

DIS-33

NAVORD REPORT 1488 (Vol. 6)

AD-243285

Bureau of Naval Weapons

FILE COPY

Return to Technical Library
Do Not Forward this copy to other
activities without authorization of
BuWeps, DIS-3.

NAVORD
1488, v. 6
Sect. 18
c. 1

HANDBOOK OF SUPERSONIC AERODYNAMICS

SECTION 18

SHOCK TUBES

Bureau of Naval Weapons
FILE COPY
Return to Technical Library
Do Not Forward this copy to other
activities without authorization of
BuWeps, DIS-3

A BUREAU OF NAVAL WEAPONS PUBLICATION

NAVORD REPORT 1488 (Vol. 6)

Bureau of Naval Weapons

FILE COPY

Return to Technical Library
Do Not Forward this copy to other
activities without authorization of
BuWeps, DIS-3.

NAVORD
1488, V 6
Sec 18
c 1

HANDBOOK OF SUPERSONIC AERODYNAMICS

Volume 6

SECTION 18

SHOCK TUBES

By

I. I. GLASS and J. GORDON/HALL

Institute of Aerophysics
University of Toronto

1488-18
1-1-59



1488-18

Produced and edited by the Aerodynamics Handbook Staff of The Johns Hopkins University Applied Physics Laboratory, Silver Spring, Maryland, under Contract NOrd 7386 with the Bureau of Ordnance, Department of the Navy. The selection and technical review of this material were functions of a Laboratory Reviewing Committee consisting of Ione D. V. Faro, Lester L. Cronvich, and Stuart L. Penn.

1488-18

For sale by the Superintendent of Documents, U.S. Government Printing Office
Washington 25, D.C. - Price \$3.75

DECEMBER 1959

3000

SERIES CONTENTS

<u>Section</u>	<u>Published</u>
Volume 1	
1 Symbols and Nomenclature	1950
2 Fundamental Equations and Formulae	1950
3 General Atmospheric Data	1950
4 Mechanics and Thermodynamics of Steady One-Dimensional Gas Flow	1950
Volume 2	
5 Compressible Flow Tables and Graphs	1953
Volume 3	
6 Two-Dimensional Airfoils	1957
7 Three-Dimensional Airfoils	1958
8 Bodies of Revolution, by D. Adamson	(in process)
Volume 4	
9 Mutual Interference Phenomena, by Cornell Aeronautical Laboratory	(In process)
10 Stability and Control Analysis Techniques, by R. S. Swanson	(In process)
11 Stability and Control Parameters, by R. S. Swanson	(In process)
12 Aeroelastic Phenomena	1952
Volume 5	
13 Viscosity Effects, by R. E. Wilson	(In process)
14 Heat Transfer Effects, by R. E. Wilson	(In process)
15 Properties of Gases	1953
16 Mechanics of Rarefied Gases, by S. A. Schaaf and L. Talbot	1959
Volume 6	
17 Ducts, Nozzles, and Diffusers, by C. L. Dailey	(In process)
18 Shock Tubes, by I. I. Glass and J. G. Hall	1959
19 Wind Tunnel Design, by A. Pope	(In process)
20 Wind Tunnel Instrumentation and Operation, by R. J. Volluz	(In process)
21 Ballistic Ranges	(No statement)

PREFACE

A preface to the entire Handbook of Supersonic Aerodynamics appears in Volume 1 and includes a brief history of the project.

The material for the Handbook has been selected on the basis of its anticipated usefulness to those who are concerned with the design and performance of supersonic vehicles. Therefore, the various sections of the Handbook present relevant data along with results of the more significant experiments and a resume of basic theory.

The Handbook is printed and distributed by the Bureau of Naval Weapons, Department of the Navy, and is being published in separate sections as material becomes available. The unpublished sections of the Handbook are now being prepared by individual authors for the Applied Physics Laboratory. The selection, editing, and technical review of Handbook material are functions of an editorial staff and a technical reviewing committee at the Applied Physics Laboratory. A list of the sections comprising the Handbook Series is presented on the facing page.

Correspondence relating to the contents of the Handbook should be directed to

Editor and Supervisor
Aerodynamics Handbook Project
Applied Physics Laboratory
The Johns Hopkins University
8621 Georgia Avenue
Silver Spring, Maryland

Communications concerning the distribution of the Handbook should be directed to

Chief, Bureau of Naval Weapons
Department of the Navy
Washington 25, D. C.

Section 18, "Shock Tubes," was prepared under a contract with G. N. Patterson, Director of the Institute of Aerophysics at the University of Toronto.

The interest of the Wind Tunnel Panel Committee of NATO-AGARD in the presentation of this material in its present form has been instrumental in obtaining financial assistance from the Defence Research Board of Canada.

Reviews of this section were prepared for Wilbur C. Nelson, Editor of the NATO-AGARD Wind Tunnel Panel, by Ira H. Abbott, Julius Lukasiewicz, Ernest H. Winkler, and Thomas D. Wilkerson and were made available to the Aerodynamics Handbook Reviewing Committee at The Johns

Hopkins University Applied Physics Laboratory. These reviews and a review by Robert N. Schwartz are gratefully acknowledged.

The pagination of Section 18 departs from the decimal system used in sections previously published. The pages are consecutively numbered on the lower margin, and the subsectional identification of text and figures has been retained on the upper margin.

As members of the Handbook staff, Anthony Strank shared with me the work of editing the manuscript for Section 18, Bruce Holland attended to many details in preparing the manuscript for publication, and Mrs. Doris Rupertus typed the reproduction copy.

Stuart L. Penn
Editor and Supervisor
Aerodynamics Handbook Project

AUTHORS' ACKNOWLEDGMENT

It is a pleasure to acknowledge the cooperation and assistance received from various shock-tube laboratories throughout the United States and the United Kingdom during the preparation of this section of the Handbook of Supersonic Aerodynamics.

The continued encouragement received from Dr. G. N. Patterson is sincerely acknowledged.

Thanks are due to E. O. Gadamer, K. Sridhar, B. W. Taylor, H. F. Waldron, and E. R. Wolff for their assistance with drawings and calculations.

The financial assistance received from The Johns Hopkins University Applied Physics Laboratory and from The Defence Research Board of Canada is gratefully acknowledged.

I. I. Glass
J. G. Hall

CONTENTS

	<u>Page</u>
List of Tables and Figures.	xiii
Symbols	xxxiii
Theory and Performance of Simple Shock Tubes, by I. I. Glass	
1. Introduction	1
1.1 General Scope of Contents.	2
References.	3
2. Performance of Simple Constant-Area Shock Tubes	5
2.1 One-Dimensional Rarefaction and Compression Waves.	5
2.1.1 Fundamental Equations	6
2.1.2 Characteristics in the (x,t)-Plane.	9
2.1.3 Rarefaction and Compression Waves in Perfect Gases.	12
2.1.4 Centred Waves in Perfect Gases.	17
2.1.5 Rarefaction and Compression Waves in Imperfect Gases.	35
2.2 Plane Shock Waves.	42
2.2.1 Shock Waves in Perfect Gases	43
2.2.2 Shock Waves in Imperfect Gases.	47
2.2.2.1 Relaxation Effects	48
2.3 The Wave System in a Simple Shock Tube	60
2.3.1 Use of the (p,u)-Plane.	60
2.3.2 Basic Equations for the Wave System and Flow Quantities in Perfect Inviscid Gases	63
2.3.3 Imperfect Gas Effects	70
2.4 Effects of One-Dimensional Wave Interactions and Finite Tube Length	81
2.4.1 Normal Reflection of a Shock Wave or a Rarefaction Wave	82
2.4.1.1 Shock Wave Reflection.	82
2.4.1.2 Rarefaction Wave Reflection	87
2.4.2 Head-on Collision of Shock Waves or Rarefaction Waves	90
2.4.2.1 Head-on Collision of Two Unequal Shock Waves	91

	<u>Page</u>
2.4.2.2 Head-on Collision of Two Unequal Rarefaction Waves	92
2.4.2.3 Head-on Collision of a Shock Wave and a Rarefaction Wave	92
2.4.3 Normal Refraction of a Shock Wave or a Rarefaction Wave at a Contact Surface	93
2.4.3.1 Refraction of a Shock Wave at a Contact Surface	93
2.4.3.2 Refraction of a Rarefaction Wave at a Contact Surface	95
2.4.4 Overtaking of Shock Waves or Rarefaction Waves.	96
2.4.4.1 The Overtaking of Two Similarly Facing Shock Waves	97
2.4.4.2 Non-Overtaking of Two Rarefaction Waves.	97
2.4.4.3 Overtaking of a Shock Wave by a Rarefaction Wave	98
2.4.4.4 Overtaking of a Rarefaction Wave by a Shock Wave	98
2.4.5 Application of One-Dimensional Wave Interactions to a Shock Tube of Finite Length	99
Supplement A: Equation of State for Thermally Imperfect Gases	103
Supplement B: Gas Imperfections at Low Pressures and High Temperatures	105
Supplement C: Relaxation Effects in Gases.	117
Supplement D: An Alternative Development of Shock-Wave Equations for Real Gases	121
Tables and Figures (See p. xiii for list)	129
References.	311
3. Observed Flows in a Constant-Area Shock Tube	317
3.1 Comparison of Idealized Theory with Experiment	317
3.1.1 Wave System Produced by Diaphragm Removal	317
3.1.2 Wave Speed Measurements	318
3.1.3 Uniform States Separated by the Contact Region.	320
3.1.4 Wave Interaction Results	322
3.2 Boundary-Layer Effects	323
3.2.1 Laminar Boundary Layer.	323
3.2.2 Transition.	331
3.2.3 Turbulent Boundary Layer	333
3.2.4 Boundary-Layer Closure.	337
3.2.5 Reflected Shock-Wave Boundary-Layer Interactions	339

	<u>Page</u>
Tables and Figures (See p. xxiii for list)	341
References.	389
Production of Strong Shock Waves, and Shock Tube Applications, Design, and Instrumentation, by J. G. Hall	
4. Production of Strong Shock Waves	393
4.1 Limitations of the Simple Shock Tube	393
4.2 Modifications to the Simple Shock Tube	396
4.2.1 Heating of Driver Gas in Constant-Area Tube	396
4.2.1.1 Electrical Heating	396
4.2.1.2 Multiple-Diaphragm Technique	400
4.2.1.3 Combustion Heating	402
4.2.2 Cross-Section Area Change	405
4.2.2.1 Monotonic Convergence at Diaphragm	405
4.2.2.2 Monotonic Convergence Along Tube	408
4.2.3 Combined Modifications and Comparisons of Theoretical Performance	409
4.3 Alternatives to the Diaphragm Shock Tube	410
4.4 Attenuation of Strong Shock Waves.	411
Tables and Figures (See p. xxvi for list)	413
References.	447
5. Applications of the Shock Tube.	451
5.1 Use as a Wind Tunnel	451
5.1.1 Shock Tube with Uniform or Constant-Area Channel	451
5.1.1.1 Use in Subsonic, Transonic, Super- sonic, and Hypersonic Research	451
5.1.1.2 Performance	453
5.1.1.3 Instrumentation	456
5.1.2 Hypersonic Shock Tunnels	457
5.1.2.1 General Characteristics	457
5.1.2.2 Non-Reflected Shock Tunnels	458
5.1.2.3 Reflected-Shock Tunnels	460
5.1.2.4 Hypersonic Gun Tunnels	462
5.2 Use in Aerophysics Research	462
5.2.1 Wave-Interaction and Non-Planar Wave Phenomena.	462
5.2.2 Condensation Phenomena.	463

	<u>Page</u>
5.2.3 Flow Transition and Boundary-Layer Phenomena	463
5.2.4 High-Temperature Gas Physics	464
5.2.4.1 Radiation Studies.	465
5.2.4.2 Ionization, Conductivity, Magneto- hydrodynamic Studies	466
5.2.4.3 Relaxation Studies	466
5.3 Use in Chemical Research	466
5.3.1 Combustion Studies.	467
5.3.2 Chemical Kinetic Studies	467
5.3.2.1 Optical Methods	468
5.3.2.2 Chemical Shock Tube	469
5.3.3 Dissociation Energies	469
5.4 Use for Calibration of Instruments	470
Figures (See p. xxix for list).	471
References.	491
 6. Shock-Tube Materials, Design, and Construction.	 499
6.1 Tube Design and Construction	499
6.1.1 Tube Length and Internal Cross-Section.	499
6.1.2 Tube Structure.	500
6.2 Diaphragms	502
6.2.1 Nonmetallic Diaphragms.	502
6.2.2 Metallic Diaphragms	503
6.2.3 Methods for Controlled Diaphragm Rupture	506
6.3 Pressure and Vacuum Technique.	506
6.4 Shock-Tube Hazards	507
Tables and Figures (See p. xxx for list)	509
References.	523
 7. Shock-Tube Flow Measurement and Instrumentation	 525
7.1 Pressure Measurement	525
7.1.1 Hydrostatic Pressure Measurement	525
7.1.2 Transient Pressure Measurement.	525
7.1.2.1 Direct Measurement	525
7.1.2.2 Indirect Measurement	531
7.2 Density Measurement	532
7.2.1 Optical Methods--Schlieren and Interferometry	532

	<u>Page</u>
7.2.1.1 Shadowgraph	533
7.2.1.2 Toepler Schlieren.	534
7.2.1.3 Wave-Speed Schlieren	537
7.2.1.4 Interferometry	537
7.2.1.5 Light Sources and Recording	541
7.2.2 Absorption Methods.	542
7.3 Heat Transfer and Temperature Measurement.	543
7.3.1 Thin-Film Resistance Thermometer	543
7.3.2 Thin-Film Thermocouple.	547
7.3.3 Calorimeter Heat-Transfer Gauge	547
7.3.4 Hot-Wire Anemometer	549
7.3.5 Interferometry.	554
7.4 Primary Shock Strength Measurement	554
7.4.1 Direct Shock-Speed Measurement.	554
7.4.1.1 Continuous Wave-Speed Methods.	554
7.4.1.2 Shock Detector Methods	555
7.4.2 Reflected-Wave Technique	560
7.5 Light-Reflectivity Measurement (Shock-Wave Transi- tion).	562
7.6 Light-Absorption Measurement	563
7.7 Electrical-Conductivity Measurement	564
7.8 Model Force Measurement	564
Tables and Figures (See p. xxxi for list)	567
References.	593
Index	601

TABLES AND FIGURES

Subsection 1.

<u>Plate</u>		<u>Page</u>
1.1.1	The wave system produced in a real shock tube from the instant the diaphragm ruptures . . .	xxxviii

Subsection 2.

<u>Table</u>		
2.1-1	Values of typical ionization energies, partition functions, and dissociation energies.	129
2.1-2	Equilibrium constant, degree of dissociation, and portion of dissociational specific heat at constant volume for O_2 at 1 atm vs translational temperature	130
2.1-3	Vibrational relaxation in gases at normal density and temperature.	130
2.1-4	Dissociational and vibrational relaxation times for O_2 vs translational temperature at a density of 1 atm	131
2.1-5	Relaxation path lengths in feet behind a normal shock wave at an altitude of 120,000 ft	131
2.1-6a	Transition through a centred Q-rarefaction wave in air; $\gamma = 1.4$	132
2.1-6b	Transition through a centred Q-compression wave in air; $\gamma = 1.4$	133
2.1-7a	Transition through a Q-centred rarefaction wave in air; $\gamma = 1.4$	134
2.1-7b	Transition through a Q-compression wave in air; $\gamma = 1.4$	135
2.1-8	List of equations	136
<u>Figure</u>		
2.1-1	Pressure waves generated by the motion of a piston	143
2.1-2	Velocity distribution in ducts of constant and varying cross sections	144
2.1-3	Degrees of freedom for different molecules.	145

<u>Figure</u>	<u>Page</u>	
2.1-4	Variation of vibrational specific heat as a function of the reduced gas translational temperature	146
2.1-5a	Variation of degree of dissociation with non-dimensional temperature for a dissociating gas	147
2.1-5b	Variation of the first degree ionization with nondimensional temperature for argon, helium, and hydrogen.	148
2.1-6	Variation of specific heat due to dissociation for oxygen with translational temperature at 1 atm	149
2.1-7	Specific heat of ionization for atomic hydrogen with translational temperature; $V_i = 13.5$ volts	150
2.1-8a	Adjustment of translational temperature and internal temperature during a slow and fast compression or expansion	151
2.1-8b	Relaxation time data for air referred to a density of atmosphere	152
2.1-9	Riemann variables in the (x,t) -plane for a steady flow through a duct of constant cross section; $\gamma = 1.4$	153
2.1-10	Riemann variables in the (x,t) -plane for a rarefaction type of pressure wave generated in a quiescent gas in a duct of constant cross section; $\gamma = 1.4$	153
2.1-11	A compression front moving to the right in a duct of constant cross section; $\gamma = 1.4$	154
2.1-12	Collision of a Q-rarefaction wave with a P-compression wave	154
2.1-13	Wave system produced by a piston accelerated from rest to a uniform velocity	155
2.1-14	Wave system produced by a piston instantaneously accelerated from rest to a uniform velocity	156
2.1-15	The generation of rarefaction waves and compression waves by a piston	157
2.1-16	Q-centred rarefaction waves in the $(a_4 t, x)$ -plane; $\gamma = 1.4$	158
2.1-17	Variation of the particle velocity through a centred Q-rarefaction wave; $\gamma = 1.4$	159
2.1-18	Variation of the sound speed ratio through a Q-centred rarefaction wave; $\gamma = 1.4$	160

<u>Figure</u>		<u>Page</u>
2.1-19	Variation of the temperature ratio through a Q-centred rarefaction wave; $\gamma = 1.4$	161
2.1-20	Variation of the density ratio through a Q-centred rarefaction wave; $\gamma = 1.4$	162
2.1-21	Variation of the pressure ratio through a Q-centred rarefaction wave; $\gamma = 1.4$	163
2.1-22	Variation of the Mach number through a Q-centred rarefaction wave; $\gamma = 1.4$	164
2.1-23	Variation of the mass flow ratio through a Q-centred rarefaction wave; $\gamma = 1.4$	165
2.1-24	Variation of the total temperature ratio through a Q-centred rarefaction wave; $\gamma = 1.4$	166
2.1-25	Variation of the isentropic pressure ratio through a Q-centred rarefaction wave; $\gamma = 1.4$	167
2.1-26	Variation of the pitot pressure ratio through a Q-centred rarefaction wave; $\gamma = 1.4$	168
2.1-27	Variation of the Reynolds number per foot and the dynamic pressure through a Q-centred rarefaction wave; $\gamma = 1.4$	169
2.1-28	Variation of the Riemann invariants P and Q through a Q-centred rarefaction wave; $\gamma = 1.4$	170
2.1-29	Flow properties of a one-dimensional, isentropic, unsteady rarefaction wave in air expanded from $p_4 = 100$ atm and $T_4 = 300^\circ\text{K}$	171
2.1-30	Flow properties of a one-dimensional, isentropic, unsteady rarefaction wave in air expanded from $p_4 = 100$ atm and $T_4 = 300^\circ\text{K}$	172
2.1-31	Rarefaction wave and compression wave with relaxation effects.	173
2.1-32	The flow about a double-wedge model in a shock tube.	174
 <u>Table</u>		
2.2-1	Initial conditions.	175
2.2-2	Enthalpy parameter; $\beta = \frac{h}{p/\rho} = 1 + \frac{e}{p/\rho}$	176
2.2-3	Number of moles per mole of cold air; $Z = PV/RT$	177
2.2-4	Entropy of dry air in chemical equilibrium, S/R per mole of cold air.	178

<u>Figure</u>	<u>Page</u>
2.2-1 Shock wave as a discontinuity	179
2.2-2 Schematic transition profiles through a weak shock front with constant specific heats.	180
2.2-3 Shock transitions in a gas with relaxation effects	181
2.2-4 Flow quantities behind a normal shock wave in CO ₂ with vibrational excitation only.	182
2.2-5a Representation of transition through a shock front with one inert (vibration) degree of freedom excited	185
2.2-5b Transition through a shock front in oxygen at M ₁ = 20 showing the approach to equilibrium of the active and inert degrees of freedom	186
2.2-6a Variation of enthalpy with temperature and pressure for a diatomic gas, oxygen	187
2.2-6b Schematic enlargement of the variation of h with T for a diatomic gas.	188
2.2-6c Dimensionless enthalpy vs temperature for a dissociating diatomic gas	189
2.2-7 Normal shock wave parameters in oxygen.	190
2.2-8a Normal shock static temperature ratio for air in dissociation equilibrium.	192
2.2-8b Normal shock density ratio for air in dissociation equilibrium	193
2.2-8c Normal shock static pressure ratio for air in dissociation equilibrium.	194
2.2-8d Normal shock pressure, temperature, and density ratios for air in dissociation equilibrium	195
2.2-9a Pressure ratio across moving normal shock vs shock velocity, equilibrium air	196
2.2-9b Density ratio across moving normal shock vs shock velocity, equilibrium air	197
2.2-9c Temperature ratio across moving normal shock vs shock velocity, equilibrium air	198
2.2-10a Velocity ratio (u_2/a_1) across moving normal shock vs shock velocity, equilibrium air	199
2.2-10b Compressibility across moving normal shock vs shock velocity, equilibrium air	200

<u>Figure</u>		<u>Page</u>
2.2-10c	Enthalpy ratio across moving normal shock vs shock velocity, equilibrium air	201
2.2-11a	Variation of the sound speed ratio with the shock Mach number in air.	202
2.2-11b	Variation of flow Mach number with the moving shock Mach number in air.	203
2.2-12	Variation of the density ratio, temperature ratio, and shock Mach number with the pressure ratio across the shock wave for various initial densities in air	204
2.2-13	Isentropic exponent γ^* for air in equilibrium	205
2.2-14	Variation of velocity ratio across a normal shock wave with altitude	206
2.2-15	Temperature behind a normal shock wave in air	207
2.2-16	Entropy increase across a shock wave in air	208
2.2-17a	Variation of the temperature ratio across a normal shock wave in argon	209
2.2-17b	Variation of the density ratio across a normal shock wave in argon	210
2.2-17c	Variation of the pressure ratio across a normal shock wave in argon	211
2.2-17d	Variation of the particle velocity ratio behind a moving normal shock wave in argon	212
2.2-17e	Variation of the degree of ionization behind a normal shock wave in argon	213
2.2-17f	Variation of the degree of ionization with temperature and pressure in argon	214
2.2-18a	Variation of particle velocity with shock wave velocity in argon	215
2.2-18b	Variation of density ratio with shock velocity in argon.	216
2.2-18c	Variation of temperature with shock velocity in argon	217
2.2-18d	Variation of pressure ratio with shock velocity in argon.	218
2.2-18e	Variation of first degree of ionization with shock velocity in argon	219

<u>Figure</u>		<u>Page</u>
2.2-18f	Variation of pressure ratio with density ratio (Hugoniot curve) in argon	220
 <u>Table</u>		
2.3-1	Physical properties of gases.	221
2.3-2	Flow quantities for strong shock waves in a perfect gas	222
2.3-3	Reynolds number per foot in states (2) and (3); $T_1 = T_4 = 288^\circ\text{K}$	223
2.3-4	Flow quantities in uniform states (2) and (3) in a shock tube	224
 <u>Figure</u>		
2.3-1	Locus of all states (2) that may be connected with a given state (1) by a forward or backward facing shock wave.	225
2.3-2	Locus of all states (2) that may be connected with a known state (1) by a forward or backward facing rarefaction wave	225
2.3-3	Locus of all the states (2) that may be reached from a given state (1) on the left by forward or backward facing waves	226
2.3-4	Locus of all the states (2) that may be reached from a given state (1) on the right by forward or backward facing waves	226
2.3-5	Initial conditions in a shock tube	227
2.3-6	The shock tube problem in the (p,u)-plane	227
2.3-7	Possible wave systems in a shock tube following the rupturing of the diaphragm.	227
2.3-8	Diagram of the (x,t)-plane of the ideal wave system produced by bursting a diaphragm in a shock tube	228
2.3-9	Variation of the shock pressure ratio with the diaphragm pressure ratio and the internal energy ratio across the diaphragm; case air/air	229
2.3-10	Variation of the shock pressure ratio with the diaphragm pressure ratio for the different gas combinations at the same temperature	230
2.3-11	Variation of Mach number with pressure ratio.	231
2.3-12	Variation of Mach number in state (3) with the diaphragm pressure ratio for different energy ratios across the diaphragm	232

<u>Figure</u>		<u>Page</u>
2.3-13	Variation of Mach number in state (3) with diaphragm pressure ratio and internal energy ratio across the diaphragm at $T_{14} = 1$	233
2.3-14	Variation of Mach number in state (2) with the diaphragm pressure ratio for different internal energy ratios across the diaphragm.	234
2.3-15	Variation of the initial shock pressure ratio with the diaphragm pressure ratio; case air/air	235
2.3-16	Variation of the initial shock-wave pressure ratio with the diaphragm pressure ratio; case He/air, $\gamma_4 = 1.665$, $\gamma_1 = 1.402$, $T_4 = T_1$	236
2.3-17	Variation of initial shock wave velocity, particle velocity, and rarefaction front velocities with the initial shock pressure ratio; case air/air.	237
2.3-18	Variation of initial shock wave velocity, particle velocity, and rarefaction front velocities with the pressure ratio across the diaphragm; case air/air	238
2.3-19	Variation of flow parameters in state (2) with the shock pressure ratio; case air/air ($E_{14} = 1$)	239
2.3-20	Variation of flow parameters in state (3) with the shock pressure ratio; case air/air ($E_{14} = 1$)	240
2.3-21	Variation of Mach number and velocity of sound ratios with the initial shock-wave pressure ratio; case He/air, $\gamma_4 = 1.665$, $\gamma_1 = 1.402$, $T_4 = T_1$	241
2.3-22	Variation of temperature ratios and density ratios with the shock wave pressure ratio; case He/air, $\gamma_4 = 1.665$, $\gamma_1 = 1.402$, $T_1 = T_4$	242
2.3-23	Variation of flow quantities behind a shock wave in air; $\gamma = 1.4$	243
2.3-24	Variation of Reynolds number per foot in the uniform states (2) and (3) with the shock pressure ratio; case air/air	244
2.3-25	Total temperature variation in uniform states (2) and (3) with shock pressure ratio; case air/air ($E_{14} = 1$)	245
2.3-26	Pitot pressure variation in uniform states (2) and (3) with shock pressure ratio; case air/air ($E_{14} = 1$)	246
2.3-27	Variation of mass flow ratios in uniform states (2) and (3) with shock pressure ratio; case air/air ($E_{14} = 1$)	247

<u>Figure</u>		<u>Page</u>
2.3-28	Variation of dynamic pressures in uniform states (2) and (3) with shock pressure ratio; case air/air ($E_{14} = 1$)	248
2.3-29a	Variation of flow properties p , ρ , and T in a shock tube	249
2.3-29b	Variation of flow properties Re/ft , M , and u in a shock tube	250
2.3-29c	Variation of flow properties $\frac{\Delta S}{C_v}$, $C_p T_o$, and $\frac{2a_4}{\gamma-1}$	251
2.3-30	Variation of shock wave Mach number with diaphragm pressure ratio for constant and variable specific heats; case air/air (vibrational excitation only)	252
2.3-31	Pressure ratio for standing normal shock vs shock velocity, equilibrium air	253
2.3-32	Density ratio for standing normal shock vs shock velocity, equilibrium air	254
2.3-33	Compressibility for standing normal shock vs shock velocity, equilibrium air	255
2.3-34	Temperature ratio for standing normal shock vs shock velocity, equilibrium air.	256
2.3-35	Enthalpy ratio for standing normal shock vs shock velocity, equilibrium air	257
2.3-36	Velocity ratio (u_s/a_1) across standing normal bow shock vs shock velocity, equilibrium air	258
2.3-37	Pressure ratio at stagnation point vs shock velocity, equilibrium air	259
2.3-38	Density ratio at stagnation point vs shock velocity, equilibrium air	260
2.3-39	Compressibility at stagnation point vs shock velocity, equilibrium air	261
2.3-40	Temperature ratio at stagnation point vs shock velocity, equilibrium air	262
2.3-41	Enthalpy ratio at stagnation point vs shock velocity, equilibrium air	263
2.4-1	Normal reflection of a shock wave and rarefaction wave	264
2.4-2	Variations of the flow parameters in air behind a normal reflected shock wave with the incident shock wave Mach number	265

<u>Figure</u>		<u>Page</u>
2.4-3	Pressure ratio for reflected normal shock vs shock velocity, equilibrium air	266
2.4-4	Density ratio for reflected normal shock vs shock velocity, equilibrium air	267
2.4-5	Compressibility for reflected normal shock vs shock velocity, equilibrium air	268
2.4-6	Temperature ratio for reflected normal shock vs shock velocity, equilibrium air	269
2.4-7	Enthalpy ratio for reflected normal shock vs shock velocity, equilibrium air	270
2.4-8	Velocity ratio (w_2/a_1) for reflected normal shock vs shock velocity, equilibrium air	271
2.4-9	Variation of the temperature ratio across a reflected shock wave with the incident shock Mach number in argon	272
2.4-10	Variation of the pressure ratio across a normal reflected shock wave with the incident shock Mach number in argon	273
2.4-11	Variation of the density ratio across a normal reflected shock wave with the incident shock Mach number in argon	274
2.4-12	Variation of the ratio of reflected to incident shock speed with the initial shock Mach number	275
2.4-13	Variation of the degree of ionization behind a reflected shock wave with the incident shock Mach number in argon	276
2.4-14	Variation of the flow parameters in state (6) with the pressure ratio across the incident rarefaction wave	277
2.4-15	Variation of time required for formation of steady-state region (6) with diaphragm pressure ratio	278
2.4-16	Head-on collision of two unequal shock waves in the (u,p)-plane	279
2.4-17	Head-on collision of two unequal shock waves in the (x,t)-plane	280
2.4-18	Head-on collision of two unequal rarefaction waves in the (u,p)-plane	281
2.4-19	Head-on collision of two unequal rarefaction waves in the (x,t)-plane	282
2.4-20	Head-on collision of a shock wave and a rarefaction wave in the (u,p)-plane	283

<u>Figure</u>		<u>Page</u>
2.4-21	Head-on collision of a shock wave and a rarefaction wave in the (x,t)-plane	284
2.4-22	Normal refraction of a shock wave at a contact surface in the (u,p)-plane	285
2.4-23	Interaction of a shock wave and a contact surface in the shock tube after the diaphragm is broken in the (x,t)-plane	286
2.4-24	Interaction of a shock wave and a stationary contact surface in the (x,t)-plane	287
2.4-25	Normal refraction of a rarefaction wave at a contact surface in the (u,p)-plane	288
2.4-26	Interaction of a rarefaction wave and a contact surface in the shock tube after the diaphragm is broken in the (x,t)-plane	289
2.4-27	Interaction of a rarefaction wave and a stationary contact surface in the (x,t)-plane	290
2.4-28	Overtaking of two similarly facing shock waves in the (u,p)-plane	291
2.4-29	Overtaking of two similarly facing shock waves in the (x,t)-plane	292
2.4-30	Overtaking of two similarly facing rarefaction waves in the (x,t) and (u,p)-planes	293
2.4-31	Overtaking of a shock wave by a weak rarefaction wave in the (u,p)-plane	294
2.4-32	Overtaking of a shock wave by a weak rarefaction wave in the (x,t)-plane	295
2.4-33	Overtaking of a shock wave by a strong rarefaction wave in the (u,p)-plane	296
2.4-34	Overtaking of a shock wave by a strong rarefaction wave in the (x,t)-plane	297
2.4-35	Overtaking of a rarefaction wave by a weak shock wave in the (u,p)-plane	298
2.4-36	Overtaking of a rarefaction wave by a weak shock wave in the (x,t)-plane	299
2.4-37	Overtaking of a rarefaction wave by a strong shock wave in the (u,p)-plane	300
2.4-38	Overtaking of a rarefaction wave by a strong shock wave in the (x,t)-plane	301
2.4-39	Points in the (X, ζ)-plane where the head of the reflected rarefaction wave overtakes the tail of the incident rarefaction wave, the contact surface, and the shock wave	302

<u>Figure</u>		<u>Page</u>
2.4-40	Variation of X_3 , X_c , and X_s with the pressure ratio across the diaphragm for air/air	303
2.4-41	Variation of X_3 , X_c , and X_s with the pressure ratio across the diaphragm for He/air	304
2.4-42	Variation of τ_3 , τ_c , and τ_s with the pressure ratio across the diaphragm for air/air	305
2.4-43	Variation of τ_3 , τ_c , and τ_s with the pressure ratio across the diaphragm for He/air	306
2.4-44	Points of maximum flow duration X_3 and X_c for regions (3) and (2)	307
2.4-45	Variation of X_5 and X_2 with the pressure ratio across the diaphragm for different gas combinations	308
2.4-46	Testing time as a function of shock Mach number and initial pressure.	309

Subsection 3.

<u>Table</u>		
3.1-1	Speed of sound in gases	341
3.1-2	Deviations in state (3) behind the rarefaction wave generated in a shock tube	342
3.1-3	Imperfect gas properties behind an incident and reflected shock wave in nitrogen and carbon monoxide.	343

<u>Figure</u>		
3.1-1a	Typical variation of shock Mach number with distance in a 3 x 3-in. shock tube	344
3.1-1b	Distance attenuation of shock waves as a function of shock strength; $P_{21} = 5.15$ to 13.1	345
3.1-2	Velocity attenuation of shock waves in 24-in. diameter tube	346
3.1-3a	Representation of the total attenuation in a shock tube	347
3.1-3b	Effect of initial pressure on attenuation with hydrogen as driver gas	347

<u>Figure</u>		<u>Page</u>
3.1-3c	Comparison of the effects of hydrogen and helium driver gases on shock-wave attenuation	348
3.1-4	Schematic growth of the boundary layer in a shock tube	349
3.1-5	Representation of the velocity of the front of the contact zone in a shock tube	350
3.1-6	Typical variation of the velocity of the contact region front with distance in a 3 x 3-in. shock tube	351
3.1-7	Theoretical and experimental variation of rarefaction wave pressure ratio with diaphragm pressure ratio	352
3.1-8	Theoretical and experimental variation of rarefaction wave stagnation temperature ratio with diaphragm pressure ratio	353
3.1-9	Theoretical and experimental variation of rarefaction wave mass flow ratio with diaphragm pressure ratio	354
3.1-10	Variation of density ratio across incident rarefaction wave with diaphragm pressure ratio	355
3.1-11	Variation of the Riemann invariants with diaphragm pressure ratio	356
3.1-12a	Mass flow distribution derived from density measurements in a 1-3/8-in. diameter shock tube.	357
3.1-12b	Particle velocity distribution derived from density measurements in a 1-3/8-in. diameter shock tube	358
3.1-13	Density as a function of time in a 1-3/8-in. diameter shock tube	359
3.1-14	Pressure as a function of time in a 1-3/8-in. diameter shock tube ($x = 3m$)	360
3.1-15	Temperature derived from pressure and density measurements as a function of time in a 1-3/8-in. diameter shock tube ($x = 3m$)	361
3.1-16a	Variation of Mach number with diaphragm pressure ratio; case air/air.	362
3.1-16b	Variation of Mach number with diaphragm pressure ratio; case air/air.	363
3.1-17a	Comparison with theory of flow Mach numbers in air, obtained from the Mach angle caused by a small disturbance on the shock tube wall	364

<u>Figure</u>	<u>Page</u>
3.1-17b Comparison with theory of flow Mach numbers in air, obtained from measurements of the flat plate Mach angle	365
3.1-18 Experimental results for the normal reflection of a shock wave	366
3.1-19 Variation of the transmitted wave speed with the incident wave speed for the head-on collision of two shock waves in air	367
3.1-20 Head-on collision of shock and rarefaction waves; rarefaction strength = 0.500	368
3.1-21 Variation of the transmitted shock pressure ratio for the refraction of a shock wave at a contact surface; case air argon	369
3.1-22 Variation of the transmitted shock Mach number with the pressure ratio across the incident shock wave; case air He	370
3.1-23 Double refraction at a layer of helium showing variation of the emergent shock Mach number with incident wave Mach number; case air He air	371
3.1-24 Double refraction at a layer of helium showing variation of the emergent shock Mach number and the overtaken shock-amplified Mach number with incident shock Mach number; case air He air.	372
3.1-25 Variation of the reflected wave speed, the refracted wave speed, and the overtaken shock-amplified wave speed with the incident wave speed; case He/air	373
3.1-26 Variation of pressure ratio across the rarefaction waves after interaction with the pressure ratio across the incident rarefaction wave; case air argon	374
3.1-27 Variation of pressure ratio across the rarefaction waves after interaction with the pressure ratio across the incident rarefaction wave; case air He	375
3.1-28 Hot-wire anemometer and piezo pressure gauge traces for the refraction of a rarefaction wave at a contact front	376
3.2-1 Coordinate axes for a moving and stationary shock or expansion wave in a shock tube.	377
3.2-2 Limiting boundary layer profiles in a shock tube in air; $\gamma = 1.4$	378
3.2-3 Velocity and temperature profiles in the boundary layer behind a moving shock wave	379

<u>Figure</u>		<u>Page</u>
3.2-4	Boundary layer velocity profiles for a moving wall in the range of wall to free stream velocity ratios of $0 \leq v_1/v_2 \leq 6$	380
3.2-5	Comparison of experimental (interferometric) and theoretical laminar boundary layer velocity profiles.	381
3.2-6	Illustration of the measurement of boundary layer transition with a thin-film heat gauge	382
3.2-7	Theoretical and experimental temperature profiles in a turbulent boundary layer behind a plane shock wave in a 2 x 7-in. shock tube; case He/air	383
3.2-8	Theoretical and experimental velocity profiles in a turbulent boundary layer behind a plane shock wave in a 2 x 7-in. shock tube	384
3.2-9	Theoretical and experimental variation of the boundary layer thickness, displacement thickness, and momentum thickness with the distance behind the shock wave and the Reynolds number in a 2 x 7-in. shock tube	385
3.2-10	Theoretical and experimental variation of the boundary layer thickness, displacement thickness, and momentum thickness with the distance behind the shock wave and the Reynolds number in a 2 x 7-in. shock tube	386
3.2-11	Variation of the local skin friction coefficient with Reynolds number for turbulent boundary layer behind a plane shock wave	387
3.2-12	Variation of the boundary layer growth behind a moving plane shock wave	388

Subsection 4.

<u>Table</u>		
4.1-1	Maximum shock Mach number attainable with cold driver in simple shock tube at infinite diaphragm pressure ratio	413

<u>Figure</u>		
4.1-1	Shock Mach number vs diaphragm pressure ratio for a simple constant-area shock tube	414
4.1-2	Theoretical perfect-gas performance of ideal constant-area shock tube; shock Mach number vs diaphragm pressure ratio for various diaphragm sound speed ratios; $\gamma_4 = 1.2$, $\gamma_1 = 1.4$	415

<u>Figure</u>		<u>Page</u>
4.1-3	Theoretical perfect-gas performance of ideal constant-area shock tube; shock Mach number vs diaphragm pressure ratio for various diaphragm sound speed ratios; $\gamma_4 = 1.2$, $\gamma_1 = 1.667$	416
4.1-4	Theoretical perfect-gas performance of ideal constant-area shock tube; shock Mach number vs diaphragm pressure ratio for various diaphragm sound speed ratios; $\gamma_4 = 1.4$, $\gamma_1 = 1.4$	417
4.1-5	Theoretical perfect-gas performance of ideal constant-area shock tube; shock Mach number vs diaphragm pressure ratio for various diaphragm sound speed ratios; $\gamma_4 = 1.4$, $\gamma_1 = 1.667$	418
4.1-6	Theoretical perfect-gas performance of ideal constant-area shock tube; shock Mach number vs diaphragm pressure ratio for various diaphragm sound speed ratios; $\gamma_4 = 1.667$, $\gamma_1 = 1.4$	419
4.1-7	Theoretical perfect-gas performance of ideal constant-area shock tube; shock Mach number vs diaphragm pressure ratio for various diaphragm sound speed ratios; $\gamma_4 = 1.667$, $\gamma_1 = 1.667$	420
4.1-8	Theory and experiment for simple constant-area shock tube; shock Mach number vs diaphragm pressure ratio	421
4.1-9	Comparison of theory and experiment for simple shock tube; maximum shock Mach number (about 60 diameters from diaphragm) vs diaphragm pressure ratio	422
4.2-1	Pulsed discharge tubes	423
4.2-2	Electric discharge drive; shock Mach number vs energy transferred to unit volume of driver gas.	424
4.2-3	Initial flow in double-diaphragm constant-area tube; unsteady expansion method	425
4.2-4	Initial flow in double-diaphragm constant-area tube; reflected shock method	426
4.2-5	Comparison of reflected shock and unsteady expansion methods for double-diaphragm constant-area tube; second shock Mach number vs pressure ratio across second diaphragm	427

<u>Figure</u>	<u>Page</u>
4.2-6 Double-diaphragm constant-area tube performance for helium-air combinations; reflected shock method; second shock Mach number vs pressure ratio across second diaphragm	428
4.2-7 Multiple-diaphragm constant-area tube performance; reflected shock method; maximum final shock Mach number vs number of diaphragms	429
4.2-8 Theoretical calculation of adiabatic constant-volume combustion assuming no dissociation	430
4.2-9 Theoretical shock Mach number in constant-area shock tube vs peak diaphragm pressure ratio after combustion (adiabatic constant-volume combustion, various driving mixtures)	431
4.2-10 Comparison of theory and experiment for O ₂ -H ₂ -He combustion drive; shock Mach number vs peak diaphragm pressure ratio after combustion	432
4.2-11 Idealized flow with monotonic area reduction at diaphragm	433
4.2-12 Parameter for monotonic-convergent shock tube vs isentropic index for driver gas	434
4.2-13 General shock-tube performance curves	435
4.2-14 Ratio of diaphragm pressure ratio for constant-area tube to diaphragm pressure ratio for convergent tube vs shock Mach number in driven N ₂	436
4.2-15 Idealized wave diagrams for impingement of incident shock on monotonic area reduction.	437
4.2-16 Double-diaphragm technique with area reduction.	438
4.2-17 Calculated performance of double-diaphragm convergent tube with argon buffer and large contraction ratio; pressure ratio across upstream diaphragm vs shock Mach number and combustion drive at various peak over-all pressure ratios	439
4.2-18 Comparison of various modifications to simple shock tube. Theoretical shock Mach number in driven air vs peak over-all pressure ratio after combustion; perfect gases assumed.	440
4.3-1 Electric discharge shock tube with magnetic push	441
4.3-2 Solid-explosive and piston drives.	442
4.4-1 Experimental shock-wave attenuation in air with distance X from diaphragm for cold hydrogen drive; constant-area shock tube, 3.75-in. I.D.	443

<u>Figure</u>		<u>Page</u>
4.4-2	Experimental shock-wave attenuation in air with distance X from diaphragm for cold helium drive and for cold helium and hydrogen; constant-area shock tube, 3.75-in. I.D.	444
4.4-3	Experimental wall pressure results with air in low-pressure channel for cold hydrogen drive; constant-area shock tube, 3.75-in. I.D.	445
Subsection 5.		
5.1-1	Range of shock Mach numbers in air and pressure ahead of shock producing hypersonic flight stagnation enthalpy and stagnation density in region (2) of uniform channel shock tube	471
5.1-2	Estimated vibration and dissociation relaxation distance for air set into motion by shock wave	472
5.1-3	Distance-time diagram showing minimum chamber and channel lengths for maximum hot flow duration at station X_T	473
5.1-4a	$L_1/\Delta t$ for air as a function of M_S (1 to 4)	474
5.1-4b	$L_1/\Delta t$ for air as a function of M_S (4 to 18)	475
5.1-5a	L_1/X_T for air vs shock Mach number (1 to 4)	476
5.1-5b	L_1/X_T for air vs shock Mach number (4 to 18)	477
5.1-6	L_1/L_4 for constant-area shock tube with various drives and air as driven gas as a function of shock Mach number (1 to 4)	478
5.1-7	L_1/L_4 for constant-area shock tube with various drives and air as driver gas as a function of shock Mach number (4 to 18)	479
5.1-8	Measured shock detachment distance as a function of time following passage of primary shock wave for two-dimensional 30-degree wedges	480
5.1-9	Measured shock detachment distance as a function of time following passage of primary shock wave for two-dimensional 45-degree wedges	481
5.1-10	Wave diagram of non-reflected shock tunnel	482
5.1-11	Cornell Aeronautical Laboratory 11 x 15-in. hypersonic shock tunnel	483
5.1-12	Primary shock Mach number required to produce perfect-gas flight stagnation temperature for flight Mach number; $\gamma = 1.4$	484

<u>Figure</u>		<u>Page</u>
5.1-13	Reynolds number performance of non-reflected shock tunnel for stagnation temperatures equal to those in flight at M_f ; perfect gas assumed . . .	485
5.1-14	Nominal testing times of hypersonic shock tunnel modifications based on equilibrium real-gas calculations; stagnation temperatures equal to those in flight at M_f	486
5.1-15	Wave diagram for reflected shock tunnel . . .	487
5.1-16	Wave diagrams illustrating variations of the tailored-interface modification of the shock tunnel which give increased testing times . . .	488
5.1-17	Reynolds number performance of reflected shock tunnel for stagnation temperatures equal to those in flight at M_f ; perfect gas assumed . . .	489
5.3-1	Chemical shock tube for producing a single high-temperature pulse	490

Subsection 6.

<u>Table</u>		
6.1-1	Survey of unclassified shock tubes in the U.S.A. and Canada up to 1956	509
6.2-1	Nonmetallic diaphragm materials	512

<u>Figure</u>		
6.1-1	Example of square cross-section construction; 3 x 3-in. wave interaction tube	513
6.1-2	Square cross section encased in circular pipe; 2 x 2-in. combustion driven tube.	514
6.2-1	Clamping arrangement for diaphragm tests	515
6.2-2	Diaphragm bursting test results; bursting pressure difference in psi vs thickness-diameter ratio	516
6.2-3	Examples of diaphragm petalling; scribed cold-rolled mild steel	517
6.2-4	Examples of diaphragm petalling; cold-burst annealed copper	518
6.2-5	Free-piston clamping arrangement for diaphragm tests	519
6.2-6	Spring-driven, solenoid-actuated diaphragm breaker	520

<u>Figure</u>		<u>Page</u>
6.2-7	Diaphragm-piercing plungers driven by shock waves generated in the auxiliary shock tube. . . .	521
6.2-8	Electrical method of diaphragm rupture	522
Subsection 7.		
<u>Table</u>		
7.1-1	Transducer diaphragm performance parameters. . . .	567
7.2-1	Values of Gladstone-Dale constant K.	568
<u>Figure</u>		
7.1-1	Two-pile crystal element	569
7.1-2	Equivalent circuit of piezo transducer	569
7.1-3	Response to shock wave (ringing)	570
7.2-1	Refraction of light ray.	571
7.2-2	Component angular deflections α_x and α_y	571
7.2-3	Direct shadowgraph method	572
7.2-4	Toepler schlieren system	572
7.2-5	Offset schlieren system.	573
7.2-6	Wave-speed schlieren system.	574
7.2-7	Shock trace on wave-speed record	575
7.2-8	Mach-Zehnder interferometer.	575
7.2-9	Fringe shift referred to uniform flow region	576
7.2-10	Low-inductance spark gap	576
7.2-11	Transmission-line spark gap.	577
7.3-1	Thin-film surface thermometer	578
7.3-2	Per cent difference between actual surface temperature and that for zero film thickness; constant heat transfer rate	579
7.3-3	Response of thin-film thermometer mounted flush in shock-tube wall to passage of shock wave	580
7.3-4	Hot-wire anemometer.	580
7.3-5	Calculated heat loss from calorimeter gauge element (thickness δ_m) to infinite pyrex backing for various element materials; constant rate of heat input to element and perfect contact with pyrex . .	581

<u>Figure</u>		<u>Page</u>
7.4-1	Pressure contactor.	582
7.4-2	Schlieren light screen, using one lens.	582
7.4-3	Reflection light screen	583
7.4-4	Use of lucite guide enabling one photocoell to serve three stations.	583
7.4-5	Glow discharge probe	583
7.4-6	Ionization probe	584
7.4-7	Shaped ionization probe	584
7.4-8	Multiple ionization probe unit.	585
7.4-9	Film-resistance thermometer as shock detector.	585
7.4-10	\bar{U} function.	586
7.4-11	Hot-wire shock detector	586
7.4-12	Hot-wire response to primary shock wave in air.	587
7.4-13	Positive-ion beam trigger	587
7.4-14	Cylindrical-wave reflection method of shock strength measurement; state (2) subsonic.	588
7.4-15	Normal shock reflection method of shock strength measurement	588
7.4-16	Cylindrical-wave reflection method of shock strength measurement; state (2) supersonic	589
7.5-1	Light-reflectivity measurement.	589
7.7-1	Probe technique for measuring gas conductivity.	590
7.7-2	Magnetic method for measuring gas conductivity.	590
7.8-1	Internal balance system of shock-tube cone- cylinder model	591
7.8-2	Balance system with cone-cylinder shell removed	592

SYMBOLS

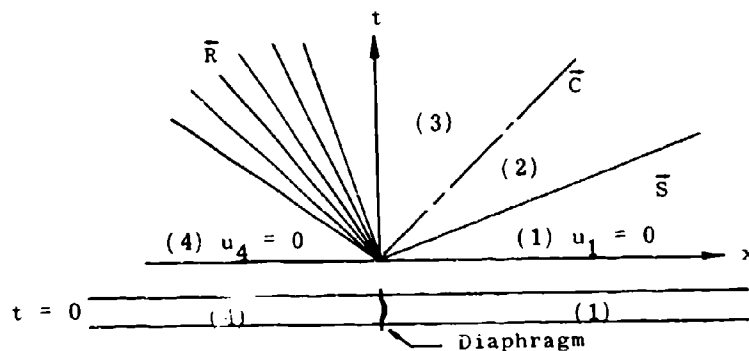
a	sound speed
A	area
Å	Angstrom unit: 10^{-7} mm
B	mass flow; light source brightness
C_p	heat capacity per unit mass at constant pressure
C_v	heat capacity per unit mass at constant volume
C_f	skin friction coefficient: $\tau/(1/2 \rho u^2)$
d	length
D	hydraulic diameter: $(\frac{4 \times \text{area}}{\text{perimeter}})$; mirror diameter
e	internal energy per unit mass
E	voltage; illumination; energy
f	resultant body force per unit mass; focal length
g	see Eq. (2), Subsec. 4.2.2.1
h	heat transfer coefficient, enthalpy per unit mass; Planck's constant
I	electric current
k	heat conduction coefficient; Boltzmann's constant
K	equilibrium constant; Knudsen number; Gladstone-Dale constant
l_d	heat of dissociation per unit mass
l_i	heat of ionization per unit mass
L	length
m	mass; molecular weight; magnification
M	Mach number
M_s	shock wave Mach number referred to sound speed of stationary gas ahead of shock: $\frac{w}{a_1}$
n	index of refraction; number of diaphragms

N	dimensionless characteristic slope: $\frac{x}{a_4 t}$
p	static pressure
p_0	stagnation pressure
p'_0	pitot pressure
P	bursting pressure difference across diaphragm; also Riemann variable: $\frac{2}{\gamma - 1} a + u$
Pr	Prandtl number: $\frac{\mu C_p}{k}$
q	rate of heat transfer/unit area
Q	Riemann variable: $\frac{2}{\gamma - 1} a - u$
R	universal gas constant
R	gas constant per unit molecular mass: $\frac{R}{m}$; electrical resistance; radius of curvature
S	specific entropy; area; sensitivity
t	time
T	absolute temperature
T_0	stagnation temperature
u	velocity along x-axis
v	relative velocity; specific volume: $(\frac{1}{\rho})$; volume of driver section
w	shock wave velocity
x	distance; degree of ionization
X	dimensionless distance: $\frac{x}{L}$
y	distance
z	distance
Z	compressibility factor: $\frac{p}{\rho RT}$
α	temperature coefficient of resistivity; degree of dissociation; angle
β	enthalpy parameter: $\frac{h}{p/\rho}$
γ	specific heat ratio: $\frac{C_p}{C_v}$

γ	isentropic index: $\rho a^2/p$
δ	boundary-layer thickness; film thickness; resistance element thickness
η	efficiency of energy transfer
θ	angle; characteristic absolute temperature
θ_d	characteristic temperature for dissociation: $\frac{l_d}{R}$
θ_i	characteristic temperature for ionization: $\frac{l_i}{R}$
θ_v	characteristic temperature for vibration: $\frac{h\nu}{k}$
λ	wavelength, mean free path
μ	coefficient of viscosity; Mach angle
ν	frequency
ξ	distance (fringe shift)
ρ	mass density
τ	dimensionless time: $\frac{a_4 t}{L}$; wall shearing stress: $\frac{C_f \rho u^2}{2}$; relaxation time

Subscripts

- i denotes initial condition
- 1, 2, 3, etc. denote a quasi-steady uniform state of the basic shock-tube flow shown below or of a particular flow described in the text



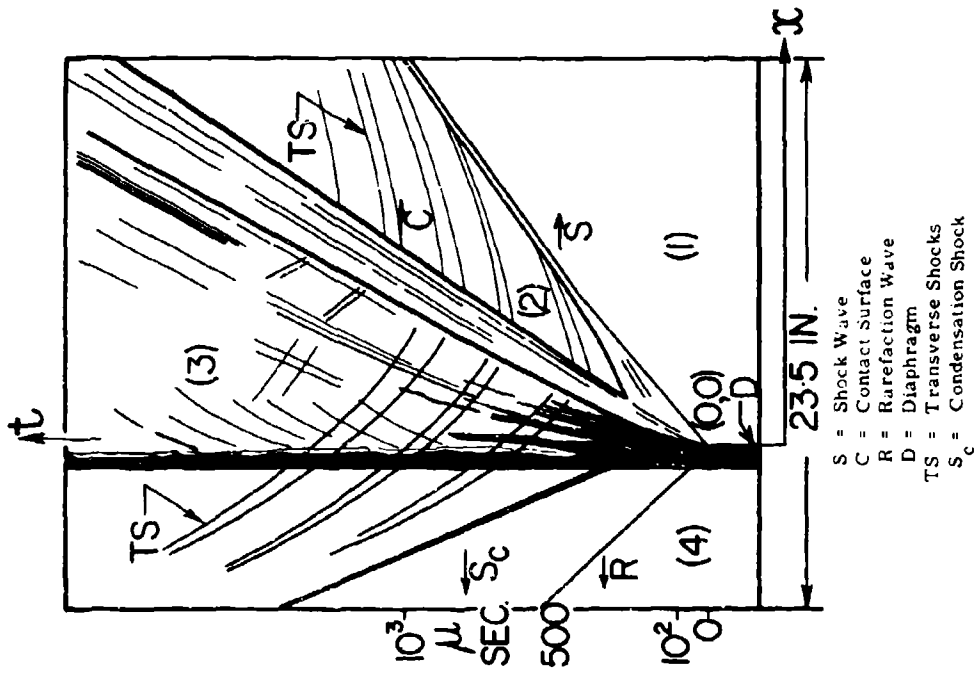
(x, t) Diagram of Basic Shock-Tube Flow

Special Notation

Dimensionless ratios of velocities and thermodynamic variables are denoted below; subscripts i and j refer to quasi-steady uniform states 1, 2, 3, etc.

$A_{ij} = \frac{a_i}{a_j}$	sound speed ratio
$C_{ij}^- = \frac{C_i}{a_j} = \frac{u_i - a_i}{a_j}$	speed ratio of Q-characteristic line
$C_{ij}^+ = \frac{C_i}{a_j} = \frac{u_i + a_i}{a_j}$	speed ratio of a P-characteristic line
$E_{ij} = \frac{e_i}{e_j}$	specific internal energy ratio
$M_i = \frac{u_i}{a_i}$	Mach number
$P_{ij} = \frac{p_i}{p_j}$	static pressure ratio
$P_{oij} = \frac{p_{oi}}{p_j}$	stagnation pressure to reference static pressure ratio
$Q_{ij} = \left(\frac{1}{2} \rho u^2\right)_i / p_j$	dynamic pressure to reference pressure ratio
$T_{ij} = \frac{T_i}{T_j}$	static temperature ratio
$T_{oij} = \frac{T_{oi}}{T_j}$	stagnation temperature to reference state temperature ratio
$U_{ij} = \frac{u_i}{a_j}$	particle velocity to reference sound speed ratio
$V_{ij} = \frac{v_i}{a_j}$	relative gas velocity to reference sound speed ratio ($V_{ij} = W_{ij} - U_{ij}$)
$\sqrt{v}_{ij} = \frac{v_i}{v_j}$	ratio of relative velocities

$M_{ij} = M_s = \frac{w_i}{a_j}$	shock Mach number
$\Lambda_{ij} = \frac{\rho_i u_i}{\rho_j a_j}$	mass flow ratio
$\Gamma_{ij} = \frac{\rho_i}{\rho_j}$	density ratio
$\alpha_i = \frac{\gamma_i + 1}{\gamma_i - 1}$	perfect gas quantity
$\beta_i = \frac{\gamma_i - 1}{2\gamma_i}$	perfect gas quantity
$\frac{D}{Dt} = \frac{\partial}{\partial t} + u \frac{\partial}{\partial x}$	derivative along a line whose slope is $\frac{dx}{dt} = u$, or in the direction of a particle path (substantive or material derivative)
$\frac{\delta^+}{\delta t} = \frac{\partial}{\partial t} + (u \pm a) \frac{\partial}{\partial x}$	derivative along a line whose slope is $\frac{dx}{dt} = u \pm a$, or in the direction of a characteristic line
\bar{C}, \bar{C}	represent contact regions travelling to the left and right, respectively
\bar{R}, \bar{S}	represent forward facing or P-type rarefaction waves and shock waves, respectively, in which the particles enter from right to left
\bar{R}, \bar{S}	represent backward facing or Q-type rarefaction waves and shock waves, respectively, in which the particles enter from left to right
air/argon	represents a diaphragm initially separating air and argon in a shock tube
air helium	represents a contact surface separating air and helium in a shock tube



$P_4 = 1500 \text{ mm. Hg.}$
 $a_{4,1} = 1132 \text{ f.p.s.}$
 $P_{21} = 2.1, M_2 = .50$
 $P_1 = 300 \text{ mm. Hg.}$
 $W_{11} = 1.39$
 $P_{41} = 5.00$
 $U_{21} = .60$
 $M_3 = .65$

Plate 1.1-1. The wave system produced in a real shock tube from the instant the diaphragm ruptures.

SECTION 18: SHOCK TUBES

1. Introduction

A shock tube is a device for generating gas flows of very short duration. In its simplest form it consists of a tube of constant cross section in which a diaphragm initially separates two bodies of gas at different pressures. Rapid removal of the diaphragm generates a flow of short duration containing waves of finite amplitude separated by quasi-steady regions. Initially, after diaphragm removal, a shock wave travels into the low pressure gas while an expansion or rarefaction wave travels into the high pressure gas. The quasi-steady flow regions induced behind these waves are separated by a contact surface across which pressure and velocity are equal, but density and temperature are in general different. The shock heating of the low pressure gas and the expansion cooling of the high pressure gas permit a very wide range of flow temperatures to be achieved. One important application of the shock tube has been to the study of gases under extreme temperature conditions.

The shock tube was first used in France by Paul Vieille as early as 1899 (Ref. 1). Vieille's tube was 22 mm in diameter and over 6 m long, with a chamber length of 271 mm. He used diaphragms of collodion, paper, glass, and steel foil. The collodion diaphragms proved most successful, since like cellophane they had very desirable rupturing properties. Collodion diaphragms 0.29 and 0.11 mm thick burst when the chamber pressures were 27 and 16 atmospheres, respectively, while the paper diaphragms ruptured at an overpressure of 1 atmosphere. The records appear to indicate that the velocity recording apparatus was rather limited. Nevertheless, Vieille came very close to obtaining the theoretical shock velocity of almost twice the speed of sound in air at a diaphragm pressure ratio of 27. It might be noted that he was at that time also concerned with shock wave attenuation and the effect of chamber length on the shock strength.

No further work appears to have been done in shock tubes until Payman and Shepherd in 1940 (Ref. 2) made a detailed study of the flow in the channel following the rupture of copper diaphragms. They successfully used a wave-speed camera with a schlieren system that they had developed more than a decade earlier while working on combustion studies for the Explosives in Mines Research Committee of Britain.

Work in this field in America was initiated by Prof. W. Bleakney and his associates at Princeton University around 1942. Their shock tube was used initially for calibrating crystal pressure gauges (Refs. 3 and 4). Later it was applied to problems in gas dynamics in the form of a study of regular and Mach type reflections of shock waves from a solid surface (Ref. 5). The potentialities of the shock tube for investigating many problems in physics and fluid mechanics were soon recognized, and its use in university and other laboratories became quite widespread in the United States soon after the Second World War (see Refs. 6, 7, 8, 9, 10, and 11, for example).

A theoretical analysis applicable to the shock tube was first given by Kobes in Austria in 1910 (Ref. 12), when he investigated a pneumatic brake system used in railway cars. This work was referred to by Schardin in Germany (Ref. 13) in connection with his own development of the shock-tube theory relating to bursting diaphragms in a pipe. The

shock-tube equation, relating diaphragm pressure ratio and shock-wave pressure ratio, was later developed independently by G. I. Taylor in England (Ref. 2), A. H. Taub (Ref. 3) in the U. S. A., and by G. N. Patterson (Ref. 14) in Canada. Some recent accounts of shock-tube theory and experiment can be found in Refs. 15, 16, and 17.

Some of the research applications of the shock tube have been as follows: Study of transitions through the shock front, contact surface and rarefaction wave; collision, overtaking, and refraction of shock waves and rarefaction waves; shock wave diffraction; shock-loading of structures; relaxation effects and imperfect gas effects; chemical kinetics; combustion and flame propagation; condensation effects; sound-speed measurements; unsteady boundary layers induced by shock and expansion waves, dissociation, ionization, electrical conductivity, radiation, heat transfer, spectra, and other physical effects produced in gases at extremely high temperatures; magnetogasdynamics; and use as an aerodynamic test facility in the subsonic, transonic, and supersonic flow regions, as well as a means of driving hypersonic shock tunnels. This wide utilization of the shock tube has resulted in a large research output, and a sizeable literature on shock tube studies has now accumulated.

1.1 General Scope of Contents

This section of the Handbook of Supersonic Aerodynamics presents a comprehensive account of shock tube theory and application. Subsections 1 through 3, by I. I. Glass, treat the detailed theory and performance of idealized cold-driven constant-area shock tubes (simple shock tubes), including a discussion of real-gas effects (Subsec. 2), and a comparison with theory of experimentally observed flows in shock tubes with a discussion of viscous and heat transfer effects (Subsec. 3). Subsections 4 through 7, by J. G. Hall, treat the production of strong shock waves by various modifications to the simple shock tube (such as driver-gas heating and area reduction from driver to driven sections) and comparison of the relative effectiveness of such modifications (Subsec. 4); applications of the shock tube as an aerodynamic facility, including the hypersonic shock tunnel, and applications to aerophysics, chemical kinetics, and combustion research (Subsec. 5); shock-tube materials, design, and construction (Subsec. 6); and finally, shock-tube instrumentation (Subsec. 7).

REFERENCES

1. Vieille, P., "Sur les discontinuités produites par la détente brusque de gas comprimés," Comptes Rendus de L'Académie des Sciences, Vol. 129 (1899), p. 1228.
2. Payman, W., Sheperd, W. C. F., and others. "The Detonation-Wave in Gaseous Mixtures and the Pre-Detonation Period," Proc. Roy. Soc., Vol. A120 (1928), pp. 90-109.
- _____. "Explosion Waves and Shock Waves, Part I: The Wave-Speed Camera and its Application to the Photography of Bullets in Flight," Proc. Roy. Soc., Vol. A132 (1931), pp. 200-213.
- _____. "Explosion Waves and Shock Waves, Part II: The Shock Wave and Explosion Products Sent Out by Blasting Detonators," Proc. Roy. Soc., Vol. A148 (1935), pp. 604-622.
- _____. "Explosion Waves and Shock Waves, Part III: The Initiation of Detonation in Mixtures of Ethylene and Oxygen and of Carbon Monoxide and Oxygen," Proc. Roy. Soc., Vol. A152 (1935), pp. 418-455.
- _____. "Explosion Waves and Shock Waves, Part IV: Quasi-Detonation in Mixtures of Methane and Air," Proc. Roy. Soc., Vol. A158 (1937), pp. 348-367.
- _____. "Explosion Waves and Shock Waves, Part VI: The Disturbance Produced by Bursting Diaphragms with Compressed Air," Proc. Roy. Soc., Vol. A186 (1946), pp. 243-321.
3. Reynolds, G. T. A Preliminary Study of Plane Shock Waves Formed by Bursting Diaphragms in a Tube. OSRD No. 1519. Washington: Office of Scientific Research and Development, 1943.
4. Fletcher, C. H., Read, W. T., Stoner, R. G., and Weimer, D. K. Final Report on Shock Tube, Piezoelectric Gauges and Recording Apparatus. OSRD No. 6321. Washington: Office of Scientific Research and Development, 1946.
5. Smith, L. G. Photographic Investigation of the Reflection of Plane Shock Waves in Air. OSRD No. 6271. Washington: Office of Scientific Research and Development, 1945.
6. Bleakney, W., Weimer, D., and Fletcher, C. H. "The Shock Tube - A Facility for Investigations in Fluid Dynamics," Rev. Sci. Inst., Vol. 20 (1949), p. 807.
7. Geiger, F. W. and Mautz, C. W. The Shock Tube as an Instrument for the Investigation of Transonic and Supersonic Flow Patterns. Ann Arbor: Engineering Research Institute, University of Michigan, 1949.
8. Huber, P. W., Fitton, C. W., and Delpino, F. Experimental Investigation of Moving Pressure Disturbances and Shock Waves and Correlation with One-Dimensional Unsteady Flow Theory. NACA TN 1903, 1949.

9. Lobb, R. K. A Study of Supersonic Flows in a Shock Tube. UTIA Report 8. Institute of Aerophysics, University of Toronto, 1950.
10. Glass, I. I. Design of a Wave Interaction Tube. UTIA Report 6. Institute of Aerophysics, University of Toronto, 1950.
11. Bitondo, D. Experiments on the Amplification of a Plane Shock Wave. UTIA Report 7. Institute of Aerophysics, University of Toronto, 1950.
12. Kobes, K. "Die Durchschlagsgeschwindigkeit bei den Luftsaug- und Druckluft-bremsen." Zeitschrift des Osterreichischen Ingenieur- und Architekten-Vereines, Vol. 62 (1910), p. 558.
13. Schardin, H. "Bemerkungen zum Druckausgleichsvorgang in einer Rohrleitung." Phy. Zeits., Vol. 33 (1932), p. 60.
14. Patterson, G. N. Theory of the Shock Tube. NOL Memorandum 9903. White Oak, Md.: Naval Ordnance Laboratory, 1948.
15. Lukaszewicz, J. Shock Tube Theory and Application. NAE Report 15. Ottawa, Canada: National Aeronautical Establishment, 1952.
16. Glass, I. I., Martin, W. A., and Patterson, G. N. A Theoretical and Experimental Study of the Shock Tube. UTIA Report 2. Institute of Aerophysics, University of Toronto, 1953.
17. Duff, R. E. The Use of Real Gases in a Shock Tube. Report 51-3. Engineering Research Institute, University of Michigan, 1951.

2. Performance of Simple Constant-Area Shock Tubes

2.1 One-Dimensional Rarefaction and Compression Waves

A disturbance or pressure wave of finite amplitude in a one-dimensional nonstationary flow may be considered as being composed of an infinite number of infinitesimal disturbance fronts or pulses. A basic property of the pressure wave is that each small pulse (Mach wave or characteristic line) travels at the local sound speed with respect to the gas at the point under consideration (Ref. 1). It will be shown that each sound wave changes p , ρ , and u , so that $\Delta p = (\rho a) (\Delta u) = a^2 \Delta \rho$. The above concept is illustrated in Fig. 2.1-1. Consider a piston held by a peg in the duct as shown. At $t = 0$ the peg is released and the piston moves to the right as shown on the (x, t) -plane. Approximate the piston path by small reversible steps 0-1-2-3. At point 0, acoustic pulses of identical speed are transmitted into regions A and B, and at different speeds for points 1, 2, and 3. The gas to the right is being compressed and heated by the piston, whereas to the left the gas is expanded and cooled. Consequently the acoustic pulses in the compression wave (CW) separating states a-b, b-c, and c-D are travelling with progressively increasing sonic speeds, while those in the rarefaction wave (R) between e-f, f-g, and g-C travel with a diminishing speed. Therefore, rarefaction waves are disturbances which spread and become less steep with time. Through the wave, the thermodynamic properties decrease along a particle path, while the flow velocity increases. Whereas through a compression wave, both the thermodynamic and dynamic properties increase along a particle path, so that this disturbance steepens and finally forms into a shock wave. These waves are really transition fronts which are non-linear and aperiodic.

In nonstationary flows such rarefaction and compression waves may be generated and modified at pressure and internal energy discontinuities, at area changes, through skin friction and heat transfer, and by mass removal or addition. The flows may be analysed by applying the appropriate equations of motion and thermodynamic relations.

For duct flows, such as in the shock tube, the analysis is greatly simplified by the assumption of one-dimensional flow whereby the flow properties are assumed to be uniform over any cross section and to vary only with distance along the duct axis and, in general, with time. Departures from this idealization are caused by friction at the duct walls, duct cross-section area change, and significant curvature of the duct axis. Figure 2.1-2(a) shows idealized one-dimensional flow through a straight constant-area duct. Such a flow is fictitious, for in a real gas viscosity causes a boundary layer to grow at the wall which changes the velocity profile to the one shown in Fig. 2.1-2(b). In this case, due to the condition of no slip (gas adjacent to the wall adheres to it), the velocity is zero at the wall and increases to the free stream value u_1 at a distance δ from the wall. In this thin boundary layer of thickness δ , the flow is viscous and diabatic, whereas outside of it the flow is frictionless. When the boundary layer growth is very large the entire flow becomes viscous and diabatic, i.e., becomes a fully developed pipe flow. Here the velocity distribution varies continuously from zero at the wall to a maximum at the pipe centre. Even in large ducts with relatively thin boundary layers it is quite difficult to achieve truly uniform flow quantities at any cross section. Consequently, one-dimensional representation of real flows requires the use of average flow quantities at each cross section. Even in steady flow no unique definition of an average Mach number of flow velocity

exists which will satisfy all of the relations connecting the flow quantities (Ref. 2). In the present note it will be assumed that the dynamic and thermodynamic quantities (u , p , ρ , etc.) are averaged over a cross-section A . While the method of averaging is not prescribed, the mean quantities are functions of distance x (along the duct axis) and time t only.

When the cross-section area varies, the velocity must change in magnitude and direction even with inviscid flow. If the area change is sufficiently gradual so that $\frac{d}{dx} (\ln A)$ is small compared to unity, the transverse velocity components (v and w) are small (see Fig. 2.1-2) by comparison with the axial component (u), and the flow may be treated as one-dimensional whether inviscid (c) or viscous (d). The relation of an actually measured flow velocity or other physical quantity to the corresponding average quantity must be carefully considered in each particular experiment in order to avoid misleading comparisons (Ref. 2). However, it should be noted that small stream-tubes in a flow can always be treated on a one-dimensional basis.

The assumption of one-dimensional flow is made in deriving the differential equations governing fluid motion which follow in Subsec. 2.1.1. For straight duct flows such as in the shock tube, the one-dimensional representation will involve only small errors in the change of average flow quantities along the duct axis provided (Ref. 8):

1. The fractional rate of change of cross-section area with respect to distance along the duct axis is small, i.e.,

$$\frac{d}{dx} \ln A = \frac{1}{A} \frac{dA}{dx} \ll 1$$

2. The velocity and temperature profile shapes remain approximately unchanged from section to section along the duct axis.

2.1.1 Fundamental Equations

The fundamental equations which govern a nonstationary one-dimensional flow can be found in general texts such as Liepmann and Roshko (Ref. 3).

1. Continuity Equation

This equation expresses the principle that mass is conserved:

$$\frac{\partial(\rho A)}{\partial t} + \frac{\partial(\rho u A)}{\partial x} = 0 \quad (1)$$

2. Momentum Change

This equation expresses Newton's Second Law which states that the resultant force on a particle equals the time rate of change of the momentum of the particle:

$$\frac{Du}{Dt} = \frac{\partial u}{\partial t} + u \frac{\partial u}{\partial x} = -\frac{1}{\rho} \frac{\partial p}{\partial x} + f \quad (2)$$

All body and viscous forces are assumed as represented by a resultant body force denoted by f . The properties of f must be given in a particular case. For example, if only the wall friction forces are important, $f = -f_s$,

where

$$f_s = \frac{\text{perimeter} \times l \times \tau_w}{\rho \times \text{area} \times l} = \frac{2u^2 C_f}{D}$$

3. Energy Equation

Neglecting gravitational forces, the total energy, E , per unit mass is the sum of the internal and kinetic energy per unit mass, or (assuming an ideal gas with constant specific heats) $E = C_v T + \frac{1}{2} u^2$. The rate of heat transfer per unit mass per unit time is given by q . The heat transfer may be through the walls or as a result of heat addition due to combustion or chemical reactions.

Therefore,

$$\frac{\partial}{\partial t} [\rho A E dx] = - \frac{\partial}{\partial x} [\rho u A E + p A u] dx + q \rho A dx$$

or,

$$q \rho A dx = \frac{\partial}{\partial t} [\rho A dx (C_v T + \frac{1}{2} u^2)] + \frac{\partial}{\partial x} [\rho u A (C_v T + \frac{p}{\rho} + \frac{1}{2} u^2)] dx \quad (3)$$

Substituting in Eq. (3) the applicable continuity and momentum equations ($f = -f_s$),

$$\frac{\partial(\rho A)}{\partial t} + \frac{\partial}{\partial x} (\rho u A) = 0$$

$$\frac{\partial u}{\partial t} + u \frac{\partial u}{\partial x} + \frac{1}{\rho} \frac{\partial p}{\partial x} + f_s = 0$$

then,

$$q + u f_s = \frac{D}{Dt} (C_v T) + \frac{p}{\rho A} \frac{\partial}{\partial x} (A u) \quad (4)$$

The above states that the sum of the rate of heat transferred by external sources and internally by the power of the friction force times the average velocity is equal to the total time rate of change of internal energy along a particle path plus the power generated by the pressure forces.

4. Equation of State

A thermal equation of state of the form $p = p(v, T)$ connects the three thermodynamic variables p , T , and $v = \frac{1}{\rho}$. Gases in thermal

equilibrium at low pressure or density and at temperatures sufficiently below the onset of dissociation or ionization approximately obey the so-called perfect equation of state:*

$$pv = \frac{RT}{m} = RT \quad \text{or} \quad \frac{p}{\rho} = RT \quad \text{per unit mass} \quad (5)$$

In general, the caloric equation of state of a gas expresses the specific internal energy of a gas e as a function of specific volume v and temperature T , i.e., $e = e(v, T)$. The specific heats of a gas at constant volume (C_v) and constant pressure (C_p) are given, in general, by

$$C_v = \left(\frac{\partial e}{\partial T} \right)_v \quad C_p = \left(\frac{\partial h}{\partial T} \right)_p$$

where $h = e + pv =$ specific enthalpy. For a thermally perfect gas, e is independent of v and depends only on T . Thus, for a thermally perfect gas, C_v and C_p are functions of T only and can be shown to be related by

$$C_p - C_v = \frac{R}{m} = R \quad (6)$$

A gas for which C_v and C_p are constants, independent of both volume and temperature, is termed calorically perfect.

A relation of the form $p = p(S, \rho)$ is sometimes called an entropic equation of state, for example $p = A\rho$, where $A = \frac{p_o}{\rho_o^\gamma} \exp(S - S_o)/C_v$, and the subscript "o" refers to some unknown reference state.

5. Velocity of Sound

The speed of sound (propagation of a small pulse) in gas causes the particles to undergo slow changes. Velocity and temperature gradients are negligibly small, and even though coefficients of viscosity and heat conduction exist, no entropy change is produced (except in the region of ultrasonic sound absorption) as their products, $\mu \left(\frac{du}{dx} \right)$ and $\frac{d}{dx} \left(k \frac{dT}{dx} \right)$, required for entropy production are essentially zero (see Ref. 3, for example). For an imperfect gas, the sound speed a becomes quite a complex quantity to evaluate (Ref. 6) and will be considered in Supplement B. However, for a thermally perfect gas, it reduces to the following simple form:

$$a^2 = \left(\frac{\partial p}{\partial \rho} \right)_s = \frac{\gamma p}{\rho} = \gamma RT \quad (7)$$

*Equation (5) is for thermally perfect gases. The equation of state for thermally imperfect gases is discussed in Supplement A.

For a thermally perfect gas, the entropy change of a fluid element may be expressed from thermodynamic considerations as

$$dS = C_p \frac{dT}{T} - R \frac{dp}{p} \quad (8a)$$

For a thermally and calorically perfect gas (C_p , C_v constants), the speed of sound and the entropy may be used as the independent variables to give two alternate forms of the equation of state as follows:

$$\frac{p}{p_1} = \left(\frac{a}{a_1}\right)^{2\gamma/(\gamma-1)} \cdot e^{-(S-S_1)/R} \quad (8b)$$

$$\frac{\rho}{\rho_1} = \left(\frac{a}{a_1}\right)^{2/(\gamma-1)} \cdot e^{-(S-S_1)/R} \quad (8c)$$

2.1.2 Characteristics in the (x,t)-Plane

The equations of continuity and momentum, Eqs. (1) and (2) in Subsec. 2.1.1, may be expressed, with the aid of Eq. (8), in the following form:

$$\frac{\partial \ln \rho}{\partial t} + u \frac{\partial \ln \rho}{\partial x} + \frac{\partial u}{\partial x} = -u \frac{\partial \ln A}{\partial x} - \frac{\partial \ln A}{\partial t} \quad (1)$$

$$\frac{\partial u}{\partial t} + u \frac{\partial u}{\partial x} = -\frac{a^2}{\gamma} \frac{\partial \ln p}{\partial x} + f \quad (2)$$

From Eq. (8) in Subsec. 2.1.1

$$d \ln p = \frac{2\gamma}{\gamma-1} d \ln a - \frac{dS}{R} = \frac{2\gamma}{\gamma-1} \frac{da}{a} - \frac{dS}{R} \quad (3a)$$

$$d \ln \rho = \frac{2}{\gamma-1} d \ln a - \frac{dS}{R} = \frac{2}{\gamma-1} \frac{da}{a} - \frac{dS}{R} \quad (3b)$$

Substituting the above relations in Eqs. (1) and (2) yields the following results (see Ref. 7):

$$\frac{2}{\gamma-1} \frac{\partial a}{\partial t} + \frac{2}{\gamma-1} u \frac{\partial u}{\partial x} + a \frac{\partial u}{\partial x} = -au \frac{\partial \ln A}{\partial x} - a \frac{\partial \ln A}{\partial t} + \frac{a}{R} \frac{DS}{Dt} \quad (4)$$

$$\frac{\partial u}{\partial t} + u \frac{\partial u}{\partial x} + \frac{2}{\gamma-1} a \frac{\partial a}{\partial x} = \frac{a^2}{\gamma R} \frac{\partial S}{\partial x} + f \quad (5)$$

Adding to, and subtracting Eq. (5) from Eq. (4) gives

$$\begin{aligned} \frac{\partial}{\partial t} \left(\frac{2}{\gamma - 1} a \pm u \right) + (u \pm a) \frac{\partial}{\partial x} \left(\frac{2}{\gamma - 1} a \pm u \right) = \\ - au \frac{\partial \ln A}{\partial x} - a \frac{\partial \ln A}{\partial t} + \frac{a}{R} \left(\frac{DS}{Dt} \pm \frac{a}{\gamma} \frac{\partial S}{\partial x} \right) \pm f \end{aligned} \quad (6)$$

Special curves, known as characteristics, exist in the (x, t) -plane along which the fluid properties are continuous, but derivatives of fluid properties can be discontinuous. The characteristic curves have slopes given by

$$\frac{dx}{dt} = u \pm a \quad (7)$$

The left hand side of Eq. (6) therefore represents the derivative of the parameter $\left(\frac{2}{\gamma - 1} a \pm u \right)$ in the direction of the characteristic curves. Characteristics can also be defined as curves with slopes given by Eq. (7), along which changes in the flow parameter $\left(\frac{2}{\gamma - 1} a \pm u \right)$ are governed by Eq. (6). As a consequence, it is possible for a large disturbance to be propagated by means of the characteristic curves in a nonstationary flow. It should be noted that a particle path has a characteristic slope given by $\frac{dx}{dt} = u$. Therefore $\frac{D}{Dt} = \frac{\partial}{\partial t} + u \frac{\partial}{\partial x}$ represents the derivative along a third characteristic line, whereas

$$\frac{\delta_+}{\delta t} = \frac{\partial}{\partial t} + (u + a) \frac{\partial}{\partial x} \quad \text{and} \quad \frac{\delta_-}{\delta t} = \frac{\partial}{\partial t} + (u - a) \frac{\partial}{\partial x}$$

represent derivatives along the characteristics with slopes $(u \pm a)$. Applying these differential operators, the terms in $\frac{\partial S}{\partial x}$ may be eliminated from Eq. (5), since

$$a \frac{\partial}{\partial x} = \frac{\delta_+}{\delta t} - \frac{D}{Dt} = - \frac{\delta_-}{\delta t} + \frac{D}{Dt} \quad (8)$$

The Riemann variables P and Q are defined as

$$P = \frac{2}{\gamma - 1} a + u \quad Q = \frac{2}{\gamma - 1} a - u$$

Using the above one can rearrange Eq. (6) as follows:

$$\frac{\delta_+ P}{\delta t} = -au \frac{\partial \ln A}{\partial x} - a \frac{\partial \ln A}{\partial t} + \frac{a}{\gamma R} \frac{\delta_+ S}{\delta t} + (\gamma - 1) \frac{a}{\gamma R} \frac{DS}{Dt} + f \quad (9)$$

$$\frac{\delta_- Q}{\delta t} = -au \frac{\partial \ln A}{\partial x} - a \frac{\partial \ln A}{\partial t} + \frac{a}{\gamma R} \frac{\delta_- S}{\delta t} + (\gamma - 1) \frac{a}{\gamma R} \frac{DS}{Dt} - f \quad (10)$$

Similar results can be obtained in a more formal manner (Ref. 8) by using the energy equation (Eq. (4), Subsec. 2.1.1).

Assuming that A can be given as a function of x and t , then the third equation for the three dependent variables a , u , and S is provided by an entropy equation of the general form

$$\frac{DS}{Dt} = F(a, u, S, x, t) \quad (11)$$

If the force f is due to wall friction only, i.e., $f = -f_s$, then from the energy equation it may be shown that

$$\frac{DS}{Dt} = \frac{q + uf_s}{T} \quad (\text{see also Eq. (3a), Subsec. 2.2.1})$$

Problems illustrating the use of Eq. (11) may be found in Refs. 7 and 9. Relations (9), (10), and (11) are a set of non-linear partial differential equations which theoretically provide the means of solving non-stationary flow problems. They may be regarded as forms of the wave equation since they indicate how the quantities P , Q , and S vary along characteristic curves whose slopes in the (x, t) -plane are given by

$$\begin{aligned} \frac{dx}{dt} &= u + a && \text{for P-waves} \\ \frac{dx}{dt} &= u - a && \text{for Q-waves} \\ \frac{dx}{dt} &= u && \text{for S (particle paths)} \end{aligned} \quad (12)$$

Consequently, curves of slopes $(u + a)$ and $(u - a)$ are known as P-waves and Q-waves, respectively, while those of slope u are the paths of fluid elements or particle paths. Equations (9), (10), and (11) are not solvable except in the most simplified cases, and, in general, one must resort to numerical or graphical finite difference methods (Refs. 7 and 8).

In the special case of isentropic (homotropic) flows in ducts of constant area without heat transfer or friction forces, Eqs. (9), (10), (11), and (12) reduce to the following simple forms:

$$\begin{aligned}
 P &= \text{constant} \\
 Q &= \text{constant} \\
 S &= \text{constant} \\
 \frac{dx}{dt} &= u + a \quad \text{for P-waves} \\
 \frac{dx}{dt} &= u - a \quad \text{for Q-waves}
 \end{aligned}
 \tag{13}$$

The flow problem thus reduces to one with two dependent variables, i.e., (u, a) only.

It is of interest to note from Eq. (13) that the rate of advance of the P- and Q-waves is given by $(u + a)$ and $(u - a)$, respectively. However, when this rate is referred to the local flow velocity, it is given by $(+a)$ and $(-a)$. Thus the P- and Q-pulses propagate at the local sound speed relative to the gas and justifiably may be defined as sound waves from a gas-dynamical consideration of infinitesimally weak pulses.*

2.1.3 Rarefaction and Compression Waves in Perfect Gases

The conditions presented in Eq. (13), Subsec. 2.1.2, define the P-wave and Q-wave for an isentropic flow through a duct of constant cross section. If the flow is steady, the P- and Q-waves may be thought to form two families of parallel lines as shown in Fig. 2.1-9. If a local flow disturbance occurs, its effects can be felt at other points only after the arrival of the P- and Q-pulses from the origin of the disturbance. The P- and Q-waves or the characteristic curves therefore may be considered as signals which transmit information about infinitesimal local flow disturbances to other parts of the duct. Finite amplitude pressure fronts are composed of an entire family of P- or Q-pulses which do not remain parallel, but converge or diverge, depending on the type of disturbance. This point is illustrated in Fig. 2.1-10, which shows a disturbance front composed of a family of diverging P-waves moving to the right. It is seen that to the right (1) and to the left (4) of the disturbance front the flow is quasi-steady and the P-pulses are parallel, although their values in states (1) and (2) are different. (A finite amplitude disturbance front which separates two uniform flow regions is also called a simple wave.) Although the value of $P(P_1$ to $P_4)$ throughout the disturbance decreases monotonically, the value of Q remains a constant, since no disturbance was generated at the right side of the duct. The slope of a Q-pulse changes as it moves through the

*A discussion of "Gas Imperfections at Low Pressures and High Temperatures" is presented in Supplement B. This discussion considers caloric and thermal imperfections resulting from high temperature effects only. A treatment of "Relaxation Effects in Gases" is presented in Supplement C.

P-disturbance, owing to the change in u and a , but in the uniform states (1) and (2) the slope remains constant. The Q-waves also remain parallel owing to identical changes in u and a throughout the flow field. Hence, for the particular case of isentropic flow in a duct of constant cross section shown in Fig. 2.1-10, the value of $P = \frac{2a}{\gamma - 1} + u$ is a constant along each Mach wave and $Q = \frac{2a}{\gamma - 1} - u$ is constant across the entire disturbance front. Therefore, on a given P-wave,

$$u = \frac{P - Q}{2} \quad (\text{a constant}) \quad (1)$$

$$a = \frac{(P + Q)(\gamma - 1)}{4} \quad (\text{a constant}) \quad (2)$$

and the P-waves are straight lines because

$$\frac{dx}{dt} = u + a = \frac{P(\gamma + 1) - Q(3 - \gamma)}{4} \quad (3)$$

is also a constant. However, the Q-waves cross P-waves for which the value of P varies from wave to wave; therefore $\frac{dx}{dt} = (u - a)$ will change at every P-wave. Consequently, the Q-waves become curved whenever the value of P changes. Analogous results are obtained by considering a disturbance front from the right composed of Q-waves.

P-waves and Q-waves in turn are subdivided into compression and rarefaction (or expansion) waves, depending on whether or not they increase or decrease the pressure of the gas into which they advance. The above may be illustrated by referring to Fig. 2.1-10. If the disturbance is an expansion wave moving to the right, then the pressure, density, and temperature fall from P_1 to P_4 . Consequently (e.g., for P_2),

$$a_2 < a_1 \quad (4)$$

However, since the P-waves are crossed by Q-waves of constant value, as no disturbance is propagated from the right side of the duct, the following also applies:

$$Q = \frac{2}{\gamma - 1} a_2 - u_2 = \frac{2}{\gamma - 1} a_1 - u_1 \quad (5)$$

From Eqs. (4) and (5) it follows that

$$u_2 < u_1, \quad (u_1 = 0)$$

$$u_2 + a_2 < u_1 + a_1 \quad (6)$$

$$P_2 < P_1$$

Since an increasing inclination of a wave towards the x-axis represents an increasing wave velocity, it is seen that each P-wave propagates at a slower velocity than the preceding one. Therefore the P-waves in a rarefaction front diverge. As indicated by Eq. (6), although the absolute value of u_2 increases, u becomes monotonically more negative throughout the rarefaction front. Conversely, for a compression front (see Fig. 2.1-11) the P-waves converge and

$$\begin{aligned} u_2 &> u_1, \quad (u_1 = 0) \\ u_2 + a_2 &> u_1 + a_1 \\ P_2 &> P_1 \end{aligned} \quad (7)$$

The converging P-pulses brought about by an increased temperature, owing to isentropic compression and increased particle velocity in the direction of the wave propagation, soon overtake and coalesce to form a shock front. Where the P-waves meet, the values of the flow quantities are no longer unique; they undergo discontinuous changes and the flow ceases to be isentropic.

This difficulty is not generally encountered with a rarefaction wave since the characteristic lines diverge and the flow remains isentropic. However, it may be seen from Fig. 2.1-10 that if the P-waves were extended back in the (x, t) -plane, they too would intersect. If the Mach waves meet at a point, the wave is called a centred rarefaction wave. Such a wave has a discontinuity at the focal point. However, it is assumed that it is smoothed out very quickly (Ref. 1). This type of wave is difficult to generate in practice, as it implies an instantaneous drop in pressure at some point. Usually, the rarefaction wave is of the non-centred type.

It is of interest to note that the diverging or converging properties of P- or Q-waves are maintained regardless of the wave which may cross their path. This is illustrated in Fig. 2.1-12, which shows the collision of P- and Q-wave fronts. Initially, $P_2 > P_1$ and $(u_4 + a_4) > (u_1 + a_1)$ for the P-wave front.

$$\begin{aligned} u_3 + a_3 &= \frac{P_1(\gamma + 1) - Q_2(3 - \gamma)}{4} \\ u_2 + a_2 &= \frac{P_2(\gamma + 1) - Q_2(3 - \gamma)}{4} \end{aligned} \quad (8)$$

Therefore, $u_2 + a_2 > u_3 + a_3$, and the compression characteristics remain converging. Similarly, the expansion characteristics remain diverging.

A physical insight into the properties of compression and rarefaction waves may be obtained by considering the motion of a piston in an infinite cylinder (Fig. 2.1-13). A piston of a given mass and area moves under the influence of certain forces such that it accelerates from rest to a uniform velocity u_2 . It is seen that during the

period when the piston accelerates it gives rise to P-characteristic lines which overtake and steepen to form a shock wave. Simultaneously, the piston generates a Q-rarefaction wave which moves into state (4). Here the characteristic lines fan out with time. The gas adjacent to the piston in states (4) and (1) follows the piston, whose velocity is communicated along the characteristic lines to the particle paths. The piston path generates a Q-rarefaction and a P-compression wave, where the particle velocity is positive in each case. However, the particles move in a direction opposite to the rarefaction wave head, but follow the compression wave head. This feature distinguishes a compression wave from a rarefaction wave.

Since the gases in states (1) and (4) are initially at rest, one may write for the P-compression wave:

characteristic slope

$$\frac{dx}{dt} = u + a \quad (9)$$

along each characteristic

$$P = \frac{2a}{\gamma_1 - 1} + u \quad (10)$$

across the entire P-compression wave

$$Q = \frac{2a}{\gamma_1 - 1} - u = \frac{2a_1}{\gamma_1 - 1} \quad (11a)$$

or

$$\frac{a}{a_1} = 1 + \frac{\gamma_1 - 1}{2} \frac{u}{a_1} \quad (11b)$$

Combining Eqs. (9) and (11b),

$$a = \frac{2}{\gamma_1 + 1} a_1 + \frac{\gamma_1 - 1}{\gamma_1 + 1} \left(\frac{dx}{dt} \right) \quad (12)$$

$$u = \frac{-2}{\gamma_1 + 1} a_1 + \frac{2}{\gamma_1 + 1} \left(\frac{dx}{dt} \right) \quad (13)$$

Similarly, for the Q-rarefaction wave:

characteristic slope

$$\frac{dx}{dt} = u - a \quad (14)$$

along each characteristic

$$Q = \frac{2a}{\gamma_4 - 1} - u \quad (15)$$

across the entire wave

$$P = \frac{2a}{\gamma_4 - 1} + u = \frac{2a_4}{\gamma_4 - 1} \quad (16a)$$

$$\frac{a}{a_4} = 1 - \frac{\gamma_4 - 1}{2} \frac{u}{a_4} \quad (16b)$$

$$a = \frac{2}{\gamma_4 + 1} a_4 - \frac{\gamma_4 - 1}{\gamma_4 + 1} \left(\frac{dx}{dt} \right) \quad (17)$$

$$u = \frac{2a_4}{\gamma_4 + 1} + \frac{2}{\gamma_4 + 1} \left(\frac{dx}{dt} \right) \quad (18)$$

Equations (9) to (18) are of particular importance since they make it possible to determine u and a from the slope of a characteristic line. If the piston path is established in the form of $x = f(t)$ or $u = f'(t)$, then from the initial conditions and Eqs. (11a) and (16a) the sound speed is determined at every point along the piston path, the characteristic lines can be drawn, and the entire flow pattern as shown in Fig. 2.1-13 is determined. Each characteristic line would have a straight line equation

$$x = mt + b \quad (19)$$

where m depends on u , and a and b is the intercept on the x -axis. The heads of the expansion and compression waves go through the origin, and their equations, regardless of the piston path, are given by $x = -a_4 t$ and $x = a_1 t$, respectively. In addition, one may obtain the thermodynamic properties of the homentropic flow from $p = \rho RT$, $p = A_0^\gamma$ and $a^2 = \frac{\gamma p}{\rho}$, so that for the compression wave and the rarefaction wave,

$$\frac{a}{a_n} = \left(\frac{T}{T_n} \right)^{1/2} = \left(\frac{\rho}{\rho_n} \right)^{\frac{\gamma_n - 1}{2}} = \left(\frac{p}{p_n} \right)^{\frac{\gamma_n - 1}{2\gamma_n}} \quad (20)$$

$n = 1$ or $n = 4$

It may be emphasized that the piston path fixes the starting point, the position, and the slope of the characteristic lines in the (x, t) -plane. Without the piston path, the compression or rarefaction wave cannot be drawn. The piston path generally may be of a form which gives a non-centred expansion or compression wave. However, there is a particular piston path which can result in a centred type rarefaction wave (i.e., if the characteristics were projected back they would meet at a point which is not at the origin of the (x, t) -plane). This type of piston path is given by the equation of the particle path for a centred rarefaction wave (see Subsec. 2.1.4). It will be noted from

Fig. 2.1-13 that in the case of the non-centred compression wave the shock is initiated as soon as two Mach lines overtake. The shock front continues to grow as additional Mach lines catch up until it achieves its full strength. The entropy change increases simultaneously and this gives rise to an entropy layer separating states (2) and (2)¹. It will be shown (Subsec. 2.4.7) that when two shock waves overtake, only a reflected rarefaction wave is possible in a real gas. In the limit the coalescing compression pulses will therefore reflect expansion pulses. This expansion fan will increase the particle velocity and reduce the pressure such that these quantities are identical with those produced by the shock. Subsequently, the reflected rarefaction pulses will interact with this layer and will give rise to a complex pattern of weak reflected and transmitted P- and Q-pulses as indicated schematically in Fig. 2.1-13. (The wave system outlined above is closely reproduced in a shock tube, as shown on Plate 1.1-1. Even some entropy lines, from overtaking and coalescing shock waves, appear near the origin and they are quickly absorbed by the thick and spreading contact front from the diaphragm.)

In the case where the piston path generates a centred compression wave and a focused shock wave, the entropy layer reduces to a contact surface, and a reflected centred rarefaction wave propagates into region (2) (Fig. 2.1-15d).

2.1.4 Centred Waves in Perfect Gases

Of particular interest for the study of shock tube flows is the rarefaction wave which is centred at the origin of the (x, t)-plane (see Fig. 2.1-14). A comparison of Fig. 2.1-13 and Fig. 2.1-14 shows that the initial portion of the piston curve has degenerated to a single point; that is, the piston is instantly accelerated to a uniform velocity. Under this condition a plane shock wave is propagated into state (1) and the compression wave disappears. The advantage of this type of simplification is that for a given uniform piston speed all wave elements start from the origin and their positions in the (x, t)-plane are fixed. For an accelerating piston which is producing a non-centred wave, this is not the case, and the position and extent of the wave system differs for each piston curve.

For a rarefaction front centred at the origin the Q-waves or characteristics are straight lines whose equation may be expressed in terms of one parameter as $\frac{x}{t} = (u - a)$. This mathematical simplification is not possible for a non-centred wave where $\frac{x}{t} = (u - a) + \frac{\text{const.}}{t}$. Hence, for a centred Q-rarefaction wave:

$$(a) \quad \frac{x}{t} = u - a$$

$$(b) \quad Q = \frac{2a}{\gamma_4 - 1} - u \quad (\text{along a characteristic line})$$

$$(c) \quad P = \frac{2a}{\gamma_4 - 1} + u = \frac{2a_4}{\gamma_4 - 1} \quad (\text{across the entire wave})$$

$$(d) \quad \frac{a}{a_4} = 1 - \frac{\gamma_4 - 1}{2} \cdot \frac{u}{a_4}$$

$$\begin{aligned}
 \text{(e)} \quad a &= \frac{2}{\gamma_4 + 1} a_4 - \frac{\gamma_4 - 1}{\gamma_4 + 1} \left(\frac{x}{t}\right) \\
 \text{(f)} \quad u &= \frac{2}{\gamma_4 + 1} a_4 + \frac{2}{\gamma_4 + 1} \left(\frac{x}{t}\right)
 \end{aligned} \tag{1}$$

From

$$\begin{aligned}
 p &= \rho RT \quad p = A \rho^\gamma \quad \text{and} \quad a^2 = \frac{\gamma p}{\rho} \\
 \frac{a}{a_4} &= \left(\frac{T}{T_4}\right)^{1/2} = \left(\frac{\rho}{\rho_4}\right)^{\frac{\gamma_4 - 1}{2}} = \left(\frac{p}{p_4}\right)^{\frac{\gamma_4 - 1}{2\gamma_4}}
 \end{aligned} \tag{2}$$

It will be noted that Eqs. (1) and (2) would be identical with Eqs. (14) to (18) and (20) of Subsec. 2.1.3 except that for the centred wave the position of the characteristic lines are known from the initial and final gas states $x = (u - a) t$, whereas for a non-centred wave the piston curve must also be given ($x = (u - a) t + \text{constant}$) before the Mach lines can be positioned in the (x, t) -plane. The above is the only essential difference between the two types of waves. Parts (e) and (f) of the above equations show that the slope of the characteristic determines u and a . For example, a centred or non-centred wave having the same characteristic slope at the tail of the wave will also have identical dynamic and thermodynamic properties, although the position of the tail of the wave in the (x, t) -plane will be different. To verify whether or not a wave is centred, when the piston path is not known, it is essential to extend at least three characteristic lines to determine if they meet at the same focal point.

If a centred rarefaction wave of the type shown in Fig. 2.1-14 is generated, then all the characteristics converge at the origin or focal point where the dynamic and thermodynamic quantities (u , p , ρ , and T) as functions of (x, t) are discontinuous. It is assumed that these discontinuities are rapidly smoothed out in the subsequent motion. This is an example of an initial discontinuity which immediately undergoes a transition to continuous flow (Ref. 1).

A theoretical limiting case of the centred rarefaction wave occurs when the temperature behind the wave becomes zero and the particle velocity attains its maximum possible value, the so-called escape speed \hat{u} . A vacuum would exist behind such a wave which is known as a complete centred rarefaction wave. Since for a Q-wave

$$\frac{2}{\gamma_4 - 1} a + u = \frac{2a_4}{\gamma_4 - 1}$$

applies, the value of \hat{u} is given by

$$\hat{u} = \frac{2a_4}{\gamma_4 - 1} \tag{3}$$

when $a = 0$. At the tail of such a wave, the characteristic slopes and the particle paths are given by $Q_T = (u - a)_T = \hat{u}$, $P_T = (u + a)_T = \hat{u}$, and $u_T = \hat{u}$. Hence for a complete centred rarefaction the tail of the wave, the piston path, and the Q- and P-characteristics at the tail are all coincident, i.e., $x/a_4 t = N = 2/(\gamma_4 - 1)$. As a perfect vacuum is impossible to achieve physically, a complete centred rarefaction wave is only of hypothetical interest.

If a centred or noncentred rarefaction wave is generated by a piston which is instantly started from rest or attains a velocity greater than the escape speed, then "cavitation" exists between the tail of the wave and the piston. The particles cannot follow the piston and a hypothetical vacuum exists.

The equation of the particle path for a centred Q-rarefaction wave may be determined from Eq. (1f):

$$u = \frac{dx}{dt} = \frac{2}{\gamma_4 + 1} \cdot \frac{x}{t} + \frac{2}{\gamma_4 + 1} \cdot a_4$$

From Fig. 2.1-15 (a) it is seen that

$$\frac{x}{t} = \frac{x - x_0}{t - t_0}$$

or

$$\frac{dx}{dt} = \frac{2}{\gamma_4 + 1} \left(\frac{x - x_0}{t - t_0} \right) + \frac{2}{\gamma_4 + 1} \cdot a_4 \quad (4)$$

Equation (4) is an ordinary linear differential equation which has the solution,

$$t = \left[\frac{2}{\gamma_4 + 1} \left(1 - \frac{\gamma_4 - 1}{2} N \right) \right]^{\frac{(\gamma_4 + 1)}{(\gamma_4 - 1)}} (t_p - t_0) + t_0 \quad (5)$$

When $N = -1$ (head of wave), $t = t_p$. For a gas with, for example, $\gamma_4 = 1.4$, when $N \rightarrow 5$ (tail of complete centred wave), $t \rightarrow \infty$. The last result indicates that the particle path in the limit approaches the slope of the tail characteristic of a complete wave after an infinitely long time. Alternatively, the escape speed \hat{u} is attained after an infinitely long time in a centred type of rarefaction wave.

A piston moving in accordance with Eq. (5) will generate a rarefaction wave which is focused at the point 0 of the (x, t) -plane. The farther away point P (the real origin of the physical (x', t') -plane) is from 0, the more gentle will be the transition through the rarefaction wave.

It is of interest to determine the acceleration produced on a particle path of a Q-centred rarefaction wave:

$$u = \frac{2}{\gamma_4 + 1} \left(\frac{x}{t} \right) + \frac{2a_4}{\gamma_4 + 1}$$

or

$$u = \frac{2}{\gamma_4 + 1} (N + 1) a_4$$

$$\frac{du}{dN} = \frac{2a_4}{\gamma_4 + 1}$$

$$\frac{\partial u}{\partial t} = \frac{du}{dN} \cdot \frac{\partial N}{\partial t} = -\frac{N}{t} \cdot \frac{du}{dN}$$

$$\frac{\partial u}{\partial x} = \frac{du}{dN} \cdot \frac{\partial N}{\partial x} = \frac{N}{x} \cdot \frac{du}{dN}$$

The fluid acceleration

$$b = \frac{du}{dt} = \frac{\partial u}{\partial t} + u \frac{\partial u}{\partial x}$$

or

$$b = \frac{2a_4}{(\gamma_4 + 1)t} \left[\frac{2}{\gamma_4 + 1} (N + 1) - N \right] = \frac{2a_4}{(\gamma_4 + 1)t} \quad (6)$$

At the head of the wave $N = -1$, and $b = \frac{2a_4}{(\gamma_4 + 1)t}$, that is, b varies inversely as t . At the tail of the complete centred wave $N = 5$, and $b = 0$ regardless of t . Thus the acceleration is a maximum at the head of the wave and decreases across the wave to zero for a complete wave. It is worth noting that at $t = 1 \mu\text{sec}$, the acceleration for air is of the order of $0.92 \times 10^9 \text{ ft/sec}^2$ ($2.8 \times 10^7 \text{ g}$) at the head of the wave.

Similarly, the equation for a P-characteristic crossing a Q-rarefaction wave (Fig. 2.1-14) may be obtained as follows:

$$\frac{dx}{dt} = u + a$$

or from Eq. (1c) and (1f)

$$\frac{dx}{dt} = \frac{4a_4}{\gamma_4 + 1} + \left(\frac{x - x_0}{t - t_0} \right) \frac{3 - \gamma_4}{\gamma_4 + 1}$$

or

$$(x - x_0) = \frac{2a_4}{\gamma_4 - 1} (t - t_0) \left[1 - \frac{\gamma_4 + 1}{2} \left(\frac{t_p - t_0}{t - t_0} \right)^{\frac{2(\gamma_4 - 1)}{\gamma_4 + 1}} \right] \quad (7)$$

which gives

$$t = \left[\frac{2}{\gamma_4 + 1} \left(1 - \frac{\gamma_4 - 1}{2} N \right) \right]^{\frac{\gamma_4 + 1}{2(\gamma_4 - 1)}} (t_p - t_0) + t_0 \quad (8)$$

When $N = -1$, $t = t_p$, as $N \rightarrow 5$, $t \rightarrow \infty$, and the previous remark regarding the particle path applies here as well. A comparison of Eqs. (5) and (8) shows that they differ as the square root of the power. Consequently the P-characteristic will approach the tail of a complete wave faster ($dx/dt = u + a$) than the particle path ($dx/dt = u$).

Typical particle paths and characteristic lines are shown on Fig. 2.1-14. It is of interest to point out that a P-characteristic originating in state (4) penetrates the rarefaction wave as well as state (3) and state (2), and therefore will influence all of these regions. On the other hand, a Q-wave originating in state (1) penetrates states (2) and (3), but cannot enter the rarefaction wave because it becomes parallel to the tail of the wave (Q_3) and cannot overtake it. Thus the rarefaction wave is isolated from any downstream influence.

The previous discussion on rarefaction waves applies to compression waves. However, in this case the characteristic lines or pulses soon overtake as shown in Fig. 2.1-15. The characteristic slope is given by $\frac{dx}{dt} = (u + a)$ for the P-compression wave. The particle velocity u increases with time and the temperature or sound speed rises behind each pulse. Consequently, $\frac{dx}{dt} = (u + a)$ increases and the Mach waves converge to form a shock wave. At the points of intersection of these pulses, the values of u and a are no longer unique. This is resolved by the generation of a shock wave which has a change in entropy across it, so that the original isentropic equations are invalidated. The shock wave may be generated at the head or within the compression wave (see Ref. 1), and depends on the piston acceleration.

Consider the motion of a piston which starts from rest with a constant acceleration b as shown on Fig. 2.1-15 (c). Along and across the P_1 -pulse,

$$x = a_1 t$$

$$u = \frac{2a}{\gamma_1 - 1} = - \frac{2a_1}{\gamma_1 - 1}$$

or

$$\frac{dx}{dt} = u + a = \frac{\gamma_1 + 1}{2} u + a_1$$

For the P_2 -pulse, $x = x_0 + (u + a) \tau$

or

$$x = \frac{1}{2} b \epsilon^2 + \left(a_1 + \frac{\gamma_1 + 1}{2} b \epsilon \right) (t - \epsilon) \quad (9)$$

The time parameter ϵ depends on the piston position. Solving for x_1 and t_1 from the P_1 and P_2 characteristics:

$$t_1 = \frac{2}{(\gamma_1 + 1)b} \left[a_1 + \frac{\gamma}{2} b \epsilon \right] \quad (10)$$

$$x_1 = a_1 t_1 = \frac{2}{(\gamma_1 + 1)} \cdot \frac{a_1}{b} \left[a_1 + \frac{\gamma}{2} b \epsilon \right]$$

This gives the birth point of the shock (x_1, t_1) for a piston of constant acceleration b , where

$$u = b \epsilon$$

$$a = \frac{\gamma_1 - 1}{2} b \epsilon + a_1$$

$$u + a = \frac{\gamma_1 + 1}{2} b \epsilon + a_1$$

In order to get the envelope, Eq. (9) may be considered as a one parameter family of curves for $\epsilon \geq 0$, and the required conditions are that $G(x, t, \epsilon) = 0$ and $\frac{dG}{d\epsilon} = 0$. Thus

$$\frac{\gamma_1 + 1}{2} b t = \gamma_1 b \epsilon + a_1$$

or

$$t = \frac{2}{\gamma_1 + 1} \cdot \frac{a_1}{b} + \frac{2\gamma_1}{\gamma_1 + 1} \epsilon$$

and from Eq. (9),

$$x = \frac{2}{\gamma_1 + 1} \cdot \frac{a_1^2}{b} + \epsilon \left(\frac{\gamma_1 b \epsilon}{2} + \frac{2\gamma_1}{\gamma_1 + 1} a_1 \right)$$

Eliminating ϵ yields

$$x = \frac{(\gamma_1 + 1)^2}{8\gamma_1} bt^2 + \frac{\gamma_1 - 1}{2\gamma_1} a_1 t + \frac{a_1^2}{2\gamma_1 b} \quad (11)$$

Thus the shock wave starts at (x_1, t_1) and grows from that point until it has achieved its full strength.

The case of a centred compression wave that gives rise to a focussed shock wave is shown in Fig. 2.1-15 (d). In this idealized case, all the Mach lines converge at the focal point $F(x_F, t_F)$, where the shock wave forms and attains its full strength instantly.

If the condition that the particle velocity and the pressure must be constant across the contact surface is to be met ($p_2 = p_3$; $u_2 = u_3$), then a centred rarefaction wave must be reflected as shown. The reason for this can be explained from wave interaction considerations, as noted above, or from the following. For the same pressure ratio across a compression wave and shock wave, the compression wave generates a lower temperature (or higher density), sound speed, and particle velocity than the shock front. If the boundary conditions at the shock wave are to be satisfied, then the compression wave must be of higher strength in order that the reflected rarefaction wave can reduce its pressure and increase the particle velocity to give $p_2 = p_3$ and $u_2 = u_3$.

The piston path which yields a focussed compression wave may be found from the following considerations (Fig. 2.1-15 (d)).

Let the piston path be given by $x = f(t)$, and the focal point by (x_F, t_F) . The slope of any Mach wave emanating from the piston is given by

$$\frac{x - x_F}{t - t_F} = u + a$$

For a Q-pulse across the P-compression wave,

$$u - \frac{2a}{\gamma_1 - 1} = - \frac{2a_1}{\gamma_1 - 1}$$

Combining the above,

$$a = \frac{2a_1}{\gamma_1 + 1} + \frac{\gamma_1 - 1}{\gamma_1 + 1} \left(\frac{x - x_F}{t - t_F} \right)$$

$$u = \frac{dx}{dt} = \frac{2}{\gamma_1 + 1} \left(\frac{x - x_F}{t - t_F} \right) - \frac{2a_1}{\gamma_1 + 1}$$

That is, the same results apply for a P-compression wave as for a P-rarefaction wave, except that (u) is positive for the former and negative for the latter.

Integrating the equation for u yields

$$x - x_F = -\frac{2a_1}{\gamma_1 - 1} (t - t_F) + A(t - t_F)$$

On the first P-pulse

$$\frac{x_o - x_F}{t_o - t_F} = a_1$$

and

$$\frac{A}{a_1} = \frac{\gamma_1 + 1}{\gamma_1 - 1} (t_o - t_F)^{\frac{\gamma_1 - 1}{\gamma_1 + 1}}$$

or

$$(x - x_F) = \frac{2a_1}{\gamma_1 - 1} (t - t_F) \left[\frac{\gamma_1 + 1}{2} \left(\frac{t_o - t_F}{t - t_F} \right)^{\frac{\gamma_1 - 1}{\gamma_1 + 1}} - 1 \right] \quad (12)$$

Since the characteristic slope

$$N = \frac{x - x_F}{a_1(t - t_F)}$$

then an alternate form of the piston path is

$$t = \left[\frac{2}{\gamma_1 + 1} \left(1 + \frac{\gamma_1 - 1}{2} N \right) \right]^{-\frac{\gamma_1 + 1}{\gamma_1 - 1}} (t_o - t_F) + t_F \quad (13)$$

When $N = 1$, $t = t_o$, and when $N \rightarrow \infty$, $t \rightarrow t_F$. The above relations give the piston path x as a function of the focal point t_F and t , or t as a function of N and the focal point t_F .

In this case as well, the farther away F is from 0 , the more gentle will be the compression wave transition profiles. Compression waves are chiefly of academic interest, since in practice they quickly turn into a shock front.

The piston velocity $u = \frac{2a_1}{\gamma_1 + 1} (N - 1)$, and following the method of Eq. (6), the piston acceleration is given by

$$b = \frac{du}{dt} = \frac{2a_1}{(\gamma_1 + 1)(t - t_F)} \left[\frac{2}{\gamma_1 + 1} (N - 1) - N \right] = \frac{-2a}{(\gamma_1 + 1)(t - t_F)} \quad (14)$$

It should be noted that although Eq. (14) will yield accelerations to the left of the piston curve (Fig. 2.1-15(d)), they have no physical meaning. The accelerations on each characteristic pulse are a minimum at the piston face and increase in value as the focal point is approached.

Since $(t - t_F)$ is negative, b is positive, and increases from $2a_1/(\gamma_1 + 1)t_F$ at the head of the wave to an infinite value when $t \rightarrow t_F$. The acceleration decreases with large t_F as expected.

The flow properties through unsteady expansion waves may be described in terms of the local Mach number or the local characteristic slope by the following alternate forms (see Eqs. (1) and (2)).

For a Q-rarefaction wave in a perfect gas:

1. Speed of sound ratio

$$\frac{a}{a_4} = 1 - \frac{\gamma_4 - 1}{2} \cdot \frac{u}{a_4} = \left[1 + \frac{(\gamma_4 - 1)}{2} M \right]^{-1} \quad (15)$$

when

$$u \rightarrow \frac{2a_4}{\gamma_4 - 1} \quad \text{or} \quad M \rightarrow \infty, \quad a \rightarrow 0$$

2. Flow temperature ratio

$$\frac{T}{T_4} = \left[1 - \frac{\gamma_4 - 1}{2} \cdot \frac{u}{a_4} \right]^2 = \left[1 + \frac{\gamma_4 - 1}{2} M \right]^{-2} \quad (16)$$

when

$$M \rightarrow \infty, \quad T \rightarrow 0$$

3. Flow density ratio

$$\frac{\rho}{\rho_4} = \left[1 - \frac{\gamma_4 - 1}{2} \cdot \frac{u}{a_4} \right]^{\frac{1}{(\beta\gamma)_4}} \left[1 + \frac{\gamma_4 - 1}{2} M \right]^{\frac{-1}{(\beta\gamma)_4}} \quad (17)$$

when

$$M \rightarrow \infty, \quad \rho \rightarrow 0$$

4. Static pressure ratio

$$\frac{p}{p_4} = \left[1 - \frac{\gamma_4 - 1}{2} \cdot \frac{u}{a_4} \right]^{\frac{1}{\beta_4}} = \left[1 + \frac{\gamma_4 - 1}{2} M \right]^{\frac{-1}{\beta_4}} \quad (18a)$$

or

$$\frac{u}{a_4} = \frac{2}{\gamma_4 - 1} \left[1 - \left(\frac{p}{p_4} \right)^{\beta_4} \right] \quad (18b)$$

when

$$M \longrightarrow \infty, \quad p \longrightarrow 0; \quad \frac{u}{a_4} \longrightarrow \frac{2}{\gamma_4 - 1} = \hat{u}, \quad p \longrightarrow 0$$

5. Particle velocity ratio

$$\frac{u}{a_4} = \frac{M}{1 + \frac{\gamma_4 - 1}{2} M} \quad (19)$$

when

$$M \longrightarrow \infty, \quad \frac{u}{a_4} \longrightarrow \frac{2}{\gamma_4 - 1}$$

6. Mass flow ratio

$$\frac{\rho u}{(\rho a)_4} = \frac{M}{\left(1 + \frac{\gamma_4 - 1}{2} M \right)^\alpha} \quad (20)$$

when

$$M \longrightarrow \infty, \quad \frac{\rho u}{(\rho a)_4} \longrightarrow 0$$

7. Stagnation temperature ratio

$$\frac{T_o}{T_4} = \frac{T_o}{T} \cdot \frac{T}{T_4} = \frac{\left(1 + \frac{\gamma_4 - 1}{2} M^2 \right)}{\left(1 + \frac{\gamma_4 - 1}{2} M \right)^2} \quad (21)$$

when

$$M \longrightarrow \infty, \quad \frac{T_o}{T_4} \longrightarrow \frac{2}{\gamma_4 - 1}$$

8. Isentropic stagnation pressure ratio

$$\frac{p_o}{p_4} = \frac{p_o}{p} \cdot \frac{p}{p_4} = \frac{\left[1 + \frac{\gamma_4 - 1}{2} M^2\right]^{\frac{1}{2\beta_4}}}{\left[1 + \frac{\gamma_4 - 1}{2} M\right]^{\frac{1}{\beta_4}}} \quad (22)$$

when

$$M \rightarrow \infty, \quad p_o/p_4 \rightarrow \left(\frac{2}{\gamma_4 - 1}\right)^{\frac{1}{2\beta_4}}$$

9. Pitot pressure ratio for subsonic flow ($M < 1$)

This relation is identical to Eq. (22)

$$\frac{p_o}{p_4} = \frac{\left[1 + \frac{\gamma_4 - 1}{2} M^2\right]^{\frac{1}{2\beta_4}}}{\left[1 + \frac{\gamma_4 - 1}{2} M\right]^{\frac{1}{\beta_4}}} \quad (23a)$$

when

$$M \rightarrow 1, \quad \frac{p_o}{p_4} \rightarrow \left(\frac{2}{\gamma_4 + 1}\right)^{\frac{1}{2\beta_4}}$$

10. Pitot pressure ratio for supersonic flow ($M > 1$)

$$\frac{p'_o}{p_4} = \frac{p'_o}{p} \cdot \frac{p}{p_4} = \frac{\gamma_4 + 1}{2} M^2 \left[\frac{\frac{\gamma_4 + 1}{2} M^2}{\frac{2\gamma_4}{\gamma_4 + 1} M^2 - \frac{\gamma_4 - 1}{\gamma_4 + 1}} \right]^{\frac{1}{2(\beta\gamma)_4}} \cdot \frac{1}{\left[1 + \frac{\gamma_4 - 1}{2} M\right]^{\frac{1}{\beta_4}}} \quad (23b)$$

when

$$M \rightarrow 1, \quad \frac{p'_o}{p_4} \rightarrow \left(\frac{2}{\gamma_4 + 1}\right)^{\frac{1}{2\beta_4}}$$

$$M \rightarrow \infty, \quad \frac{p'_o}{p_4} \rightarrow 0, \quad \frac{p'_o}{p_4} \sim 0.545 \text{ at } M \sim \frac{5}{3}, \quad \gamma_4 = 1.4$$

11. Reynolds number per foot ratio

$$\frac{(\rho u/\mu)}{(\rho a/\mu)_4} = \frac{\rho u}{(\rho a)_4} \cdot \left(\frac{T_4}{T}\right)^n = \frac{M}{\left(1 + \frac{\gamma_4 - 1}{2} M^2\right)^{\alpha - 2n}} \quad (24)$$

For

$$M \longrightarrow 0 \quad \text{and} \quad M \longrightarrow \infty, \quad \text{Re} \longrightarrow 0$$

For

$$\gamma_4 = 1.4 \quad \text{and} \quad n = 1, \quad \text{Re}_{\max} \text{ occurs when } M = \frac{5}{3}$$

where n is the exponent in the viscosity-temperature relation.

12. Dynamic pressure

$$\frac{\frac{1}{2} \rho u^2}{p_4} = \frac{q}{p_4} = \frac{\frac{\gamma_4}{2} M^2}{\left[1 + \frac{\gamma_4 - 1}{2} M^2\right]^{1/\beta_4}} \quad (25)$$

For

$$M \longrightarrow 0 \quad \text{or} \quad M \longrightarrow \infty, \quad q/p_4 \longrightarrow 0$$

For

$$\gamma_4 = 1.4, \quad q/p_4 \text{ max occurs when } M = 2$$

It should be noted that in Eqs. (21), (22), and (23) it is assumed that the steady flow adiabatic equations apply locally at a measuring instrument in an unsteady flow. The correctness of this assumption must be verified by experiment.

The physical quantities of the flow can also be expressed in a very useful form in terms of the slope of the characteristic lines of a Q-centred (noncentred) rarefaction wave. The slope is expressed in nondimensional form as

$$N = \frac{x}{a_4 t} = \frac{u - a}{a_4} \quad (\text{centred})$$

$$N = \frac{1}{a_4} \cdot \frac{dx}{dt} = \frac{u - a}{a_4} \quad (\text{noncentred})$$

From Eq. (1d)

$$\frac{a}{a_4} = 1 - \frac{\gamma_4 - 1}{2} \cdot \frac{u}{a_4}$$

From Eq. (1f)

$$\frac{u}{a_4} = \frac{2}{\gamma_4 + 1} + \frac{2}{\gamma_4 + 1} \cdot \frac{x}{a_4 t}$$

Combining the above gives:

1. Particle velocity ratio

$$\frac{u}{a_4} = \frac{2}{\gamma_4 + 1} [N + 1] = \frac{1}{(\alpha\beta\gamma)_4} [N + 1] \quad (26)$$

For

$$\gamma_4 = 1.4, \text{ when } N = -1, \frac{u}{a_4} = 0; N = 5, \frac{\hat{u}}{a_4} = 5$$

2. Sound speed ratio

$$\frac{a}{a_4} = 1 - \frac{\gamma_4 - 1}{\gamma_4 + 1} \left(\frac{x}{a_4 t} + 1 \right) = 1 - \frac{1}{\alpha_4} (N + 1) \quad (27)$$

For

$$\gamma_4 = 1.4, \text{ when } N = -1, \frac{a}{a_4} = 1; N = 5, \frac{u}{a_4} = 0$$

3. Static temperature ratio

$$\frac{T}{T_4} = \left[1 - \frac{1}{\alpha_4} (N + 1) \right]^2 \quad (28)$$

For

$$\gamma_4 = 1.4, \text{ when } N = -1, \frac{T}{T_4} = 1; N = 5, \frac{T}{T_4} = 0$$

4. Density ratio

$$\frac{\rho}{\rho_4} = \left[1 - \frac{1}{\alpha_4} (N + 1) \right]^{\frac{1}{(\beta\gamma)_4}} \quad (29)$$

For

$$\gamma_4 = 1.4, \text{ when } N = -1, \frac{\rho}{\rho_4} = 1; N = 5, \frac{\rho}{\rho_4} = 0$$

5. Static pressure ratio

$$\frac{p}{p_4} = \left[1 - \frac{1}{\alpha_4} (N + 1) \right]^{\frac{1}{\beta_4}} \quad (30)$$

For

$$\gamma_4 = 1.4, \text{ when } N = -1, \frac{p}{p_4} = 1; N = 5, \frac{p}{p_4} = 0$$

6. Mach number

$$M = \left| \frac{u}{a} \right| = \left[\frac{N + 1}{1 - (\beta\gamma)_4 N} \right] \quad (31)$$

For

$$\gamma_4 = 1.4, \text{ when } N = -1, M = 0; N = 5, M \rightarrow \infty$$

7. Mass flow ratio

$$\frac{\rho u}{(\rho a)_4} = \left[1 - \frac{1}{\alpha_4} (N + 1) \right]^{\frac{1}{(\beta\gamma)_4}} (N + 1) \frac{1}{(\alpha\beta\gamma)_4} \quad (32)$$

For

$$\gamma_4 = 1.4, \text{ when } N = -1, \frac{\rho u}{(\rho a)_4} = 0; N = 5, \frac{\rho u}{(\rho a)_4} = 0$$

8. Stagnation temperature ratio

$$\frac{T_o}{T_4} = \frac{T_o}{T} \cdot \frac{T}{T_4} = \left[1 + \frac{\gamma_4 - 1}{2} \left(\frac{N + 1}{1 - (\beta\gamma)_4 N} \right)^2 \right] \left[1 - \frac{1}{\alpha_4} (N + 1) \right]^2 \quad (33)$$

For

$$\gamma_4 = 1.4, \text{ when } N = -1, \frac{T_o}{T_4} = 1; N = 5, \frac{T_o}{T_4} = 5$$

9. Pitot pressure ratio (subsonic flow), and isentropic stagnation pressure ratio

$$\frac{p_o}{p_4} = \frac{p_o}{p} \cdot \frac{p}{p_4} = \left[1 + \frac{\gamma_4 - 1}{2} \left(\frac{N + 1}{1 - (\beta\gamma)_4 N} \right)^2 \right]^{\frac{1}{2\beta_4}} \left[1 - \frac{1}{\alpha_4} (N + 1) \right]^{\frac{1}{\beta_4}}$$

For

$$\gamma_4 = 1.4$$

(34)

when

$$N = -1, \quad \frac{p_0}{p_4} = 1; \quad N = 0, \quad \frac{p_0}{p_4} = \left[\frac{2}{\gamma_4 + 1} \right]^{\frac{1}{2\beta_4}} = 0.528$$

$$N = 5, \quad \frac{p_0}{p_4} \rightarrow \left[\frac{2}{\gamma_4 - 1} \right]^{\frac{1}{2\beta_4}} = 280$$

10. Pitot pressure ratio (supersonic flow)

$$\frac{p'_0}{p_4} = \frac{p'_0}{p} \cdot \frac{p}{p_4} = \frac{\gamma_4 + 1}{2} \left[\frac{N+1}{1 - (\beta\gamma)_4 N} \right]^2 \left[\frac{\frac{\gamma_4 + 1}{2} \left(\frac{N+1}{1 - (\beta\gamma)_4 N} \right)^2}{\frac{2\gamma_4}{\gamma_4 + 1} \left(\frac{N+1}{1 - (\beta\gamma)_4 N} \right)^2 - \frac{\gamma_4 - 1}{\gamma_4 + 1}} \right]^{1/2 (\beta\gamma)_4} \left[1 - \frac{1}{\alpha_4} (N+1) \right]^{\frac{1}{\beta_4}} \quad (35)$$

For

$$\gamma_4 = 1.4, \quad \text{when } N = 0, \quad \frac{p'_0}{p_4} = 0.528; \quad N = 5, \quad \frac{p'_0}{p_4} = 0$$

11. Reynolds number per foot ratio

$$\frac{\rho u / \mu}{(\rho \mu / \mu)_4} = \frac{\rho u}{(\rho \mu)_4} \left(\frac{T_4}{T} \right)^n = \left[1 - \frac{1}{\alpha_4} (N+1) \right] \frac{1}{(\beta\gamma)_4} \cdot \frac{1}{(N+1)} \frac{1}{(\alpha\beta\gamma)_4} \quad (36)$$

For

$$\gamma_4 = 1.4, \quad \text{Re} = 0 \quad \text{when } N = -1 \quad \text{and } N = 5$$

12. Dynamic pressure

$$\frac{\frac{1}{2} \rho u^2}{p_4} = \frac{q}{p_4} = \frac{\gamma_4}{2} \left[\frac{N+1}{1 - (\beta\gamma)_4 N} \right]^2 \left[1 - \frac{1}{\alpha_4} (N+1) \right] \quad (37)$$

For

$$\gamma_4 = 1.4, \quad q = 0 \quad \text{when } N = 1 \quad \text{and } N = 5$$

The above relations are tabulated in Table 2.1-6 as functions of the nondimensional slope ($N = \frac{x}{a_4 t} = \frac{u - a}{a_4}$) of the characteristic lines of a centred rarefaction wave. The value of $N = -1$ corresponds

to the head of a Q-rarefaction wave, while $N = 5$ is the limiting value of the slope of the tail of a complete centred rarefaction wave. The intermediate values of $-1 \leq N \leq 5$ represent characteristic lines or the tails of rarefaction waves greater than a Mach wave but less than a completed centred wave.

Some of the features of Eqs. (15) to (37) and of Table 2.1-6 are illustrated in Figs. 2.1-16 to 2.1-28 for $\gamma = 1.4$.

Similar results may be plotted for a Q-compression wave. However, in this case the range of N is $-\infty \leq N \leq -1$. That is, it is hypothetically assumed that a piston can be accelerated from rest to infinite speed. In a real flow a shock wave would form long before such a condition is reached, and the assumptions of isentropic flow would become invalid.

Figure 2.1-16 shows that in the $(a_4 t, x)$ -plane, for a gas with $\gamma = 1.4$, the complete centred rarefaction wave occupies the region between $N = -1$ and $N = 5$, i.e., from a slope of -45° to $+78.70^\circ$. Figure 2.1-17 indicates that the velocity ratio has a value of 0 at $N = -1$ and increases linearly to the escape speed value of 5 at $N = 5$. Similarly, Fig. 2.1-18 shows that the sound speed ratio decreases linearly from 1 at $N = -1$ to 0 at $N = 5$.

The thermodynamic quantities of temperature, density, and pressure ratio decrease monotonically from 1 at $N = -1$ to 0 at $N = 5$. The rate of decrease is also in the same order, as shown in Figs. 2.1-19 to 2.1-21. On the other hand, the Mach number increases monotonically from $M = 0$ at $N = -1$ to $M \rightarrow \infty$ at $N = 5$, as shown on Fig. 2.1-22.

By analogy with steady flow, the mass flow has a maximum $(\rho v / \rho a)_4 = 0.334$ when $N = 0$ or $M = 1$. It is zero at $N = -1$ and $N = 5$, as shown in Fig. 2.1-23.

Figure 2.1-24 shows that the total temperature ratio T_0/T_4 has a minimum (0.833) when $N = 0$ or $M = 1$. It is 1 at $N = -1$ and has a value of 5 at $N = 5$. The isentropic stagnation pressure ratio p_0/p_4 (Fig. 2.1-25) has a minimum (0.528) at $N = 0$, and has a value of unity at $N = -1$. It has a limiting value of 280 at $N = 5$. The pitot pressure behind a normal shock wave in the rarefaction region appears in Fig. 2.1-26. It is seen to increase slightly up to $N \sim 0.5$ from a value of 0.528 at $N = 0$ (it has no real values for subsonic flows $-1 \leq N \leq 0$) and then decreases to 0 at $N = 5$.

If the temperature-viscosity relationship is assumed to be of the form $\frac{\mu}{\mu_4} = \left(\frac{T}{T_4}\right)^n$, $n = 1$ (which is only good in a very narrow range for real flows), then the Reynolds number per foot ratio can be plotted in a simple form as shown on Fig. 2.1-27. It rises from 0 at $N = -1$ to a maximum value of 0.528 at $N = 1/2$ or $M = 5/3$ and decreases to 0 at $N = 5$. Similarly, the dynamic pressure has a maximum value of 0.265 at $M = 2$ or $N = 5/7$ (Fig. 2.1-27).

The Riemann invariants are shown on Fig. 2.1-28. For a Q-centred rarefaction wave the value of $\frac{P}{a_4} = 5$ is a constant throughout. The values of Q decrease linearly from $\frac{Q}{Q_4} = 5$ at $N = -1$ to

$$\frac{Q}{Q_4} = -5 \text{ at } N = 5.$$

It is of interest to differentiate the above relations with respect to N , or normal to the characteristic lines, giving

$$\begin{aligned} \frac{du}{dN} &= \frac{a_4}{(\alpha\beta\gamma)_4} && \text{(a constant)} \\ \frac{da}{dN} &= -\frac{a_4}{\alpha_4} && \text{(a constant)} \\ \frac{dT}{dN} &= -\frac{2T_4}{\alpha_4} \left[1 - \frac{1}{\alpha} (N + 1) \right] \\ \frac{d\rho}{dN} &= -\frac{\rho_4}{(\alpha\beta\gamma)_4} \left[1 - \frac{1}{\alpha_4} (N + 1) \right]^{\frac{3-\gamma_4}{\gamma_4-1}} \\ \frac{dp}{dN} &= -\frac{p_4}{(\alpha\beta)_4} \left[1 - \frac{1}{\alpha_4} (N + 1) \right]^{\alpha_4} \\ \frac{dM}{dN} &= \frac{(\alpha\beta\gamma)_4}{(1 - (\beta\gamma)_4 N)^2} \end{aligned} \quad (37)$$

The derivatives listed in Eq. (37) are evaluated in Table 2.1-7a for the range $-1 \leq N \leq 5$, for Q-rarefaction waves. Table 2.1-7a illustrates what is shown graphically in Figs. 2.1-17 to 2.1-22 inclusive. The slopes of a and u versus N remain constant since they are linear relations. The slopes of the curves of T , ρ , and p versus N are monotonically decreasing, respectively, whereas $\frac{dM}{dN}$ increases rapidly with N . Similar results for a Q-compression wave appear in Table 2.1-7b.

A consideration of Fig. 2.1-14 will indicate that since states (3) and (4) are uniform flow regions, there the derivatives of the dynamic and thermodynamic quantities are zero. However, at the head and tail of the Q-rarefaction wave the same quantities change discontinuously and their values are shown in Table 2.1-7. Similar discontinuities exist in the derivatives of higher order and illustrate the following important property of characteristic lines: if a uniform state exists beside a non-uniform region, the two are separated by a characteristic line, for example, the head of the Q-rarefaction wave in Fig. 2.1-14. Therefore, despite the fact that the values of u , p , ρ , and T are continuous across this characteristic, their derivatives can be discontinuous. Consequently, the transition from one region to another occurs through characteristic lines where the derivatives of first and higher order can change discontinuously (Ref. 1). (In a real flow any sharp discontinuities would probably be smoothed out by the action of viscosity and heat conduction.)

Tables 2.1-6 and 2.1-7 show that the shape of a given flow-quantity transition profile through a rarefaction wave depends on the initial and final conditions. Also, the extent of the wave in the (x, t) -plane depends on the initial and final states, for example, on states (4) and (3) in Fig. 2.1-14. If state (3) is theoretically a vacuum, then a complete centred Q-rarefaction wave connects states (4) and (3). Under this condition all of the derivatives are discontinuous at the head of the wave, and those of a , u , and M are discontinuous at the tail of the wave. For an incomplete wave ($N < 5$), the derivatives are all discontinuous at the head as well as at the tail of the wave.

Since

$$\left(\frac{\partial}{\partial x}\right)_t = \frac{d}{dN} \left(\frac{\partial N}{\partial x}\right)_t = \frac{1}{a_4 t} \cdot \frac{d}{dN} \quad (38)$$

and

$$\left(\frac{\partial}{\partial t}\right)_x = \frac{d}{dN} \left(\frac{\partial N}{\partial t}\right)_x = -\frac{N}{t} \cdot \frac{d}{dN} \quad (39)$$

the derivatives in Table 2.1-7 could have been rewritten in a somewhat different form in order to illustrate the above remarks. For example,

$$\left(\frac{\partial \rho}{\partial x}\right)_t = -\frac{1}{a_4 t} \cdot \frac{2\rho_4}{\gamma_4 + 1} \left[1 - \frac{\gamma_4 - 1}{\gamma_4 + 1} \left(\frac{x}{a_4 t} + 1\right)\right]^{\frac{3-\gamma_4}{\gamma_4-1}} \quad (40)$$

$$\left(\frac{\partial \rho}{\partial t}\right)_x = \frac{x}{a_4 t^2} \cdot \frac{2\rho_4}{\gamma_4 + 1} \left[1 - \frac{\gamma_4 - 1}{\gamma_4 + 1} \left(\frac{x}{a_4 t} + 1\right)\right]^{\frac{3-\gamma_4}{\gamma_4-1}} \quad (41)$$

It is seen that at the origin, when $t = 0$, the derivatives are discontinuous and must be smoothed out to give a continuous flow through the rarefaction wave. Since the rarefaction wave profiles spread with time, when $t \rightarrow \infty$ their derivatives become vanishingly small. Although the value of the discontinuity $\frac{d}{dN}$ on each characteristic line remains unchanged, as shown in Table 2.1-7, it is important to note from Eqs. (40) and (41) that the derivatives of the physical quantities with respect to x and t will be smaller for any wave whose centre is not located at the origin of the physical (x, t) -plane. Thus, in a schlieren record, a wave which is centred at the physical origin will appear sharper than one which may be centred elsewhere. From Eq. (40) it is seen that for a given $x = x_1$ from the origin where $t = t_1$ and

$$\frac{x}{a_4 t} = -1, \quad \left(\frac{\partial \rho}{\partial x}\right)_t = -\frac{1}{a_4 t_1} \cdot \frac{2\rho_4}{\gamma_4 + 1}$$

is a maximum at this station. As t becomes $> t_1$ and $\frac{x}{a_4 t}$ becomes more positive, $\left(\frac{\partial \rho}{\partial x}\right)_t$ decreases.

It is sometimes of practical importance to obtain very fast temperature changes in a shock tube. From Eq. (28) it is possible to determine the time rate of change of temperature that a particle of gas would experience on passing through a rarefaction wave, i.e.,

$$\frac{dT}{dt} = \frac{dT}{dN} \cdot \frac{\partial N}{\partial t} + u \frac{dT}{dN} \cdot \frac{\partial N}{\partial x}$$

$$\frac{1}{T_4} \frac{dT}{dN} = -2 \left[1 - \frac{1}{\alpha_4} (N + 1) \right] \frac{1}{\alpha_4} \quad (42)$$

$$\frac{\partial N}{\partial t} = -\frac{N}{t} \quad \text{and} \quad \frac{\partial N}{\partial x} = \frac{N}{x}$$

$$\frac{1}{T_4} \cdot \frac{dT}{dt} = \frac{2}{\alpha_4 t} \left[1 - \frac{1}{\alpha_4} (N + 1) \right] \left[N - \frac{2}{\gamma_4 + 1} (N + 1) \right] \quad (43)$$

For

$$\gamma_4 = 1.4, \quad \text{when } N = -1, \quad \frac{dT}{dt} = -\frac{T_4}{3t}; \quad N \rightarrow 5, \quad \frac{dT}{dt} \rightarrow 0$$

Hence, close to the rarefaction wave head, the cooling temperature gradient is very high. For example, if $T_4 = 300^\circ\text{K}$ and $t = 10 \mu\text{sec}$, then

$$\frac{dT}{dt} = -10^7 \text{ }^\circ\text{K/sec.}$$

Some of the above results are summarized in Table 2.1-8 for Q- and P-rarefaction and compression waves as a ready and convenient reference.

2.1.5 Rarefaction and Compression Waves in Imperfect Gases

A simple deviation from the perfect gas flow assumed in Subsecs. 2.1.3 and 2.1.4 occurs when the specific heat is dependent on temperature. It is assumed that the gas is thermally perfect ($p = \rho RT$) but calorically imperfect with $\gamma = \gamma_0 (1 + aT + bT^2 + \dots)$ where γ_0 , a , b , etc., are known gas constants. A further assumption is made that there are no variations in entropy in the flow.

The equations of motion are unchanged, and consequently, for a P-wave,

$$\frac{dx}{dt} = u + a$$

$$\frac{du}{d\rho} = \frac{a}{\rho} \quad (1)$$

and for a Q-wave,

$$\frac{dx}{dt} = u - a \quad (2)$$

$$\frac{du}{d\rho} = \frac{-a}{\rho}$$

From the First Law of thermodynamics and the equation of state,
 $p = \rho RT$,

$$\frac{dT}{d\rho} = \frac{T}{\rho} (\gamma - 1) \quad (3)$$

If $\gamma = \text{constant}$, then the usual relation between ρ and T can be obtained by direct integration $\rho = CT^{1/(\gamma-1)}$. From Eqs. (1) and (3),

$$\frac{du}{dT} = \pm \frac{a}{\rho} \frac{d\rho}{dT} = \pm \frac{1}{\gamma - 1} \sqrt{\frac{\gamma R}{T}} \quad (4)$$

Since $\gamma = \gamma(T)$ was assumed as known analytically or from an experimental curve, Eq. (4) can in principle be integrated and

$$u + f(T) = \text{constant } (C_1) \quad (5)$$

$$u - f(T) = \text{constant } (C_2)$$

Adding and subtracting the above equations shows that along a characteristic line u and T are constant, and from Eqs. (1) and (2) it is seen that the characteristics in the (x, t) -plane are straight lines.

Since $a^2 = \gamma RT$ and

$$2a \frac{da}{dT} = \gamma R + RT \frac{d\gamma}{dT} \cdot \frac{da}{dT}$$

therefore,

$$\frac{dT}{da} = \left(1 - \frac{a}{2\gamma} \cdot \frac{d\gamma}{da} \right) \frac{2a}{\gamma R}$$

Similarly,

$$\frac{du}{d\rho} = \frac{du}{da} \cdot \frac{da}{dT} \cdot \frac{dT}{d\rho}$$

or,

$$du = \pm \frac{2da}{\gamma - 1} \left(1 - \frac{a}{2\gamma} \cdot \frac{d\gamma}{da} \right) \quad (6)$$

From Eq. (6) it is seen that when $\gamma = \text{constant}$, $\frac{du}{da} = \frac{2}{\gamma - 1}$, a constant. That is, the characteristic lines in the (u, a) -plane are also straight lines. However, when $\gamma = \gamma(T)$ these characteristics become curved.

An alternative method for showing the relation between u and p for a perfect gas and for a gas with vibrational excitation is given in Ref. 24. It is shown that when changes in the specific heats are small, that is, $C_p = C_{p4} (1 + \epsilon T)$ for a compression wave where ϵ is a small quantity, then from Eq. (18), Subsec. 2.1.4, for a perfect gas,

$$\frac{u}{a_4} = \frac{2}{\gamma_4 - 1} \left[1 - \left(\frac{p}{p_4} \right)^{\beta_4} \right] \quad (7)$$

becomes,

$$\frac{u}{a_4} = \frac{2}{\gamma_4 - 1} \left[1 - \left(\frac{p}{p_4} \right)^{\beta_4} \phi \right] \quad (8)$$

where $\phi \leq 1$ for a compression wave. Consequently, for the same pressure ratio $\frac{p}{p_4}$, the particle velocity is greater for the variable specific heat case. Similarly for a rarefaction wave $C_p = C_{p4} (1 - \epsilon T)$ and $\phi \geq 1$, and for the same pressure ratio, the particle velocity is less than for the constant specific heat case.

If imperfect or real gas flow tables or Mollier diagrams are available (Refs. 34, 35, and 36), then all the flow properties through rarefaction and compression waves can be determined quite accurately by using graphical integration (Ref. 34b) without having to make any of the above assumptions. This is accomplished by determining the initial entropy of the real gas and then finding the pressure, density, temperature, and speed of sound at a constant entropy for an expansion or compression wave.

The method is illustrated in Figs. 2.1-29 and 2.1-30 (from Ref. 34b), where air is expanded from 100 atmospheres and 300°K to lower values.

Figure 2.1-29 (a) shows that for a given pressure, the real gas temperature is somewhat lower than the perfect gas value.

Figure 2.1-29 (b) indicates that the initial higher sound speed for the real gas is decreased as the expansion proceeds, and finally, at low pressures, the perfect gas sound speed is greater.

From Fig. 2.1-29 (c) it is seen that the density for the same pressure is greater for the real gas, since it is expanded to a lower temperature than the perfect gas over most of the range.

From Eqs. (1) and (2) and the definition of sound speed ($a^2 = dp/d\rho$), one can write

$$\text{for a P-wave} \quad \frac{du}{dp} = \frac{1}{\rho a} \quad (1a)$$

$$\text{for a Q-wave } \frac{du}{dp} = -\frac{1}{\rho a} \quad (2a)$$

The quantity $\frac{1}{\rho a}$ is plotted against p on Fig. 2.1-30 (a). It is seen that the perfect gas values are only slightly greater over the pressure range. A graphical integration of (a) gives the particle velocity directly at a given pressure (since $u = \pm \int \frac{dp}{\rho a}$), and is shown on Fig. 2.1-30 (b). At a given pressure, the particle velocity is greater for the perfect gas than for the real gas in an expansion wave, as noted above. A cross plot of Fig. 2.1-29(b) and Fig. 2.1-30 (b) gives the variation of u with a , and is shown on Fig. 2.1-30 (c). It is seen that for a forward facing rarefaction wave $\frac{du}{da} = -5$ for a perfect gas, whereas for a real gas du/da becomes increasingly larger as the expansion proceeds. It also illustrates the previous remark that for the perfect gas the characteristic lines in the (u, a) -plane are straight, and for the real gas they are curved. The method of obtaining the characteristics in a real gas are discussed in Ref. 22. In addition, it is worth noting that the Riemann invariant

$$P = u + \frac{2a}{\gamma_4 - 1} = \frac{2a_4}{\gamma_4 - 1}$$

for a perfect gas is no longer a constant in a real gas. The deviations noted in Figs. 2.1-29 and 2.1-30 would be very much greater for an expansion from an initially high temperature and low pressure, where the real gas effects are more significant.

It should be noted that the above effects are important only when imperfect gas effects for isentropic flows are noticeable. For shock tube work at ordinary temperatures these effects in a rarefaction wave would be small. However, for expansions from high temperatures, gas imperfections can be quite significant. In addition, when such expansions occur very rapidly (near the focal point of a centred rarefaction wave) the flow along each particle path can no longer be regarded as isentropic (Fig. 2.1-31). Such flows are discussed in Refs. 22, 22a, 22b, 22c, 22d, 22e, 23, and 23a.

It is of interest to use the definition of the sound speed along a particle path as defined in Ref. 22 to illustrate some of the forms it can take in a relaxing gas (agreement on the correctness of this procedure has not been reached; see the discussions in the above noted references).

$$a^2 = \frac{Dp}{Dt} / \frac{D\rho}{Dt} = \left[\frac{D}{Dt} (E + U + RT) / \frac{D}{Dt} (E + U) \right] RT \quad (9)$$

In Eq. (9), $(E + U + RT)$ is the enthalpy, $(E + U)$ the internal energy, E the adjusted portion, and U the lagging part. Their derivatives

define an effective isentropic index for the sound speed, where

$$p = \rho RT$$

$$E = E(T)$$

$$\frac{DU}{Dt} = f(\rho, T, U)$$

$$R = R(\rho, T, U)$$

$$U = \sum U_i \quad (10)$$

The lagging part (i) of the internal energy is designated by (U_i).

The value of a^2 can be found for different cases of lagging specific heat. Consider the case of lagging rotational heat capacity (in practice this would not occur readily, since it only requires a few collisions (2 to 4) for adjustment).

Let

$$\frac{dE}{dT} = C_t \quad \text{and} \quad \frac{dU_r}{d\theta_r} = C_r$$

where θ_r is a temperature typifying U_r . For a perfect diatomic gas $R = R_0$ (a constant), $E = \frac{3}{2} R_0 T$ and $U_r = R_0 \theta_r$.

Therefore,

$$a^2 = \frac{R \frac{DT}{Dt} + T \frac{DR}{Dt} + \frac{D}{Dt} (E + U)}{\frac{D}{Dt} (E + U)} \cdot RT \quad (9b)$$

or

$$a^2 = \frac{5 \frac{DT}{Dt} + 2 \frac{D\theta_r}{Dt}}{3 \frac{DT}{Dt} + 2 \frac{D\theta_r}{Dt}} \cdot R_0 T \quad (11)$$

If $\theta_r = \text{constant}$, then

$$\frac{D\theta_r}{Dt} = 0 \quad \text{and} \quad a^2 = \frac{5}{3} R_0 T \quad (\text{the monatomic value})$$

If $\theta_r = T$, then

$$a^2 = \frac{7}{5} R_0 T \quad (\text{the diatomic value})$$

If θ_v lags T , then intermediate sound speed between the monatomic and diatomic value is obtained.

In the case of lagging vibrational heat capacity for a diatomic gas, $E = \frac{5}{2} R_o T$ and $U_v =$ vibrational energy summed over all modes. Or, $U_v = U_v(\theta_v)$, where $\theta_v =$ vibrational temperature which typifies the vibrational energy, and

$$\frac{DU_v}{Dt} = \frac{DU_v}{D\theta_v} \cdot \frac{D\theta_v}{Dt} = C_{vib} \frac{D\theta_v}{Dt}$$

Substituting in Eq. (11) yields

$$a^2 = \frac{7 \frac{DT}{Dt} + \frac{2}{R_o} C_{vib} \frac{D\theta_v}{Dt}}{5 \frac{DT}{Dt} + \frac{2}{R_o} C_{vib} \frac{D\theta_v}{Dt}} \cdot R_o T \quad (12)$$

If $\theta_v =$ constant, then

$$\frac{D\theta_v}{Dt} = 0 \quad \text{and} \quad a^2 = \frac{7}{5} R_o T$$

When

$$\theta_v = T \quad \text{then,} \quad a^2 = \frac{7 + \frac{2}{R_o} C_{vib}}{5 + \frac{2}{R_o} C_{vib}} \cdot R_o T$$

For a diatomic gas $C_{vib} \rightarrow R_o$ at high T (assuming no other modes) and $a^2 \rightarrow \frac{9}{7} R_o T$.

Similarly, for a dissociating gas with vibrational heat capacity lag, if α is the degree of dissociation then $R = (1 + \alpha) R_o$, where R_o is the molecular gas constant per unit mass, and

$$\frac{DR}{Dt} = R_o \frac{D\alpha}{Dt} ; \quad E = \frac{5}{2} (1 - \alpha) R_o T + \frac{3}{2} (2\alpha) R_o T = \left(\frac{5 + \alpha}{2} \right) R_o T$$

$$\frac{DE}{Dt} = \frac{5 + \alpha}{2} R_o \frac{DT}{Dt} + \frac{R_o T}{2} \cdot \frac{D\alpha}{Dt}$$

$$U = \alpha l_d + U_v(\theta_v) (1 - \alpha)$$

$$\frac{DU}{Dt} = l_d \frac{D\alpha}{Dt} + C_{vib} \frac{D\theta_v}{Dt} (1 - \alpha) - U_v \frac{D\alpha}{Dt}$$

A substitution into Eq. (9b) gives

$$a^2 = \frac{\left[(7 + 3\alpha) \frac{DT}{Dt} + T \frac{D\alpha}{Dt} \left(3 + \frac{21_d}{R_o T} - \frac{2U_v}{R_o T} \right) + \frac{2 C_{vib} (1 - \alpha)}{R_o} \frac{D\theta_v}{Dt} \right]}{\left[(5 + \alpha) \frac{DT}{Dt} + T \frac{D\alpha}{Dt} \left(1 + \frac{21_d}{R_o T} - \frac{2U_v}{R_o T} \right) + \frac{2 C_{vib} (1 - \alpha)}{R_o} \frac{D\theta_v}{Dt} \right]} (1 + \alpha) R_o T \quad (13)$$

It will be noted that when $\alpha = 0$, Eq. (13) becomes identical with Eq. (12), and when $\alpha \rightarrow 1$, $a^2 \rightarrow \frac{5}{3} (2R_o)T$. That is, for the atomic gas the gas constant is twice the molecular gas constant.

For example, consider Eq. (11) and assume that θ_r does not follow T instantly when a rarefaction or compression wave passes over a gas, but maintains the temperature T_1 for a few collisions. Then $\theta_r = T_1$ and $a^2 = \frac{5}{3} R_o T$. This implies that the head (H) of the rarefaction wave (R) (Fig. 2.1-31) starts out from the origin (O) with a sound speed appropriate to a monatomic gas, and then the speed decreases to the equilibrium value at the particle path (d), where flow changes are now very gradual. That is, particle paths (a), (b), and (c) have diminishing entropy changes, and for particles (d) and beyond, the flow is isentropic. For the compression wave, the entropy increases as the shock is approached, and the head (H) of the wave (CW) speeds up as it approaches the shock wave. Whether the head speeds up to the monatomic sound speed will depend on whether or not the compression wave which is steepening to form the shock wave is strong enough to yield a sharp or diffuse type of shock wave (Subsec. 2.2.2). If a sharp shock is formed, then the head will speed up until it has achieved the monatomic sound speed. If the shock is diffuse, this would not occur and would be similar to the case of a rarefaction wave which is not centered at the physical origin, and changes along a particle path may be small enough to avoid relaxation effects.

Some special cases may be derived from Eq. (13) for a diatomic gas.

1. If the chemical reaction rate or change in dissociation is very small, the composition is fixed or frozen, i.e., α is constant across a sound wave. If in addition vibration does not change, then the sound speed is one of frozen composition and frozen vibration. From Eq. (13),

$$a^2 = \left(\frac{7 + 3\alpha}{5 + \alpha} \right) (1 + \alpha) R_o T \quad (14)$$

or

$$a^2 = \frac{4 + 3Z}{4 + Z} \cdot Z R_o T \quad (14a)$$

2. If the vibrational degrees do participate at their classical value of $R_o T$ when the translational temperature is high,

$$C_{vib} = R_o$$

and

$$a^2 = \left(\frac{9 + \alpha}{7 - \alpha} \right) (1 + \alpha) R_0 T \quad (15)$$

or

$$a^2 = \frac{8 + Z}{8 - Z} \cdot Z R_0 T \quad (15a)$$

3. If the chemical reaction rates and the rotational degrees can follow the changes across a sound wave and the vibrational degree cannot, then (from Eqs. (B-25) and (B-26), Supplement B)

$$a^2 = \frac{C_p}{C_v} \cdot \frac{2}{2 + \alpha - \alpha^2} (1 + \alpha) R_0 T \quad (16)$$

where C_p and C_v are evaluated with fixed vibrational energies along an isentrope.

4. If the vibrational degrees also can follow the change across a sound wave, then complete equilibrium exists, and

$$a^2 = \frac{C_p}{C_v} \cdot \frac{2}{2 + \alpha - \alpha^2} (1 + \alpha) R_0 T \quad (17)$$

where C_p and C_v now include the change in the vibrational energy.

The above definitions of sound speed are quite useful when dealing with flows through shock waves and rarefaction waves (Ref. 24b). They apply to nonstationary flows in a shock tube or stationary flows over a model where these waves exist and relaxation effects occur.

For example, consider Fig. 2.1-32, where the flow over a model in a shock tube is illustrated schematically. Behind the moving shock wave (S) in the quasi-steady region (2), equilibrium is established after a relaxation distance (L). Relaxation effects can occur in region (3), through the rarefaction fan and in state (4), depending on whether or not the flow time through a wave element along a streamline (τ_f) is very much greater or less than the equilibrium time (τ_e) for external, internal, and chemical degrees of freedom (Supplement C).

2.2 Plane Shock Waves

In Subsecs. 2.1.3 and 2.1.4, it was shown that a compression wave generated by a piston in a duct of constant area steepens to form a plane shock wave. The properties of the shock wave now will be considered in some detail. It can be noted that the shock relations to be derived also apply locally without restriction across spherical or cylindrical shocks.

2.2.1 Shock Waves in Perfect Gases

In its simplest form the shock front in a perfect gas is regarded as a discontinuity across which changes occur in the dynamic and thermodynamic flow quantities (Fig. 2.2-1). In real flows viscosity and heat conduction change the discontinuity into a thin front (of the order of a few molecular mean free paths thick, see Ref. 26) through which a rapid but continuous transition in velocity, pressure, density, and temperature takes place (Fig. 2.2-2). A further and much greater thickening of the shock front takes place whenever relaxation phenomena occur in imperfect gases (Subsec. 2.2.2). If viscous and diabatic effects are assumed to act within the transition front only, then regions (1) and (2) can be considered as isentropic, one-dimensional states (behind the shock wave a boundary layer is formed in a real flow and the flow is no longer strictly one-dimensional). The equations of motion of one-dimensional steady flow are as follows:

Continuity equation

$$\frac{d}{dx} (\rho v) = 0 \quad (1)$$

Momentum equation

$$\frac{d}{dx} (\rho v^2 + p - \frac{4}{3} \mu \frac{dv}{dx}) = 0 \quad (2)$$

Energy equation

$$\rho v T \frac{dS}{dx} = \rho v \frac{dQ}{dx} = \rho C_v v \frac{dT}{dx} + p \frac{dv}{dx} = \frac{4}{3} \mu \left(\frac{dv}{dx} \right)^2 + \frac{d}{dx} \left(k \frac{dT}{dx} \right) \quad (3a)$$

Alternately,

$$\frac{d}{dx} \left[\rho v \left(C_p T + \frac{1}{2} v^2 \right) - \frac{4}{3} \mu v \frac{dv}{dx} - k \frac{dT}{dx} \right] = 0 \quad (3b)$$

The energy equation as given in Eq. (3a) is a restatement of the First Law of thermodynamics. It is useful in showing the terms that contribute to the entropy production in a shock wave. The form given in Eq. (3b) is the usual one which contains the enthalpy and kinetic energy terms.

Equation of state for a perfect gas

$$p = \rho \frac{R}{m} T = \rho R T \quad (4)$$

where $R = C_p - C_v$, a constant.

Entropic equation of state

$$p = A \rho^\gamma \quad (5)$$

where $A = \frac{p_0}{\rho_0^\gamma} \cdot e^{\frac{s-s_0}{C_v}}$, a constant for isentropic flow.

For all values of x ,

$$\rho v = C_1 \quad (6)$$

$$p + \rho v^2 - \frac{4}{3} \mu \frac{dv}{dx} = C_1 C_2 \quad (7)$$

$$\rho v \left(C_p T + \frac{1}{2} v^2 \right) - \frac{4}{3} \mu v \frac{dv}{dx} - k \frac{dT}{dx} = C_1 C_3 \quad (8)$$

where C_1, C_2, C_3 are constants that can be evaluated in terms of a known state (1) ahead of the shock wave, and where

$$\left(\frac{dv}{dx} \right)_1 = 0, \quad \left(\frac{dT}{dx} \right)_1 = 0$$

Therefore,

$$C_1 = \rho_1 v_1$$

$$C_1 C_2 = p_1 + \rho_1 v_1^2 \quad (9)$$

$$C_3 = C_p T_1 + \frac{1}{2} v_1^2$$

When the viscous diabatic equations (Eqs. (6) to (9)) are solved for the shock front (Refs. 26 and 26a to 26c), a continuous transition front is obtained which is shown schematically in Fig. 2.2-2. The thickness of this front is considered in detail in Ref. 26. From Eq. (3), if k is treated as a constant (just to indicate the physical effects, e.g., for a weak shock front) it can be shown that the contribution to the entropy production by d^2T/dx^2 is positive when there is a net heat flow into the element and negative when it flows out. Consequently, the curves of entropy and total enthalpy

$$\frac{d}{dx} \left(C_p T + \frac{1}{2} v^2 \right) = \frac{dh_0}{dx} = T \frac{dS}{dx} + \frac{4}{3} \frac{\mu}{\rho} \frac{d^2v}{dx^2}$$

have a maximum value. The final result is a net increase in entropy (in accordance with the Second Law of thermodynamics) but there is no change in the total enthalpy of the states separated by the shock. That is, the heat which is generated remains within the shock front.

If the conditions that $\frac{dv}{dx} = 0$ and $\frac{dT}{dx} = 0$ are also applied to state (2) downstream from the shock wave, then Eqs. (6), (7), and (8) reduce to algebraic form and are known as the Rankine-Hugoniot equations for a normal shock wave. The resulting algebraic equations are

$$\rho_2 v_2 = \rho_1 v_1 \quad (10)$$

$$p_2 + \rho_2 v_2^2 = p_1 + \rho_1 v_1^2 \quad (11)$$

$$c_p T_2 + \frac{1}{2} v_2^2 = c_p T_1 + \frac{1}{2} v_1^2 \quad (12a)$$

or

$$h_2 + \frac{1}{2} v_2^2 = h_1 + \frac{1}{2} v_1^2 \quad (12b)$$

$$\frac{p_2}{p_1} = \frac{1 - \frac{\gamma - 1}{\gamma + 1} \cdot \frac{\rho_1}{\rho_2}}{\frac{\rho_1}{\rho_2} - \frac{\gamma - 1}{\gamma + 1}} \quad (13)$$

$$\frac{s_2 - s_1}{C_v} = \ln \left[\frac{p_2}{p_1} \left(\frac{\rho_1}{\rho_2} \right)^\gamma \right] \quad (14)$$

$$e_2 - e_1 = \frac{1}{2} (p_2 + p_1) \left(\frac{1}{\rho_1} - \frac{1}{\rho_2} \right) \quad (15)$$

$$h_2 - h_1 = \frac{1}{2} (p_2 - p_1) \left(\frac{1}{\rho_1} + \frac{1}{\rho_2} \right) \quad (16)$$

The ratios $\frac{p_2}{p_1}$ and $\frac{\rho_1}{\rho_2}$ may be expressed in terms of shock wave Mach number $M_s = \left(\frac{v}{a} \right)_1 = M_{11}$, and it can be shown that $S_2 \geq S_1$ only for $M_s \geq 1$.

A comparison in series form of Eq. (13) with the isentropic relation

$\frac{p_2}{p_1} = \left(\frac{\rho_2}{\rho_1} \right)^\gamma$ indicates that they differ only in the third order term $\left(\frac{\rho_2 - \rho_1}{\rho_1} \right)^3$, showing that for a very weak disturbance the two expressions are equivalent.

For a shock wave moving at speed w into gas at rest, $v_1 = w$ and $v_2 = w - u_2$, where u_2 is the flow speed induced behind the shock wave. From Eqs. (10) and (11)

$$\rho_1 w = \rho_2 (w - u_2) \quad (17)$$

$$\rho_1 w^2 + p_1 = \rho_2 (w - u_2)^2 + p_2 \quad (18)$$

or

$$w = \sqrt{\frac{\rho_2}{\rho_1} \cdot \frac{(p_2 - p_1)}{(\rho_2 - \rho_1)}} \quad (19)$$

$$u_2 = \sqrt{\frac{(\rho_2 - \rho_1)(p_2 - p_1)}{\rho_1 \rho_2}} \quad (20)$$

$$\frac{w}{u_2} = \frac{w/a_1}{u_2/a_1} = \frac{w_{11}}{u_{21}} = \frac{\rho_2/\rho_1}{\rho_2/\rho_1 - 1} = \frac{\Gamma_{21}}{\Gamma_{21} - 1} \quad (21)$$

$$\frac{\rho_2}{\rho_1} = \Gamma_{21} = \frac{w}{w - u_2} = \frac{w_{11}}{w_{11} - u_{21}} \quad (22)$$

$$\frac{p_2}{p_1} = P_{21} = 1 + \frac{w u_2}{RT_1} = 1 + \gamma w_{11} u_{21} \quad (23)$$

Therefore, from a measurement of the shock velocity w and particle velocity u_2 the pressure and density relation (Hugoniot) for the state behind the shock wave can be determined (Ref. 27). It is seen from Eq. (23) that when

$$\rho_2 \rightarrow \rho_1, \quad p_2 - p_1 \rightarrow \Delta p \quad \text{and} \quad \rho_2 - \rho_1 \rightarrow \Delta \rho$$

or

$$w \rightarrow a_1 = \sqrt{\Delta p / \Delta \rho}$$

That is, in the limit a weak shock becomes a sound pulse. In this case $u_2 \rightarrow 0$, i.e., there is no mass motion behind a Mach wave.

From Eq. (13) it is seen that $P_{21} \rightarrow \infty$ when $\frac{\rho_1}{\rho_2} \rightarrow \frac{\gamma - 1}{\gamma + 1}$, that is, in the limit for strong shock waves

$$\Gamma_{21} = \frac{\rho_2}{\rho_1} \rightarrow \frac{\gamma + 1}{\gamma - 1} \quad (22)$$

Substituting this value in Eq. (21) for strong shocks

$$\frac{w_{11}}{u_{21}} \rightarrow \frac{\gamma + 1}{2} \quad (23)$$

or

$$\frac{v_{21}}{w_{11}} = \frac{w_{11} - u_{21}}{w_{11}} \rightarrow \frac{\gamma - 1}{\gamma + 1} \quad (23a)$$

A substitution of Eq. (23) into Eq. (21) yields, for strong shocks,

$$P_{21} = 1 + \frac{2\gamma}{\gamma + 1} w_{11}^2 \approx \frac{2\gamma}{\gamma + 1} w_{11}^2 \quad (24)$$

$$T_{21} = \frac{P_{21}}{\rho_{21}} = \frac{2\gamma}{\gamma + 1} w_{11}^2 \frac{\gamma - 1}{\gamma + 1} = \frac{2\gamma(\gamma - 1) w_{11}^2}{(\gamma + 1)^2} \quad (25)$$

$$A_{21} = w_{11} \sqrt{2\gamma(\gamma - 1)} / (\gamma + 1) \quad (26)$$

$$M_2 = \frac{u_{21}}{A_{21}} = \frac{u_{21}}{w_{11}} \cdot \frac{\gamma + 1}{\sqrt{2\gamma(\gamma - 1)}} = \sqrt{\frac{2}{\gamma(\gamma - 1)}} \quad (27)$$

For the case of air, e.g., with $\gamma = 1.4$, $M_2 \rightarrow 1.89$ as $P_{21} \rightarrow \infty$. It is worth noting that $1 \leq \gamma \leq 5/3$. Consequently, a monatomic gas (e.g., He) is least compressible ($\rho_2/\rho_1 \rightarrow 4$); and a gas of a complex structure (e.g., SF_6), is most compressible ($\rho_2/\rho_1 \rightarrow 21$). For such a gas, $w_{11}/u_{21} \rightarrow 1$ and $\rho_{21} \rightarrow \rho_1$ if γ remains constant. This condition is not satisfied for strong shocks (Supplement B).

Physical quantities behind a normal shock wave in a perfect gas are plotted in Figs. 2.2-8 to 2.2-13. The same results also apply locally across spherical and cylindrical shocks as well as to the normal velocity components of oblique shock waves since the tangential velocity components remain unchanged.

2.2.2 Shock Waves in Imperfect Gases

The present section deals with shock waves in imperfect gases.* The effects of thermal [$p = \rho RT(1 + \alpha)$] and caloric imperfections

*An alternative development of shock-wave equations in real gases is discussed in Supplement D.

$[C_v = C_v(T, p)]$, and relaxation processes are considered. Entropy increases are encountered considerably beyond that for shock waves in perfect gases at high Mach numbers.

2.2.2.1 Relaxation Effects

When a gas is suddenly compressed by a shock front (Supplement C), thermodynamic equilibrium is disturbed and a relaxation time is required to restore it. If the relaxation time τ is much longer than the times τ_c of molecular collisions ($\tau/\tau_c = Z \gg 1$), then the shock wave becomes quite extended and very marked changes occur in the flow properties through the transition front.

The distinct shock transition fronts shown in Fig. 2.2-3 may occur in a gas (Refs. 11 and 28). Sketch (a) illustrates the adiabatics in the (p, v) -plane. The value of γ_2^* for complete equilibrium is in this case less than the constant value of γ_{1-2} for the so-called "frozen" state, which considers the active degrees as immediately excited, but the inert degrees as unexcited. (Translation and rotation are usually lumped together, since they reach equilibrium in a few collisions.) Consequently, the gas is more compressible ($v = 1/\rho$), and the complete equilibrium adiabatic lies closer to the p -axis. A plot of p against x through the weak shock does not exhibit the familiar Rankine-Hugoniot pressure ratio P_2 discussed in Subsec. 2.2.1. Instead, a smooth transition or a "diffuse" shock occurs. This is analogous to the action of heat conduction and viscosity in the transition front for a perfect gas or frozen γ case. As a matter of fact, relaxation effects can be treated by adding bulk or compression viscosity terms in the Navier-Stokes equations (see Refs. 29, 30, and 31 for example). Such a profile is found when $w < (a_1 \text{ active})$, that is, the compression or weak shock front travels with a velocity less than the sound speed for the Rankine-Hugoniot adiabatic with γ evaluated on the basis of the active degrees. This may be seen in sketch (a) of Fig. 2.2-3. If a discontinuous shock is to be generated then state (2), which lies on the Rankine-Hugoniot adiabatic, must be formed first. Since the tangent ratio for state (1) is

$$\left(\frac{\partial p}{\partial v}\right)_{1-2} / \left(\frac{\partial p}{\partial v}\right)_{1-2}^* > 1$$

then

$$a_{1-2}^2 > a_{1-2}^{2*} \text{ or } w > (a_1 \text{ active})$$

is the condition for the formation of a sharp shock. If $w < (a_1 \text{ active})$ then the sharp front is replaced by a smooth transition. (A gas with a very long relaxation time ($L = w\tau$ is large) would be most useful for observing such a shock. A systematic experimental study of this problem has not been done to date.) This transition is propagated without change of shape. The front is of the order of the vibrational mean free path. The pressure, temperature, and density all increase continuously through the transition front, while the velocity decreases until it has attained the equilibrium sound speed (a_1), and then decreases further until it is subsonic.

An example similar to the case of Fig. 2.2-3 (a) occurs when a subsonic steady flow with $w < a_1$ is decelerated by a small pitot tube (Ref. 32). Along the stagnation streamline, near the pitot orifice, the pressure rises from the free stream static pressure to the equilibrium stagnation pressure, giving a smooth transition curve similar to that in Fig. 2.2-3 (a). The compression is accompanied by an entropy increase even in the decelerated subsonic flow.

Figure 2.2-3 (b) illustrates the condition $w > (a_1 \text{ active})$. A discontinuous jump in pressure occurs from (1) to (2) along the Rankine-Hugoniot adiabetic as the translational and rotational degrees adjust in a few collisions. This is followed by a further, almost exponential, rise in pressure (2^*), as the inert degrees adjust through an increasing number of molecular collisions (see Supplement C).

Another possible shock transition profile that may occur is shown in Fig. 2.2-3 (c). For example, consider a very strong shock wave propagating into a diatomic gas. Immediately behind the front the pressure jumps from (1) to (2). However, if the translational temperature is very high, the collisions are very effective and the gas dissociates almost completely before vibration or any other inert degree can be excited (assuming no electronic excitation or ionization). Under these conditions the gas is nearly monatomic and cannot be compressed to the same extent as a diatomic gas. (The perfect gas limit is $\rho_2/\rho_1 = 4$ for $\gamma = 5/3$ and 21 for $\gamma = 1.1$.) Alternately, there are no new heat sinks available to further cool the gas in order to increase its density. Consequently, the pressure behind the shock front jumps to the perfect gas value and then drops exponentially as the gas reaches thermal equilibrium (2^*). It is of interest to note that two adiabatics cross at (i). Beyond (i), the equilibrium adiabetic now lies to the right of the Rankine-Hugoniot adiabetic, having a constant γ evaluated for the active degrees, and gives rise to a decreasing pressure and density. Analyses for the weak shock case shown in Fig. 2.2-3 (a) may be found in Refs. 11, 19, and 28. An experimental verification can be found in Ref. 28d. Although this is an interesting problem in gas dynamics, it is not of immediate practical importance for actual flight problems. Some recent work on strong shock wave profiles including radiation effects can be found in Refs. 28a to 28c.

Shock waves shown in Fig. 2.2-3 (b) can be readily produced even for weak shock waves in a gas where the inert degrees are already excited (e.g., CO_2 at NTP). The almost discontinuous jump (L_a is very small, $\sim 10^6$ in. at NTP, see Supplement C) from p_1 to p_2 is found from the Rankine-Hugoniot relation Eq. (13), Subsec. 2.2.1, with $\gamma = 7/5$ for any diatomic or linear polyatomic molecule, and with $\gamma = 4/3$ for any other polyatomic molecule. This very interesting result arises from a consideration of the energy equation,

$$C_{pa} T_1 + e_1 + \frac{1}{2} v_1^2 = C_{pa} T_2 + e_1 + \frac{1}{2} v_2^2 \quad (1)$$

where $C_{pa} T_1$ and $C_{pa} T_2$ are the enthalpies excluding the inert internal energy e_1 , which the initial gas possesses to start with. It is seen that this energy cancels out, and since the mass and momentum equations are unchanged, only the γ for the active degrees is involved. It should

be strongly emphasized that the use of $\gamma = \text{constant}$ for the determination of the properties behind the shock applies only to the active portion of the front. It will be seen subsequently that γ ceases to have an important role in calculating the shock properties when inert or imperfect gas effects are present.

Flow Quantities in the Equilibrium Region behind the Shock Wave (Region 2*).--The almost exponential rise in pressure from p_2 to p_2^* is considered in some detail in Refs. 18, 33, and 34a. However, since the equilibrium flow quantities in (2*) are independent of the intervening processes which establish equilibrium between the active and inert degrees of freedom (Ref. 11), it is not necessary to consider the relaxation zone in order to compute the equilibrium (*) values behind the shock front. Consequently, the final equilibrium flow quantities far enough behind the shock front can be determined from a knowledge of the enthalpy or internal energy content of the gas. It is worthwhile illustrating the above by considering the case of CO_2 , as shown in Fig. 2.2-4, for vibrational excitation only (Ref. 34b). It is seen that the equilibrium pressure (p_2^*) and density (ρ_2^*) exceed the Rankine-Hugoniot values based on the active degrees only ($\gamma = 7/5$), while the temperature (T_2^*) is less. The above result is shown in an alternate manner in Fig. 2.2-5a. On the other hand, if for CO_2 $\gamma = 1.3$ is considered as constant throughout the transition, then the Rankine-Hugoniot equations give results roughly intermediate between the active and equilibrium values for density and temperature and a lower value for pressure.

The transition through a shock front for the case where dissociation is also present is shown in Fig. 2.2-5b for the case of oxygen. The sharp change L_1 for the active degrees and the exponential approach to equilibrium for vibration (L_v) and dissociation (L_d) as equipartition of energy takes place are shown. The total shock thickness or relaxation zone is given by L .

The method of obtaining the equilibrium values is as follows. Consider the equations of motion for adiabatic one-dimensional shock flow in stationary co-ordinates ($v_2 = w - u$, $v_1 = w$):

Continuity,

$$\rho_1 v_1 = (\rho_2 v_2)^* \quad (2)$$

Momentum,

$$(p_1 + \rho_1 v_1^2) = (p_2 + \rho_2 v_2^2)^* \quad (3)$$

Energy,

$$\frac{1}{2} v_1^2 + h_1 = \left(\frac{1}{2} v_2^2 + h_2\right)^* \quad (4)$$

Equation (3) may be rewritten as

$$p_{21}^* = 1 + \gamma_1 M_s^2 (1 - \sqrt{v_{21}^*}) \quad (5)$$

where γ has the free stream value, M_s is the free stream or shock Mach number $\frac{w}{a_1}$, and $V_{21}^* = v_2^*/v_1$.

Similarly, from Eq. (4),

$$H_{21}^* = \frac{h_2^*}{h_1} = 1 + \frac{\gamma_1 - 1}{2} M_s^2 (1 - V_{21}^{*2}) \quad (6)$$

The thermally perfect equation of state for an undissociated or non-ionized gas is given by

$$p = \rho \frac{R}{m} T = \rho RT \quad (7a)$$

The thermally imperfect equation of state for a dissociated or ionized gas can be expressed as

$$p = \rho \frac{RT}{m(p, T)} = \rho RT \cdot Z(p, T) \quad (7b)$$

The calorically imperfect equation of state without dissociation or ionization is given by

$$h = h(T) = \int_0^T C_p(T) dT \quad (8a)$$

and with dissociation or ionization by

$$h = h(p, T) = \int_0^T C_p(p, T) dT \quad (8b)$$

where

m = molecular weight of cold gas

$m(p, T)$ = molecular weight of hot gas behind the shock

$$Z(p, T) = \frac{m}{m(p, T)} \geq 1 \quad (9a)$$

or, for a single diatomic gas,

$$Z = [1 + \alpha(p, T)] [1 + x(p, T)] \quad (9b)$$

where

x = degree of ionization

α = degree of dissociation

and Z and h are tabulated in such standard references as Refs. 4, 35, and 36. A plot of $h(p, T)$ for a pure diatomic gas (Ref. 37) is shown schematically in Fig. 2.2-6a. It should be noted that

$$C_p(p, T) = (\partial h / \partial T)_p$$

Consequently, the slope of a curve at any point yields $C_p(p, T)$. For a diatomic gas with only translation and rotation excited, C_p is a constant, that is, $C_p = \frac{dh}{dT} = \frac{7}{2} \frac{R}{m}$ per unit mass. When the gas is fully dissociated (no ionization) it is monatomic and the molecular weight is halved, or $C_p = \frac{dh}{dT} = \frac{5}{2} \frac{R}{m/2} = \frac{5R}{m}$. The dissociation energy l_d is the difference between the $\alpha = 0$ and the $\alpha = 1$ curves and is nearly constant with temperature (except for the effect of vibrational energy). As noted in Supplements B and C, the degree of dissociation α increases with temperature and at a given temperature increases rapidly with decreasing pressure. At the lower pressures especially, the temperature changes are small as l_d increases from zero to its full value and is typical of the variation of enthalpy with temperature of a substance as the latent heat l is added.

The effects produced by the excitation of the inert degrees of freedom can be clearly illustrated on a plot of h with T of which Fig. 2.2-6b is a portion. For a strong shock ($M_s \gg 1$) that can produce dissociation, v_{21}^{*2} is a small quantity, and from Eq. (6)

$$\frac{h_2^*}{h_1} \approx \frac{\gamma_1 - 1}{2} M_s^2 \quad (6a)$$

$$\approx \text{constant}$$

Consequently, for a given $h_2 = h_2^*$ the excitation of the inert degrees means a decrease in the translational temperature ($T_{2c} < T_{2b} < T_{2a}$, where (a), (b), and (c) are assumed as possible equilibrium states). Similarly, $v_2/v_1 = \rho_1/\rho_2 = P_{12} \cdot T_{21} \cdot Z(p_2, T_2)$. Since P_{12} does not change very much and T_{21} decreases rapidly as each new mode becomes excited and outweighs any change in Z ,

$$v_{2c} < v_{2b} < v_{2a}$$

By assuming that the vibrational degree has achieved its full molecular excitation energy of $\frac{R}{m}$ per mode over most of the range for $M_s \gg 1$, the curve of $h = h(T)$ including vibration has a slope of $C_p = \frac{9}{2} \cdot \frac{R}{m}$. Under this rough approximation $\gamma = 9/7$, and

$$\frac{v_{2b}}{v_1} \sim \frac{\gamma - 1}{\gamma + 1} = \frac{1}{8}$$

or

$$\frac{v_{2b}}{v_{2a}} \sim \frac{3}{4} \quad (\text{see Fig. 2.2-6b})$$

The temperature, at a given pressure, at which dissociation starts depends on the dissociation energy of the gas. At 1 atm hydrogen dissociates at approximately 2200°K, oxygen at 2400°K, and nitrogen at 4400°K (Ref. 17). Figure 2.2-6c shows a normalized plot of h/l_d versus T/θ_d which applies approximately for all diatomic gases (see Ref. 3 and also Supplement C).

Six equations (Eqs. (2), (5), (6), (7), (8), and (9)) permit the solution of the six unknowns p_2^* , ρ_2^* , T_2^* , v_2^* , h_2^* , and Z . This cannot be done explicitly and an iteration procedure, which converges quite rapidly, must be used as follows:

1. Compute P_{21}^* and H_{21}^* from Eqs. (5) and (6) for several values of V_{21}^* . (Assume the Rankine-Hugoniot value for a given M_s and γ , as a start and several lower values.) Note that $V_{21}^* = M_s - U_{21}^*$ connects the steady and unsteady velocities behind the shock wave. (V_{21}^* is always subsonic but U_{21}^* can be subsonic or supersonic.)
2. From thermodynamic tables and charts (Refs. 4, 35, and 36) obtain T_2^* and Z corresponding to the values of p_2^* and h_2^* obtained in (1). Compute ρ_2^* from Eq. (7).
3. Plot $\Gamma_{21}^* = \frac{\rho_2^*}{\rho_1}$ obtained from (2) as a function of $\frac{v_1}{v_2^*} = \frac{1}{V_{21}^*}$ assumed originally. The intercept of this curve with the line $\Gamma_{21}^* = \frac{1}{V_{21}^*}$ gives the correct value of V_{21}^* .

A solution of the above equations for oxygen is shown in Fig. 2.2-7 for $T_1 = 218^\circ\text{K}$ and $p_1 = 10^{-2}$ atmospheres (conditions at an altitude $\sim 100,000$ ft).

The contributions by each degree of freedom to temperature and density as the shock Mach number $M_{11} = M_s$ is increased are clearly illustrated. Of special interest are the density curves. Curve (a)

from Fig. 2.2-7 is for the case where $\rho = \rho_2$ and $\frac{\rho_2}{\rho_1} \rightarrow \frac{\gamma+1}{\gamma-1}$ for $\gamma = \frac{7}{5}$, $\frac{\rho_2}{\rho_1} = 6$. If vibration is fully excited $\gamma \rightarrow \frac{9}{7}$ and $\frac{\rho_2}{\rho_1} \rightarrow 8$

as shown for curve (b). It should be noted that the calculation of curve (b) with $\gamma = 9/7$ is a rough approximation, since γ in front of the shock is not $9/7$ but $7/5$ and the Rankine-Hugoniot equations cannot

be applied directly. In curve (c) the density reaches a maximum at $M_s \sim 20$, when $\alpha \sim 80$ per cent, and then the density decreases. The reason for this behaviour is given following Eq. (D-31) in Supplement D.

Of considerable interest is the entropy change ($S_2 - S_1$) across the shock front. In curve (a) from Fig. 2.2-7 the entropy is computed from Subsec. 2.2.1, Eq. (14), using a constant $\gamma = \gamma_1 = 7/5$. As the gas relaxes and achieves its vibrational energy through an increasing number of collisions, the entropy is increased. Assuming that the classical value of RT per mode is achieved, then curve (b) can be plotted on the basis of $\gamma = \gamma_1 = 9/7$. This is a rough approximation, since γ in front of the shock is $7/5$, and Eq. (14) noted above does not apply directly.

Finally, the entropy change is a monotonically increasing function of temperature given by curve (c). It becomes increasingly larger as the degree of dissociation (α) rises, or as the shock intensity increases.

It is seen that at $M_s = 20$, the entropy change in oxygen for an imperfect gas for the given initial conditions is more than double the perfect gas value. A similar result applies to air (see Fig. 2.2-16 for $h = 100,000$ ft). Why this comes about may be seen from the entropy change between state (1) and any of the other states (2)

$$dS = \frac{dh}{T} - \frac{R}{m} d \ln p$$

or

$$S_2 - S_1 = \int_1^2 \frac{dh}{T} (p_2, T) - \frac{R}{m} \ln \frac{p_2}{p_1} \quad (10)$$

$$S_2 - S_1 = \int_1^2 C_p (p_2, T) \frac{dT}{T} - \frac{R}{m} \ln \frac{p_2}{p_1}$$

S is the entropy per unit mass, and the integration takes place over any reversible path. The pressure integration can be done at low temperature T_1 so that dissociation is absent, otherwise $m = m(p, T)$ and the pressure integrator could not be written explicitly. Finally, the temperature integration is performed from T_1 to T_2 at constant p_2 . The reversible path of integration for T or h corresponds to the constant pressure curves of Fig. 2.2-6a for h versus T . The pressure p_2 does not change very much in going from state (a) to state (c) behind a shock front. As a result, the entropy rise on going from state 2(a) to 2(c) is given approximately by (Ref. 37)

$$S_{2c} - S_{2a} = \int_1^{2c} \frac{dh(p_2, T)}{T} - \int_1^{2a} \frac{dh}{T}$$

The integration paths are shown on Fig. 2.2-6b, and it is seen that for an identical change dh , the temperature T for the first integral is always less than or equal to T for the second integral. Since h_2 is the same for both paths, therefore $S_{2(c)} > S_{2(a)}$. This difference grows increasingly larger for a given set of initial conditions. As the strength of the shock increases, $t_{2(c)}$ on the curve of $h_{2(c)}$ changes little with increasing h_2 , whereas $T_{2(a)}$ increases very rapidly with h_2 .

Making use of Eqs. (15), (16), and (19) in Subsec. 2.2.1, and Eq. (7) above, one may express the shock relations in dimensionless form. For $\gamma_1 = 1.4$, they become

$$P_{21}^* = Z \sqrt{\Gamma_{21}^*} T_{21}^* \quad (11)$$

$$\left[\frac{P_{21}^* + 1}{5} \right] \left[1 - \frac{Z T_{21}^*}{P_{21}^*} \right] = \left[E_{21}^* - 1 \right] \quad (12)$$

or

$$\left[\frac{P_{21}^* - 1}{5} \right] \left[1 + \frac{Z T_{21}^*}{P_{21}^*} \right] = \left[H_{21}^* - 1 \right] \quad (13)$$

$$W_{11}^2 = M_1^2 = M_s^2 = \frac{\Gamma_{21}^*}{\gamma_1} \left[\frac{P_{21}^* - 1}{\Gamma_{21}^* - 1} \right] \quad (14)$$

$$U_{21}^* = \left[\frac{P_{21}^* - 1}{\gamma_1} \right] \left[1 - \frac{1}{\Gamma_{21}^*} \right] \quad (15)$$

which again may be solved by an iterative procedure.

The remaining quantities to be found in state (2*) are the sound speed (a_2^*) and the Mach number (M_2^*). Since the usual perfect gas relation for the sound speed ($a^2 = \gamma RT$) no longer applies, it may be determined for an imperfect gas in the following way. From the condition of isentropic flow, $dS = 0$, or

$$de + \rho dv = dh - v dp = 0 \quad (16)$$

Therefore,

$$\left(\frac{\partial h}{\partial e} \right)_s = \frac{\rho}{p} \left(\frac{\partial p}{\partial \rho} \right)_s \quad (17)$$

The speed of sound is now defined with the aid of Eq. (17) and the thermally imperfect equation of state as

$$\left(\frac{\partial p}{\partial \rho}\right)_s = \left(\frac{\partial h}{\partial e}\right)_s \frac{p}{\rho} = \frac{p}{\rho} \gamma^* = \gamma^* Z \frac{R}{m} T = a^2 \quad (18)$$

where

$$\gamma^* = \left(\frac{\partial h}{\partial e}\right)_s = \left(\frac{\partial \ln p}{\partial \ln \rho}\right)_s \quad (19)$$

$$\frac{1}{\gamma^* - 1} = \left(\frac{\partial \ln \rho}{\partial \ln ZT}\right)_s \quad (20)$$

and

$$\frac{\gamma^*}{\gamma^* - 1} = \left(\frac{\partial \ln p}{\partial \ln ZT}\right)_s \quad (21)$$

The isentropic exponent $\gamma^* = \gamma^*(p, T)$ for an imperfect gas is not equal to the usual specific heat ratio (see Supplement B, Eqs. (B-15), (B-23), (B-24), (B-25), and (B-26)). It can be found graphically from Mollier diagrams, by plotting h against e or $\ln \rho$ against $\ln ZT$ along isentropes, and where the local slopes give the value of γ^* . Such results are given in Fig. 2.2-13 from Ref. 40. (Another approach using a numerical method of computing a_2^* can be found in Ref. 41. It might also be noted that for single ionization (up to 25 per cent) γ^* can be determined from Eq. (B-15), Supplement B.

Since U_{21}^* is assumed as known now, therefore the flow Mach number in the quasi-steady region (2*) can be calculated from the expression,

$$M_2^* = \frac{u_2^*}{a_2^*} = \frac{U_{21}^*}{A_{21}^*} \quad (22)$$

A summary of imperfect gas flow properties obtained from graphical methods or those using computation machines is given on Figs. 2.2-8 through 2.2-16. The marked increase in the density ratio (Γ_{21}^*), with increasing shock or flight Mach number (M_s) and decreasing ambient pressure (p_1) is very striking. The same applies to the large decrease in flow temperature ratio (T_{21}^*). The changes in the pressure ratio (P_{21}^*) are not large for different values of p_1 at a given M_s (Fig. 2.2-9a). As a result they are often drawn as a single curve (Figs. 2.2-8c and 2.2-12). The noticeable waviness in the plots of M_s with temperature (T_{21}^*), density (Γ_{21}^*), compressibility factor (Z), sound speed (A_{21}^*), flow Mach number (M_2^*), isentropic index (γ^*), steady

flow velocity ratio $(\frac{v^*}{M_1})$, and entropy change $(S_2^* - S_1)$ is brought about by the addition of the energies of dissociation and first, second, and third degrees of ionization, respectively. (Additional data are given in Tables 2.2-1 to 2.2-4.) Of some interest is the variation of entropy with flight Mach number for given altitudes (Fig. 2.2-16). It is seen that at $M_1 = 19$ the imperfect entropy change increases with altitude until at 200,000 ft it is double the perfect gas value. The rise comes from the larger degrees of dissociation and ionization for a given M_1 with increasing height (or decreasing p_1 , that is, about an order of magnitude for every 50,000 ft). This increase in dissociation and ionization means a larger disturbance (P_{21}^*) , and since the absolute pressure or density is low, the number of collisions and time between collisions ($\tau = Z \tau_c$, Eq. (C-3), Supplement C) for an imperfect gas at higher altitude are both increased for a given Mach number. Consequently, the shock front is more extended, the molecular readjustment to the new state is more severe, and the entropy is greater; or roughly speaking, the entropy varies directly with the total relaxation distance or time under these conditions (Fig. 2.2-16).

Specialization to the Monatomic Gas.--The methods employed in Supplement D for the solution of properties behind strong shock waves in air can be used in a similar manner for monatomic gases. Assuming for simplicity that only single ionization is produced, then the equations of continuity, momentum, energy, and state (Eqs. (2), (3), (4), (7), and (8)), and the Saha equation (Eq. (B-12b), Supplement B) provide six equations for the six unknowns p_2 , ρ_2 , T_2 , h_2 , x and u_2 in state (2*):

$$\rho_1 w = \rho_2 (w - u_2) \quad (23)$$

$$p_1 + \rho_1 w^2 = p_2 + \rho_2 (w - u_2)^2 \quad (24)$$

$$\frac{1}{2} w^2 + h_1 = \frac{1}{2} (w - u_2)^2 + h_2 \quad (25)$$

$$p = (1 + x) \rho \frac{R}{m} T \quad (26)$$

$$h_2 = \frac{5}{2} (1 + x) \frac{R}{m} T + x \frac{1}{m} \quad (27)$$

or

$$h_2 = \frac{5}{2} \cdot \frac{p}{\rho} + x \frac{1}{m} \quad (27a)$$

$$x = \left[3.04 \times 10^6 \frac{p}{T^{5/2}} e^{1.16 \times 10^4 v_i/T} \frac{p_a}{p_i p_e} + 1 \right]^{-1/2} \quad (28)$$

The two main techniques of solving these equations can be used. That is, for the cold gas T_1 , M_s , γ_1 , and β_1 are known. Assume a p_2^* and T_2^* and solve for x , h_2^* , ρ_2^* and V_{21}^* (see Eq. (D-12) in Supplement D). Obtain ρ_1 and p_1 . Cross plot the results for regular intervals of ρ_1/ρ_0 as outlined above. If tables or graphs are available, then the method of iteration using Eqs. (10) to (14) can be used to advantage.

Alternately, given state (1) and w , assume several values of u_2 and get ρ_2 from Eq. (23), p_2 from Eq. (24), h_2 from Eq. (25) and x from Eq. (27a). With the known values of p_2 and T_2 obtain an independent value of x from Eq. (28). Plot the difference of these two values (Δx) against u_2 . When $\Delta x = 0$, the correct value of u_2^* is found. This procedure can be programmed for a computing machine.

Typical results for argon (from Refs. 42 and 43) are shown in Figs. 2.2-17a to 2.2-17f and Figs. 2.2-18a to 2.2-18f.

Some worthwhile approximations (for a gas like H_2 or D_2) can be made for Eqs. (23) to (27) by considering the shock wave as very strong. Consequently p_1 and e_1 ahead of the shock may be neglected. With $p_1 \sim 0$, then from Eqs. (23), (24), and (25),

$$\rho_2 u_2 (w - u_2) = p_2 \quad (29)$$

$$(w - u_2) u_2 + \frac{1}{2} u_2^2 = \frac{p_2}{\rho_2} + e_2 \quad (30)$$

Combining Eqs. (29) and (30),

$$\frac{1}{2} u_2^2 = e_2 \quad (31)$$

The above interesting result shows that for the nonstationary case of state (2), the internal energy and the kinetic energy of the gas per unit mass induced by the shock are equal. Similarly, from Eq. (25), since $(w - u_2)^2$ is small,

$$\frac{1}{2} w^2 = h_2 \quad (32)$$

From Eqs. (29) and (30) or from Eqs. (31) and (32),

$$\rho_2 \left(\frac{1}{2} u_2^2 + e_2 \right) (w - u_2) = p_2 u_2 \quad (33)$$

If the gas is fully dissociated and is approaching full single ionization, then per unit mass, (since $p_2/\rho_2 = \frac{R}{m} T_2 (1 + \alpha) (1 + x)$)

$$e_2 = \frac{3}{2} \frac{R}{m} T_2 2(1 + x) + 2x \frac{l_i}{m} + \frac{l_d}{m} = \frac{3}{2} \frac{p_2}{\rho_2} + 2x \frac{l_i}{m} + \frac{l_d}{m}$$

and as $x \rightarrow 1$

$$e_2 = \frac{3}{2} \cdot \frac{p_2}{\rho_2} + I$$

where

$$I = \frac{l_d + 2l_i}{m}$$

Applying Eq. (29)

$$e_2 = \frac{3}{2} u_2^w - 3e_2 + I$$

or

$$e_2 = \frac{3}{8} u_2^w + \frac{I}{4} = \frac{1}{2} u_2^2 \quad (34)$$

Solving for u_2 (Ref. 44),

$$e_2 = \frac{1}{2} u_2^2 = \frac{1}{2} \left\{ \frac{9}{32} w^2 \left[1 + \left(1 + \frac{32}{9w^2} \right)^{1/2} \right]^2 + \frac{I}{2} \right\} \quad (35)$$

Since

$$\frac{\rho_2}{\rho_1} = \frac{w}{w - u_2}$$

substituting Eq. (34),

$$\frac{\rho_2}{\rho_1} = \frac{4e_2 - I}{e_2 - I} \quad (36)$$

Since the shock velocity is generally one of the quantities that can be measured, and I is known for a given gas (assuming full single ionization), then the properties in state (2) can be found approximately from the above relations. The translational temperatures behind the incident and normal shock waves are found from the equation

$$4\left(\frac{3}{2} k T_2\right) + I' = e_2' \quad (37)$$

where e_2' and I' are the internal and dissociation plus ionization energies per molecule. Since I' is known (see Table 2.1-1 for hydrogen $I' = 2 \times 13.54 + 4.48 = 31.56$ ev) and e_2' can be found from Eq. (35), T_2 can be calculated.

For the reflection of a shock from a rigid wall the mass motion is reduced to zero and the kinetic energy (Eq. 31) is converted into internal energy. For a fully ionized gas like H_2 or D_2 ,

$$6 k T_5 + I' = 2 e_2' \quad (38)$$

and T_5 is found. For example, in order to raise the temperature of a H_2 molecule to 3 ev, nearly full ionization, (1 ev = 11,600 degrees) a shock must impart an internal energy $e_2' \sim 6 \times 3 + 32 = 50$ ev, and a kinetic energy of the same value $(1/2)u^2 = 50$ ev, or a total energy of 100 ev. If the shock is reflected $kT_5 \sim 11$ ev, and a nearly fourfold temperature rise results, which is quite significant.

2.3 The Wave System in a Simple Shock Tube

The nonisentropic shock wave and the isentropic rarefaction and compression waves are the basic transition fronts which can be generated in a shock tube. In addition, a contact front can also be formed. Ideally, it is represented as a discontinuity in temperature, density, entropy, and internal energy. That is, it is a surface separating two thermodynamically different states which are moving at the same flow velocity and pressure. In a real gas, the heat conductivity (and diffusivity) provides a continuous transition front for the changing flow properties. (In Ref. 45, it is shown that this front grows as the square root of time.)

The shock tube problem can be stated as follows: Given an inviscid, perfect gas at high pressure and another at low pressure that are separated by a diaphragm in an infinite tube of uniform cross section, what type of flow is generated when the diaphragm is removed instantaneously? The answer to such a problem and many others can be deduced from a discussion of the transition relations for shocks and isentropic waves by utilizing the (p, u) -plane for their graphical representation (Ref. 1).

2.3.1 Use of the (p, u) -Plane

It was shown in Subsec. 2.2.1 that the following relations apply across an ideal normal shock wave:

$$\rho_2 v_2 = \rho_1 v_1 = m \quad (1)$$

where

$$v_1 = (w - u_1) \quad \text{and} \quad v_2 = (w - u_2)$$

$$p_2 + \rho_2 v_2^2 = p_1 + \rho_1 v_1^2 \quad (2)$$

$$\frac{\rho_2}{\rho_1} = \frac{\frac{\gamma-1}{\gamma+1} + \frac{p_2}{p_1}}{\frac{\gamma-1}{\gamma+1} \cdot \frac{p_2}{p_1} + 1} = \frac{v_1}{v_2} \quad (3)$$

The above may be recomined to give

$$\frac{p_2 - p_1}{v_2 - v_1} = -m \quad (4)$$

$$\frac{p_2 - p_1}{\frac{1}{\rho_1} - \frac{1}{\rho_2}} = m^2 \quad (5)$$

$$u_2 = u_1 \pm \theta_1(p_2) \quad (6)$$

where

$$\theta_1(p_2) = (p_2 - p_1) \left(\frac{2}{\rho_1 [(\gamma - 1)p_1 + (\gamma + 1)p_2]} \right)^{1/2} \quad (7)$$

or

$$\theta_1(p_2) = -\theta_2(p_1) = (p_1 - p_2) \left(\frac{2}{\rho_2 [(\gamma - 1)p_2 + (\gamma + 1)p_1]} \right)^{1/2} \quad (8)$$

The equations are plotted in Fig. 2.3-1. The positive sign applies to shock waves facing in the positive x-direction \bar{S} (forward facing or P-wave). A forward facing wave is one in which the particles enter it from right to left. The opposite is true for a backward facing or Q-wave \bar{S} . For example, by considering the particular state (2) shown in the sketch, it is seen that this unknown state (2) is connected to the known state (1) on its right, by a forward facing shock wave (\bar{S}).

In a similar manner for a rarefaction wave (Subsec. 2.1.3),

$$u_2 \pm \frac{2a_2}{\gamma - 1} = u_1 \pm \frac{2a_1}{\gamma - 1} \quad (9)$$

$$u_2 = u_1 \pm \psi(p_2) \quad (10)$$

where

$$\psi_1(p_2) = \frac{2a_1}{\gamma - 1} \left[\left(\frac{p_2}{p_1} \right)^{\frac{\gamma-1}{2\gamma}} - 1 \right] \quad (11)$$

or

$$\psi_2(p_1) = \frac{2a_2}{\gamma - 1} \left[1 - \left(\frac{p_1}{p_2} \right)^{\frac{\gamma-1}{2\gamma}} \right] \quad (12)$$

These curves are plotted in Fig. 2.3-2.

By combining Figs. 2.3-1 and 2.3-2, the two diagrams on Figs. 2.3-3 and 2.3-4 are obtained.

This combination is justified, since at the point of intersection (1),

$$\theta_1'(p_1) = \psi_1'(p_1) = \sqrt{\frac{1}{\gamma p_1 \rho_1}}$$

and

$$\theta_1''(p_1) = \psi_1''(p_1) = -\frac{\gamma + 1}{2} \cdot \frac{1}{(\gamma p_1)^{3/2} \cdot \rho_1^{1/2}}$$

and the curves join at (1) in a smooth manner. Although

$$\theta_1'''(p_1) \neq \psi_1'''(p_1)$$

this has little effect on a physical flow.

These diagrams may now be applied to the shock tube problem in the following manner. Given a shock tube as shown in Fig. 2.3-5, which has two gaseous states (4) and (1) separated by a diaphragm such that $p_4 > p_1$ and $u_4 = u_1 = 0$ at $t = 0$, plot the two states in the (p, u) -plane and draw the waves for the left state (4) and the right state (1) as shown in Fig. 2.3-6.

States of the type (2*) (Fig. 2.3-7(b)) are impossible because the two waves are approaching. This implies the existence of a pressure discontinuity at infinity at $t = 0$, and is contrary to the initial condition that at $t = 0$ the pressure discontinuity is at the origin. The only physically possible solution is that given by state (2) (Fig. 2.3-7(a)), that is, when the diaphragm is ruptured a shock moves into the low pressure state (1) and a rarefaction wave into the high pressure state (4), and a new state (2) is formed such that $p_4 > p_2 > p_1$ and $u_2 > u_4 = u_1 = 0$. It will be noted that nothing is learned about the possibility of the formation of a contact surface from the (p, u) -plane because across the contact surface p and u were assumed equal. Its existence is deduced from entropy considerations of the shock and rarefaction waves. Thus, so far as the (p, u) -plane

is concerned, states (2) and (3) are equivalent. The ideal wave system and quasi-steady states (2) and (3) that are produced in a shock tube are shown in the (x, t) -plane on Fig. 2.3-8.

The (p, u) -plane method will be applied subsequently to the analysis of other wave interactions in one-dimensional nonstationary flow. Its validity has been well established by numerous experiments (Ref. 46).

2.3.2 Basic Equations for the Wave System and Flow Quantities in Perfect Inviscid Gases

In Subsec. 2.3.1 it was shown that the wave system in a simple shock tube can be represented ideally as in Fig. 2.3-8. At $t = 0$ the diaphragm is at $x = 0$ and separates two infinite tubes (4) and (1) containing gases of different thermodynamic state, which are at rest and in thermal equilibrium. The diaphragm is ruptured at $t = 0$, and the position of the waves at any subsequent time $t = t_1$ is obtained from the (x, t) -plane as illustrated. The states (3) and (2) as predicted from the (p, u) -plane analysis in the previous section have equal pressure and particle velocity. The (p, u) -plane analysis did not predict the existence of a contact surface since across it p and u are constant. A contact surface must be assumed for the coexistence of the two states (3) and (2) which were formed by two different processes and have different densities, temperatures, internal energies, and entropies. The states (3) and (2) are assumed to be uniform since changes of state occur through the waves.

The basic shock tube problem is to find the unknown flow parameters in states (3) and (2) in terms of the known quantities in the initial states (4) and (1). This is done by matching the pressures and velocities across the contact surface as a result of expansion through the rarefaction wave and compression by the shock wave, that is,

$$u_3 = u_2 \quad (1)$$

$$p_3 = p_2 \quad (2)$$

For a backward facing or Q-rarefaction wave (Subsec. 2.1.4)

$$\frac{u_3}{a_4} = \frac{2}{\gamma_4 - 1} \left[1 - \left(\frac{p_3}{p_4} \right)^{\frac{\gamma_4 - 1}{2\gamma_4}} \right] \quad (3)$$

For a forward facing or P-shock wave (Subsec. 2.3.1)

$$\frac{u_2}{a_1} = \left(\frac{p_2}{p_1} - 1 \right) \left(\frac{2}{\gamma_1 [(\gamma_1 + 1) \frac{p_2}{p_1} + (\gamma - 1)]} \right)^{1/2} \quad (4)$$

Consequently, there are four equations for the four unknowns, u_3 , u_2 , p_3 , and p_2 . It should be noted that, in general, $\gamma_4 \neq \gamma_1$, as the gas in the chamber may be different from the gas in the channel.

Equations (1) and (4) have the following dimensionless forms:

$$u_{34} = A_{14} u_{21} \quad (5)$$

$$p_{34} = p_{14} p_{21} \quad (6)$$

$$u_{34} = \frac{1}{\gamma_4 \beta_4} \left(1 - p_{34}^{\beta_4} \right) \quad (7)$$

$$u_{21} = \frac{p_{21} - 1}{\gamma_1 \sqrt{\beta_1 (\alpha_1 p_{21} + 1)}} \quad (8)$$

and they may be combined to form a relation between the shock pressure ratio p_{21} and the known parameters p_{14} , A_{14} , γ_4 , and γ_1 , which may be written as

$$(p_{14} p_{21})^{\beta_4} + \frac{\gamma_4}{\gamma_1} \beta_4 A_{14} (p_{21} - 1) \sqrt{\frac{1}{\beta_1 (\alpha_1 p_{21} + 1)}} - 1 = 0 \quad (9)$$

Since

$$A_{14} = \frac{\gamma_1}{\gamma_4} \sqrt{\frac{\beta_1}{\beta_4}} E_{14} \quad (10)$$

Equation (9) can be reduced to a simpler form,

$$(p_{21} - 1) \sqrt{\frac{\beta_4 E_{14}}{\alpha_1 p_{21} + 1}} + (p_{14} p_{21})^{\beta_4} - 1 = 0 \quad (11)$$

It should be noted that this step is justified as long as no dissociation or ionization occurs in a gas; otherwise it is imperative to use the sound speed ratio (see Supplement E), and A_{14} is therefore a more basic parameter than the internal energy ratio E_{14} .

Equation (11) has a complex algebraic form and an explicit solution, $P_{21} = P_{21}(P_{14}, E_{14}, \gamma_4, \gamma_1)$, has not been obtained. The following form is convenient for plotting curves of Eq. (11):

$$P_{14} = \frac{1}{P_{21}} \left[1 - (P_{21} - 1) \sqrt{\frac{\beta_4 E_{14}}{\alpha_1 P_{21} + 1}} \right]^{1/\beta_4} \quad (12)$$

Equation (12) gives a relation between the strength of the shock wave (P_{21}) produced in a shock tube as a function of the pressure ratio across the diaphragm (P_{14}), the specific heat ratios (γ_4, γ_1), and the internal energy ratio (E_{14}) of the gases used in the channel and the chamber.

Some interesting mathematical limits may be derived from Eq. (12). When $P_{14} = 0$ (i.e., $p_1 \rightarrow 0$ or $p_4 \rightarrow \infty$, conditions which are not realistic physically),

$$\left[P_{21} \right]_{P_{14}=0} = 1 + \frac{\alpha_1}{2\beta_4 E_{14}} + \sqrt{\frac{1}{\beta_4 \beta_1 E_{14}} + \left(\frac{\alpha_1}{2\beta_4 E_{14}} \right)^2} \quad (13)$$

This is the relation for the strongest possible shock wave that may be produced in a simple shock tube with an infinite pressure ratio P_{14} across the diaphragm. It is seen that the strongest waves are produced for small values of

$$E_{14} = \frac{(C_v T)_1}{(C_v T)_4} = KT_{14}$$

and immediately suggests the use of a combination such as H_2/A , H_2/N_2 , or He/Air for the production of strong shock waves even at room temperature (E_{14} is 0.0309, 0.0735, and 0.231 for the three combinations respectively; see Tables 2.3-1 and 2.3-2).

For example, using the combination Air/Air at room temperature, $E_{14} = 1$ and $\left[P_{21} \right]_{P_{14}=0} = 44$; for He/Air at room temperature, $E_{14} = 0.231$ and $\left[P_{21} \right]_{P_{14}=0} = 132$; and for H_2/N_2 at room temperature, $E_{14} = 0.0735$ and $\left[P_{21} \right]_{P_{14}=0} = 574$. The advantage of using such gas combinations for the production of strong waves is quite evident.

It may be worth noting that when $E_{14} \leq 1$, a good approximation to Eq. (13) is

$$\left[P_{21} \right]_{P_{14}=0} \approx \frac{\alpha_1}{\beta_4 E_{14}} + 1 \quad (14)$$

It will be noted that from Eq. (13), when $E_{14} \rightarrow 0$, $[P_{21}]_{P_{14} \rightarrow 0} \rightarrow \infty$, and when $E_{14} \rightarrow \infty$, $[P_{21}]_{P_{14} \rightarrow 0} \rightarrow 1$. The mathematical limits of $E_{14} = 0$ or $E_{14} = \infty$ are physically impossible since they imply that either T_1 or T_4 have zero or infinite values.

The criteria for strong shock waves are, therefore,

1. A very large diaphragm pressure ratio, $P_{41} \rightarrow \infty$.
2. A gas combination which will give a small energy ratio across the diaphragm, $E_{14} \rightarrow 0$.

A graphical solution of Eq. (12) is shown on Fig. 2.3-9 for the case of Air/Air. It is seen that the curves occupy the region between two straight lines which pass through the point (1, 1). These lines correspond to the theoretical limiting values of E_{14} , that is, when $E_{14} = 0$, $P_{21} = P_{41}$ and when $E_{14} \rightarrow \infty$, $P_{21} = 1$ regardless of the value of P_{41} , and illustrate the previous discussion on the production of strong shock waves. A similar plot is shown on Fig. 2.3-10 for different gas combinations at the same temperature, ($T_{14} = 1$).

Once the shock pressure ratio (P_{21}) has been determined from the given initial conditions in the tube (Eq. 12), all other quantities of the flow may be calculated as follows:

1. Density Ratios

$$\Gamma_{34} = \frac{\rho_3}{\rho_4} = P_{34}^{1/\gamma_4} = [P_{14} P_{21}]^{1/\gamma_4} \quad (15)$$

when

$$P_{14} \rightarrow 0, \quad \Gamma_{34} \rightarrow 0$$

$$\Gamma_{21} = \frac{\rho_2}{\rho_1} = \frac{1 + \alpha_1 P_{21}}{\alpha_1 + P_{21}} \quad (16)$$

when

$$P_{21} \rightarrow \infty, \quad \Gamma_{21} \rightarrow \alpha_1$$

2. Speed of Sound and Temperature Ratios

$$A_{34} = \frac{a_3}{a_4} = \left[\frac{T_3}{T_4} \right]^{1/2} = T_{34}^{1/2} = P_{34}^{\beta_4} = [P_{14} P_{21}]^{\beta_4} \quad (17)$$

when

$$P_{41} \longrightarrow 0, \quad A_{34} \longrightarrow 0$$

$$A_{21} = \frac{a_2}{a_1} = \left[\frac{T_2}{T_1} \right]^{1/2} = T_{21}^{1/2} = \left[\frac{P_{21}(\alpha_1 + P_{21})}{1 + \alpha_1 P_{21}} \right]^{1/2} \quad (18)$$

when

$$P_{21} \longrightarrow \infty, \quad A_{21} \longrightarrow \infty, \quad T_{21} \longrightarrow \infty$$

3. Velocity of the Shock Wave or Shock Mach Number

By definition, for stationary flow,

$$M_s = \frac{|v_1|}{a_1} = \frac{|u_1 - w_1|}{a_1} = \frac{w_1}{a_1} = w_{11}$$

since

$$\Gamma_{21} = \frac{1 + \alpha_1 P_{21}}{\alpha_1 + P_{21}} = \frac{\alpha_1}{1 + \frac{\alpha_1 - 1}{M_s^2}}$$

when

$$P_{21} \longrightarrow \infty \text{ or } M_1 \longrightarrow \infty, \quad \Gamma_{21} \longrightarrow \alpha_1$$

therefore

$$w_{11} = M_s = [\beta_1(1 + \alpha_1 P_{21})]^{1/2} \quad (19)$$

when

$$P_{21} \gg 1, \quad w_{11}^2/P_{21} \longrightarrow \alpha_1 \beta_1 \sim 1, \quad \text{or } P_{21} \sim w_{11}^2$$

4. Particle Velocity or Contact Surface Velocity

$$U_{21} = \frac{u_2}{a_1} = \frac{(P_{21} - 1)}{\gamma_1 [\beta_1(\alpha_1 P_{21} + 1)]^{1/2}} \quad (20)$$

when

$$P_{21} \longrightarrow \infty, \quad U_{21} \longrightarrow \infty$$

For strong shocks

$$P_{21} \sim \frac{\gamma(\gamma - 1)}{2} U_{21}^2, \quad \frac{W_{11}}{U_{21}} = \frac{\gamma_1 \beta_1 (\alpha_1 P_{21} + 1)}{P_{21} - 1} \quad (21)$$

when

$$P_{21} \rightarrow \infty, \quad \frac{W_{11}}{U_{21}} \rightarrow \alpha_1 \beta_1 \gamma_1 = (\gamma_1 + 1)/2$$

$$U_{34} = \frac{u_3}{a_4} = \frac{1}{\gamma_4 \beta_4} \left[1 - (P_{14} P_{21})^{\beta_4} \right] = A_{14} U_{21} \quad (22)$$

when

$$P_{14} \rightarrow 0, \quad U_{34} \rightarrow 1/\alpha_4 \beta_4 = 2/(\gamma_4 - 1)$$

5. Speed of Head and Tail of Rarefaction Waves

For a backward facing rarefaction wave the head and tail of the wave have the following characteristic speeds:

$$C_{44}^- = \frac{C_4^-}{a_4} = \frac{u_4 - a_4}{a_4} = -1 \quad (23)$$

$$C_{34}^- = \frac{C_3^-}{a_4} = \frac{u_3 - a_3}{a_4} = U_{34} - A_{34}$$

$$C_{34}^- = \frac{1}{\beta_4 \gamma_4} \left[1 - (P_{14} P_{21})^{\beta_4} \right] - \left[P_{14} P_{21} \right]^{\beta_4}$$

when

$$P_{14} \rightarrow 0, \quad C_{34}^- \rightarrow \frac{1}{\gamma_4 \beta_4} = \frac{2}{\gamma_4 - 1} \quad (24)$$

6. Local Mach Numbers

$$M_3 = \frac{u_3}{a_3} = \frac{U_{34}}{A_{34}} = \frac{1}{\beta_4 \gamma_4} \left[(P_{14} P_{21})^{-\beta_4} - 1 \right] \quad (25)$$

when

$$P_{14} \longrightarrow 0, \quad M_3 \longrightarrow \infty$$

$$M_2 = \frac{u_2}{a_2} = \frac{u_{21}}{a_{21}} = \frac{P_{21} - 1}{\gamma_1 [\beta_1 P_{21} (\alpha_1 + P_{21})]^{1/2}} \quad (26)$$

when

$$P_{21} \longrightarrow \infty, \quad M_2 \longrightarrow \frac{1}{\gamma_1 \sqrt{\beta_1}} = \sqrt{\frac{2}{\gamma_1 (\gamma_1 - 1)}}$$

Some of the above relations may be transformed into an alternate form involving the shock Mach number ($M_s = W_{11}$). For example, the diaphragm pressure ratio,

$$P_{41} = \frac{1}{\alpha_1} \left[\frac{M_s^2}{\beta_1} - 1 \right] \left[1 - \sqrt{\frac{\beta_4}{\beta_1}} E_{14} \left(M_s - \frac{1}{M_s} \right) \right]^{-1/\beta_4} \quad (12a)$$

or

$$P_{41} = \frac{1}{\alpha_1} \left[\frac{M_s^2}{\beta_1} - 1 \right] \left[1 - \frac{\gamma_4 - 1}{\gamma_1 + 1} \cdot \frac{a_1}{a_4} \left(M_s - \frac{1}{M_s} \right) \right]^{-1/\beta_4} \quad (12b)$$

For the special case of Air/Air, $E_{14} = 1$, $\gamma = 7/5$

$$P_{41} = \frac{1}{6} \left[7M_s^2 - 1 \right] \left[1 - \frac{1}{6} \left(M_s - \frac{1}{M_s} \right) \right]^{-7} \quad (12c)$$

$$P_{41} \longrightarrow \infty, \quad \text{when } M_s \longrightarrow 3 + \sqrt{10} = 6.16$$

Similarly,

$$\frac{6M_3}{5 + M_3} = M_s - \frac{1}{M_s} \quad (25a)$$

$$M_3 \longrightarrow \infty \quad \text{when } M_s \longrightarrow 6.16$$

$$M_2 = 5(M_s^2 - 1) \left[(7M_s^2 - 1)(M_s^2 + 5) \right]^{-1/2} \quad (26a)$$

Similar results may be obtained for other gas combinations.

It is of interest to examine the mathematical limits of the above relations for very strong shock waves. The values appear in Table 2.3-2 for three gas combinations in the shock tube. In all cases considered in Table 2.3-2, the diaphragm pressure ratio $P_{41} = p_4/p_1$ is taken as infinite; that is, p_1 is of order zero by comparison with the magnitude of p_4 . For Air/Air, when $E_{14} = 1$, the limiting shock strength $P_{21} = 44$, and the pressure ratio across the rarefaction wave $P_{21} P_{14} = P_{34} = 0$. The speed of the tail of the rarefaction wave in state (3), C_{34} , and the particle velocity in state (2), U_{21} , are both equal to 5, the escape speed (see Eqs. (22) and (24) above). In other words, the tail of the rarefaction wave coincides with the contact surface, and state (3) is non-existent. At a first glance it appears as if the conditions in the shock tube are violated at the contact surface, since on the one hand a complete centred rarefaction wave results from the assumption of $P_{41} \rightarrow \infty$, and on the other hand the results show that a shock wave pressure ratio $P_{21} = 44$ exists. It is recalled that the shock tube equation (Eq. (11)) was developed with the conditions that $p_3 = p_2$ and $u_3 = u_2$ exist at the contact surface. By assuming that $P_{41} = p_4/p_1 \rightarrow \infty$, then $P_{34} = P_{14} P_{21}$ or $p_3/p_4 = p_2/p_4$ has in it an assumption with regard to the order of magnitude, that is, p_2, p_3 , and p_1 are zero by comparison with p_4 ; and this tends to violate the initial conditions that $p_3 = p_2 \neq 0$. Therefore, the results from the basic shock tube equation will apply except for the error in the order of magnitude introduced by $p_4/p_1 \rightarrow \infty$. Thus, even if $p_2/p_1 = 44$, $P_{34} = P_{14} P_{21}$ still applies because p_2/p_4 is also of order zero. Physically, the condition that $P_{41} \rightarrow \infty$ is impossible. It could be achieved by having $p_1 = 0$ and p_4 finite, in which case a complete expansion wave only would result; or else $p_4 \rightarrow \infty$ and p_1 finite, in which case the above discussion applies, that is, a shock is produced such that $p_2 = 44 p_1$, but whose order of magnitude by comparison to p_4 is zero. A centred rarefaction wave is also formed such that p_3 is of order zero by comparison to p_4 , and therefore the complete centred rarefaction wave solution is approached and yields the escape speed as the particle velocity as noted in Table 2.3-2.

If, in addition to $P_{41} \rightarrow \infty$, $E_{14} = 0$, i.e., $T_1 = 0$ or $T_4 \rightarrow \infty$, then the flow quantities are as shown, for the case Air/Air. The interesting limits are for $\Gamma_{21} = \rho_2/\rho_1 \rightarrow 6$ and $M_2 = u_2/a_2 \rightarrow 1.89$ when $P_{21} \rightarrow \infty$. Again, these conditions are not attainable physically. For the case Air/Air, $E_{14} = 0.1$ could be obtained by having $T_1 = 300^\circ\text{K}$ and $T_4 = 3000^\circ\text{K}$. Assuming γ_1 constant, then

$$P_{21} = 422 \quad ; \quad U_{34} = A_{14} U_{21} = 15.8/\sqrt{10} = 5 = C_{34}$$

In this case as well, the tail of the rarefaction wave coincides with the contact surface and they move with the escape speed $\frac{2a_4}{\gamma_4 - 1}$ of the gas in the chamber. At room temperature (or equal temperatures in the chamber and channel) $E_{14} = 1$ for Air/Air, $E_{14} = 0.231$ for He/Air and $E_{14} = 0.0735$ for H_2/N_2 . The great advantage in using the latter two combinations for the production of strong shock waves and high values of the other flow quantities is illustrated in Table 2.3-2. Subsection 4 gives a further discussion of the limitations of the simple shock tube as a generator of strong shock waves. Various modifications to the simple shock tube giving increased shock strength, such as driver gas heating or tube cross-section area change, are considered in Subsec. 4 in detail.

If aerodynamic testing is required in the constant state region (3) and (2), then the best type of gas to be used for the production of high Mach numbers may be obtained by differentiating Eqs. (12), (25), and (26) with respect to the diaphragm pressure ratio (P_{41}), and obtaining the maximum limits when $P_{41} = 1$; that is, when very weak shock waves are produced.

$$\left(\frac{\partial P_{21}}{\partial P_{41}} \right)_{P_{41}=1} = \frac{1}{1 + \sqrt{\frac{\beta_1 E_{14}}{\beta_4}}} = \frac{1}{1 + \sqrt{B_{14} E_{14}}} \quad (27)$$

$$\left(\frac{\partial M_3}{\partial P_{41}} \right)_{P_{41}=1} = \frac{1}{\gamma_4 \left(1 + \sqrt{\frac{\beta_4}{\beta_1 E_{14}}} \right)} = \frac{1}{\gamma_4 \left(1 + \frac{1}{\sqrt{B_{14} E_{14}}} \right)}$$

$$\left(\frac{\partial M_2}{\partial P_{41}} \right)_{P_{41}=1} = \frac{1}{\gamma_1 \left(1 + \sqrt{\frac{\beta_1 E_{14}}{\beta_4}} \right)} = \frac{1}{\gamma_1 \left(1 + \sqrt{B_{14} E_{14}} \right)}$$

where $B_{14} = \beta_1/\beta_4$

A comparison of the above derivatives when $P_{41} = 1$ gives a good indication over most of the range of the important parameters required for the production of strong shock waves and high Mach number flows. The derivative $(\partial P_{21}/\partial P_{41})_{P_{41}=1}$ shows that the greatest increase

in shock strength with an increase in the diaphragm pressure ratio occurs when $E_{14} \rightarrow 0$ (i.e., $P_{21} = P_{41}$, see Fig. 2.3-5). For strong shocks the product $(BE)_{14}$ must be made small by an appropriate choice of a gas combination, e.g., H_2/SF_6 or H_2/A .

On the other hand, the derivative $\left[\frac{\partial M_3}{\partial P_{41}} \right]_{P_{41}=1}$ shows that for the production of a high Mach number flow in state (3), E_{14} should be very large. Thus there is an opposing demand in this case for a gas combination, say A/H_2 or SF_6/H_2 , which will give weak shocks. The reason for this may be seen from a plot of M_3 versus $P_{34} = P_{14} P_{21}$ (Fig. 2.3-11). For the production of a shock wave of reasonable strength (P_{21}) it will require a very much larger diaphragm pressure ratio (P_{41}), when a gas combination is used which has a large value of E_{14} . Hence $P_{34} = P_{14} P_{21}$ is very small, and as a result M_3 is very large. Although the values of γ for real gases do not differ very radically (γ ranges from about 1.1 to 1.66), nevertheless the best result for a high Mach number flow (M_3) is obtained by using a gas combination with a large value of E_{14} and a low value of γ_4 , which also implies a large value of $(BE)_{14}$. For example, the value of $\left[\frac{\partial M_3}{\partial P_{41}} \right]_{P_{41}=1}$ for SF_6/H_2 is 0.804, whereas it is only 0.497 for A/H_2 . In this case the low value of γ and β for SF_6 has a telling effect. Furthermore, the index of refraction of SF_6 is considerably greater than that of A and is advantageous for optical studies of the flow. The above is illustrated on Figs. 2.3-12 and 2.3-13.

Inspection of the equation for the derivative $\left[\frac{\partial M_2}{\partial P_{41}} \right]_{P_{41}=1}$ shows that for high Mach number flows in state (M_2) it is important to use a gas combination with a low value of $(BE)_{14}$ and a low value of γ_1 . Combinations such as H_2/A and H_2/SF_6 are very useful for the production of strong shocks and high Mach number flow behind the shock wave. The combination H_2/SF_6 is much better than H_2/A since it has a higher $\left[\frac{\partial M_2}{\partial P_{41}} \right]_{P_{41}=1}$ value (0.8 and 0.5, respectively). Also for SF_6 , $M_2 \text{ max} = 4.86$ as compared to $M_2 \text{ max} = 1.34$ for argon. However, the combination H_2/A is useful for the production of strong shock waves in a monatomic gas (A). Since it is not affected by dissociation, ionization phenomena may be studied much more readily. The variation of M_2 with P_{14} and E_{14} is shown for Air/Air on Fig. 2.3-14.

Although the above curves are useful for illustrating the range of the parameters involved in the shock tube problem, they cannot be utilized too readily for experimental comparisons. As a result the curves are replotted so that they may be applied to actual problems; Fig. 2.3-15 shows the variation of P_{41} versus P_{21} for the case Air/Air, $T_{14} = 1$. Figure 2.3-16 shows the variation of P_{41} versus P_{21} for He/Air,

$T_{14} = 1$. The relations for the wave speeds in Air/Air as a function of shock pressure ratio (P_{21}) and diaphragm pressure ratio (P_{41}) appear in Figs. 2.3-17 and 2.3-18. The variation of the flow parameters in regions (3) and (2) as a function of shock strength (P_{21}) are shown on Figs. 2.3-19 and 2.3-20. The above graphs make it possible to determine quickly the flow parameters in a shock tube as a function of shock strength P_{21} , diaphragm pressure ratio P_{41} , or shock wave Mach number W_{11} . Similar curves for the case He/Air are shown on Figs. 2.3-21 and 2.3-22. The values of P_{21} , \bar{I}_{21} , U_{21} , and T_2 ($T_1 = 300^\circ\text{K}$) are also plotted against W_{11} in Fig. 2.2-23, as a ready reference for the shock Mach number.

It will be noted that the curves which give the variation of the physical quantities with shock pressure ratio P_{21} for air are not extended beyond $P_{21} = 33$. The reason for this is that the specific heat ratio γ_1 can no longer be assumed as a constant and the properties across the shock front must be found by using the theory with imperfect gas effects.

For the strong shock range, further perfect gas results for shock Mach number (up to 25) versus diaphragm pressure ratio are given in Subsec. 4 for various values of γ_4 and γ_1 , and a range of sound speed ratio A_{41} (Figs. 4.1-1 to 4.1-7).

7. Reynolds Number

In order to compare some of the experimental results obtained in various shock tubes on shock wave attenuation, boundary layer growth, shock-boundary layer interactions, and model tests in the uniform state regions, it is necessary to maintain dynamic similarity, and the flow Reynolds number becomes one of the important non-dimensional parameters. Strictly speaking, this implies that for two flows the Reynolds number for corresponding points in the flow must be identical in order to achieve dynamic similarity. Since the flow in a shock tube is assumed as one-dimensional, a typical length dimension is not readily available, unless the shock thickness or the mean free path is used. (A cross-sectional dimension, boundary layer thickness, the product of a particle transit time and its velocity, or a model dimension, could also be used for actual flows.) However, for any point in the flow the mean free path could be used as a fundamental length parameter and the Reynolds number is given then by the relation

$$R_\lambda = \frac{\rho u \lambda}{\mu} \quad (28)$$

where ρ = gas density

u = mass motion of the gas or the free stream velocity

λ = equilibrium molecular mean free path of the gas

μ = gas viscosity

From the kinetic theory of gases

$$\mu = 0.499 \rho \bar{c} \lambda \sim 0.5 \rho \bar{c} \lambda$$

where \bar{c} = the mean molecular velocity ($\bar{c} = \sqrt{\frac{8}{\pi\gamma}} a$) and

where a = speed of sound of the gas.

Combining the above,

$$R_\lambda = 1.5M, \quad \gamma = 1.4 \quad (29)$$

Hence, for isentropic flow, the Reynolds number at a point depends only on Mach number. The form that the Reynolds number usually takes is

$$Re = \frac{R_\lambda}{\lambda/l} = 1.5 \left(\frac{M}{K} \right) \quad (30)$$

where $K = \lambda/l$, Knudsen number.

Here l = an arbitrary linear dimension which fixes the scale. For most shock tube work the Knudsen number is very small, and in order to compare the Reynolds numbers in the uniform state regions (2) and (3), the Reynolds number per foot is arbitrarily used and is given by $Re/l = \rho u/\mu$. Thus, for state (3),

$$\left(\frac{Re}{l} \right)_3 = \frac{\rho_3 u_3}{\mu_3} \quad (31)$$

or

$$\left(\frac{Re}{l} \right)_3 = \frac{\gamma_4}{\mu_4} \frac{p_1}{a_4} P_{41} P_1 \frac{\Gamma_{34} U_{34}}{T_{34}^{0.76}} \quad (32)$$

where the viscosity as a function of temperature is assumed as

$$\frac{\mu_3}{\mu_4} = T_{34}^{0.76} \quad (33)$$

Similarly,

$$\left(\frac{Re}{l} \right)_2 = \frac{\gamma_1}{a_1} \frac{p_1}{\mu_1} \cdot \frac{\Gamma_{21} U_{21}}{T_{21}^{0.76}} \quad (34)$$

For the case Air/Air, the Reynolds number ratio is

$$\frac{(Re)_3}{(Re)_2} = P_{41} \frac{\Gamma_{34}}{\Gamma_{21}} \left(\frac{T_{21}}{T_{34}} \right)^{0.76} \quad (35)$$

Assuming an initial temperature in the shock tube of 15°C, and a pressure in the channel $p_1 = 1 \text{ mm Hg}$, then

$$T_1 = T_4 = 288^\circ\text{K}$$

$$a_1 = a_4 = 1117 \text{ ft/sec}$$

$$\mu_1 = \mu_4 = 3.7194 \times 10^{-7} \text{ slugs/ft-sec}$$

$$\rho_1 = 3.13 \times 10^{-6} \text{ slugs/cu ft}$$

$$p_1 = 1 \text{ mm Hg}$$

and the variation of the Reynolds number per foot in state (2) and the Reynolds number ratio with diaphragm pressure ratio (P_{41}) is as shown in Table 2.3-3 and plotted in Fig. 2.3-24.

It is seen that even at a low channel pressure ($p_1 = 1 \text{ mm Hg}$) the Reynolds number per foot is sizeable. The Reynolds number per foot in state (3) is considerably greater than in state (2), and the ratio $\frac{(Re)_3}{(Re)_2}$ increases with increasing diaphragm pressure ratio. Thus, by varying the channel pressure (p_1) and the diaphragm pressure ratio (P_{41}), it is possible to get a large range of Reynolds and Mach numbers in a shock tube for aerodynamic testing in the uniform state regions. Although theoretically region (3) has the larger Mach and Reynolds number range, the gas temperature is low; in practice this region passes over the jagged remains of the diaphragm and is found to be quite turbulent. It is therefore not as useful for testing purposes as state (2). It should be noted that the Reynolds number per foot could just as well have been referred to state (4), and a curve similar to Fig. 2.1-27 is obtained.

8. Total Temperatures

The total temperature behind the shock wave may be derived from the energy equation,

$$c_p T_2 + \frac{1}{2} u_2^2 = c_p T_{o2} \quad (36)$$

or

$$T_{o2} = \frac{T_{o2}}{T_2} = 1 + \frac{\gamma_1 - 1}{2} M_2^2 \quad (37)$$

when

$$P_{21} \rightarrow \infty, \quad M_2 \rightarrow \sqrt{\frac{2}{\gamma_1(\gamma_1 - 1)}}$$

or

$$\frac{T_{o2}}{T_2} = \frac{\gamma_1 + 1}{\gamma_1}$$

for

$$\gamma_1 = 1.4, \quad \frac{T_{o2}}{T_2} \rightarrow 1.71$$

For $\gamma = 1.4$, Eq. (37) may be expressed as

$$\frac{T_{o2}}{T_1} = 1 + \frac{1}{3} (w_{11}^2 - 1) \quad (37a)$$

From stationary flow considerations the stagnation temperature arising from adiabatic deceleration is given by

$$\frac{1}{2} w_1^2 + c_p T_1 = \frac{1}{2} (w_1 - u_2)^2 + c_p T_2 = c_p T_o$$

or

$$\frac{1}{2} w_1^2 + h_1 = \frac{1}{2} (w_1 - u_2)^2 + h_2 = c_p T_o \quad (38)$$

Therefore

$$\frac{T_{o2}}{T_o} = \frac{1 + \frac{\gamma_1 - 1}{2} M_2^2}{1 + \frac{\gamma_1 - 1}{2} \left(\frac{w_{11}}{U_{21}} - 1 \right)^2 M_2^2} \quad (39)$$

when

$$P_{21} \rightarrow 1, \quad \frac{T_{o2}}{T_o} \rightarrow 1$$

$$P_{21} \rightarrow \infty, \quad \frac{w_{11}}{U_{21}} \rightarrow \frac{\gamma_1 + 1}{2}, \quad M_2 \rightarrow \sqrt{\frac{2}{\gamma_1(\gamma_1 - 1)}}$$

or

$$\frac{T_{o2}}{T_o} \rightarrow \frac{4}{\gamma_1 + 1}$$

For

$$\gamma_1 = 1.4, \quad \frac{T_{o2}}{T_o} \rightarrow 1.66$$

That is, the total temperature experienced by a model in the hot gas behind a moving shock wave is considerably larger than the stagnation temperature in a steady flow at the equivalent shock Mach numbers. An examination of Eqs. (36) and (38) shows that this increase in total temperature arises from the fact that u_2 can be supersonic, whereas

$(w_1 - u_2)$ is always subsonic. It is worth noting that since $\frac{w_{11}}{u_{21}} \gtrsim 1$ as $P_{21} \rightarrow \infty$, therefore $(w_1 - u_2)^2 \rightarrow 0$, or from Eq. (38),

$$h_2 \rightarrow C_p T_o = \frac{1}{2} w_1^2 + h_1 \sim \frac{1}{2} w_1^2$$

that is, the enthalpy behind a strong shock front $\rightarrow \frac{1}{2} w_1^2$.

The total temperatures available in state (3) is given by (see Subsec. 2.1.4, Eq. (21))

$$T_{o34} = \frac{T_{o3}}{T_4} = \frac{1 + \frac{\gamma_4 - 1}{2} M_3^2}{\left[1 + \frac{\gamma_4 - 1}{2} M_3\right]^2} \quad (40)$$

$$\frac{T_{o3}}{T_4} \rightarrow \frac{2}{\gamma_4 - 1} \quad \text{as } M_3 \rightarrow \infty$$

For

$$\gamma_4 = 1.4, \quad T_{o3}/T_4 \rightarrow 5$$

Alternatively,

$$\frac{T_{o3}}{T_4} = 1 - 2 \left[3(P_{34})^{1/7} - 2 \right] \left[1 - (P_{34})^{1/7} \right] \quad (40a)$$

A plot of Eqs. (39) and (40) versus P_{21} is shown in Fig. 2.3-25, where Eq. (37) has been restated as

$$T_{o21} = \frac{T_{o2}}{T_1} = \frac{T_{o2}}{T_2} \cdot \frac{T_2}{T_1} \quad (41)$$

9. Pitot Pressures

For $M_2 < 1$

$$P_{o21} = \frac{P_{o2}}{P_1} = \frac{P_{o2}}{P_2} \cdot \frac{P_2}{P_1} = \left(1 + \frac{\gamma_1 - 1}{2} M_2^2 \right)^{\frac{\gamma_1}{\gamma_1 - 1}} \cdot P_{21} \quad (42)$$

For $M_2 > 1$, the Rayleigh relation applies,

$$P'_{o21} = \frac{p_{o2}}{p_2} = \frac{p'_{o2}}{p_2} \frac{p_2}{p_1} = \frac{\gamma_1 + 1}{2} M_2^2 \left[\frac{\frac{\gamma_1 + 1}{2} M_2^2}{\frac{2\gamma_1}{\gamma_1 + 1} M_2^2 - \frac{\gamma_1 - 1}{\gamma_1 + 1}} \right]^{\frac{1}{2\beta_1 \gamma_1}} \cdot P_{21} \quad (43)$$

For state (3), for $M_3 < 1$

$$P_{o34} = \frac{p_{o3}}{p_4} = \frac{\left[1 + \frac{\gamma_4 - 1}{2} M_3^2 \right]^{1/2\beta_4}}{\left[1 + \frac{\gamma_4 - 1}{2} M_3^2 \right]^{1/\beta_4}} \quad (44)$$

when $M_3 > 1$,

$$P'_{o34} = \frac{p'_{o3}}{p_4} = \frac{\gamma_4 + 1}{2} M_3^2 \left[\frac{\frac{\gamma_4 + 1}{2} M_3^2}{\frac{2\gamma_4}{\gamma_4 + 1} M_3^2 - \frac{\gamma_4 - 1}{\gamma_4 + 1}} \right]^{\frac{1}{2\beta_4 \gamma_4}} \frac{1}{\left[1 + \frac{\gamma_4 - 1}{2} M_3^2 \right]^{1/\beta_4}} \quad (45)$$

Equations (42) to (45) are shown on Fig. 2.3-26 and in Table 2.3-4.

10. Mass Flow Ratios

$$\Lambda_{21} = \frac{\rho_2 u_2}{\rho_1 a_1} = \Gamma_{21} \cdot U_{21} \quad (46)$$

$$\Lambda_{34} = \frac{\rho_3 u_3}{\rho_4 a_4} = \frac{M_3}{\left[1 + \frac{\gamma_4 - 1}{2} M_3^2 \right]^{\alpha_4}} \quad (47)$$

Relations (46) and (47) are shown on Fig. 2.3-27 and in Table 2.3-4.

11. Dynamic Pressure

$$Q_{21} = \frac{1}{2} \rho_2 \frac{u_2^2}{p_1} = \frac{q_2}{p_1} = \frac{\gamma_1}{2} M_2^2 \cdot P_{21} \quad (48)$$

$$q_{34} = \frac{1}{2} \rho_3 \frac{u_3^2}{p_4} = \frac{q_3}{p_4} = \frac{\frac{\gamma_4}{2} M_3^2}{\left[1 + \frac{\gamma_4 - 1}{2} M_3^2\right]^{1/\beta_4}} \quad (49)$$

A plot of Eqs. (48) and (49) is shown on Fig. 2.3-28 and Table 2.3-4. In order to illustrate the variation of the physical and thermodynamic quantities of the flow in a shock tube, a particular case has been computed for illustration and is shown on Fig. 2.3-29. The initial conditions are for a temperature $T_{1,4} = 288^\circ\text{K}$, a channel pressure

$p_1 = 100$ mm Hg, a diaphragm pressure ratio $p_{41} = 20$, case Air/Air, for $t_1 = 1000$ μsec after rupturing the diaphragm. The pressure p , density ρ , temperature T , particle velocity u , Mach number M , Reynolds number Re , entropy $\frac{\Delta S}{C_v}$, and the conserved flow parameters, $C_p T_0$ and

$\frac{2}{\gamma_4 - 1} a_4$, are shown along the tube length x . The actual values of the quantities are also given and were obtained from the previous graphs.

Referring to Fig. 2.3-29, it is of interest to note that at the contact surface only the particle velocity and the pressure are continuous and all other parameters are discontinuous. Since the temperature and the density are discontinuous at the contact surface, there exists a molecular transfer of heat between region (3) and (2). It should be noted that the greatest change in entropy exists at the contact front and not at the shock front, and arises from the fact that state (4), being a region of high pressure but at the same temperature as state (1), has a very much lower entropy.

In order to solve the shock tube problem the particle velocities $u_3 = u_2$ and the pressures $p_3 = p_2$ were matched. The process for the rarefaction wave was shown to be unsteady and isentropic. The differential equations of continuity and motion defining this flow were not solved directly; instead, the equations of the characteristics were found. On the other hand, the shock wave process was shown to be equivalent to an irreversible adiabatic steady process. The integrated equations of continuity, momentum, and energy were applied directly for this case. As a result of the matching of these two different flows, two conserved flow parameters appear on Fig. 2.3-29 at the contact surface, i.e., $C_p T_0$ and $\frac{2}{\gamma_4 - 1} a_4$. Due to the steady state process,

$$C_p T_0 = \frac{1}{2} w_1^2 + C_p T_1 = \frac{1}{2} (w_1 - u_2)^2 + C_p T_2$$

the stagnation enthalpy remains constant for regions (1) and (2); but due to the unsteady state process,

$$u + \frac{2a}{\gamma_4 - 1} = \frac{2a_4}{\gamma_4 - 1}$$

the constant of the P- family of characteristics applies to regions (4) and (3) and throughout the Q-rarefaction wave.

It is interesting to note that the constant per unit mass for states (1) and (2) is an energy constant, and for (4) and (3) a momentum constant. The above along with the distinctly different results for the "escape speed," total temperature, and pitot pressure illustrates the fundamental difference between steady and unsteady flows.

2.3.3 Imperfect Gas Effects

The relations derived in Subsec. 2.3.2 apply when the gas is thermally and calorically perfect. If the gas is imperfect, then two deviations will occur. First, consider the case when a gas in state (4) is heated and a considerable amount of dissociation occurs. If the diaphragm is now ruptured, the high-temperature, high-pressure gas in the chamber goes through the rarefaction wave and is cooled. Relaxation and recombination take place giving rise to a flow with variable chemical properties, specific heat, and entropy (see Supplements B and C and Subsec. 2.1.5). Consequently, the resulting flow will deviate from that predicted by the perfect gas theory. That is, Eq. (11), Subsec. 2.3.2, no longer applies.

Second, if the gas is imperfect, then the other relations in Subsec. 2.3.2 for states (3) and (2) must be replaced by their equivalent imperfect gas-flow properties. For example, all of the relations for state (2) behind a shock wave in an imperfect gas developed in Subsec. 2.2.2 apply.

In order to cope with the first deviation, the variable entropy region can be neglected and numerical integration along an isentrope of Eqs. (1) and (2), Subsec. 2.1.5 can be done, that is, for a P-wave the integral

$$u = \int \frac{a}{\rho} d\rho \quad (1)$$

is evaluated along an isentrope. If a Mollier chart is available (Ref. 36a), then this can be done in a step by step manner since the state properties are known along an isentrope and the particle velocity can be determined from

$$\Delta u = \frac{a}{\rho} \Delta \rho \quad (1a)$$

In practice it is found (see Subsec. 4.3) that one may approximate by neglecting the imperfect gas effects and use the perfect rarefaction wave relation (Eq. (22), Subsec. 2.3.2)

$$U_{34} = \frac{1}{\gamma_4 \beta_4} \left[1 - (P_{14} P_{21})^{\beta_4} \right] = A_{14} U_{21} \quad (2)$$

to obtain the diaphragm pressure ratio P_{14} . To do this, γ_4 must be the value appropriate to the high temperature, high pressure gas (including dissociation effects after combustion) and P_{21}^* and U_{21}^* are the appro-

appropriate imperfect shock wave values. For a given shock Mach number $W_{11} = M_s$, P_{21}^* and U_{21}^* are known. If the chamber conditions have been calculated for the given method of heating, γ_4 is known. Consequently, P_{14} is found from Eq. (2).

It can be noted that under ordinary temperatures (300°K) the effects of variable specific heat through the rarefaction wave have a very small influence. However, hydrogen is an exception since at moderate pressures at 300°K it has a value of $\gamma = 1.40$, whereas at low pressures and a temperature of 50°K, $\gamma = 1.66$ (Ref. 4). That is, rotation is practically de-excited and hydrogen behaves like a monatomic gas. It should also be noted that even for the case of Air/Air at 300°K, with a diaphragm pressure ratio of 1.3×10^5 , the temperature behind the rarefaction wave for a perfect gas is $0.08 \times 300 = 24^\circ\text{K}$. This temperature is considerably below the boiling point of nitrogen and oxygen, and liquefaction should occur. Under such conditions the effects of variable specific heat can be quite significant. However, as will be noted in Subsec. 3.1.3, the temperature in the rarefaction region (3), in a real flow, is usually much above the ideal temperature, and it is doubtful if such extreme low temperatures would be attained. However, a recent calculation (Ref. 55) on hydrogen as an imperfect-gas driver shows that the high-pressure effects (50 to 125 atm) compensate for the gas imperfections, and using $\gamma = 1.4$ (perfect gas) gives very good agreement for P_{41} vs W_{11} .

Figure 2.3-30 shows a plot of shock Mach number W_{11} with diaphragm pressure ratio (P_{41}) for Air/Air when $\gamma = 1.4$, and when air is considered as an imperfect gas behind the shock wave (perfect gas in chamber and vibrational energy included behind the shock wave). The properties behind the shock wave are those calculated in Ref. 11. It is seen that a higher diaphragm pressure ratio P_{41} is required to produce a given shock speed W_{11} for an imperfect gas. The reason for this lies in the fact that the shock wave in an imperfect gas has a higher pressure and particle velocity than in the perfect gas case. At high shock Mach numbers, the deviation becomes quite significant. For example at $W_{11} = 4.3$, a $P_{41} = 6 \times 10^4$ is required for a perfect gas, and a $P_{41} = 8 \times 10^4$ for an imperfect gas, an increase of over 30 per cent in P_{41} . If a $P_{41} = 6 \times 10^4$ was used in both cases, then the imperfect gas $W_{11} = 4.24$ as compared to 4.30 for the perfect gas case. Very little gain is achieved with air as a driver at high diaphragm pressure ratios.

Typical curves of the state properties for air in equilibrium in state (2*) as compared to the ideal values given for state (2) in Subsec. 2.3.2 are shown in Figs. 2.3-31 to 2.3-41, inclusive. The above plots are taken from Ref. 36a. The effects of dissociation and ionization at low pressure are quite evident.

2.4 Effects of One-Dimensional Wave Interactions and Finite Tube Length

In the previous subsections the chamber and the channel were assumed to be of infinite length. In actual shock tube work the chamber and the channel are of finite length with open or closed ends. As a result, after a short time (milliseconds, depending on the channel length) the flow in a shock tube becomes quite complex due to the ensuing interactions.

When the diaphragm in a shock tube is ruptured, the shock wave proceeds along the channel, and if it strikes a closed end, it undergoes normal reflection in a non-linear manner. If the channel is open, the shock wave undergoes diffraction and reflection. If the flow behind the shock wave is subsonic, $M_2 < 1$; theoretically, a rarefaction wave is reflected back into the channel. (Actually, due to the complex three-dimensional flow that takes place, a shock wave is also reflected back into the channel. Real flows at open chamber and channels will be discussed in Subsec. 3.) When the flow behind the shock wave is supersonic $M_2 > 1$, then theoretically a rarefaction wave cannot be reflected back from the open end of the channel.

In the case of the rarefaction wave which is propagated into the chamber: if it encounters a closed end, then it undergoes normal reflection as a rarefaction wave; if it strikes an open chamber, then theoretically a reflected compression wave steepening into a shock wave enters the chamber. Again, owing to the three-dimensional effects, this is modified somewhat for a real flow (see Subsec. 3).

Eventually, the reflected waves will interact with the contact surface and with each other and will give rise to a very complex flow pattern in the shock tube. As a result the reflected waves will determine the duration of the steady state flows in regions (3) and (2) and will control the selection of the theoretical lengths of the chamber and channel of a finite shock tube for aerodynamic testing. Some of these interactions now will be considered in some detail. It should be noted that the final states resulting from these interactions can be predicted from the (p, u)-plane solutions as outlined in Subsec. 2.3.1. Numerical and graphical solutions may be found in Ref. 7.

2.4.1 Normal Reflection of a Shock Wave or a Rarefaction Wave

2.4.1.1 Shock Wave Reflection

Figure 2.4-1 shows a simple shock tube with both ends closed and the resulting normal reflection of the rarefaction wave at the end of the chamber and the normal reflection of the shock wave at the end of the channel. From Eq. (20) in Subsec. 2.3.2, the particle velocity behind the incident shock wave for constant γ is given by

$$u_{21} = \frac{u_2}{a_1} = \frac{P_{21} - 1}{\gamma_1 [\beta_1 (\alpha_1 P_{21} + 1)]^{1/2}} \quad (1)$$

The boundary condition at the closed end of the channel is that the particle velocity, after the head-on reflection, must be zero. If this condition is to be satisfied, then the particle velocity behind the reflected shock wave travelling into a gas at rest must be equal to the particle velocity behind the incident shock wave also entering a gas at rest.

Hence,

$$u_2 = u_5 \quad (2)$$

and

$$u_{21} = u_{52} A_{21} \quad (3)$$

or

$$u_{21} = \frac{P_{52} - 1}{\gamma_1 [\beta_1 (\alpha_1 P_{52} + 1)]^{1/2}} \left[\frac{P_{21} (\alpha_1 + P_{21})}{1 + \alpha_1 P_{21}} \right]^{1/2} \quad (4)$$

or

$$\frac{P_{21} - 1}{\gamma_1 [\beta_1 (\alpha_1 P_{21} + 1)]^{1/2}} = \frac{P_{52} - 1}{\gamma_1 [\beta_1 (\alpha_1 P_{52} + 1)]^{1/2}} \left[\frac{P_{21} (\alpha_1 + P_{21})}{1 + \alpha_1 P_{21}} \right]^{1/2} \quad (5)$$

and

$$P_{52} = \frac{\alpha_1 + 2 - P_{12}}{1 + \alpha_1 P_{12}} \quad (6)$$

Equation (6) gives the variation of the pressure ratio across the reflected shock wave in terms of the pressure ratio across the incident shock wave. It is seen that for an incident Mach wave $P_{21} = 1$ and $P_{52} = 1$. When the incident shock wave $P_{21} \rightarrow \infty$, then $P_{52} \rightarrow \alpha_1 + 2$. Thus for air, assuming a constant $\gamma = 1.40$, the strongest possible reflected wave $P_{52} = 8$. (The limits of the absolute value of P_{21} obtainable in a simple shock tube, as outlined in Table 2.3-2, should be noted.)

The excess pressure ratio is defined as

$$\frac{P_5 - P_1}{P_2 - P_1} = 1 + \frac{P_{21}(1 + \alpha)}{P_{21} + \alpha} \quad (7)$$

For a Mach wave, $P_{21} \rightarrow 1$ and the excess pressure ratio $\rightarrow 2$, which is the acoustic result for sonic reflection. If $P_{21} \rightarrow \infty$, then the excess pressure ratio $\rightarrow P_{52} \rightarrow 8$, as for Eq. (6).

The density ratio ρ_{52} and the temperature ratio T_{52} are obtained from Subsec. 2.3.2, Eqs. (16) and (18).

$$\rho_{52} = \frac{1 + \alpha_1 P_{52}}{\alpha_1 + P_{52}} \quad (8)$$

$$T_{52} = \frac{P_{52} (\alpha_1 + P_{52})}{1 + \alpha_1 P_{52}} \quad (9)$$

Thus, these ratios for $1 \leq P_{52} \leq 8$ are identical with the values given for $1 \leq P_{21} \leq 8$ on Fig. 2.3-19.

The limiting values of the above ratios when $P_{21} \rightarrow \infty$ and $P_{52} \rightarrow 8$, for air (assuming constant specific heat), are

$$\left[\frac{r_{52}}{P_{21}} \right]_{P_{21} \rightarrow \infty} = 3.50$$

$$\left[\frac{T_{52}}{P_{21}} \right]_{P_{21} \rightarrow \infty} = 2.29$$

The variation of these flow parameters with the initial shock wave Mach number W_{11} is shown on Fig. 2.4-2, for constant γ (and for an imperfect gas with vibrational specific heat only included).

The ratio of the incident shock wave velocity W_{11} to the reflected shock wave velocity W_{21} may be determined in a similar manner. The incident wave speed (Eq. (19), Subsec. 2.3.2) is given by

$$\frac{w_1}{a_1} = W_{11} = \left[\beta_1 (1 + \alpha_1 P_{21}) \right]^{1/2} \quad (10)$$

The reflected wave speed, if the gas in state (2) were at rest, would be given by

$$\frac{w_2}{a_2} = \left[\beta_1 (1 + \alpha_1 P_{52}) \right]^{1/2} \quad (11)$$

From this, the particle velocity u_2/a_1 must be subtracted to obtain the absolute velocity $|w_{21}|$, which is directed along the negative x-axis.

Thus

$$\left| \frac{w_2}{a_1} \right| = |w_{21}| = \frac{w_2 - u_2}{a_1} = \frac{w_2}{a_2} \cdot \frac{a_2}{a_1} - \frac{u_2}{a_1} = w_{21} \quad (12)$$

or

$$w_{21} = \left[\beta_1 (1 + \alpha_1 P_{52}) \right]^{1/2} \left[\frac{P_{21} (\alpha_1 + P_{21})}{1 + \alpha_1 P_{21}} \right]^{1/2} - \frac{P_{21} - 1}{\gamma_1 \left[\beta_1 (\alpha_1 P_{21} + 1) \right]^{1/2}} \quad (13)$$

Substituting for P_{52} from Eq. (6),

then

$$w_{21} = \frac{P_{21}(\gamma_1 - 1) + 1}{\gamma_1 \left[\beta_1 (\alpha_1 P_{21} + 1) \right]^{1/2}} \quad \text{or} \quad w_{21} = \frac{2 + (\alpha_1 - 1) P_{12}}{\left[(\alpha_1 + 1) P_{12} (\alpha_1 + P_{12}) \right]^{1/2}} \quad (14)$$

and

$$\frac{w_{21}}{w_{11}} = \frac{P_{21}(\gamma_1 - 1) + 1}{\gamma_1 \beta_1 (\alpha_1 P_{21} + 1)} \quad \text{or} \quad \frac{w_{21}}{w_{11}} = \frac{2 + (\alpha_1 - 1) P_{12}}{\alpha_1 + P_{12}} \quad (15)$$

For weak shock waves $P_{21} \rightarrow 1$ and $\frac{w_{21}}{w_{11}} \rightarrow 1$.

For infinitely strong shock waves $P_{21} \rightarrow \infty$ and

$$\left(\frac{w_{21}}{w_{11}} \right)_{P_{21} \rightarrow \infty} \rightarrow \frac{2}{\alpha_1} \quad (16)$$

For air with constant specific heat $\gamma_1 = 1.4$, $\alpha_1 = 6$ and

$$\left(\frac{w_{21}}{w_{11}} \right)_{P_{21} \rightarrow \infty} = \frac{1}{3} \quad (17)$$

The reflected shock wave has a speed equal to the incident wave when they are both Mach waves (sound waves). The speed ratio of the reflected to incident shock waves then decreases as the incident wave strength increases until it reaches the value of one third the incident wave velocity as $P_{21} \rightarrow \infty$. For the case of Air/Air with $E_{14} = 1$,

$$\left(\frac{w_{21}}{w_{11}} \right)_{P_{21} \rightarrow 44} = 0.351, \text{ which is the minimum value of the wave speed}$$

ratio, and $w_{21} = 0.351 \times 6.16 = 2.16$. It is important to realize that in a plot of w_{21} versus w_{11} , the curve exhibits a minimum. In the case of an ideal gas, $\gamma_1 = 1.40$, $(w_{21})_{\min} = 0.94$ when $w_{11} = 1.39$ (see Fig. 2.4-2), and is due to the nonlinear relation between particle velocities and shock speeds.

It is of interest to note that in case of normal reflection the ratios P_{52} , $\sqrt{52}$, T_{52} and w_{21}/w_{11} remain finite when $P_{21} \rightarrow \infty$. These may be compared with the equivalent ratios in Table 2.3-2, for the incident shock wave.

In the case of variable specific heats, the methods of Subsec. 2.2.2 are applied to the equations of motion with respect to the reflected shock wave w_2 as follows.

Let the velocities with respect to the reflected shock wave (w_2) be

$$v = u + w_2 \quad (18)$$

and with respect to the incident shock wave (w_1),

$$v = u - w_1 \quad (19)$$

The condition for normal reflection is that the reflected shock must bring the gas particles to rest,

$$u_5 = 0 \quad (20)$$

Consequently,

$$v_5 = u_5 + w_2 = w_2 \quad ; \quad u_2 = v_2 - v_1$$

where

$$v_1 = u_1 - w_1 = -w_1 \quad ; \quad v_2 = u_2 - w_1$$

The continuity equation becomes, in nonstationary co-ordinates,

$$\rho_5 w_2 = \rho_2 (u_2 + w_2) \quad (21)$$

and in stationary co-ordinates,

$$\rho_5 v_5 = \rho_2 (v_2 - v_1 + v_5) \quad (21a)$$

Momentum,

$$p_5 + \rho_5 w_2^2 = p_2 + \rho_2 (u_2 + w_2)^2 \quad (22)$$

$$p_5 + \rho_5 v_5^2 = p_2 + \rho_2 (v_2 - v_1 + v_5)^2 \quad (22a)$$

Energy,

$$\frac{1}{2} w_2^2 + h_5 = \frac{1}{2} (u_2 + w_2)^2 + h_2 \quad (23)$$

$$\frac{1}{2} v_5^2 + h_5 = \frac{1}{2} (v_2 - v_1 + v_5)^2 + h_2 \quad (23a)$$

Thermally imperfect equation of state,

$$p = Z \rho RT \quad (24)$$

Calorically imperfect equation of state,

$$h = h(p, T) = \int_0^T C_p(p, T) dT \quad (25)$$

Equations (21), (22), (23), (24), and (25) and the equation for Z (Supplement B) are six relations for the solution of the six unknowns p_5 , ρ_5 , T_5 , Z_5 , h_5 , and w_2 . A solution for air without dissociation using the computation methods of Subsec. 2.2.2 is shown on Fig. 2.4-2. A solution for air including dissociation and other states in chemical equilibrium is shown in Figs. 2.4-3 to 2.4-8, inclusive (Ref. 30a).

Similar plots for Argon, from Ref. 42, are shown on Figs. 2.4-9 to 2.4-13, inclusive.

2.4.1.2 Rarefaction Wave Reflection

The rarefaction wave which is formed when the diaphragm is ruptured travels along the chamber and undergoes normal reflection at the closed end (see Fig. 2.4-1).

It is shown in Ref. 47, that a steady state (6) is theoretically still possible behind the reflected rarefaction wave if the initial diaphragm pressure ratio produces a rarefaction wave such that the speed of the tail of the wave $\frac{dx}{dt} \leq 2a_4$ for a diatomic gas and $\frac{dx}{dt} \leq a_4$ for a monatomic gas. At the limiting value of $\frac{dx}{dt}$, after an infinite time, a total vacuum is produced in state (6) and $p_6 = 0$. In practice, owing to the ensuing wave interactions, a uniform high vacuum state would be very difficult to achieve.

The physical quantities in state (6) behind the reflected rarefaction wave may be determined from the following considerations.

For a backward facing or Q-rarefaction wave (Subsec. 2.1.4),

$$u_3 + \frac{2a_3}{\gamma_4 - 1} = u_4 + \frac{2a_4}{\gamma_4 - 1} \quad (26)$$

Similarly for a forward facing or P-rarefaction wave,

$$u_6 - \frac{2a_6}{\gamma_4 - 1} = u_3 - \frac{2a_3}{\gamma_4 - 1} \quad (27)$$

The boundary conditions are that initially $u_4 = 0$, and finally $u_6 = 0$ behind the reflected rarefaction wave. Subtraction of the above two equations yields

$$\frac{4a_3}{\gamma_4 - 1} = \frac{2}{\gamma_4 - 1} (a_4 + a_6) \quad (28)$$

or

$$\frac{a_6}{a_4} = \frac{2a_3}{a_4} - 1 \quad (29)$$

but

$$\frac{a}{a_4} = \left(\frac{T}{T_4}\right)^{1/2} = \left(\frac{\rho}{\rho_4}\right)^{\frac{\gamma_4-1}{2}} = \left(\frac{P}{P_4}\right)^{\frac{\gamma_4-1}{2\gamma_4}} \quad (30)$$

Therefore

$$P_{64}^{\beta_4} = 2 P_{34}^{\beta_4} - 1 = 2(P_{14} P_{21})^{\beta_4} - 1 \quad (31)$$

Similarly

$$T_{64}^{1/2} = 2 P_{34}^{\beta_4} - 1 \quad (32)$$

$$\Gamma_{64}^{\beta_4 \gamma_4} = 2 P_{34}^{\beta_4} - 1 \quad (33)$$

Thus the flow quantities in state (6) may be determined from the known pressure ratio ($P_{34} = P_{14} P_{21}$) across the incident rarefaction wave. Also from Eqs. (26) and (27)

$$\frac{2u_3}{a_3} = \frac{2}{\gamma_4 - 1} \left(\frac{a_4 - a_6}{a_3} \right) \quad (34)$$

Substituting Eq. (29)

$$M_3 = \frac{2}{\gamma_4 - 1} \left(\frac{1 - \frac{a_6}{a_4}}{1 + \frac{a_6}{a_4}} \right) \quad (35)$$

$$A_{64} = \frac{\left[\frac{2}{\gamma_4 - 1} - M_3 \right]}{\left[\frac{2}{\gamma_4 - 1} + M_3 \right]} = \frac{\left[1 - (\gamma\beta)_4 M_3 \right]}{\left[1 + (\gamma\beta)_4 M_3 \right]} \quad (36)$$

or from Eq. (30)

$$P_{64} = \left[\frac{1 - (\gamma\beta)_4 M_3}{1 + (\gamma\beta)_4 M_3} \right]^{1/\beta_4} \quad (37)$$

$$T_{64} = \left[\frac{1 - (\gamma\beta)_4 M_3}{1 + (\gamma\beta)_4 M_3} \right]^2 \quad (38)$$

$$\Gamma_{64} = \left[\frac{1 - (\gamma\beta)_4 M_3}{1 + (\gamma\beta)_4 M_3} \right]^{\frac{1}{(\gamma\beta)_4}} \quad (39)$$

It is worth noting that (Subsec. 2.1.4)

$$P_{34} = \left[1 - \frac{1}{\alpha_4} \left(\frac{x}{a_4 t} + 1 \right) \right]^{1/\beta_4} \quad (40)$$

From Eq. (31), when

$$P_{64} = 0, \quad P_{34} = \left(\frac{1}{2} \right)^{1/\beta_4} \quad (41)$$

From Eqs. (40) and (41),

$$\frac{x}{t} = a_4 \left(\frac{\alpha_4}{2} - 1 \right) \quad (42)$$

For a monatomic gas

$$\alpha_4 = 4 \quad \text{and} \quad \left(\frac{x}{t} \right)_{\text{tail}} = a_4 \quad (43)$$

For a diatomic gas

$$\alpha = 6 \quad \text{and} \quad \left(\frac{x}{t} \right)_{\text{tail}} = 2a_4 \quad (44)$$

That is, a diatomic gas needs a greater incident rarefaction wave tail slope or greater expansion $\left\{ (1/2)^7 \right\}$ than a monatomic gas $\left\{ (1/2)^5 \right\}$ to achieve a hypothetical vacuum in state (6) after an infinitely long time. For tail slopes greater than the above values, this state is never achieved.

In the case of Air/Air, this limiting value may be obtained when $P_{34} = (1/2)^7 = 0.00781$, or from Eq. (12) when $M_3 = 5$. This occurs at a diaphragm pressure ratio $P_{41} = 1620$ when the shock pressure $P_{21} = 12.63$ for the case Air/Air, $\gamma = 1.40$, at $E_{14} = 1$. The values of the flow quantities in state (6) are plotted on Fig. 2.4-14. The dimensionless time (τ_6) of formation of the steady state (6) is given in Ref. 47 for the case of a monatomic gas in the chamber as

$$\tau_6 = \frac{a_4 t_6}{L} = \frac{1 - 2 P_{34}^{1/5} + 2 P_{34}^{2/5}}{(2 P_{34}^{1/5} - 1)^3} \quad (45)$$

and for a diatomic gas in the chamber as

$$\tau_6 = \frac{a_4 t_6}{L} = \frac{1}{(2 P_{34}^{1/7} - 1)^3} + \frac{6 P_{34}^{2/7} (1 - P_{34}^{1/7})^2}{(2 P_{34}^{1/7} - 1)^5} \quad (46)$$

where L = chamber length, and t_6 (time state (6) forms at the instant the diaphragm is ruptured. For example, case Air/Air, with $P_{41} = 10.5$ and $P_{21} = 2.90$, the tail of the rarefaction wave has a slope

$\frac{dx}{dt} = 0$ and $M_3 = 1$. If $a_4 = 1130$ ft/sec (22°C) and $L = 1$ ft, then $t_6 = 3.82$ millisecc; for $P_{41} = 100$, $P_{21} = 6.35$, $t_6 = 71.1$ millisecc. The variation of t_6 with P_{41} for the combinations He/Air, A/Air, and Air/Air is shown on Fig. 2.4-15.

The duration of state (6) will be governed by the reflection of the refracted rarefaction wave which gives rise to a reflected rarefaction or shock wave from the contact surface; or, in the case of a short channel, by the reflected shock wave. Hence the duration must be determined for a given experiment when state (6) is to be investigated.

The effects of heat addition and gas imperfection arising from condensation and de-excitation, respectively, should be considered if they are sizeable.

2.4.2 Head-on Collision of Shock Waves or Rarefaction Waves

One-dimensional wave interactions may be analysed by using the method of the (p, u) -plane outlined in Subsec. 2.3.1. The resulting waves and states are predicted and they may be plotted in the physical (x, t) -plane.

The head-on collision of two shocks, two rarefaction waves, and of a shock and a rarefaction wave will be considered below. It can be noted that the normal reflections treated in Subsec. 2.4.1 are particular cases of the head-on collision of two shock waves and two rarefaction waves of equal strength.

2.4.2.1 Head-on Collision of Two Unequal Shock Waves

This problem is illustrated in Figs. 2.4-16 and 2.4-17. States (1), (2), and (5), and the two approaching shock waves are given. The final states and receding shock waves are obtained from the (p, u)-plane. The contact surface is deduced from physical considerations. The solution in the (p, u)-plane shows that the pressure ratio of both receding shock waves, with respect to the initial state, has been increased.

An exact algebraic solution can be obtained by making use of the shock equations and the fact that across the contact surface

$$p_3 = p_4 \quad \text{and} \quad u_3 = u_4$$

The strength of the two shocks, P_{45} and P_{32} , is given in terms of state (1) and the initial shocks P_{21} and P_{51} as (Ref. 46)

$$P_{45} = \sqrt{1 + \alpha_1 P_{45}} \left\{ A - C \left[B + \frac{P_{12} P_{45} - P_{15}}{\sqrt{P_{15}(\alpha_1 P_{12} P_{45} + P_{15})}} \right] \right\} + 1 \quad (1)$$

where

$$A = \frac{1 - P_{15}}{\sqrt{1 + \alpha_1 P_{15}}}, \quad B = \frac{P_{12} - 1}{\sqrt{1 + \alpha_1 P_{12}}} \quad (2)$$

and

$$C = \sqrt{\frac{(\alpha_1 P_{12} + 1)}{P_{12}(\alpha_1 + P_{12})} \cdot \frac{P_{15}(\alpha_1 + P_{15})}{(\alpha_1 P_{15} + 1)}}$$

Since $P_{32} = P_{45} \cdot P_{12} \cdot P_{51}$, then for the case of equal shocks where $P_{15} = P_{12}$, the two roots of Eq. (1) yield the following solutions:

For the positive root

$$P_{45} = (2 + \alpha_1 - P_{15}) / (1 + \alpha_1 P_{15}) \quad (3)$$

This is identical with Subsec. 2.4.1, Eq. (6). It indicates that the head-on collision of two equal shocks is equivalent to the normal reflection from a solid boundary, and no contact surface will be observed in the flow.

The negative root of Eq. (1) yields $P_{45} = P_{15}$, which applies to acoustic reflection. Equation (1) may also be applied to the interaction of a sound wave with a shock wave.

2.4.2.2 Head-on Collision of Two Unequal Rarefaction Waves

The interaction is illustrated in Figs. 2.4-18 and 2.4-19. From the (p, u)-plane it may be seen that the pressure in state (3), after the two rarefaction waves have receded, is the lowest existing pressure. The problem has been solved in a closed form for a monatomic and diatomic gas even in the region of penetration using Riemann's method of integration (Ref. 47). Because the waves are isentropic, only one thermodynamic state (3) results, which may be computed from the following. Given the initial state (1) and the strength of the two colliding rarefaction waves P_{41} and P_{21} , then

$$u_{31} = (1/\gamma_1 \beta_1) (P_{41}^{\beta_1} - P_{21}^{\beta_1}) \quad (4)$$

$$P_{31}^{\beta_1} = P_{41}^{\beta_1} + P_{21}^{\beta_1} - 1 \quad (5)$$

If the waves are of equal strength, then $P_{41} = P_{21}$, and $u_{31} = 0$, resulting in

$$P_{31}^{\beta_1} = 2 P_{41}^{\beta_1} - 1 \quad (6)$$

Equation (6) is identical to Subsec. 2.4.1, Eq. (31) for the normal reflection of a rarefaction wave from a solid boundary.

2.4.2.3 Head-on Collision of a Shock Wave and a Rarefaction Wave

This collision is illustrated in Figs. 2.4-20 and 2.4-21. From the (p, u)-plane it is seen that the particle velocity in states (3) and (4) is greater than that in state (5). It is found that the pressure ratio across the receding shock wave is increased; that is, it is a stronger shock wave, but with a lower absolute pressure behind it ($p_3 < p_5$). Similarly, the rarefaction wave pressure ratio is increased; that is, it is a weaker wave, but is advancing into a higher pressure region ($p_5 > p_4$).

It should be noted that because the shock wave is increasing in strength as it penetrates the rarefaction wave, the entropy behind it is continuously increasing. Consequently, a contact region rather than a surface separates the receding waves.

The algebraic solution for the interaction is given in Ref. 48. Given state (1) and the strength of the shock (P_{51}) and

rarefaction wave (P_{12}), the strength of the receding shock (P_{32}) and rarefaction wave ($P_{45} = P_{32} \cdot P_{21} \cdot P_{15}$) is obtained from

$$P_{32} = 1 + \sqrt{1 + \alpha_1} P_{32} \left\{ D - E \left[(P_{32} P_{15})^{\frac{1}{\alpha_1+1}} - (P_{12})^{\frac{1}{\alpha_1+1}} \right] \right\} \quad (7)$$

where

$$D = P_{12}^{\frac{1}{\alpha_1+1}} \frac{P_{51} - 1}{\sqrt{1 + \alpha_1} P_{51}} + \sqrt{\alpha_1 + 1} \left[1 - P_{12}^{\frac{1}{\alpha_1+1}} \right]$$

$$E = \sqrt{\alpha_1 + 1} \sqrt{P_{51} \left[(\alpha_1 + P_{51}) / (1 + \alpha_1 P_{51}) \right]} \quad (8)$$

Although Eq. (7) makes it possible to calculate the final states and wave strengths from the initial conditions, it is not sufficient to give the path of the curved shock wave. A procedure for doing this is given in Ref. 48. Equation (7) also provides a means of computing the collision of an acoustic pulse with a rarefaction wave.

2.4.3 Normal Refraction of a Shock Wave or a Rarefaction Wave at a Contact Surface

The one-dimensional refraction of shock waves or expansion waves is pictorially analogous to the same problem in light or acoustics. It will be shown that when a finite amplitude pressure wave refracts at a contact surface, the non-linear interaction gives rise to a transmitted wave, which can have a higher or lower pressure ratio than the incident wave. The reflected wave may be of the same type as the incident wave, a Mach wave, or of a kind opposite to the incident wave. Consequently, it is possible to raise or lower the pressure ratio across the refracted wave, as well as increase or decrease the particle velocity by a suitable choice of gas combinations at the contact surface. These properties are useful in the studies of wave attenuation or amplification, chemical kinetics, and in the design of hypersonic shock tunnels.

2.4.3.1 Refraction of a Shock Wave at a Contact Surface

This interaction is illustrated in the (p, u)-plane in Fig. 2.4-22. Three cases are predicted. It is possible to have a reflected shock wave, a Mach wave (when states (2), (3), and (4) are coincident), or a rarefaction wave after the interaction of the shock with the contact surface. Which case occurs depends on the shock strength (P_{45}) and the internal energy ratio (E_{15}).

The same interactions appear on Figs. 2.4-23 and 2.4-24, in the (x, t)-plane for the moving and stationary contact surfaces. The analysis applies to both contact surfaces since they differ only by a velocity component. In closed form the interaction for the stationary contact surface is described by the following equations (Ref. 49).

For the case of a reflected shock wave,

$$E_{15} = \frac{\alpha_1 + P_{54} P_{43}}{(1 - P_{54} P_{43})^2} \left[k \sqrt{P_{43}} - \frac{P_{43} - 1}{\sqrt{\alpha_5 + P_{43}}} \right]^2 \quad (1)$$

where

$$h = (\alpha_5 P_{54} + 1) / (\alpha_5 + P_{54})$$

$$k = (1 - P_{54}) / \sqrt{\alpha_5 P_{54} + 1} \quad (2)$$

$$E_{15} \leq (\alpha_1 + P_{54}) / (\alpha_5 + P_{54})$$

It may be seen from Fig. 2.4-22 that the absolute pressure and the pressure ratio across the transmitted shock wave are increased. In the limit, as $E_{15} \rightarrow 0$,

$$P_{43} = \frac{2 + \alpha_5 - P_{54}}{1 + \alpha_5 P_{54}} \quad (3)$$

for the positive root, and

$$P_{43} = P_{54} \quad (4)$$

is the acoustic result for the negative root.

Equation (3) is identical with Eq. (6), Subsec. 2.4.1, and shows that for very large energy ratios E_{15} the contact surface behaves as if it were a rigid wall and remains stationary. This has an important application in generating high temperatures through multiple shock reflection from the contact surface at the end of a closed channel in a shock tube. The limit of $E_{15} \rightarrow 0$ is, of course, not possible to attain in practice.

The condition for a reflected Mach wave is that across the contact surface

$$E_{15} = \frac{\alpha_1 + P_{54}}{\alpha_5 + P_{54}} \quad (5)$$

In this case the incident shock strength is unchanged.

The case of a reflected rarefaction wave is given by

$$P_{34}^{\beta_5} + f (P_{34} - P_{54}) \sqrt{\frac{\beta_5 E_{15}}{\alpha_1 P_{34} + P_{54}}} - g - 1 = 0 \quad (6)$$

where

$$f = \left[(\alpha_5 + P_{54}) / (\alpha_5 P_{54} + 1) \right]^{1/2}$$

$$g = (1 - P_{54}) \left[\beta_5 / (\alpha_5 P_{54} + 1) \right]^{1/2} \quad (7)$$

$$E_{15} \geq (\alpha_1 + P_{54}) / (\alpha_5 + P_{54})$$

As seen from Fig. 2.4-22, the absolute pressure and the pressure ratio across the refracted shock wave are both reduced. By using a gas combination across the contact surface such as Air || H₂ or Air || He, a considerable attenuation of the shock strength is possible. Conversely, a combination such as Air || A or Air || CO₂ will give an amplified shock strength.

2.4.3.2 Refraction of a Rarefaction Wave at a Contact Surface

When a rarefaction wave refracts at a contact surface, three wave systems are possible. A rarefaction wave is always transmitted, but the reflected wave can be a rarefaction wave, a Mach wave, or a compression wave that steepens into a shock wave. Since weak shock waves have the same properties as compression waves, the analysis will assume that the shock wave equations apply for both shock waves and compression waves. With this assumption, the varying entropy field behind the forming shock front is also neglected and is taken as a constant. The type of wave that is reflected after the interaction depends on the internal energy ratio E_{15} and the strength of the incident rarefaction wave P_{45} .

Figure 2.4-26 shows the interaction in the (x, t) -plane for the case of a moving contact surface, and Fig. 2.4-27 for the case of a stationary contact surface. The analysis applies to both cases and they differ by a velocity component only.

Consider the stationary case and the algebraic equations for the case of a reflected rarefaction wave as given by (Ref. 50):

$$E_{15} = \frac{(\beta_1/\beta_5) \left[(P_{34} P_{45})^{\beta_5} - 2 (P_{45})^{\beta_5} + 1 \right]^2}{\left[1 - (P_{34} P_{45})^{\beta_1} \right]^2} \quad (8)$$

$$E_{15} \leq (\beta_1/\beta_5) \left[(1 - P_{45}^{\beta_5})^2 / (1 - P_{45}^{\beta_1})^2 \right] \quad (9)$$

From Fig. 2.4-25, it can be seen that the absolute pressure behind the refracted rarefaction wave is reduced, or a stronger rarefaction wave is transmitted. It can be noted that when $E_{15} \rightarrow 0$,

$$(P_{34} P_{45})^{\beta_5} - 2 (P_{45})^{\beta_5} + 1 = 0 \quad (10)$$

Equation (10) is identical to Eq. (31), Subsec. 2.4.1, and shows that when $E_{15} \rightarrow 0$, the transmitted wave behaves as if it were reflected from a rigid wall, and the contact surface is stationary. The limit $E_{15} \rightarrow 0$ is physically not attainable.

For a reflected Mach wave, states (2), (3), and (4) are coincident and this condition is given by

$$E_{15} = \frac{\beta_1}{\beta_5} \left[\frac{1 - P_{45}^{\beta_5}}{1 - P_{45}^{\beta_1}} \right]^2 \quad (11)$$

and the rarefaction wave strength is unchanged. The reflected Mach waves form a fan of parallel lines.

For a reflected compression wave that steepens into a shock wave, the solution is given by

$$\sqrt{\frac{\beta_5}{\beta_1}} E_{15} = \frac{P_{45}^{\beta_5} \left[\frac{\sqrt{\beta_5} (1 - P_{34})}{\sqrt{\alpha_1 P_{34} + 1}} \right] + P_{45}^{\beta_5} - 1}{[(P_{34} P_{45})^{\beta_1} - 1]} \quad (12)$$

$$E_{15} \geq (\beta_1/\beta_5) \left[(1 - P_{45}^{\beta_5}) / (1 - P_{45}^{\beta_1}) \right]^2 \quad (13)$$

From Fig. 2.4-25 it can be seen that the absolute pressure behind the transmitted rarefaction wave has been increased or the wave strength has been attenuated.

2.4.4 Overtaking of Shock Waves or Rarefaction Waves

The problems of overtaking waves are not only of interest in themselves but they also affect the operation of conventional shock tubes and hypersonic shock tunnels. They may also be used to generate ideal contact surfaces, shock waves, and centred rarefaction waves without being affected by the diaphragm of the shock tube. Such ideal wave elements are sometimes very necessary in the study of the wave transition properties or wave interactions.

2.4.4.1 The Overtaking of Two Similarly Facing Shock Waves

The interaction in the (p, u) -plane is shown on Fig. 2.4-28. It is seen that three cases can take place. A transmitted shock always occurs. The reflected wave can be a shock wave, a Mach wave, or a rarefaction wave. It is shown in Ref. 51 that for all real gases ($\gamma \leq 5/3$), a rarefaction wave is always reflected, whereas for a gas with $\gamma > 5/3$ a reflected shock is possible.

The algebraic equation for the case of a reflected rarefaction wave (Fig. 2.4-29) for all real gases is given by

$$\begin{aligned} & \sqrt{\frac{\beta_1 (1 + \alpha_1 P_{45})}{(\alpha_1 + P_{45}) (\alpha_1 P_{15} + 1) P_{45}}} \left[(P_{34} - P_{14}) \sqrt{\frac{(P_{15} + \alpha_1) P_{45}}{P_{14} + \alpha_1 P_{34}}} \right. \\ & \left. - (P_{45} - 1) \sqrt{\frac{\alpha_1 P_{15} + 1}{1 + \alpha_1 P_{45}}} - (1 - P_{15}) \right] + P_{34}^{\beta_1} - 1 = 0 \end{aligned} \quad (1)$$

where

$$P_{34} = P_{14} \cdot P_{21} \quad (2)$$

It is of interest to note that after the two waves overtake, the wave diagram in the (x, t) -plane appears just like the one for the ideal shock tube problem, and the wave elements can be studied as such. This fact is also borne out by Eq. (2), where P_{41} is the equivalent diaphragm pressure ratio. Consequently, the final strength of the transmitted shock wave P_{21} is always less than the combined strengths of the two overtaking waves P_{41} . However, the particle velocity $u_2 = u_3$ is greater than that behind the two shock waves (u_4) due to the acceleration across the reflected rarefaction wave.

2.4.4.2 Non-Overtaking of Two Rarefaction Waves

Although the initial conditions can readily be illustrated in the (x, t) -plane (Fig. 2.4-30), the two waves can never overtake and no interaction results. The reason may be seen by considering the above figure. State (2) is common to both P-rarefaction waves and as it is a uniform region, the head (H) of R_2 must travel with the identical velocity as the tail (T) of R_1 . Consequently, they cannot overtake.

The problem can be drawn in the (p, u) -plane as shown in Fig. 2.4-30. It is seen that in a sense state (2) is merely the condition on any characteristic line which includes (H) of R_2 and (T) of R_1 , and the two waves can be joined to form one single rarefaction wave of pressure ratio $P_{31} = P_{32} \cdot P_{21}$. That is, state (3) on the left is

connected to state (1) on the right by the same rarefaction wave locus, and state (2) can be considered as just another Mach line in the rarefaction wave fan. Consequently, there is no interaction between the two waves.

2.4.4.3 Overtaking of a Shock Wave by a Rarefaction Wave

This interaction is shown in the (p, u) -plane (Fig. 2.4-31) for the case of a weak overtaking rarefaction wave. It is seen that three wave systems are possible. A weakened or decayed transmitted shock wave always occurs ($P_{21} < P_{51}$). However, a reflected rarefaction wave, Mach wave, or compression wave steepening into a shock wave can result.

As the shock wave decays, its strength decreases and the entropy change across it diminishes. This gives rise to a variable entropy field in the form of a contact region rather than a contact surface (Fig. 2.4-32), which moves to the right.

If the overtaking rarefaction wave is strong, it will decay the shock to an extent that finally it becomes one of the Mach lines of the rarefaction wave fan. Consequently, the wave system can consist of a transmitted rarefaction wave and either a reflected rarefaction wave, Mach wave, or compression wave steepening into a shock wave.

The three possible wave systems are shown in Figs. 2.4-33 and 2.4-34. The contact surface in these cases moves to the left. It is also possible to have a transmitted Mach wave as well as a transmitted and a reflected Mach wave occurring simultaneously as limiting cases.

A method for computing this type of interaction is outlined in Ref. 1. In the case where uniform states result after the interaction, it is possible to obtain an algebraic solution in closed form as for the other interactions given above. Such solutions are given in Ref. 51a.

2.4.4.4 Overtaking of a Rarefaction Wave by a Shock Wave

In this case as well, the wave system is determined by the strength of the overtaking shock wave. For a weak shock, Fig. 2.4-35 shows that a transmitted rarefaction wave always occurs. However, the reflected wave can be a rarefaction wave, a Mach wave, or a compression wave steepening into a shock wave. From Fig. 2.4-36, it is seen that the overtaking shock is decayed until it becomes one of the Mach lines in the rarefaction wavefan. The decaying shock gives rise to a variable entropy field in the form of a contact region moving to the left.

If the pursuing P-shock wave is very strong, it goes right through the P-rarefaction wave (Fig. 2.4-37). It comes out weaker ($P_{21} < P_{45}$). However, the reflected wave is turned into a Q-wave and it can be either a rarefaction wave, a Mach wave, or compression wave which steepens into a shock wave. The interaction is also shown in the (x, t) -plane on Fig. 2.4-38. It has been shown in Ref. 1a that only reflected compression waves steepening into shock waves are possible for all physical gases ($1 \leq \gamma \leq 5/3$). Algebraic solutions in closed form can also be obtained for the above cases. For further details see Ref. 51b.

2.4.5 Application of One-Dimensional Wave Interactions to a Shock Tube of Finite Length

The previous results are very useful for the determination of optimum chamber and channel lengths that may be required for aerodynamic testing in a shock tube of constant cross section or in a hypersonic shock tunnel, and for chemical kinetics and wave interaction problems.

For example, consider the wave system in a shock tube of finite length in the (x, t) or the nondimensional (X, τ) -plane (Fig. 2.4-39). The relations that determine the points (X_3, τ_3) , (X_c, τ_c) and (X_s, τ_s) are developed in detail in Ref. 52.

$$X_3 = (\alpha_4 - 1 - \alpha_4 P_{34}^{\beta_4}) P_{34} - \frac{\beta_4 \alpha_4}{2} \quad (1)$$

$$\tau_3 = P_{34} - \frac{\beta_4 \alpha_4}{2} \quad (2)$$

$$X_c = 2 (\alpha_4 - 1) (1 - P_{34}^{\beta_4}) P_{34} - \frac{\beta_4 \alpha_4}{2} \quad (3)$$

$$\tau_c = 2 \tau_3 \quad (4)$$

$$X_s = W_{11} A_{14} \tau_s \quad (5)$$

$$\tau_s = \frac{2 A_{21} \tau_3}{U_{21} + A_{21} - W_{11}} \quad (6)$$

The relations for A_{14} , A_{21} , W_{11} , and U_{21} are given by Eqs. (10), (18), (19), and (20), Subsec. 2.3.2.

Equations (1) to (6) are plotted in Figs. 2.4-40 to 2.4-43 for different gas combinations against the diaphragm pressure ratio P_{41} for the same chamber and channel temperature ($T_{14} = 1$).

It is interesting to note that the position where the head of the reflected rarefaction wave will overtake the shock wave has a minimum value at a low diaphragm pressure ratio, which in the case of Air/Air, $P_{41} \sim 4$; and for He/Air, $P_{41} \sim 5$. For a chamber length of one foot, the minimum channel length occurs for Air/Air at about 15 ft, and for He/Air at 4 ft. For diaphragm pressure ratios approaching one or infinity, the overtaking process theoretically takes place at an infinite distance. If shock wave studies are conducted at the lower diaphragm pressure ratios, they should be made before the overtaking process takes place in order to prevent shock wave decay. This is especially important for gas combinations such as He/Air or H_2 /Air.

It may be seen from Fig. 2.4-44 that the maximum flow duration $\Delta\tau_3$ for the uniform state (3) occurs at X_3 for all diaphragm pressure ratios P_{41} for which $M_3 > 1$. If $M_3 < 1$, then the maximum occurs at $X = 0$. Similarly the maximum $\Delta\tau_2$ for region (2) occurs at X_c .

These values may be obtained from the above figures. If aerodynamic testing is to be done in regions (3) or (2), then the maximum testing time for a set of initial conditions is obtained by placing the model at X_3 and X_c , respectively. In order to eliminate the possibility of the reflected shock wave decreasing the maximum flow duration $\Delta\tau_2$ for region (2), the channel should be of a length (X_5) such that the reflected shock wave meets the head of the reflected rarefaction wave at the contact surface, i.e., the point (X_c, τ_c). The length X_5 may be determined as follows. The dimensionless time τ_c it takes for the shock wave to hit the end of the tube, reflect, and interact with the contact surface follows at once from geometrical considerations:

$$\tau_c = \frac{X_5}{w_{11} A_{14}} + \frac{X_5 - X_c}{w_{21} A_{14}} \quad (7)$$

Solving for X_5 , one obtains the required channel length,

$$X_5 = \frac{\tau_c A_{14} + X_c/w_{21}}{1/w_{11} + 1/w_{21}} \quad (8)$$

where w_{11} and w_{21} are the absolute magnitudes of the incident and reflected shock speeds as given by Eq. (19), Subsec. 2.3.2 and Eq. (14), Subsec. 2.4.1. Again, τ_c is given by Eq. (4).

In order to avoid excessive channel lengths when region (3) is under investigation, it is sufficient to use a length X_2^- such that the reflected shock wave strikes the contact surface when the head of the reflected rarefaction wave overtakes the tail of the incident wave, i.e., the time τ_3 . This practical simplification eliminates the necessity of solving the complex shock-contact surface interaction. Since from Eq. (4) $\tau_c = 2\tau_3$, therefore

$$X_2^- = \frac{1}{2} X_5 \quad (9)$$

The variation of X_5 with the diaphragm pressure ratio P_{41} is plotted on Fig. 2.4-45. It is seen that X_5 is only slightly greater than X_c for the higher diaphragm pressure ratios (Figs. 2.4-40 to 2.4-43) because the reflected shock speed w_{21} decreases as P_{41} increases. If the channel length is increased beyond that required for maximum $\Delta\tau_3$ and $\Delta\tau_2$, then these values are unaffected; if they are decreased, the testing time is reduced by the wave interactions.

Another useful method of calculating Δt_2 directly in microseconds for strong shock waves in air (as a perfect or imperfect gas) in the form of nomograph, is shown in Fig. 2.4-46 (Ref. 53). It should be noted that in practice the testing time is reduced due to imperfect gas effects as well as viscous effects. The boundary layer attenuates the shock wave, and the contact front spreads and accelerates so that the test time interval is reduced. Since the test time, in seconds, per foot of channel is given by

$$\Delta t_2 = \frac{1}{u_2} - \frac{1}{w_1} = \frac{1}{u_2 \sqrt{r_{21}}} = \frac{1}{w_1 (\sqrt{r_{21}} - 1)} \quad (10)$$

then, at the higher shock strengths when $\sqrt{r_{21}}$ for an imperfect gas can readily be twice the perfect gas value, the flow duration is halved due to real gas effects alone. The viscous effects noted above can in addition reduce the flow time by half again at higher shock strengths. Consequently, the expected flow duration might be about a quarter of the perfect gas value, or less.

SUPPLEMENT A

Equation of State for Thermally Imperfect Gases

Thermally imperfect gases do not follow the relation between p , ρ , and T as stated in Eq. (5) of Subsec. 2.1.1, except at very low density (large specific volumes). Many equations of state, some empirical, others based on molecular properties, have been proposed for imperfect gases. Van der Waals' equation is typical and is given by

$$\left(p + \frac{a}{v^2}\right) (v - b) = RT \quad (\text{A-1})$$

or

$$p = \rho RT \left(\frac{1}{1 - b\rho} + \frac{a\rho}{RT} \right)$$

where

$$\frac{a}{b} = \frac{27}{8} RT_c, \quad \frac{a}{b^2} = 27 p_c, \quad b = \frac{v_c}{3}, \quad \frac{RT_c}{p_c v_c} = \frac{8}{3}$$

All real (imperfect) gases can be liquified. The highest temperature at which this occurs is known as the critical temperature T_c ; the corresponding critical pressure and density are given by p_c and ρ_c . These critical quantities are characteristic of the gas and depend on intermolecular forces. It is seen that when ρ is very small (or v is very large) then Eq. (A-1) reduces to Eq. (5) of Subsec. 2.1.1 for a thermally perfect gas. It should be noted that equations for a real gas of the type given in Eq. (A-1) can be written in terms of a "compressibility" factor Z as (Ref. 4)

$$\frac{pV}{RT} = Z(p, T) \quad (\text{A-2})$$

where $Z = 1 \pm \delta$ and δ is a small quantity, usually.

The deviation δ is due to intermolecular forces at low temperature and high pressure, under which conditions the van der Waals forces are important. At sufficiently high temperature and low pressure the van der Waals forces are usually unimportant, but dissociation and ionization processes may take place in the gas. As a result of dissociation, for example, the number of particles per unit volume increases. If the mixture of undissociated and dissociated particles is assumed to be a mixture of two thermally perfect gases, then Dalton's law of partial pressures applies, and it is easily shown that

$$\frac{pV}{RT} = 1 + \alpha = Z \quad (\text{A-3})$$

where α is the degree of dissociation or the fraction of the original number of particles which are dissociated. If ionization takes place at still higher temperatures, then for a single diatomic gas, for example,

$$\frac{pV}{RT} = (1 + \alpha) (1 + x) = Z \quad (A-4)$$

where x is the degree of ionization. It will be noted from Eqs. (A-3) and (A-4) that the dissociated or ionized mixture itself does not behave as a thermally perfect gas even though the component gases of the mixture are assumed thermally perfect.

If the heat required to dissociate a unit mass of gas at constant p and T is given by l_d , the ratio $l_d/R = \theta_d$ has the dimensions of temperature and may be termed a characteristic temperature for dissociation. For example, $ml_d = 118,000$ cal/mole for O_2 (Ref. 5) and $\theta_d = 118,000/2 = 59,000^\circ K$ for O_2 (see Fig. 2.2-6a). The heat of dissociation l_d is a function of T . However, its variation with T can often be neglected. It should be noted that l_d is related to interatomic forces that hold the atoms together in a molecule, whereas the latent heat of vaporization l_v is related to the forces that hold the molecules together (van der Waals forces). Consequently, $C_v \ll l_d$ and, as stated above, van der Waals forces are usually unimportant at temperatures giving dissociation effects (for O_2 , $ml_v = 1640$ cal/mole at $90^\circ K$, whereas $ml_d \sim 118,000$ cal/mole). As for dissociation, a characteristic temperature $\theta_i = l_i/R$ may be defined for ionization, where l_i is the heat required to ionize a unit mass of gas. For atomic oxygen, for example, $ml_i = 284,000$ cal/mol. for single ionization, i.e., removal of one electron from the outer shell, and $\theta_i = 284,000/2 = 142,000^\circ K$ (see Table 2.1-1).

SUPPLEMENT B

Gas Imperfections at Low Pressures and High Temperatures

It was stated in Subsec. 2.1.1 that a perfect gas (thermally and calorically perfect) obeys the thermal equation of state $p v = RT$ and has constant specific heats C_v and C_p . It was also noted that in gas dynamics, high-pressure low-temperature flows, where van der Waals intermolecular forces exist, are seldom encountered. Consequently, this Supplement will consider caloric and thermal imperfections resulting from high temperature effects only, i.e., from molecular vibration, dissociation, ionization, and electronic excitation.

Consider first a monatomic gas like helium at a temperature such that the internal energy consists of translational energy only. Each atom has three degrees of freedom, i.e., the three co-ordinates defining its position in physical space (Fig. 2.1-3). According to the classical law of equipartition of energy, each degree of freedom will contribute on the average an amount $1/2 kT$ to the total kinetic energy, where k is Boltzmann's constant and T is the absolute temperature. Thus the internal energy per unit mass will be

$$e = \frac{3}{2} \frac{NkT}{m} = \frac{3}{2} RT$$

where N is Avogadro's number, m is the molecular weight, and R is the gas constant per unit molecular weight. The heat capacity per unit mass at constant volume is then

$$C_v = \left(\frac{\partial e}{\partial T} \right)_v = \frac{3}{2} R$$

and

$$C_p = C_v + R = \frac{5}{2} R$$

with

$$\gamma = \frac{C_p}{C_v} = \frac{5}{3}$$

If helium is now heated (the same result applies if work in the form of adiabatic compression is done on the gas) at constant volume, the gas temperature increases ($\Delta T = \Delta Q/C_v$) and the kinetic energy of the atoms increases. The atomic collisions add quanta of energy to the electrons and increase their energy. The electrons move from their ground state to outer orbits and the atom is now electronically excited. When the electrons fall to their original stable orbit or minimum energy level in a single-step transition or in a multi-step transition, they return their acquired quanta of energy by emitting photons of radiation whose frequencies will depend on the energy acquired during a collision and in the manner the transition to the ground state is made. If more heat is added, the kinetic energy of atoms becomes sufficiently large to knock out an electron from an atomic orbit. The gas is said to be ionized, and consists of a gaseous mixture (plasma) of neutral atoms,

ionized atoms, and electrons. Atom-atom collisions are not very effective in producing ionization (Ref. 10). Once enough free electrons are generated, they complete the ionization process very efficiently since they are light, small, travel at high velocity, and provide a long enough collision contact. During this process millions of atoms are involved and many electrons are recaptured, and the electrons transit to the ground state radiating at every conceivable frequency.

If the energy required to ionize an atom is V_i electron volts (ev), the ionization potential of that atom is said to be V_i volts. In the case of helium, $V_i = 24.58$ volts. This is the highest known ionization potential, and helium is the most difficult gas to ionize. The velocity v_e that an electron of mass m_e must acquire to produce ionization of helium is found from $1/2 m_e v_e^2 = 24.58 \text{ ev} = 24.58 \times 1.60 \times 10^{-19}$ joules. The electron mass $m_e = 9.1 \times 10^{-31}$ k gm giving $v_e = 2.94 \times 10^6$ meters/sec. The rare earths by comparison to helium are much easier to ionize. For example, the ionization potential of Na is $V_i = 5.14$ volts, and $v_e = 1.3 \times 10^6$ meters/sec.

If sufficient heat is added, then more than one electron can be removed by collision (second degree ionization). Entire electron shells can be stripped, and the gas can become fully ionized (Ref. 10a). Ionized atoms emit their own particular spectra.

From the above, it is seen that the contributions to the internal energy of an atomic gas come from the following sources:

1. Kinetic energy of atom translation (e_t)
2. Energy of electronic excitation (e_e)
3. Energy of ionization (e_i)

For a polyatomic gas the contributions to the internal energy come from the following sources:

1. Kinetic energy of molecular translation (e_t)
2. Kinetic energy of molecular rotation (e_r)
3. Energy of molecular vibration (e_v)
4. Energy of molecular dissociation (e_d)
5. Energy of electronic excitation (e_e)
6. Energy of ionization (e_i)

Therefore, in the general case,

$$e = e_t + e_r + e_v + e_d + e_e + e_i \quad (\text{B-1})$$

The above energy contributions arise in the following manner:

A molecule that consists of n atoms will require $3n$ co-ordinates to describe its state. A linear molecule like H_2 or CO_2 (Fig. 2.1-3) has 3 translational degrees of freedom which are described by co-ordinates x, y, z of its mass centre. It can also rotate about 2 axes (x^1, y^1), and these modes of motion are described by θ and ϕ . Consequently, a linear type molecule has $(3n - 5)$ additional degrees or energy sinks, i.e., H_2 has 1 and CO_2 has 4, as shown on Fig. 2.1-3. The energy sinks help to reduce the gas temperature. For example, with a given heat addition ΔQ , for translation $\Delta T = \Delta Q / \frac{3}{2} R$, and for rotation and translation $\Delta T = \Delta Q / \frac{5}{2} R$. Consequently, the temperature rise is reduced by a factor of $3/5$ with rotation. A nonlinear polyatomic molecule possesses 3 degrees of rotation and consequently has $(3n - 6)$ vibrational degrees (for example, SF_6 has 15 modes).

The rotational degrees are fully excited even at low temperatures and contribute $1/2 R$ each to C_v . The vibrational modes are due to the oscillations of the atoms of the molecule about their equilibrium position arising from the forces of attraction (valence forces) and repulsion (matter resists penetration). The vibrating molecule may be treated approximately as a quantum mechanical harmonic oscillator. That is, the vibrating atoms are assumed to obey Hooke's law and the atomic forces to vary linearly with distance. In the limit at very high temperatures, the kinetic and potential energy terms each contribute $1/2 R + 1/2 R = R$ per mode to C_v , which is the classical value for a particle executing simple harmonic motion. However, at high temperatures the oscillations are no longer small, and the motion is anharmonic.

The quantum harmonic oscillator energy per mode e'_v is given by (Ref. 11).

$$e'_v = RT \frac{Z}{e^Z - 1} \quad (B-2)$$

where

$$Z = \frac{h\nu}{kT} = 1.438 \frac{\bar{\nu}}{T}$$

$$\bar{\nu} = \frac{1}{\lambda}, \text{ wave number, or waves/cm}$$

$\lambda =$ wave length in cm

$h =$ Planck's constant (4.135×10^{-15} ev sec)

$k =$ Boltzmann's constant (86.1×10^{-6} ev/deg)

$$\left(\text{Since } C = \lambda \nu, \text{ therefore } Z = \frac{4.135 \times 10^{-15} \times 3 \times 10^{10} \times \bar{\nu}}{86.1 \times 10^{-6} T} = 1.438 \frac{\bar{\nu}}{T} \right)$$

It is seen that in the limit as $T \rightarrow 0$, $e'_v \rightarrow 0$ and as $T \rightarrow \infty$, $e'_v \rightarrow RT$.

The vibrational constant-volume specific heat per mode is

$$C'_{\text{vib}} = \frac{\partial}{\partial T} (e'_{\text{vib}})_v \quad \text{or} \quad C'_{\text{vib}} = R e^Z \left(\frac{Z}{e^Z - 1} \right)^2 \quad (\text{B-4})$$

Quite often $Z = \frac{h\nu}{kT}$ is expressed as $Z = \frac{\theta_v}{T}$, where $\theta_v = \frac{h\nu}{k}$ is a characteristic vibrational temperature. Consequently,

$$C'_{\text{vib}} = R \left(\frac{\theta_v}{T} \right)^2 \frac{e^{\theta_v/T}}{\left(e^{\theta_v/T} - 1 \right)^2} \quad (\text{B-5})$$

The above equation is shown in Fig. 2.1-4 for oxygen ($\bar{\nu} = 1570$ waves/cm and $\theta_v = 2260^\circ\text{K}$).

All the vibrational modes will make their own contribution to

$$C_{\text{vib}}. \quad \text{In general, } C_{\text{vib}} = R \sum_1^{3n-6} e^Z \left(\frac{Z}{e^Z - 1} \right)^2 \quad (\text{B-6})$$

For example, SF_6 has the following 15 modes: $1 \times \bar{\nu}_1$ at 775 cm^{-1} , $2 \times \bar{\nu}_2$ at 664 cm^{-1} , $3 \times \bar{\nu}_3$ at 960 cm^{-1} , $3 \times \bar{\nu}_4$ at 615 cm^{-1} , $3 \times \bar{\nu}_5$ at 524 cm^{-1} , and $3 \times \bar{\nu}_6$ at 363 cm^{-1} . At 30.00°C or 303.16°K , the respective contributions are as follows: $C_{\text{vib}}/R = 0.360 + 0.968 + 0.705 + 1.542 + 1.836 + 2.356 = 7.769$. As expected from Eq. (B-6) the largest contributions come from the low frequencies. Therefore SF_6 at 30.00°C has a $C_v = C_t + C_r + C_{\text{vib}} = \frac{3}{2}R + \frac{3}{2}R + 7.769R$, or $C_v = 21.398 \text{ cal/gm mole}$, $C_p = 23.385 \text{ cal/gm mole}$, and $\gamma = 1.093$.

If the molecules are heated still further, when an atom reaches the highest quantum vibrational energy level, the molecular binding forces are overcome and the molecule dissociates into atoms. Therefore, at high temperatures a dissociational heat capacity exists.

Consider the case of a diatomic molecule like O_2 . The dissociation equation is given by $2\text{O} \rightleftharpoons \text{O}_2$. If the degree or per cent dissociation is α , then $p_v = \frac{RT}{m} (1 + \alpha)$, where R is the universal gas constant, and m the molecular weight. If $K(T)$ is the equilibrium constant for dissociation (dimensions of pressure) derived from the law of mass action (ref. 3), then

$$\frac{K(T)}{p} = \frac{4\alpha^2}{1 - \alpha^2} \quad (\text{B-7})$$

or

$$\alpha = \sqrt{\frac{K}{4p + K}} \quad (\text{B-7a})$$

That is, α increases with decreasing pressure and increasing temperature. It is highly temperature dependent. A plot of α against T/θ_d from Ref. 3 is shown on Fig. 2.1-5a, where θ_d is the characteristic temperature for dissociation. It was noted in Supplement A that for O_2 , $ml_d = 118,000$ cal/mole, or $\theta_d = l_d/R = 59,000^\circ K$. This reduced or normalized plot makes it possible to use a single graph (approximately) for all diatomic gases (see Eq. (B-12)).

At higher temperatures electronic excitation and ionization set in, giving rise to the specific heat contributions C_e and C_i . For example, for the hydrogen atom in the ground state, an electron revolves at an orbit whose radius $r_0 \sim 0.5\text{\AA}$. It requires an energy of 10.20 eV to move the electron to the next energy level or first excited state. To remove the electron completely an energy of 13.58 eV is required. To dissociate a hydrogen molecule it requires 4.477 eV and to ionize it 15.42 eV (Ref. 5). Consequently, the contributions by electronic excitations to the molecular specific heat is negligible because dissociation will set in first. However, such contributions to the atomic specific heat are not insignificant (Ref. 12).

In general, the separation between the lowest state and the first excited state is 2 to 10 eV for electronic energies, 0.2 to 2 eV for vibrational energies, and about 10^{-5} to 10^{-3} eV for rotational energies. An electronic transition will therefore also generate entire series of vibrational and rotational bands and spectral lines.

The specific heats of dissociation and ionization can be determined by very similar methods. Consider the case of a monatomic gas like argon. The single ionization reaction is given by $A \rightleftharpoons A^+ + \text{electron}$. If K is the equilibrium constant for single ionization and x the degree or fraction of the gas that is ionized, then (Ref. 3)

$$p = \rho \frac{Q}{m} T(1 + x) \quad (\text{B-8})$$

and

$$\frac{K}{P} = \frac{x^2}{1 - x^2} \quad (\text{B-9})$$

or

$$x = \sqrt{\frac{K}{p + K}} \quad (\text{B-9a})$$

A plot of x with T/θ_1 is shown in Fig. 2.1-5b. It is seen that in this case the normalized plot does not apply to all gases. Hydrogen is an exception, but helium and argon agree very well. The reason is given later on (Eq. B-12).

It is shown in Refs. 11 and 12 that in general for the reaction $A + B \rightleftharpoons AB$, that is, $2O \rightleftharpoons O_2 + l_d$ or $A^+ + e \rightleftharpoons A + l_i$, the equilibrium constant K_{AB} is given by

$$K_{AB} = \frac{v_o}{N_o} \cdot \frac{(2\pi k)^{3/2}}{h^3} \cdot m^{3/2} \cdot T^{3/2} \cdot e^{-l/kT} \frac{P_A P_B}{P_{AB}} \quad (B-10)$$

where

$$\frac{v_o}{N_o} = (1 + \alpha)k \frac{T}{p} \quad (\text{for dissociation})$$

$$\frac{v_o}{N_o} = (1 + x)k \frac{T}{p} \quad (\text{for ionization})$$

$$K_{AB} = \frac{4\alpha^2}{1 - \alpha^2} \quad (\text{for dissociation})$$

$$K_{AB} = \frac{x^2}{1 - x^2} \quad (\text{for ionization})$$

$$m = \frac{m_A \cdot m_B}{m_A + m_B}, \quad \frac{N_o}{v_o} = \text{particles/cc}$$

$$m = \frac{m_A}{2} = \frac{1}{2} \text{ atomic mass, in the case of a diatomic molecule (mass of hydrogen atom} = 1.673 \times 10^{-24} \text{ gm)}$$

$$m = m_e = \text{electron mass, in the case of ionization } m_{ion} \gg m_e \\ (m_e = 9.1066 \times 10^{-28} \text{ gm})$$

$$l = \text{heat of dissociation } (l_d) \text{ or ionization } (l_i)$$

$$p = \text{pressure in dynes/cm}^2 \text{ (1 atm} = 1.0132 \times 10^6 \text{ dynes/cm}^2)$$

$$T = \text{temperature in } ^\circ\text{K}$$

$$h = \text{Planck's constant} = 6.624 \times 10^{-27} \text{ erg sec (4.135} \times 10^{-15} \text{ ev sec)}$$

$$k = \text{Boltzmann's constant} = 1.3805 \times 10^{-16} \text{ erg/}^\circ\text{K (8.616} \times 10^{-5} \text{ ev/}^\circ\text{K)}$$

P_{AB} , P_A , P_B are the partition functions or statistical weights of the molecule and atoms in the case of dissociation, and of the atom (a), ion (i), and electron (e) in the case of ionization.

The partition functions are highly temperature dependent and mildly density dependent for dissociation equilibrium (Ref. 12). They are sometimes assumed as constant for the case of ionization by neglecting higher excited electronic levels, and such values for typical elements are given in Table 2.1-1. At high temperatures or low densities, the more accurate values should be used to avoid significant errors. (The error is generally small for $x \approx 0.25$; see Ref. 13a for a discussion.)

Equation (B-10) may be rearranged for the case of dissociation of a diatomic gas, using Eq. (B-7), as

$$\alpha = \left[A(p, T) \frac{p}{T^{5/2}} e^{\theta_d/T} + 1 \right]^{-1/2} \quad (\text{B-11})$$

where

$$A(p, T) = \frac{4h^3}{\left(2\pi \frac{m_a}{2}\right)^{3/2} k^{5/2}} \cdot \frac{P_{AB}}{P_A P_B}$$

It is worth noting that α may be plotted against the reduced or normalized temperature T/θ_d . For a given value of T/θ_d , the temperature T will vary with the gas θ_d . If for two or more different gases the ratio $A(p, T)/T^{5/2}$ remains constant, then a normalized plot of α versus T/θ_d for varying p will produce a set of curves that are identical for each p (this is approximately true for diatomic gases as shown in Fig. 2.1-5a).

Similarly, for the case of ionization,

$$x = \left[A(p, T) \frac{p}{T^{5/2}} e^{\theta_1/T} + 1 \right]^{-1/2} \quad (\text{B-12})$$

where

$$A(p, T) = \frac{h^3}{(2\pi m_e)^{3/2} k^{5/2}} \cdot \frac{p_a}{P_i P_e} \approx \frac{3p_a}{P_i P_e}$$

Equation (B-12) is also known as Saha's equation (Ref. 13). Some typical values for l_1 , P , and x are listed in Table 2.1-1. If x is very small, then Eq. (B-12) may be written by neglecting unity in the bracket as

$$x \sim \frac{T^{5/4}}{(Ap)^{1/2}} \cdot e^{-\theta_1/2T} \quad (\text{B-12a})$$

The previous remarks regarding a universal set of curves for monatomic gases on a plot of x against T/θ_1 for various p apply to helium and argon but not to hydrogen, where $A(p, T)/T^{5/2}$ varies considerably from the others. If p is in atmospheres and l_1 is in volts, then from Eq. (B-12)

$$x = \left[3.04 \times 10^6 \frac{p}{T^{5/2}} e^{1.16 \times 10^4 V_1/T} \frac{P_a}{P_i P_e} + 1 \right]^{-1/2} \quad (\text{B-12b})$$

For the case of argon $\frac{P_a}{P_1 P_e} = \frac{1}{12}$, $v_1 = 15.76$ volts, and

$$x = \left[2.54 \times 10^5 \frac{p}{T^{5/2}} e^{1.83 \times 10^5/T} + 1 \right]^{-1/2} \quad (\text{B-12c})$$

In order to illustrate how the specific heats are determined with the aid of the above equations, consider the case of single ionization. A relation derived from the First Law of thermodynamics and the condition of isentropic flow is given by

$$C_v \left(\frac{\partial T}{\partial p} \right)_v dp + C_p \left(\frac{\partial T}{\partial v} \right)_p dv = 0 \quad (\text{B-13})$$

Since

$$T = \frac{pv}{R(1+x)}$$

$$\left(\frac{\partial T}{\partial p} \right)_v = \left[\frac{T}{p} - \frac{T}{1+x} \left(\frac{\partial x}{\partial p} \right)_T \right] / \left[1 + \frac{T}{1+x} \left(\frac{\partial x}{\partial T} \right)_p \right]$$

$$\left(\frac{\partial T}{\partial v} \right)_p = \frac{T}{v} / \left[1 + \frac{T}{1+x} \left(\frac{\partial x}{\partial T} \right)_p \right]$$

From Eq. (B-13), and $a^2 = \left(\frac{\partial p}{\partial \rho} \right)_s = \gamma^* pv$, by definition,

$$\left(\frac{\partial p}{\partial v} \right)_s = - \frac{C_p}{C_v} \left(\frac{\partial T}{\partial v} \right)_p / \left(\frac{\partial T}{\partial p} \right)_v = - \frac{1}{v^2} \left(\frac{\partial p}{\partial \rho} \right)_s \quad (\text{B-14})$$

and

$$\gamma^* = \frac{C_p}{C_v} \frac{1}{1 - \frac{p}{1+x} \left(\frac{\partial x}{\partial p} \right)_T} \quad (\text{B-14a})$$

From Eq. (B-12), if the partition functions are assumed as constant, then

$$x = \left[A \frac{p}{T^{5/2}} e^{\theta_1/T} + 1 \right]^{-1/2} \quad (\text{B-14b})$$

where $A = \text{constant}$.

Consequently,

$$\left(\frac{\partial x}{\partial p} \right)_T = - \frac{1}{2} \cdot \frac{x(1-x^2)}{p}$$

and

$$\gamma^* = \frac{C_p}{C_v} \cdot \frac{2}{2 + x - x^2} \quad (\text{B-15})$$

Equation (B-15) shows that the isentropic index or exponent γ^* of an ionized gas depends on the degree of ionization. It is equal to the specific heat ratio only when $x = 0$ or $x = 1$. When $x \rightarrow 1$, Eq. (B-15) is no longer correct as the higher electronically excited states have been omitted. A discussion of this particular point is given in Ref. 13a with numerical examples.

The internal energy per unit mass of ionized gas is given by

$$e = \frac{3}{2} (1 + x) RT + l_1 x \quad (\text{B-16})$$

Similarly, the enthalpy per unit mass is given by

$$h = e + pv = \frac{5}{2} (1 + x) RT + l_1 x \quad (\text{B-17})$$

The specific heats are defined by

$$C_v = \left(\frac{\partial e}{\partial T} \right)_v = \frac{3}{2} R(1 + x) + \left(\frac{\partial x}{\partial T} \right)_v \left(l_1 + \frac{3}{2} RT \right) \quad (\text{B-18})$$

$$C_p = \left(\frac{\partial h}{\partial T} \right)_p = \frac{5}{2} R(1 + x) + \left(\frac{\partial x}{\partial T} \right)_p \left(l_1 + \frac{5}{2} RT \right) \quad (\text{B-19})$$

For $x = x(p, T)$ and $p = \frac{RT}{v} (1 + x)$, it can be shown that

$$\left(\frac{\partial x}{\partial T} \right)_v = \frac{T \left(\frac{\partial x}{\partial T} \right)_p + p \left(\frac{\partial x}{\partial p} \right)_T}{T \left[1 - \frac{p}{1 + x} \left(\frac{\partial x}{\partial p} \right)_T \right]} \quad (\text{B-20})$$

Assuming Eq. (B-14b)

$$\left(\frac{\partial x}{\partial T} \right)_p = \frac{1}{2} \frac{x}{T} (1 - x^2) \left(\frac{5}{2} + \frac{\theta_1}{T} \right) \quad (\text{B-21})$$

and

$$\left(\frac{\partial x}{\partial p} \right)_T = -\frac{1}{2} x \left(\frac{1 - x^2}{p} \right) \quad (\text{B-22})$$

Substitution of Eqs. (B-21) and (B-22) into Eq. (B-20) gives

$$\left(\frac{\partial x}{\partial T}\right)_v = \frac{x(1-x)}{T(2-x)} \left(\frac{3}{2} + \frac{\theta_1}{T}\right) \quad (\text{B-20a})$$

Further substitution into Eqs. (B-18) and (B-19) gives

$$C_v = \frac{3}{2} R(1+x) + Rx \frac{(1-x)}{(2-x)} \left(\frac{3}{2} + \frac{\theta_1}{T}\right)^2 \quad (\text{B-23})$$

$$C_p = \frac{5}{2} R(1+x) + \frac{Rx}{2} (1-x^2) \left(\frac{5}{2} + \frac{\theta_1}{T}\right)^2 \quad (\text{B-24})$$

For $\frac{\theta_1}{T} \gg \frac{3}{2}$ and $x \ll 1$ the specific heat per unit mass at constant volume may be written as

$$C_v = \frac{3}{2} R + \frac{3}{2} Rx + \frac{R}{2} \left(\frac{\theta_1}{T}\right)^2 x \quad (\text{B-23a})$$

The first term is a contribution arising from the translational energy of the nonionized gas. The second term is the contribution to the translational energy of the additional particles formed by ionization. The last term is essentially due to the addition of the heat of ionization.

Although Eqs. (B-23) and (B-24) apply only for small ionization, i.e., at low temperature and not too low densities, they indicate qualitatively how the specific heats vary with temperature. The contribution to C_p or C_v from ionization is initially zero at sufficiently low temperature ($x = 0$), increases with increasing temperature (increasing x) to a maximum which can be much larger than $\frac{3}{2} R$, and then decreases asymptotically to $\frac{3}{2} R$ for very high temperature ($x \rightarrow 1$). Correspondingly, γ is initially $\frac{5}{3}$ for $x = 0$, decreases to a minimum as x increases, and then increases towards $\frac{5}{3}$ as $x \rightarrow 1$.

Similar considerations for dissociation show that for a diatomic gas

$$\gamma = \frac{C_p}{C_v} = \frac{2}{2 + \alpha - \alpha^2} \quad (\text{B-25})$$

However, owing to rotation and vibration, C_v and C_p become more complex; for example,

$$C_v = \frac{3}{2} \frac{R}{m} (1 + \alpha) + (1 - \alpha) \frac{R}{m} \left\{ 1 + e^z \left(\frac{z}{e^z - 1} \right)^2 \right\} + \frac{\alpha(1 - \alpha)}{2 - \alpha} \frac{R}{m} \left\{ \frac{\theta_d}{T} + \frac{1}{2} - \frac{z}{e^z - 1} \right\}^2 \quad (\text{B-26})$$

For $\frac{\theta_d}{T} \gg \frac{1}{2} - \frac{Z}{e^z - 1}$ the last term of Eq. (B-26) may be written as

$$\frac{C_d^-}{R} \approx \frac{\alpha(1-\alpha)}{2-\alpha} \left(\frac{\theta_d}{T}\right)^2 \quad (\text{B-27})$$

A plot of Eq. (B-27) for O_2 is shown on Fig. 2.1-6, and typical values of K , α , and C_d^- are given in Table 2.1-2. Similarly, the contribution C_i of the ionization terms of Eq. (B-23) involving x for atomic hydrogen is shown in Fig. 2.1-7 (Ref. 15). It can be seen that C_i behaves somewhat like C_d^- (Fig. 2.1-6). At $T = 10,000^\circ\text{K}$, the C_i contribution is nearly the same as for the nonionized gas ($5.57 \times 10^3 \text{ erg/cm}^3 \text{ deg}$). The value of C_i rises with T until at $20,000^\circ\text{K}$ it achieves a maximum of about 100 times the nonionized value. It then falls steadily to the nonionized value with increasing temperatures as the gas approaches complete single ionization. An extensive treatment of specific heats may be found in Ref. 16 and additional data on dissociation phenomena in Ref. 17. An excellent summary is given in Ref. 12.

Although the above contributions to the internal energy of the gas were treated for clarity as separate processes, it should be noted that they vary continuously with temperature and may be present together in varying degrees. At the higher temperatures, dissociation, electronic excitation, and ionization become increasingly dominant. In the case of a gas mixture like air, these processes occur at different temperatures, depending on the gas constituent, and the possibility of chemical reactions of the various components is present. For example, in air at Mach numbers between 12 and 20 one can expect to find NO , NO_2 , N_2O , NO^+ , O_2 , O , N , O^- , O^+ , N^+ , and electrons as gas components behind normal shock waves (Refs. 18 and 35).

SUPPLEMENT C

Relaxation Effects in Gases

If heat is slowly added or removed from a container (Fig. 2.1-8a, graphs (a) and (c)) the equipartition of energy takes place without disturbance (that is, the molecules are able to adjust in a reversible manner) by means of molecular collisions, as was noted in Supplement B. The number of collisions required to achieve equilibrium differs for each degree of freedom. It requires only a few collisions to achieve translational (1 or 2) and rotational (2 to 6) equilibrium, but many orders of magnitude more for other degrees. However, if heat is added or removed so rapidly that only the translational degrees can come into equilibrium (Fig. 2.1-8a, graphs (b) and (d)), the gas is disturbed, and it takes some time for the other degrees of freedom to catch up and attain their portion of energy by collision. The time it takes to reach equilibrium for a particular degree of freedom is known as the relaxation time τ . The approach to equilibrium of any degree of freedom is nearly exponential, or the final state is reached without oscillation when subject to a step change.

Under these simplifying assumptions, it can be shown (Refs. 11, 14, and 19) that the rate of decrease with time of the translational temperature T in Fig. 2.1-8b behind the shock wave is proportional to the deviation from the final equilibrium value T_2^* . That is,

$$\frac{dT}{dt} = - \left[\frac{T - T_2^*}{\tau} \right] \quad (C-1)$$

The solution of Eq. (C-1) is

$$T = T_2^* + (T_2 - T_2^*) e^{-t/\tau} \quad (C-2)$$

when $t = 0$, $T = T_2$

$$t = \tau, \quad T = T_2^* + \frac{1}{e} (T_2 - T_2^*)$$

The transition curves for pressure, density, and flow velocity exhibit a similar exponential approach to equilibrium (Ref. 14) for every internal degree of freedom.

The rapid disturbance followed by relaxation causes an irreversible adjustment, and such transfer of energy shows up as an increase in the entropy of the gas. The entropy change depends on the magnitude of the disturbance (which can be characterized by the pressure ratio and other thermodynamic quantities across a shock wave, for example) and the total number of collisions required to bring the gas to the new equilibrium molecular velocity distribution. The transfer of energy therefore depends on the number of collisions which a molecule undergoes. At a given temperature the number of collisions per unit time

varies directly as the gas pressure, and the relaxation time τ therefore varies inversely as the pressure. The above may be stated roughly as (Ref. 12)

$$\tau = Z \tau_c \quad (C-3)$$

where Z = pure number that measures the number of collisions required to achieve $(1 - \frac{1}{e})$ of the equilibrium conditions and is independent of density.

τ_c = time between collisions and depends strongly on density.
 $(\tau_c \sim 2 \times 10^{-10}$ sec at N T P, or 5×10^9 collisions/molecule/sec; $\tau_c \sim \lambda/a$ or $\tau_c \sim 1/\rho \sqrt{T}$)

At a given temperature the time between collisions will decrease at higher density as there are more molecules present. If the temperature is now raised the molecular speed is also increased and the collision time is decreased.

The exchange between rotation and translation is very efficient and under standard conditions only a few collisions are required, so that $Z_r \sim 2$ to 6 and $\tau_r \sim 10^{-9}$ sec. Hydrogen is an exception, with $Z_r \sim 180$ and $\tau_r \sim 4 \times 10^{-8}$ sec. The values of Z_v and τ_v for vibrational equilibrium given in Table 2.1-3 are taken from Ref. 14. It is seen that there is a very wide range in Z_v or τ_r , and heavy gases have small vibrational relaxation times. Some impurities, like water, are very effective in reducing the number of collisions Z_v by many orders of magnitude (Ref. 19).

An increase in the temperature and densities of the gas (e.g., behind the normal shock wave) reduces τ_c and τ . It can be shown that for temperatures less than 1000°K (Refs. 20 and 21)

$$\ln \tau = - \left(\frac{\epsilon}{kT} \right)^{1/3} + \text{constant} \quad (C-4)$$

where ϵ = characteristic energy. A plot of $\ln \tau$ versus $T^{-1/3}$ shows good agreement for N_2 and O_2 but only fair agreement for CO_2 (Ref. 21). Vibrational and dissociational relaxation times measured in a shock tube (Refs. 18 and 21) are given in Table 2.1-4 and Fig. 2.1-8b.

Quite often it is of interest to know the distance or path length over which the relaxation process extends over a body or a model in order to determine the validity of exact simulation of flow properties. This length is known as the relaxation distance L or path length. In terms of L , Eqs. (C-1) and (C-2) may be rewritten as

$$\frac{dT}{dx} = - \frac{(T - T_2^*)}{L} \quad (C-1a)$$

$$T = T_2^* + (T_1 - T_2^*) e^{-x/L} \quad (C-2a)$$

For example, if a body is travelling at $M = 10$ or $10,000$ ft/sec and the relaxation times are of the order of 10^{-7} , 10^{-5} , and 10^{-3} sec, then the relaxation distance L is of the order of 10^{-3} , 10^{-1} , and 10 ft. An actual computation is given in Ref. 18 and is listed in Table 2.1-5. Recent experimental data from interferometric measurements in a shock tube are given in Refs. 21a and 54.

From the above considerations it can be concluded that the entropy change across a shock wave will be increased as each new degree of freedom such as vibration, dissociation, or ionization becomes excited since more molecular collisions are required to bring the velocity distribution of the unshocked molecules up to that found behind the shock front. The magnitude of the entropy change will increase with the intensity of the shock wave.

Equation (C-1) also applies to chemically reactive flows (such as with dissociation or recombination) and results in a chemical relaxation time τ_K given by

$$\frac{dx}{dt} = -\frac{1}{\tau_K} (x - x_e) \quad (C-1b)$$

where x = instantaneous concentration (or energy of excitation of external or internal degrees as in Eq. (C-1) and x_e = equilibrium value of x . Denote the time for a gas particle to flow a characteristic distance (e.g., model length) by τ_F . Then, if

$$\tau_F \ll \tau_K \quad (C-5)$$

the flow is said to be frozen. The flow time of the gas particle about the model is too short for any chemical reaction to occur. The flow is said to be in equilibrium when

$$\tau_K \ll \tau_F \quad (C-6)$$

For a diatomic gas like oxygen, for example, the chemical relaxation time at the same pressure and shock Mach number can be orders of magnitude greater than the vibrational relaxation time (Ref. 21a).

SUPPLEMENT D

An Alternative Development of Shock-Wave Equations
for Real Gases

Subsection 2.2.2 presents a development of the shock-wave equations. Another approach used to determine the properties behind normal shock waves is given in Ref. 11. The equations of motion (Subsec. 2.2.1) are rewritten as

$$\rho v = \rho_1 v_1 = m \quad (D-1)$$

$$\rho = \frac{m}{v} \quad (D-1a)$$

$$p + mv = p_1 + mv_1 = mV \quad (D-2)$$

$$p = m(V - v) \quad (D-2a)$$

$$v = \frac{p_1}{\rho_1 v_1} + v_1 \quad (D-2b)$$

$$v/a_1 = (1 + \gamma_1 M_s^2) / \gamma_1 M_s \quad (D-2c)$$

$$\frac{p}{\rho} = (v - v) v \quad (D-3)$$

$$\frac{\beta p}{\rho} + \frac{1}{2} v^2 = \beta_1 \frac{p_1}{\rho_1} + \frac{1}{2} v_1^2 = \frac{1}{2} c^2 \quad (D-4)$$

$$c^2 = v_1^2 + 2\beta_1 \frac{p_1}{\rho_1} \quad (D-4a)$$

where

$$c = \sqrt{\frac{2}{\gamma - 1}} a_0 = \sqrt{\frac{\gamma + 1}{\gamma - 1}} \bar{a} \quad (D-5)$$

a_0 = stagnation sound speed

\bar{a} = sound speed where locally $M = 1$

β = enthalpy parameter (enthalpy divided by $\frac{p}{\rho} \equiv \frac{h}{p/\rho}$)

or

$$h = \frac{\beta p}{\rho} \quad (D-6)$$

For a perfect gas:

$$h_1 = \frac{\gamma_1}{\gamma_1 - 1} \cdot \frac{p_1}{\rho_1} \quad \text{or} \quad \beta_1 = \frac{\gamma_1}{\gamma_1 - 1} \quad (D-7)$$

The internal energy,

$$e = h - \frac{p}{\rho} = (\beta - 1) \frac{p}{\rho} \quad (D-8)$$

for a perfect gas

$$e = \frac{1}{\gamma_1 - 1} \cdot \frac{p}{\rho} \quad (D-8a)$$

That is, only for a perfect gas can β_1 be expressed in terms of γ_1 .
The equation of state is given by

$$\frac{p}{\rho} = z \frac{R}{m} T \quad (D-9)$$

Inserting Eq. (D-3) in Eq. (D-4) yields

$$\beta(v - v) v + \frac{1}{2} v^2 = \frac{1}{2} c^2 \quad (D-10)$$

or

$$v = \frac{\beta v \pm \sqrt{\beta^2 v^2 - (2\beta - 1) c^2}}{2\beta - 1} \quad (D-10a)$$

Since

$$\frac{v_1}{a_1} = M_s = w_{j1} \quad \text{and} \quad \frac{v_2}{a_1} = v_{21}$$

The positive root gives

$$M_s = \frac{1 + \gamma_1 M_s^2}{\gamma_1 M_s} \beta_1 + \sqrt{\left(\frac{1 + \gamma_1 M_s^2}{\gamma_1 M_s} \beta_1 \right)^2 - (2\beta_1 - 1) \left(M_s^2 + \frac{2}{\gamma_1 - 1} \right)} \quad (D-11)$$

That is, $v_+ > a_1$, or the flow is supersonic in front of the shock. The negative root gives the local particle velocity at any point behind the shock wave divided by the free stream sound speed ahead of the shock front (or $v_- < a_1$, the flow is subsonic behind a sharp fronted shock).

In particular, we choose the equilibrium values after the relaxation zone,

$$v_{21}^* = \frac{\frac{1 + \gamma_1 M_s^2}{\gamma_1 M_s} \beta - \sqrt{\left(\frac{1 + \gamma_1 M_s^2}{\gamma_1 M_s} \beta\right)^2 - (2\beta - 1) \left(M_s^2 + \frac{2}{\gamma_1 + 1}\right)}}{2\beta - 1} \quad (D-12)$$

As

$$M_s \rightarrow \infty, \quad \frac{v_{21}^*}{M_s} = \frac{v_2^*}{v_1} = \frac{\rho_1}{\rho_2} \rightarrow \frac{1}{2\beta - 1} \quad (D-12a)$$

From Eq. (D-12) when $\beta = \beta_1$, then for a perfect gas, constant γ_1 ,

$$v_{21} = \frac{2}{\gamma_1 + 1} \left(\frac{\gamma_1 - 1}{2} M_s + \frac{1}{M_s} \right) \quad (D-13)$$

and when $M_s \rightarrow \infty$

$$\frac{v_{21}}{M_s} = \frac{v_2}{v_1} = \frac{\rho_1}{\rho_2} \rightarrow \frac{\gamma_1 - 1}{\gamma_1 + 1} \quad (D-13a)$$

or

$$\frac{U_{21}}{M_s} = 1 - \frac{\gamma_1 - 1}{\gamma_1 + 1} = \frac{2}{\gamma_1 + 1} \quad (D-13b)$$

Consequently, the density ratio or the velocity ratio across the shock approaches a finite limit.

From Eqs. (D-1) and (D-2)

$$\Gamma_{21}^* = M_s / v_{21}^* \quad (D-14)$$

$$P_{21}^* = \gamma_1 M_s \left(\frac{1 + \gamma_1 M_s^2}{\gamma_1 M_s} - v_{21}^* \right) \quad (D-15)$$

when

$$M_s \rightarrow \infty, \quad P_{21}^* \sim \gamma_1 M_s^2$$

$$zT_{21}^* = \frac{P_{21}^*}{\Gamma_{21}^*} = \gamma_1 v_{21}^* \left(\frac{1 + \gamma_1 M_s^2}{\gamma_1 M_s} - v_{21}^* \right) \quad (D-16)$$

$$M_s \rightarrow \infty \quad T_{21}^* \sim \frac{\gamma_1}{2} v_{21}^* M_s$$

Furthermore, from Eq. (D-10a), the sum of the roots,

$$v_1 + v_2^* = -\frac{\beta v}{2\beta - 1} \quad (D-17)$$

The product of the roots,

$$v_1 v_2^* = \frac{C^2}{2\beta - 1} \quad (D-18)$$

For a perfect gas $\beta = \beta_1$ and

$$v_1 v_2 = \frac{v_1^2 + 2(\beta_1 - 1) a_1^2}{2\beta_1 - 1} \quad (D-19)$$

From Eq. (D-4) when

$$v_2 = a_2 = \bar{a}$$

then

$$\frac{\gamma_1 - 1}{\gamma_1 + 1} v_1^2 + \frac{2a_1^2}{\gamma_1 + 1} = \bar{a}^2 \quad (D-20)$$

or

$$v_1 v_2 = \bar{a}^2 = \frac{v_1^2 + 2(\beta_1 - 1) a_1^2}{2\beta_1 - 1} = \frac{p_2 - p_1}{\rho_2 - \rho_1} \quad (D-21)$$

Equation (D-21) is the Prandtl form of the energy equation for a perfect gas. Alternately, for very strong shocks, $v_1 \gg a_1 \sim \sqrt{p/\rho}$, then from Eqs. (D-2b) and (D-4a), $v \sim C \sim v_1$, or from Eq. (D-18)

$$v_2^* = v_1 / (2\beta - 1) \quad (D-22)$$

and from Eq. (D-1)

$$\frac{\rho_2^*}{\rho_1} = \frac{v_1}{v_2^*} = (2\beta - 1) \quad (D-23)$$

Similarly, from Eqs. (D-2a) and (D-23)

$$p_2^* = \rho_1 v_1 (v_1 - v_2^*) = \frac{2\rho_1 v_1^2 (\beta - 1)}{2\beta - 1} \quad (D-24)$$

$$\frac{p_2^*}{\rho_2^*} = Z \frac{R}{m} T_2^* = \frac{2v_1^2 (\beta - 1)}{(2\beta - 1)^2} \quad (D-25)$$

or

$$P_{21}^* = \frac{2 \gamma_1 M_s^2 (\beta - 1)}{(2\beta - 1)} \quad (D-26)$$

$$T_{21}^* = \frac{2 \gamma_1 M_s^2 (\beta - 1)}{z(2\beta - 1)^2} \quad (D-27)$$

The above equations reduce to the forms given in Subsec. 2.2.1 for a perfect gas and are summarized below for the case $M_s \rightarrow \infty$, for a perfect and imperfect gas.

$$\begin{aligned} \frac{v_2}{v_1} &= \frac{\gamma_1 - 1}{\gamma_1 + 1} & \frac{v_2^*}{v_1^*} &= \frac{1}{2\beta - 1} \\ \Gamma_{21} &= \frac{\gamma_1 + 1}{\gamma_1 - 1} & \Gamma_{21}^* &= 2\beta - 1 \\ P_{21} &= \frac{2\gamma_1}{\gamma_1 + 1} M_s^2 & P_{21}^* &= \frac{2\gamma_1 M_s^2 (\beta - 1)}{2\beta - 1} \\ T_{21} &= \frac{2\gamma_1(\gamma_1 - 1)}{(\gamma_1 + 1)^2} M_s^2 & T_{21}^* &= \frac{2\gamma_1 M_s^2 (\beta - 1)}{z(2\beta - 1)^2} \end{aligned} \quad (D-28)$$

Consider the special case of air at $M_s = 20$. The value of these parameters for a perfect and imperfect gas can be compared. If $\gamma_1 = \text{constant}$, then $\beta_1 = 3.5$. Assume an enthalpy parameter value of $\beta = 10.1$ for the imperfect gas, then (Ref. 34):

$$\begin{aligned} v_{21} &= 3.375 & > & v_{21}^* = 1.053 \\ u_{21} &= (M_s - v_{21}) = 16.620 & < & u_{21}^* = (M_s - v_{21}^*) = 18.947 \\ \Gamma_{21} &= 5.926 & < & \Gamma_{21}^* = 18.988 \\ P_{21} &= 466.50 & < & P_{21}^* = 531.51 \\ T_{21} &= 78.722 & > & zT_{21}^* = 27.992 \end{aligned}$$

The above numerical results illustrate what is shown graphically in Figs. 2.2-8 to 2.2-12. The very large drop in temperature ratio behind the shock front for the imperfect gas as compared to the perfect case is quite evident. The correspondingly large density increase because of the cooling effect is also very noticeable. The increase in pressure and non-stationary particle velocity (U_{21}^*) is not too large.

A systematic solution of Eqs. (D-12), (D-14), (D-15), and (D-16) can be done as follows:

1. For a given set of initial conditions the unshocked air is cold, and β_1 and γ_1 are known from T_1 independently of ρ_1 for any M_S .
2. Choose T_2^* and ρ_2^* and obtain β_2 and Z from tables or plots of the thermodynamic properties as above.
3. Solve for V_{21}^* from Eq. (D-12).
4. Calculate Γ_{21}^* from Eq. (D-14) and obtain ρ_1 directly.

$$\text{Calculate } P_{21}^* \text{ from Eq. (D-15) and } p_1 = \frac{\rho_1 RT_1}{m}.$$

The above alternate method of choosing the thermodynamic quantities behind the shock wave and calculating ρ_1 has the advantage of eliminating successive approximations (Ref. 35). A drawback is that ρ_1 cannot be given in advance. However, by choosing $\rho_2^*/\rho_0 = 10, 1, 10^{-1}$, etc. ($\rho_0 =$ standard reference density at 273.2°K and 1 atmosphere, $\rho_0 = 1.2931 \times 10^{-3} \text{ gm/cm}^3 = 2.511 \times 10^{-3} \text{ slugs/ft}^3$), $T_1 = 273.2^\circ\text{K}$ and T_2^* takes on the range of temperatures given in the thermodynamic tables.

5. For each value of M_S and range of T_2^* , plot a graph of P_{21}^* , T_{21}^* , and Γ_{21}^* with ρ_1/ρ_0 .
6. Choose regular intervals of $\rho_1/\rho_0 = 1, 10^{-1}, 10^{-2}$, etc., and cross-plot the ratios T_{21}^* and Γ_{21}^* against P_{21}^* . Since P_{21}^* is nearly independent of ρ_1 or p_1 (see Eq. (D-15), as V_{21}^* is small for strong shocks), the graph of M_S with P_{21}^* can be drawn approximately as a single curve. The results as shown on Fig. 2.2-12 are taken from Ref. 35.

It is worthwhile noting that the quantity γ' , which is defined in Ref. 35 in order to preserve the form of the shock relations for perfect and imperfect gases as

$$\gamma' = 1 + \frac{P}{\rho E} \quad (\text{D-29})$$

is equivalent to,

$$\gamma' = \frac{\beta}{\beta - 1} \quad (\text{D-30})$$

or

$$\beta = \frac{\gamma'}{\gamma - 1} \quad (D-30a)$$

Consequently, some of the limits for the imperfect gas have an appearance similar to the perfect gas case. For example, as

$$M_s \rightarrow \infty, \quad \Gamma_{21} \rightarrow \frac{\gamma_1 + 1}{\gamma_1 - 1} \quad \text{and} \quad \Gamma_{21}^* \rightarrow (2\beta - 1) = \frac{\gamma' + 1}{\gamma' - 1}$$

An inspection of Table 2.2-2 for β for a given ρ/ρ_0 with increasing temperature shows that it is not a monotonic function. For example, consider the column for $\rho/\rho_0 = 10^{-6}$. At low temperatures (273°K) $\beta = 3.5$. As the temperature increases β rises to $\beta = 12.5$ at 5000°K; falls and rises to 11.9 at 8000°K; falls and is rising to 10.5 at 24,000°K. The reason for this may be seen from the enthalpy of a dissociating diatomic gas (see Supplement B and Subsec. 2.1.5),

$$h = \frac{5 + \alpha}{2} R_0 T + Uv (1 - \alpha) + \alpha l_d$$

$$\frac{h}{p/\rho} = \beta = \frac{5 + \alpha}{2(1 + \alpha)} + \frac{Uv}{R_0 T} \cdot \frac{(1 - \alpha)}{(1 + \alpha)} + \frac{\alpha}{1 + \alpha} \cdot \frac{\theta_d}{T} \quad (D-31)$$

As the gas reaches a high degree of dissociation the first term in β remains almost stationary, the second term is practically zero, and the third (largest) term falls with increasing translational temperature T . Consequently, β decreases. When ionization sets in β again rises, and the process is repeated as new degrees of ionization are excited, giving the characteristic waviness to the plots of the thermodynamic quantities as a function of increasing temperature. For example, since $\Gamma_{21}^* \rightarrow (2\beta - 1)$, the density ratio can be less for a more intense shock. In the above case when $\rho/\rho_0 = 10^{-6}$, $\Gamma_{21}^* = 24$ at 5000°K and 20 at 24,000°K. As the modes become fully excited the heat sink is removed. The gas cannot then be cooled down and consequently the density can be lower for the stronger shock wave.

Typical values for Z and S are given in Tables 2.2-3 and 2.2-4 (Ref. 35). As expected both of these quantities increase for the low densities at a given temperature, as new particles are formed and the disturbance caused by the strong shocks becomes increasingly greater.

Some simplification in the calculations arise when the only excited inert mode is vibration. In this case $Z = 1$ and β is only dependent on T . The continuity, momentum, and energy equations are combined to give

$$v_1(v_2^{*2} + RT_2^*) = v_2^*(v_1^2 + RT_1) \quad (D-32)$$

$$2\beta RT_2^* + v_2^{*2} = 2\beta_1 RT_1 + v_1^2 \quad (D-33)$$

Let

$$v_1 = \frac{v_1}{v_2^*} v_2^* = gv_2^*, \text{ where } g = \frac{v_1}{v_2^*} \quad (D-34)$$

From Eq. (D-32)

$$v_2^{*2} = \frac{R(T_1 - gT_2^*)}{-g(g-1)} \quad (D-35)$$

From Eq. (D-33)

$$v_2^{*2} = \frac{2R(\beta T_2^* - \beta_1 T_1)}{g^2 - 1} \quad (D-36)$$

Solving for g from Eqs. (D-35) and (D-36)

$$g = b + \sqrt{b^2 + \frac{T_1}{T_2^*}} \quad (D-37)$$

where

$$b = (\beta - \frac{1}{2}) - \frac{T_1}{T_2^*} (\beta_1 - \frac{1}{2}) \quad (D-38)$$

From Eq. (D-36)

$$v_2^{*2} = RT_2^* \frac{2b + 1 - T_1/T_2^*}{\left(\frac{v_1}{v_2^*}\right)^2 - 1} \quad (D-39)$$

where

$$R = \mathcal{R}/m$$

or

$$v_{21}^{*2} = \frac{T_{21}^*}{\gamma_1} \cdot \frac{2b + 1 - T_{12}^*}{\left(\frac{w_{11}}{v_{21}^*}\right)^2 - 1} \quad (D-40)$$

For calculation purposes assume $\beta_1 \sim 3.5$ at T_1 for the cold gas. Choose a T_2^* , and β is known. Calculate v_2^* from Eq. (D-39), v_1 from Eq. (D-34), ρ_2^* from Eq. (D-1), and p_2^* from Eq. (D-9) with $Z = 1$.

The methods employed above for the solution of properties behind strong shock waves in air can be used in a similar manner for monatomic gases.

Table 2.1-1
 Values of typical ionization energies (I_1), partition functions (P), and
 dissociation energies (I_d) (after Ref. 5)

Element	I_1 (ev)	P-atom (Pa)	P-ion (Pi)	P-electron (Pe)	Molecule	I_d (ev)
N	14.54	4	9	2	H ₂	4.477
A	15.75	1	6	2	N ₂	9.76
He	24.58	1	2	2	C ₂	5.08
Ne	21.56	1	6	2	CC	11.11
H	13.59	2	1	2	NO	6.48
O	13.61	9	4	2	OH	4.37
Kr	14.00	1	6	2	CO ₂	16.56

Table 2.1-2

Equilibrium constant (K), degree of dissociation (α), and dissociational portion of specific heat at constant volume (C_d^-/R) for oxygen at 1.0 atm as a function of the translational temperature (T)
(Values of K from Ref. 17)

T °K	K_{atm}	α	C_d^-/R
2000	5.38×10^{-7}	3.67×10^{-4}	0.159
2400	8.74×10^{-5}	4.67×10^{-3}	1.40
2800	3.35×10^{-3}	2.89×10^{-2}	6.45
3200	5.18×10^{-2}	0.106	16.9
3600	0.437	0.315	34.3
3800	1.07	0.461	38.9
4000	2.41	0.613	37.1
4200	5.01	0.745	29.8
4400	9.76	0.842	20.6
4800	31.3	0.941	7.91
5000	52.4	0.965	4.54

Table 2.1-3

Vibrational relaxation in gases at normal density and temperature (Ref. 14)

Gas	Exp. Z_v (Ref. 14)	τ_v	Calc. C_v (Ref. 20)
O ₂	2×10^7	3×10^{-3}	3.8×10^7
Cl ₂	4×10^4	4.2×10^{-6}	6.8×10^4
CO ₂	5.2×10^4	6.6×10^{-6}	9.6×10^4 (?)
Methyl-chloride	1400	1.8×10^{-7}	1700 (?)
Methyl-alcohol	200	2.3×10^{-8}	

Table 2.1-4

Dissociational (τ_d) and vibrational (τ_v) relaxation times for O_2 vs translational temperature at a density of 1 atm (after Ref. 18)

T °K	1000	1500	2000	3000	3500
τ_v Sec	10×10^{-6}	1.6×10^{-6}	$.5 \times 10^{-6}$	$.1 \times 10^{-6}$	
τ_d Sec				5×10^{-6}	$.5 \times 10^{-6}$

Table 2.1-5

Relaxation path lengths (L) in feet behind a normal shock wave at an altitude of 120,000 ft (after Ref. 18)

Mach No.	Oxygen (O_2)		Nitrogen (N_2)	
	Vibration	Dissociation	Vibration	Dissociation
10	2.1×10^{-3}	2×10^{-1}	4.5×10^{-2}	
12		1×10^{-2}	1.8×10^{-2}	
14			7.4×10^{-3}	7.5
16			4×10^{-3}	.6
18			2.4×10^{-3}	.09
20			1.8×10^{-3}	.01

Table 2.1-6a

Transition through a centred Q-rarefaction wave in air; $\gamma = 1.4$

N	$\frac{u}{a_4}$	$\frac{a}{a_4}$	$\frac{T}{T_4}$	$\frac{f}{P_4}$	$\frac{P}{P_4}$	M	$\frac{P_u}{(P_4)_4}$	$\frac{T_0}{T_4}$	$\frac{P_0}{P_4}$	$\frac{P}{P_4}$	$\frac{P_0}{P_4}$	$\frac{P_u}{(P_4)_4}$	$\frac{1/2 \rho u^2 / \rho_4}{P_4}$	$\frac{Q}{a_4}$	$\frac{P}{P_4}$
-1	0	1	1	1	1	0	0	1	1	-	-	0	0	5	5
0	$\frac{5}{6}$	$\frac{5}{6}$.684	.401	.278	1.00	.334	.833	.328	.528	1.000	.488	.195	$\frac{20}{6}$	5
1	$\frac{10}{6}$	$\frac{4}{6}$.444	.132	.058	2.50	.220	1.000	1.000	.489	.449	.495	.258	$\frac{10}{6}$	5
2	$\frac{15}{6}$	$\frac{3}{6}$.250	.031	.0078	5.00	.0775	1.500	4.13	.255	.0817	.310	.137	0	5
3	$\frac{20}{6}$	$\frac{2}{6}$.111	.0041	4.6×10^{-4}	10.00	.0136	2.335	19.95	.0608	3.045×10^{-3}	.123	.0318	$-\frac{10}{6}$	5
4	$\frac{25}{6}$	$\frac{1}{6}$.0278	1.28×10^{-4}	3.55×10^{-6}	25.00	5.33×10^{-6}	3.500	80.0	.00890	3.59×10^{-5}	.0102	.00195	$-\frac{20}{6}$	5
5	5	0	0	0	0	∞	0	5	280	0	0	0	C	-5	5

Table 2.1-6b

Transition through a centred Q-compression wave in air; $\gamma = 1.4$

N	$\frac{u}{a_4}$	$\frac{a}{a_4}$	$\frac{T}{T_4}$	$\frac{P}{P_4}$	M	$\frac{Q}{a_4}$	$\frac{P}{a_4}$
-1	0	1	1	1	0	5	5
-2	-5/6	7/6	1.36	2.16	5/7	40/6	5
-3	-10/6	8/6	1.78	4.22	10/8	50/6	5
-4	-15/6	9/6	2.25	7.60	15/9	60/6	5
-5	-20/6	10/6	2.78	12.9	20/10	70/6	5
-6	-25/6	11/6	3.76	27.5	25/11	80/6	5
-7	-5	2	4	32	30/12	90/6	5
$-\infty$	$-\infty$	∞	∞	∞	5.0	∞	5

Table 2.1-7a

Transition through a Q-centred rarefaction wave in air; $\gamma = 1.4$

N	$\frac{1}{a_4} \frac{da}{dN}$	$\frac{1}{a_4} \frac{du}{dN}$	$\frac{1}{T_4} \frac{dT}{dN}$	$\frac{1}{P_4} \frac{dP}{dN}$	$\frac{1}{P_4} \frac{dp}{dN}$	$\frac{dM}{dN}$
-1	-1/6	5/6	-6/18	-.833	-1.166	.833
0	-1/6	5/6	-5/18	-.402	-.392	1.200
1	-1/6	5/6	-4/18	-.1645	-.1014	1.875
2	-1/6	5/6	-3/18	-.0521	-.01845	3.333
3	-1/6	5/6	-2/18	-.01029	-.00164	7.500
4	-1/6	5/6	-1/18	-.00064	-2.47×10^{-5}	30.0
5	-1/6	5/6	0	0	0	∞

Table 2.1-7b
 Transition through a Q-compression wave in air; $\gamma = 1.4$

N	$\frac{1}{a_4} \frac{da}{dN}$	$\frac{1}{a_4} \frac{du}{dN}$	$\frac{1}{T_4} \frac{dT}{dN}$	$\frac{1}{P_4} \frac{dP}{dN}$	$\frac{1}{P_4} \frac{dp}{dN}$	$\frac{dM}{dN}$
-1	1/6	-5/6	6/18	.833	1.166	.833
-2	1/6	-5/6	7/18	1.54	2.92	.611
-3	1/6	-5/6	8/18	2.63	6.53	.468
-4	1/6	-5/6	9/18	4.57	13.3	.370
-5	1/6	-5/6	10/18	6.41	24.9	.300
-6	1/6	-5/6	11/18	8.57	44.3	.248
-7	1/6	-5/6	12/18	13.30	74.6	.208
$-\infty$	1/6	-5/6	∞	∞	∞	0

Table 2.1-8
List of equations

Q - WAVES	P - WAVES
<p><u>NOTE</u></p> <p>(a) $-\frac{1}{\sqrt{2}} \leq N \leq \frac{1}{\sqrt{2}}$; $0 \leq M \leq \infty$</p> <p>(b) $u > 0$ (+)</p>	<p>$1 \leq N \leq \infty$; $0 \leq M \leq 5$</p> <p>$u > 0$ (+)</p>
<p>1. <u>Characteristic Slope</u></p> $\frac{dx}{dt} = u - a$	<p>$1 \leq N \leq \infty$; $0 \leq M \leq 5$</p> <p>$u > 0$ (+)</p>
<p>2. <u>Along a Characteristic</u></p> $\frac{2a}{\sqrt{2}} - u = Q$	<p>$1 \leq N \leq \infty$; $0 \leq M \leq 5$</p> <p>$u > 0$ (+)</p>
<p>3. <u>Across Any Characteristic</u></p> $\frac{2a}{\sqrt{2}} + u = P = \frac{2a_4}{\sqrt{2}}$	<p>$1 \leq N \leq \infty$; $0 \leq M \leq 5$</p> <p>$u > 0$ (+)</p>
<p>4. <u>Sound Speed Ratio</u></p> $\frac{a}{a_4} = 1 - \frac{\sqrt{2}-1}{2} \frac{u}{a_4}$	<p>$1 \leq N \leq \infty$; $0 \leq M \leq 5$</p> <p>$u > 0$ (+)</p>
<p>As for R</p>	<p>As for R</p>

Table 2.1-8 (continued)

List of equations

	← R	← CW	← R	← CW
	Q - WAVES		P - WAVES	
5. <u>Sound Speed Ratio in Terms of Characteristic Slope</u>				
	$\frac{a}{a_4} = \frac{2}{\gamma+1} + \frac{\gamma-1}{\gamma+1} \left(\frac{1}{a_4} \frac{dx}{dt} \right)$		$\frac{a}{a_4} = \frac{2}{\gamma+1} + \frac{\gamma-1}{\gamma+1} \left(\frac{1}{a_4} \frac{dx}{dt} \right)$	
6. <u>Particle Velocity in Terms of Characteristic Slope</u>				
	$\frac{u}{a_4} = \frac{2}{\gamma+1} + \frac{2}{\gamma+1} \left(\frac{1}{a_4} \frac{dx}{dt} \right)$		$\frac{u}{a_4} = -\frac{2}{\gamma+1} + \frac{2}{\gamma+1} \left(\frac{1}{a_4} \frac{dx}{dt} \right)$	
7. <u>Thermodynamic Quantities</u>				
	$\frac{a}{a_4} = \left(\frac{T}{T_4} \right)^{1/2} = \left(\frac{p}{p_4} \right)^{\frac{\gamma-1}{2\gamma}} = \left(\frac{\rho}{\rho_4} \right)^{\frac{\gamma-1}{\gamma}}$		$\frac{a}{a_4} = \left(\frac{T}{T_4} \right)^{1/2} = \left(\frac{p}{p_4} \right)^{\frac{\gamma-1}{2\gamma}} = \left(\frac{\rho}{\rho_4} \right)^{\frac{\gamma-1}{\gamma}}$	As for P.
Flow Properties in Terms of Mach No.				
8. <u>Flow Sound Speed</u>	$\frac{a}{a_4} = \left(1 + \frac{\gamma-1}{2} M \right)^{-1}$	$\frac{a}{a_4} = \left(1 - \frac{\gamma-1}{2} M \right)^{-1}$	$\frac{a}{a_4} = \left(1 + \frac{\gamma-1}{2} M \right)^{-1}$	$\frac{a}{a_4} = \left(1 - \frac{\gamma-1}{2} M \right)^{-1}$
9. <u>Flow Temperature</u>	$\frac{T}{T_4} = \left(1 + \frac{\gamma-1}{2} M \right)^{-2}$	$\frac{T}{T_4} = \left(1 - \frac{\gamma-1}{2} M \right)^{-2}$	$\frac{T}{T_4} = \left(1 + \frac{\gamma-1}{2} M \right)^{-2}$	$\frac{T}{T_4} = \left(1 - \frac{\gamma-1}{2} M \right)^{-2}$

Table 2.1-8 (continued)

List of equations

	Q - WAVES		P - WAVES	
	\leftarrow CW	\rightarrow R	\leftarrow CW	\rightarrow R
10. <u>Flow Density</u>	$\frac{\rho}{\rho_4} = \left(\frac{1 + \gamma - 1 M}{2} \right)^{-1/\beta}$	$\frac{\rho}{\rho_4} = \left(\frac{1 + \gamma - 1 M}{2} \right)^{-1/\beta}$	$\frac{\rho}{\rho_4} = \left(\frac{1 - \gamma - 1 M}{2} \right)^{-1/\beta}$	$\frac{\rho}{\rho_4} = \left(\frac{1 - \gamma - 1 M}{2} \right)^{-1/\beta}$
11. <u>Flow Pressure</u>	$\frac{p}{p_4} = \left(\frac{1 + \gamma - 1 M}{2} \right)^{-1/\beta}$	$\frac{p}{p_4} = \left(\frac{1 + \gamma - 1 M}{2} \right)^{-1/\beta}$	$\frac{p}{p_4} = \left(\frac{1 - \gamma - 1 M}{2} \right)^{-1/\beta}$	$\frac{p}{p_4} = \left(\frac{1 - \gamma - 1 M}{2} \right)^{-1/\beta}$
12. <u>Particle Velocity</u>	$\frac{u}{a_4} = \frac{M}{1 + \gamma - 1 M}$	$\frac{u}{a_4} = \frac{M}{1 + \gamma - 1 M}$	$\frac{u}{a_4} = \frac{M}{1 - \gamma - 1 M}$	$\frac{u}{a_4} = \frac{M}{1 - \gamma - 1 M}$
13. <u>Mass Flow</u>	$\frac{\rho u}{(\rho a)_4} = \frac{M}{(1 + \gamma - 1 M)^2}$	$\frac{\rho u}{(\rho a)_4} = \frac{M}{(1 + \gamma - 1 M)^2}$	$\frac{\rho u}{(\rho a)_4} = \frac{M}{(1 - \gamma - 1 M)^2}$	$\frac{\rho u}{(\rho a)_4} = \frac{M}{(1 - \gamma - 1 M)^2}$
14. <u>Stagnation Temperature</u>	$\frac{T^0}{T_4} = 1 + \frac{\gamma - 1 M^2}{2}$	$\frac{T^0}{T_4} = 1 + \frac{\gamma - 1 M^2}{2}$	$\frac{T^0}{T_4} = 1 + \frac{\gamma - 1 M^2}{2}$	$\frac{T^0}{T_4} = 1 + \frac{\gamma - 1 M^2}{2}$

Table 2.1-8 (continued)

List of equations

	Q - WAVES		P - WAVES	
	R	CW	R	CW
15. Isentropic Stagnation Pressure				
$\frac{p^0}{p_4} = \left(\frac{1 + \frac{\gamma-1}{2} M^2}{1 + \frac{\gamma-1}{2}} \right)^{1/2\beta}$				
16. Normal Shock Wave Stagnation Pressure				
$\frac{p_0^c}{p_4} = \frac{\gamma+1}{2} \left\{ \frac{\gamma+1}{2} M^2 \right\}^{\frac{1}{\gamma-1}} \left\{ \frac{2\gamma M^2 - \gamma - 1}{\gamma+1} \right\}^{\frac{1}{\gamma+1}}$				
17. Reynolds Number Per Foot				
$\frac{\rho u}{\mu} \left(\frac{p_a}{p} \right)^{\frac{1}{\gamma}} = \frac{M}{\left(1 + \frac{\gamma-1}{2} M^2 \right)^{\frac{\gamma-1}{2\gamma}}}$				
18. Dynamic Pressure				
$\frac{q}{p_4} = \frac{\gamma M^2}{2 \left(1 + \frac{\gamma-1}{2} M^2 \right)^{\frac{\gamma}{2}}}$				

Table 2.1-8 (continued)

List of equations

	Q - WAVES ← R	CW ←	R ←	P - WAVES ←	CW ←
	$-1 \leq N \leq \frac{2}{\gamma-1}$			$N = \frac{x}{a_4^2} \text{ or } \frac{1}{a_4^2} \cdot \frac{dx}{dt}$	$1 \leq N \leq \infty$
Flow Quantities As A Function Of Characteristic Slope					
	$-1 \leq N \leq -\infty$		$-\frac{2}{\gamma-1} \leq N \leq 1$		
19. Particle Velocity	$\frac{u}{a_4} = \frac{1}{\alpha\beta\gamma} (N+1)$	$\left \frac{u}{a_4} \right = -\frac{1}{\alpha\beta\gamma} (N+1)$	$\left \frac{u}{a_4} \right = -\frac{1}{\alpha\beta\gamma} (N-1)$	$\frac{u}{a_4} = \frac{1}{\alpha\beta\gamma} (N-1)$	
20. Flow Sound Speed	$\frac{a}{a_4} = 1 - \frac{1}{\alpha} (N+1)$		$\frac{a}{a_4} = 1 + \frac{1}{\alpha} (N-1)$		
21. Flow Temperature	$\frac{T}{T_4} = \left(1 - \frac{1}{\alpha} (N+1) \right)^2$		$\frac{T}{T_4} = \left(1 + \frac{1}{\alpha} (N-1) \right)^2$		
22. Flow Density	$\frac{\rho}{\rho_4} = \left(1 - \frac{1}{\alpha} (N+1) \right)^{1/\beta\gamma}$	As for R			As for R
23. Flow Pressure	$\frac{p}{p_4} = \left(1 - \frac{1}{\alpha} (N+1) \right)^{1/\beta}$				

Table 2.1-8 (continued)

		Q - WAVES		P - WAVES	
		R	CW	R	CW
24. Mach Number		$M = \frac{u}{a} = \frac{N+1}{1-\beta\gamma N}$	$M = \frac{ u }{a} = \frac{N+1}{\beta\gamma N-1}$	$M = \frac{ u }{a} = \frac{1-N}{1+\beta\gamma N}$	$M = \frac{N-1}{1+\beta\gamma N}$
25. Mass Flow		$\frac{\rho u}{(\rho a)_4} = \left(1 - \frac{1}{\alpha}\right) \frac{1}{(N+1)} \frac{1}{\alpha\beta\gamma}$	$\left \frac{\rho u}{(\rho a)_4}\right = -\frac{\rho u}{(\rho a)_4}$	$\left \frac{\rho u}{(\rho a)_4}\right = -\left(\frac{1+(N-1)}{\alpha}\right)^{1/\beta\gamma} \frac{1}{(\rho a)_4} \left(\frac{N-1}{\alpha\beta\gamma}\right)$	$\frac{\rho u}{(\rho a)_4} = \frac{\rho u}{(\rho a)_4}$
26. Stagnation Temperature		$\frac{T^0}{T_4} = \left[1 + \frac{\gamma-1}{2} \left(\frac{N+1}{1-\beta\gamma N}\right)^2\right] \frac{1}{\alpha}$		$\frac{T^0}{T_4} = \left[\frac{1+\gamma-1}{2} \left(\frac{1-N}{1+\beta\gamma N}\right)^2\right] \frac{1}{\alpha}$	
27. Isentropic Stagnation Pressure		$\frac{p^0}{p_4} = \left[1 + \frac{\gamma-1}{2} \left(\frac{N+1}{1-\beta\gamma N}\right)^2\right]^{1/2\beta} \frac{1}{\alpha}$		$\frac{p^0}{p_4} = \left[\frac{1+\gamma-1}{2} \left(\frac{1-N}{1+\beta\gamma N}\right)^2\right]^{1/2\beta} \frac{1}{\alpha}$	
28. Normal Shock Wave Stagnation Pressure		$\frac{p^0}{p_4} = \frac{\gamma+1}{2} \left(\frac{N+1}{1-\beta\gamma N}\right)^2 \left[\frac{7+1}{7+1 - \frac{1}{\alpha}(N+1)}\right]^{1/\beta}$		$\frac{p^0}{p_4} = \frac{\gamma+1}{2} \left(\frac{1-N}{1+\beta\gamma N}\right)^2 \left[\frac{7+1}{7+1 - \frac{1}{\alpha}(N-1)}\right]^{1/\beta}$	

As for R

As for R

Table 2.1-8 (continued)

List of equations

	Q - WAVES	P - WAVES
	← R	← R
	← CW	← CW
29. Reynolds Number Per Foot	$\frac{\rho u}{\mu} \left(\frac{p_a}{\rho} \right)^{1/4} = \left[1 - \frac{1}{\alpha} (N+1) \right]^{1/\beta} \gamma^{-2n}$	$\frac{\rho u}{\mu} \left(\frac{p_a}{\rho} \right)^{1/4} = \frac{\rho u}{\mu} \left(\frac{p_a}{\rho} \right)^{1/4}$
30. Dynamic Pressure	$\frac{q}{p_a} = \frac{\gamma}{2} \left[\frac{N+1}{1-\beta\gamma N} \right]^2 \times \frac{1}{\beta}$	$\frac{q}{p_a} = \frac{\gamma}{2} \left[\frac{1-N}{1-\beta\gamma N} \right]^2 \times \frac{1}{\beta}$
	As for R	As for R

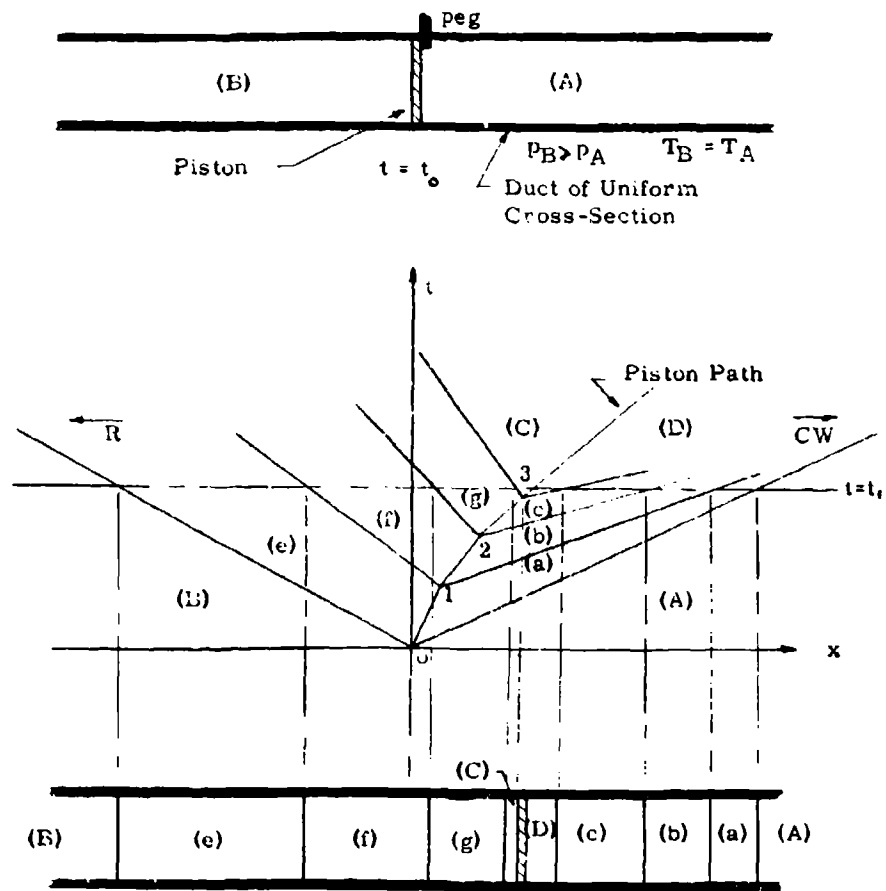


Fig. 2.1-1. Pressure waves generated by the motion of a piston.

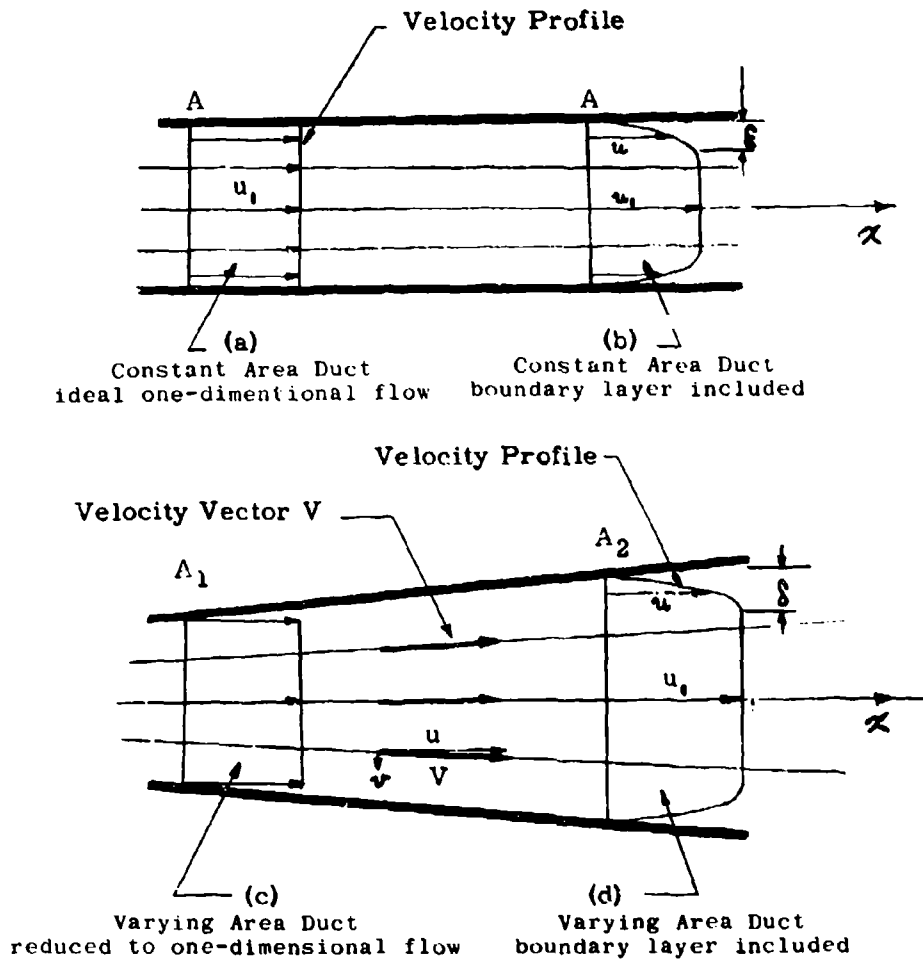


Fig. 2.1-2. Velocity distribution in ducts of constant and varying cross sections.

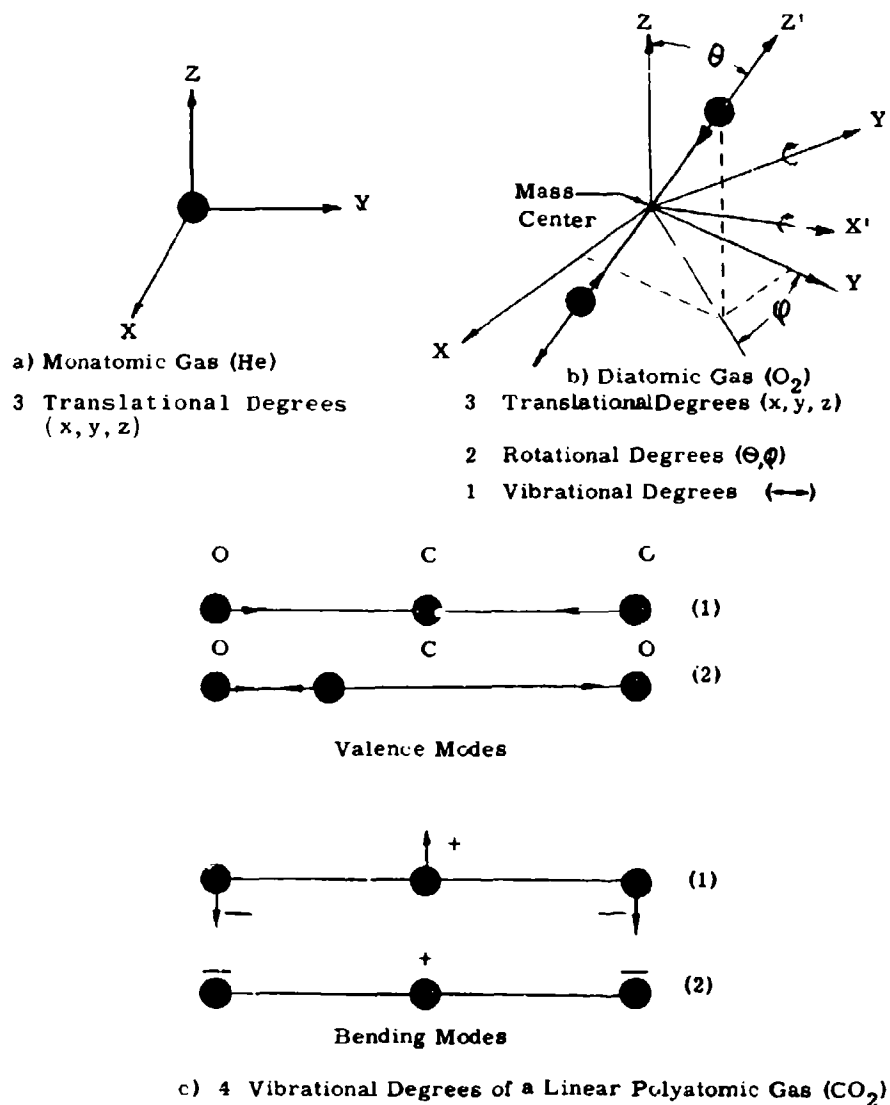


Fig. 2.1-3. Degrees of freedom for different molecules.

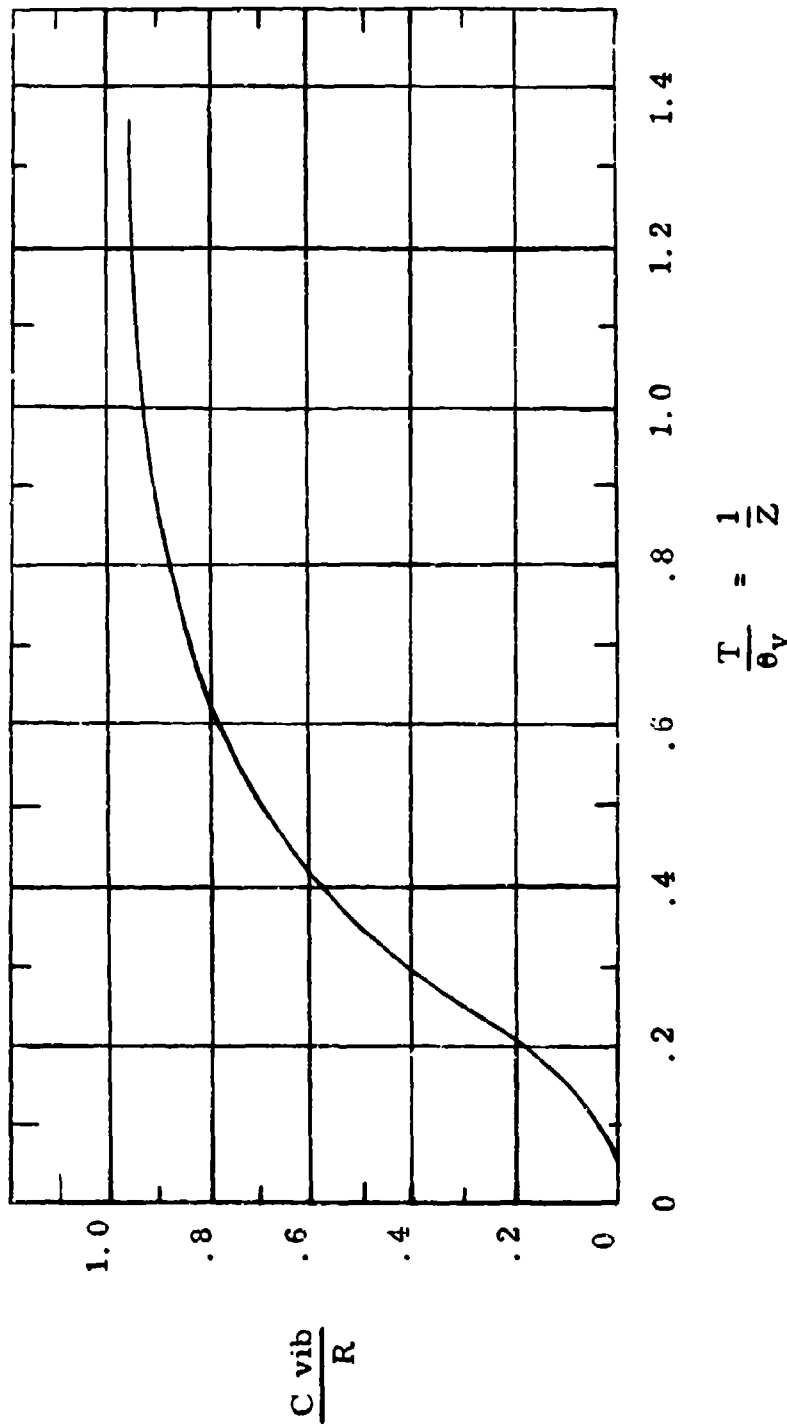


Fig. 2.1-4. Variation of vibrational specific heat as a function of the reduced gas translational temperature (T/θ_v) (Ref. 14).

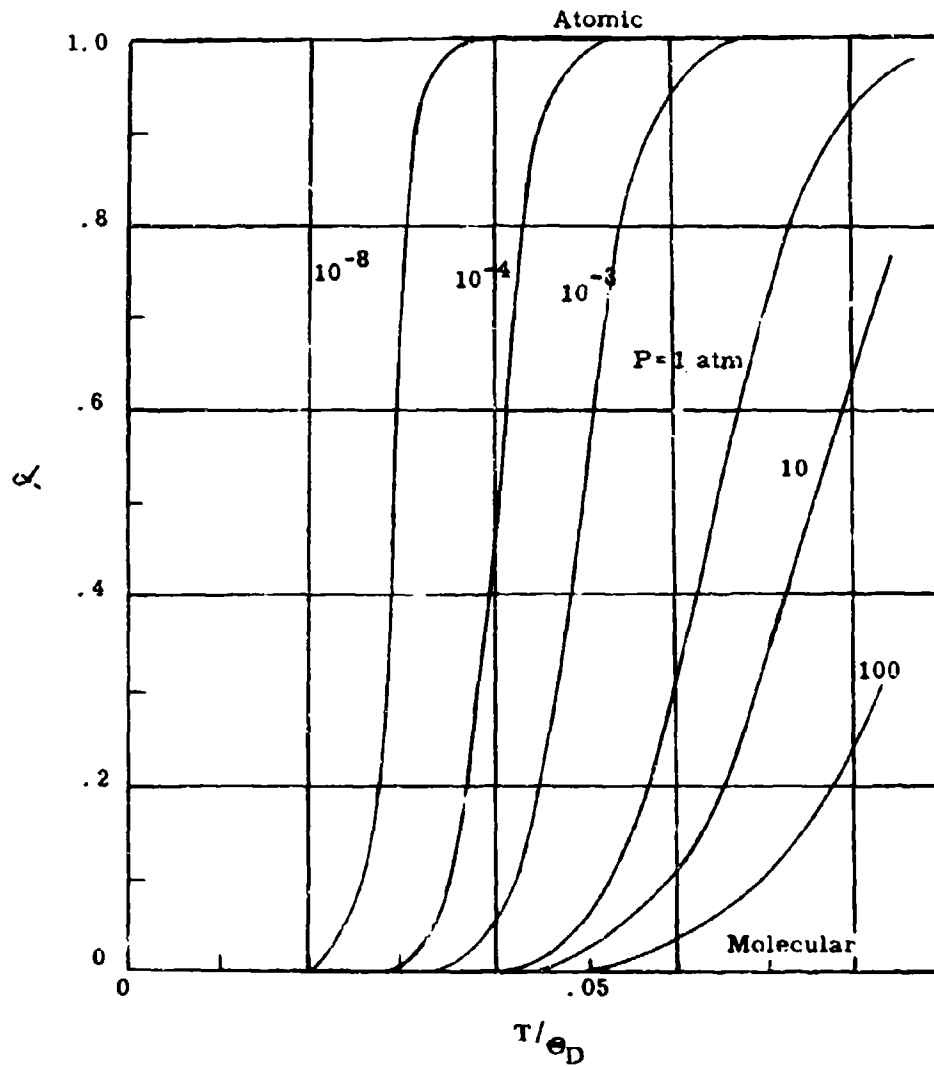


Fig. 2.1-5a. Variation of degree of dissociation (α) with nondimensional temperature (T/θ_D) for a dissociating gas (Ref. 3).

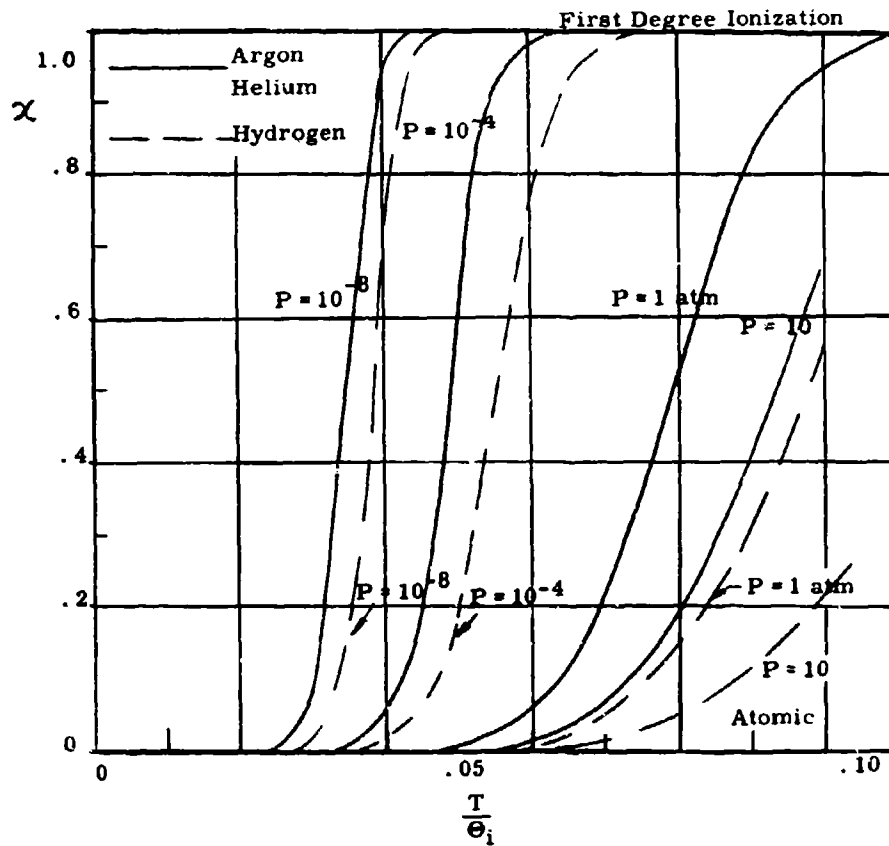
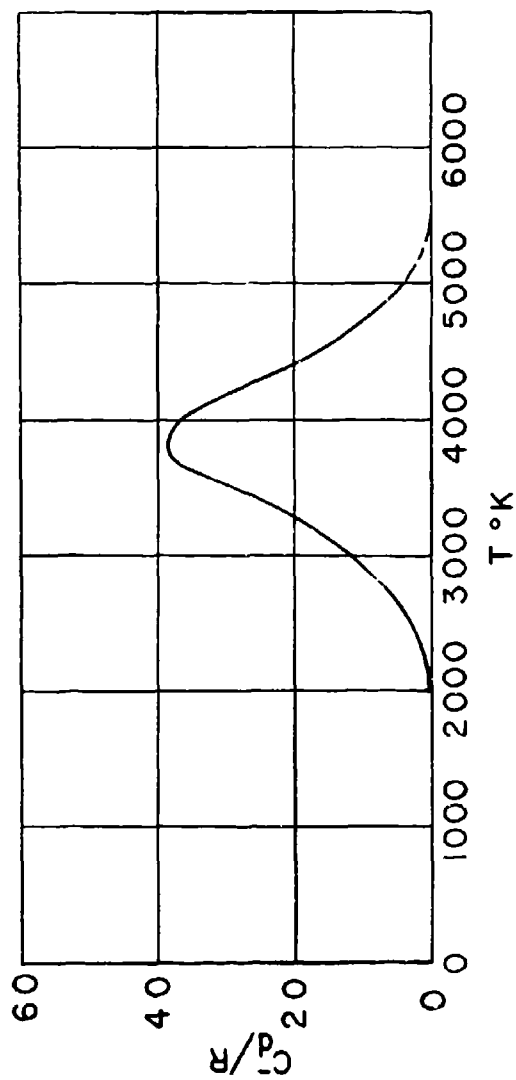
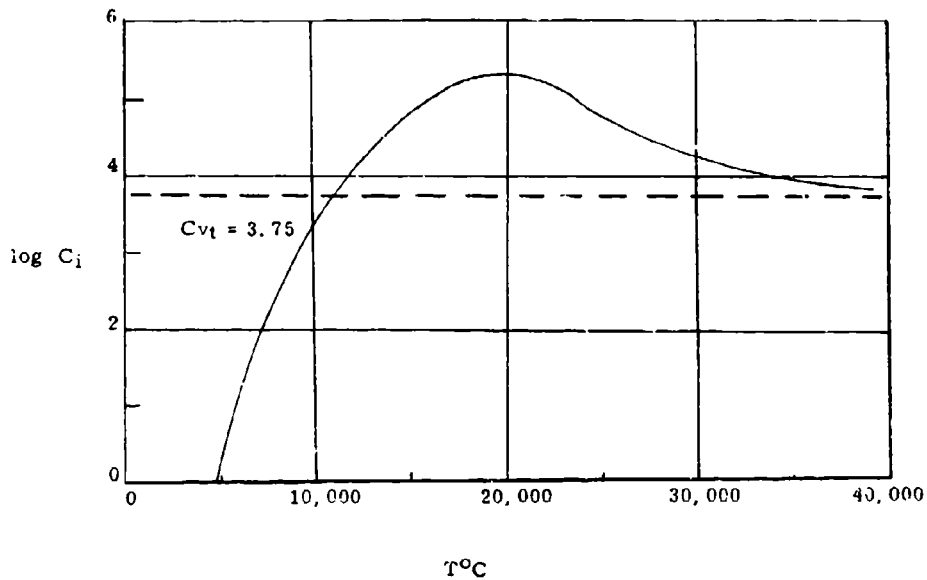


Fig. 2.1-5b. Variation of the first degree ionization (α) with nondimensional temperature (T/θ_i) for argon, helium, and hydrogen.



(The translational, rotational, and vibrational components are not included.)

Fig. 2.1-6. Variation of specific heat due to dissociation for oxygen with translational temperature at 1 atm.



(C_{vt} for a nonionized gas is 5.57×10^3 erg/cm³ deg or $\log C_{vt} = 3.746$. The translational term is not included.)

Fig. 2.1-7. Specific heat of ionization (C_i) for atomic hydrogen with translational temperature (Ref. 15); $v_i = 13.5$ volts.

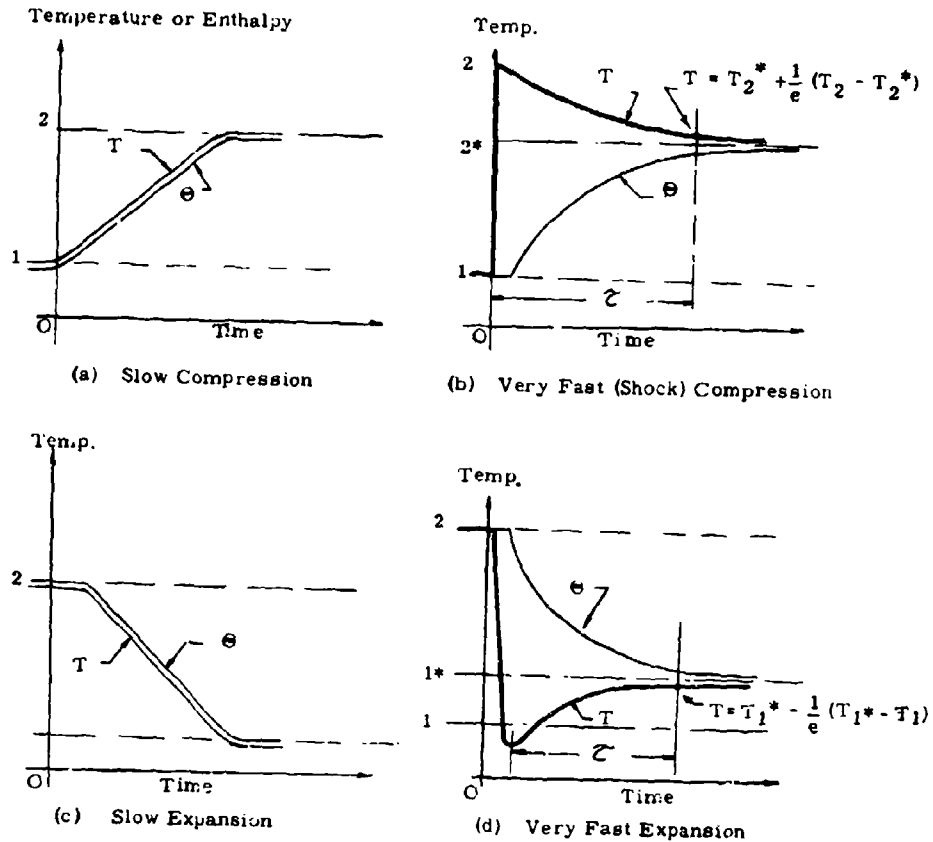


Fig. 2.1-8a. Adjustment of translational temperature (T) and internal temperature (θ) during a slow and fast compression or expansion.

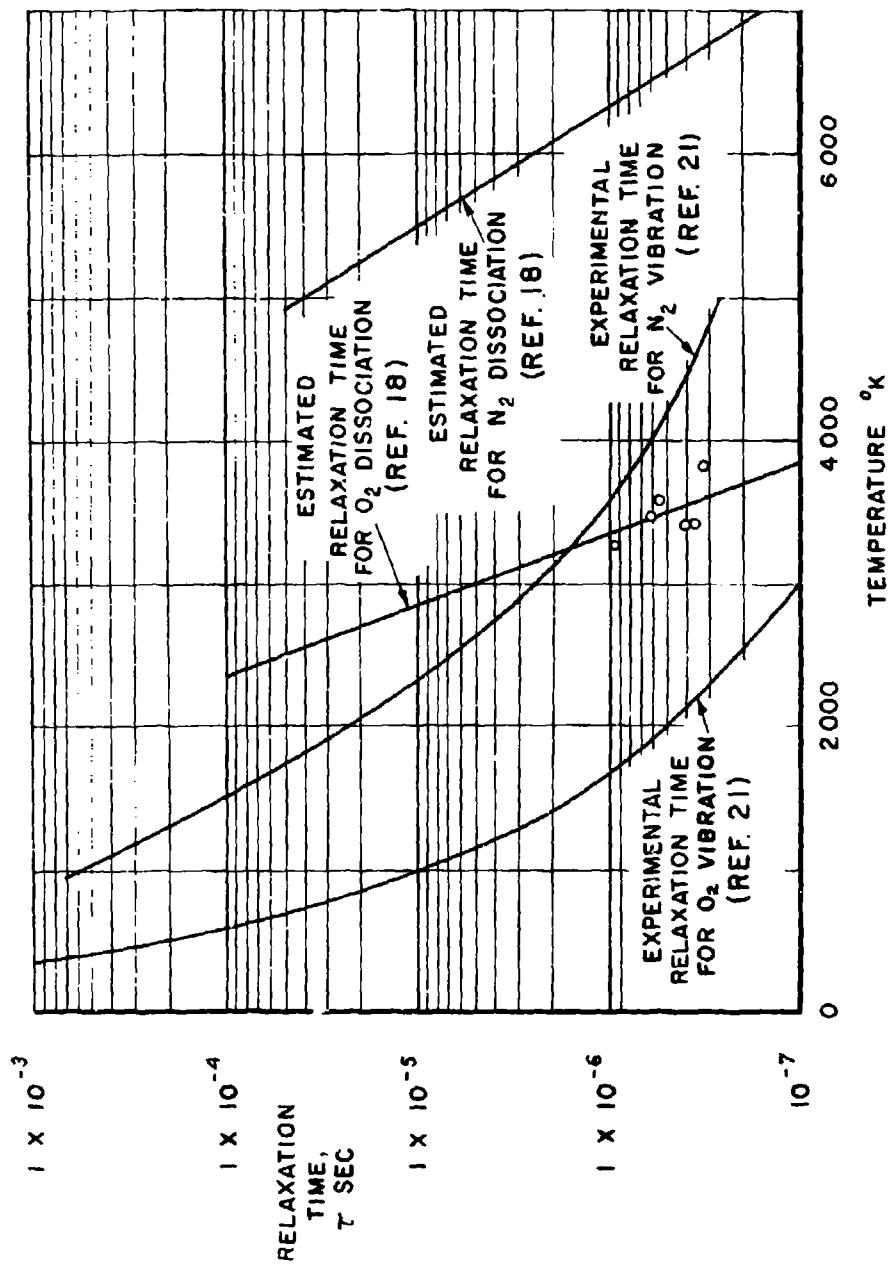


Fig. 2.1-8b. Relaxation time data for air referred to a density of atmosphere.

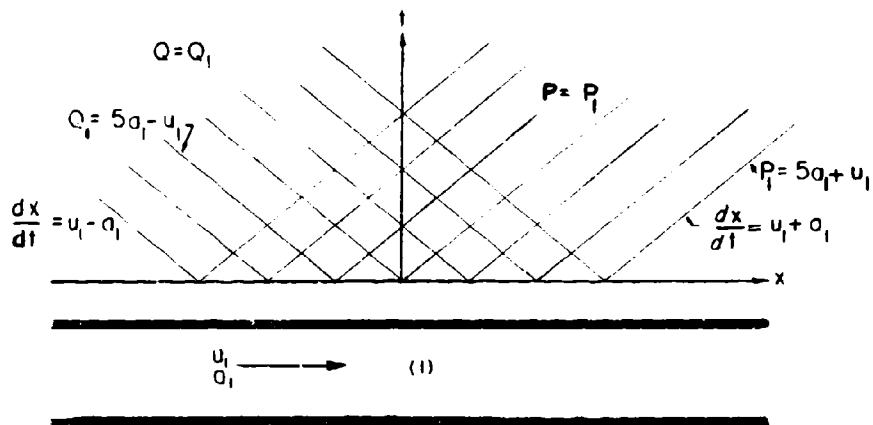


Fig. 2.1-9. Riemann variables in the (x,t) -plane for a steady flow through a duct of constant cross section; $\gamma = 1.4$.

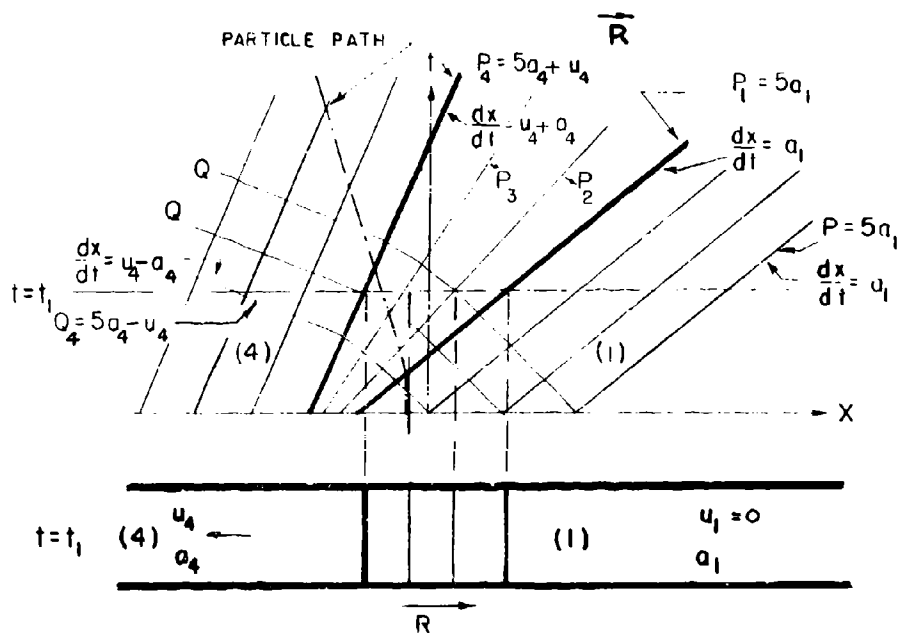


Fig. 2.1-10. Riemann variables in the (x,t) -plane for a rarefaction type of pressure wave generated in a quiescent gas in a duct of constant cross section; $\gamma = 1.4$.

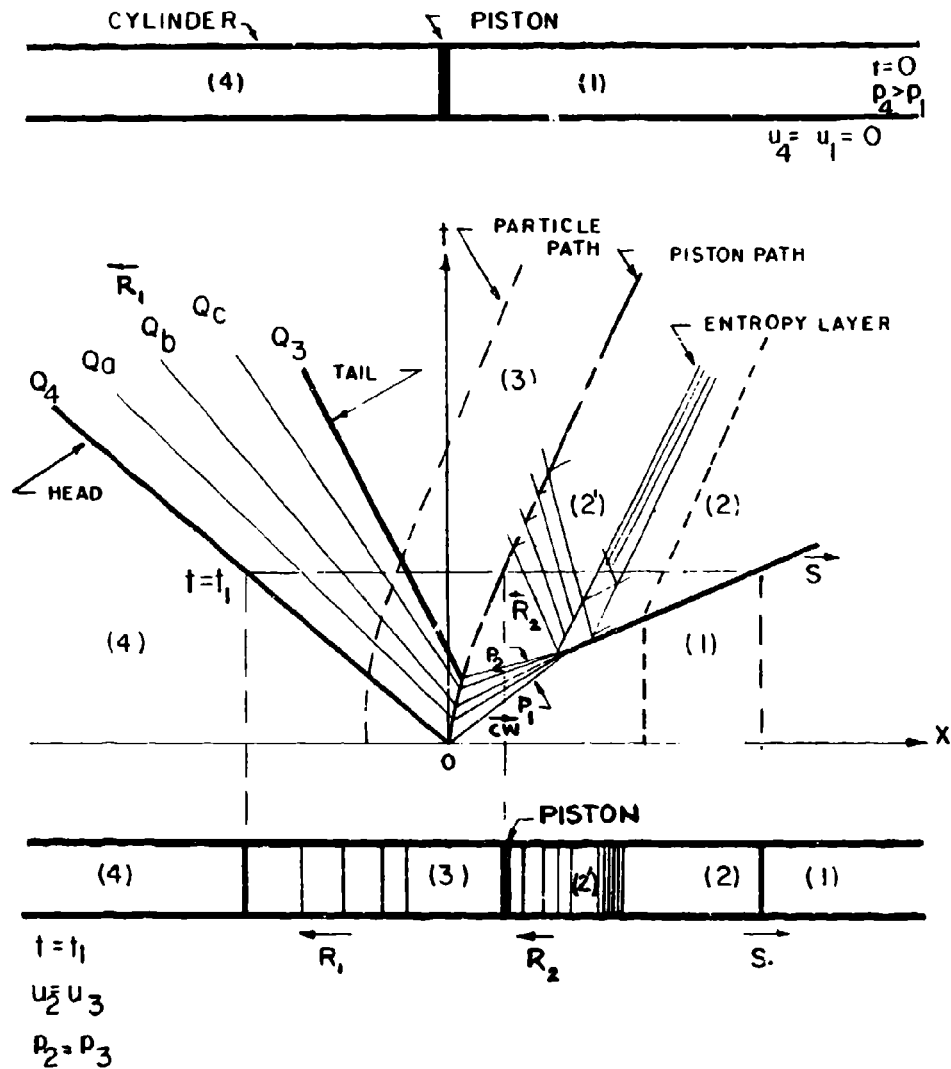
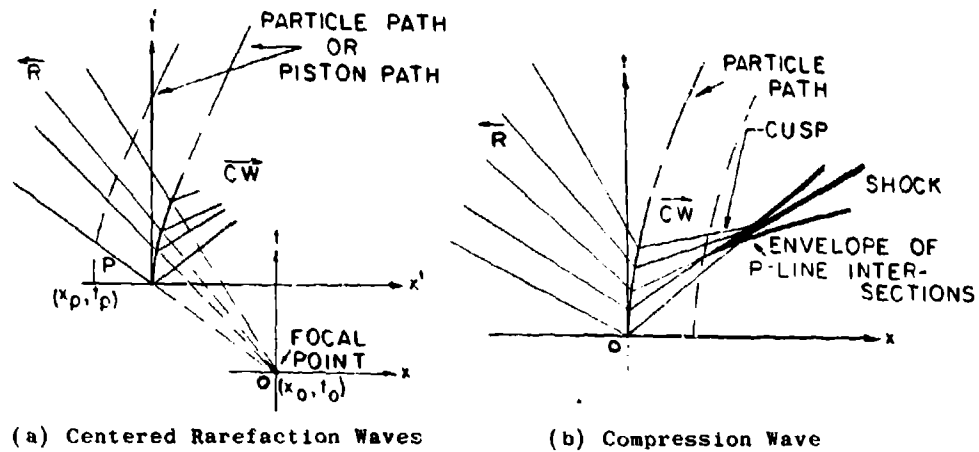
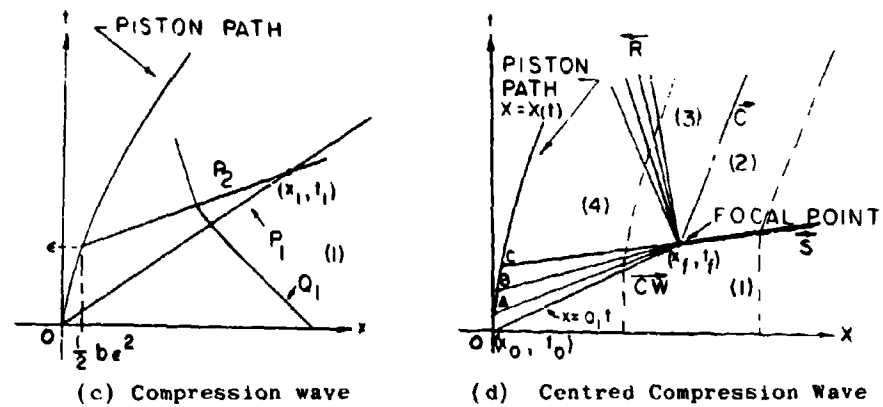


Fig. 2.1-13. Wave system produced by a piston accelerated from rest to a uniform velocity.



(a) Centered Rarefaction Waves

(b) Compression Wave



(c) Compression wave

(d) Centred Compression Wave

Fig. 2.1-15. The generation of rarefaction waves and compression waves by a piston.

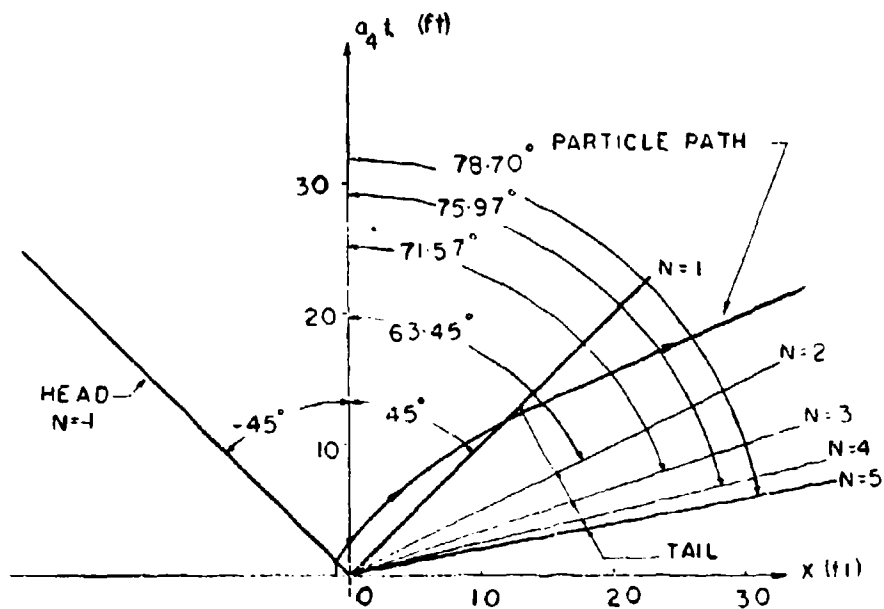


Fig. 2.1-16. Q-centred rarefaction waves in the $(a_4 t, x)$ -plane; $\gamma = 1.4$.

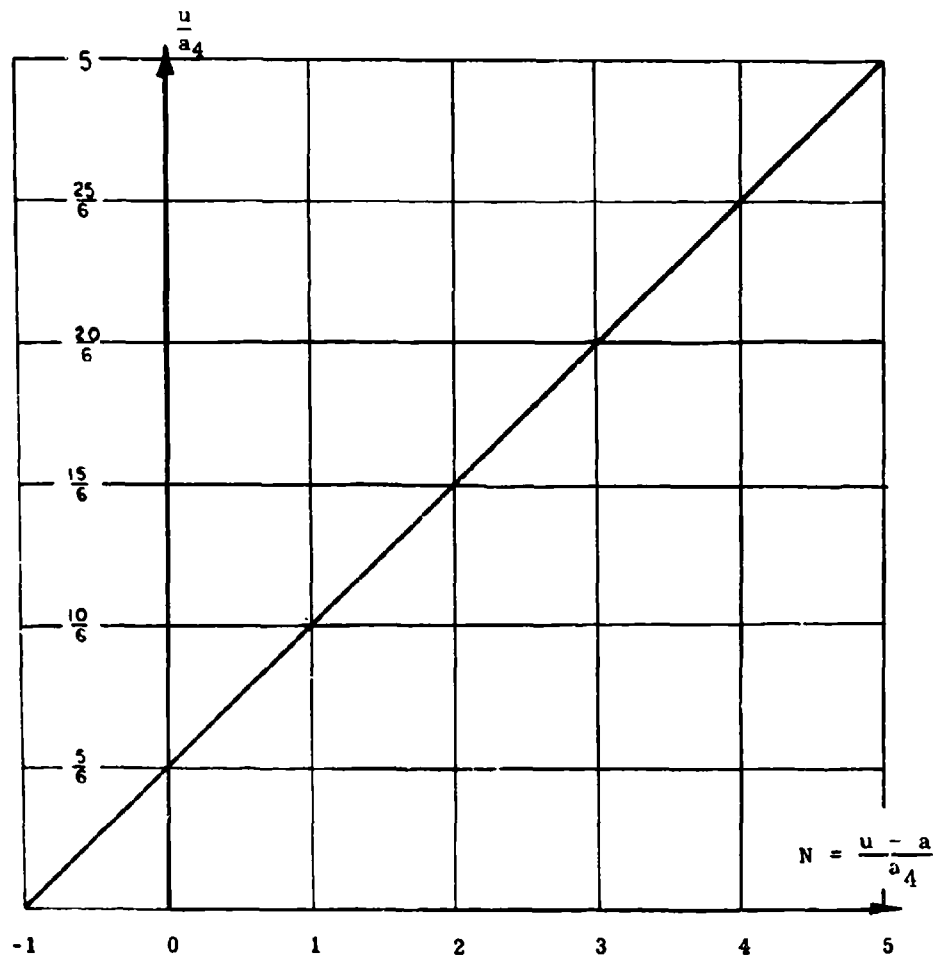


Fig. 2.1-17. Variation of the particle velocity through a centred Q-rarefaction wave; $\gamma = 1.4$.

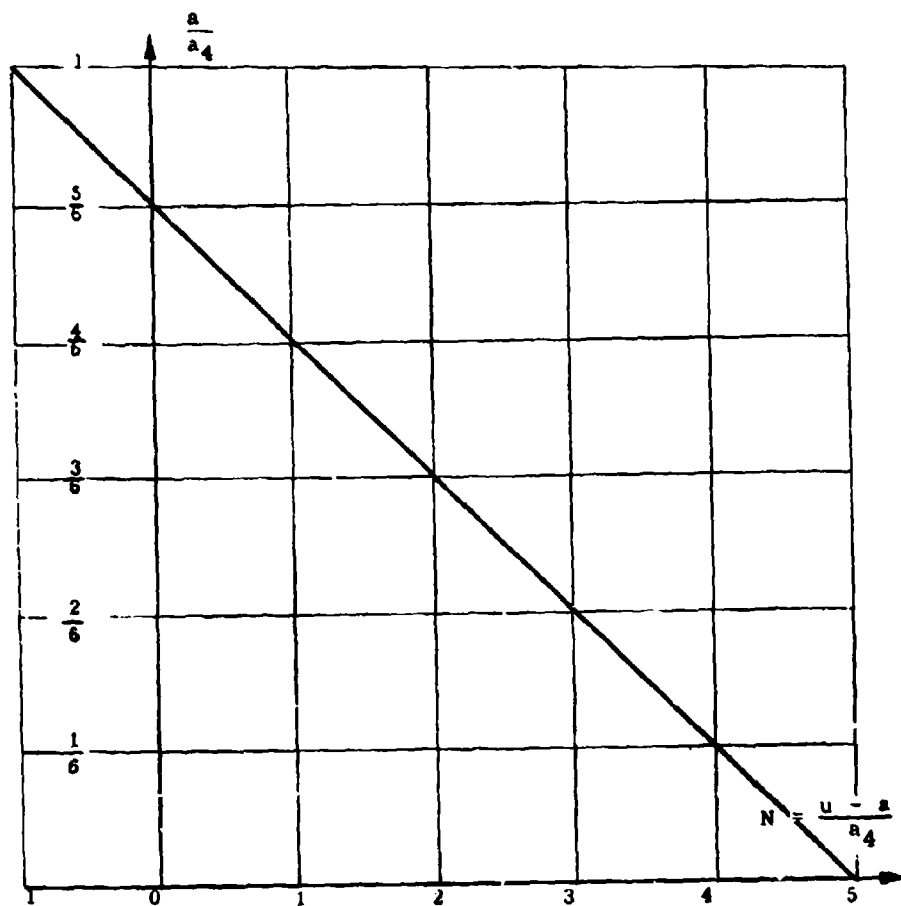


Fig. 2.1-18. Variation of the sound speed ratio through a Q-centred rarefaction wave; $\gamma = 1.4$.

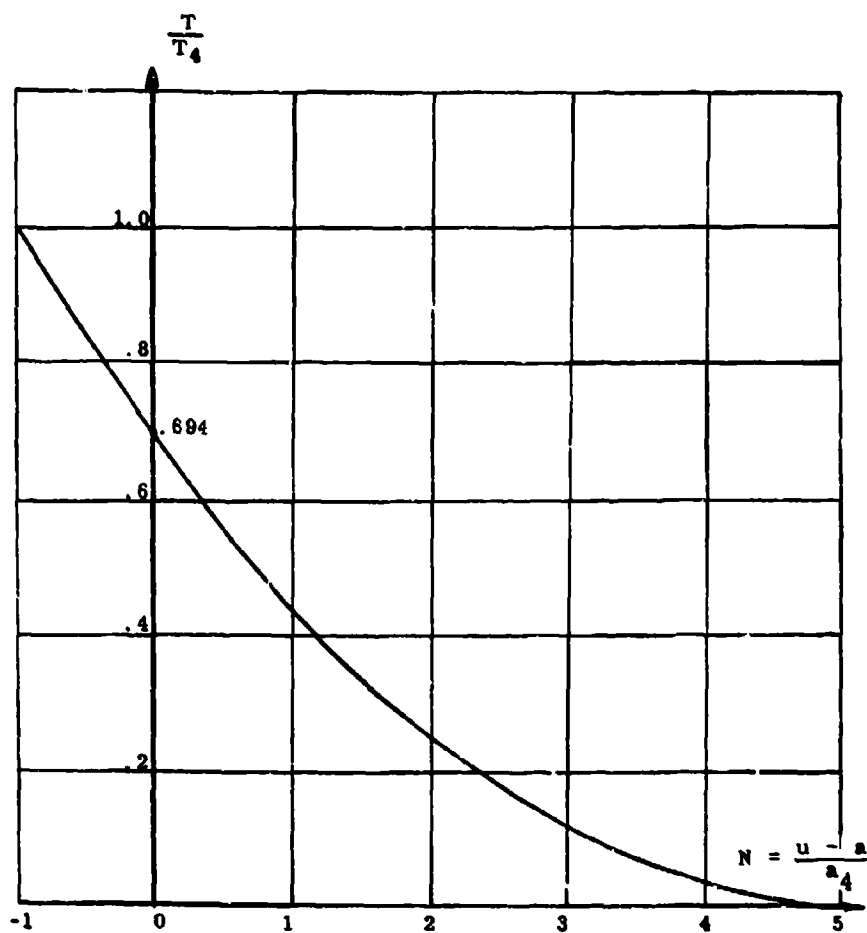


Fig. 2.1-19. Variation of the temperature ratio through a Q-centred rarefaction wave; $\gamma = 1.4$.

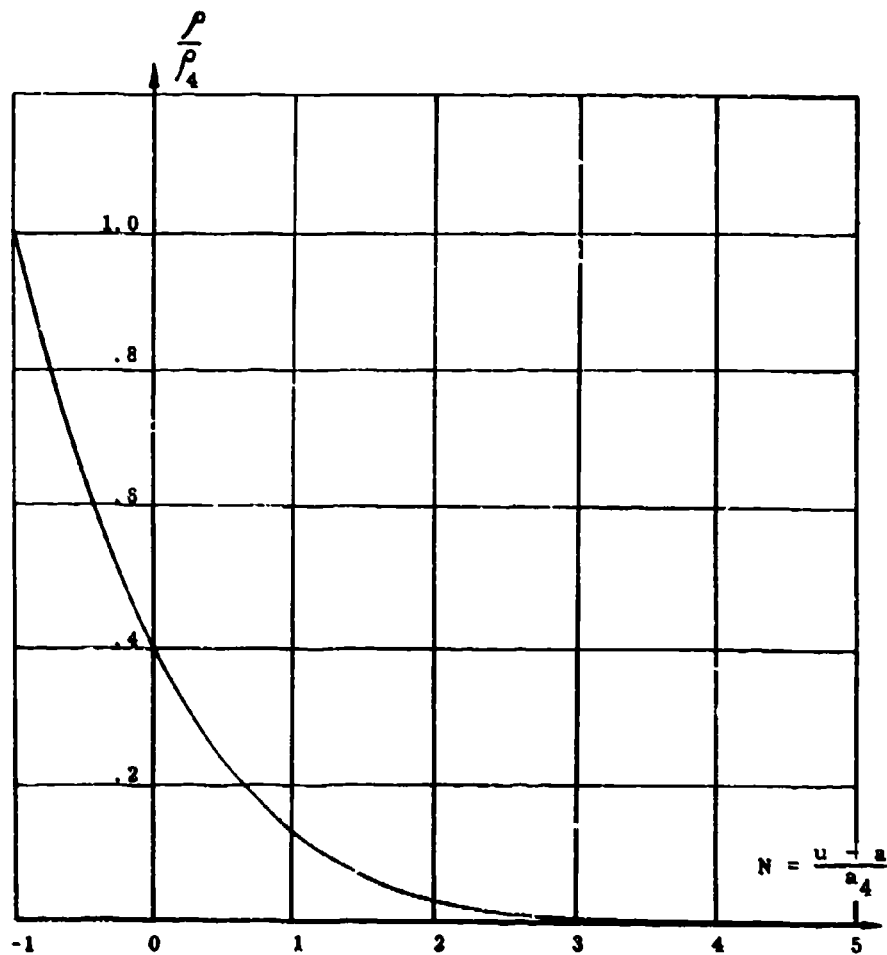


Fig. 2.1-20. Variation of the density ratio through a Q-centred rarefaction wave; $\gamma = 1.4$.

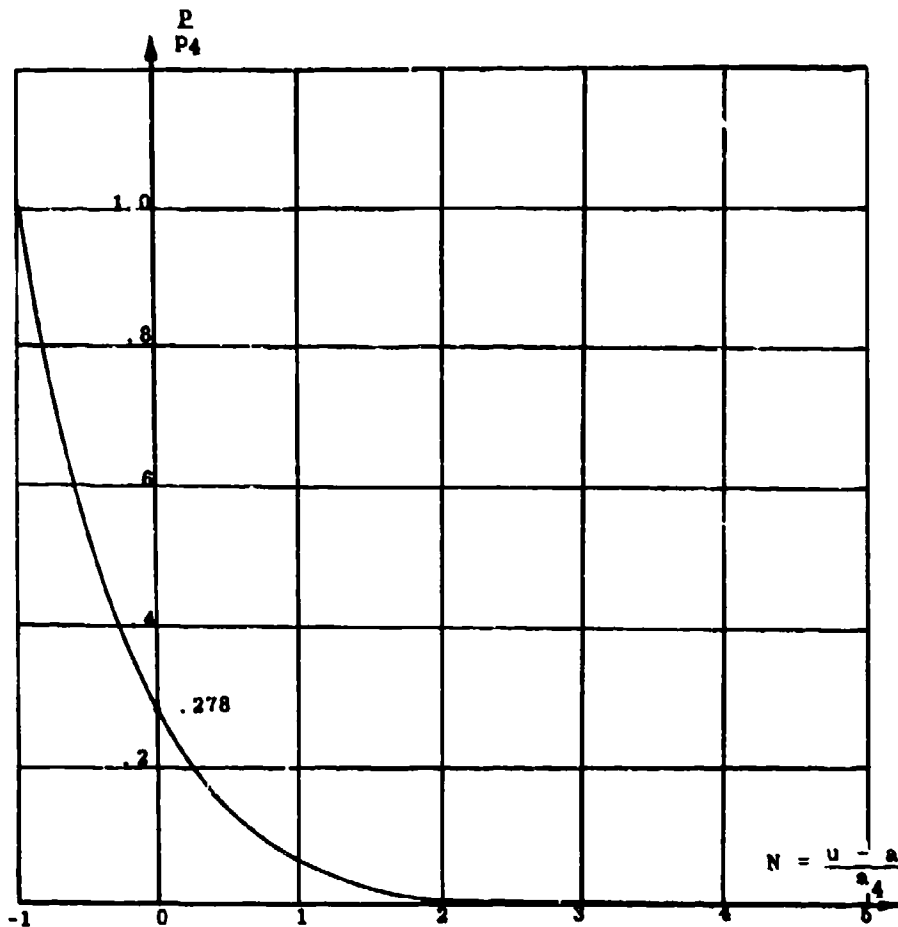


Fig. 2.1-21. Variation of the pressure ratio through a Q-centred rarefaction wave; $\gamma = 1.4$.

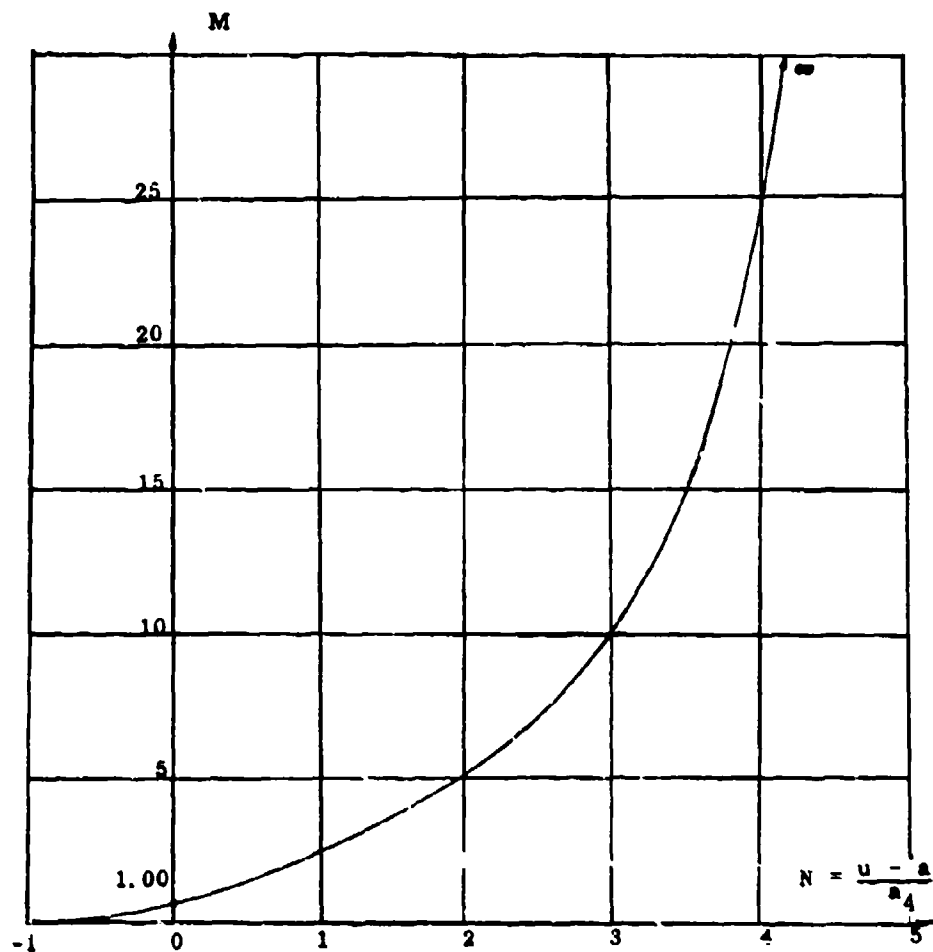


Fig. 2.1-22. Variation of the Mach number through a Q-centred rarefaction wave; $\gamma = 1.4$.

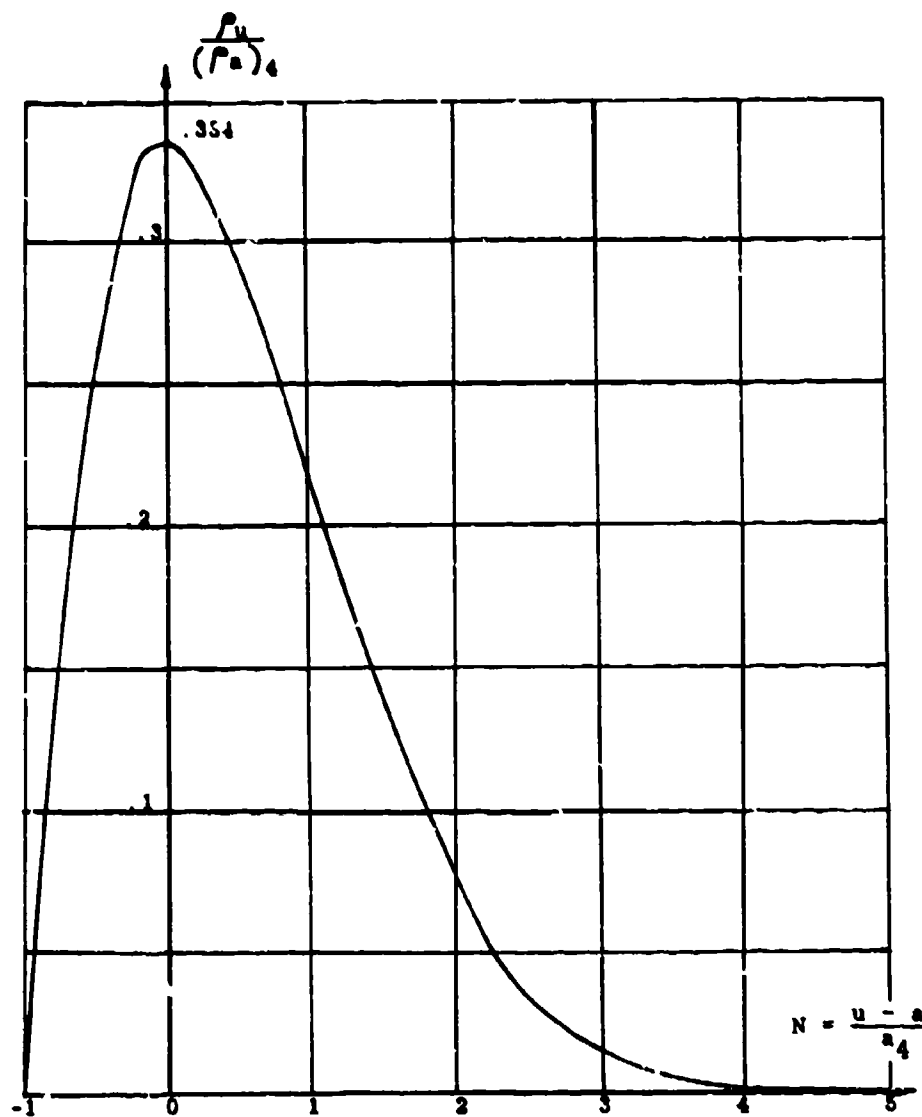


Fig. 2.1-23. Variation of the mass flow ratio through a Q-centred rarefaction wave; $\gamma = 1.4$.

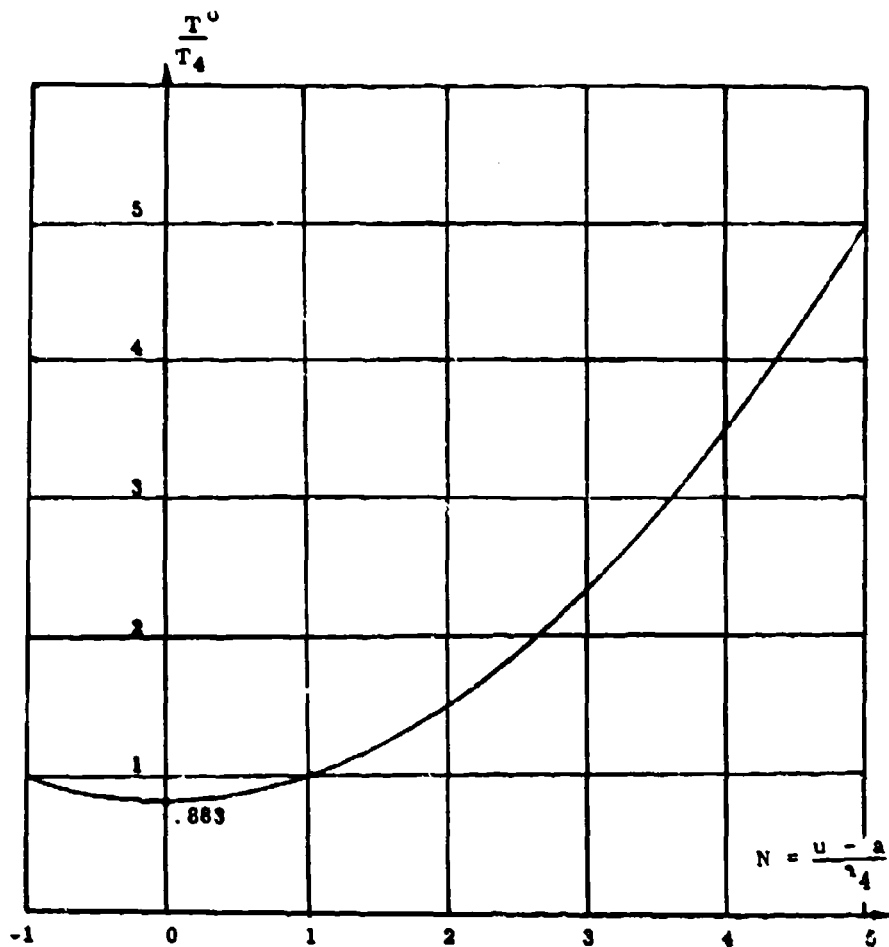


Fig. 2.1-24. Variation of the total temperature ratio through a Q-centred rarefaction wave; $\gamma = 1.4$.

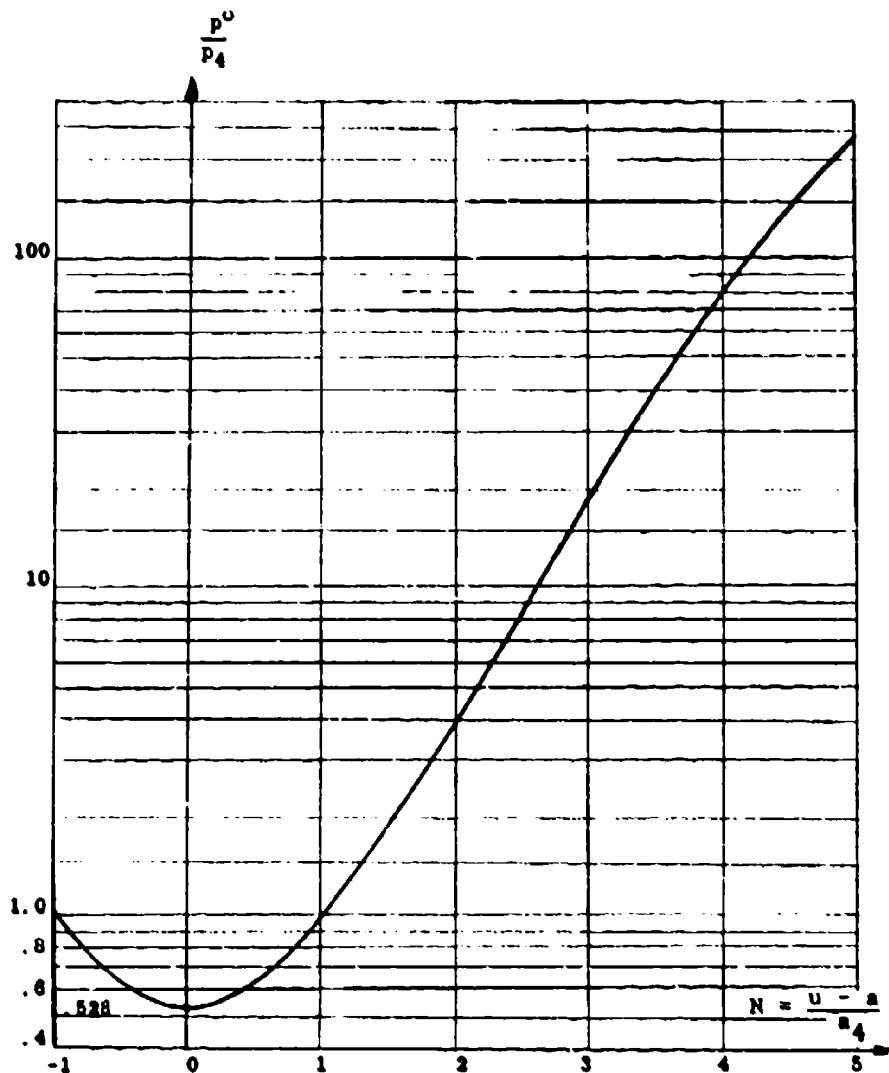


Fig. 2.1-25. Variation of the isentropic pressure ratio through a Q-centred rarefaction wave; $\gamma = 1.4$.

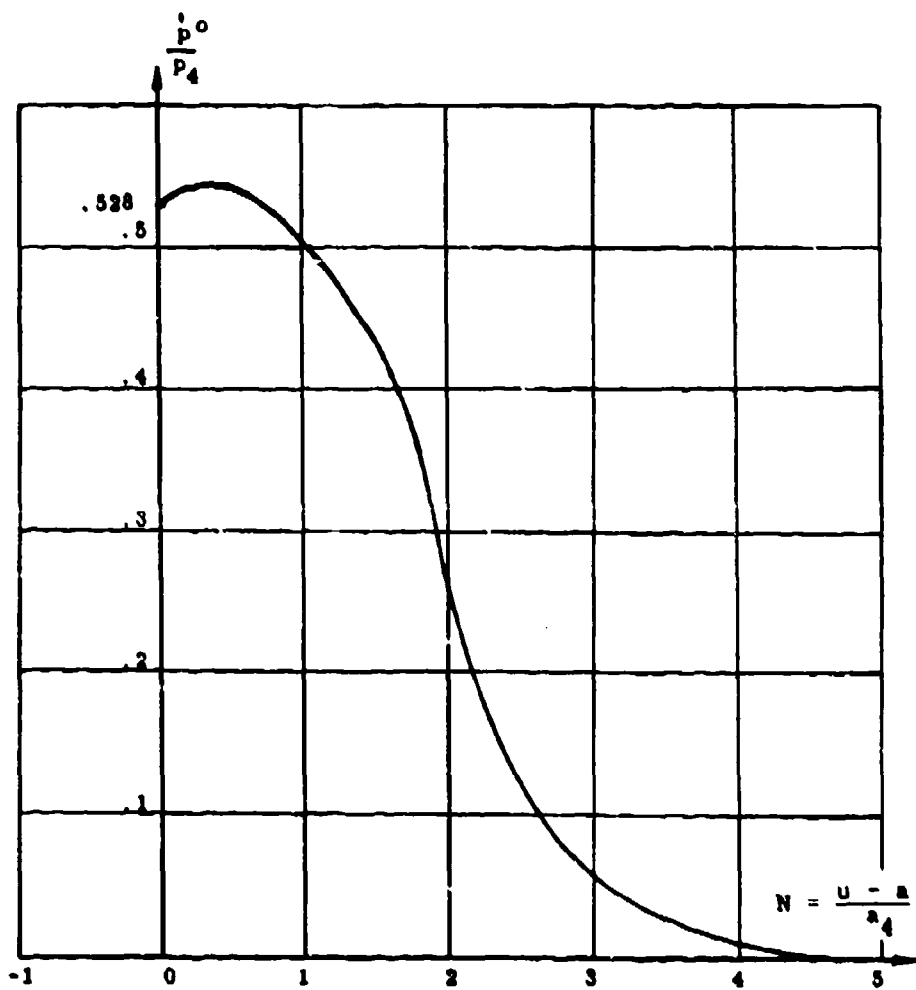


Fig. 2.1-26. Variation of the pitot pressure ratio through a Q-centred rarefaction wave; $\gamma = 1.4$.

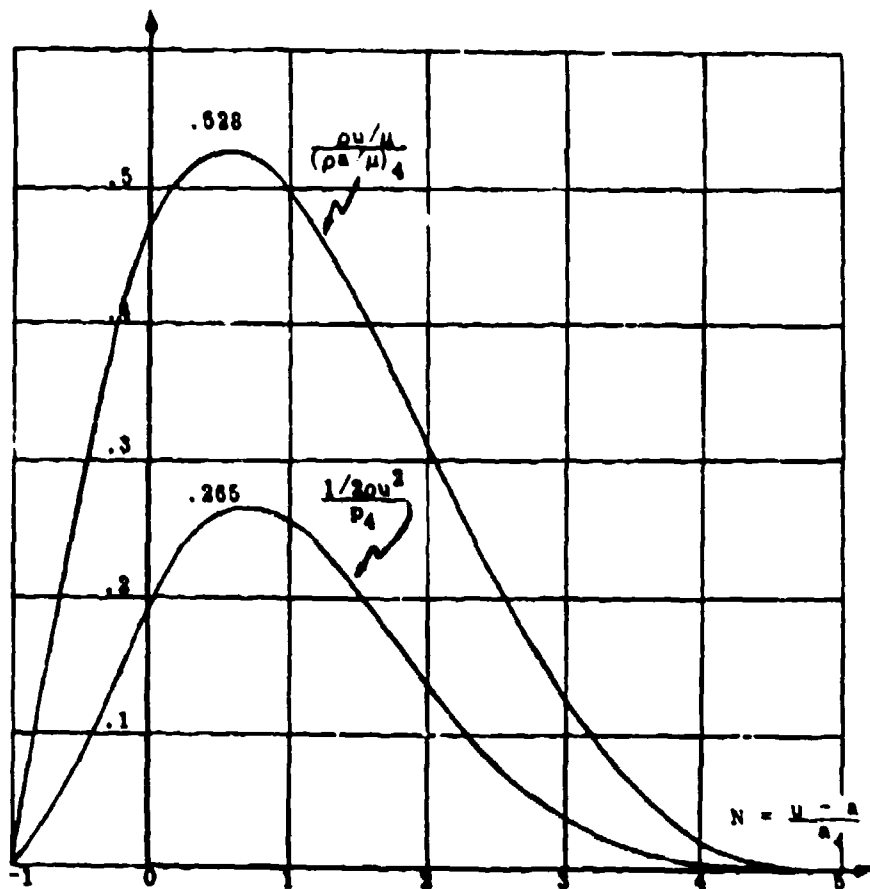


Fig. 2.1-27. Variation of the Reynolds number per foot and the dynamic pressure through a Q-centred rarefaction wave; $\gamma = 1.4$.

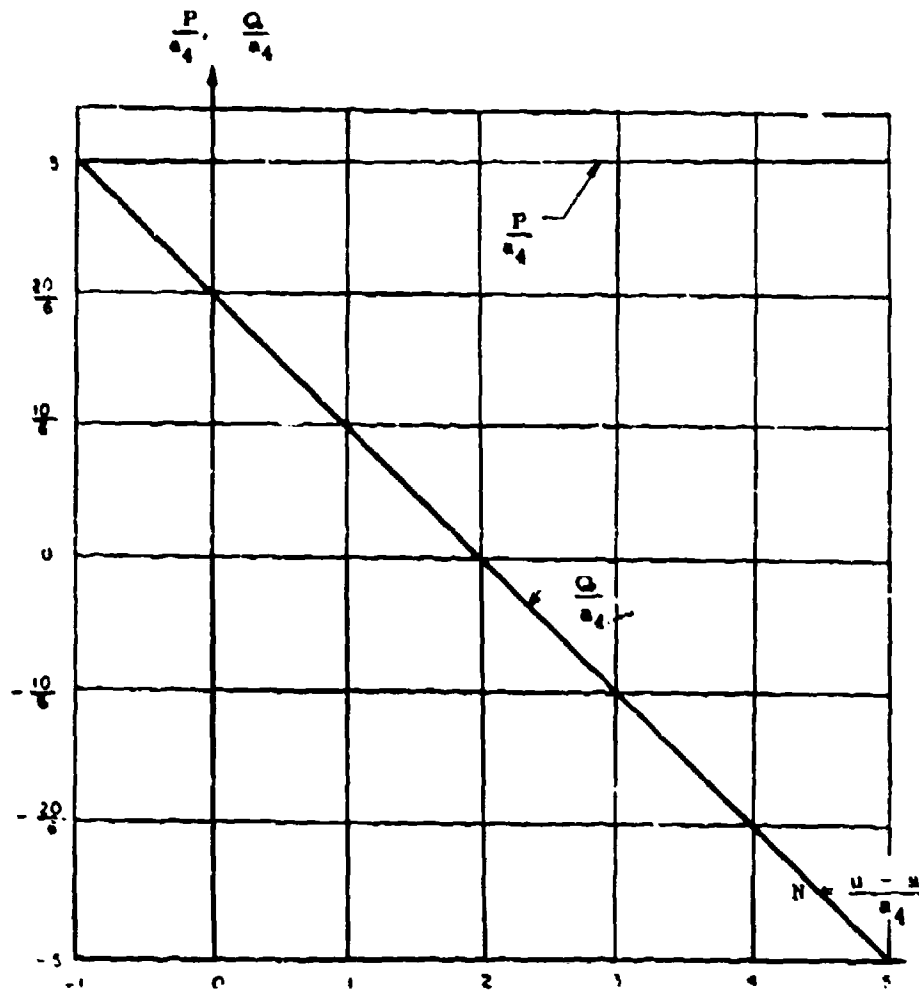


Fig. 2.1-28. Variation of the Riemann invariants P and Q through a Q-centred rarefaction wave; $\gamma = 1.4$.

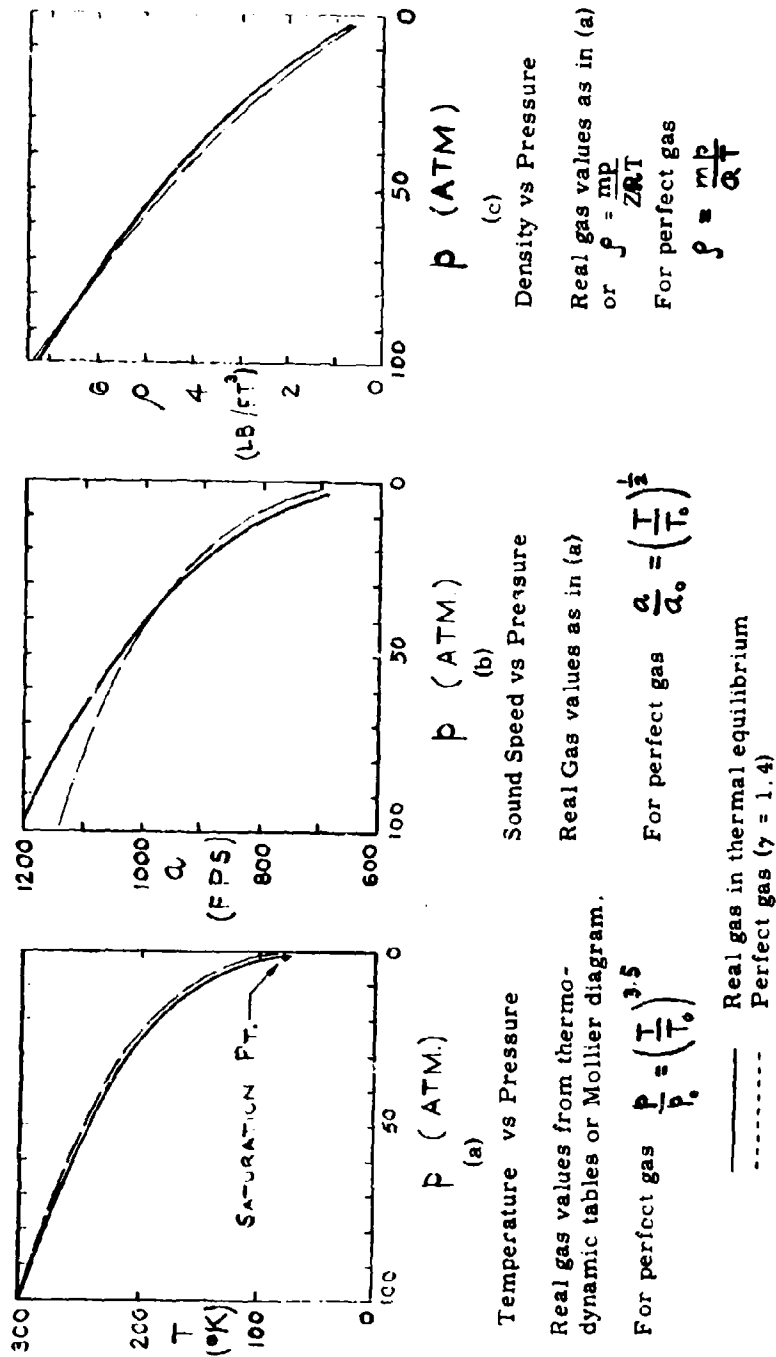


Fig. 2.1-29. Flow properties of a one-dimensional, isentropic, unsteady rarefaction wave in air expanded from $p_4 = 100$ atm and $T_4 = 300^\circ\text{K}$ (Ref. 34b).

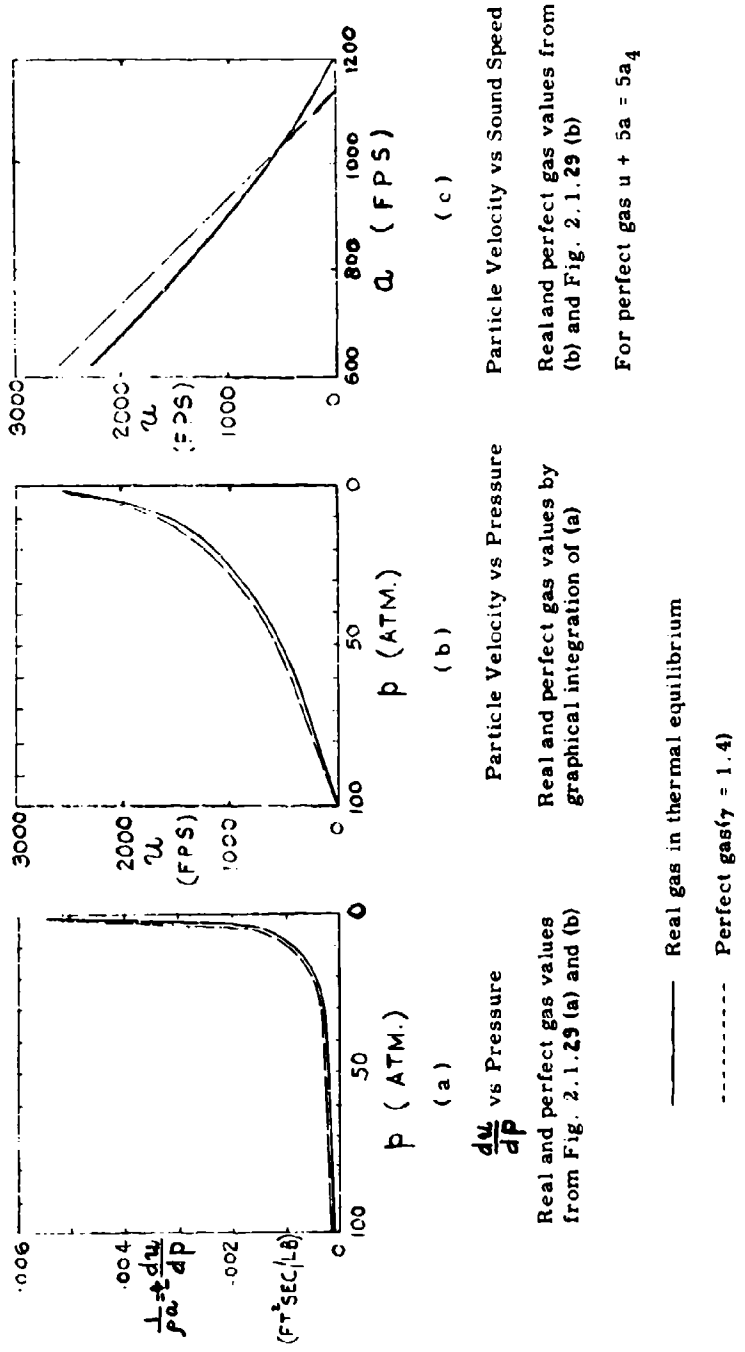


Fig. 2.1-30. Flow properties of a one-dimensional, isentropic, unsteady rarefaction wave in air expanded from $P_4 = 100$ atm and $T_4 = 300^\circ\text{K}$ (Ref. 34b).

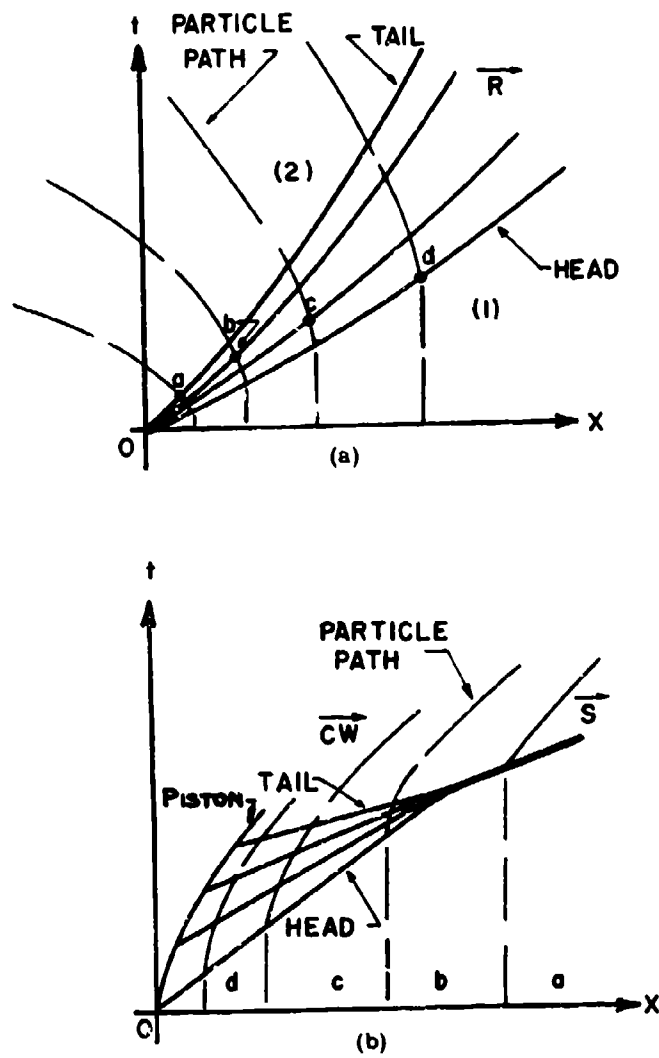


Fig. 2.1-31. Rarefaction wave and compression wave with relaxation effects.

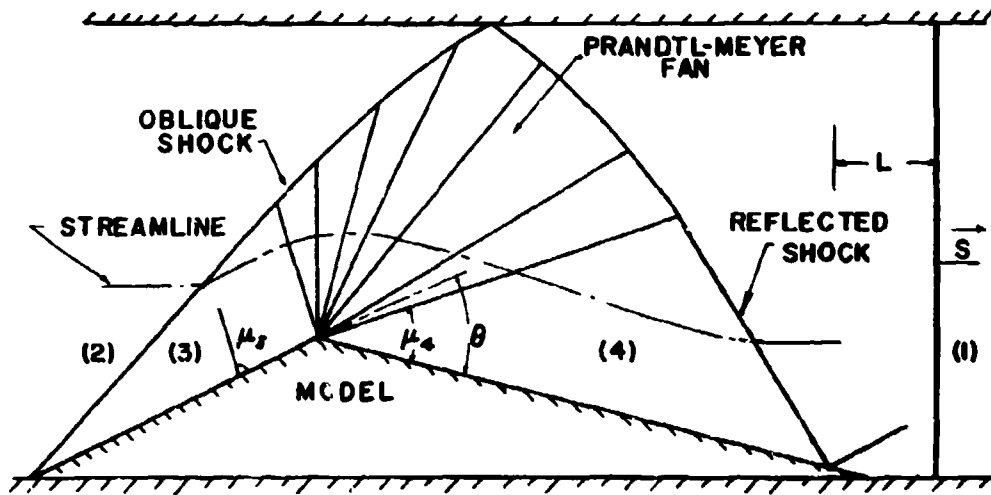


Fig. 2.1-32. The flow about a double-wedge model in a shock tube.

Table 2.2-1

Initial conditions (Ref. 40)

Altitude, ft	Pressure, P_1 , atm	Density, ρ_1 , slugs/ft ⁻³	Temperature, T_1 , °R	Dimensionless enthalpy, h_1/R_0T_0	Dimensionless entropy, S_1/R_0
0	1.0	2.38×10^{-3}	519	3.70	23.6
50,000	0.1145	3.62×10^{-4}	392.4	2.795	25.0
100,000	0.0106	3.31×10^{-5}	392.4	2.795	27.4
150,000	0.00142	3.05×10^{-6}	573.5	4.085	30.9
200,000	0.000314	6.2×10^{-7}	619.4	4.41	32.7

Table 2.2-2

$$\text{Enthalpy parameter; } \beta = \frac{h}{p/\rho} = 1 + \frac{e}{p/\rho}$$

Temperature °K	Density Ratio										
	10	1	10 ^{-1/2}	10 ⁻¹	10 ^{-3/2}	10 ⁻²	10 ^{-5/2}	10 ⁻³	10 ⁻⁴	10 ⁻⁵	10 ⁻⁶
1000	3.630							4.007	4.105	4.400	5.200
2000	3.961	3.960		3.953		3.975		6.128	6.777	6.938	7.061
3000	4.294	4.3704		4.597		5.170		6.263	6.534	7.285	9.123
4000	4.712	5.087		5.684		6.084		7.061	8.994	11.38	12.50
5000	5.083	5.486		5.792		6.160		9.347	10.72	11.06	11.20
6000	5.255	5.591	5.815	6.144	6.650	7.382	8.331				
7000	5.374	5.931	6.420	7.101	7.935	8.758	9.368	9.741	9.993	10.22	10.83
8000	5.596	6.531	7.223	7.949	8.541	8.885	9.084	9.190	9.489	10.25	11.96
12,000	6.669	7.219		7.536		8.153		9.396	10.84	11.53	11.65
18,000	6.269	6.711		7.532		8.342		8.645	8.728	8.994	10.24
24,000	6.120	6.615		7.061		7.274		7.609	8.855	10.12	10.51

Table 2.2-3

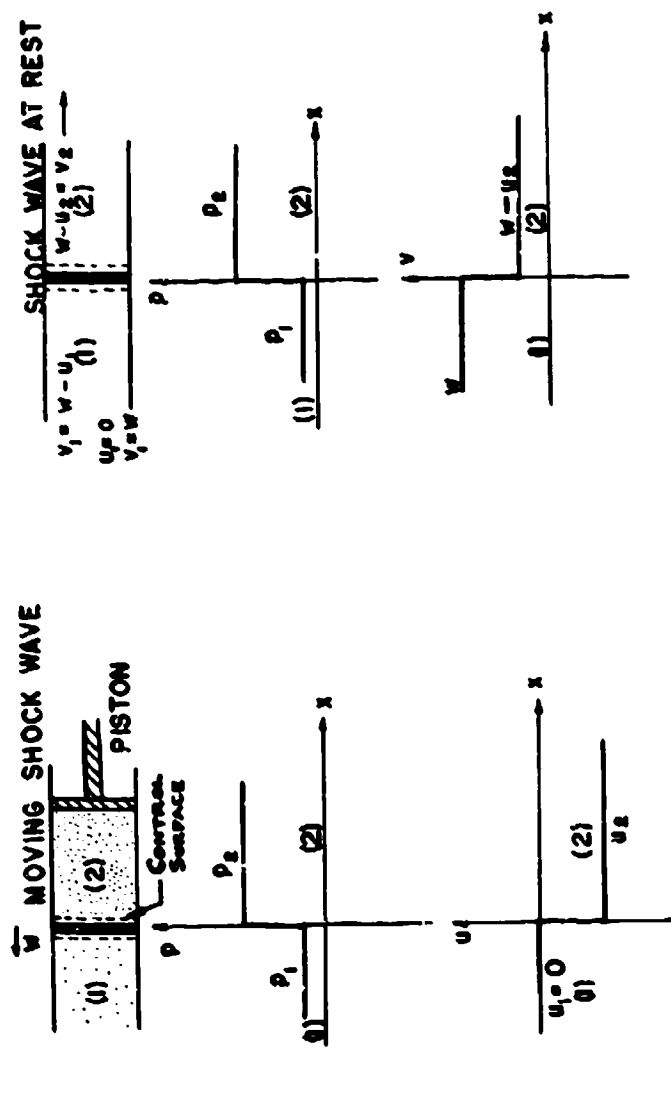
Number of moles per mole of cold air; $Z = PV/RT$ (Ref. 35)

Temperature °K	Density Ratio ρ/ρ_0										
	10	1	$10^{-1/2}$	10^{-1}	$10^{-3/2}$	10^{-2}	$10^{-5/2}$	10^{-3}	10^{-4}	10^{-5}	10^{-6}
1000	1.0000	1.0000		1.0000		1.0000		1.0000	1.0000	1.0000	1.0000
2000	1.0000	1.0000		1.0001		1.0007		1.0017	1.0055	1.0170	1.0487
3000	1.0023	1.0072		1.0218		1.0610		1.1341	1.1912	1.2069	1.2109
4000	1.0226	1.0628		1.1341		1.1896		1.2107	1.2282	1.2715	1.3383
5000	1.0728	1.1448		1.1990		1.2370		1.3081	1.4835	1.7752	1.9544
6000	1.1275	1.1984	1.2298	1.2669	1.3196	1.4001	1.5163	1.6643	1.9143	1.9664	2.0051
7000	1.1761	1.2698	1.3364	1.4315	1.5623	1.7162	1.8570	1.9364	1.9970	2.0788	2.1105
8000	1.2380	1.4001	1.5259	1.6794	1.9261	2.224	1.9763	2.0010	2.0487	2.1702	2.5007
12,000	1.708	1.957		2.062		2.224		2.636	3.365	3.865	3.968
18,000	2.063	2.284		2.775		3.518		3.910	3.984	4.078	4.530
24,000	2.322	2.865		3.602		3.930		4.143	4.778	5.623	5.931

Table 2.2-4
Entropy of dry air in chemical equilibrium, S/R per mole of cold air (Ref. 35)

Temperature °K	Density Ratio ρ/ρ_0										
	10	1	$10^{-1/2}$	10^{-1}	$10^{-3/2}$	10^{-2}	$10^{-5/2}$	10^{-3}	10^{-4}	10^{-5}	10^{-6}
1000	2.493 ⁺¹	2.883 ⁺¹	3.190 ⁺¹	3.821 ⁺¹	4.251 ⁺¹	4.165 ⁺¹	4.939 ⁺¹	3.374 ⁺¹	3.604 ⁺¹	3.835 ⁺¹	4.085 ⁺¹
2000	2.698 ⁺¹	2.929 ⁺¹	3.180 ⁺¹	3.860 ⁺¹	4.244 ⁺¹	3.391 ⁺¹	5.584 ⁺¹	3.626 ⁺¹	3.867 ⁺¹	4.133 ⁺¹	4.466 ⁺¹
3000	2.858 ⁺¹	3.098 ⁺¹	3.360 ⁺¹	3.853 ⁺¹	4.777 ⁺¹	3.675 ⁺¹	5.849 ⁺¹	4.065 ⁺¹	4.442 ⁺¹	4.747 ⁺¹	5.034 ⁺¹
4000	3.008 ⁺¹	3.303 ⁺¹	3.653 ⁺¹	3.821 ⁺¹	4.777 ⁺¹	3.995 ⁺¹	5.849 ⁺¹	4.305 ⁺¹	4.627 ⁺¹	5.035 ⁺¹	5.666 ⁺¹
5000	3.150 ⁺¹	3.491 ⁺¹	3.806 ⁺¹	3.821 ⁺¹	5.199 ⁺¹	4.165 ⁺¹	5.849 ⁺¹	4.611 ⁺¹	5.324 ⁺¹	6.353 ⁺¹	7.193 ⁺¹
6000	3.285 ⁺¹	3.825 ⁺¹	4.037 ⁺¹	4.009 ⁺¹	4.251 ⁺¹	4.556 ⁺¹	4.939 ⁺¹	5.400 ⁺¹	6.285 ⁺¹	6.876 ⁺¹	7.382 ⁺¹
7000	3.395 ⁺¹	3.768 ⁺¹	4.037 ⁺¹	4.244 ⁺¹	4.728 ⁺¹	5.153 ⁺¹	5.584 ⁺¹	5.951 ⁺¹	6.509 ⁺¹	7.047 ⁺¹	7.726 ⁺¹
8000	3.522 ⁺¹	4.032 ⁺¹	4.373 ⁺¹	4.777 ⁺¹	5.199 ⁺¹	5.348 ⁺¹	5.849 ⁺¹	6.120 ⁺¹	6.685 ⁺¹	7.437 ⁺¹	8.704 ⁺¹
12,000	4.250 ⁺¹	4.900 ⁺¹	5.494 ⁺¹	5.494 ⁺¹	5.494 ⁺¹	6.228 ⁺¹	6.228 ⁺¹	7.403 ⁺¹	9.191 ⁺¹	1.078 ⁺²	1.185 ⁺²
16,000	4.772 ⁺¹	5.488 ⁺¹	6.574 ⁺¹	6.574 ⁺¹	6.574 ⁺¹	8.067 ⁺¹	8.067 ⁺¹	9.338 ⁺¹	1.034 ⁺²	1.145 ⁺²	1.336 ⁺²
24,000	5.199 ⁺¹	6.209 ⁺¹	7.529 ⁺¹	7.529 ⁺¹	7.529 ⁺¹	8.686 ⁺¹	8.686 ⁺¹	9.893 ⁺¹	1.192 ⁺²	1.448 ⁺²	1.633 ⁺²

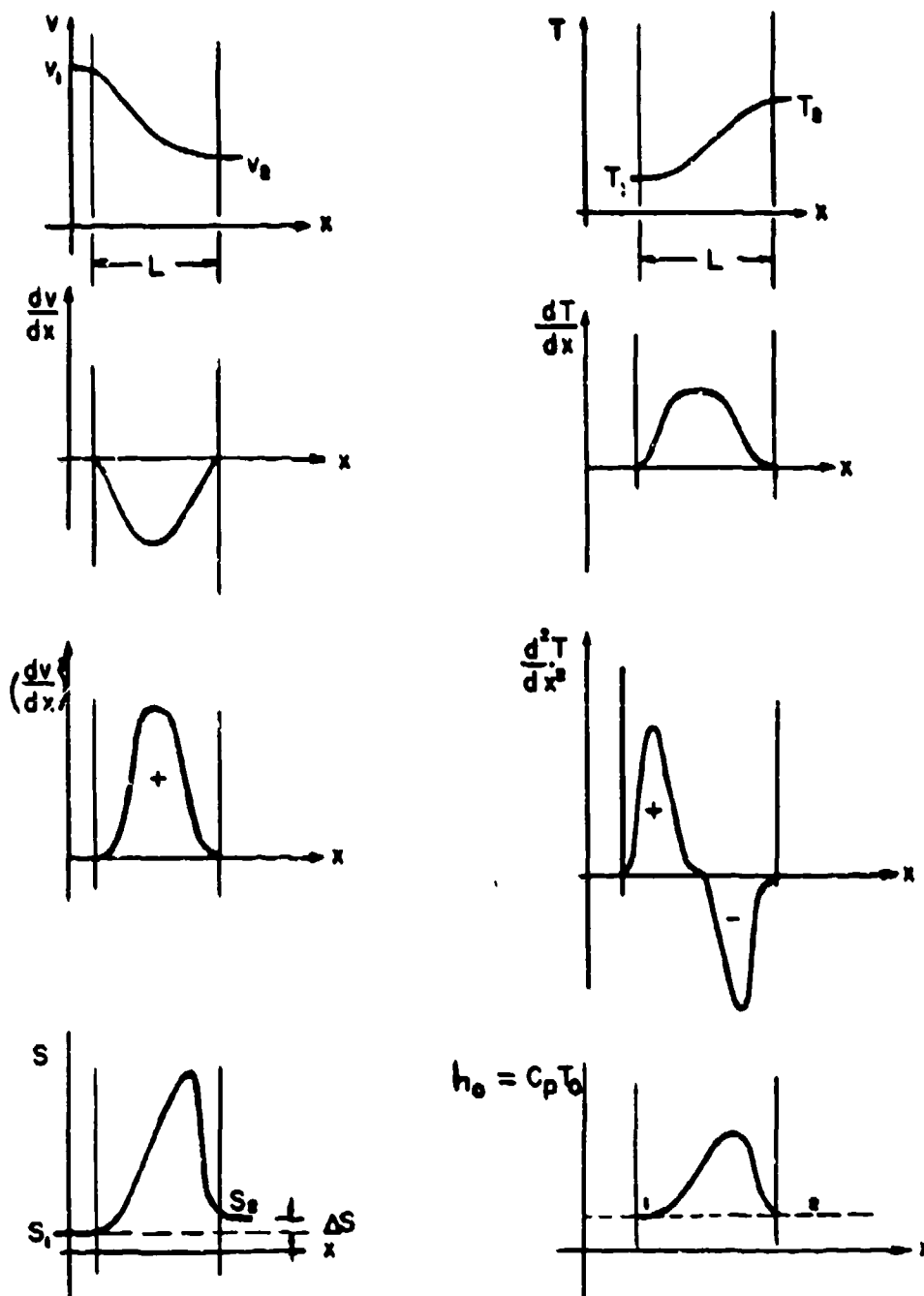
Note: For each value, the power of ten is indicated by a superscript.



(a) Nonstationary flow-moving shock wave generated by a piston.

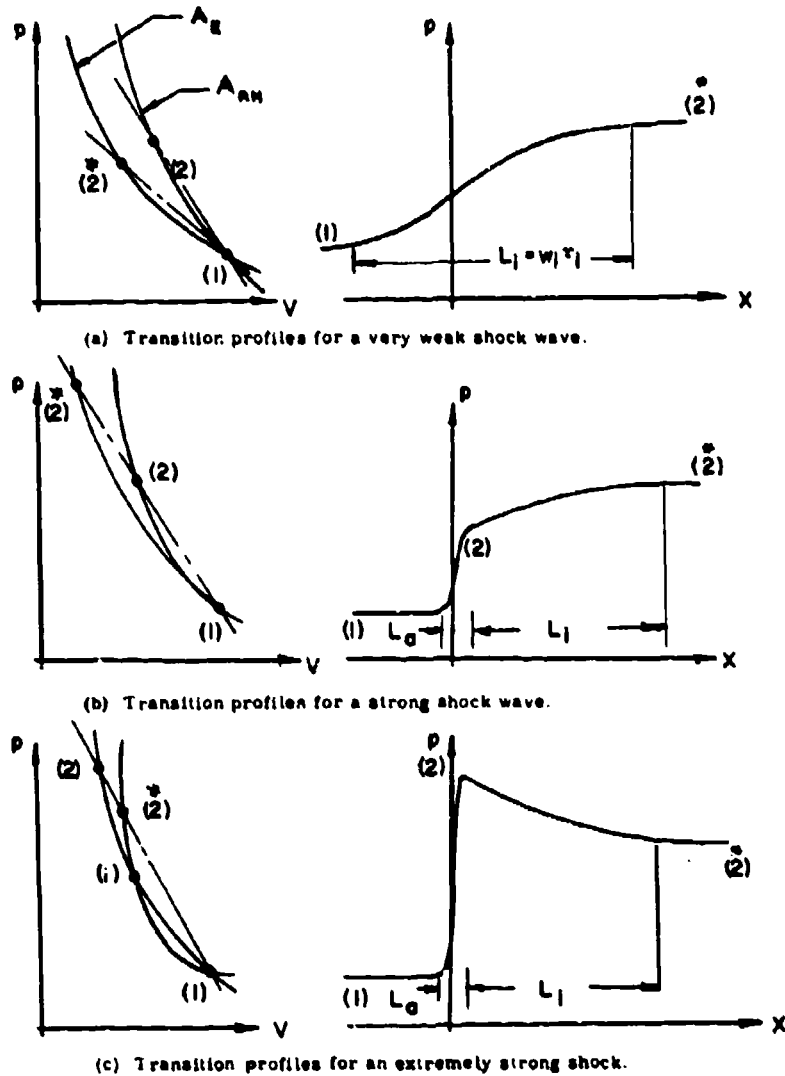
(b) Steady flow-shock wave brought to rest by velocity vector \vec{V} (reference axes fixed to shock wave).

Fig. 2.2-1. Shock wave as a discontinuity.



(L = shock thickness about 20 mean free paths at $M_g \sim 1.1$ and 4 mean free paths at $M_g \sim 2$ for monatomic and diatomic gases, Ref. 26.)

Fig. 2.2-2. Schematic transition profiles through a weak shock front with constant specific heats.



L_1 = Relaxation distance due to inert degrees.

L_a = Relaxation distance due to active degrees.

A_E = Complete equilibrium adiabatic for final state.

A_{RH} = Rankine-Hugoniot adiabatic for states evaluated by considering the active degrees only and inert degrees are considered as "frozen."

$\gamma = 5/3$ for monatomic molecule.

$\gamma = 7/5$ for linear molecule.

$\gamma = 4/3$ for other molecules.

Fig. 2.2-3. Shock transitions in a gas with relaxation effects.

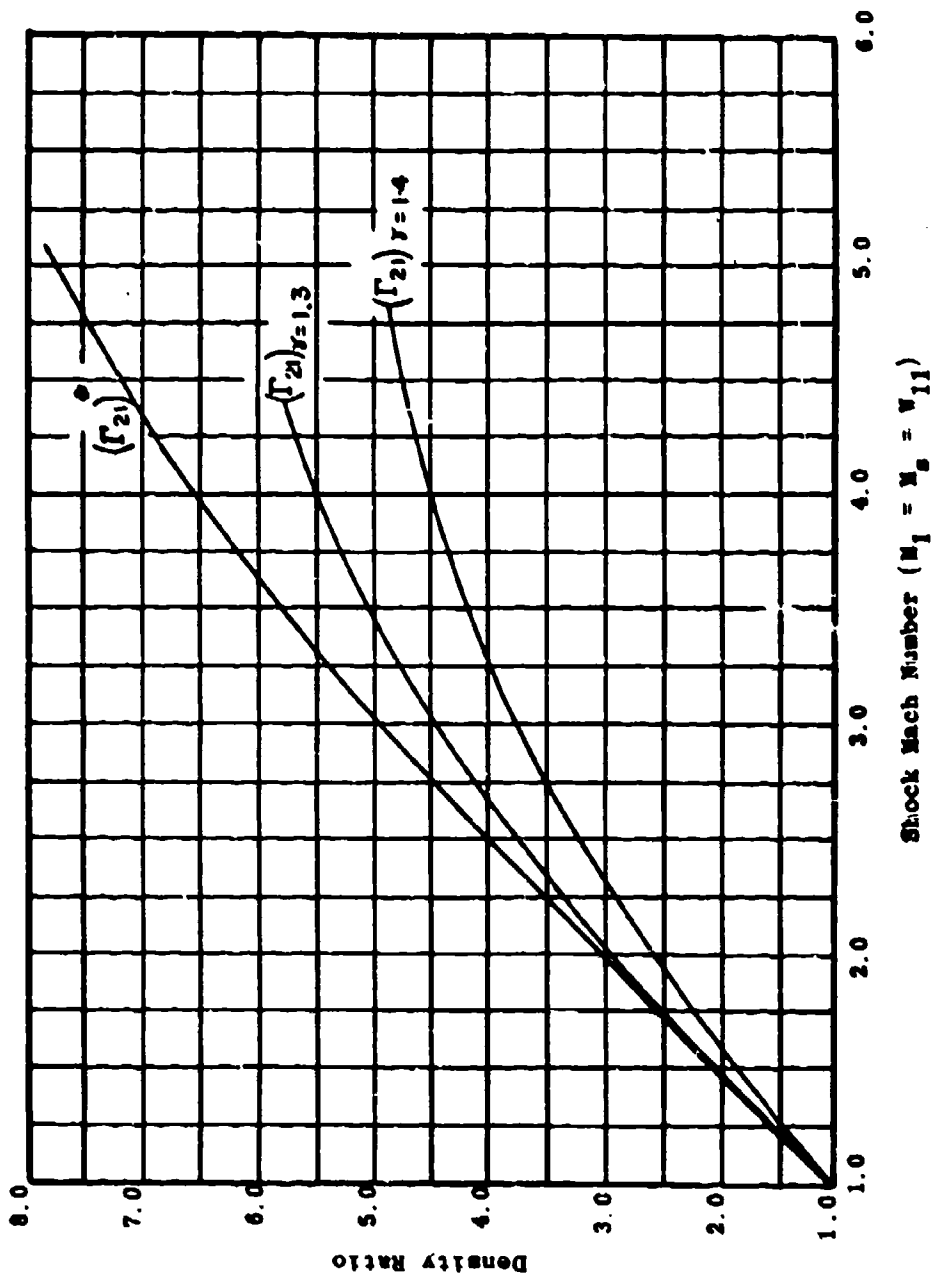


Fig. 2.2-4. Flow quantities behind a normal shock wave in CO₂ with vibrational excitation only (Ref. 34a).

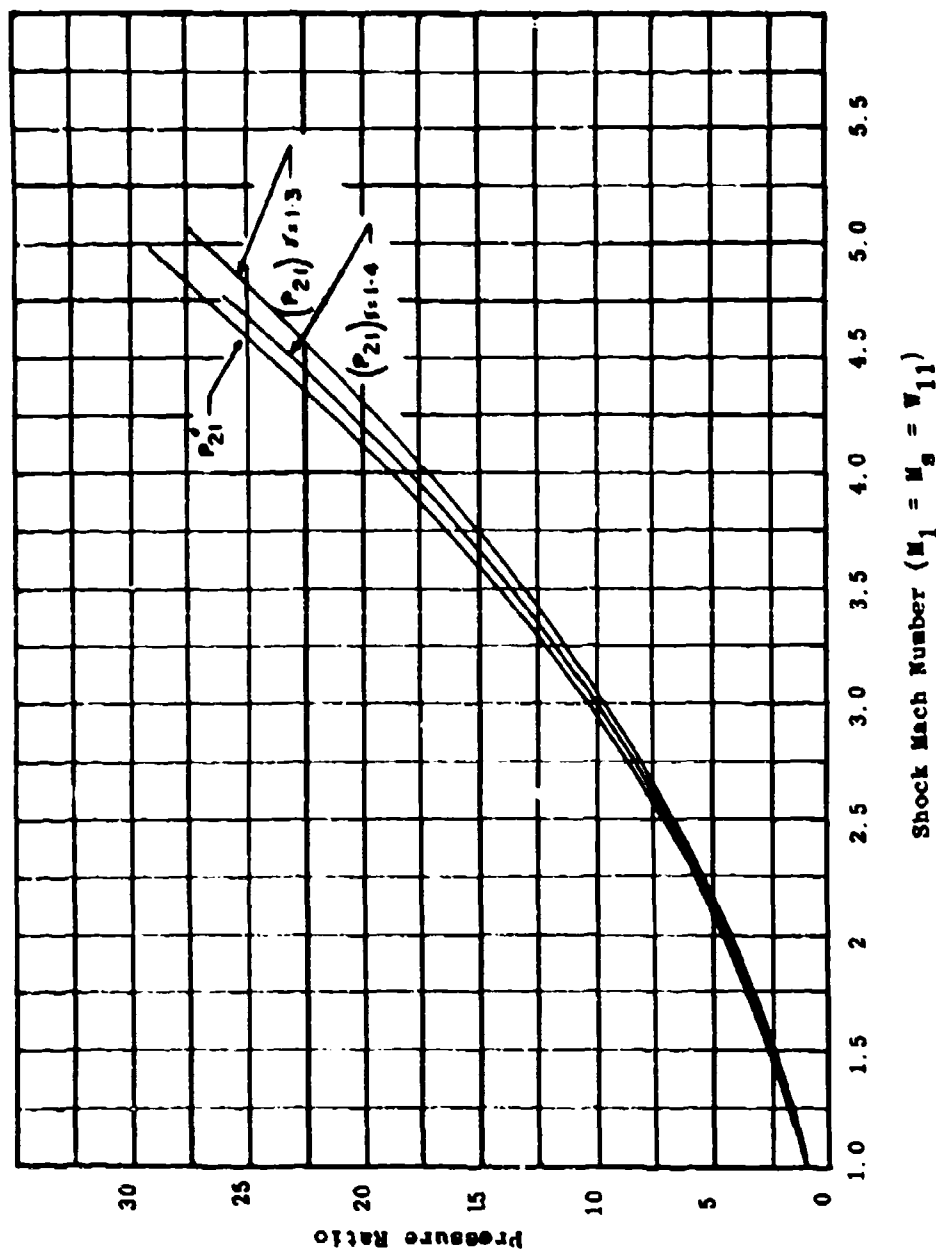


Fig. 2.2-4 (continued). Flow quantities behind a normal shock wave in CO₂ with vibrational excitation only (Ref. 34a).

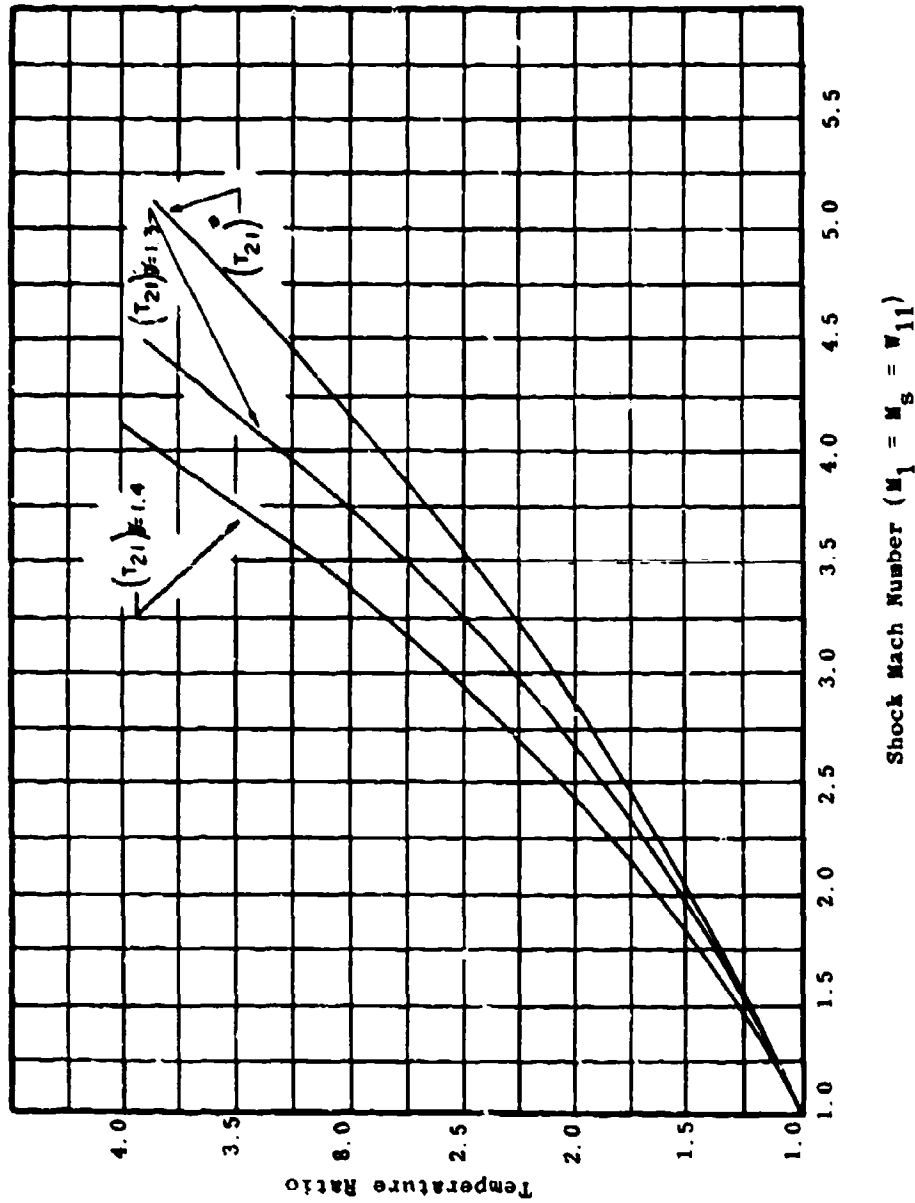


Fig. 2.2-4 (continued). Flow quantities behind a normal shock wave in CO_2 with vibrational excitation only (Ref. 34a).

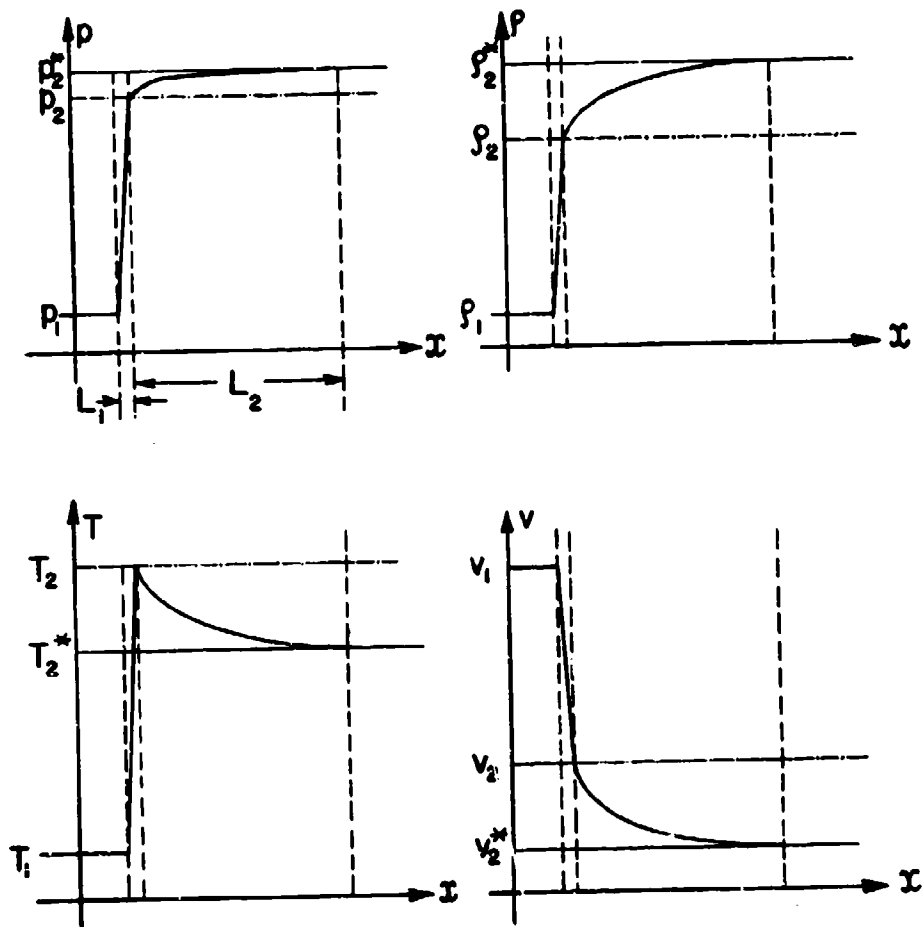


Fig. 2.2-5a. Representation of transition through a shock front with one inert (vibration) degree of freedom excited.

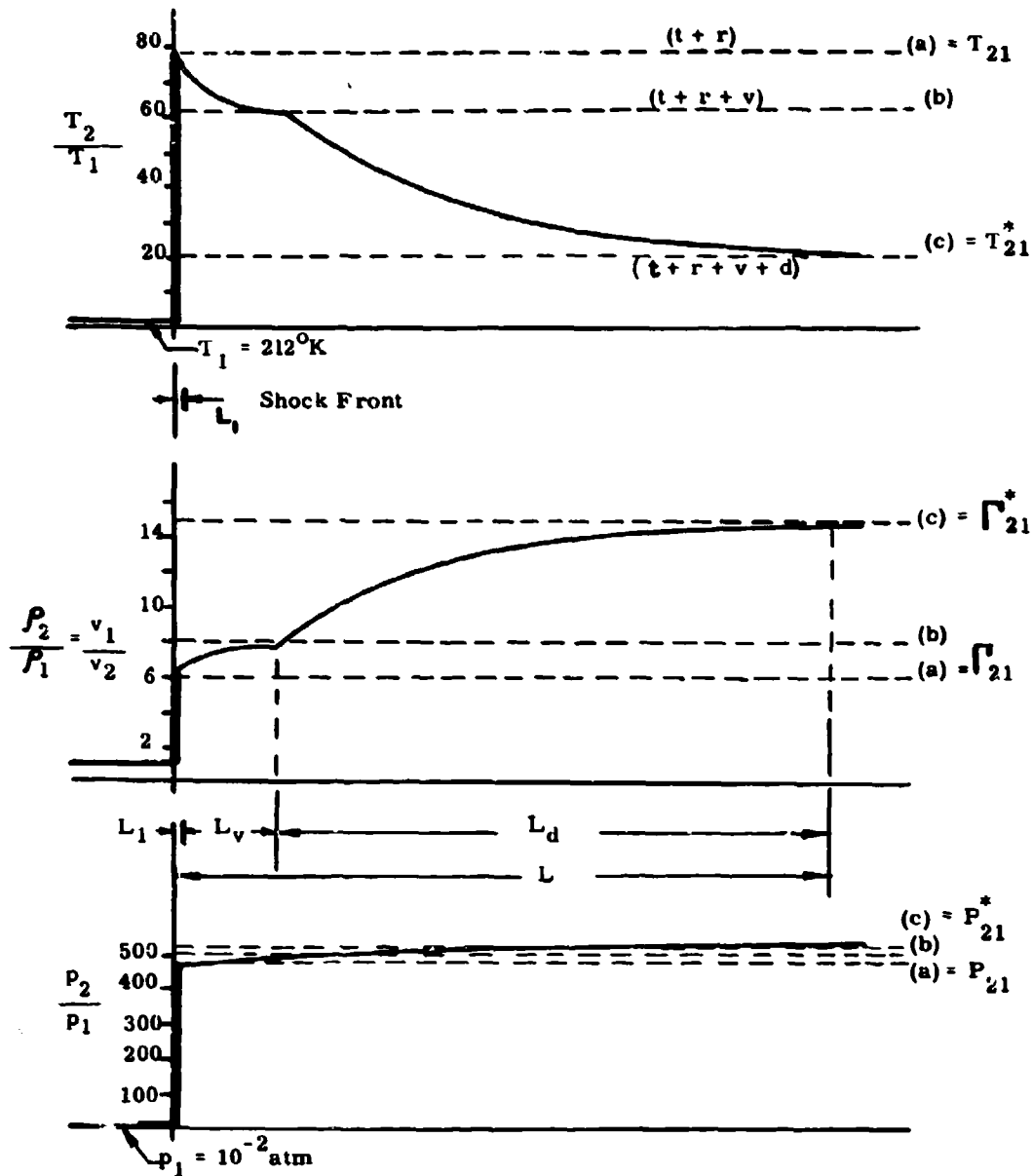


Fig. 2.2-5b. Transition through a shock front in oxygen at $M_1 = 20$ showing the approach to equilibrium of the active and inert degrees of freedom (after Ref. 37).

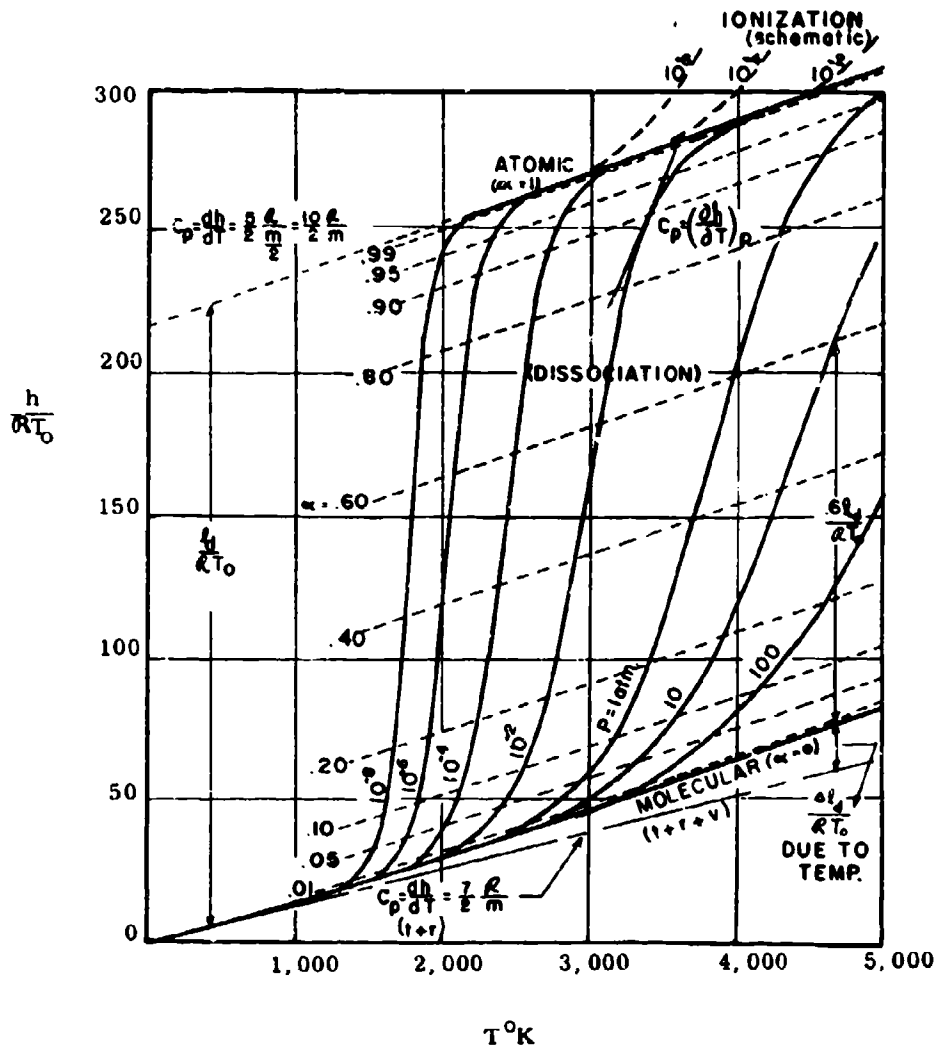


Fig. 2.2-6a. Variation of enthalpy $\frac{h}{RT_0}$ with temperature (T) and pressure (P) for a diatomic gas, oxygen (after Ref. 17).

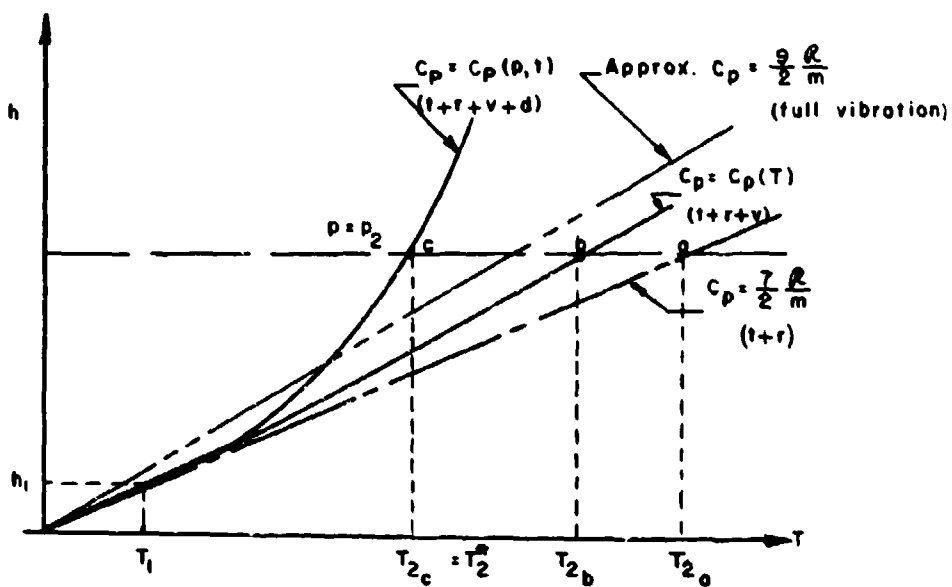


Fig. 2.2-6b. Schematic enlargement of the variation of h with T for a diatomic gas (after Ref. 37).

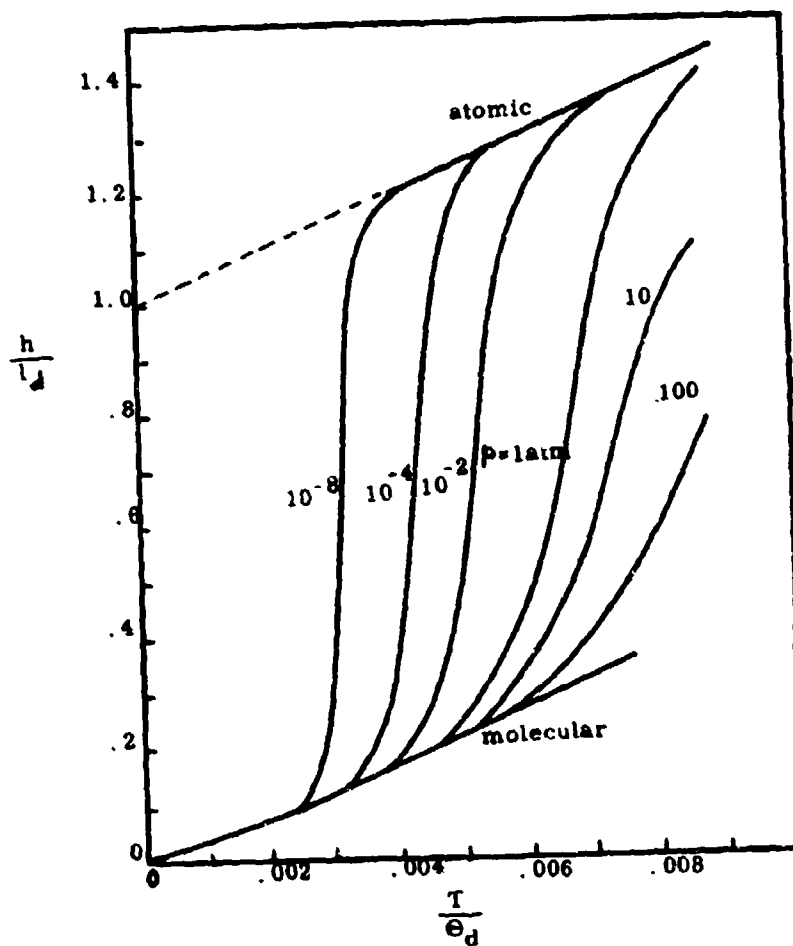


Fig. 2.2-6c. Dimensionless enthalpy vs temperature for a dissociating diatomic gas (Ref. 3).

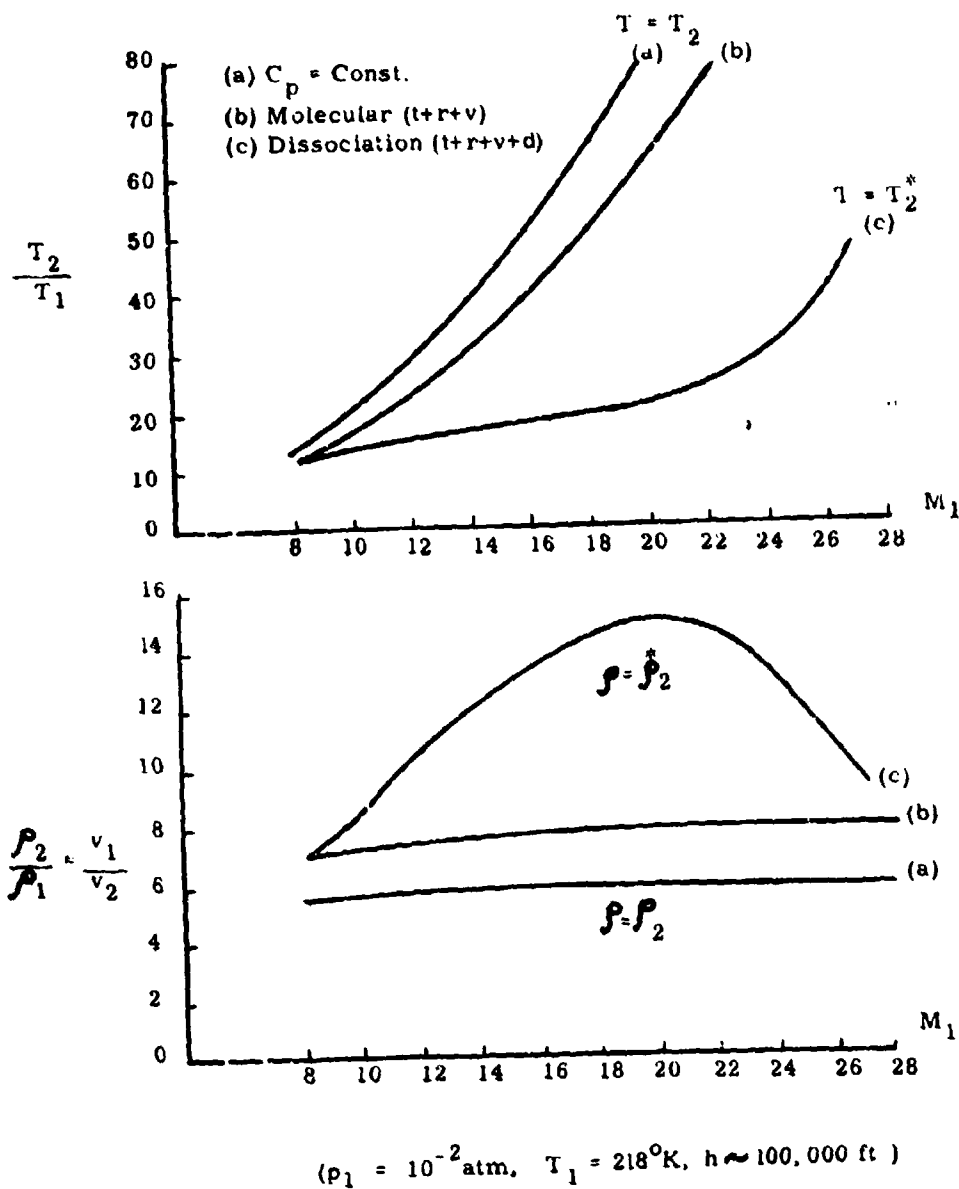


Fig. 2.2-7. Normal shock wave parameters in oxygen; $p_1 = 10^{-2}$ atm, $T_1 = 218^\circ\text{K}$, $h \sim 100,000$ ft (Ref. 37).

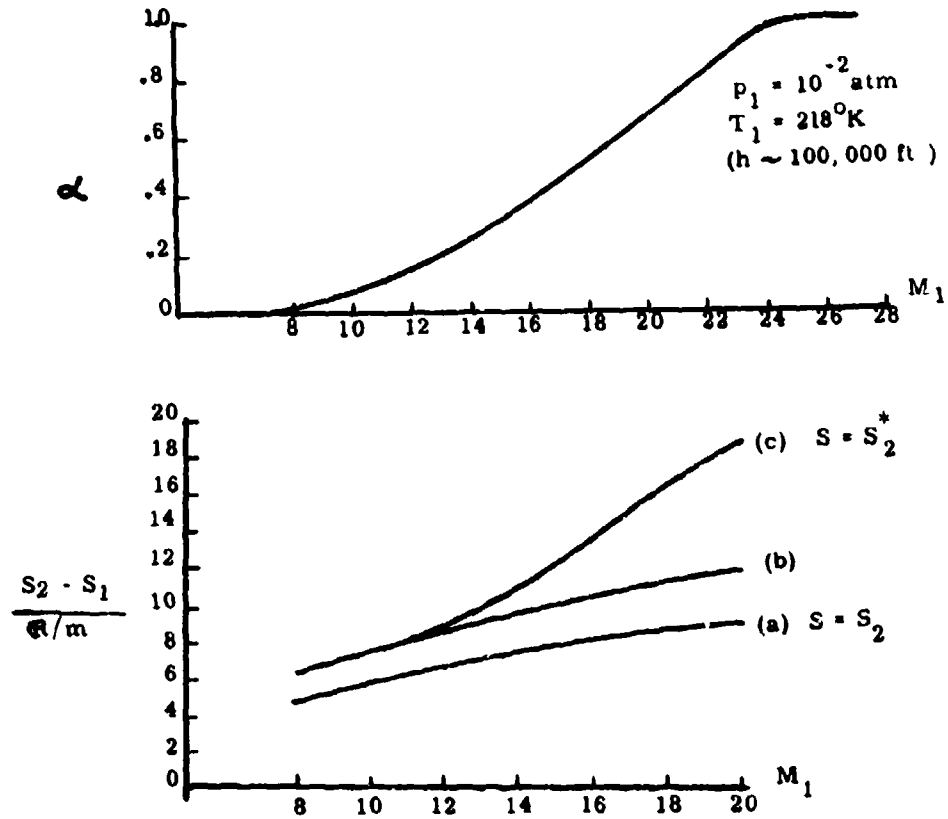


Fig. 2.2-7 (continued). Normal shock wave parameters in oxygen; $P_1 = 10^{-2}$ atm, $T_1 = 218^\circ\text{K}$, h ~ 100,000 ft (Ref. 37).

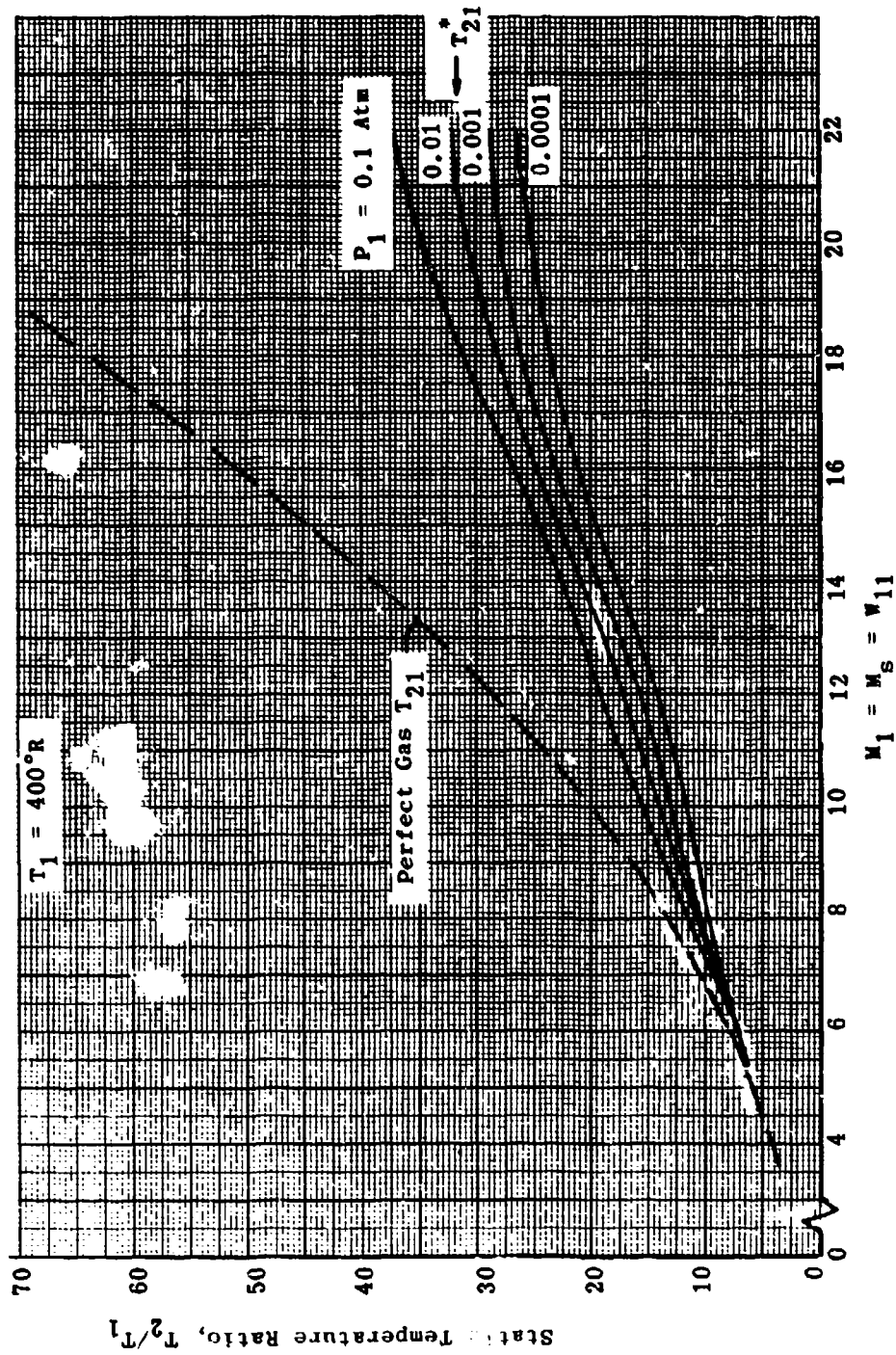


Fig. 2.2-8a. Normal shock static temperature ratio for air in dissociation equilibrium (Ref. 39).

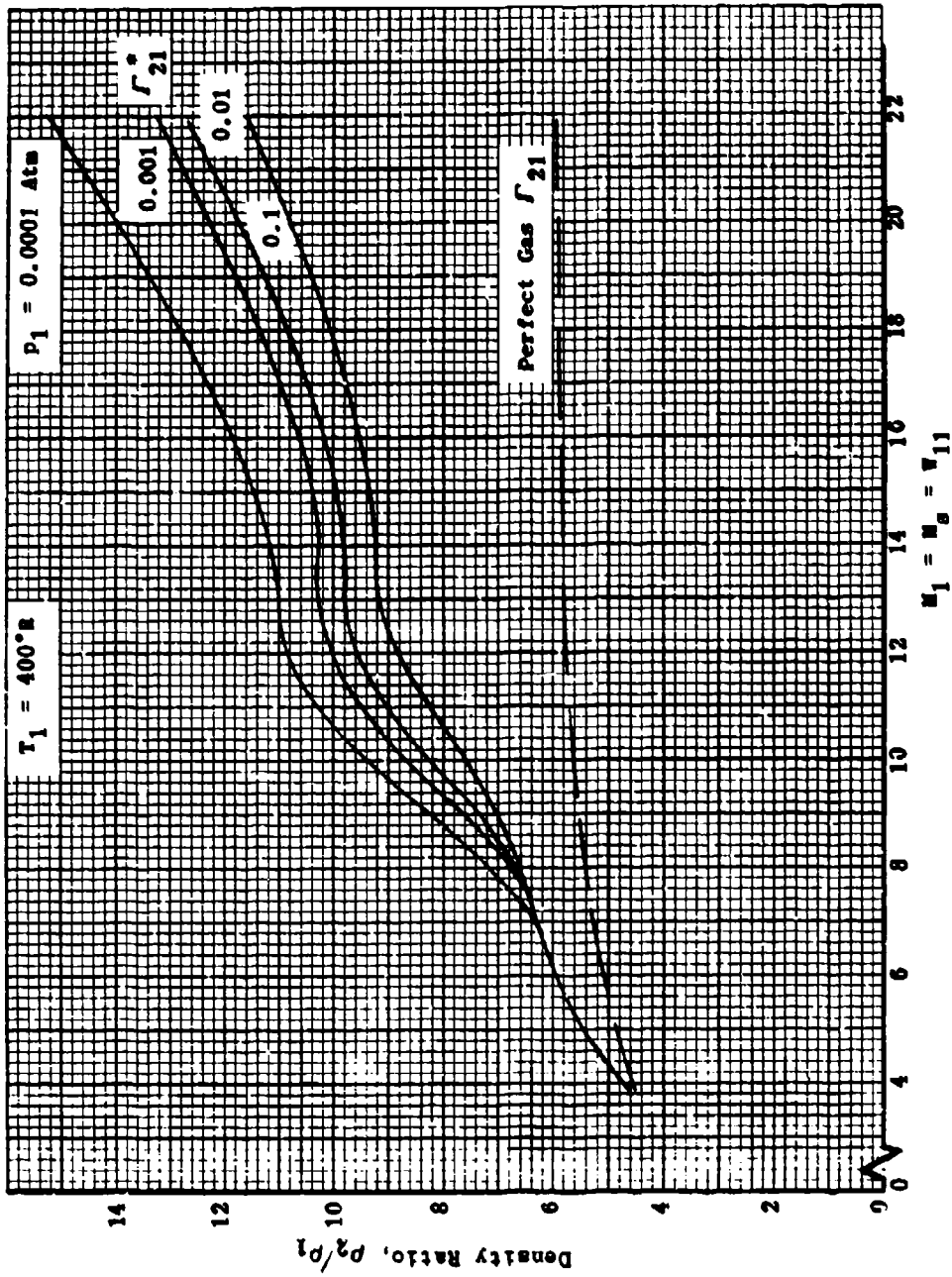


Fig. 2.2-8b. Normal shock density ratio for air in dissociation equilibrium (Ref. 39).

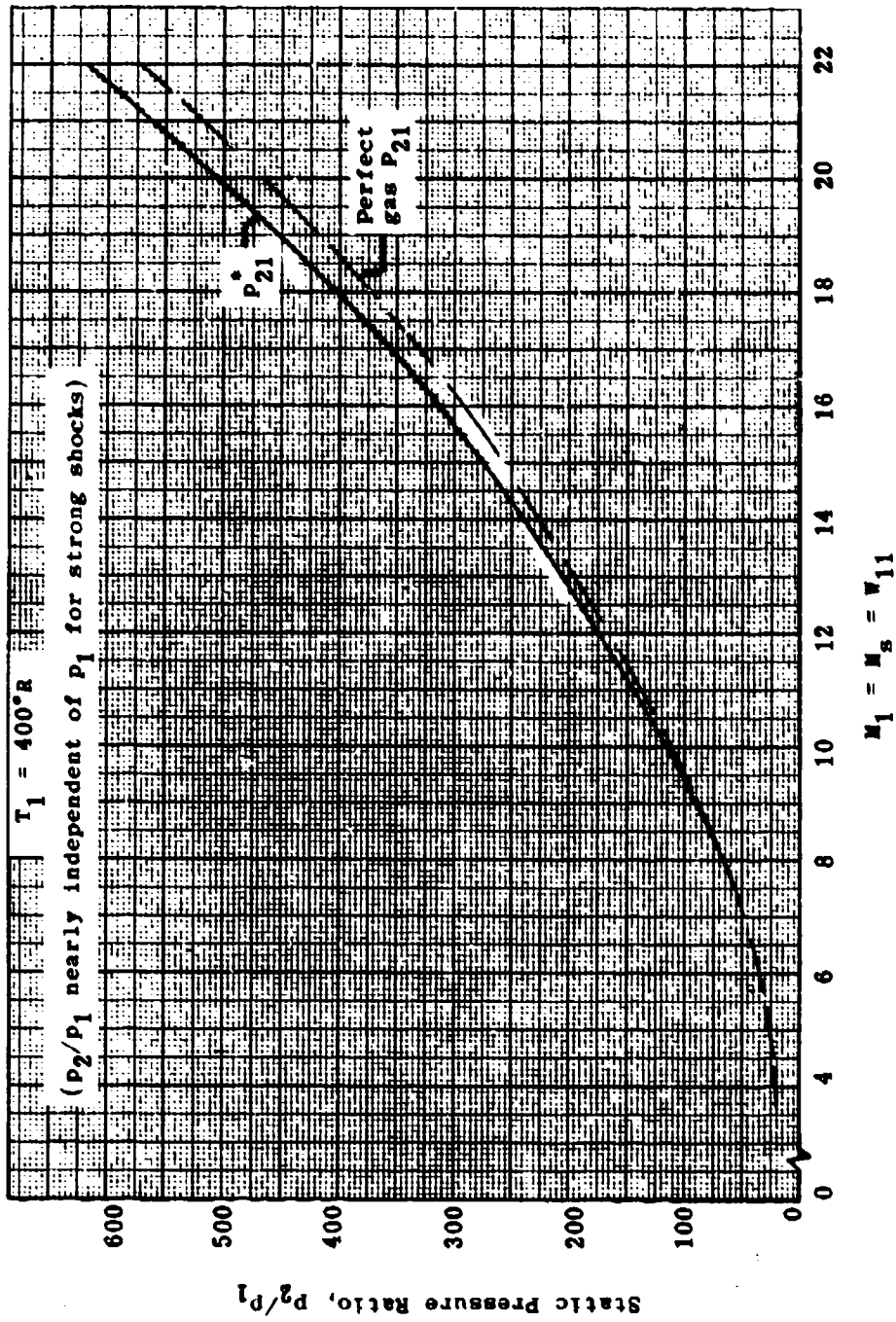


Fig. 2.2-8c. Normal shock static pressure ratio for air in dissociation equilibrium (Ref. 39).

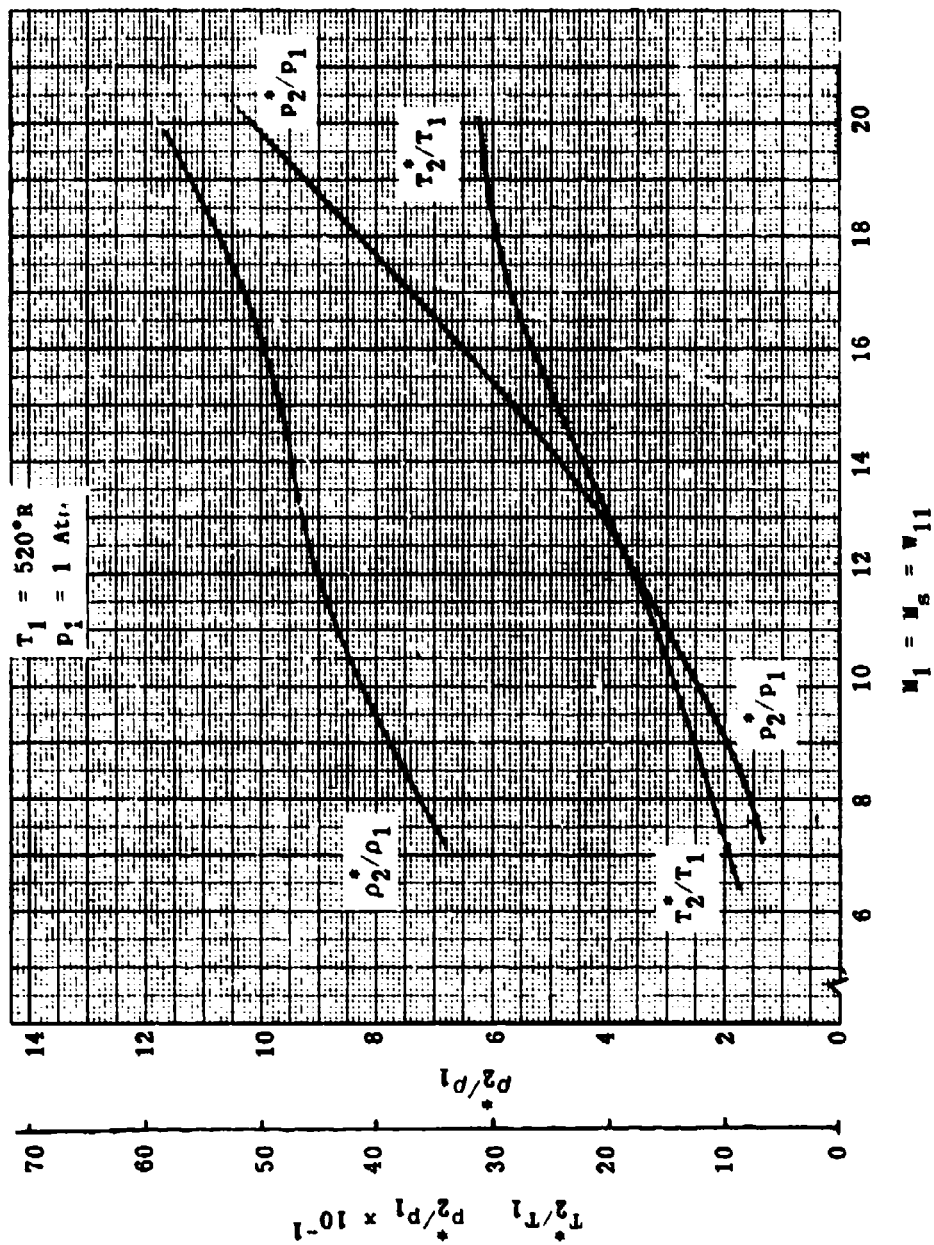


Fig. 2.2-8d. Normal shock pressure, temperature, and density ratios for air in dissociation equilibrium (Ref. 39).

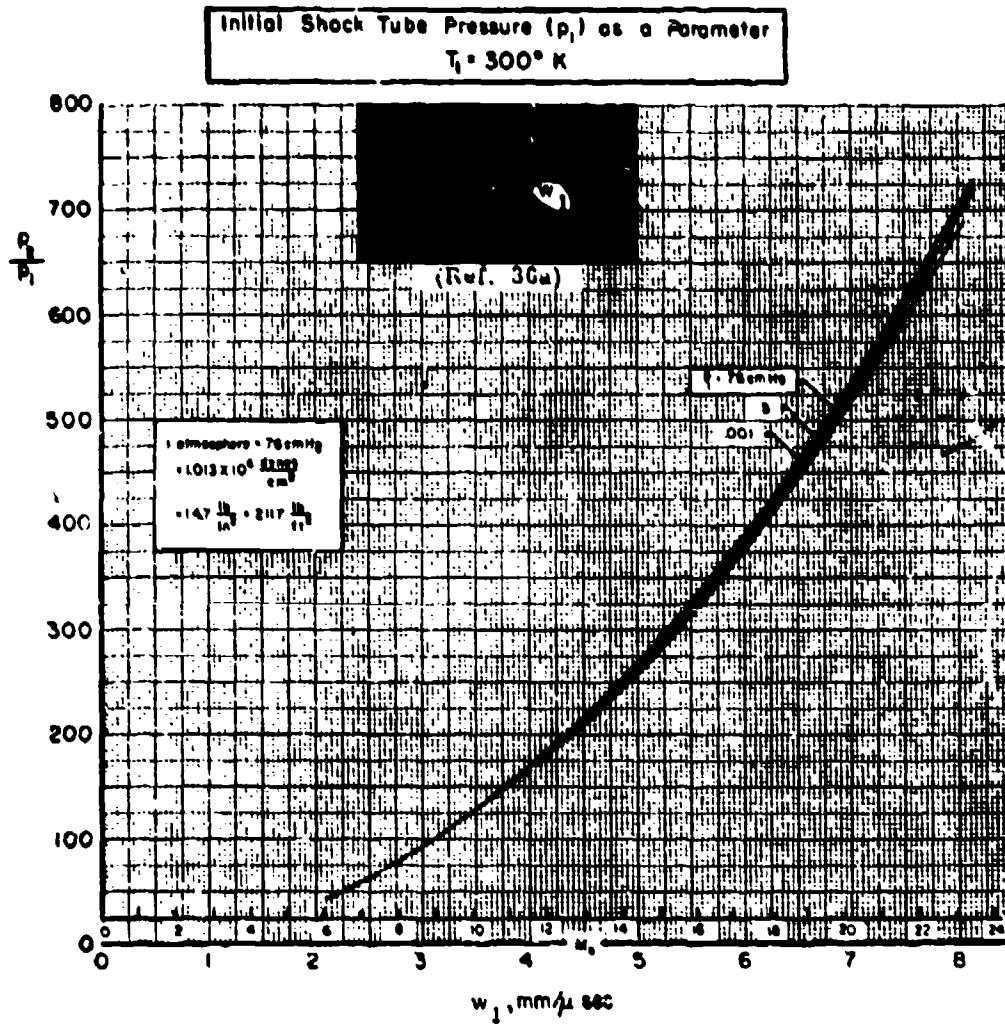


Fig. 2.2-9a. Pressure ratio (p_2/p_1) across moving normal shock vs shock velocity (w_1), equilibrium air.

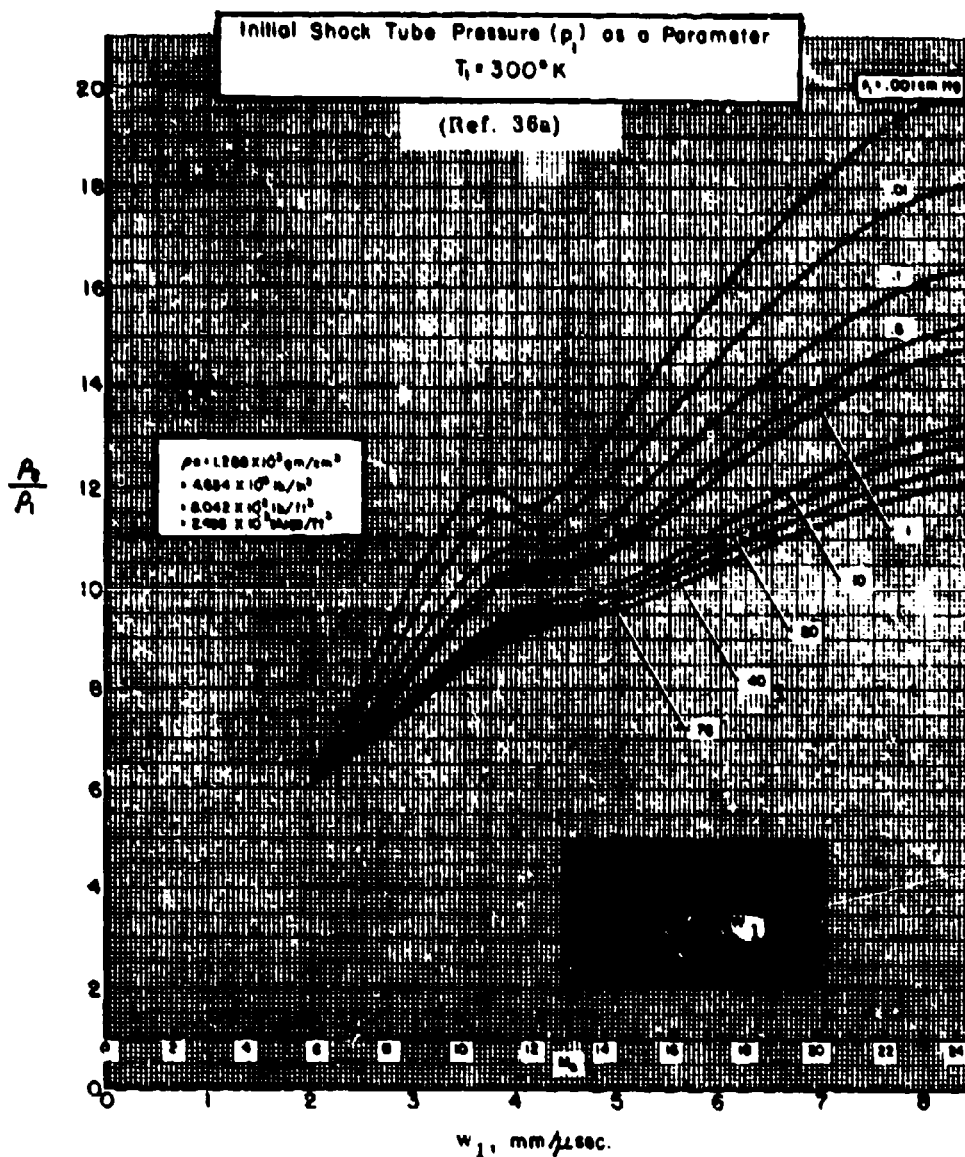


Fig. 2.2-9b. Density ratio (ρ_2/ρ_1) across moving normal shock vs shock velocity (w_1), equilibrium air.

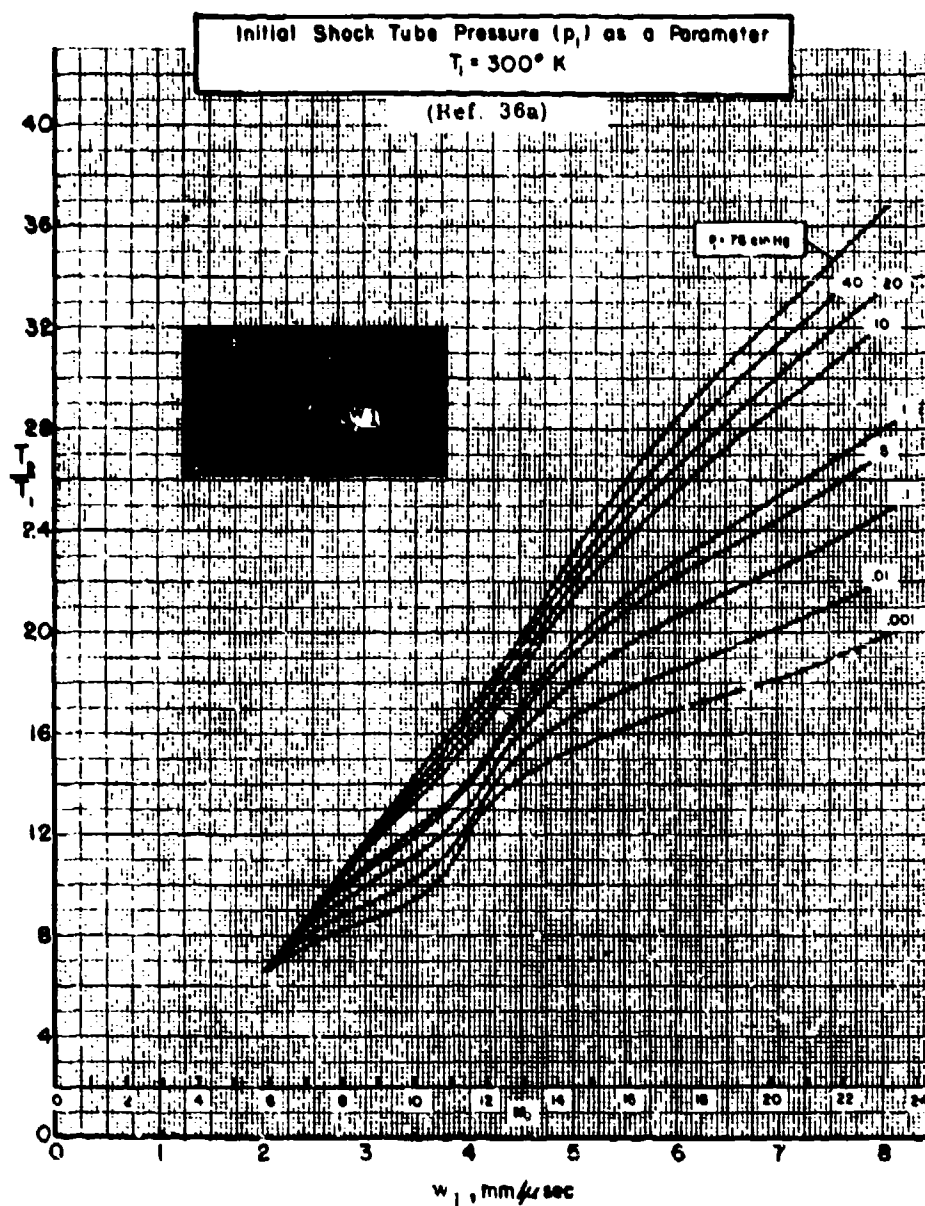


Fig. 2.2-9c. Temperature ratio (T_2/T_1) across moving normal shock vs shock velocity (w_1), equilibrium air.

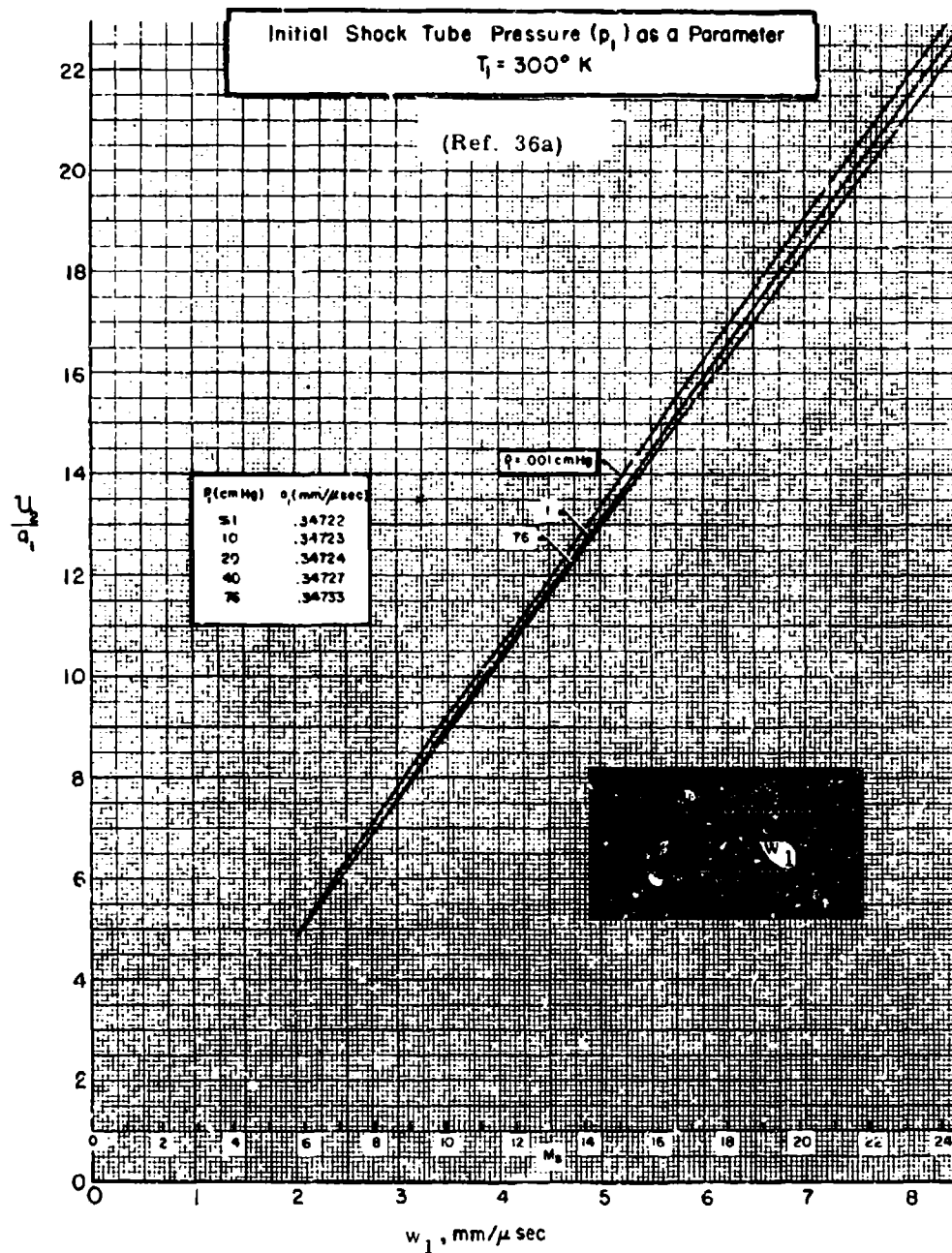


Fig. 2.2-10a. Velocity ratio (u_2/a_1) across moving normal shock vs shock velocity (w_1), equilibrium air.

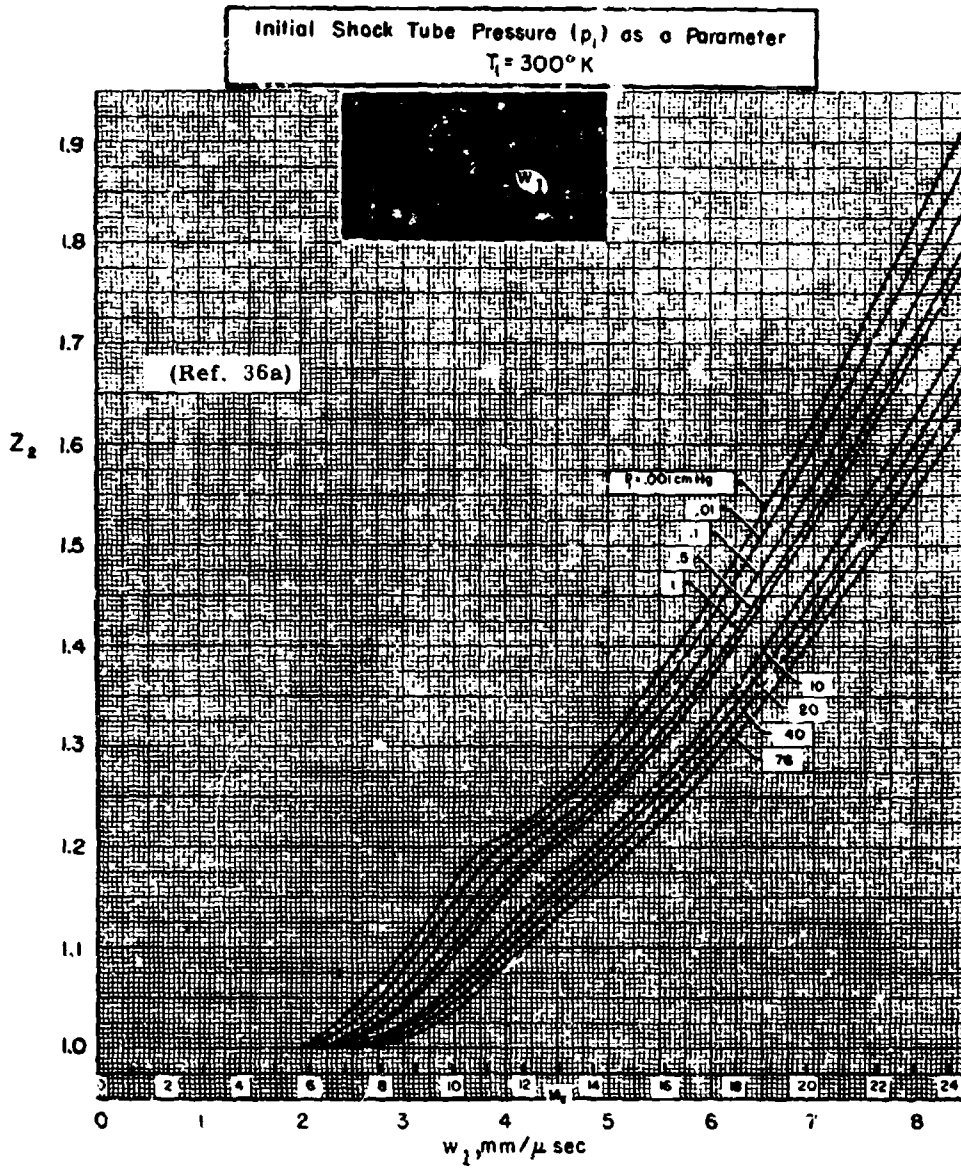


Fig. 2.2-10b. Compressibility (Z_2) across moving normal shock vs shock velocity (w_1), equilibrium air.

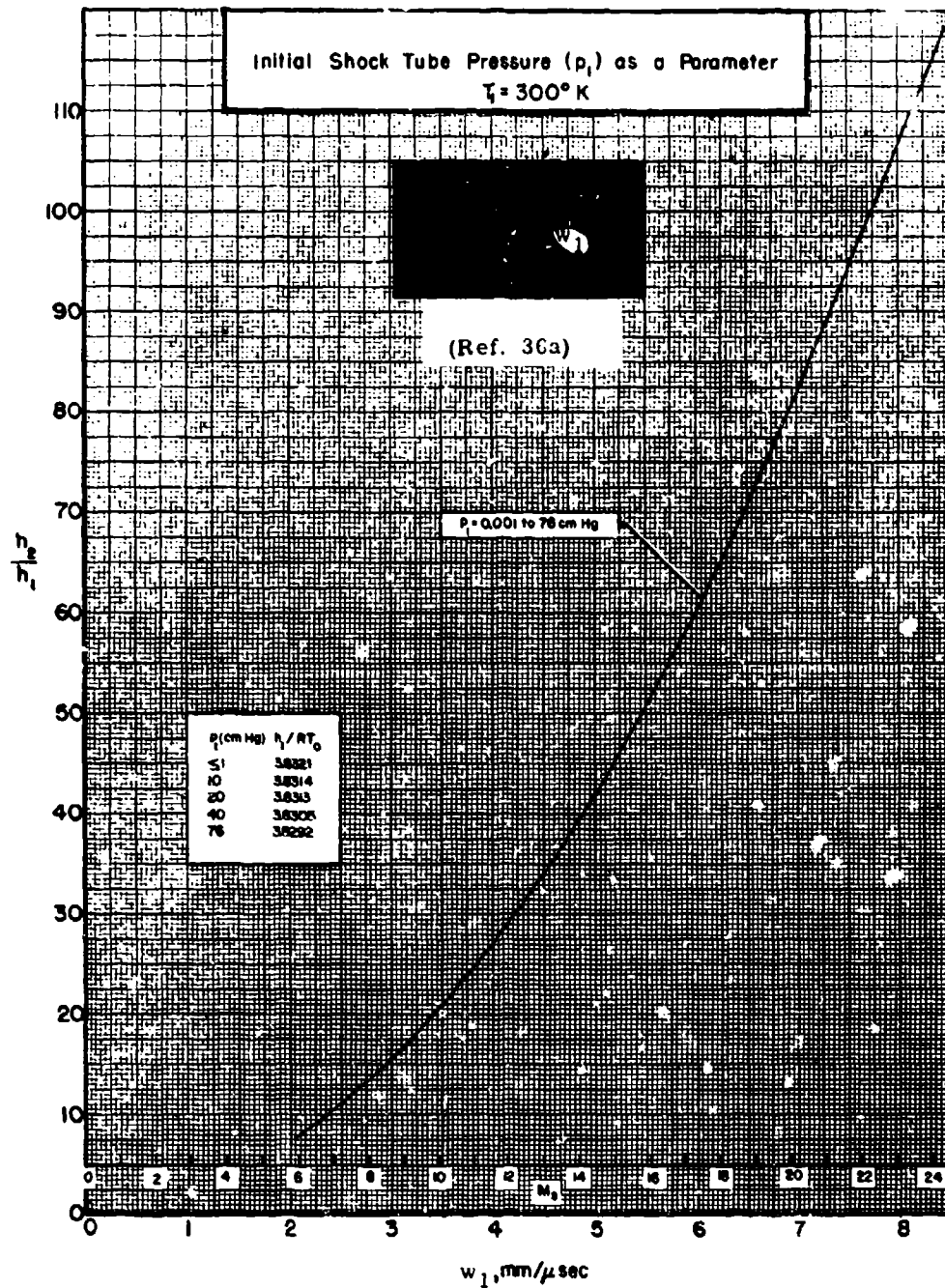
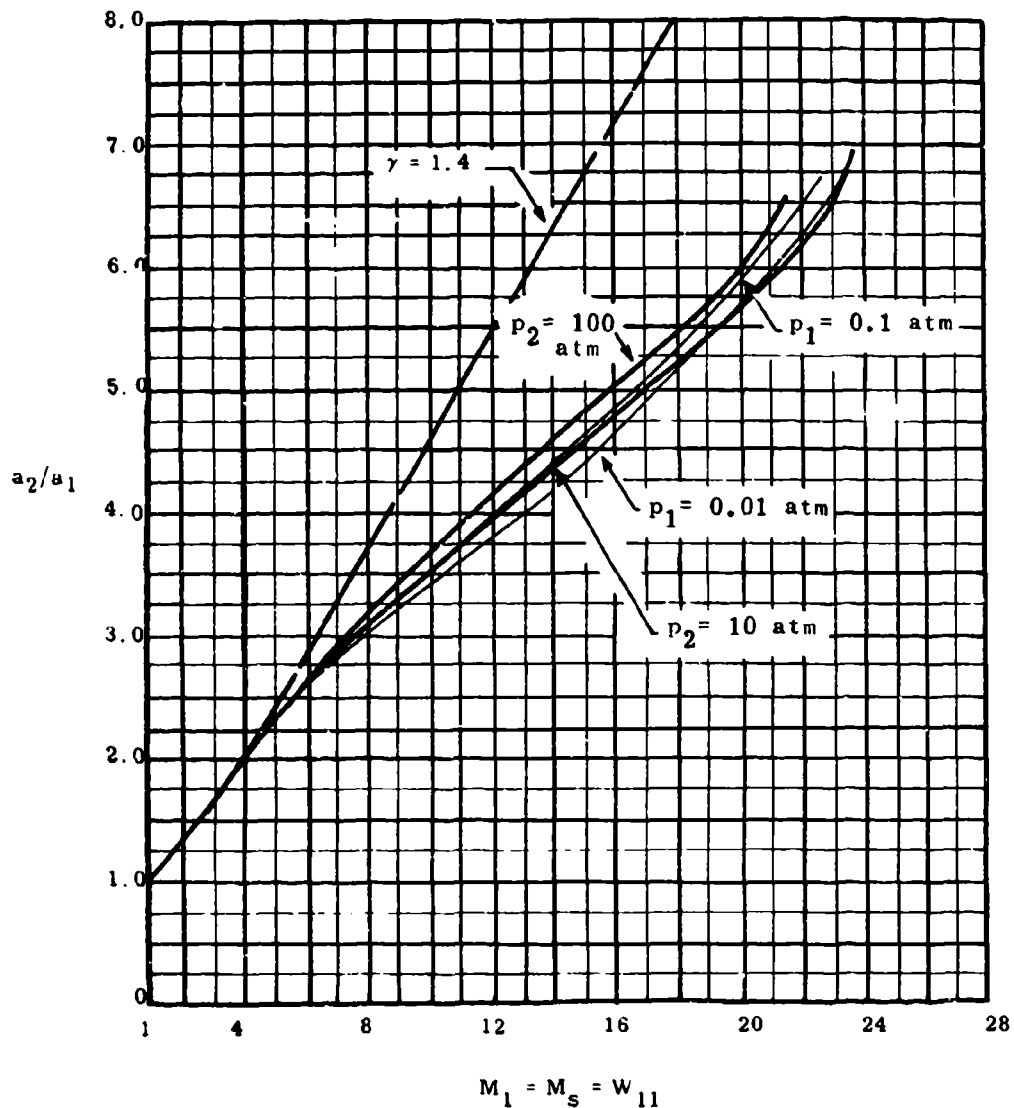
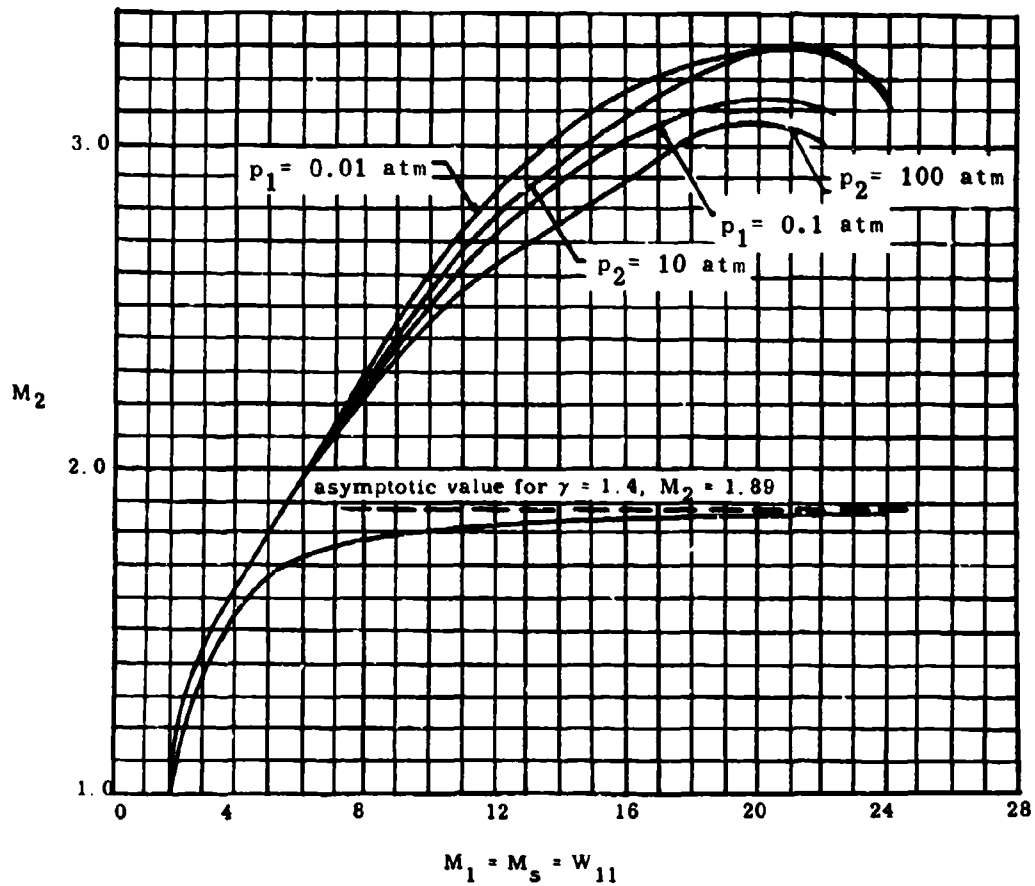


Fig. 2.2-10c. Enthalpy ratio (h_2/h_1) across moving normal shock vs shock velocity (w_1), equilibrium air.



(Curves have been computed on the basis of a nitrogen dissociation energy of 7.37 ev, instead of the presently accepted value of 9.76 ev, resulting in errors of about 5 per cent.)

Fig. 2.2-11a. Variation of the sound speed ratio $(a_2/a_1) = \Lambda_{21}$ with the shock Mach number (M_s) in air; $T_1 = 300^\circ\text{K}$ (Ref. 41).



(Curves have been computed on the basis of a nitrogen dissociation energy of 7.37 eV, instead of the presently accepted value of 9.76 eV, resulting in errors of about 5 per cent.)

Fig. 2.2-11b. Variation of flow Mach number (M_2) with the moving shock Mach number (M_s) in air; $T_1 = 300^\circ\text{K}$ (Ref. 41).

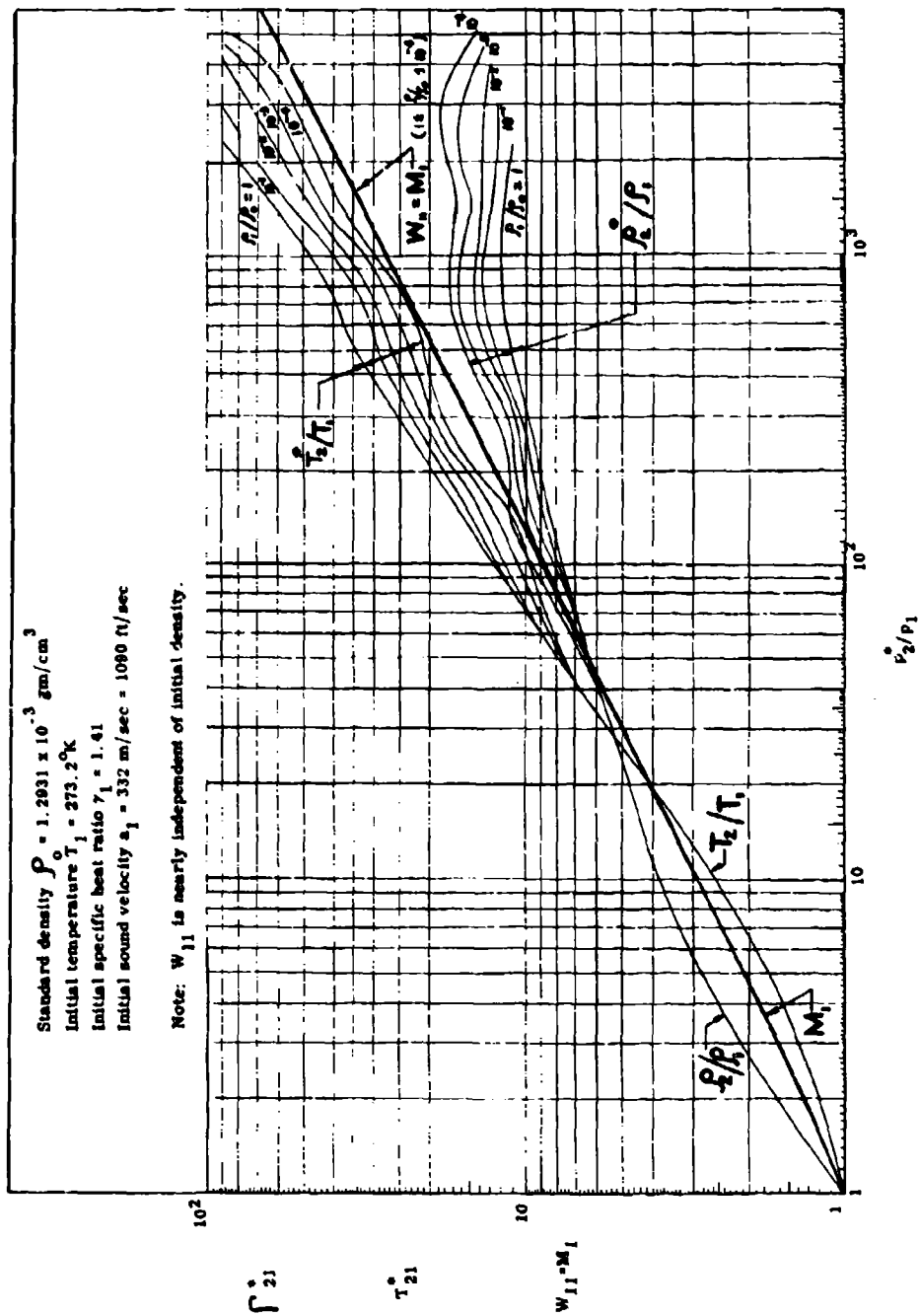


Fig. 2.2-12. Variation of the density ratio (ρ_2^*/ρ_1), temperature ratio (T_2^*/T_1), and shock Mach number ($W_{11} = M_1$) with the pressure ratio (p_2^*/p_1) across the shock wave for various initial densities (ρ_1/ρ_0) in air (Ref. 35).

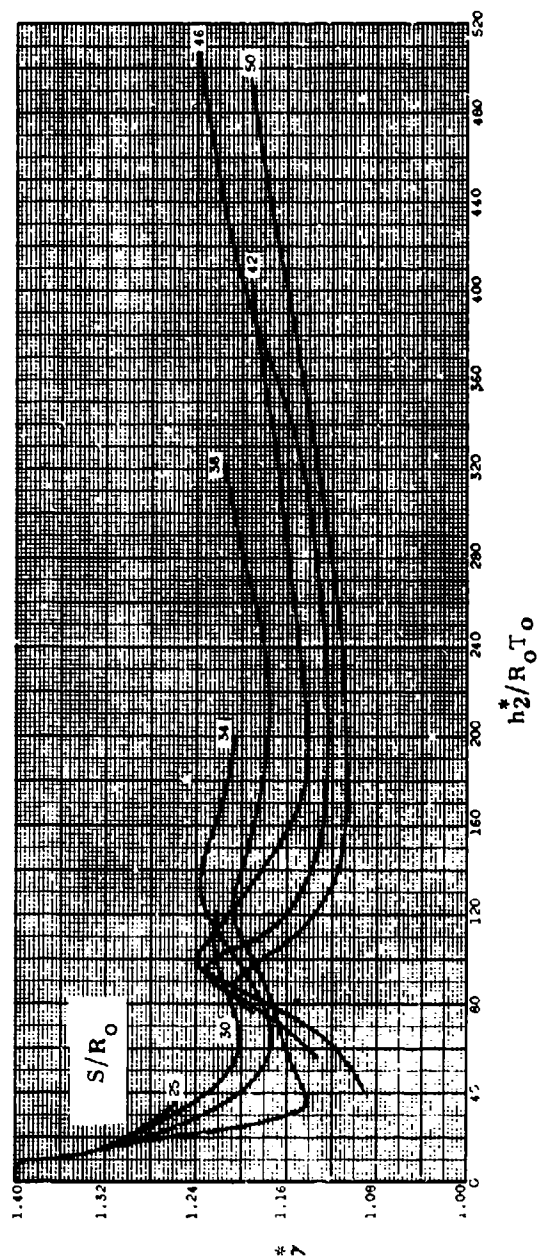
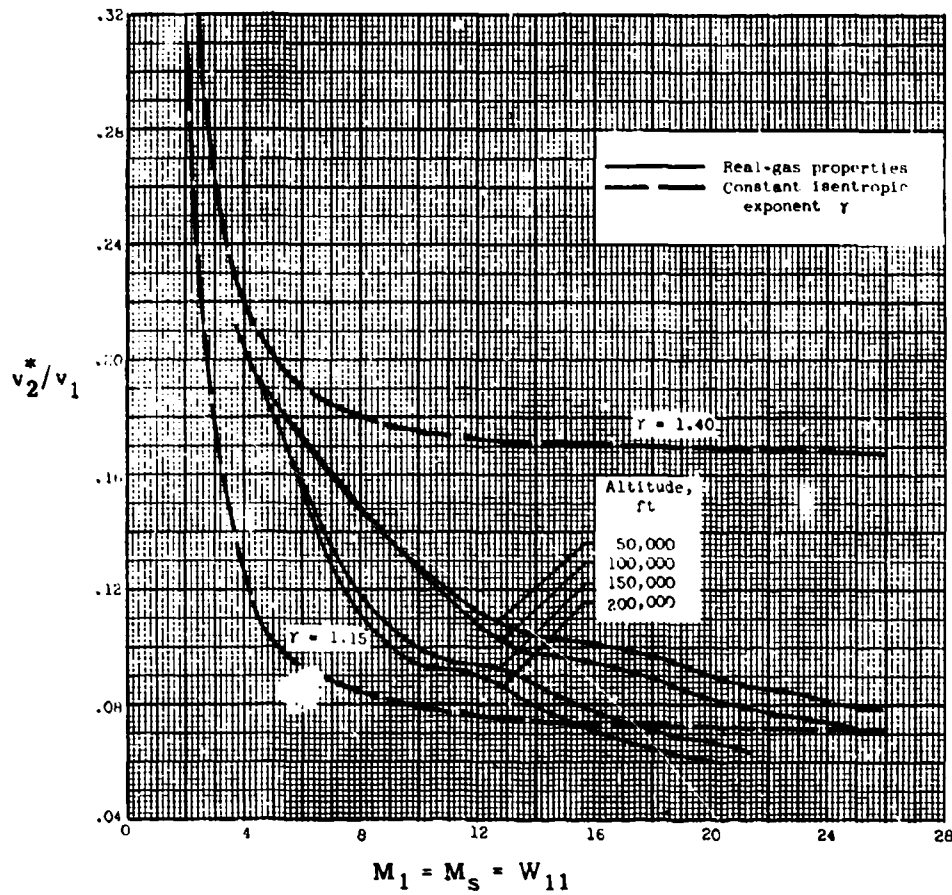


Fig. 2.2-13. Isentropic exponent γ^* for air in equilibrium (Ref. 40).



(Note: $v_2^*/v_1 = \rho_1/\rho_2^* = 1/\Gamma_{21}^* v_{21}^*/W_{11} = v_{21}/M_1$ and $U_{21}^* = M_1 - v_{21}^*$.)

Fig. 2.2-14. Variation of velocity ratio (v_2^*/v_1) across a normal shock wave (M_1) with altitude (Ref. 40).

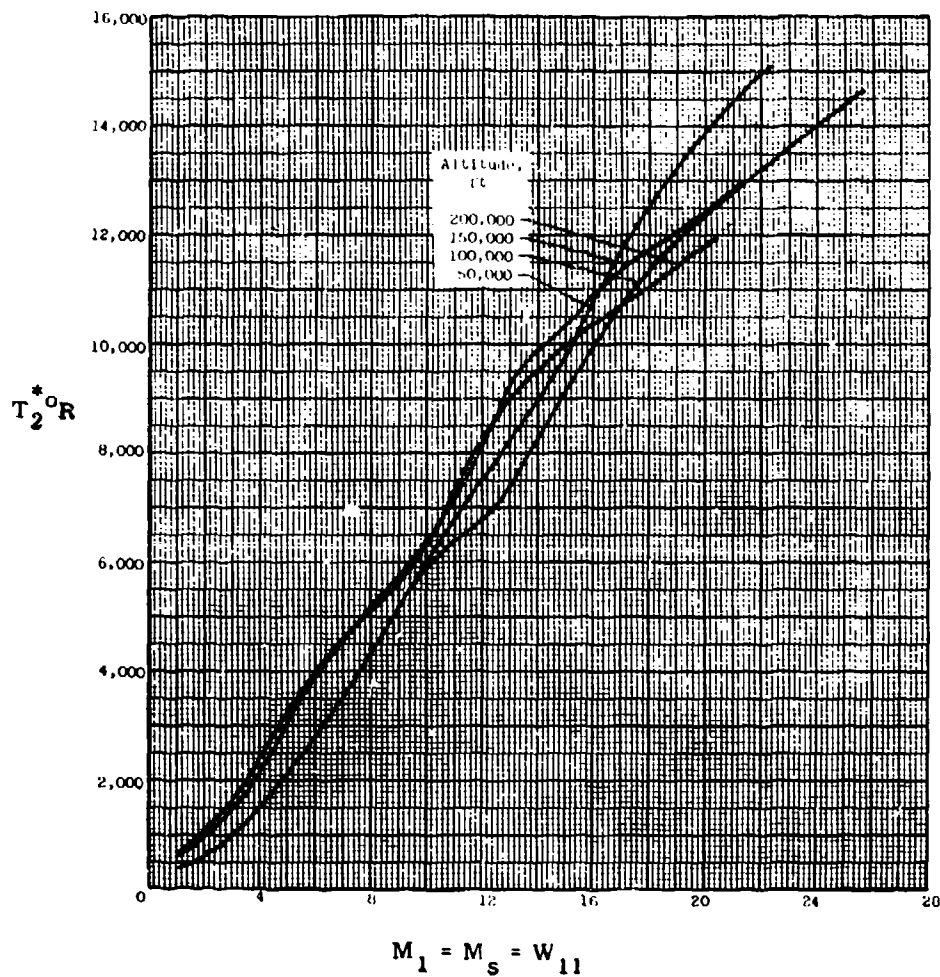


Fig. 2.2-15. Temperature (T_2^*) behind a normal shock wave (M_1) in air (Ref. 40).

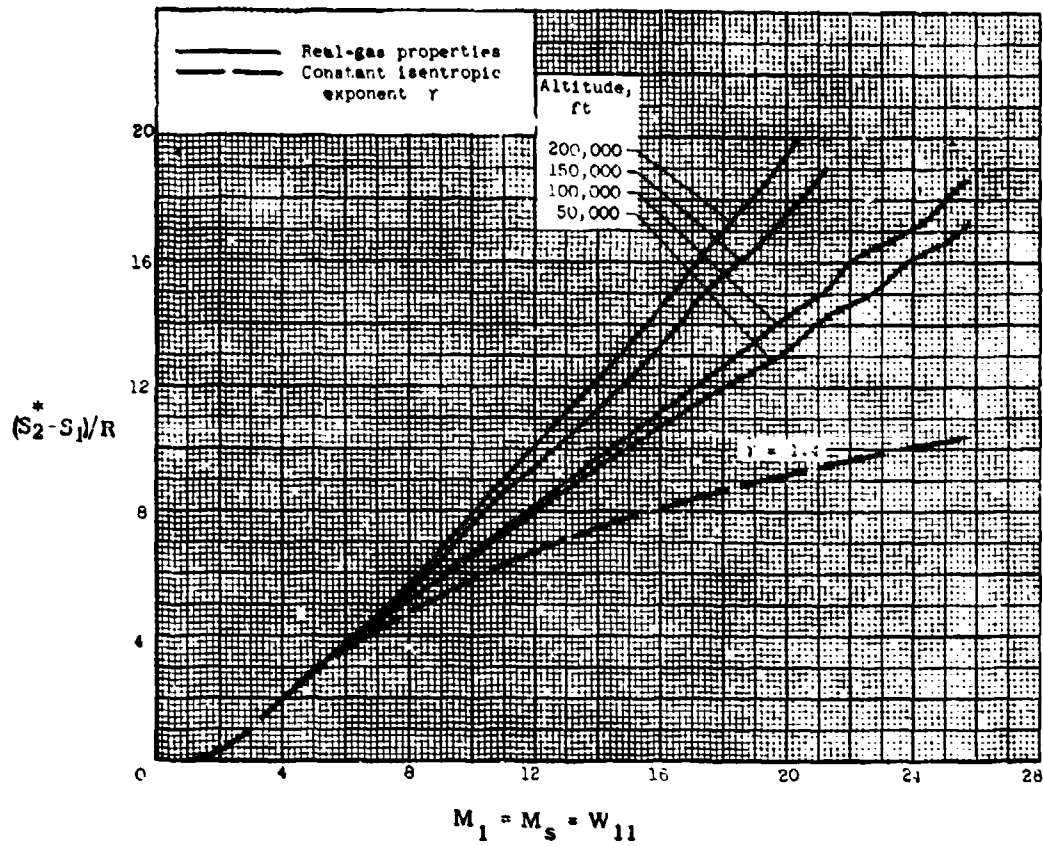


Fig. 2.2-16. Entropy increase across a shock wave in air (Ref. 40).

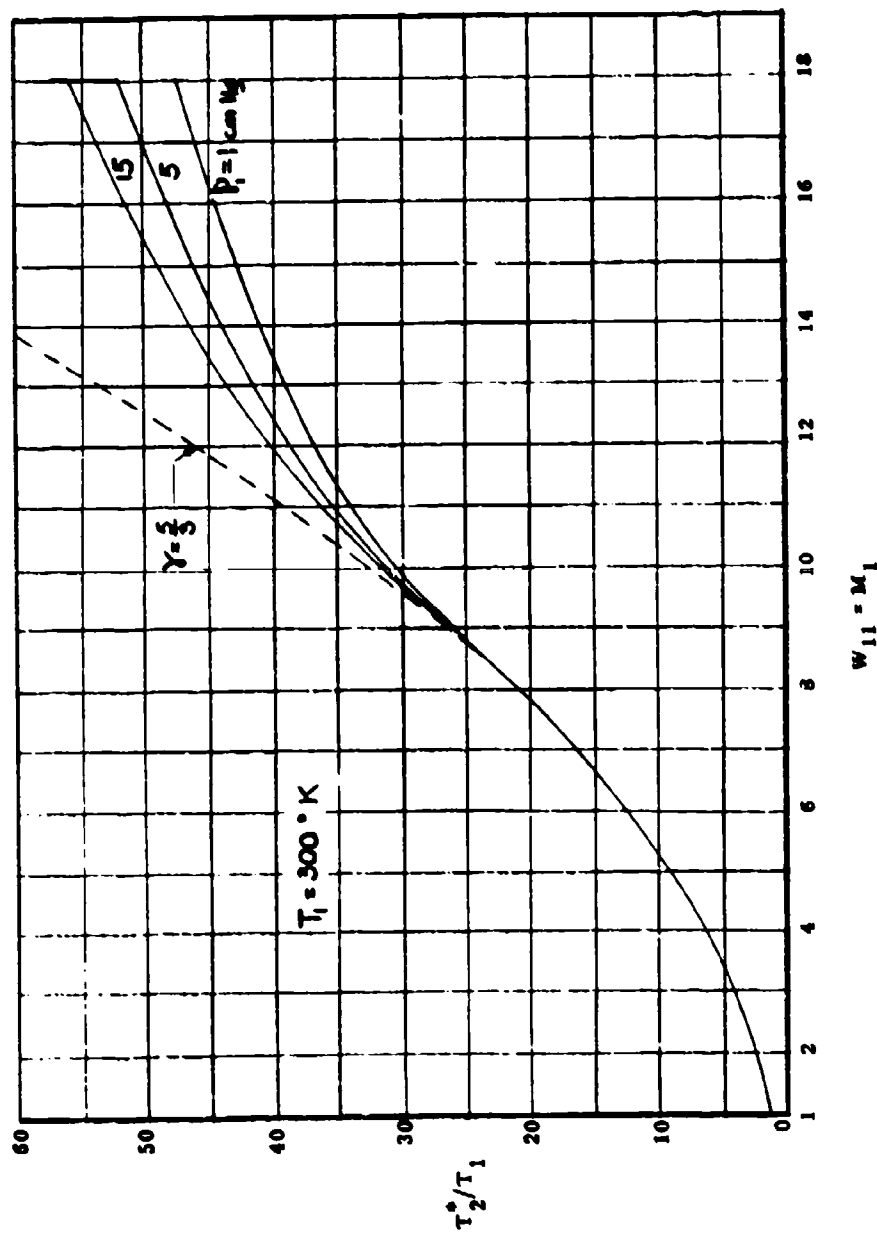


Fig. 2.2-17a. Variation of the temperature ratio (T_2^0/T_1) across a normal shock wave (W_{11}) in argon (Ref. 42).

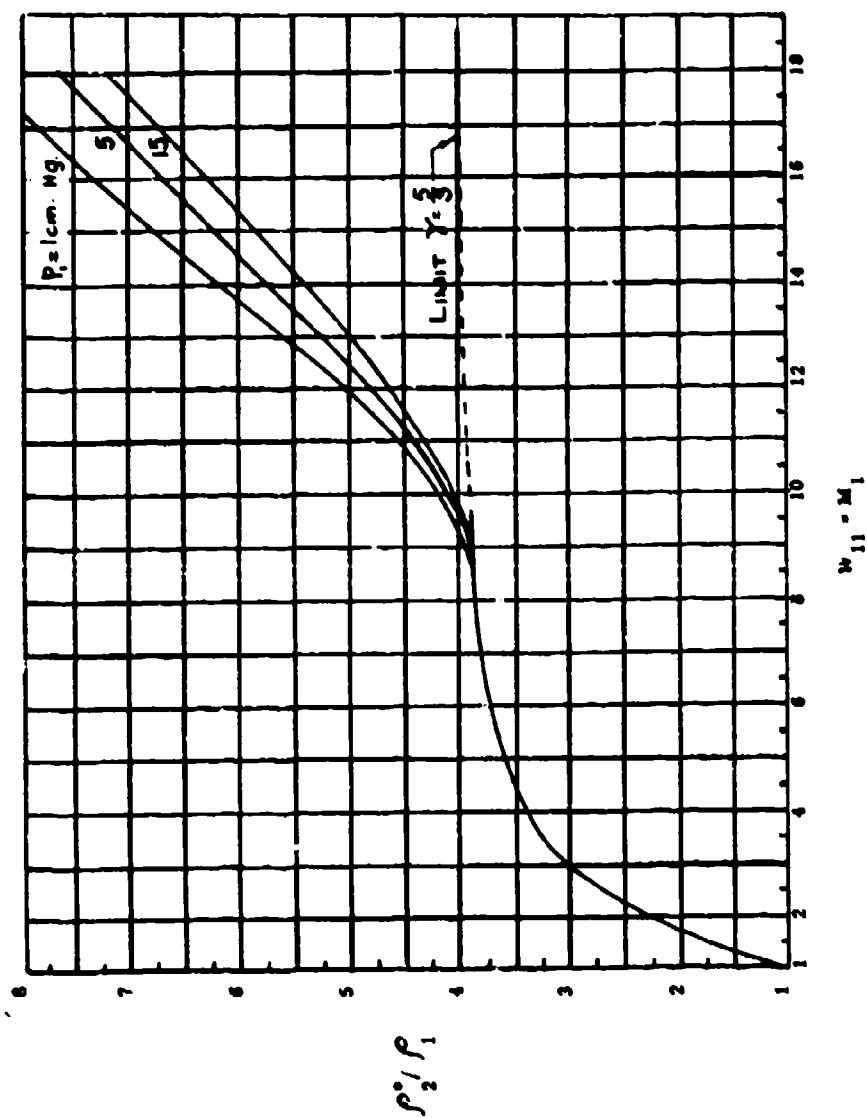


Fig. 2.2-17b: Variation of the density ratio (ρ_2/ρ_1) across a normal shock wave (W_{11}) in argon (Ref. 42).

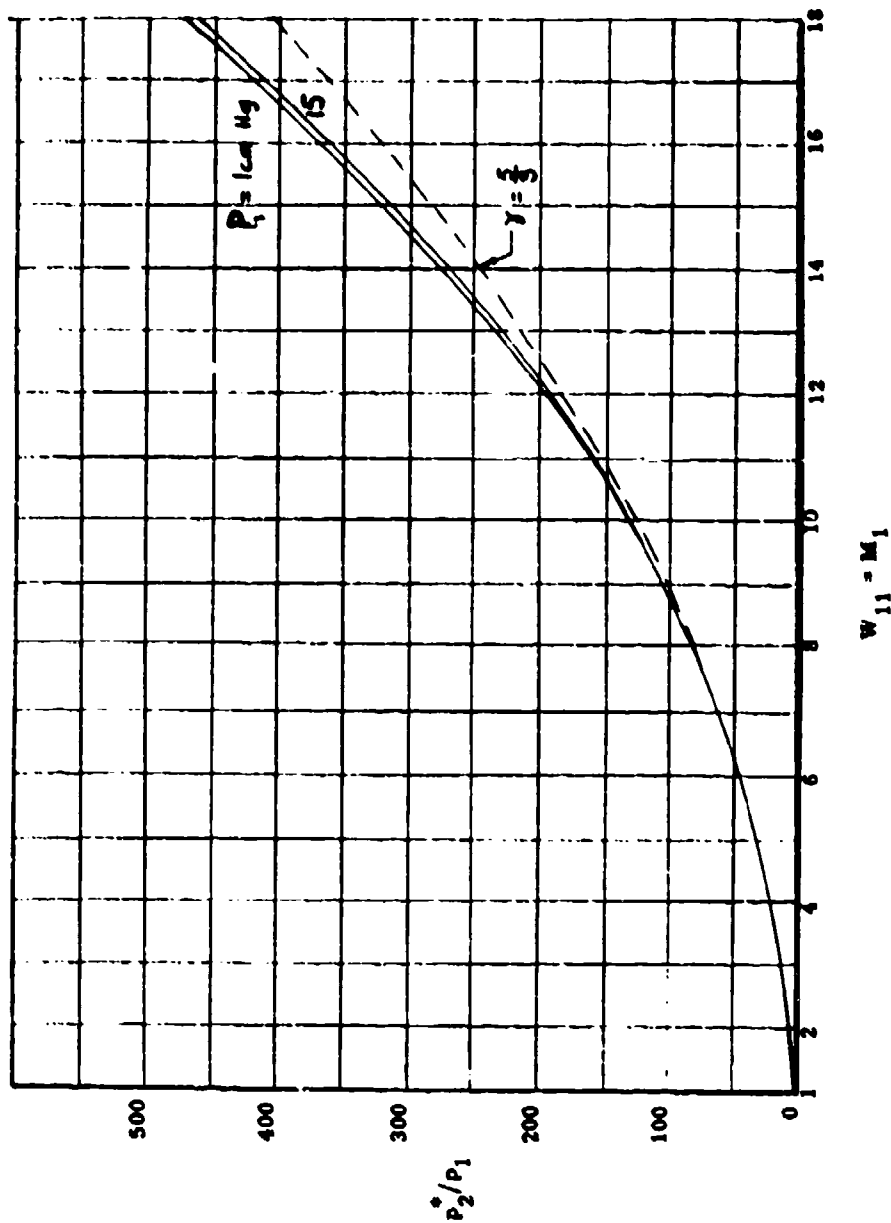


Fig. 2.2-17c. Variation of the pressure ratio (p_2^*/p_1) across a normal shock wave (W_{11}) in argon (Ref. 42).

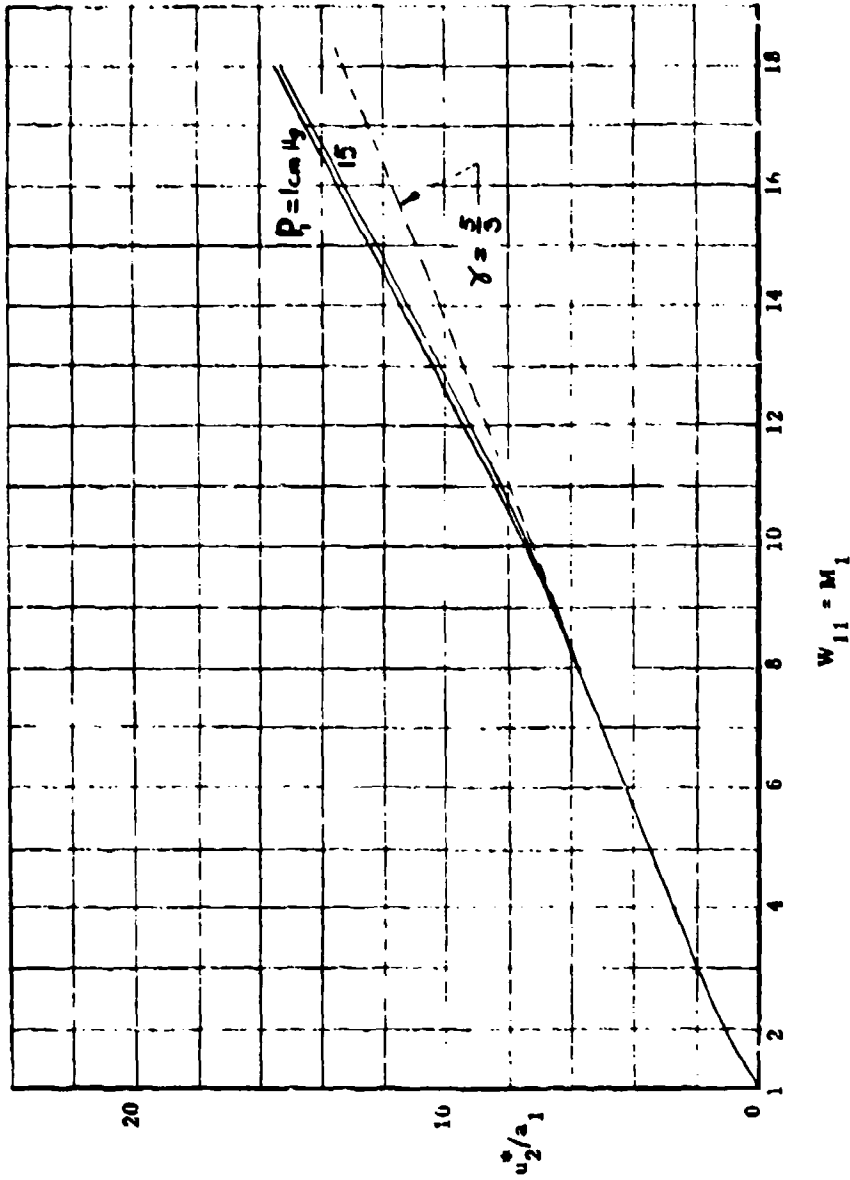


Fig. 2.2-17d. Variation of the particle velocity ratio (u_2^*/a_1) behind a moving normal shock wave (W_{11}) in argon (Ref. 42).

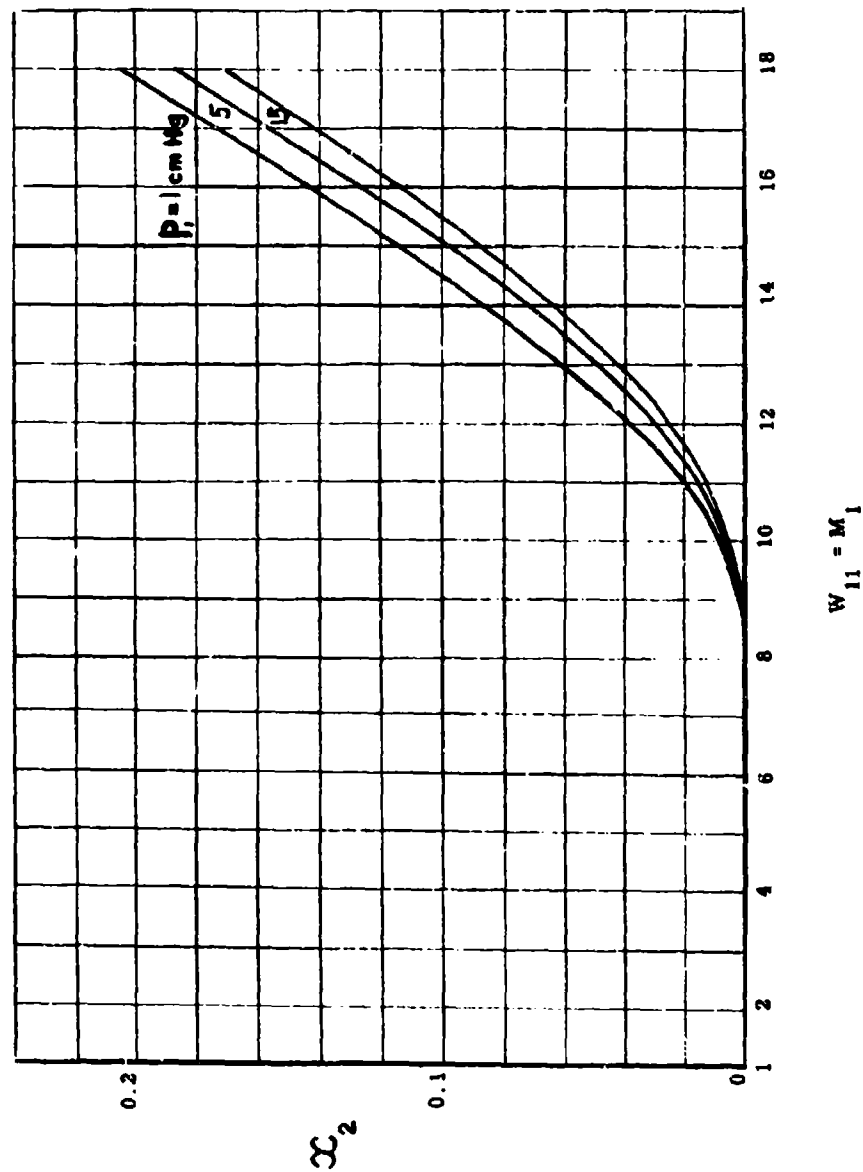


Fig. 2.2-17e. Variation of the degree of ionization (α_2) behind a normal shock wave (W_{11}) in argon (Ref. 42).

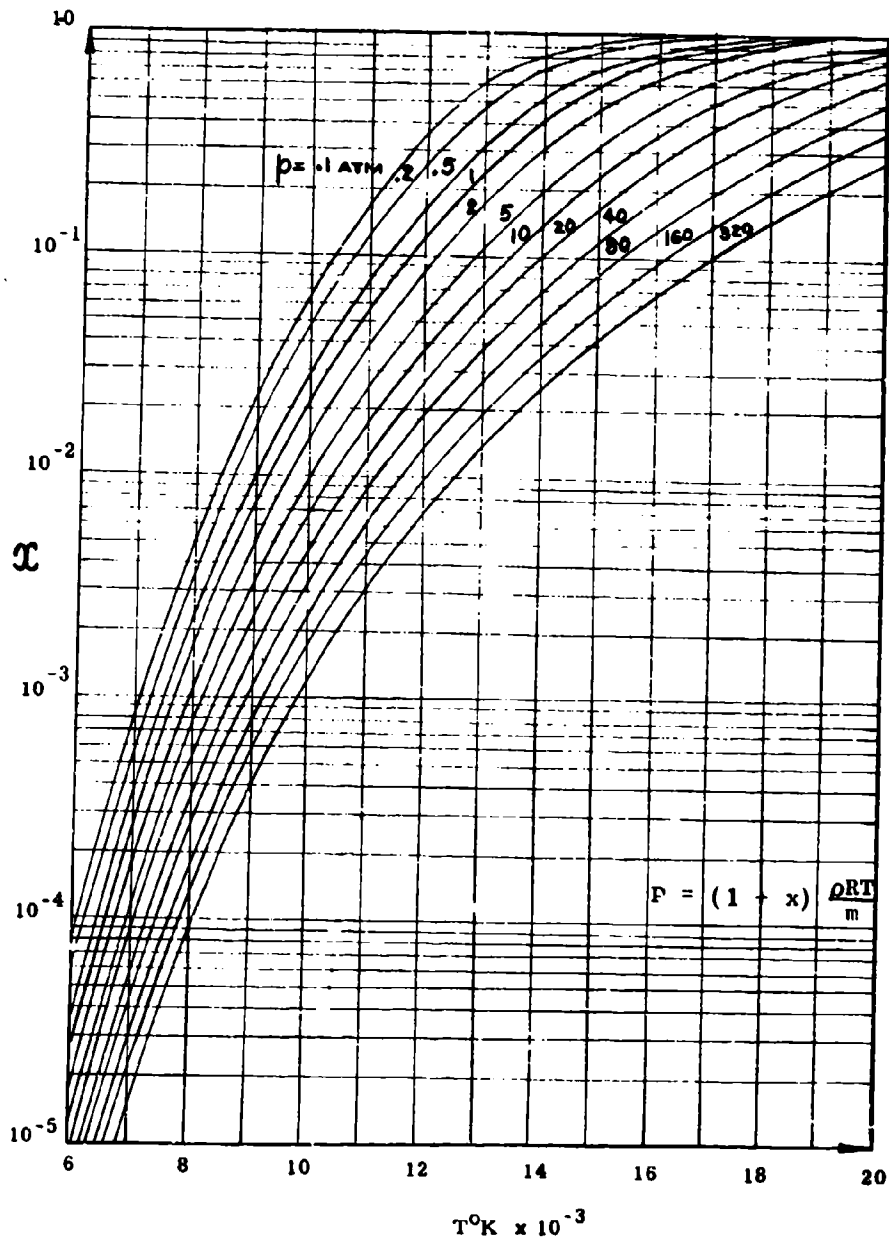


Fig. 2.2-17f. Variation of the degree of ionization (x) with temperature and pressure in argon (Ref. 42).

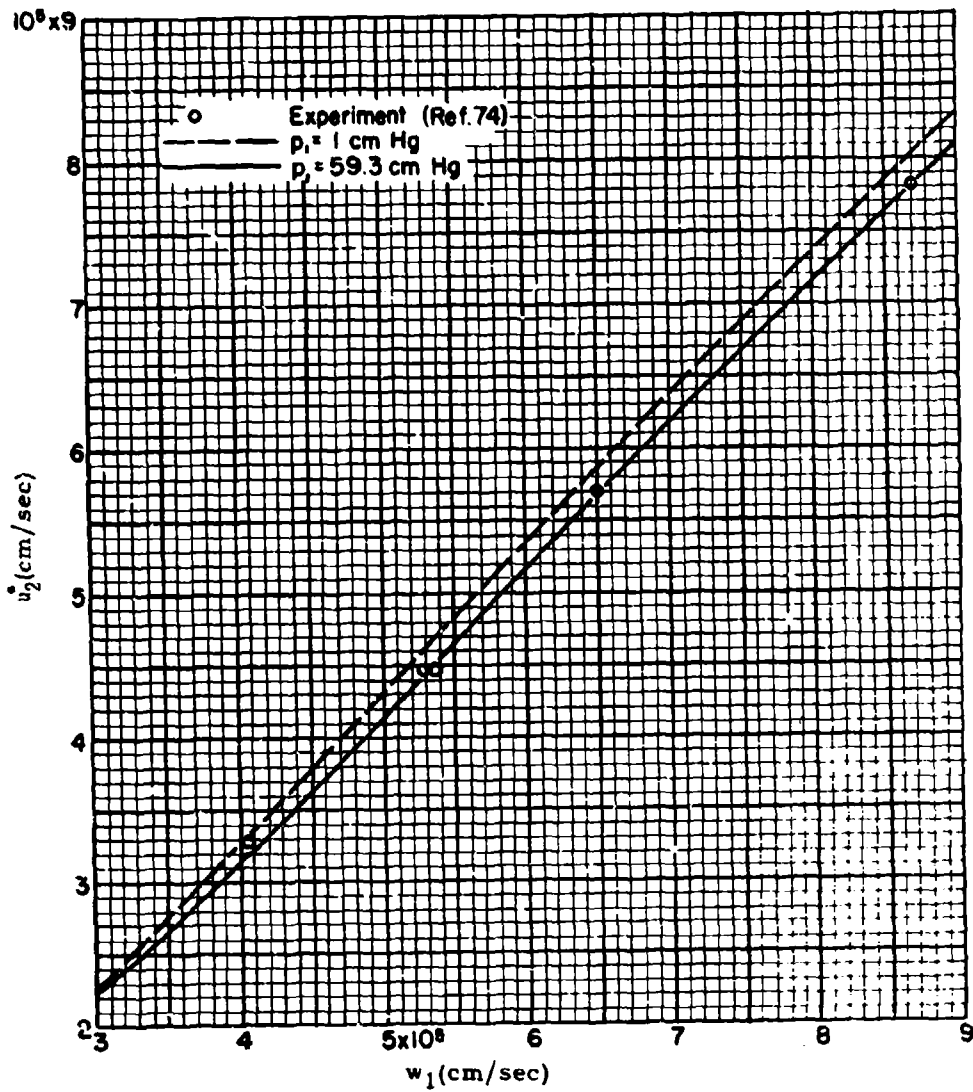


Fig. 2.2-18a. Variation of particle velocity (u_2^*) with shock wave velocity (w_1) in argon (Ref. 43).

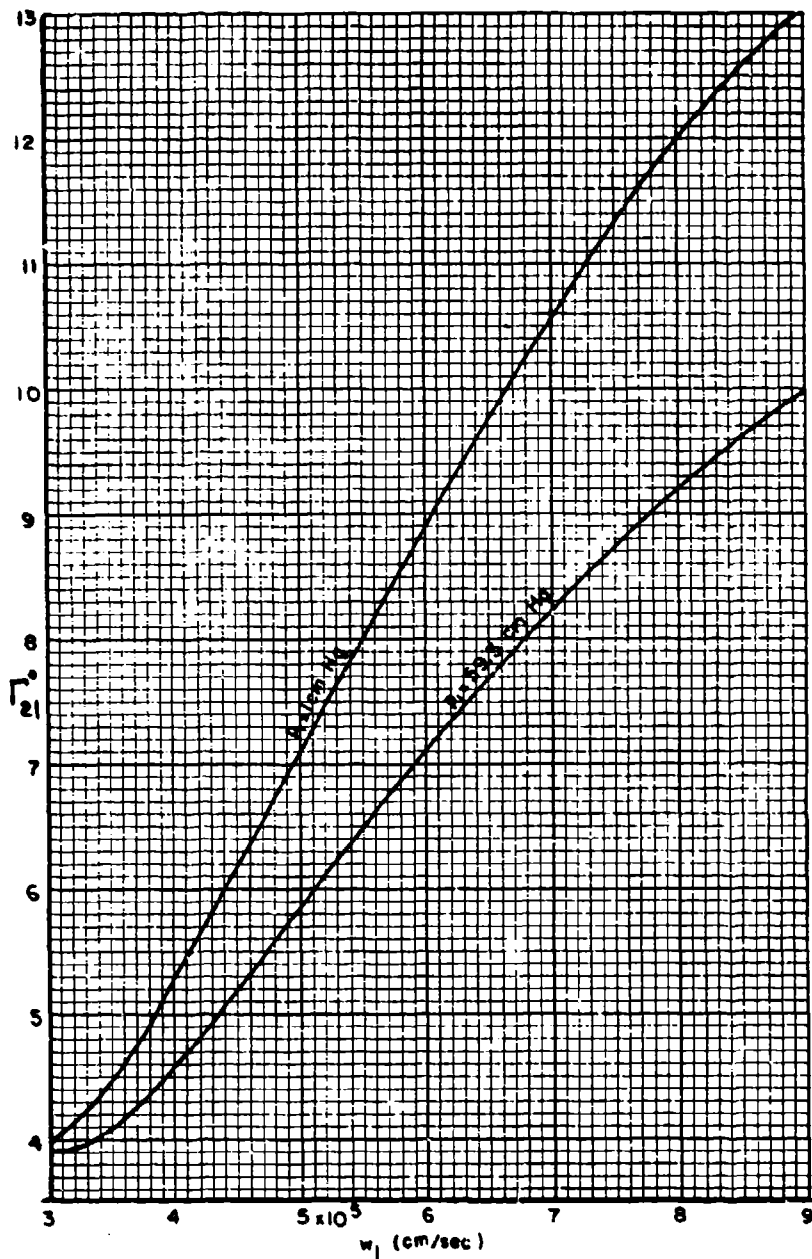


Fig. 2.2-18b. Variation of density ratio (Γ_{21}^*) with shock velocity (w_1) in argon (Ref. 43).

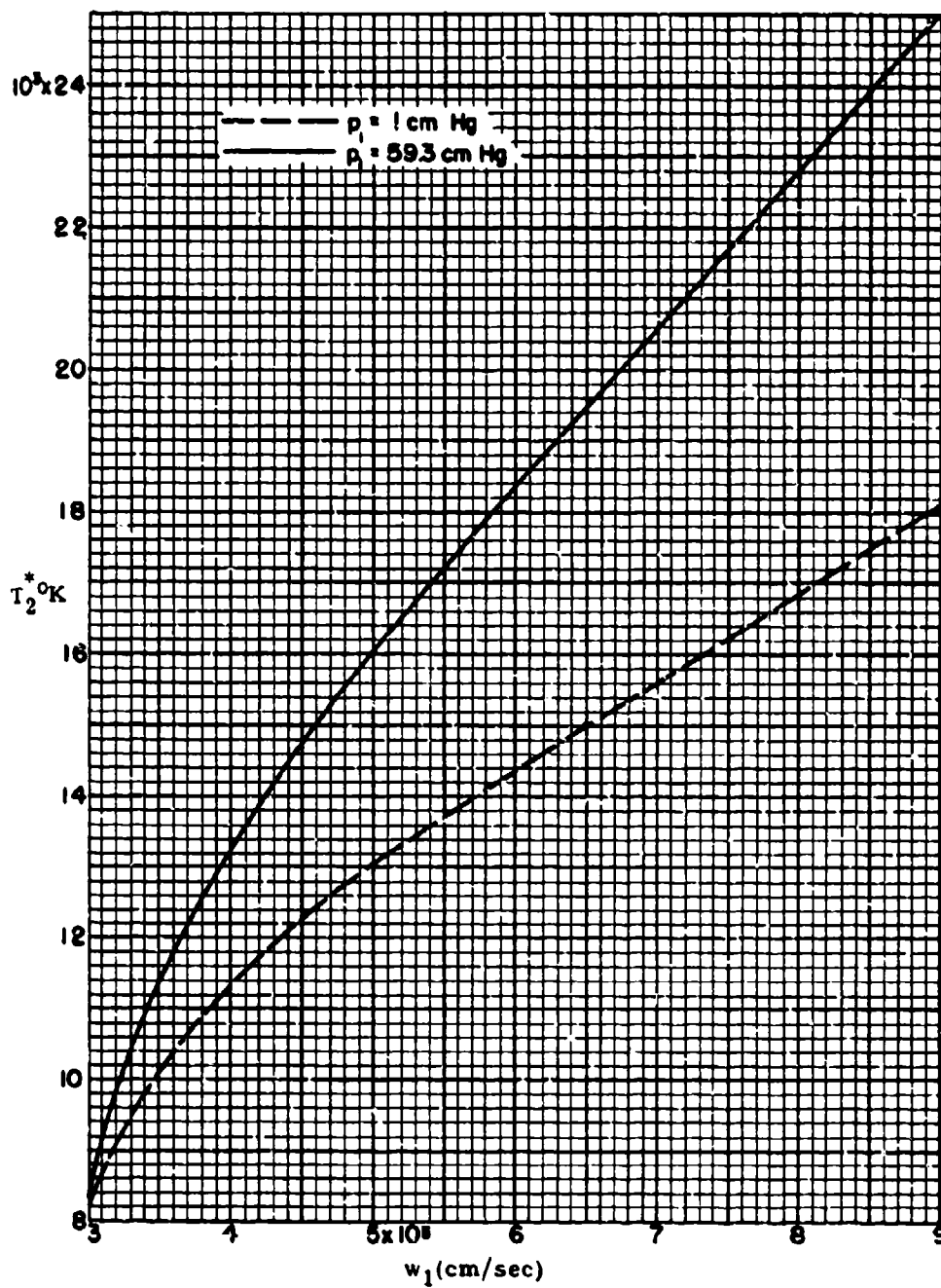


Fig. 2.2-18c. Variation of temperature (T_2^*) with shock velocity (w_1) in argon (Ref. 43).

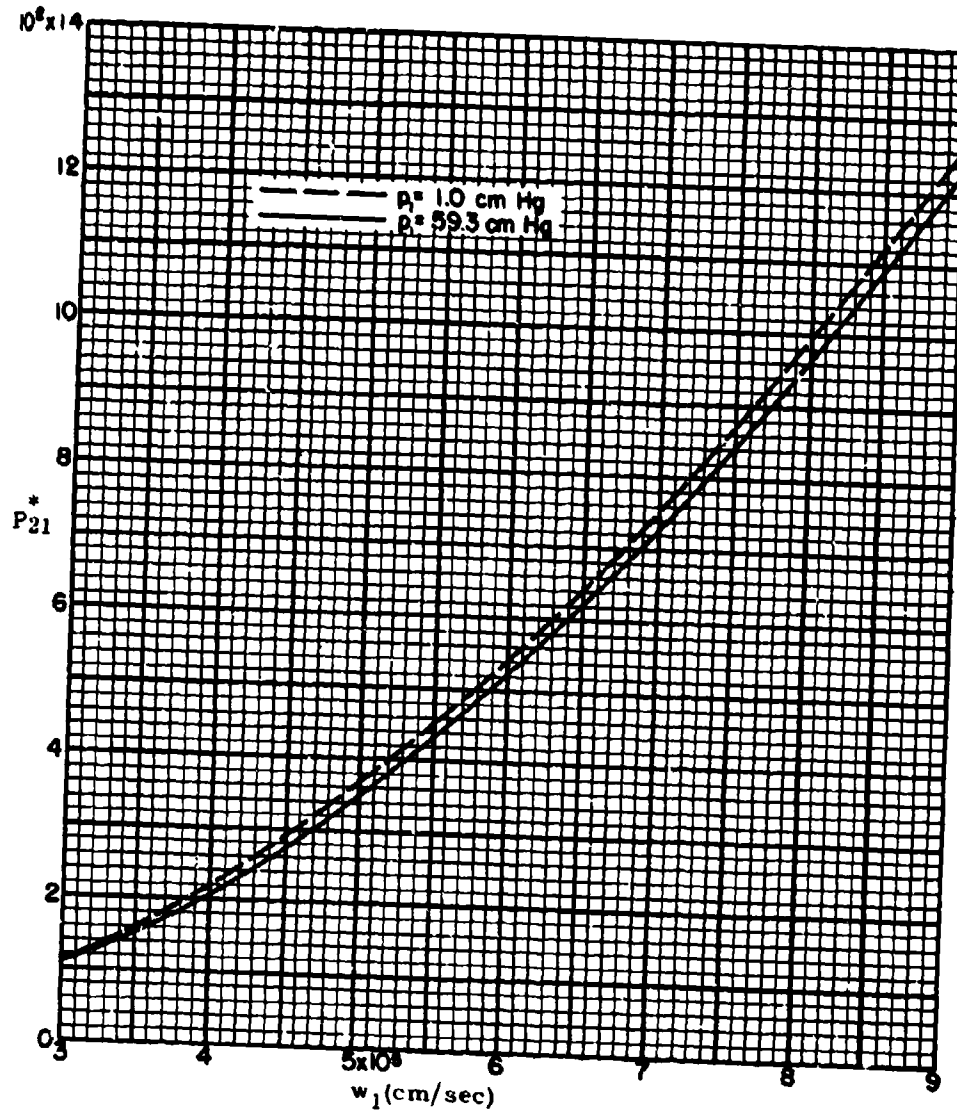


Fig. 2.2-18d. Variation of pressure ratio (P_{21}^*) with shock velocity (w_1) in argon (Ref. 43).

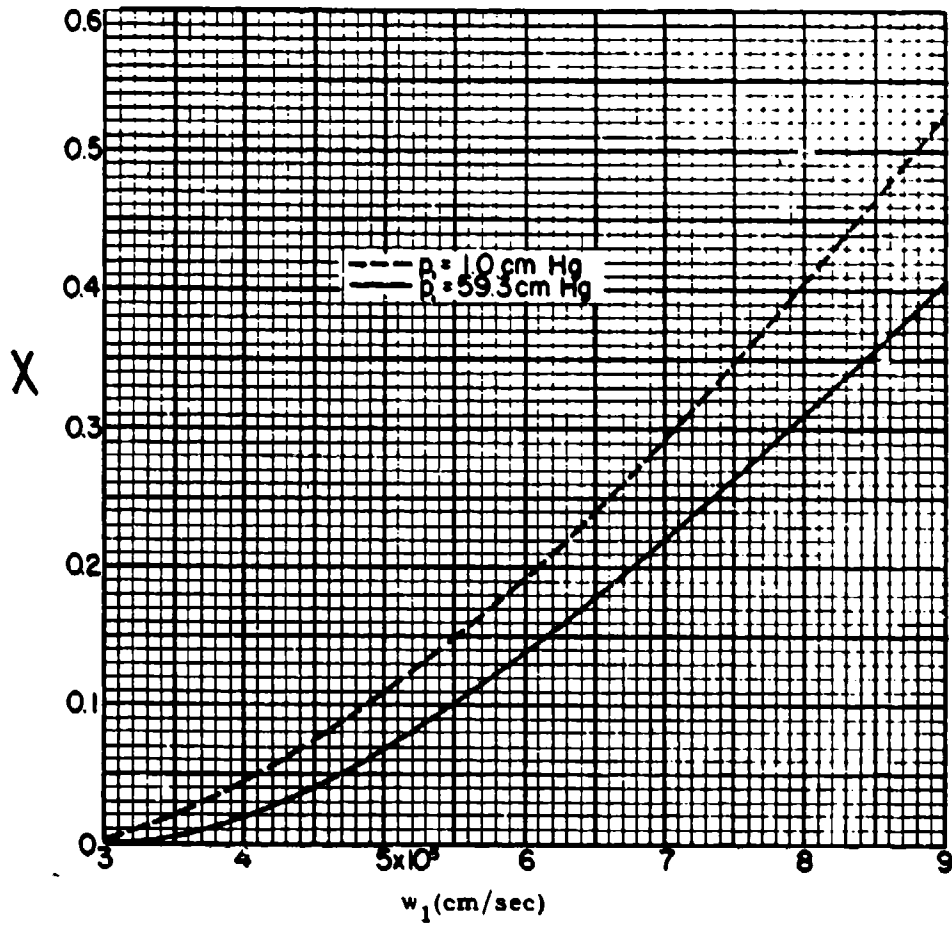


Fig. 2.2-18e. Variation of first degree of ionization (x) with shock velocity (w_1) in argon (Ref. 43).

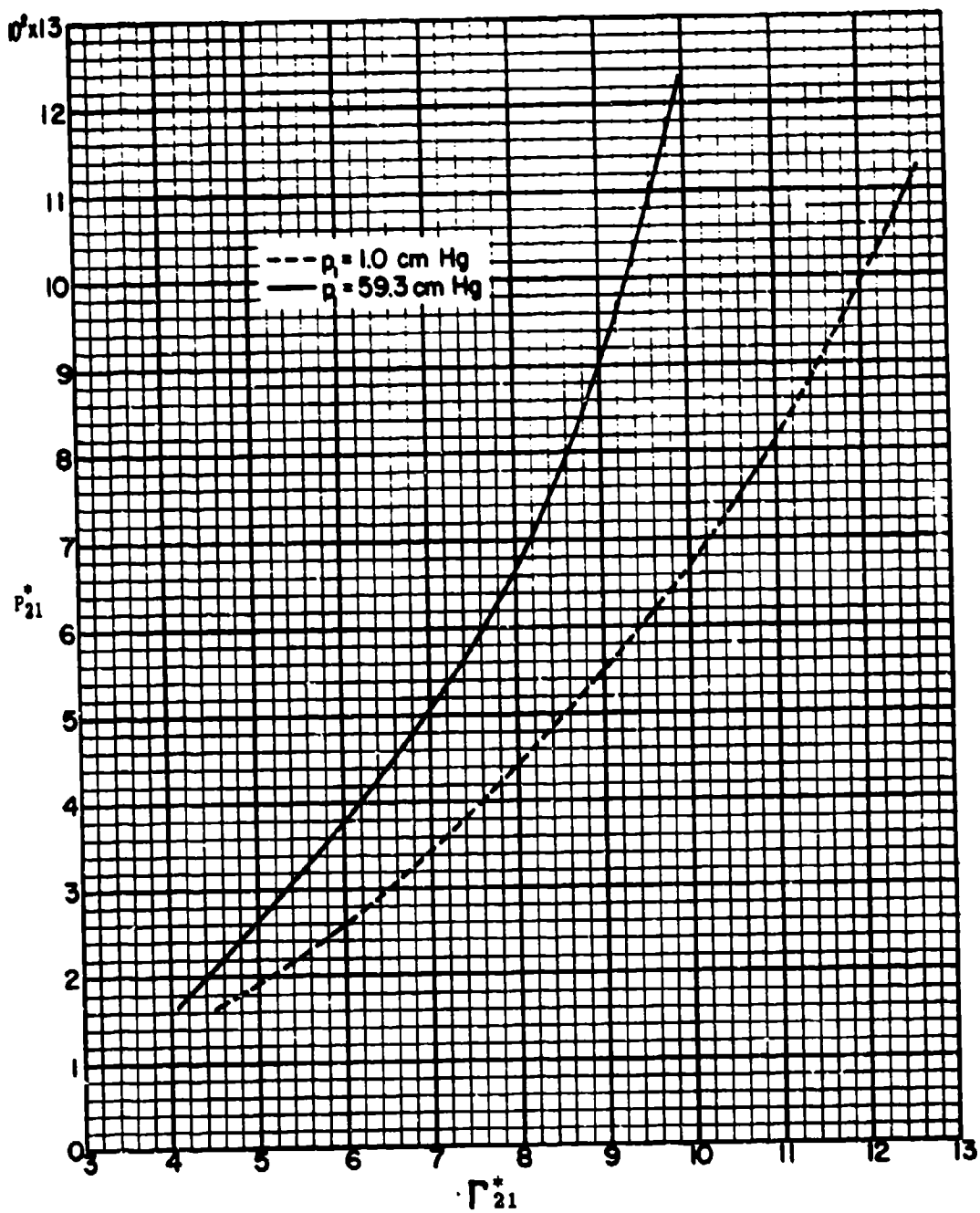


Fig. 2.2-18f. Variation of pressure ratio (P_{21}^*) with density ratio (Γ_{21}^*) (Hugoniot curve) in argon (Ref. 43).

Table 2.3-1

Physical properties of gases

Gas	Molecular Weight	γ 1 atm., 0 - 25°C	$\alpha = \frac{\gamma+1}{\gamma-1}$	$\beta = \frac{\gamma-1}{2\gamma}$	C_v Cal/gm./°C	μ Viscosity (micropoise)	n Index of Refraction	Boiling Point °C	Sound Speed 0°C, ft./sec
Air	28.96	1.404	5.8%	0.144	0.172	195	1.00029	-185.7	1087
Argon	39.94	1.667	4.00	0.200	0.375	222	1.00028		1008
CO ₂	44.01	1.300	7.67	0.115	0.151	150	1.00045	-78.5	846
† CC ₄	153.84	1.130	16.38	0.058	0.1167	100	1.0018	-76.8	433 +
C ₂ H ₂	72.15	1.066	24.3	0.039	0.416	67	1.0017	28	696 +
C ₂ H ₆	30.06	1.22	10.09	0.090	0.316	85	1.0008	-88.3	996 +
C ₂ H ₄	28.05	1.255	8.84	0.102	0.2862	100	1.00072	-103.9	1046
† CCl ₄	150.9	1.139	15.35	0.061	0.1297	123		-28	496 +
Etyletes									
Freon 12									
He	4.003	1.667	4.00	0.200	0.743	195	1.00035	-268.9	3182
H ₂	2.016	1.407	5.81	0.145	2.42	88	1.00014	-252.8	4168
Kr	82.9	1.667	3.90	0.204	0.0369	246	1.00043	-152.9	701 +
CH ₄	16.03	1.313	7.39	0.119	0.402	109	1.00045	-161.5	1417
Ne	20.18	1.667	4.12	0.196	0.1499	312	1.00067	-245.9	1429
N ₂	28.02	1.404	5.95	0.144	0.177	176	1.00030	-195.8	1096
SF ₆	146.06	1.096	21.3	0.044	0.141	150	1.00078	-63.8	432
Xe	131.3	1.667	4.00	0.200	0.073+	226	1.00070	-107.1	597 +

* Calculated (@ - 2 cal/gm mole)

† Toxic

+ Calculated from $a^2 = \frac{\gamma RT}{M}$

Table 2.3-2

Flow quantities for strong shock waves in a perfect gas

(a) Case Air/Air

 $P_{14} = 0$, $\alpha_4 = 6$, $\beta_1 = \frac{1}{2}$ $\tau = \text{indeterminate}$

E_{14}	P_{21}	Γ_{34}	A_{34}	T_{34}	Γ_{21}	A_{21}	T_{21}	W_{11}	U_{34}	U_{21}	M_3	M_2	C_{34}
0	∞	*	*	*	6	∞	∞	∞	*	∞	*	L.88	*
0.1	422	0	0	0	5.92	6.45	71.4	19.0	5	15.8	∞	L.87	5
1.0	44	0	0	0	5.30	2.88	0.30	6.16	5	5.0	∞	L.73	5

(b) Case He/Air

 $P_{14} = 0$, $\alpha_4 = 6$, $\beta_1 = \frac{1}{2}$, $\alpha_4 = 4$, $\beta_4 = \frac{1}{5}$, $T_4 = T_1$

E_{14}	P_{21}	Γ_{34}	A_{34}	T_{34}	Γ_{21}	A_{21}	T_{21}	W_{11}	U_{34}	U_{21}	M_3	M_2	C_{34}
.231	132	0	0	0	5.75	4.79	23.0	10.6	3.00	8.83	∞	L.94	3

(c) Case H_2/N_2 $P_{14} = 0$, $\alpha_4 = 6$, $\beta_1 = \frac{1}{2}$, $T_4 = T_1$

E_{14}	P_{21}	Γ_{34}	A_{34}	T_{34}	Γ_{21}	A_{21}	T_{21}	W_{11}	U_{34}	U_{21}	M_3	M_2	C_{34}
.0735	574	0	0	0	5.94	9.82	96.5	22.2	5	18.5	∞	L.88	5

Table 2.3-3
 Reynolds number per foot in states (2) and (3); $T_1 = T_4 = 288^\circ\text{K}$

P_{41}	P_{21}	$P_1 = 1 \text{ mm Hg}$						$\frac{(Re)_3}{(Re)_2}$
		Γ_{21}	Γ_{34}	T_{21}	T_{34}	U_{21}	$\left\{ \frac{Re}{L} \right\}_2$	
1	1.0	1.000	1.00	1.00	1.00	0	0	1.00
10	2.80	2.013	.420	1.387	.700	.81	11950	3.52
100	6.35	3.15	.142	2.025	.455	1.62	28300	14.0
1,000	11.4	3.96	.040	2.875	.225	2.35	39200	62.1
10,000	17.0	4.45	.010	3.825	.159	2.96	44700	255

Table 2.3-4

Flow quantities in uniform states (2) and (3) in a shock tube

(1)	(2)	(3)	(4)	(5)	(6)	(7)	(8)	(9)	(10)	(11)
P_{21}	M_2	P_{021}	T_{021}	Q_{21}	Λ_{21}	M_3	P_{034}	T_{034}	Q_{34}	Λ_{34}
1	0	1	1	0	0	0	1	1	0	0
1.25						0.1875	0.8097			0.1374
1.5						0.3178	0.6993		0.0459	0.2198
1.75						0.4522	0.6260			0.2701
2	0.4708	2.328	1.268	0.3104	0.6480	0.6886	0.5809	0.8586	0.1105	0.3013
2.25						0.7022	0.5828			0.3188
2.5						0.8288	0.5368		0.1637	0.3300
2.75						0.9390	0.5317			0.3344
2.888						1	0.5283			0.3348
3	0.7209	4.240	1.872	1.091	1.822	1.048	0.5289	0.8336	0.2031	0.3348
3.25						1.188	0.5323			0.3319
3.5						1.261	0.5387		0.2308	0.3271
3.75						1.365	0.5406			0.3208
4	0.8918	6.704	1.885	2.225	2.817	1.488	0.5434	0.8580	0.2487	0.3134
4.5						1.667	0.5447		0.2598	0.2988
4.823	1									
5	1.019	9.631	2.147	3.605	3.802	1.864	0.5408	0.8993	0.2647	0.2785
5.5						2.088	0.5316		0.2653	0.2688
6	1.108	12.92	2.436	5.158	4.757	2.253	0.5194	0.9579	0.2829	0.2413
6.5						2.448	0.5036		0.2978	0.2241
7	1.183	16.81	2.720	6.855	5.680	2.843	0.4888	1.026	0.2857	0.2071
7.5						2.940	0.4860		0.2423	0.1911
8	1.244	20.31	3.007	8.660	6.587	3.038	0.4482	1.102	0.2328	0.1760
8.5						3.239	0.4238		0.2227	0.1618
9	1.294	24.26	3.293	10.58	7.418	3.442	0.4020	1.183	0.2120	0.1488
9.5						3.648	0.3801		0.2012	0.1382
10	1.338	28.39	3.580	12.53	8.238	3.858	0.3584	1.270	0.1902	0.1248
11	1.374	32.68	3.867	14.54	9.028	4.306	0.3146	1.358	0.1677	0.1038
12	1.407	36.89	4.153	16.63	9.784	4.763	0.2743	1.452	0.1468	0.0860
13	1.435	41.23	4.440	18.74	10.52	5.237	0.2372	1.547	0.1273	0.0711
14	1.460	45.71	4.728	20.88	11.23	5.743	0.2031	1.645	0.1092	0.0586
15	1.482	50.18	5.016	23.06	11.91	6.275	0.1728	1.748	0.0930	0.0477
16	1.502	54.75	5.298	25.27	12.58	6.833	0.1467	1.848	0.0786	0.0389
17	1.520	59.31	5.582	27.49	13.23	7.437	0.1216	1.950	0.0657	0.0316
18	1.537	64.00	5.872	29.76	13.85	8.067	0.1006	2.068	0.0644	0.0252
19	1.552	68.88	6.157	32.04	14.46	8.770	0.0828	2.180	0.0448	0.0201
20	1.566	73.38	6.446	34.33	15.06	9.524	0.0672	2.268	0.0364	0.0159
21	1.578	78.05	6.729	36.60	15.63	10.33	0.0541	2.377	0.0293	0.0124
22	1.600	87.52	7.304	41.22	16.75	12.28	0.0332	2.407	0.0180	7.25. 10 ⁻³
23	1.619	97.08	7.878	45.87	17.81	14.39	0.0203	2.820	0.0110	4.23. 10 ⁻³
24	1.636	106.7	8.450	50.58	18.83	16.71	0.0112	3.084	6.06. 10 ⁻³	2.17. 10 ⁻³
25	1.651	116.5	9.024	55.34	19.81	20.00	5.63. 10 ⁻³	3.276	3.23. 10 ⁻³	1.14. 10 ⁻³
26	1.664	126.2	9.598	60.09	20.78	25.23	2.78. 10 ⁻³	3.510	1.51. 10 ⁻³	5.17. 10 ⁻⁴
27	1.675	135.8	10.17	64.82	21.66	31.50	1.16. 10 ⁻³	3.743	6.20. 10 ⁻⁴	2.08. 10 ⁻⁴
28	1.686	145.7	10.75	69.55	22.55	40.77	3.97. 10 ⁻⁴	3.978	2.16. 10 ⁻⁴	6.93. 10 ⁻⁵
29	1.695	155.5	11.32	74.41	23.40	55.88	1.01. 10 ⁻⁴	4.219	5.51. 10 ⁻⁵	1.71. 10 ⁻⁶
30	1.703	165.2	11.89	79.17	24.22	84.47	1.58. 10 ⁻⁴	4.460	8.30. 10 ⁻⁵	2.87. 10 ⁻⁶
41	1.711	173.2	12.46	84.03	25.03	158.8	7.78. 10 ⁻⁷	4.702	4.23. 10 ⁻⁷	1.24. 10 ⁻⁷
42	1.718	185.1	13.03	88.86	25.81	552.2	3.07. 10 ⁻¹⁰	4.924	1.67. 10 ⁻¹⁰	4.81. 10 ⁻¹¹
44	1.73	201.6	13.27	92.18	26.5	∞	0	5	0	0

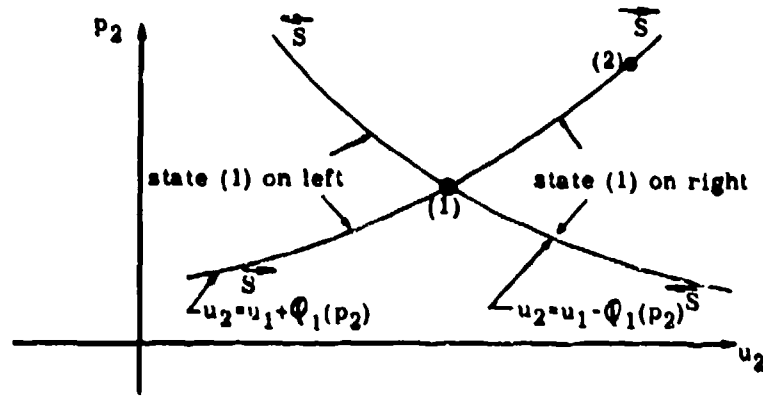


Fig. 2.3-1. Locus of all states (2) that may be connected with a given state (1) by a forward or backward facing shock wave.

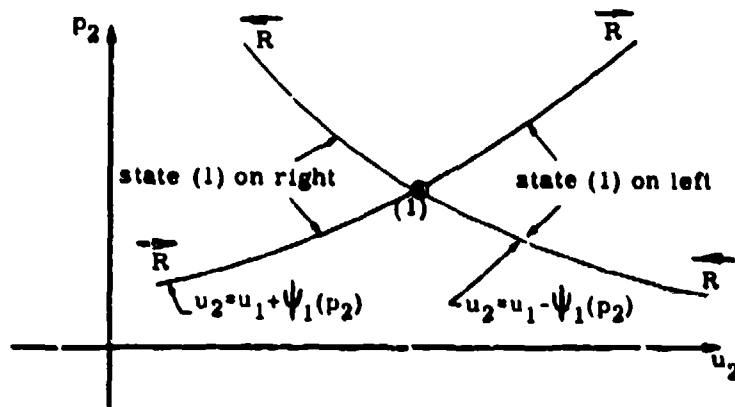


Fig. 2.3-2. Locus of all states (2) that may be connected with a known state (1) by a forward or backward facing rarefaction wave.

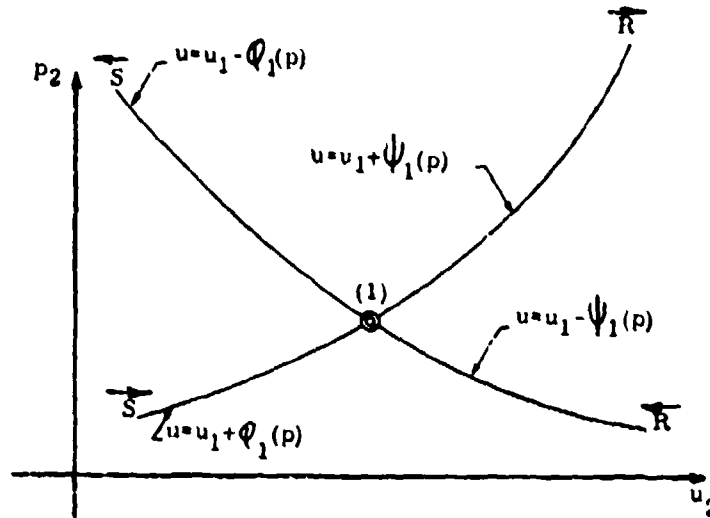


Fig. 2.3-3. Locus of all the states (2) that may be reached from a given state (1) on the left by forward or backward facing waves.

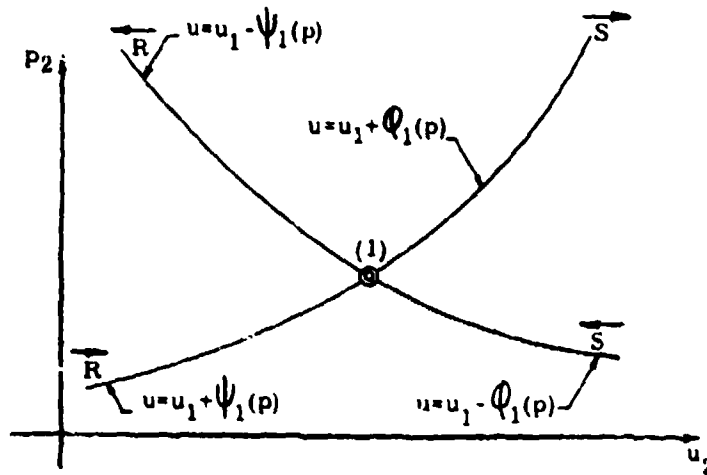


Fig. 2.3-4. Locus of all the states (2) that may be reached from a given state (1) on the right by forward or backward facing waves.

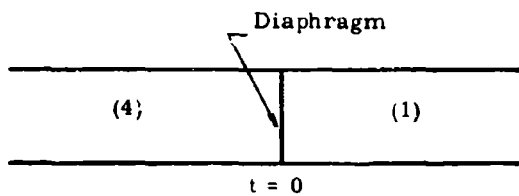


Fig. 2.3-5. Initial conditions in a shock tube.

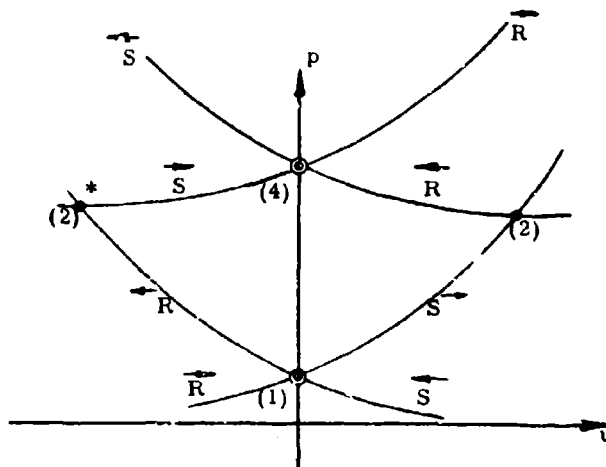


Fig. 2.3-6. The shock tube problem in the (p,u) -plane.

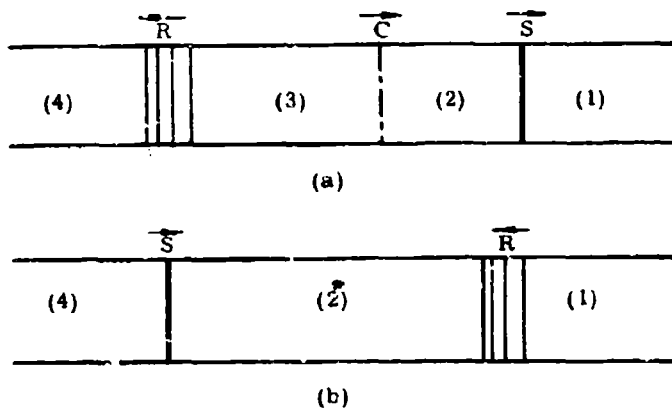
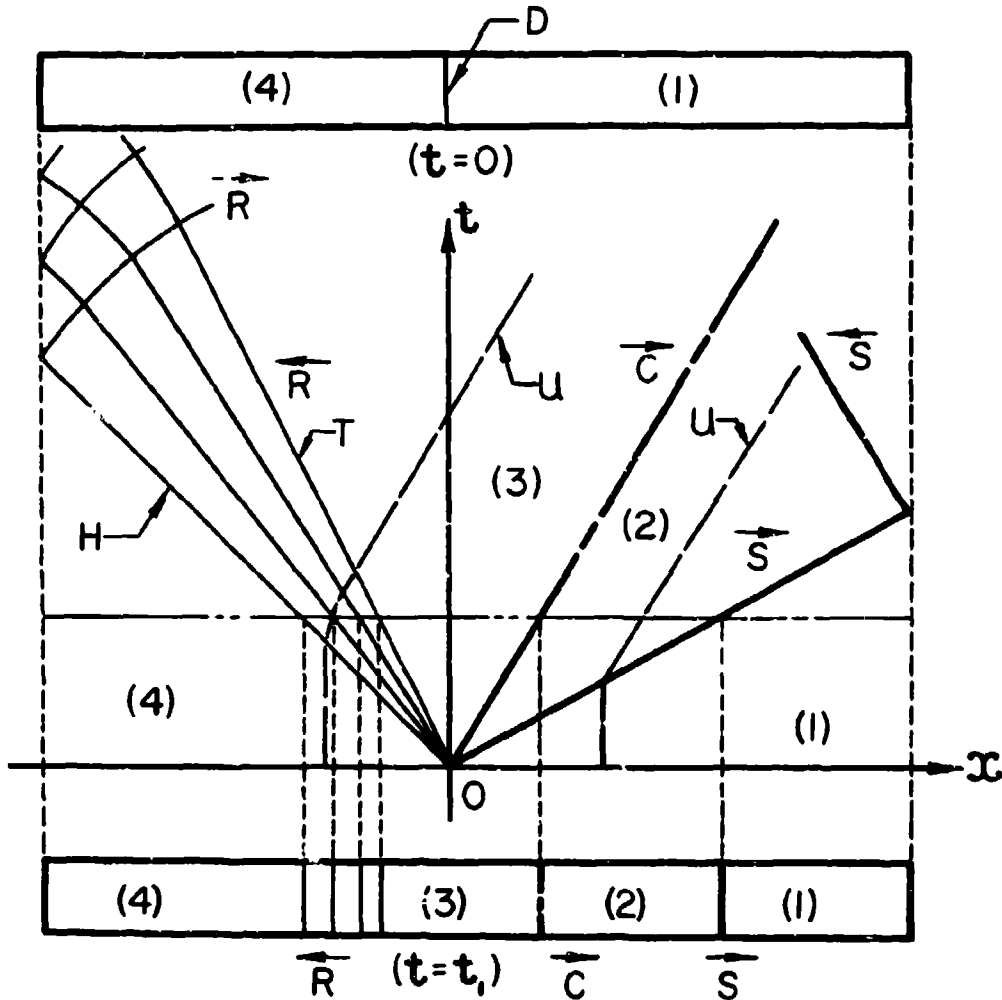


Fig. 2.3-7. Possible wave systems in a shock tube following the rupturing of the diaphragm.



- | | | |
|----------------------|-------------------|-------------------|
| (4) = Chamber | (1) = Channel | D = Diaphragm |
| S = Shock Wave | C = Contact Front | u = Particle Path |
| R = Rarefaction Wave | H = Head | T = Tail |

Fig. 2.3-8. Diagram of the (x, t) -plane of the ideal wave system produced by bursting a diaphragm in a shock tube.

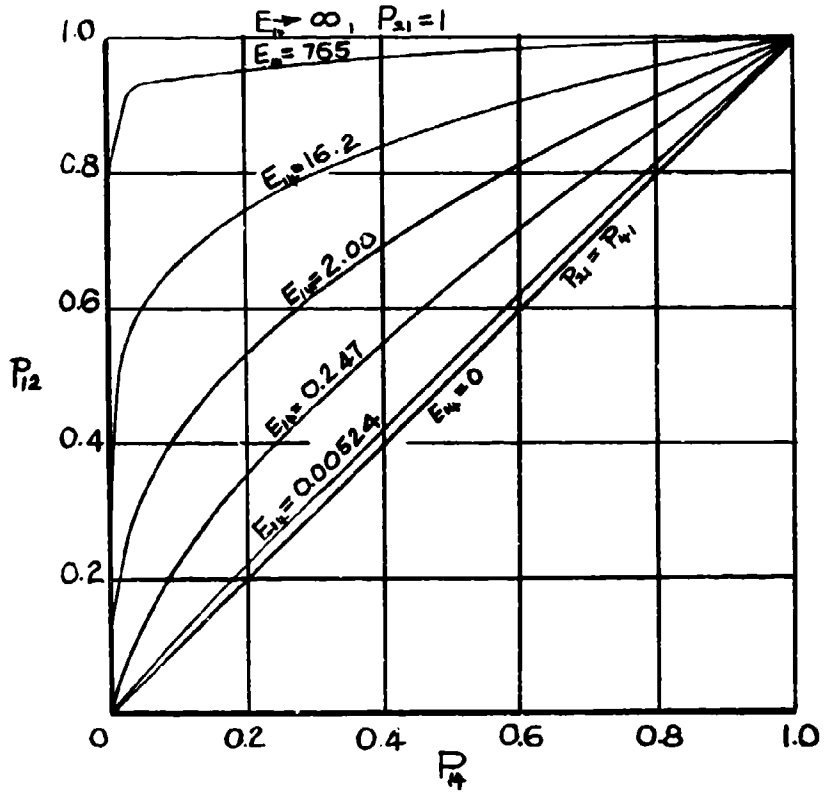


Fig. 2.3-9. Variation of the shock pressure ratio (P_{12}) with the diaphragm pressure ratio (P_{14}) and the internal energy ratio (E_{14}) across the diaphragm; case air/air.

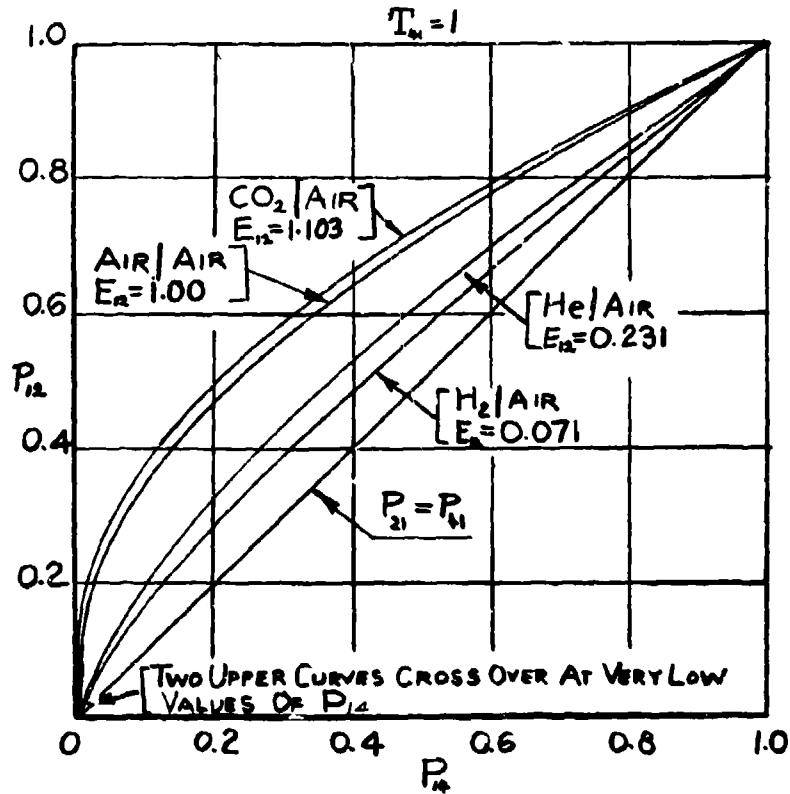


Fig. 2.3-10. Variation of the shock pressure ratio (P_{12}) with the diaphragm pressure ratio (P_{14}) for the different gas combinations at the same temperature ($T_{14} = 1$).

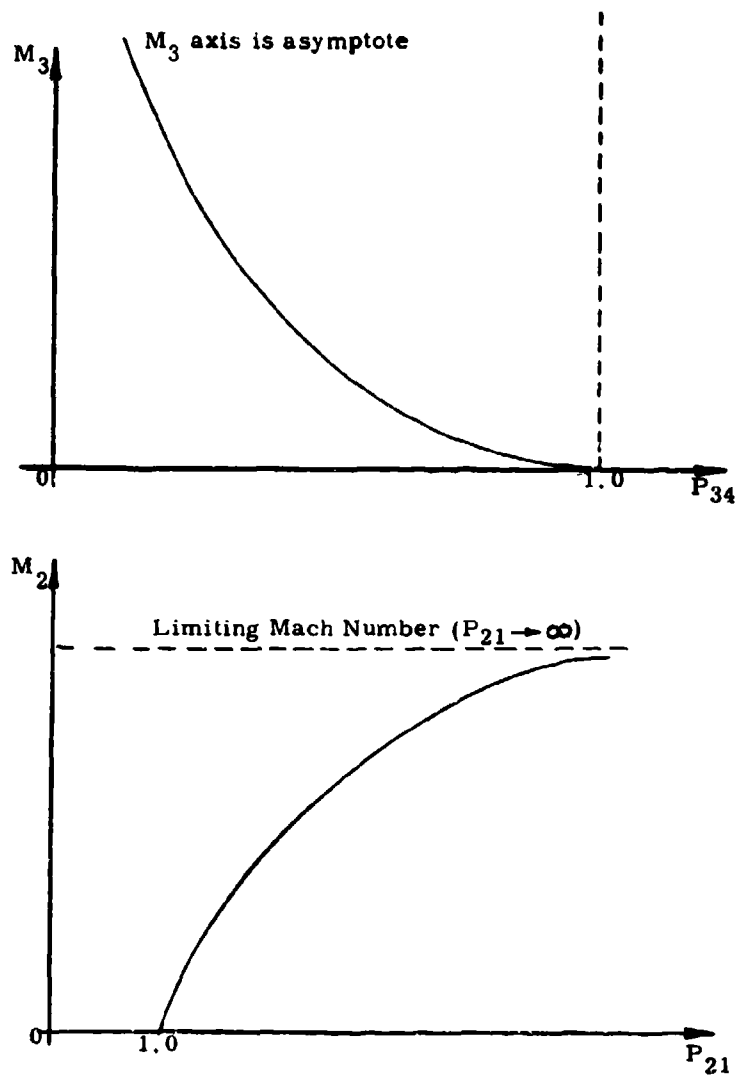


Fig. 2.3-11. Variation of Mach number with pressure ratio.

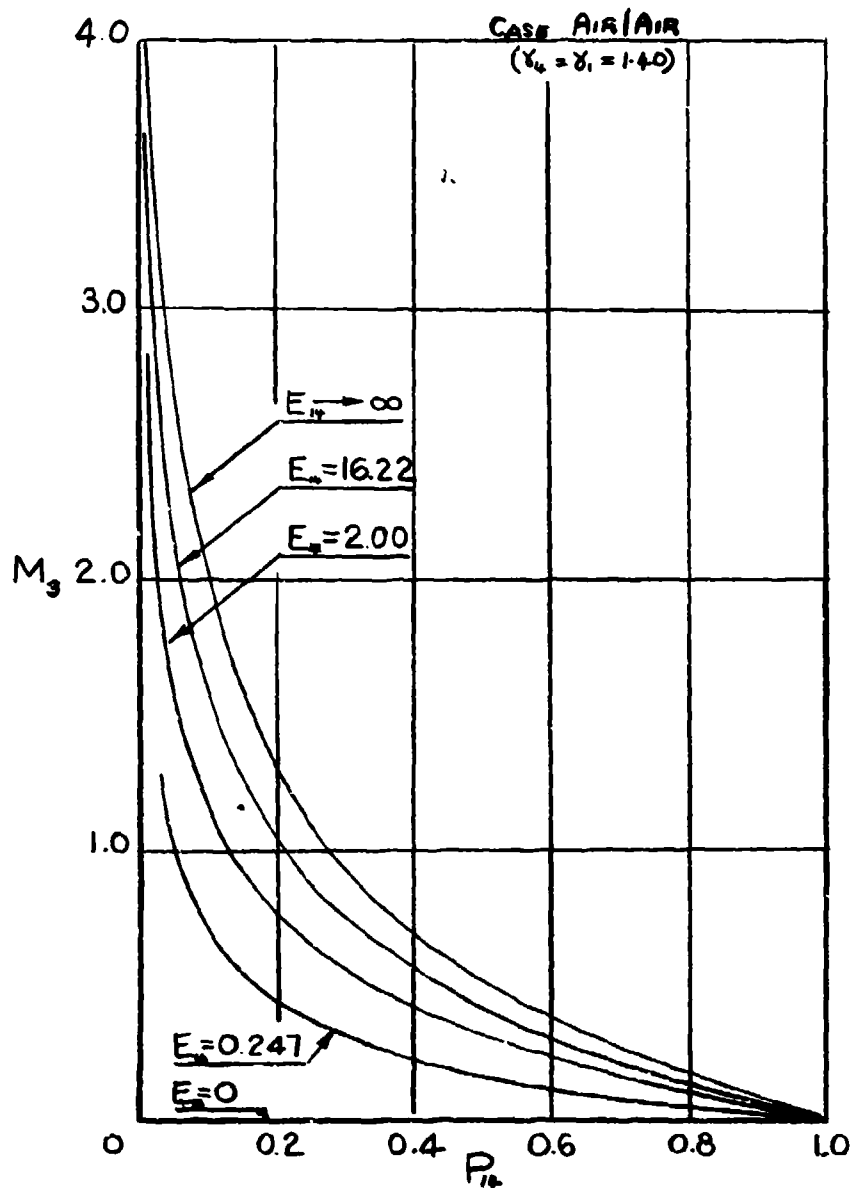


Fig. 2.3-12. Variation of Mach number in state (3) with the diaphragm pressure ratio (P_{14}) for different energy ratios (E_{14}) across the diaphragm.

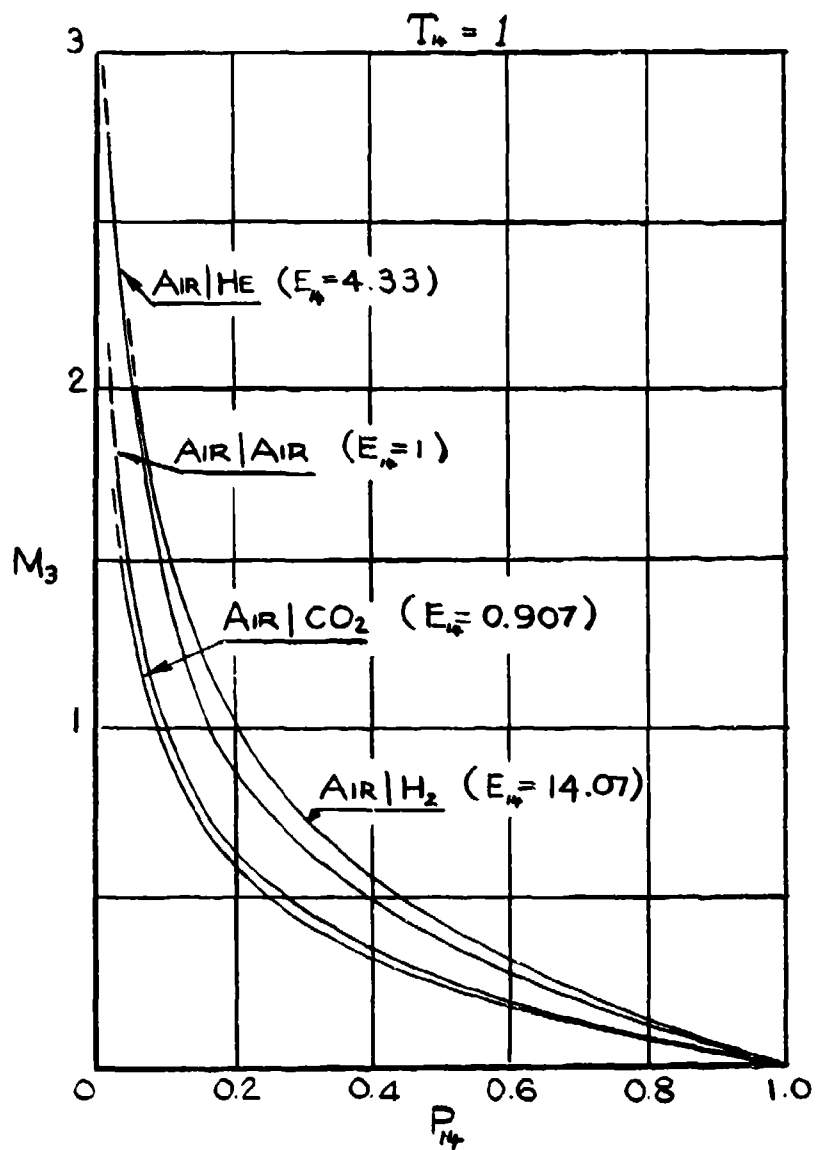


Fig. 2.3-13. Variation of Mach number in state (3) with diaphragm pressure ratio (P_{14}) and internal energy ratio (E_{14}) across the diaphragm at $T_{14} = 1$.

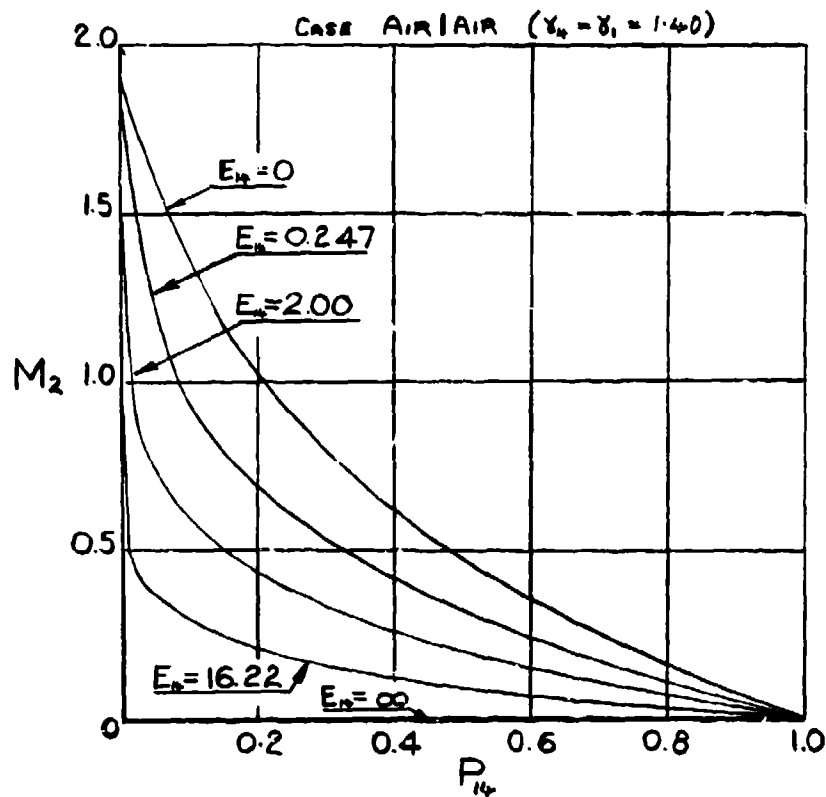


Fig. 2.3-14. Variation of Mach number in state (2) with the diaphragm pressure ratio (P_{14}) for different internal energy ratios (E_{14}) across the diaphragm.

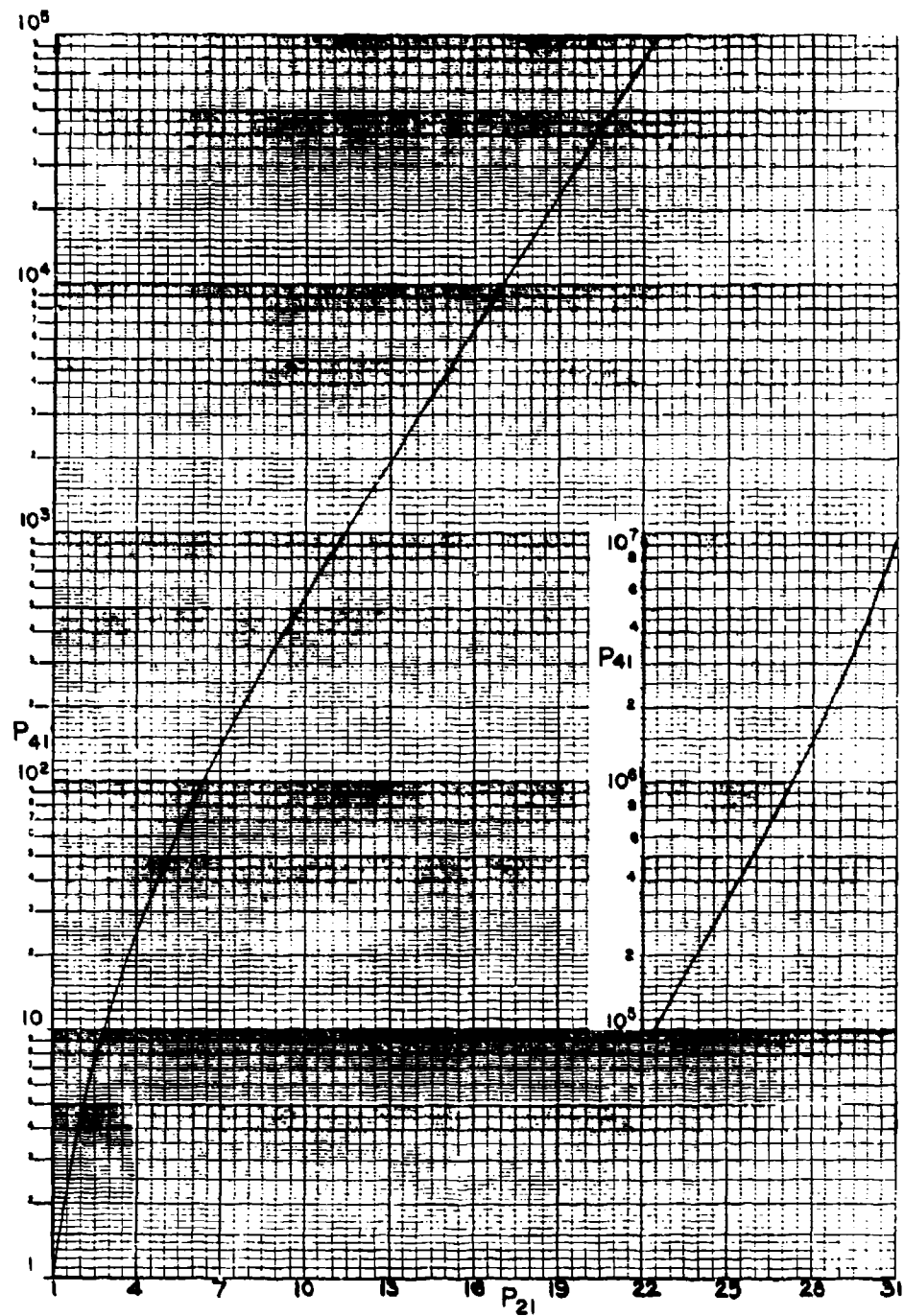


Fig. 2.3-15. Variation of the initial shock pressure ratio (P_{21}) with the diaphragm pressure ratio (P_{41}); case air/air.

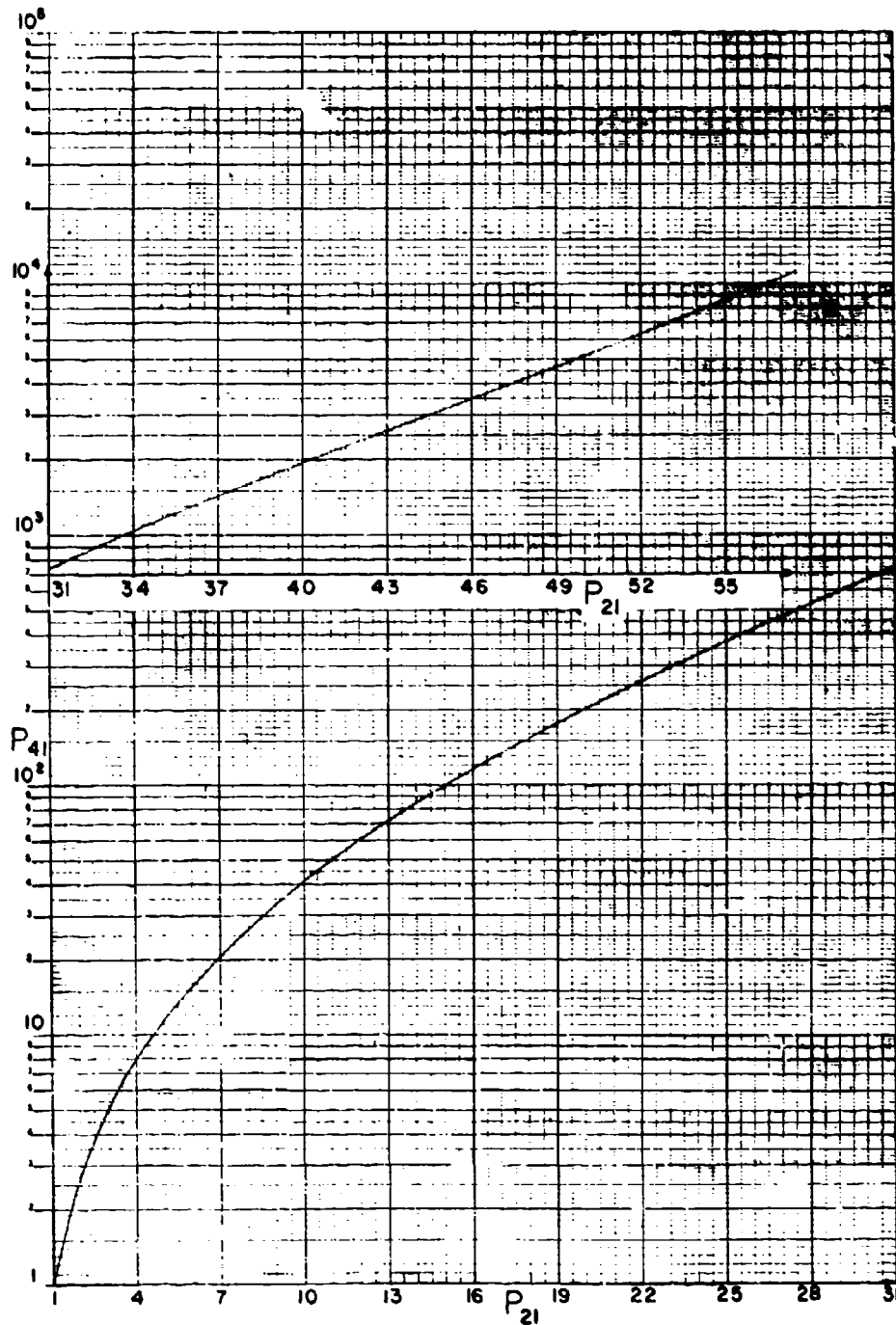


Fig. 2.3-16. Variation of the initial shock-wave pressure ratio (P_{21}) with the diaphragm pressure ratio (P_{41}); case He/air, $\gamma_4 = 1.665$, $\gamma_1 = 1.402$, $T_4 = T_1$.

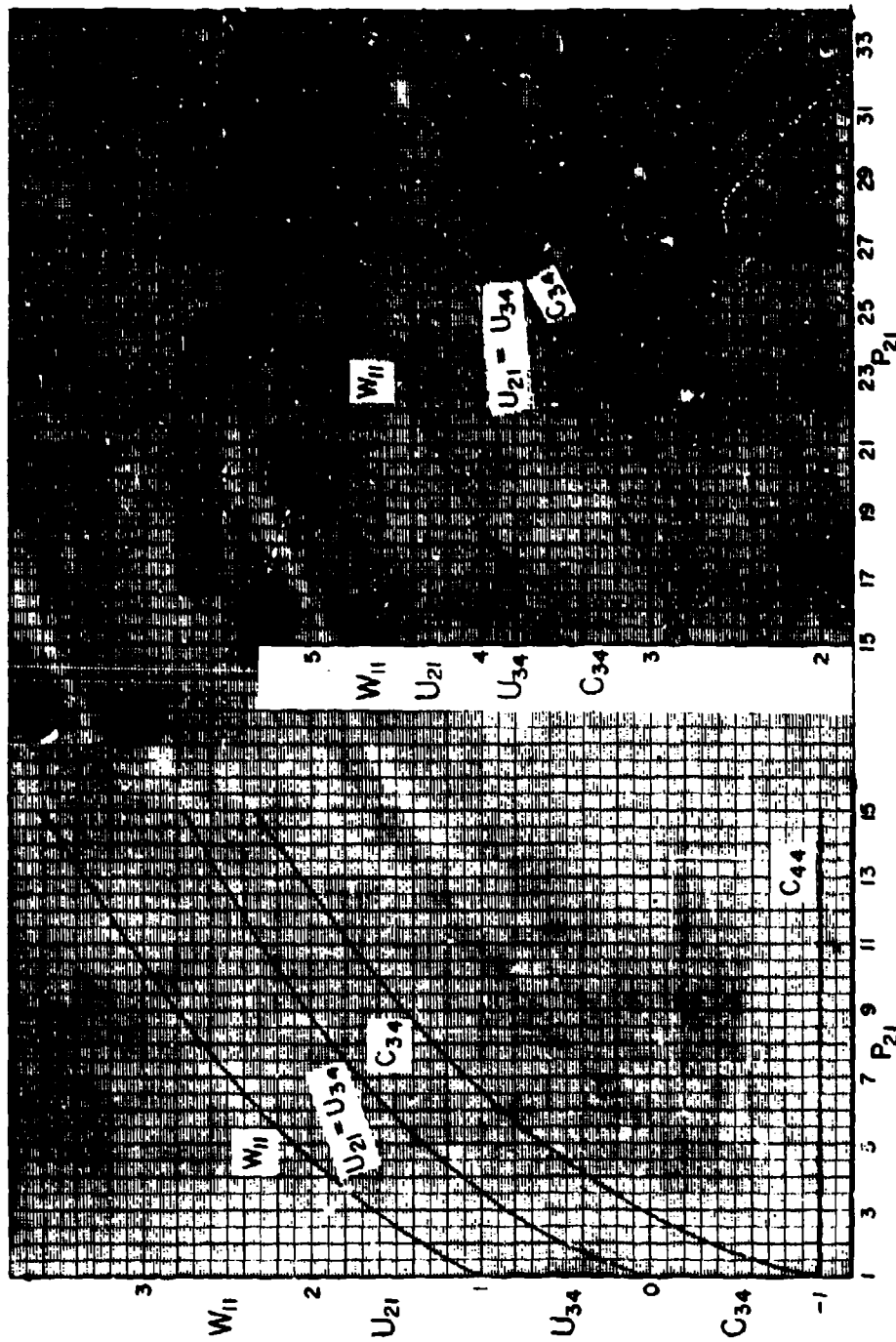


Fig. 2.3-17. Variation of initial shock wave velocity (W_{11}), particle velocity (U_{21}), and rarefaction front velocities (C_{34} and C_{44}) with the initial shock pressure ratio (P_{21}); case air/air.

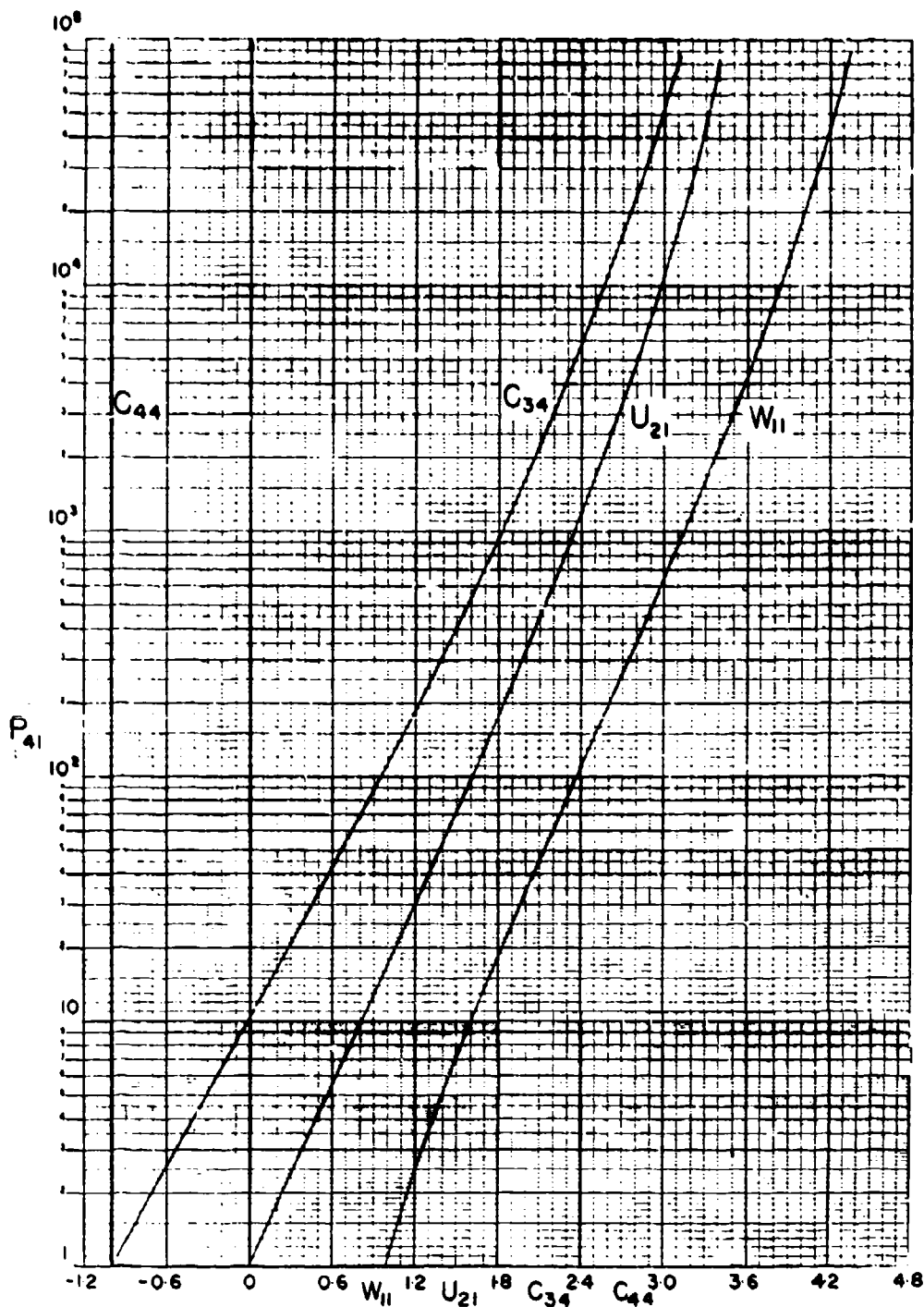


Fig. 2.3-18. Variation of initial shock wave velocity (W_{11}), particle velocity (U_{21}), and rarefaction front velocities (C_{44} and C_{34}) with the pressure ratio (P_{41}) across the diaphragm; case air/air.

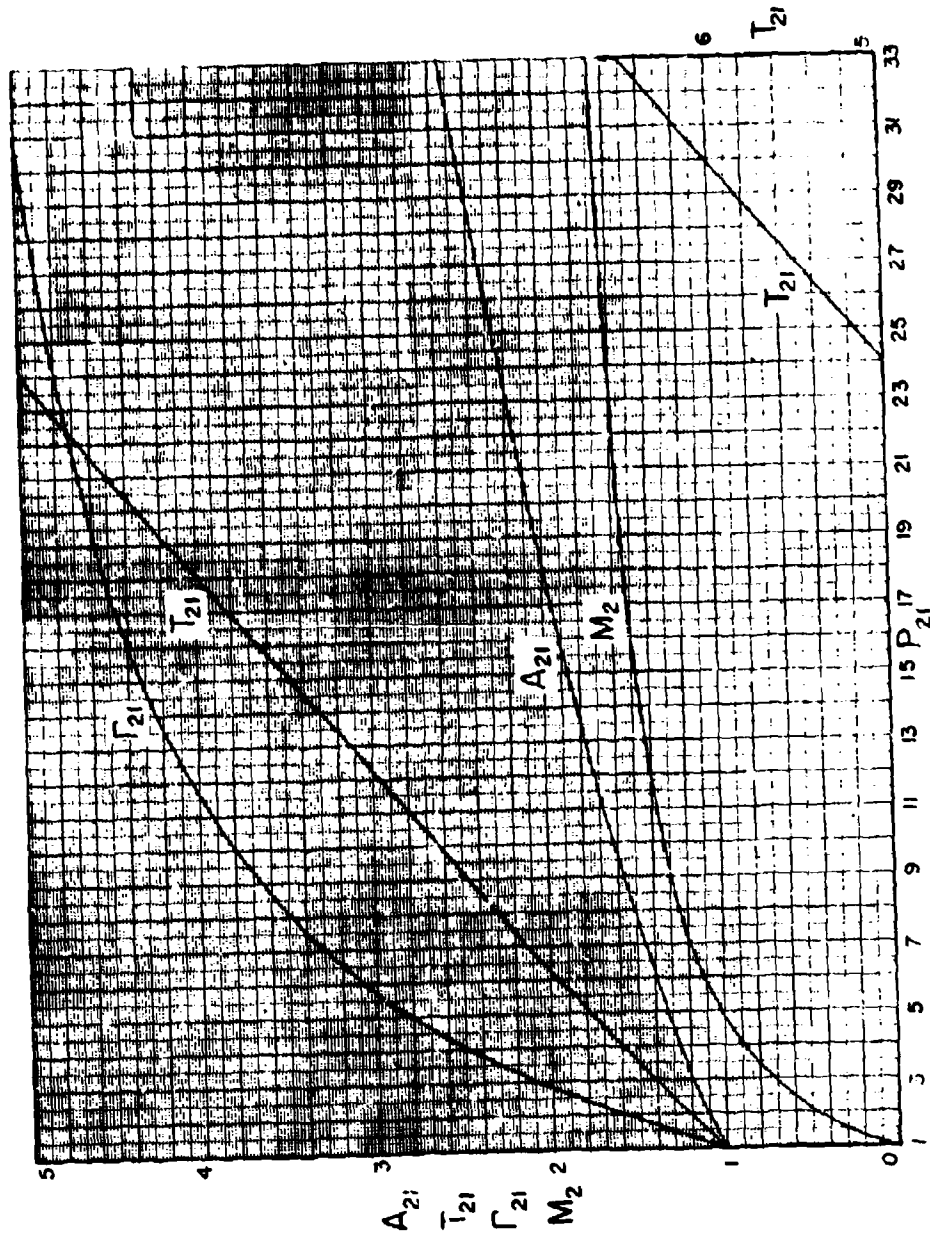


Fig. 2.3-19. Variation of flow parameters in state (2) with the shock pressure ratio (P_{21}); case air/air ($\gamma_{14} = 1$).

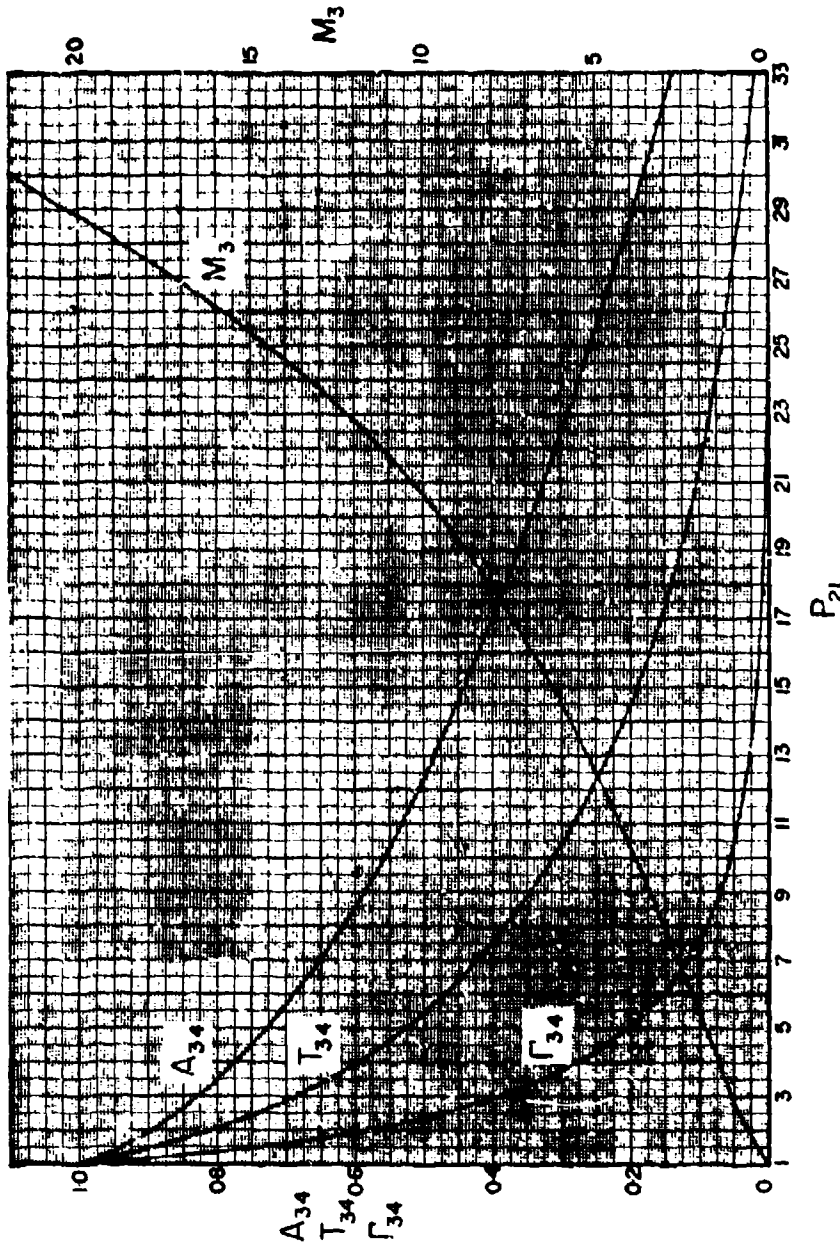


Fig. 2.3-20. Variation of flow parameters in state (3) with the shock pressure ratio (P_{21}); case air/air ($\gamma = 1.4$).

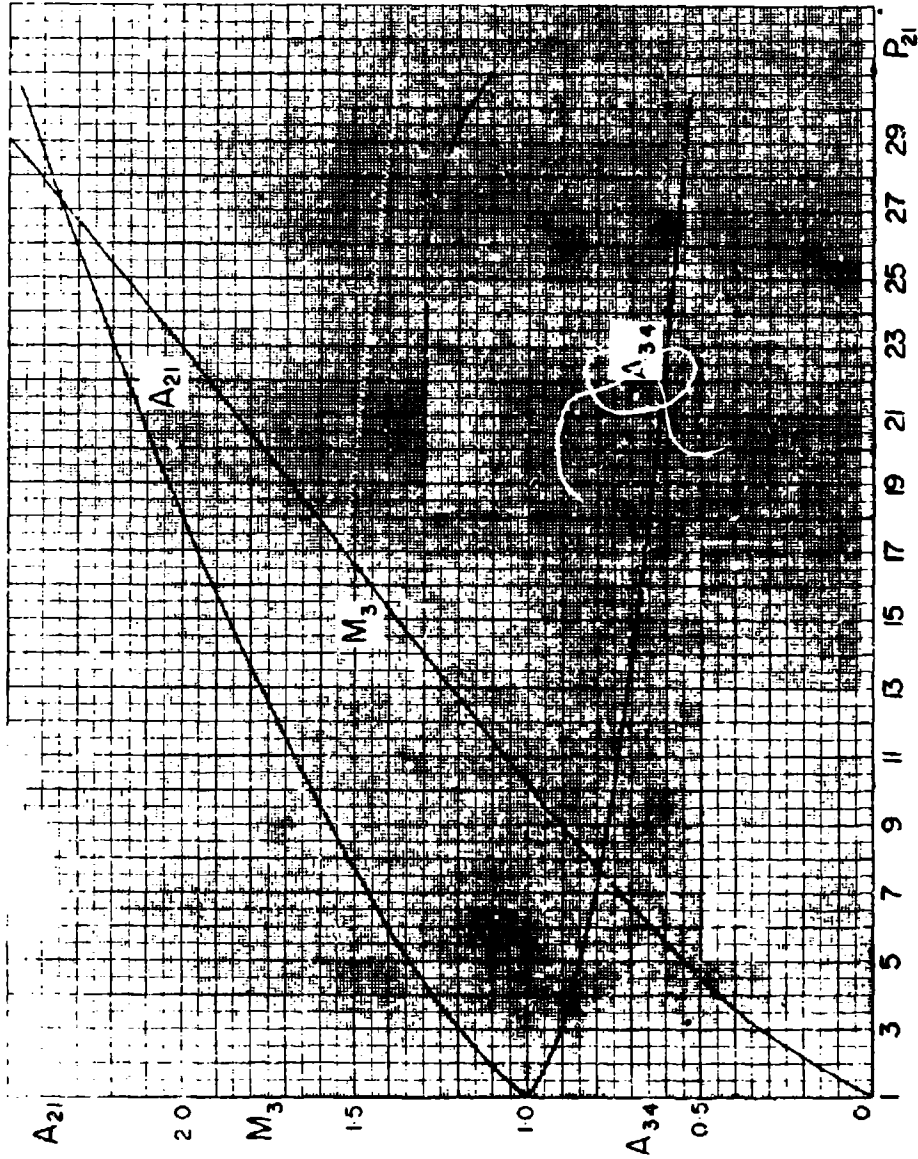


Fig. 2.3-21. Variation of Mach number M_3 and velocity of sound ratios A_{21} and A_{34} with the initial shock-wave pressure ratio P_{21} ; case He/air, $\gamma_4 = 1.665$, $\gamma_1 = 1.402$, $T_4 = T_1$.

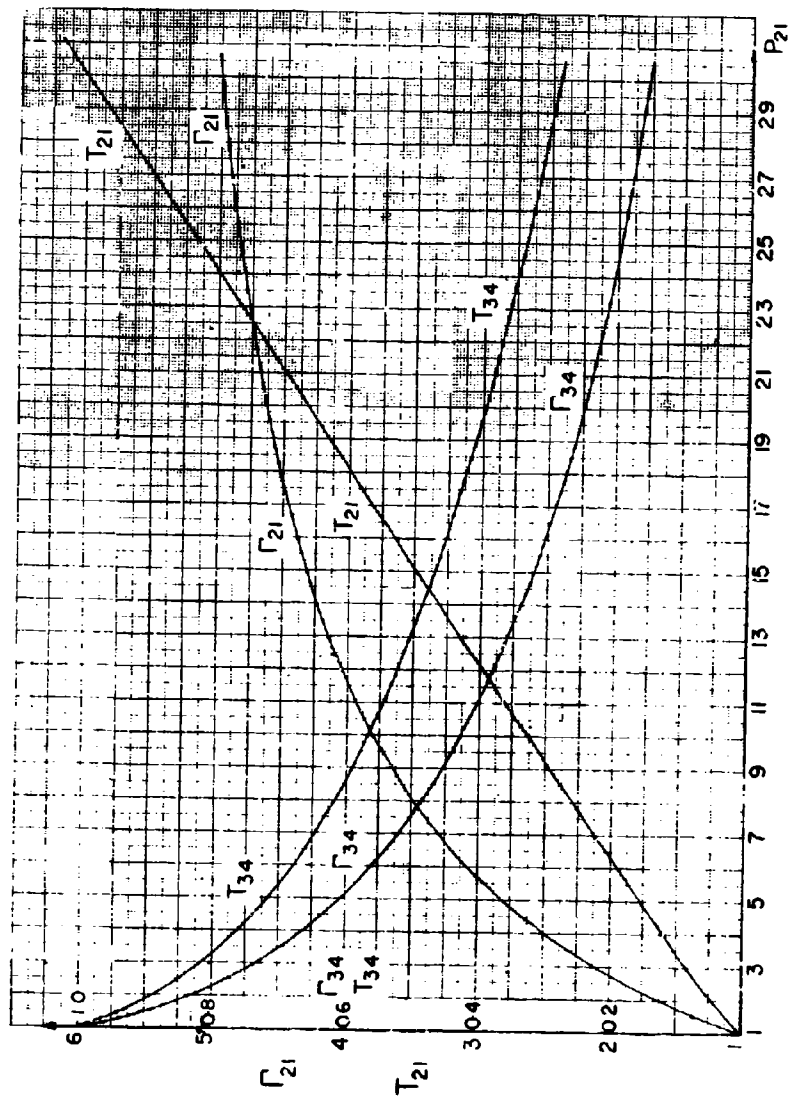


FIG. 2.3-22. Variation of temperature ratios T_{34} and T_{21} and density ratios Γ_{34} and Γ_{21} with the shock wave pressure ratio P_{21} ; case He/air, $\gamma_4 = 1.565$, $\gamma_1 = 1.402$, $\Gamma_1 = T_4$.

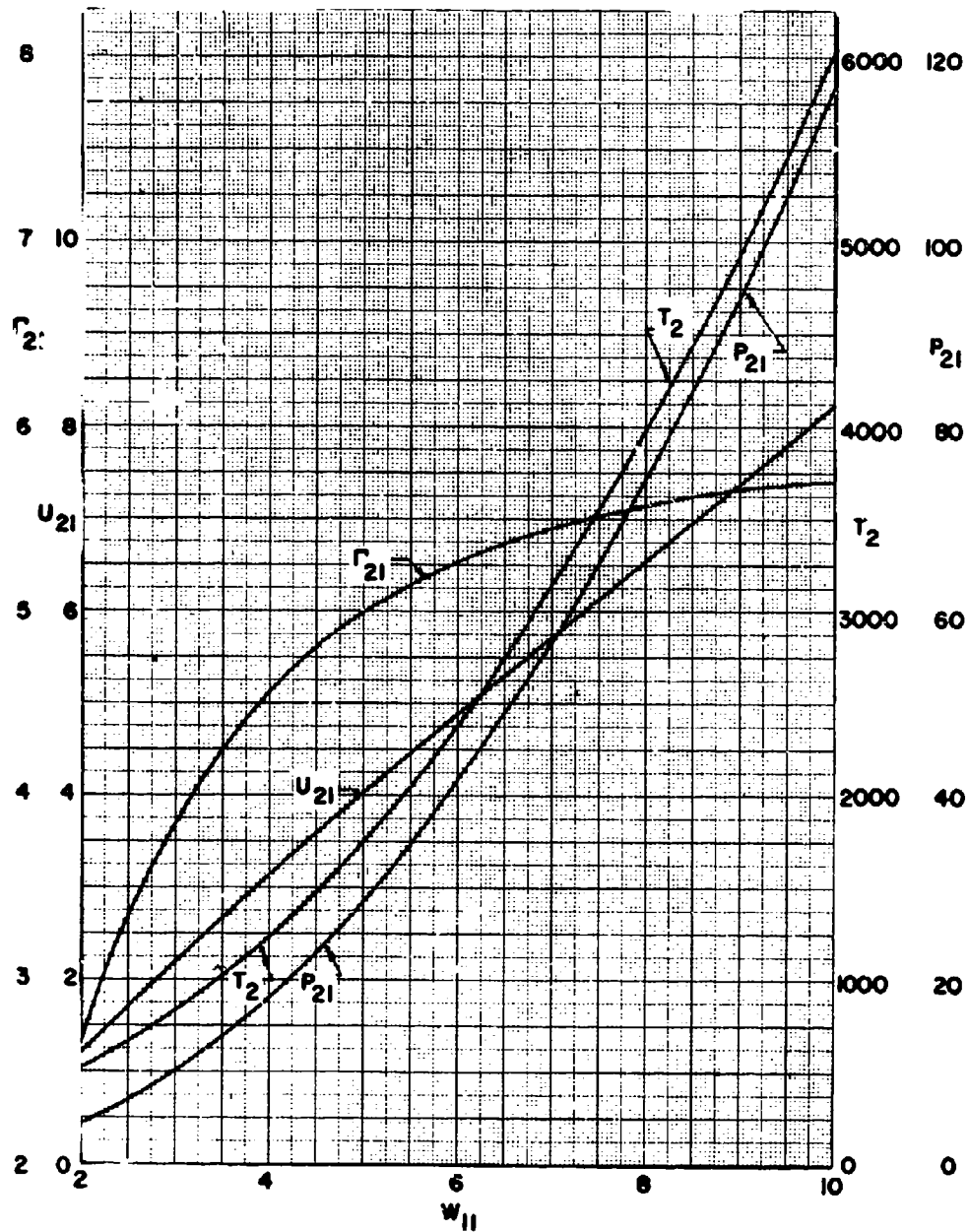


Fig. 2.3-23. Variation of flow quantities behind a shock wave in air; $\gamma = 1.4$.

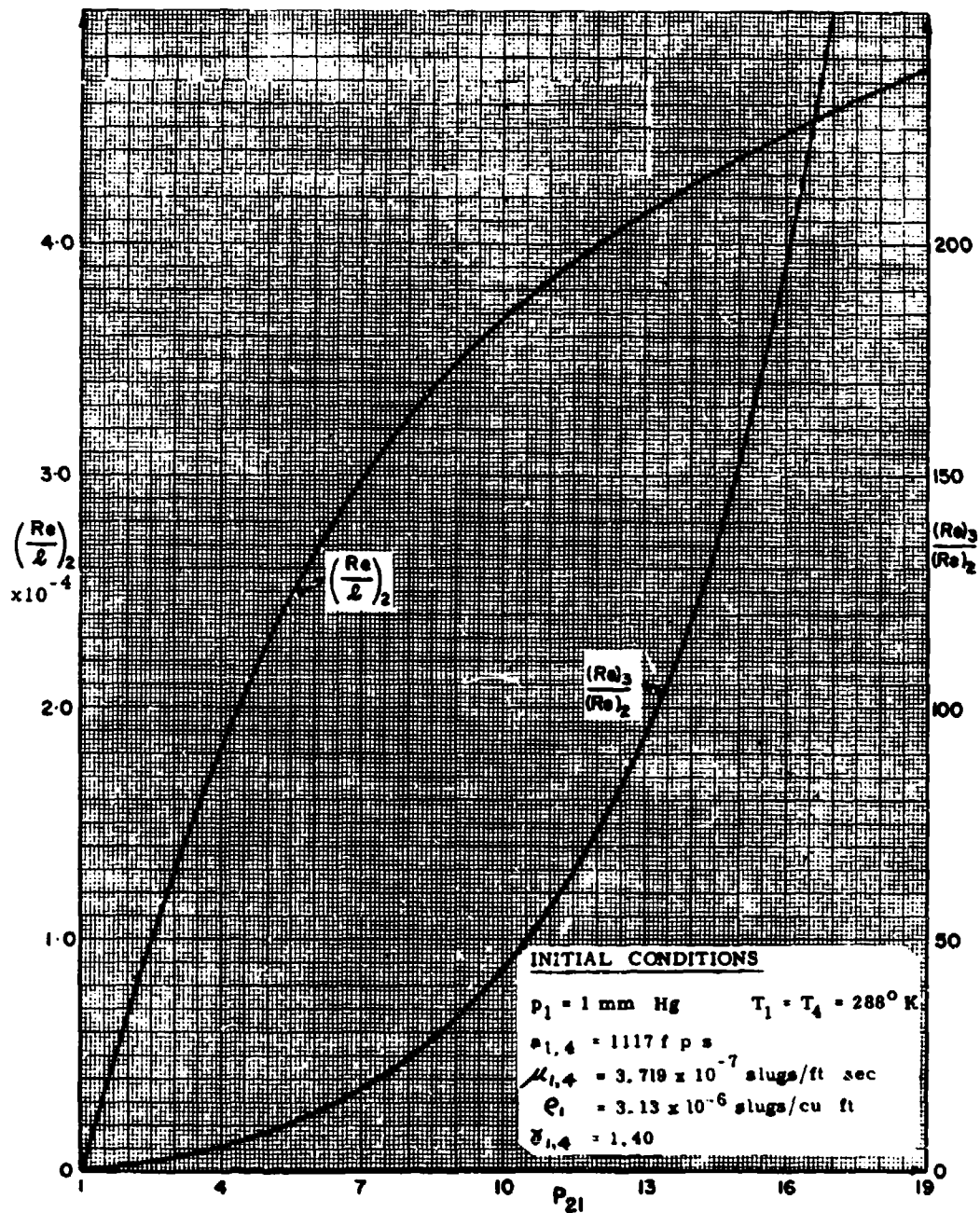


Fig. 2.3-24. Variation of Reynolds number per foot in the uniform states (2) and (3) with the shock pressure ratio (P_{21}); case air/air.

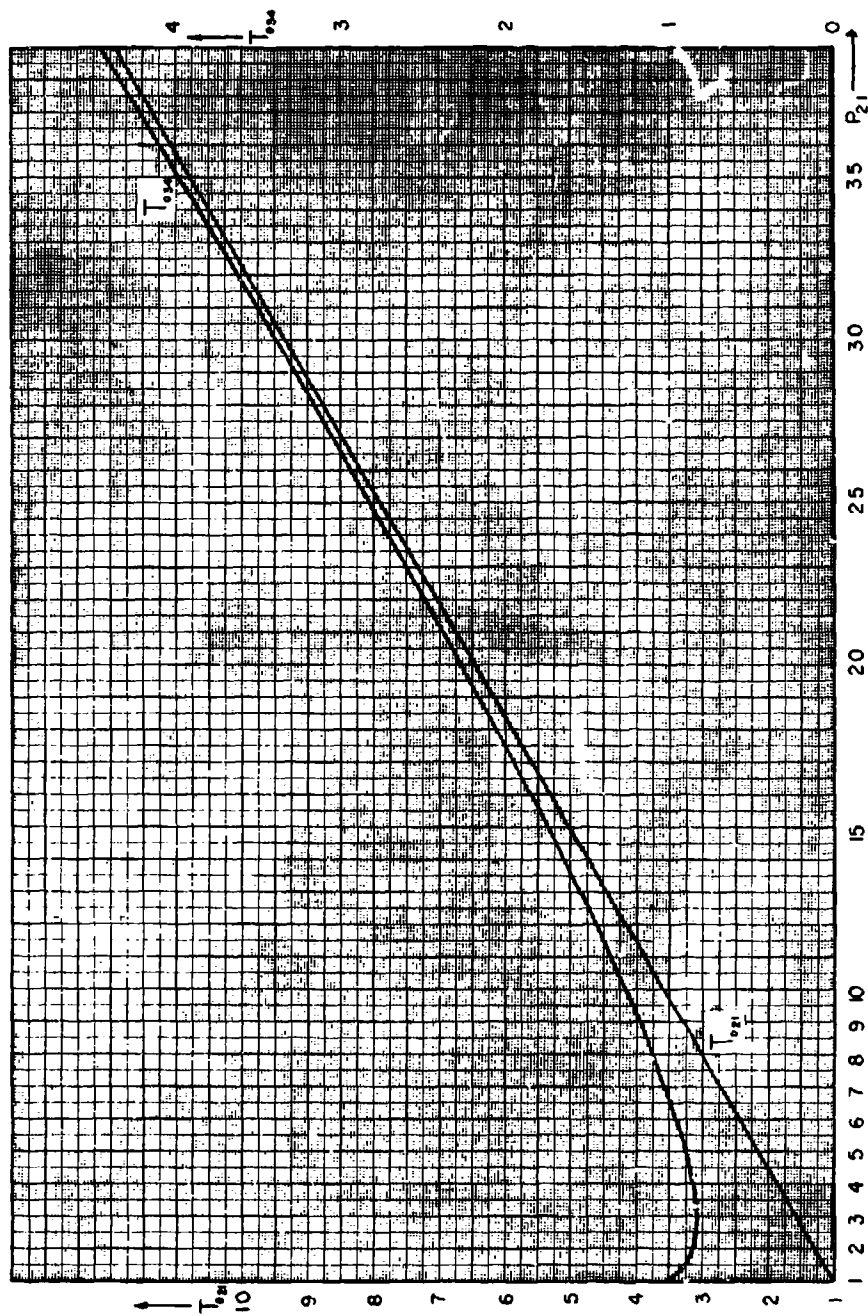


Fig. 2.3-25. Total temperature variation in uniform states (2) and (3) with shock pressure ratio (P_{21}); case air/air ($E_{14} = 1$).

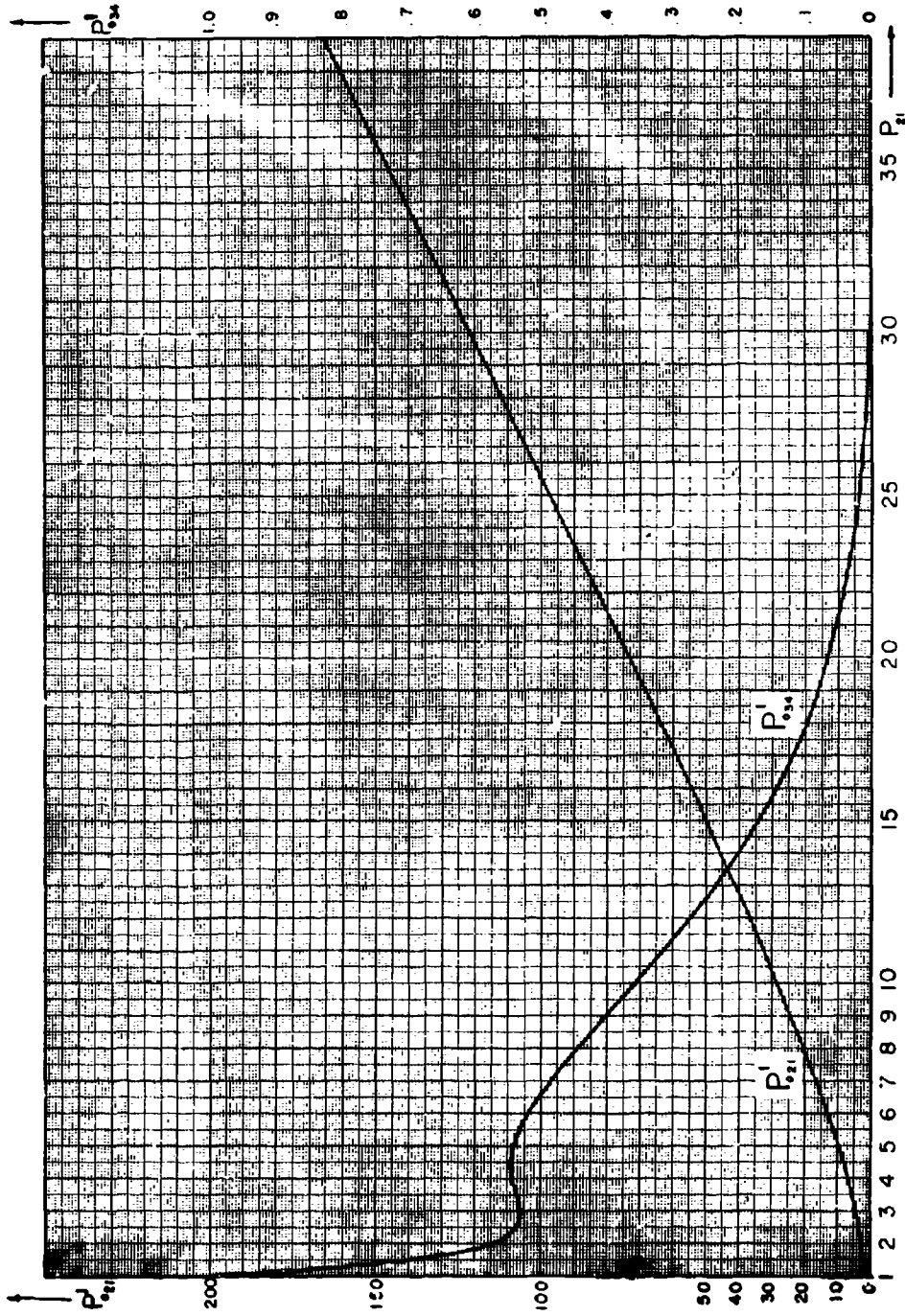


Fig. 2.3-26. Pitot pressure variation in uniform states (2) and (3) with shock pressure ratio (P_{21}); case air/air ($E_{14} = 1$).

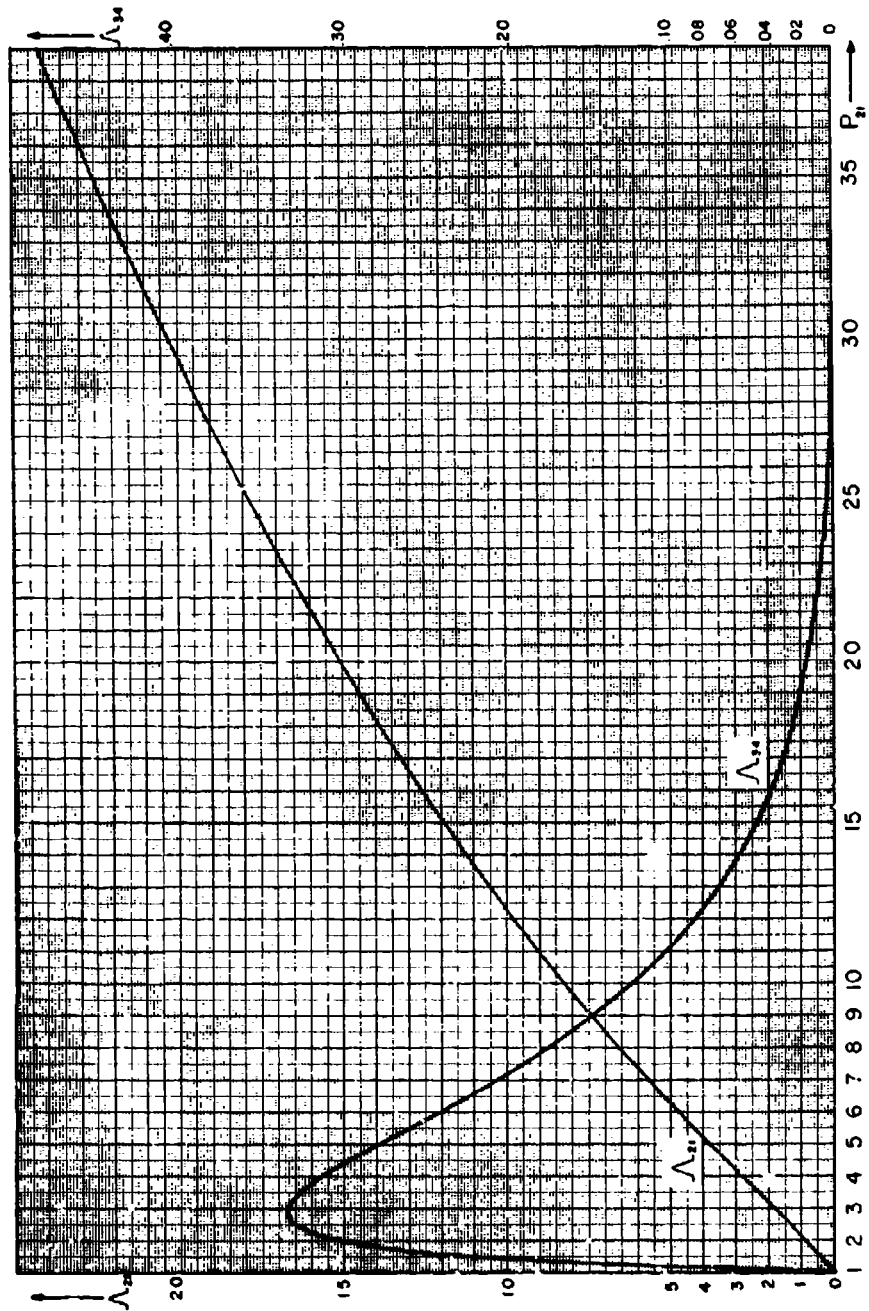


Fig. 2.3-27. Variation of mass flow ratios (A_{21} , A_{34}) in uniform states (2) and (3) with shock pressure ratio (P_{21}); case air/air ($E_{14} = 1$).

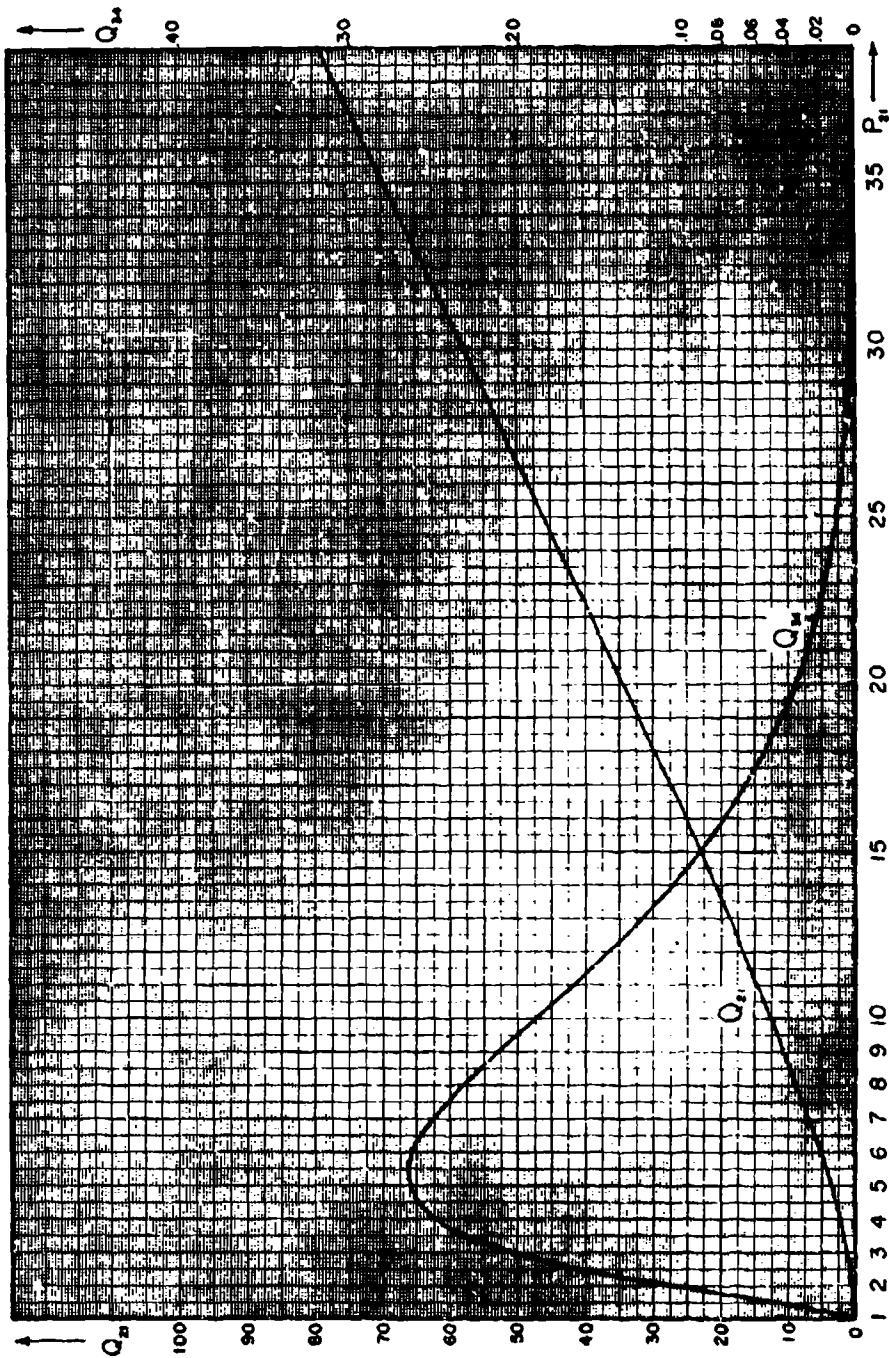
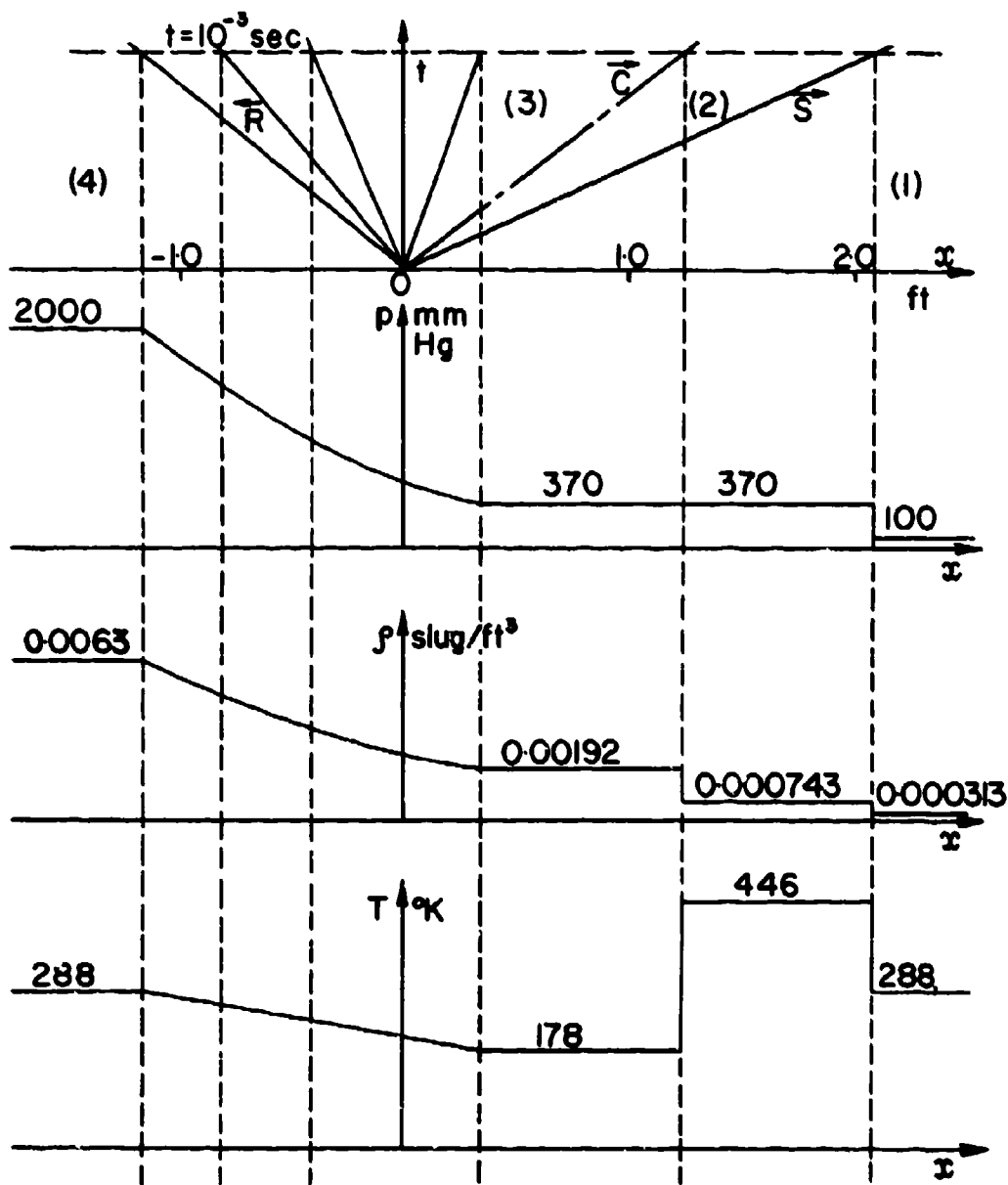


Fig. 2.3-28. Variation of dynamic pressures (Q_{21} , Q_{34}) in uniform states (2) and (3) with shock pressure ratio (P_{21}); case air/air ($E_{14} = 1$).



Initial Conditions

$t = 10^{-3}$ sec, $T = 288^\circ\text{K}$, $p = 100$ mm Hg and $P_{41} = 20$

Case Air/Air

Fig. 2.3-29a. Variation of flow properties p , ρ , and T in a shock tube.

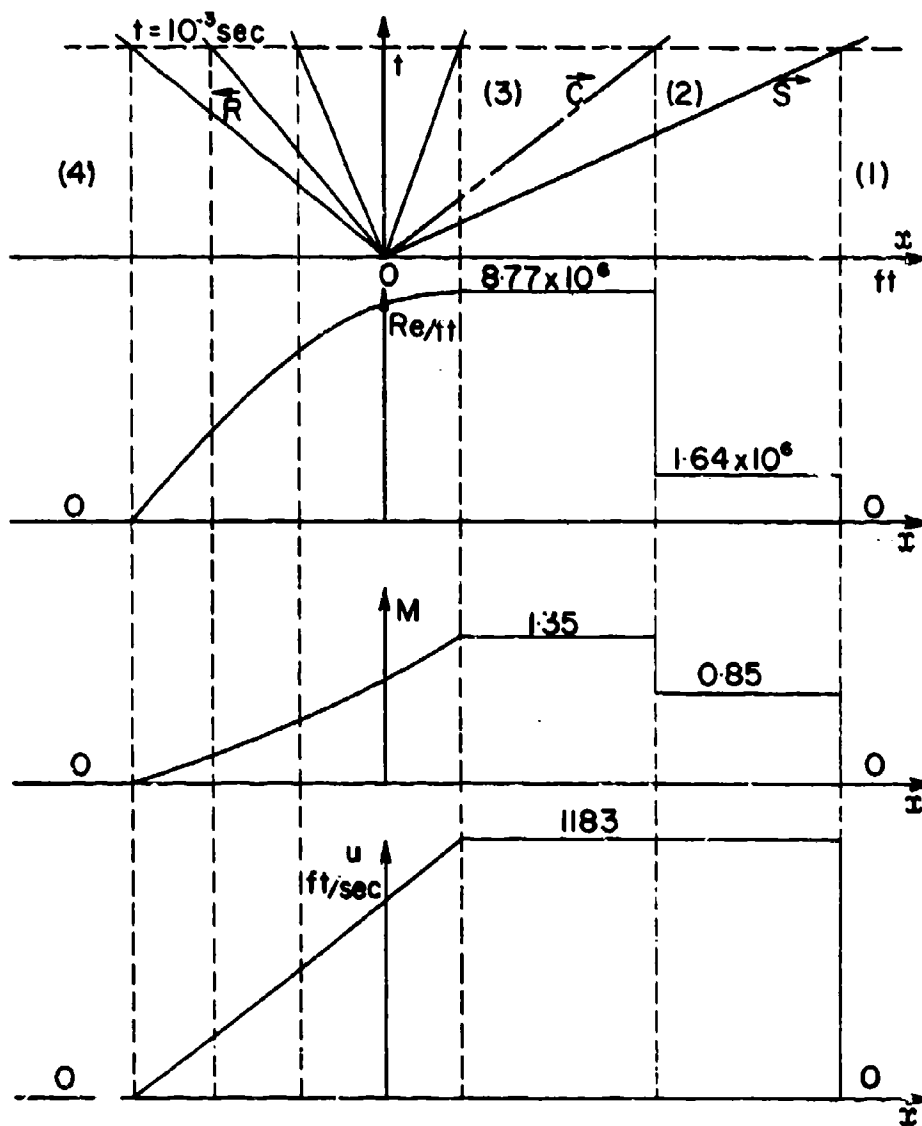


Fig. 2.3-29b. Variation of flow properties Re/ft , M , and u in a shock tube.

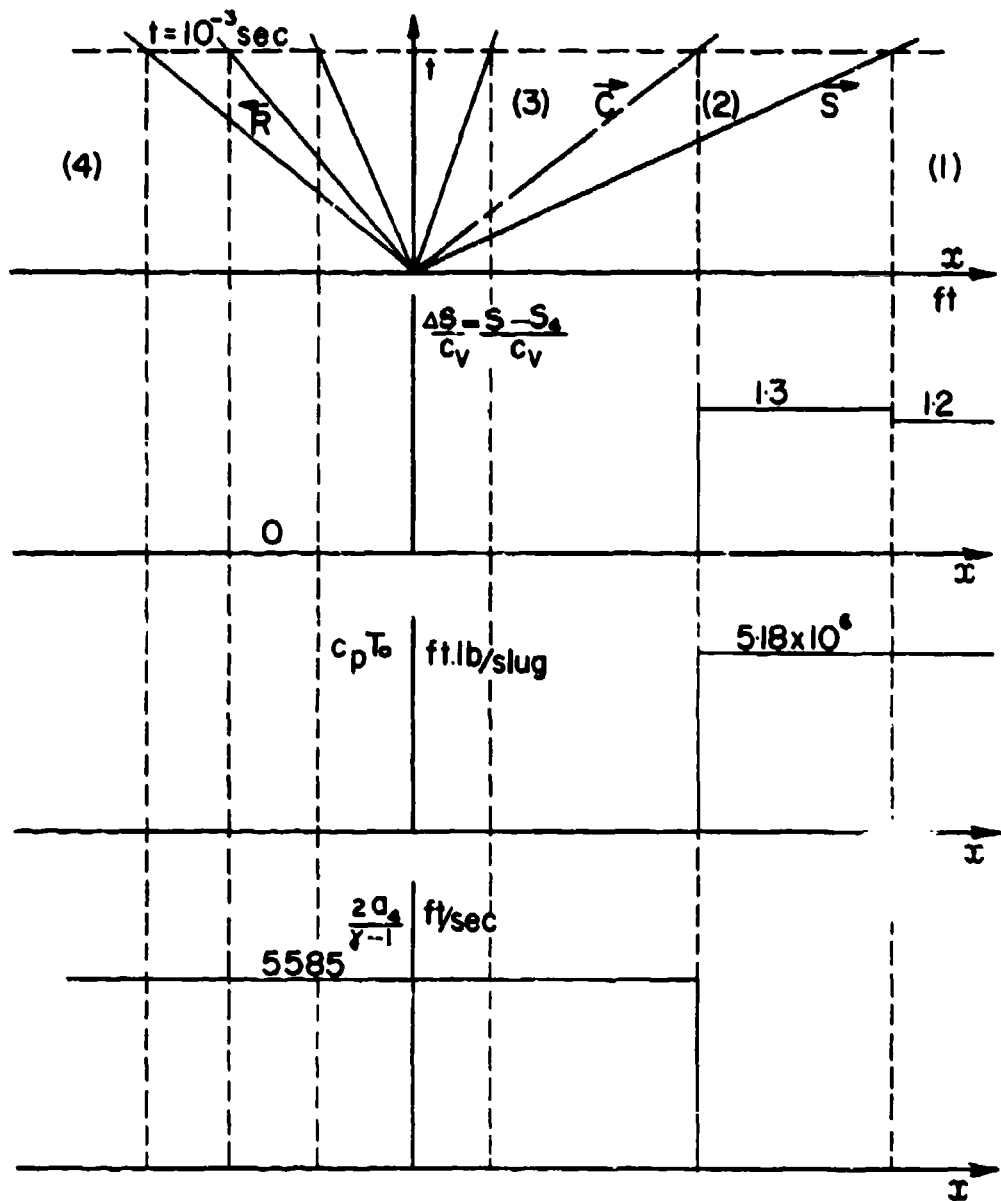


Fig. 2.3-29c. Variation of flow properties $\frac{\Delta S}{C_v}$, $c_p T_0$, and $\frac{2a_4}{\gamma - 1}$ in a shock tube.

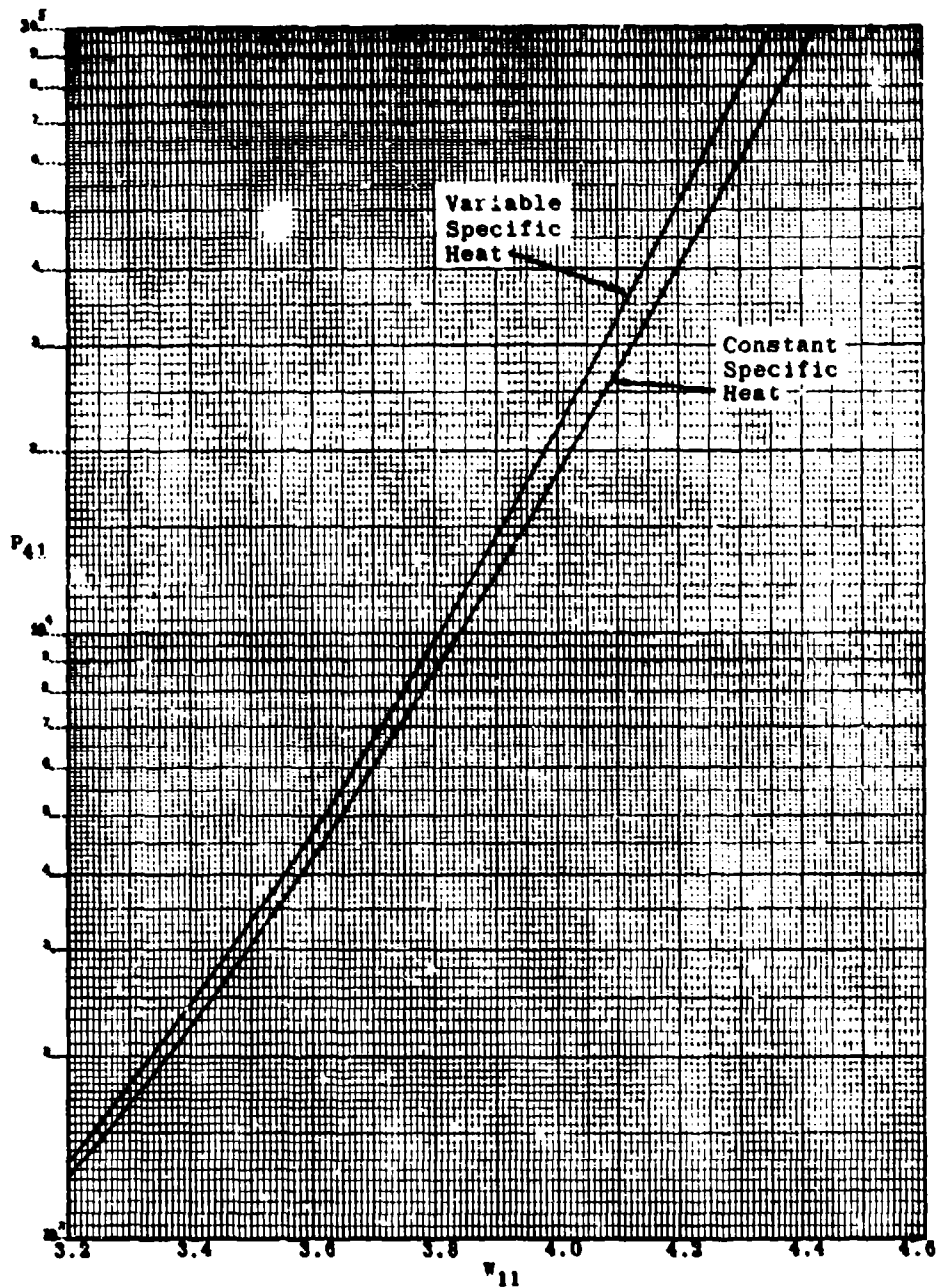


Fig. 2.3-30. Variation of shock wave Mach number (W_{11}) with diaphragm pressure ratio (P_{41}) for constant and variable specific heats; case air/air (vibrational excitation only).

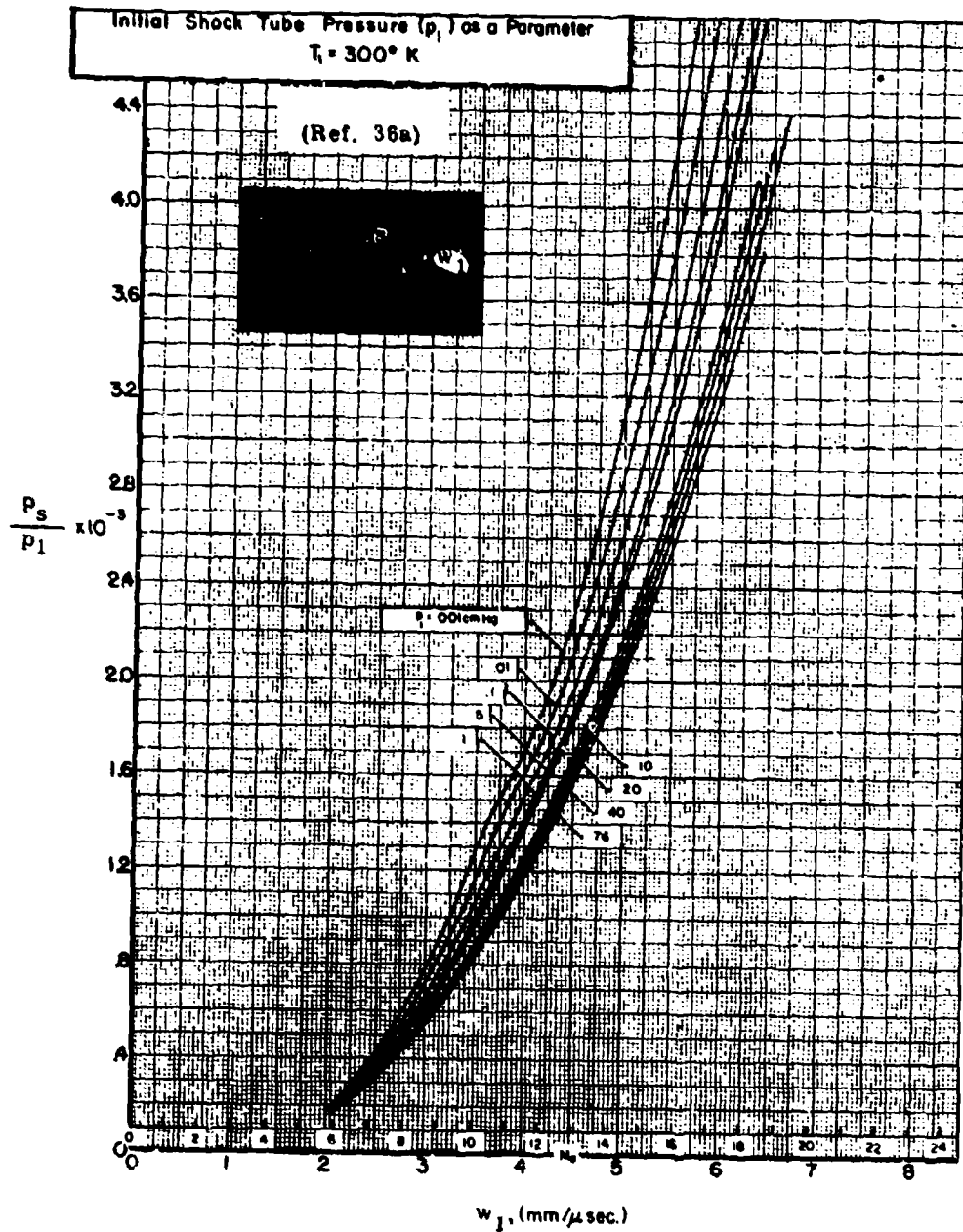


Fig. 2.3-31. Pressure ratio (p_s/p_1) for standing normal shock vs shock velocity (w_1), equilibrium air.

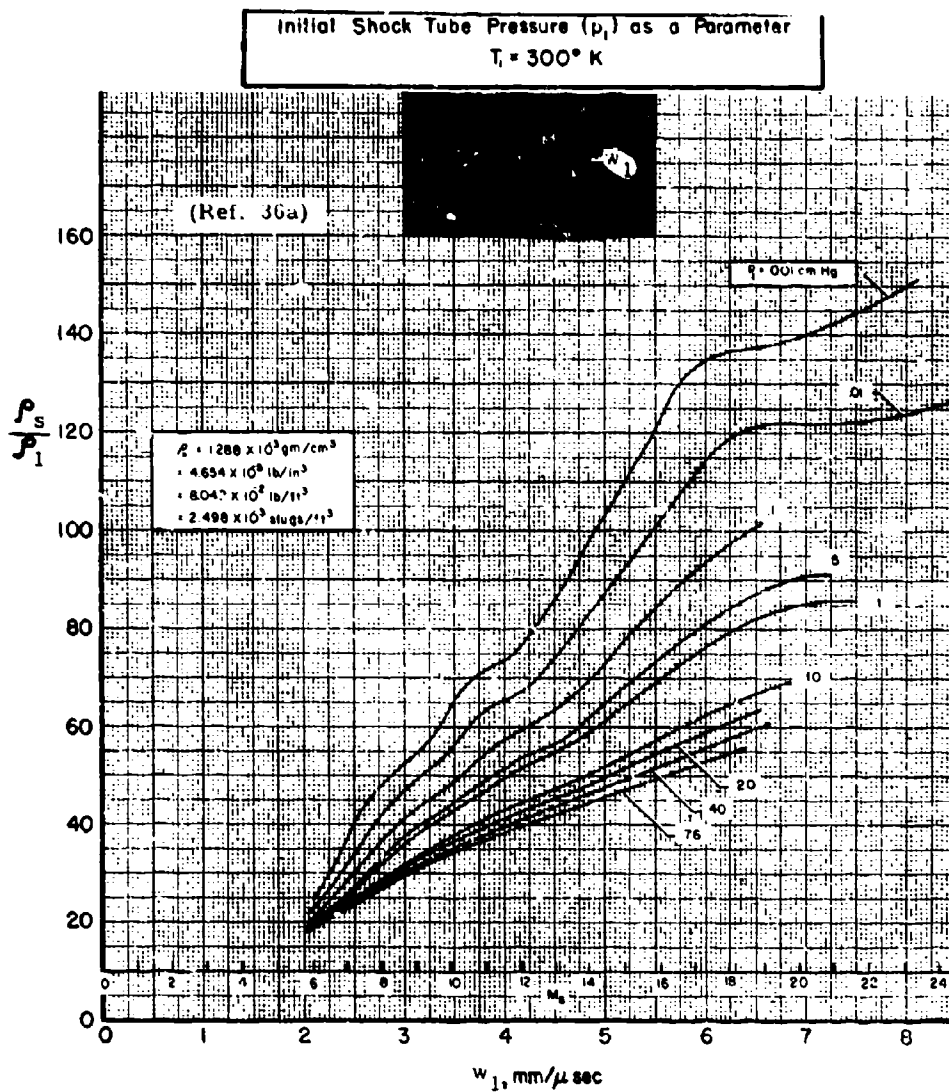


Fig. 2.3-32. Density ratio (ρ_s/ρ_1) for standing normal shock vs shock velocity (w_1), equilibrium air.

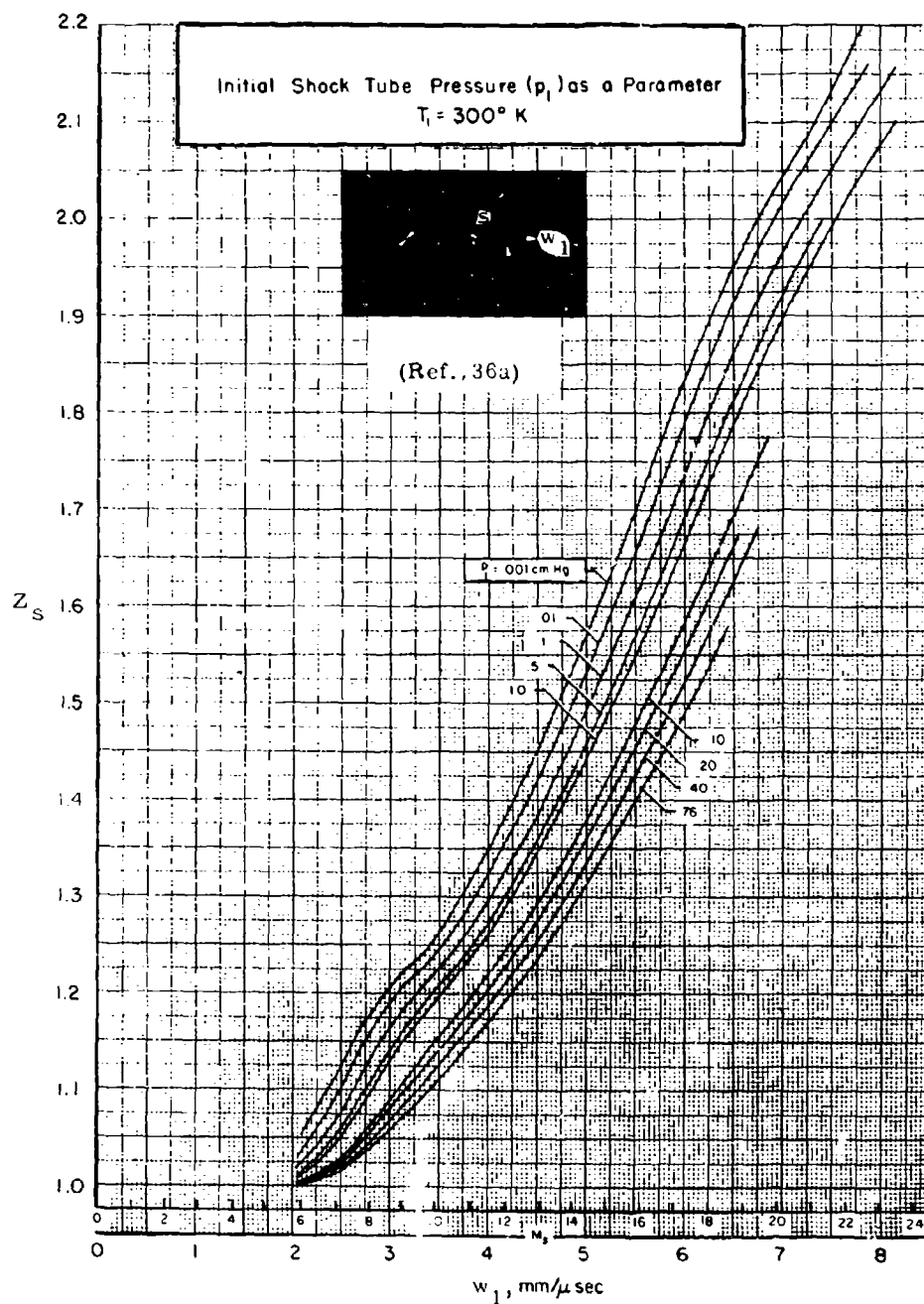


Fig. 2.3-33. Compressibility (Z_s) for standing normal shock vs shock velocity (w_1), equilibrium air.

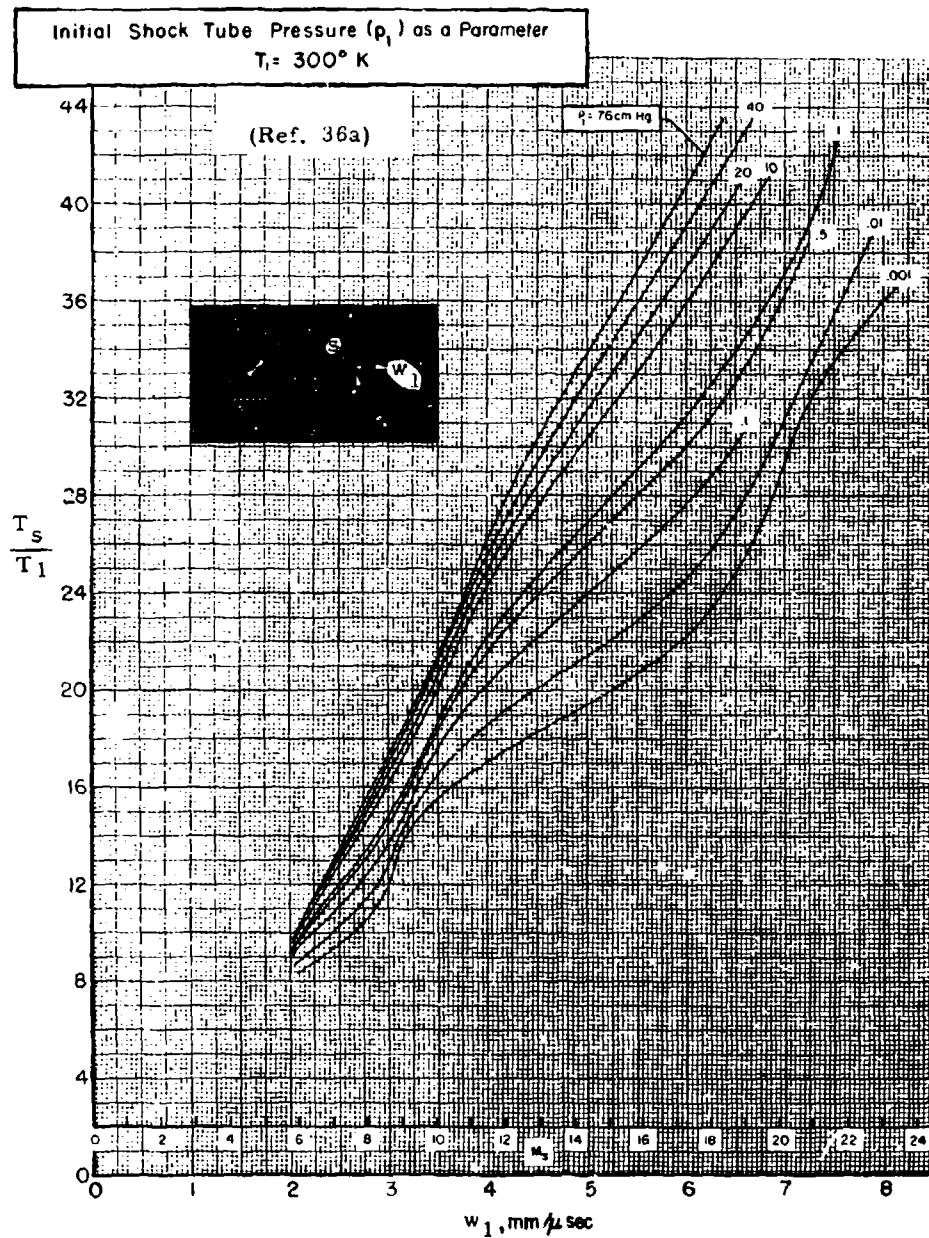


Fig. 2.3-34. Temperature ratio (T_s/T_1) for standing normal shock vs shock velocity (w_1), equilibrium air.

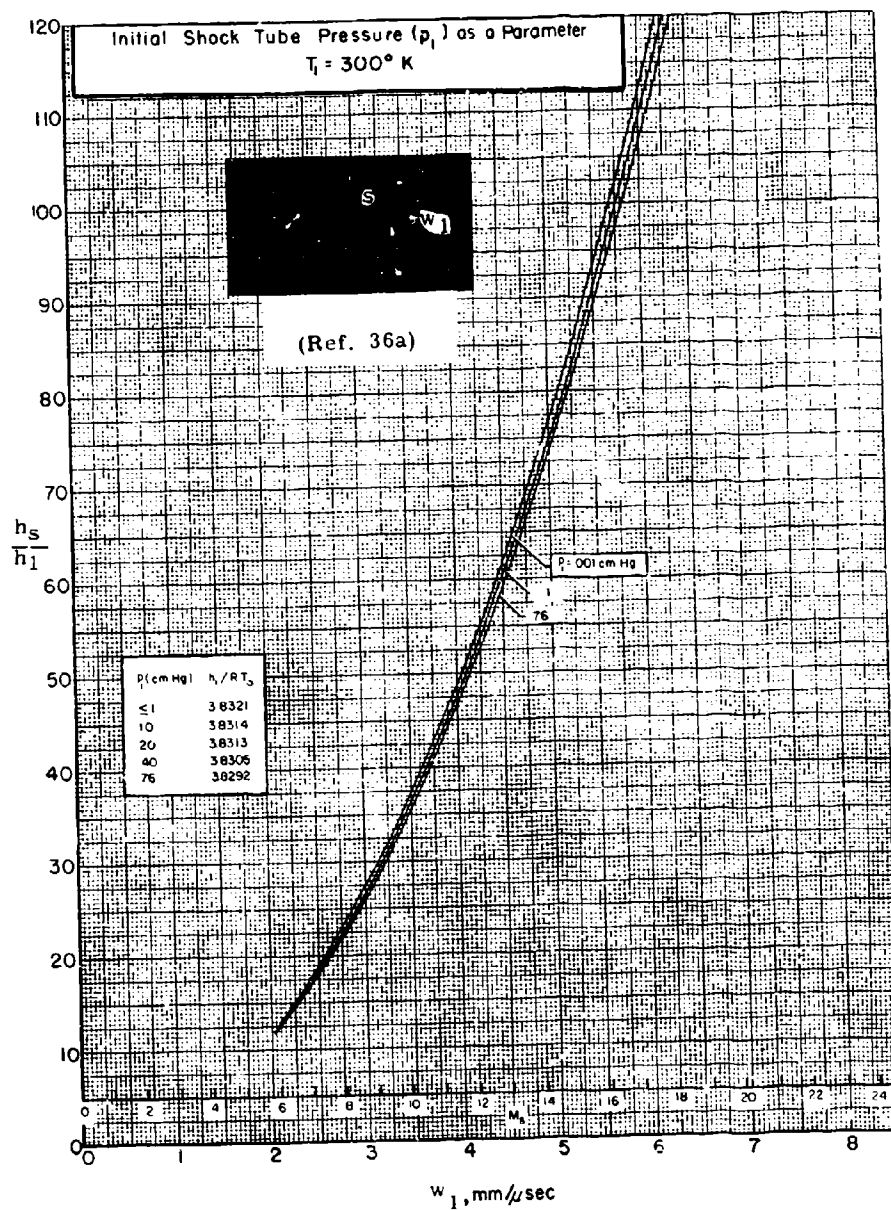


Fig. 2.3-35. Enthalpy ratio (h_s/h_1) for standing normal shock vs shock velocity (w_1), equilibrium air.

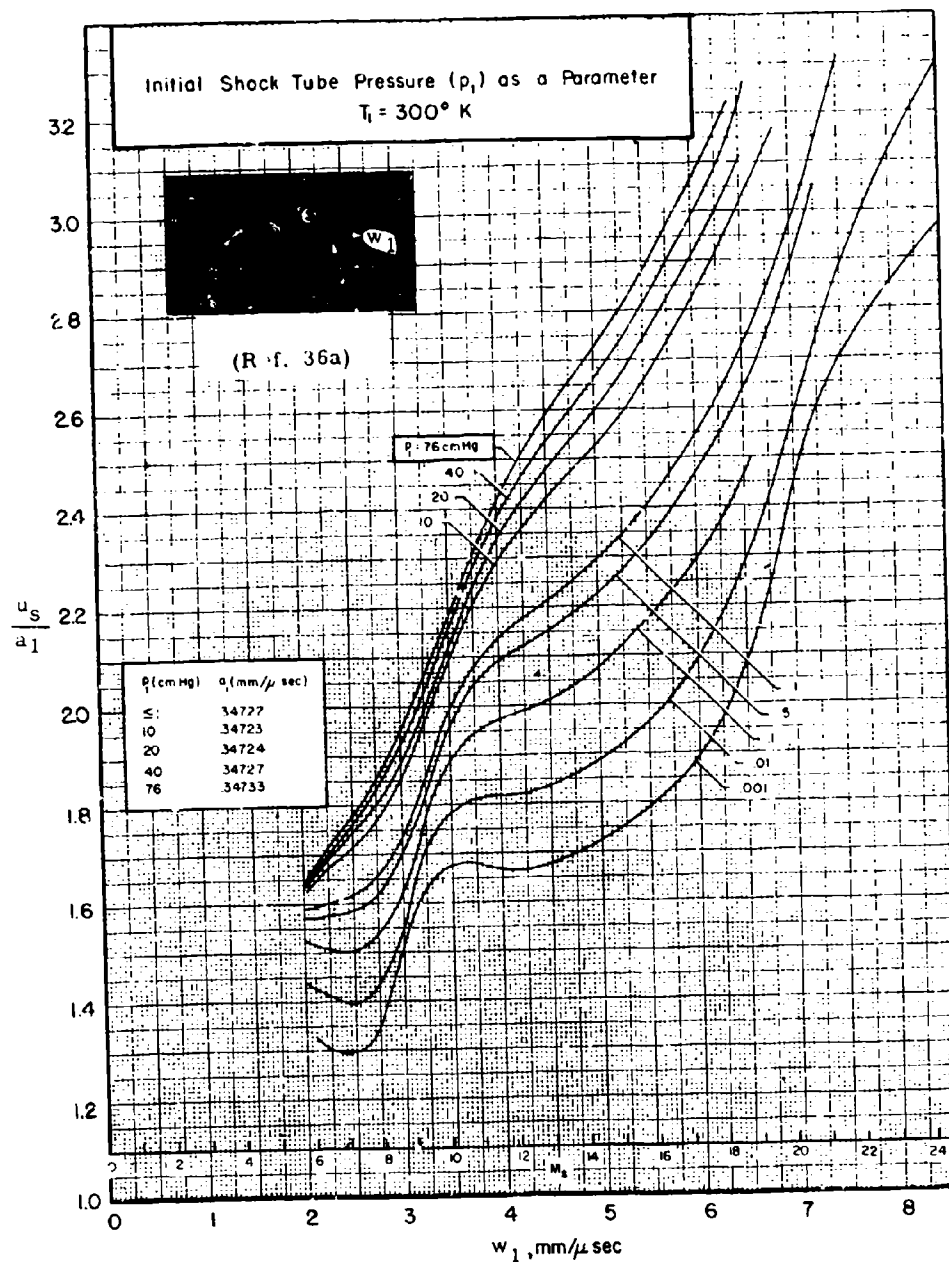


Fig. 2.3-36. Velocity ratio (u_s/a_1) across standing normal bow shock vs shock velocity (w_1), equilibrium air.

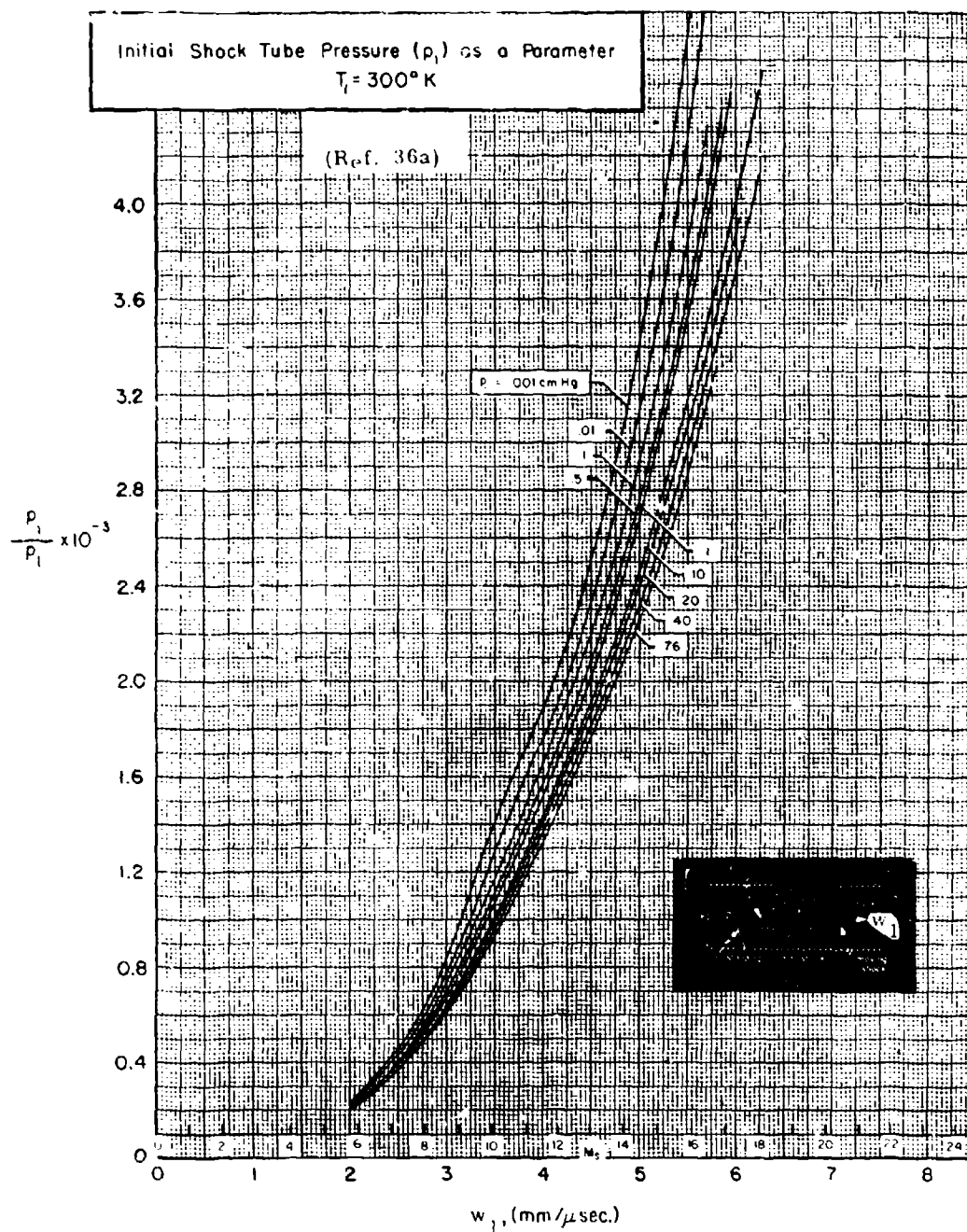


Fig. 2.3-37. Pressure ratio (p_t/p_1) at stagnation point vs shock velocity (w_1), equilibrium air.

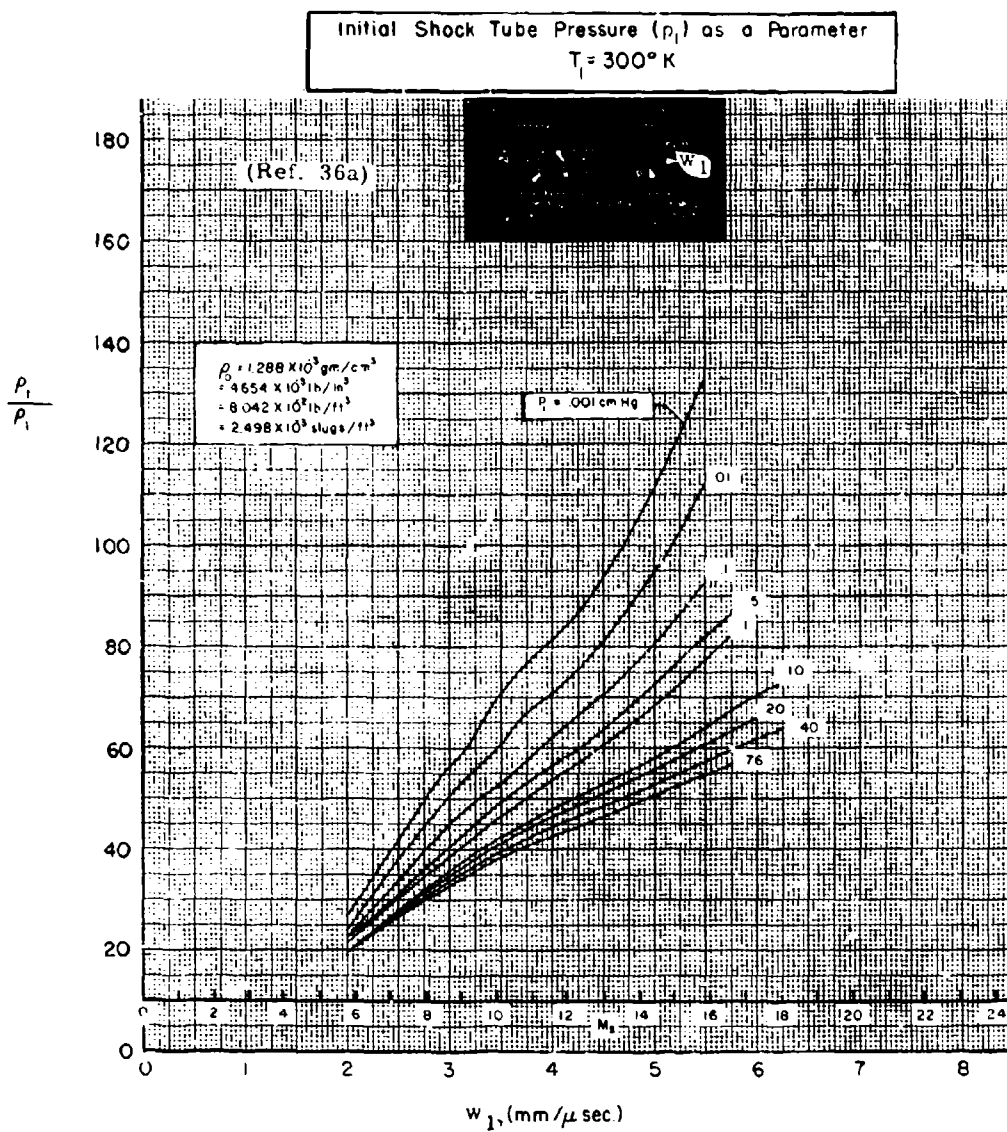


Fig. 2.3-38. Density ratio (ρ_t/ρ_1) at stagnation point vs shock velocity (w_1), equilibrium air.

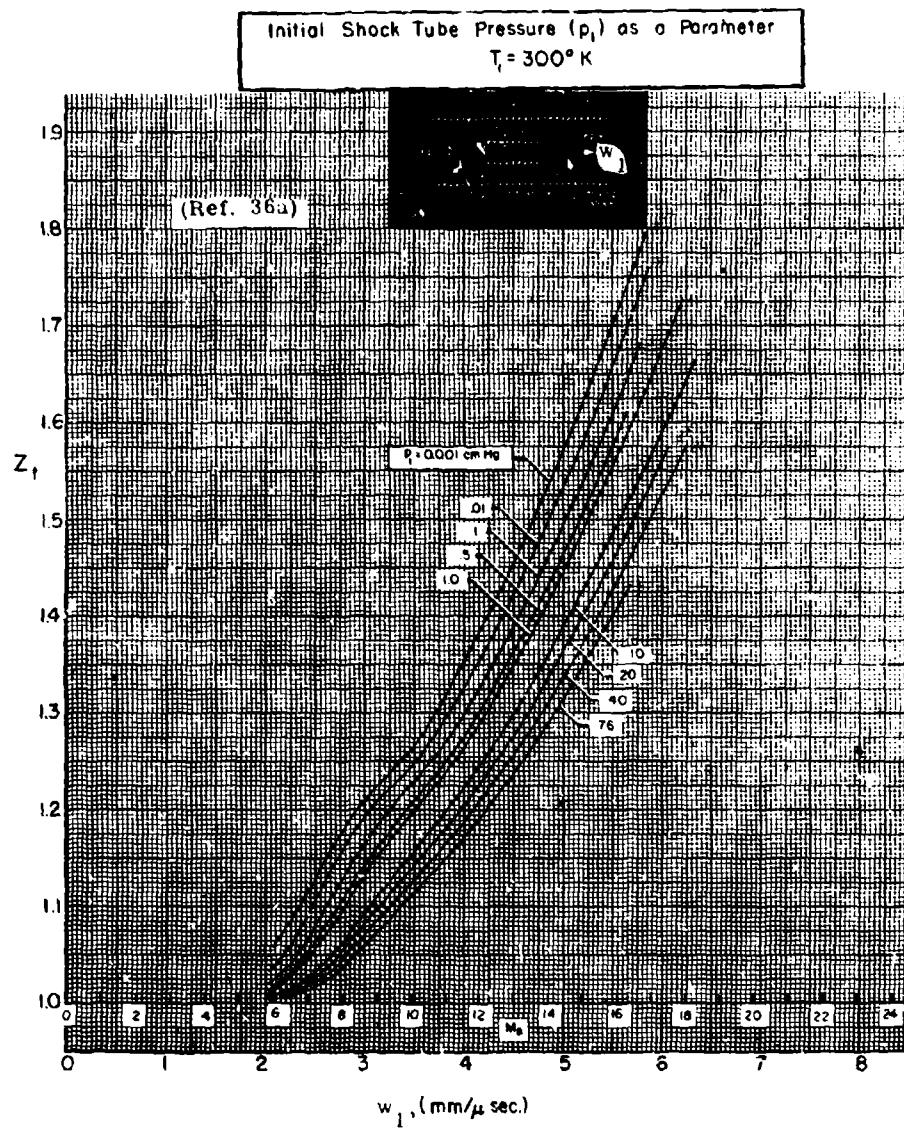


Fig. 2.3-39. Compressibility (Z_t) at stagnation point vs shock velocity (w_1), equilibrium air.

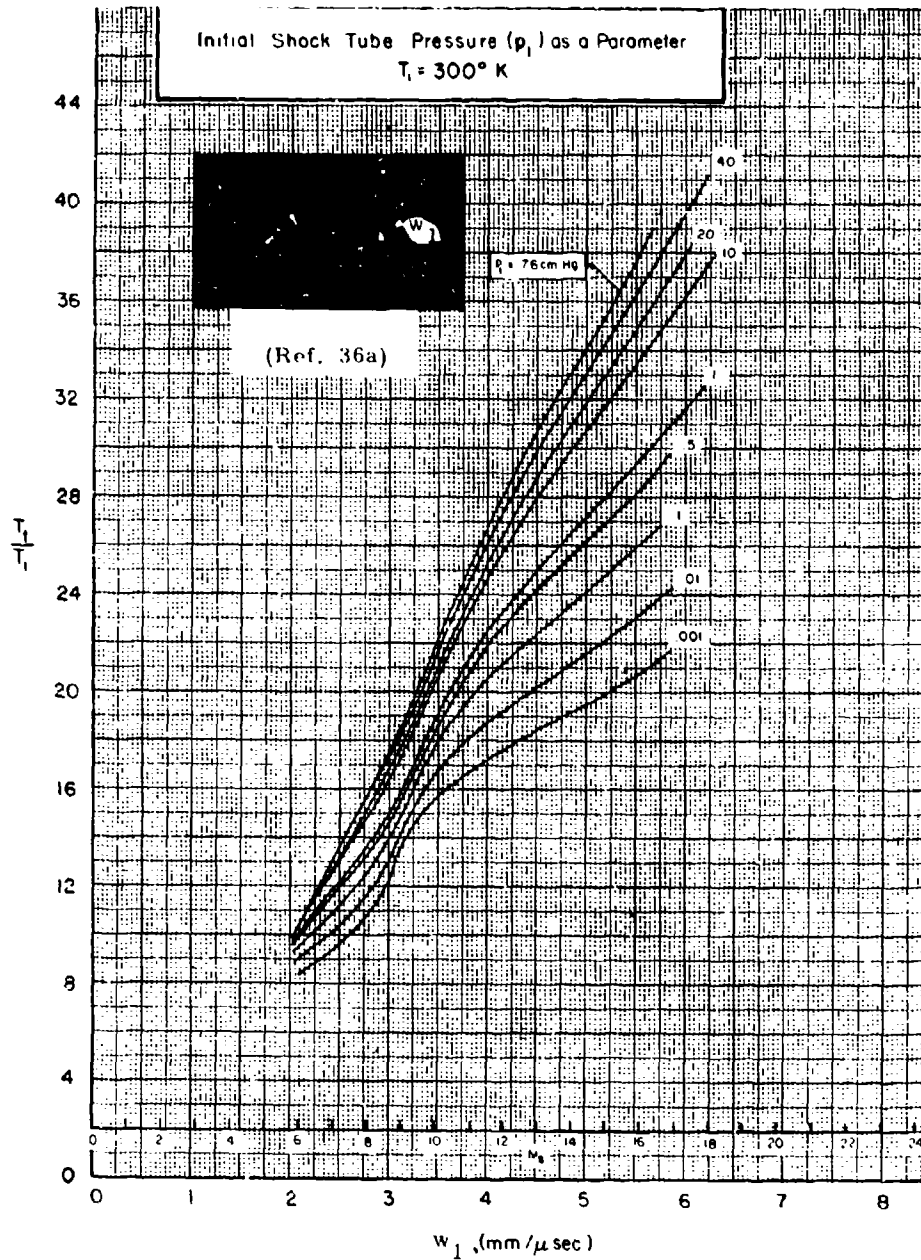


Fig. 2.3-40. Temperature ratio (T_t/T_1) at stagnation point vs shock velocity (w_1), equilibrium air.

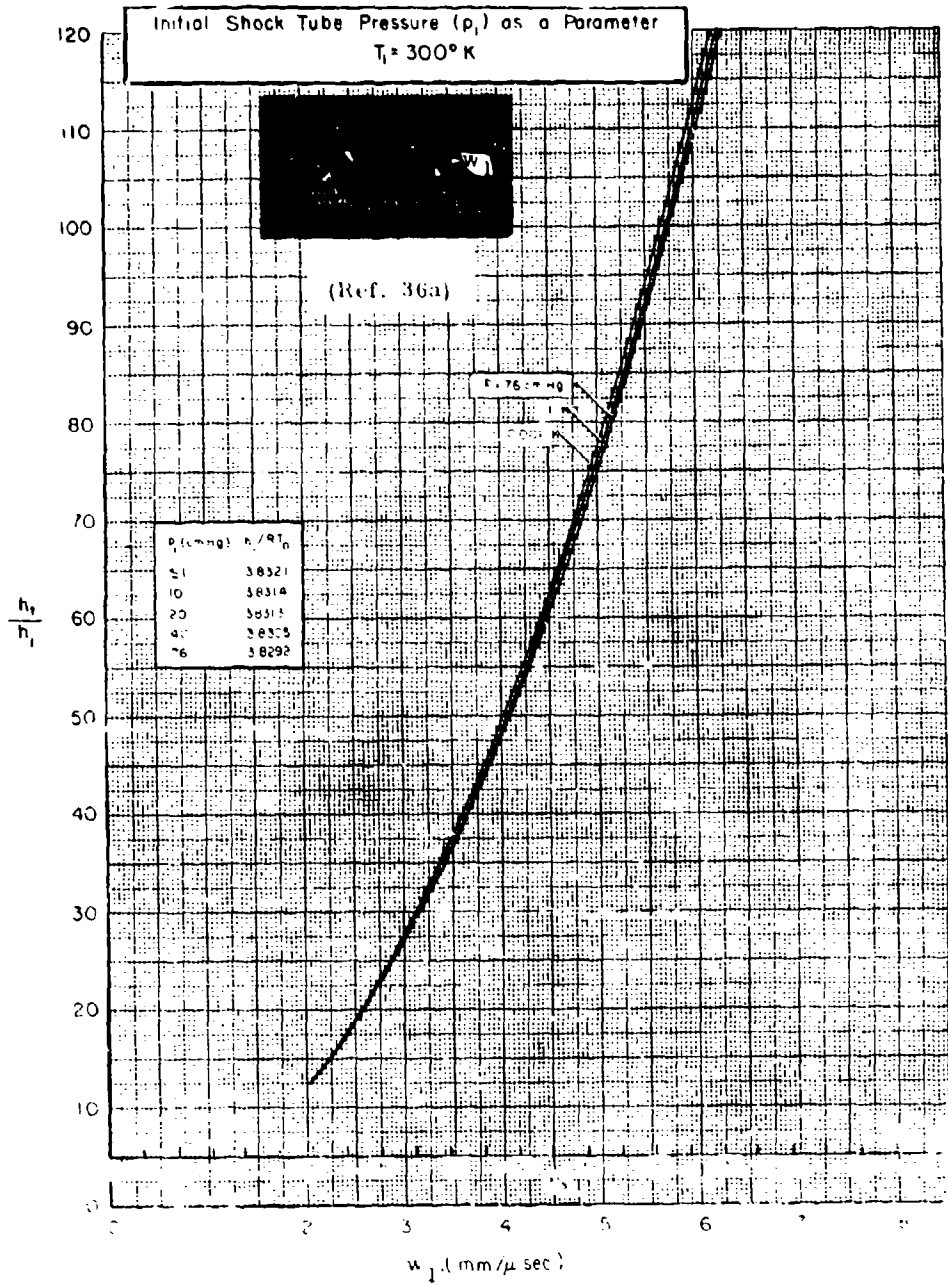


Fig. 2.3-41. Enthalpy ratio (h_2/h_1) at stagnation point vs shock velocity (w_1), equilibrium air.

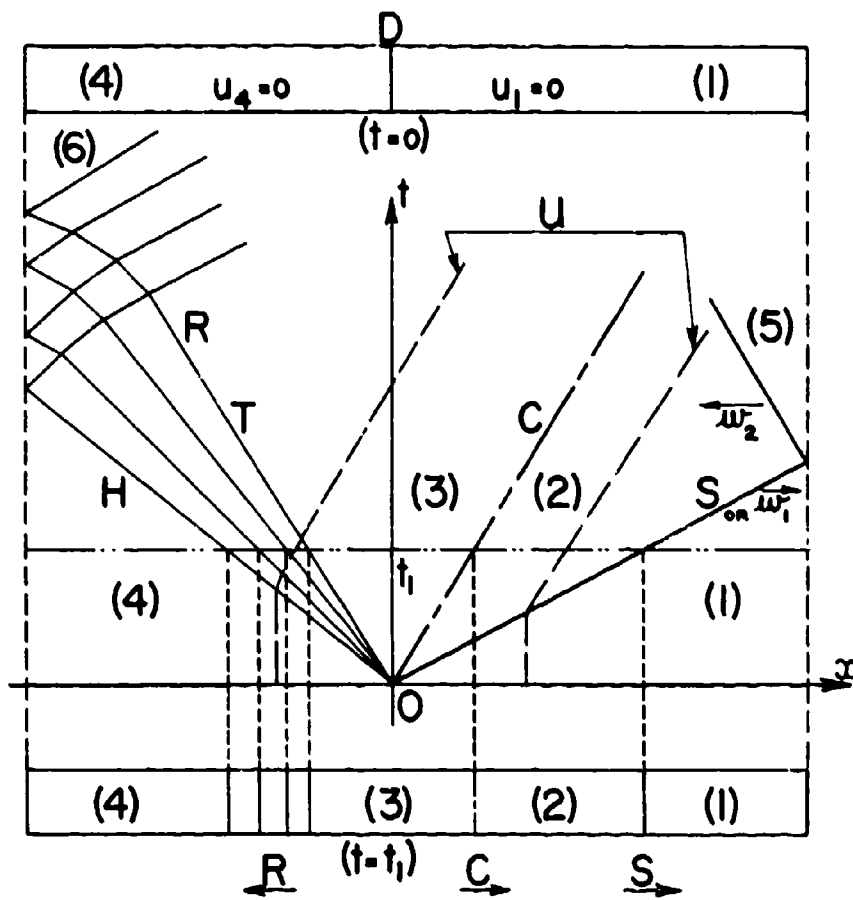


Fig. 2.4-1. Normal reflection of a shock wave and rarefaction wave.

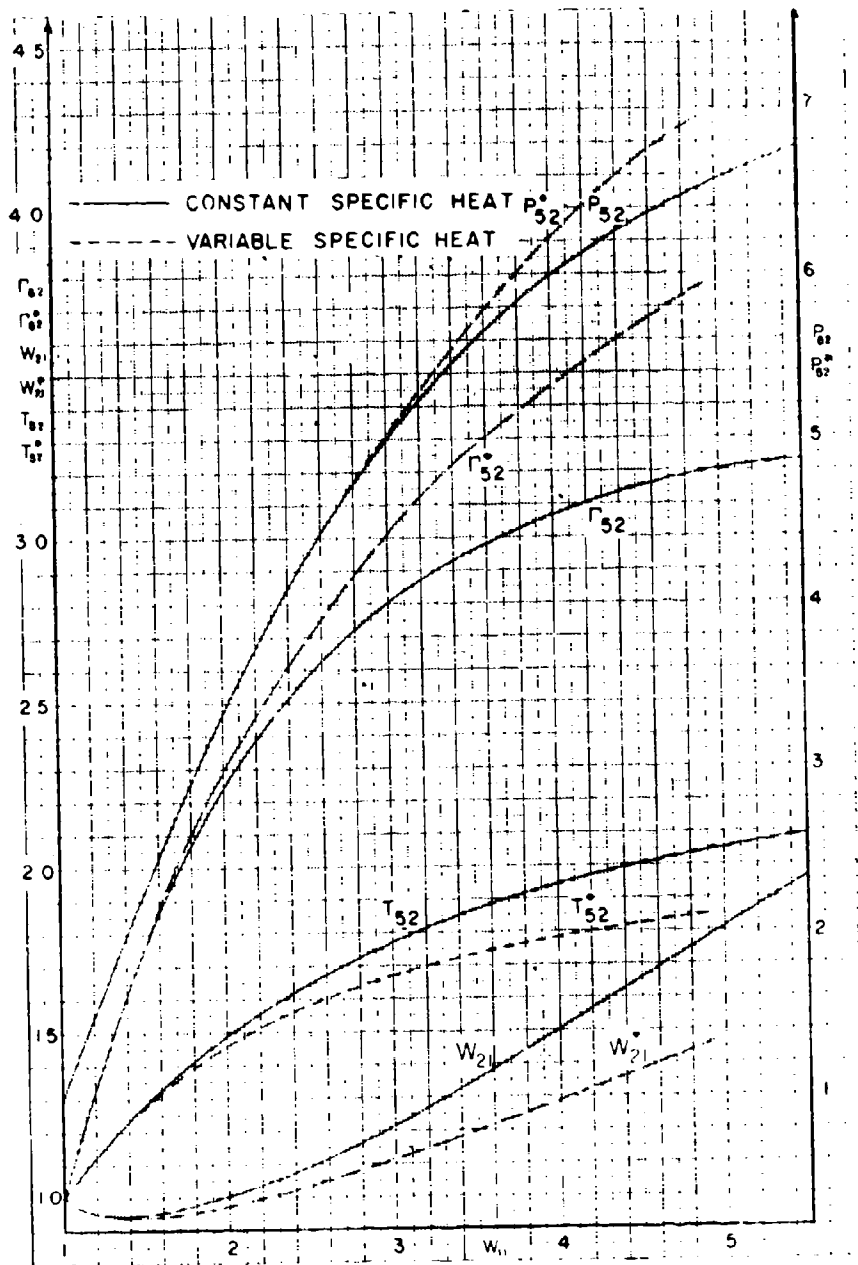


FIG. 2.4-2. Variations of the flow parameters in air behind a normal reflected shock wave with the incident shock wave Mach number (W_{11}) (vibrational excitation only).

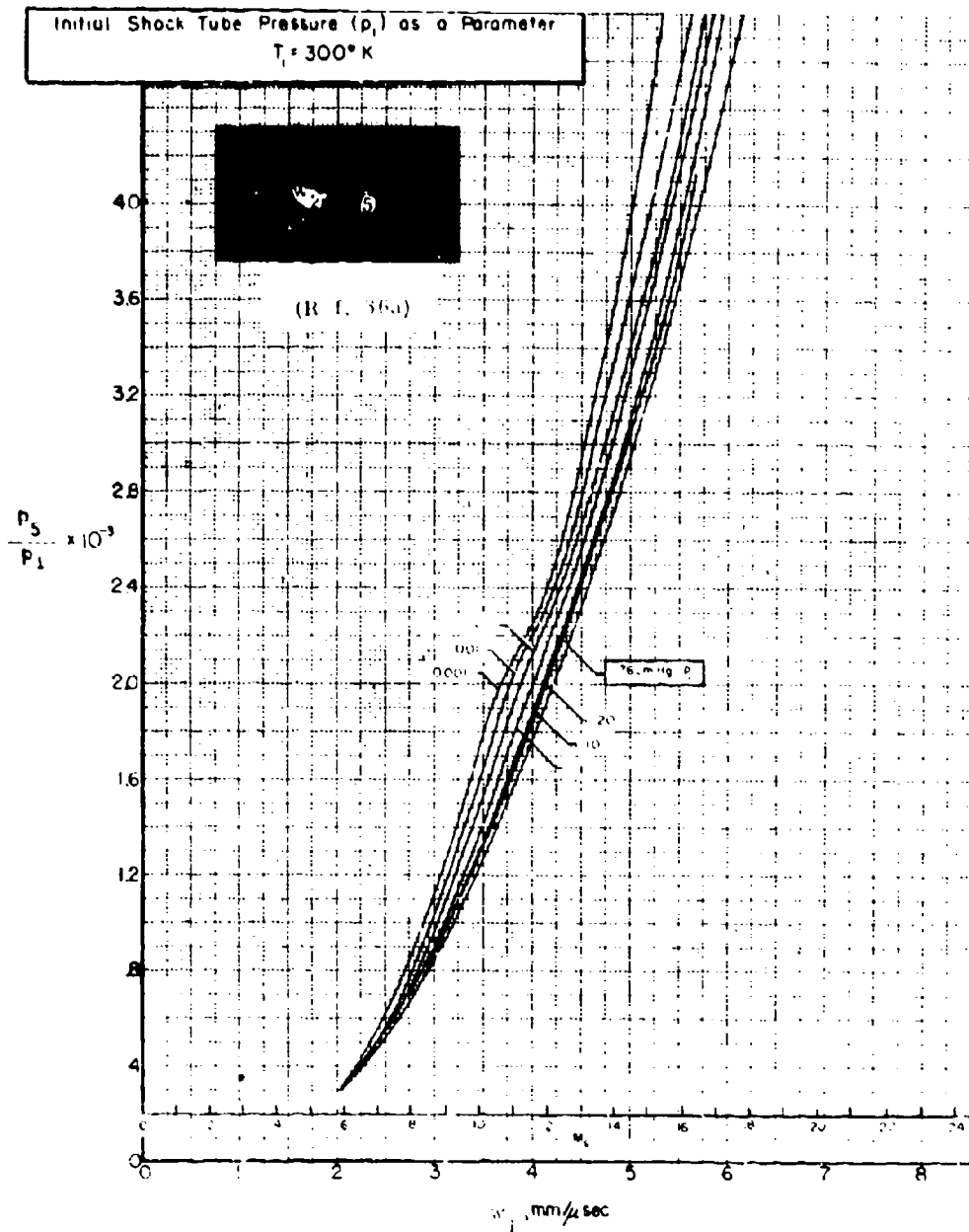


Fig. 2.4-3. Pressure ratio (p_5/p_1) for reflected normal shock vs shock velocity (w_1), equilibrium air.

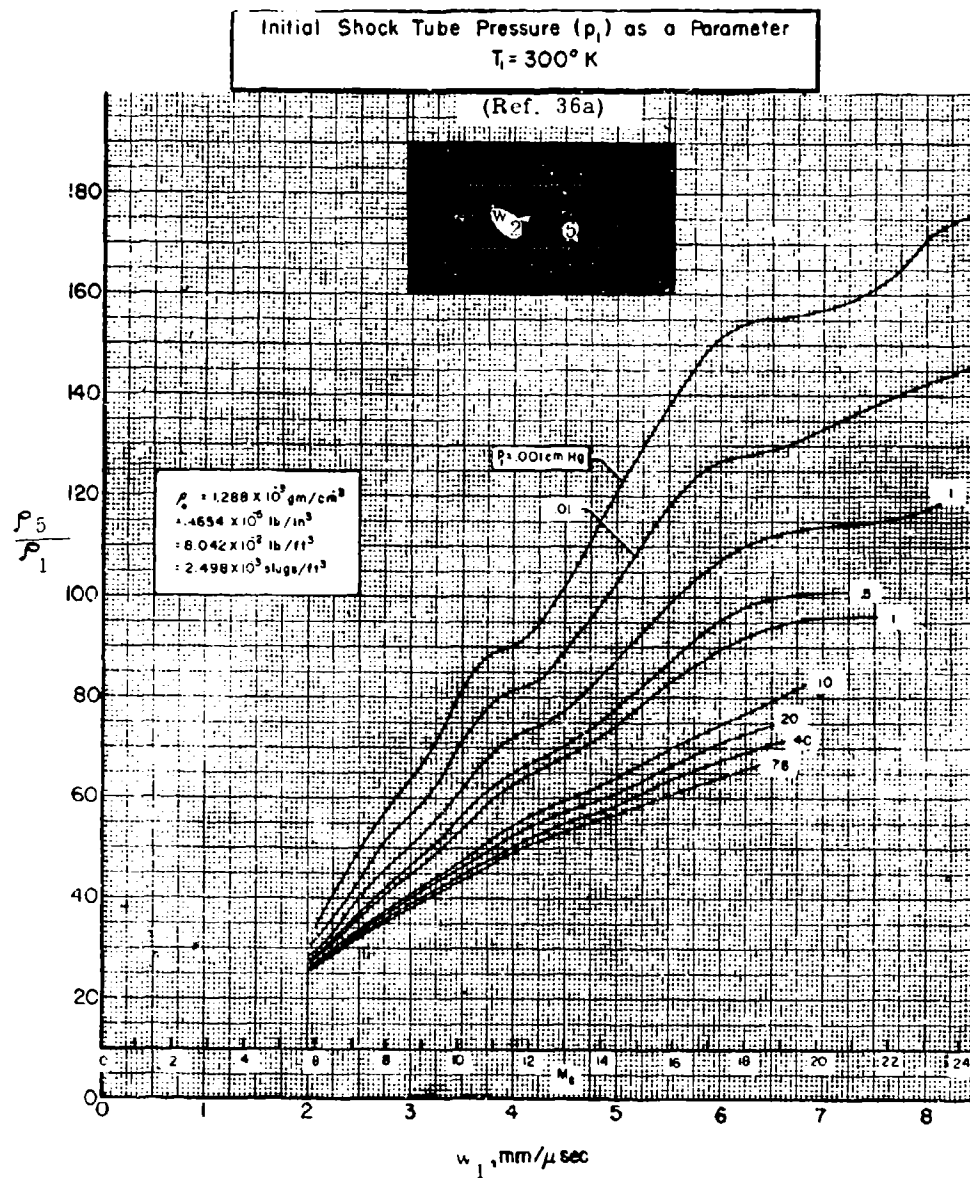


Fig. 2.4-4. Density ratio (ρ_5/ρ_1) for reflected normal shock vs shock velocity (w_1), equilibrium air.

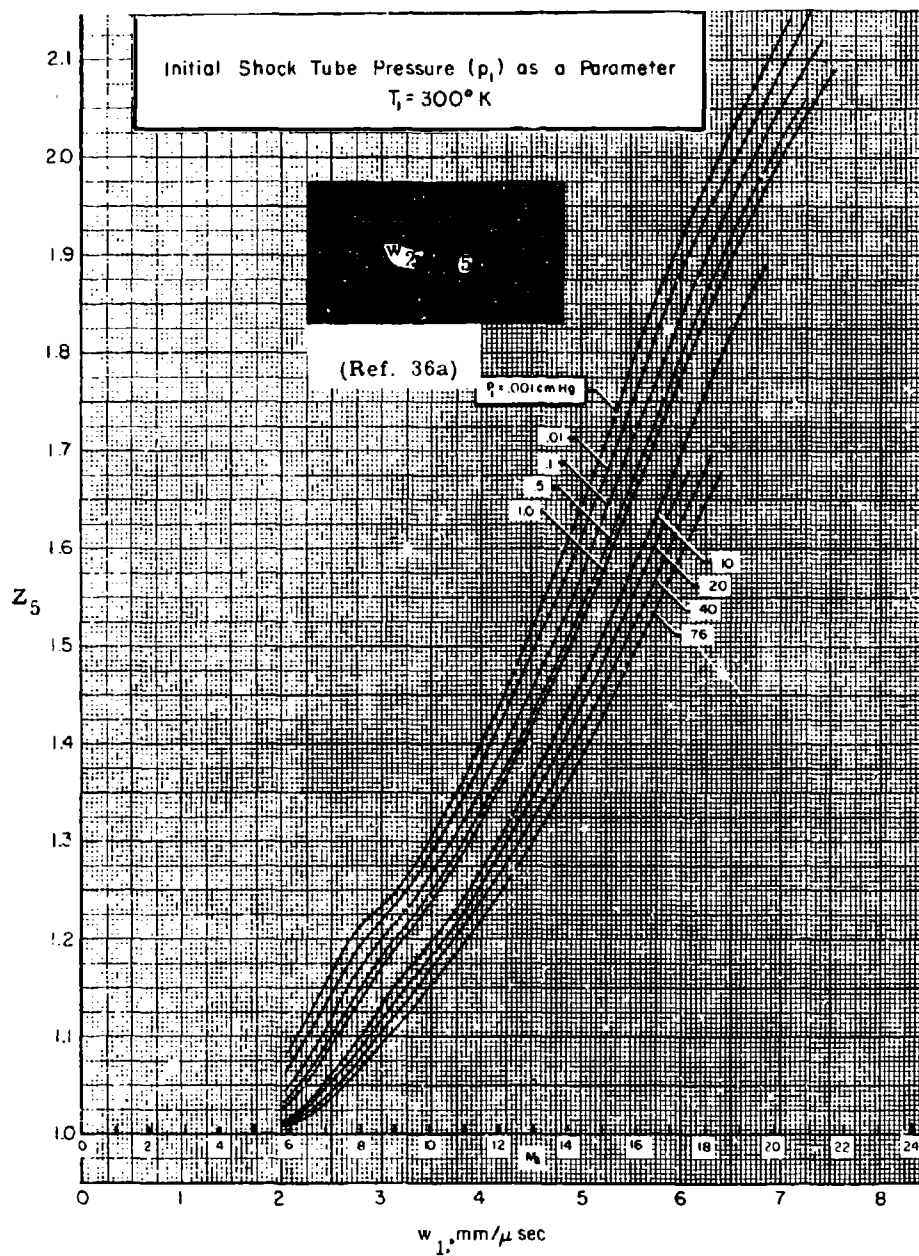


Fig. 2.4-5. Compressibility (Z_5) for reflected normal shock vs shock velocity (w_1), equilibrium air.

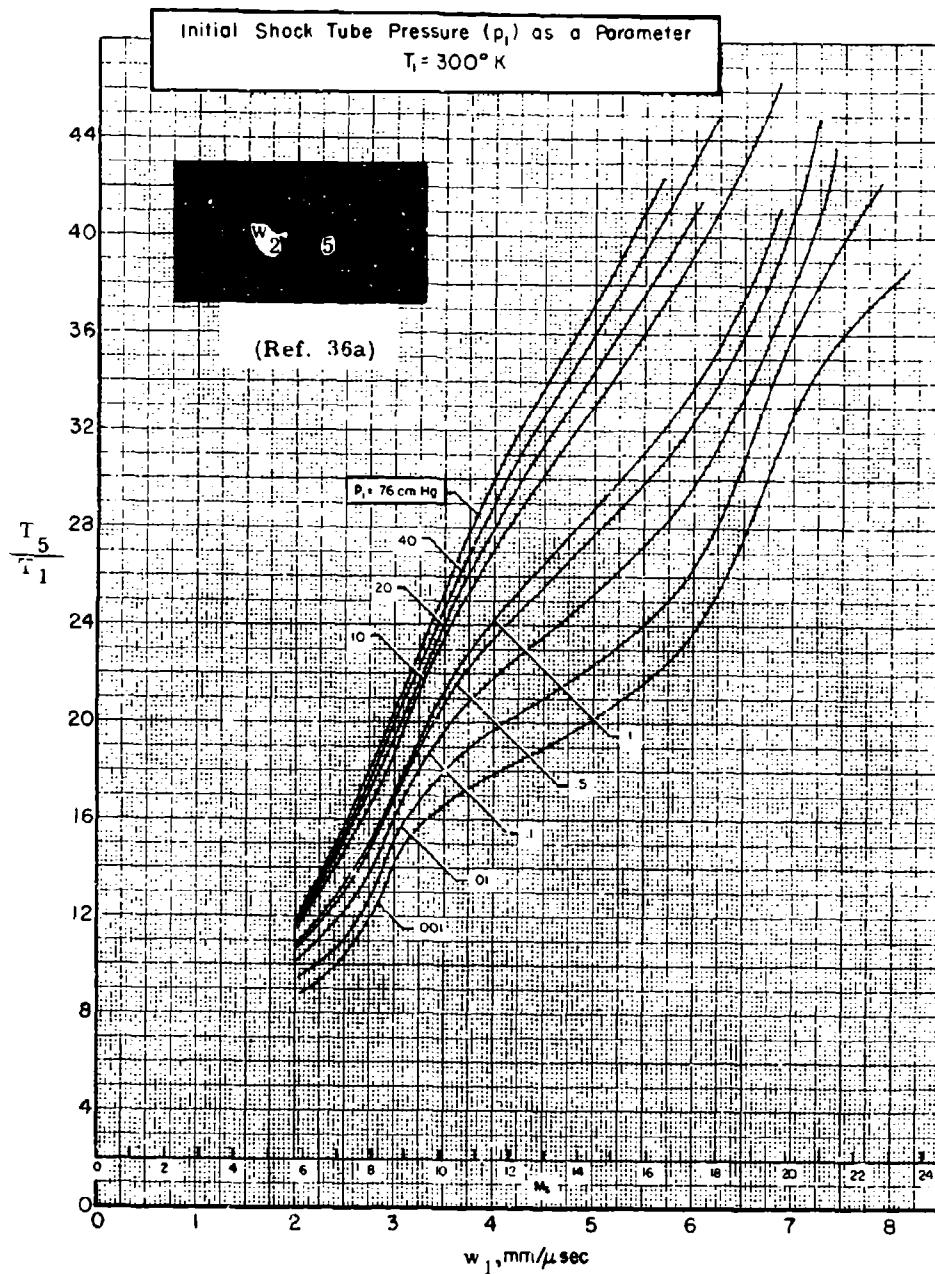


Fig. 2.4-6. Temperature ratio (T_5/T_1) for reflected normal shock vs shock velocity (w_1), equilibrium air.

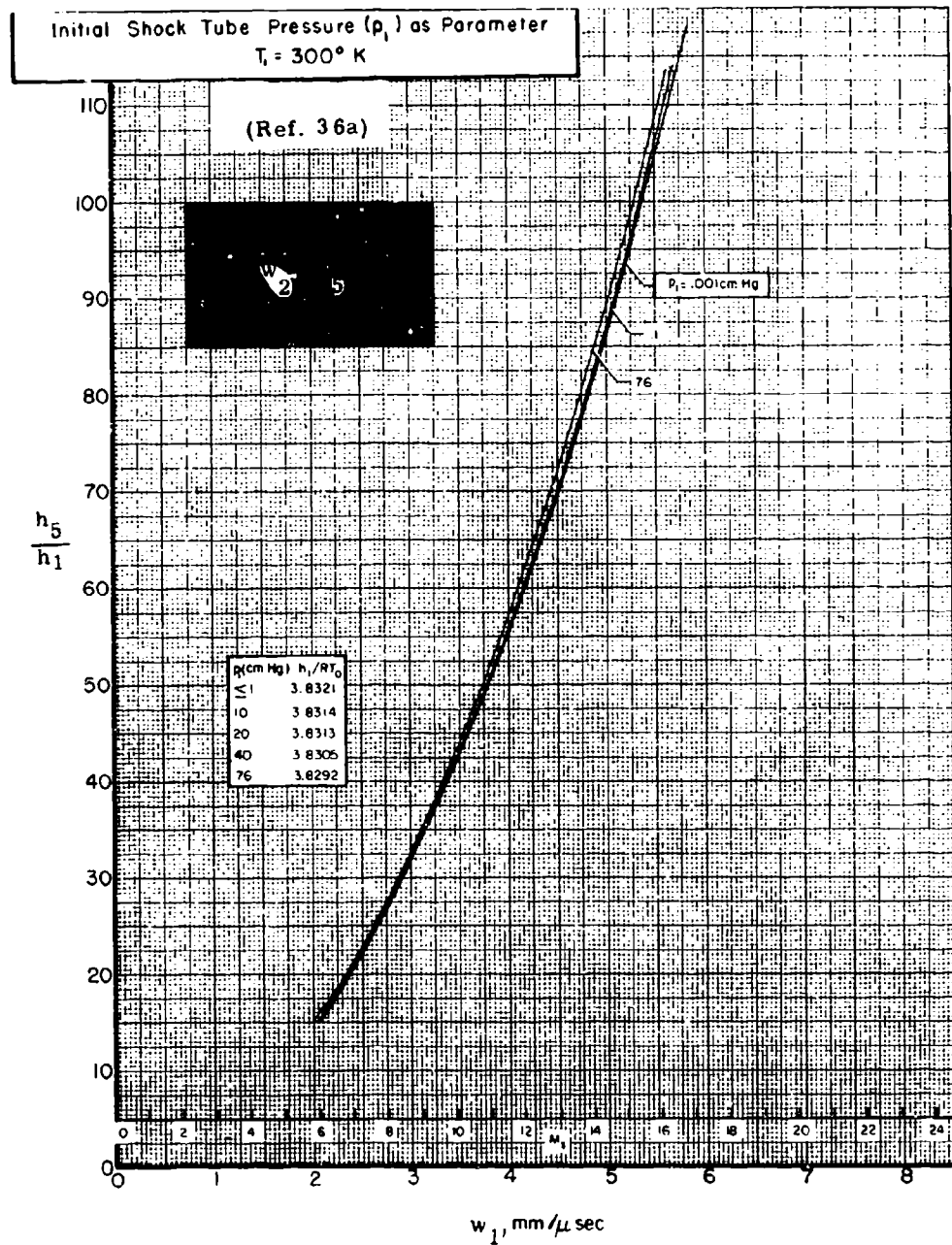


Fig. 2.4-7. Enthalpy ratio (h_5/h_1) for reflected normal shock vs shock velocity (w_1), equilibrium air.

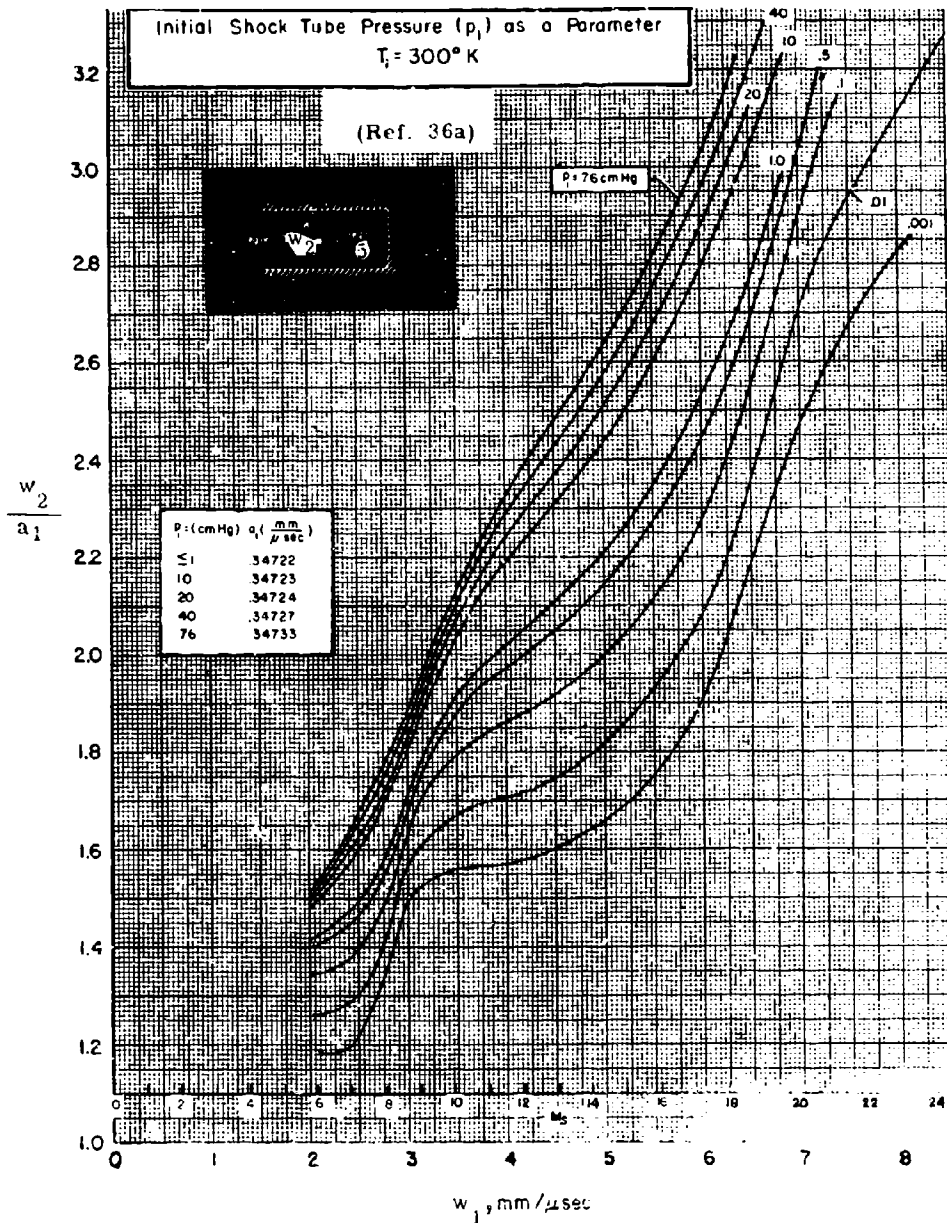


Fig. 2.4-8. Velocity ratio (w_2/a_1) for reflected normal shock vs shock velocity (w_1), equilibrium air.

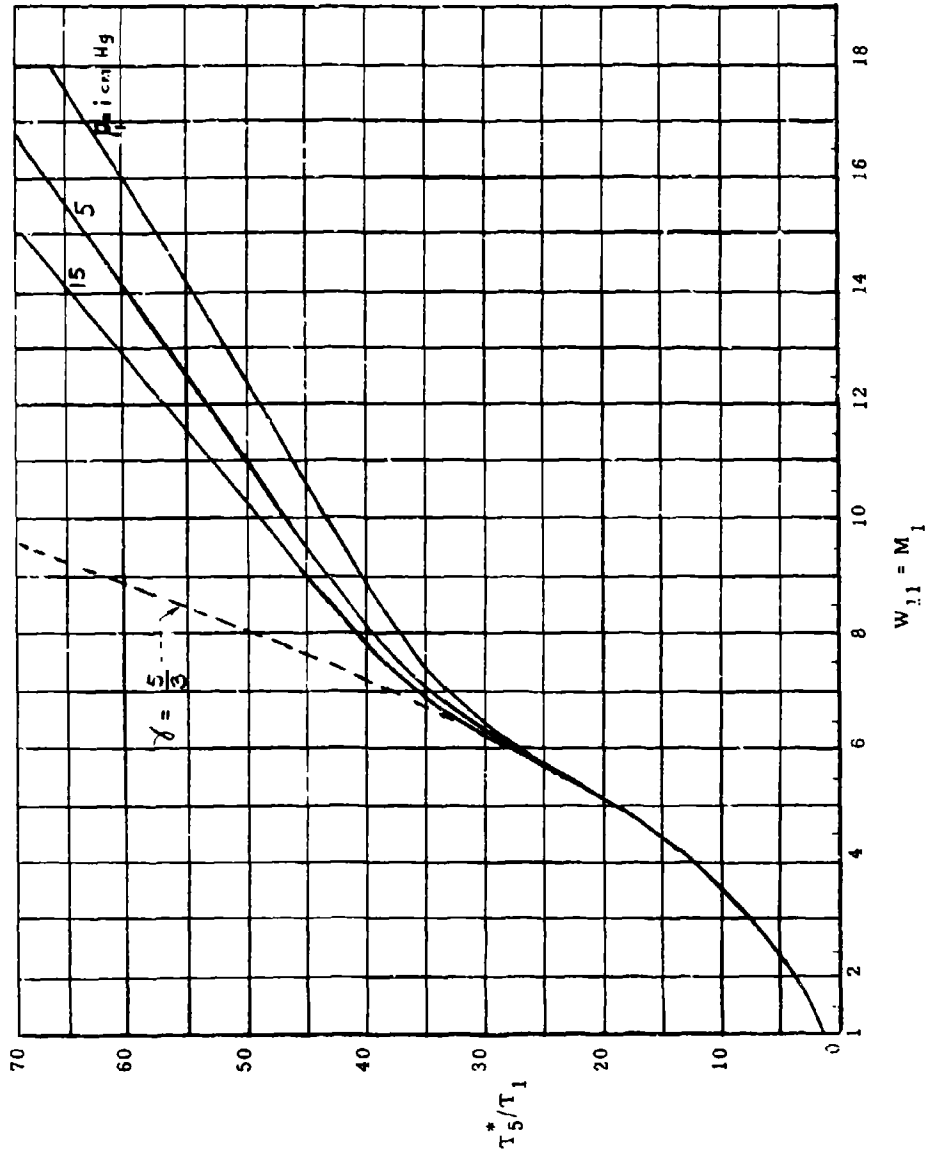


Fig. 2.4-9. Variation of the temperature ratio (T_5^*/T_1) across a reflected shock wave with the incident shock Mach number (W_{11}) in argon (Ref. 42).

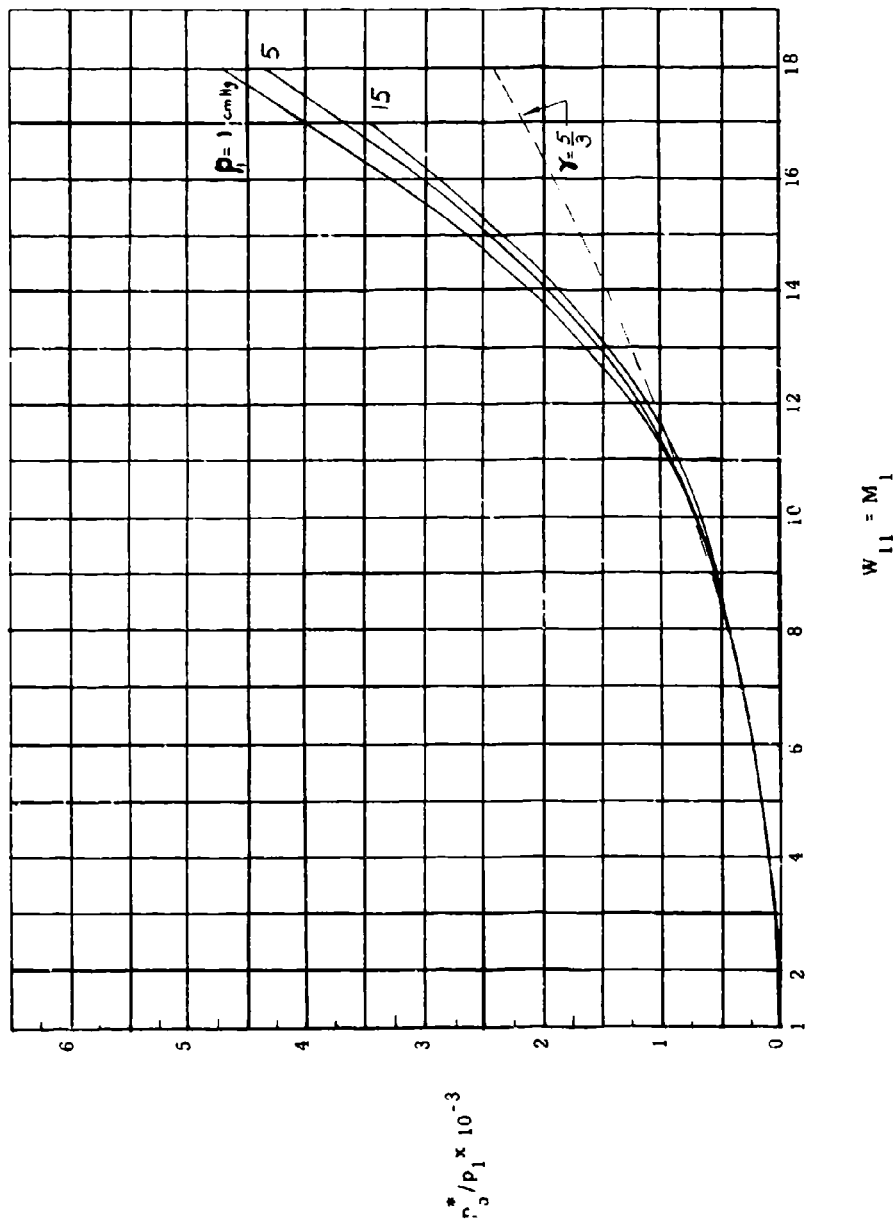


Fig. 2.4-10. Variation of the pressure ratio (p_5^*/p_1) across a normal reflected shock wave with the incident shock Mach number (W_{11}) in argon (Ref. 42).

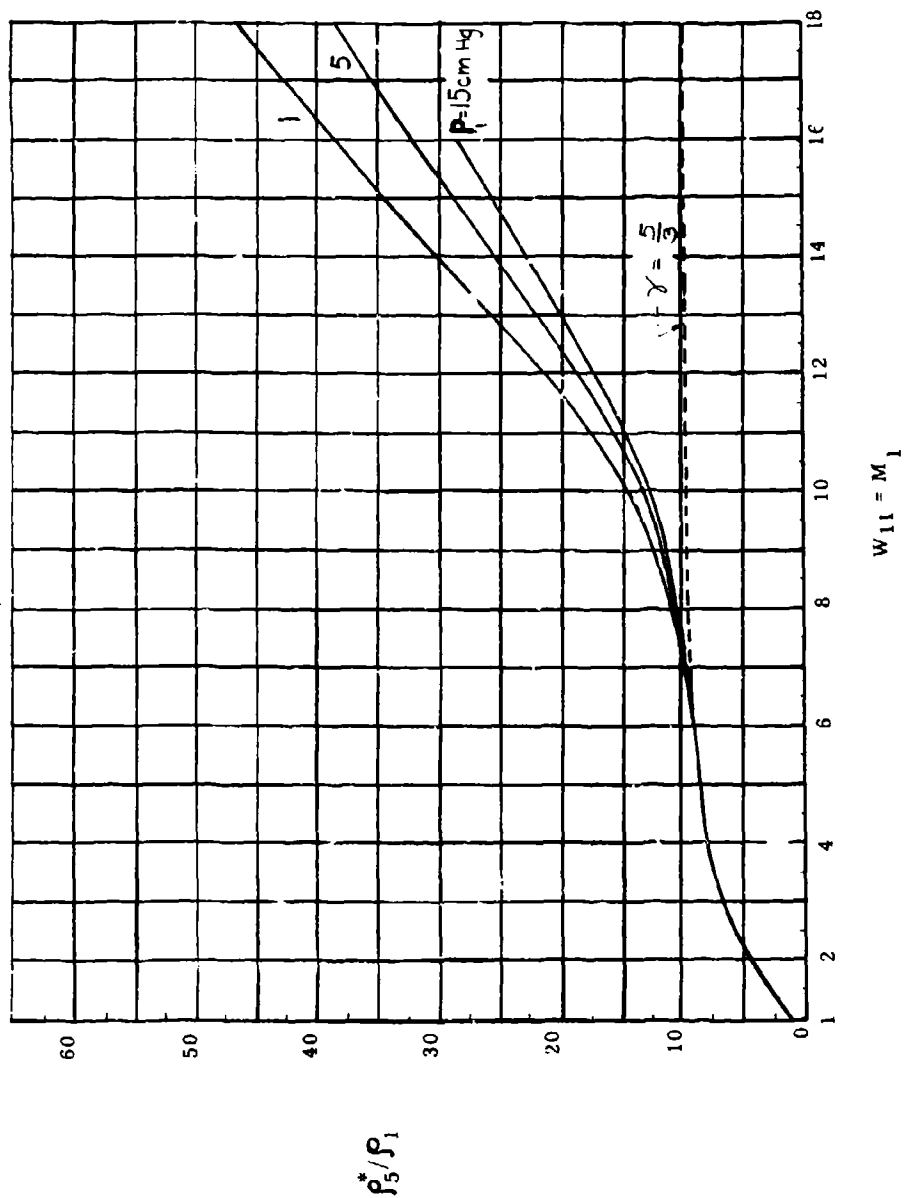


Fig. 2.4-11. Variation of the density ratio (ρ_5^*/ρ_1) across a normal reflected shock wave with the incident shock Mach number (W_{11}) in argon (Ref. 42).

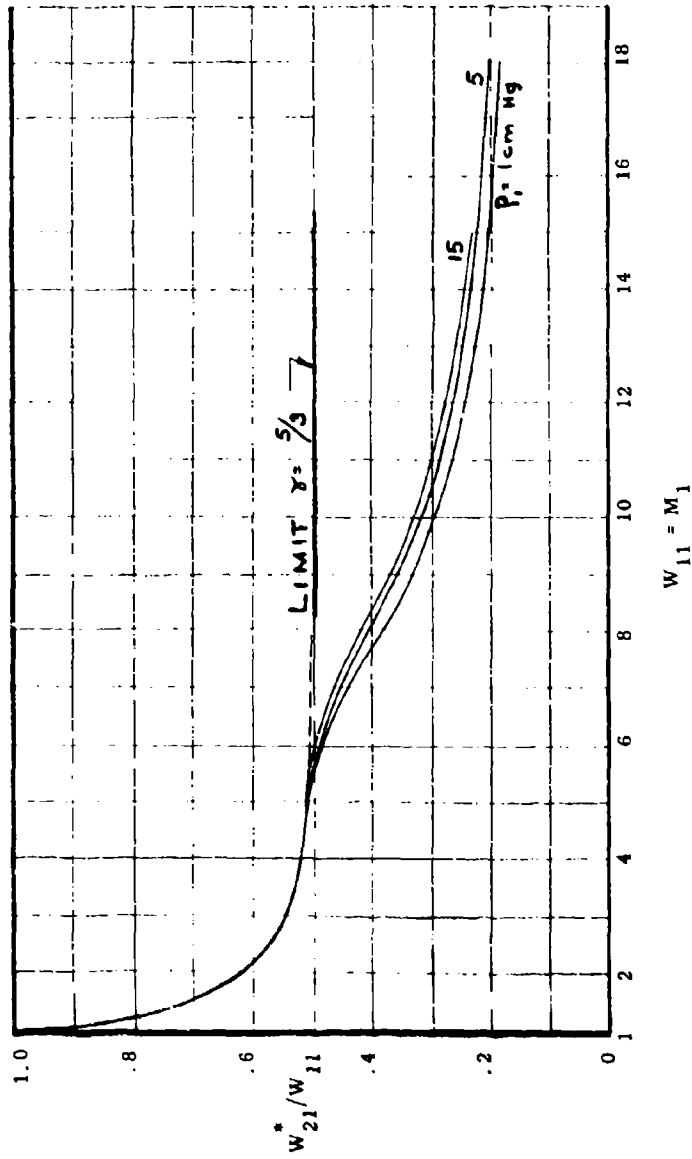


Fig. 2.4-12. Variation of the ratio of reflected to incident shock speed (W_{21}^*/W_{11}) with the initial shock Mach number (W_{11}) (Ref. 42).

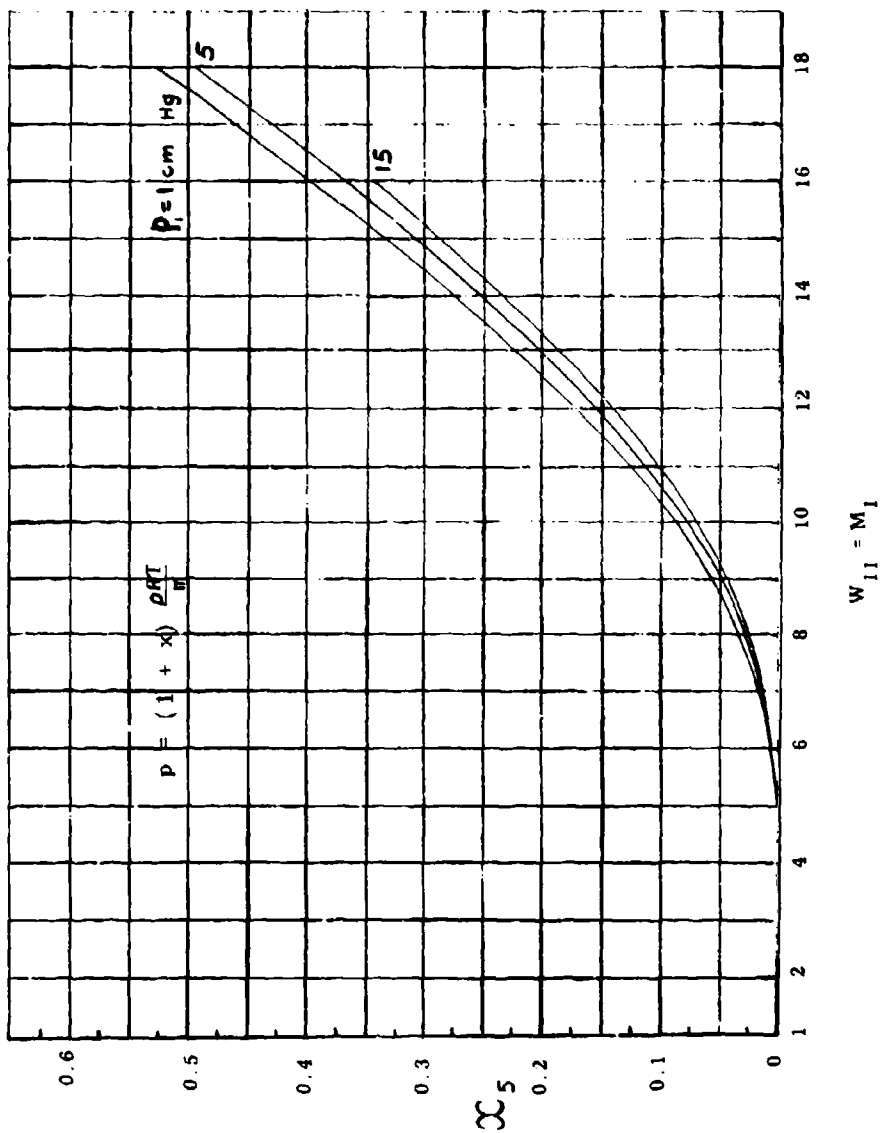


Fig. 2.4-13. Variation of the degree of ionization (x_5) behind a reflected shock wave with the incident shock Mach number (W_{11}) in argon (Ref. 42).

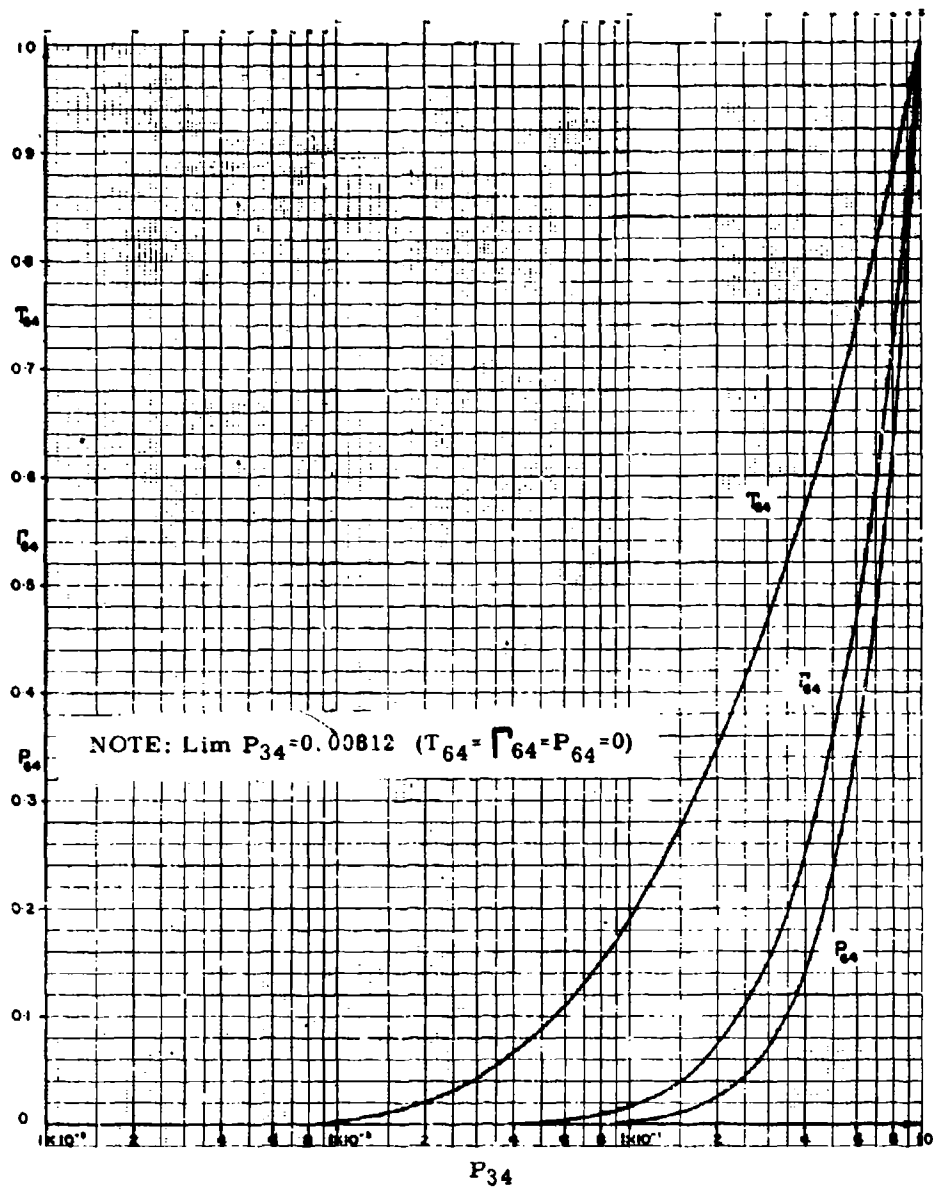


Fig. 2.4-14. Variation of the flow parameters in state (6) with the pressure ratio (P_{34}) across the incident rarefaction wave.

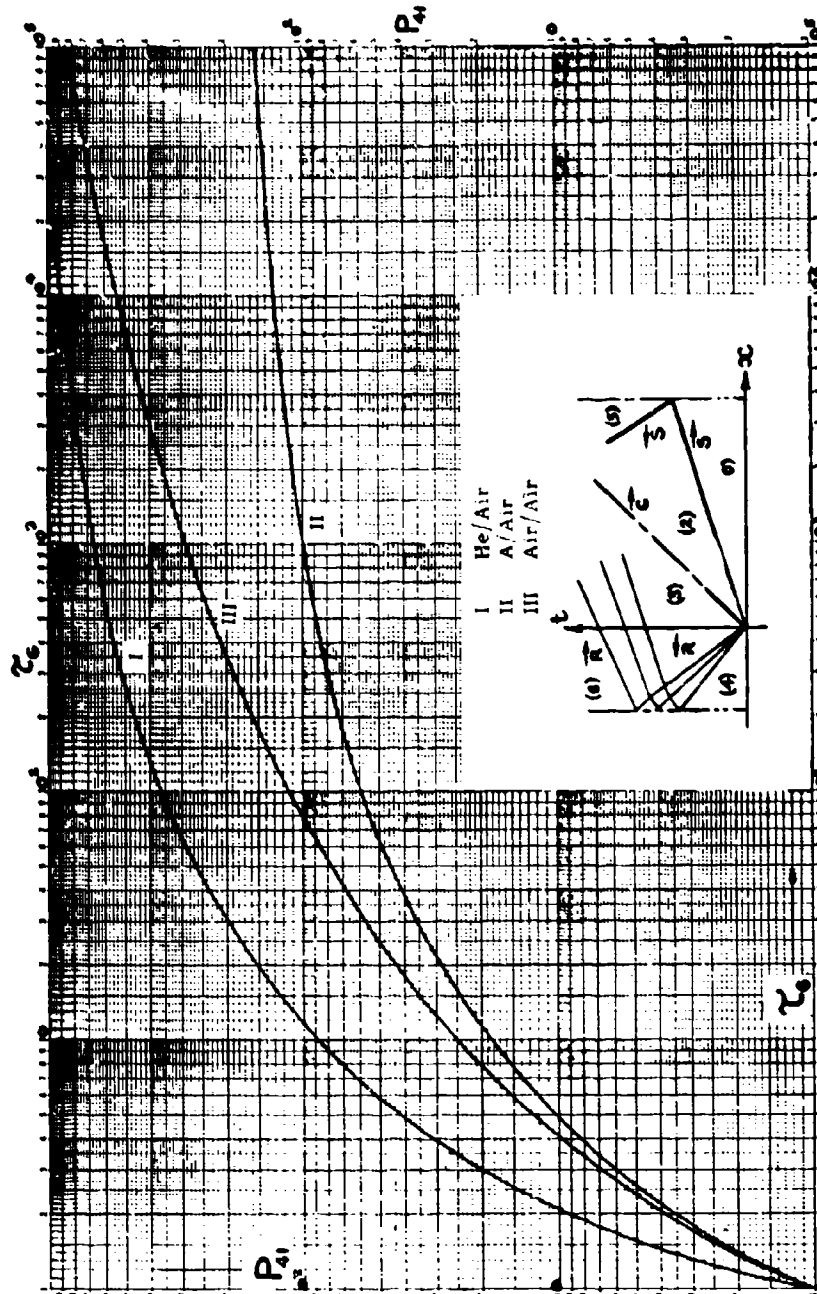


Fig. 2.4-15. Variation of time required (τ_6) for formation of steady-state region (6) with diaphragm pressure ratio (P_{41}).

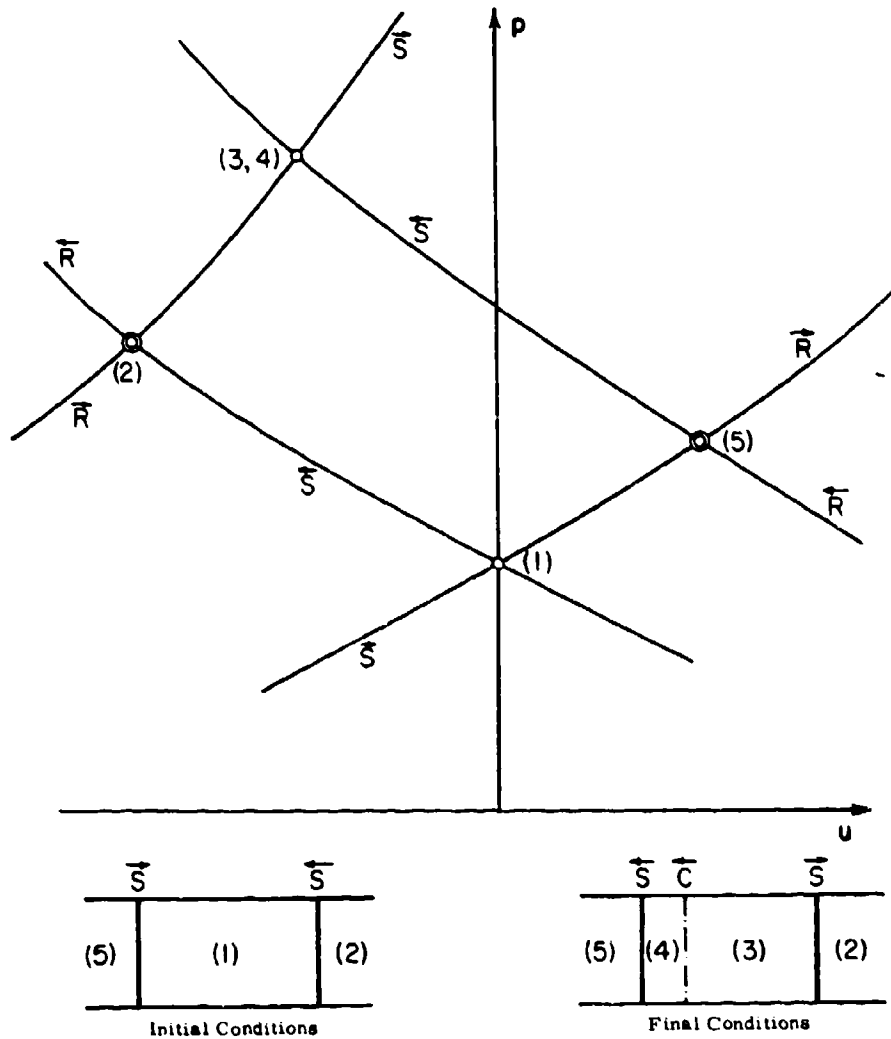


Fig. 2.4-16. Head-on collision of two unequal shock waves in the (u, p) -plane.

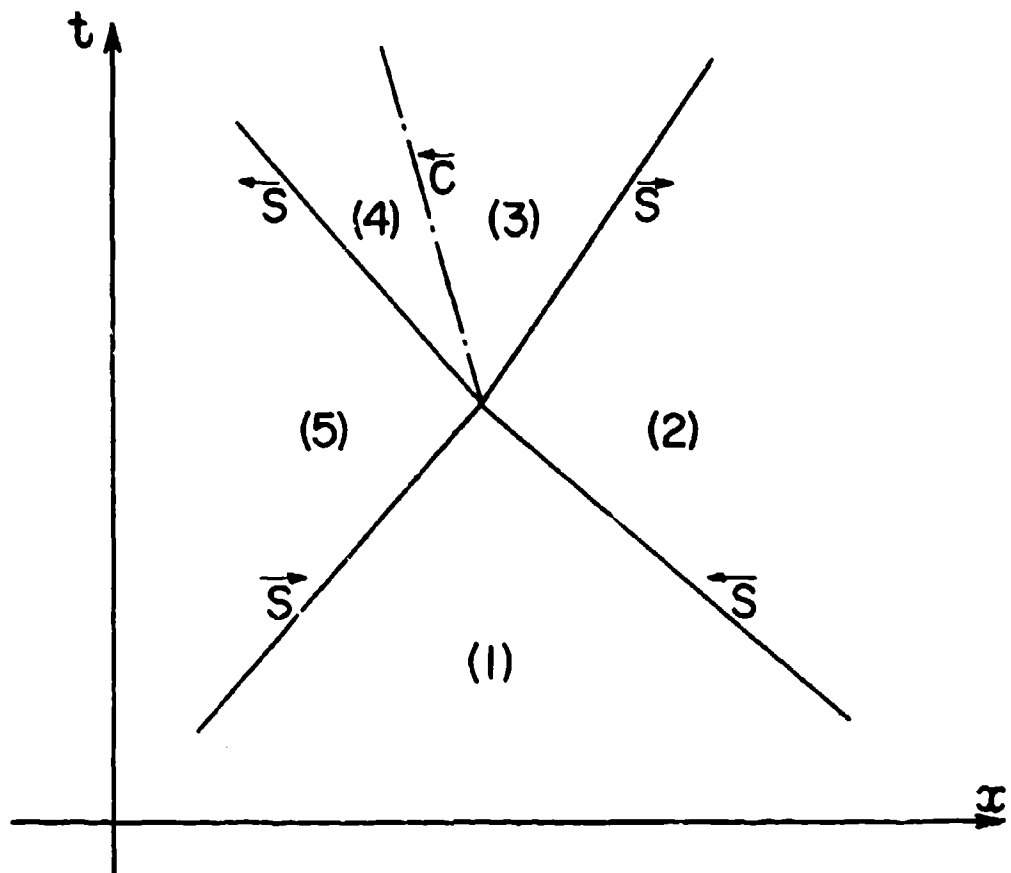


Fig. 2.4-17. Head-on collision of two unequal shock waves in the (x, t) -plane.

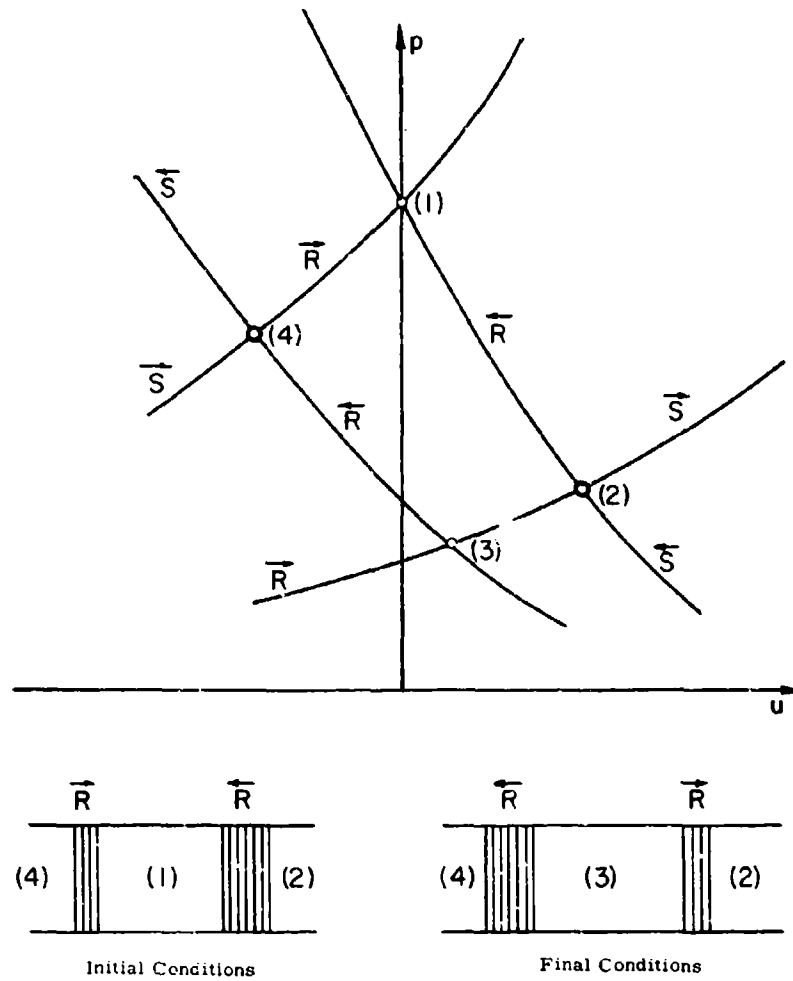


Fig. 2.4-18. Head-on collision of two unequal rarefaction waves in the (u, p) -plane.

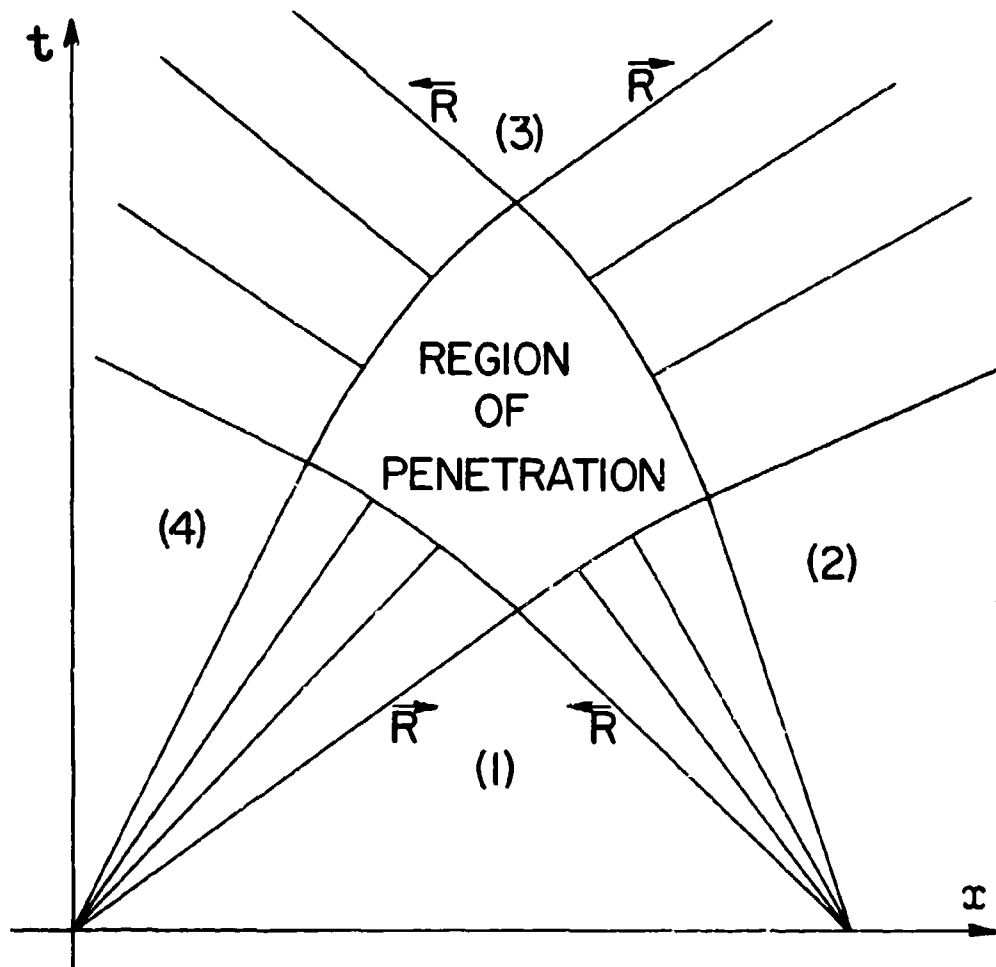


Fig. 2.4-19. Head-on collision of two unequal rarefaction waves in the (x, t) -plane.

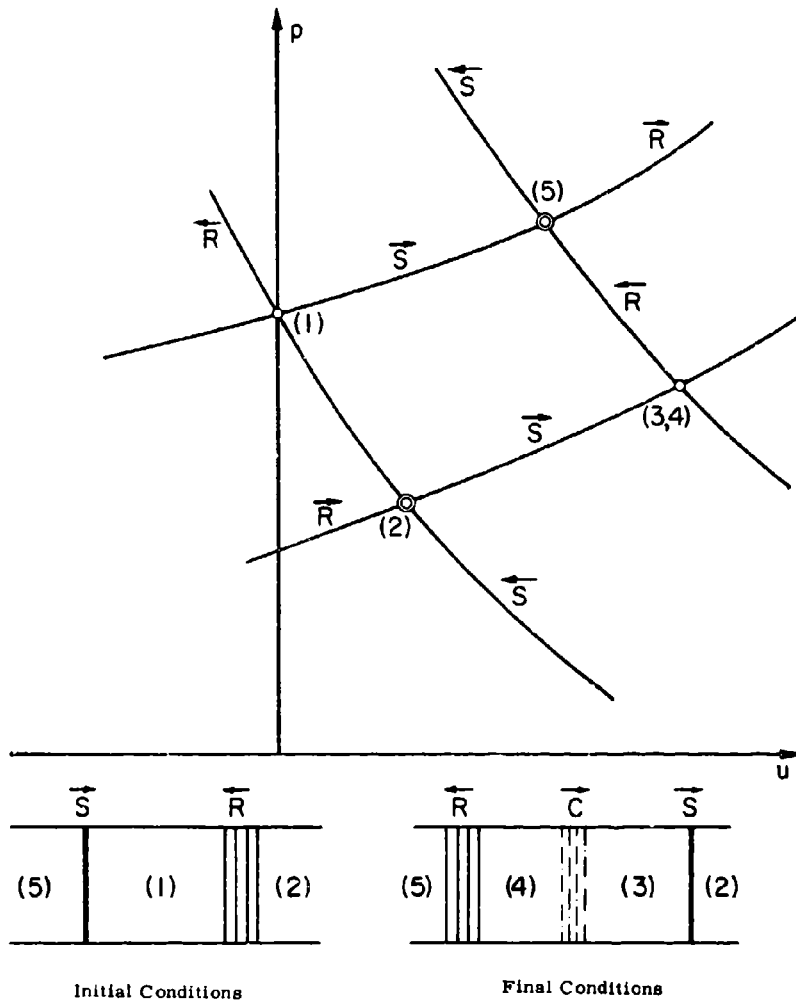


Fig. 2.4-20. Head-on collision of a shock wave and a rarefaction wave in the (u, p)-plane.

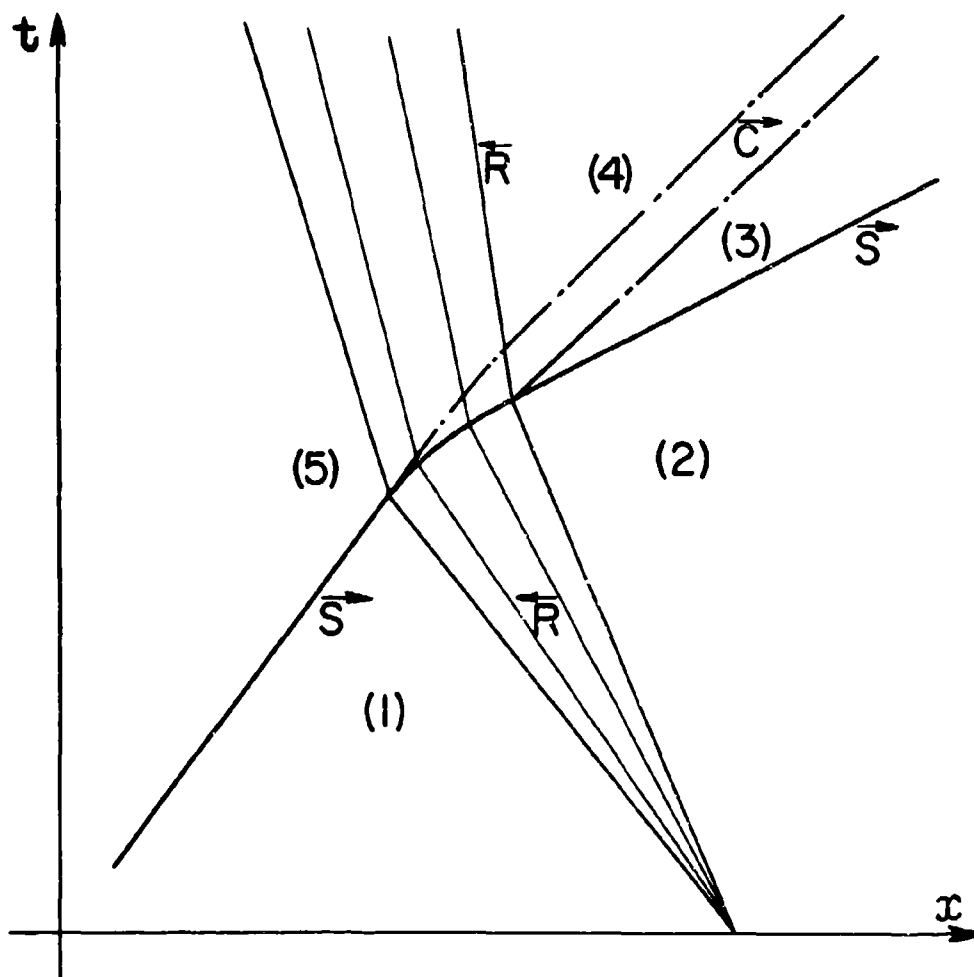


Fig. 2.4-21. Head-on collision of a shock wave and a rarefaction wave in the (x, t) -plane.

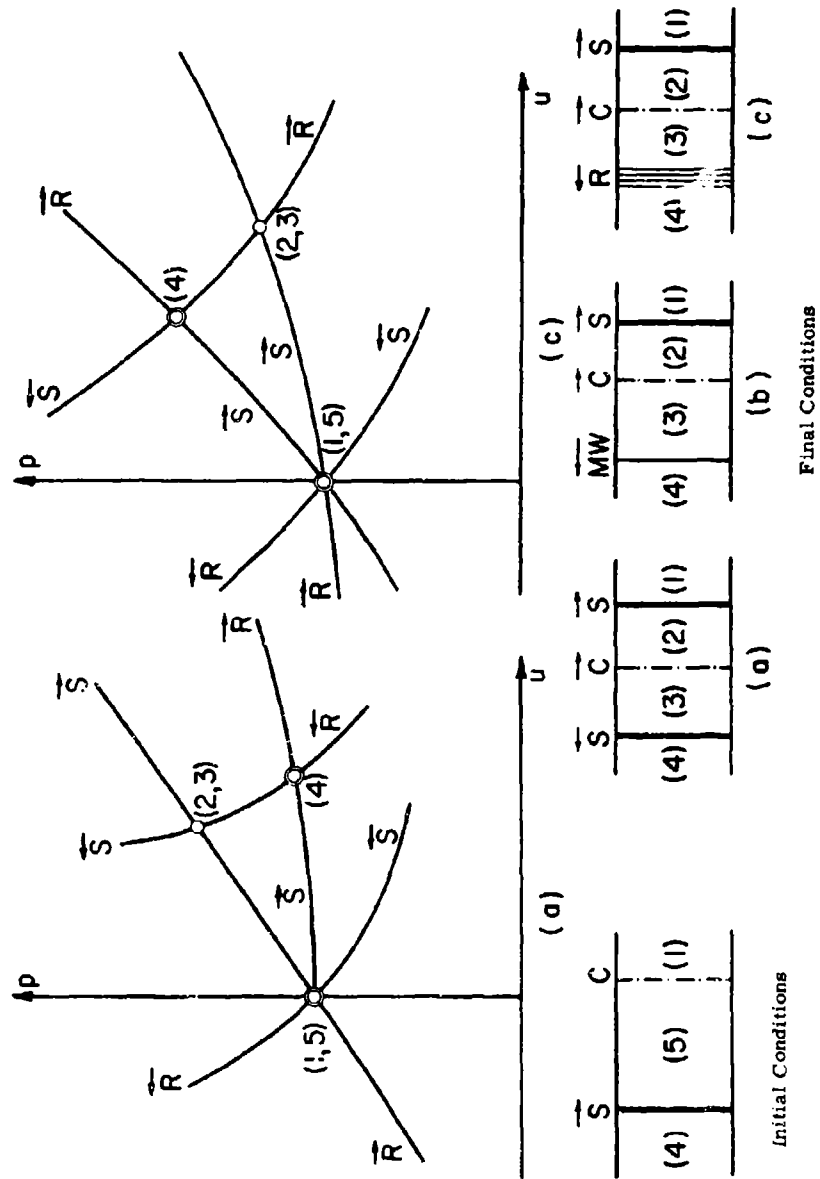


Fig. 2.4-22. Normal refraction of a shock wave at a contact surface in the (u, p) -plane.

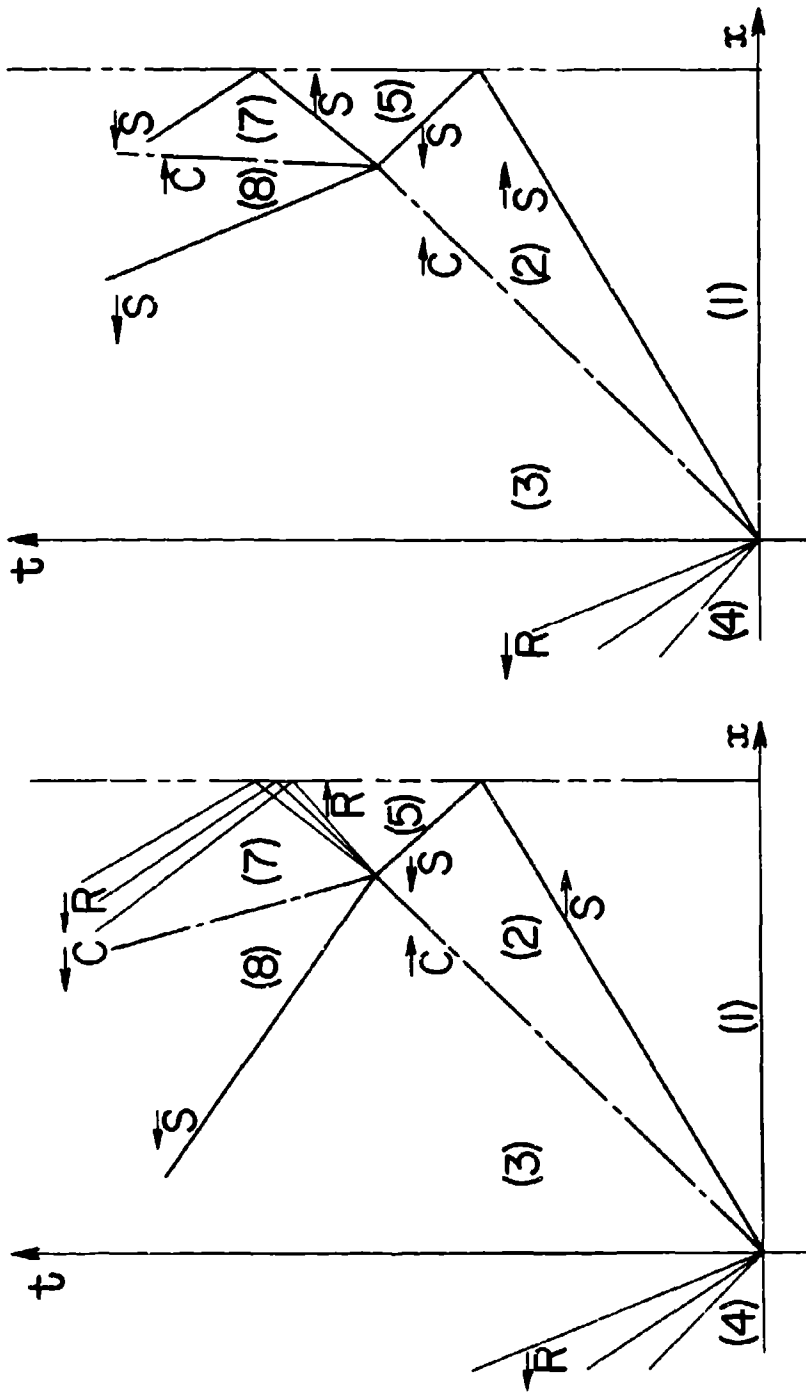


Fig. 2.4-23. Interaction of a shock wave and a contact surface in the shock tube after the diaphragm is broken in the (x, t) -plane.

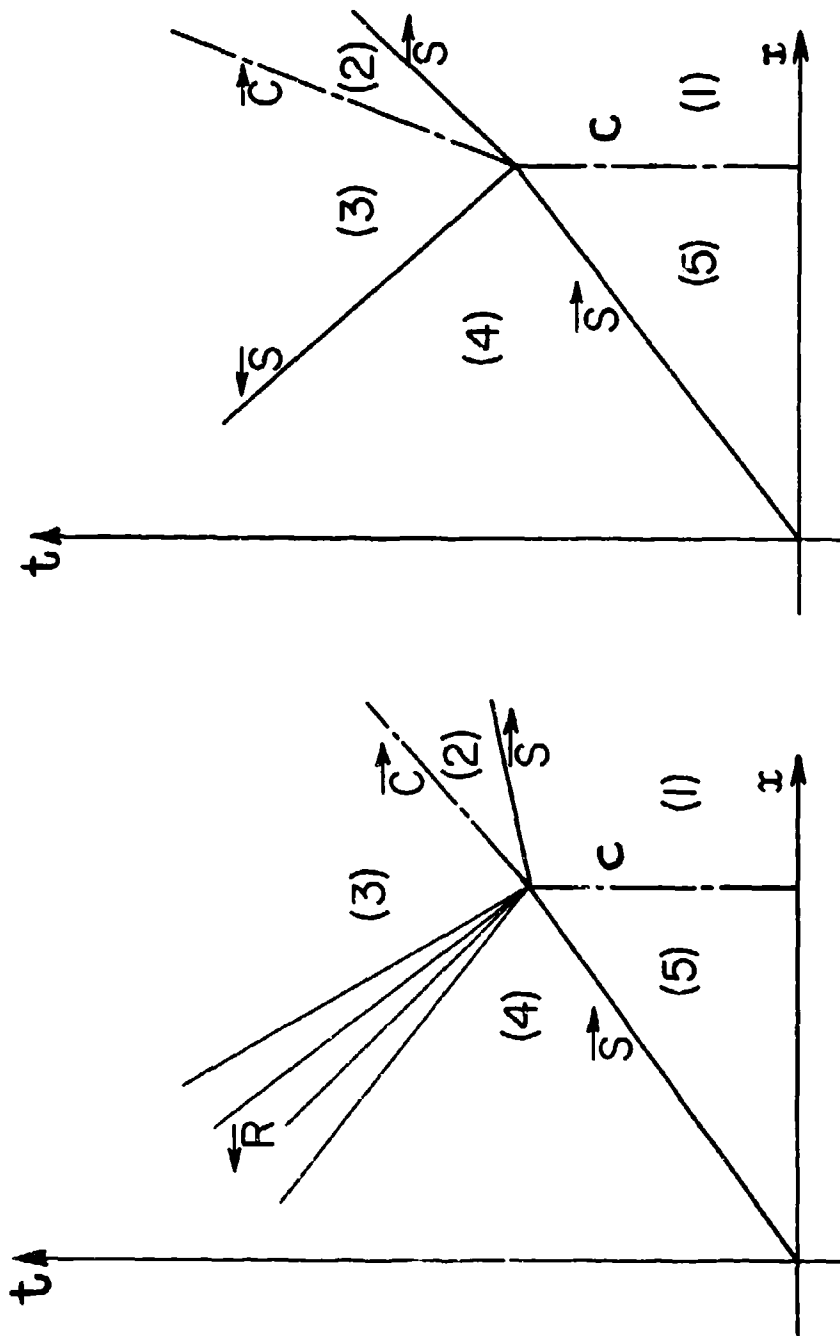


Fig. 2.4-24. Interaction of a shock wave and a stationary contact surface in the (x, t) -plane.

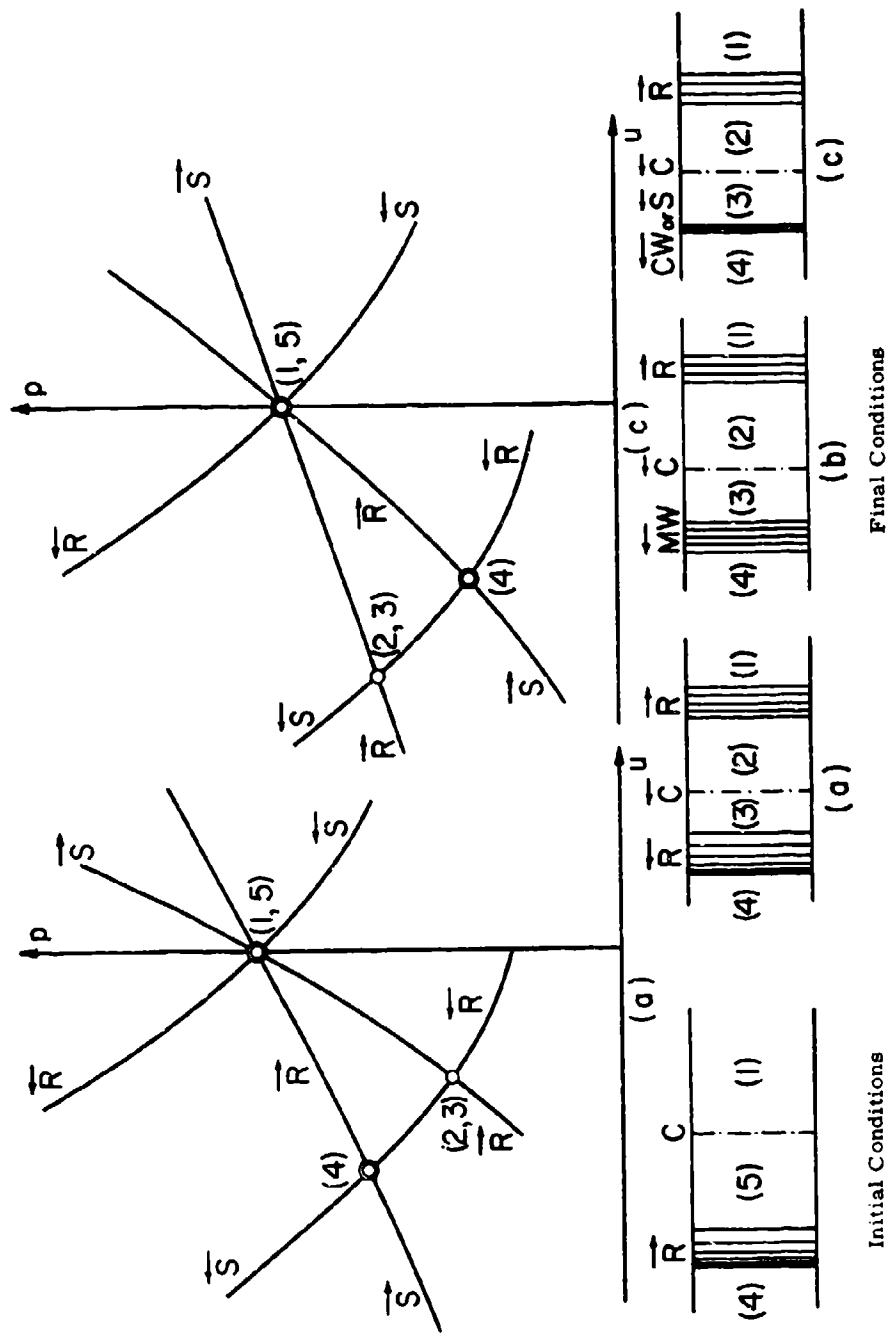


Fig. 2.4-25. Normal refraction of a rarefaction wave at a contact surface in the (u, p) -plane.

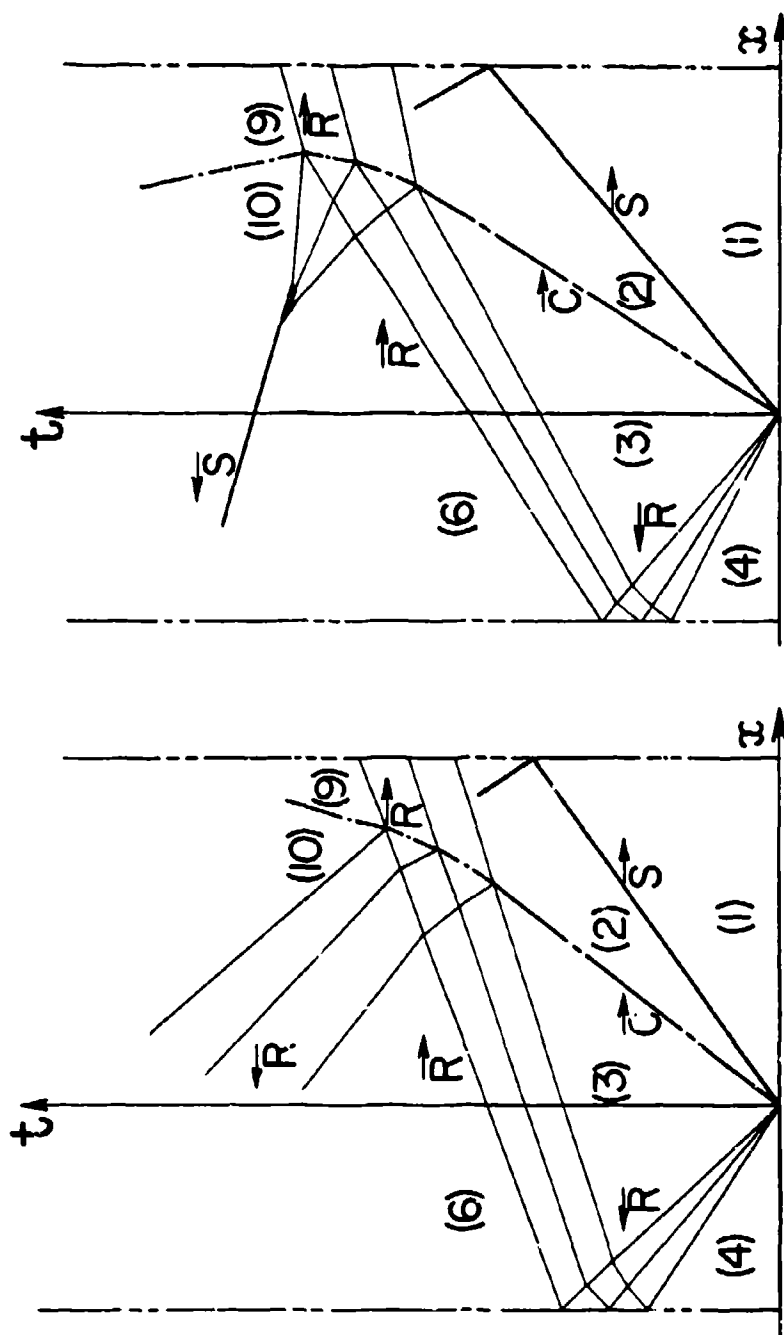


Fig. 2.4-26. Interaction of a rarefaction wave and a contact surface in the shock tube after the diaphragm is broken in the (x, t) -plane.

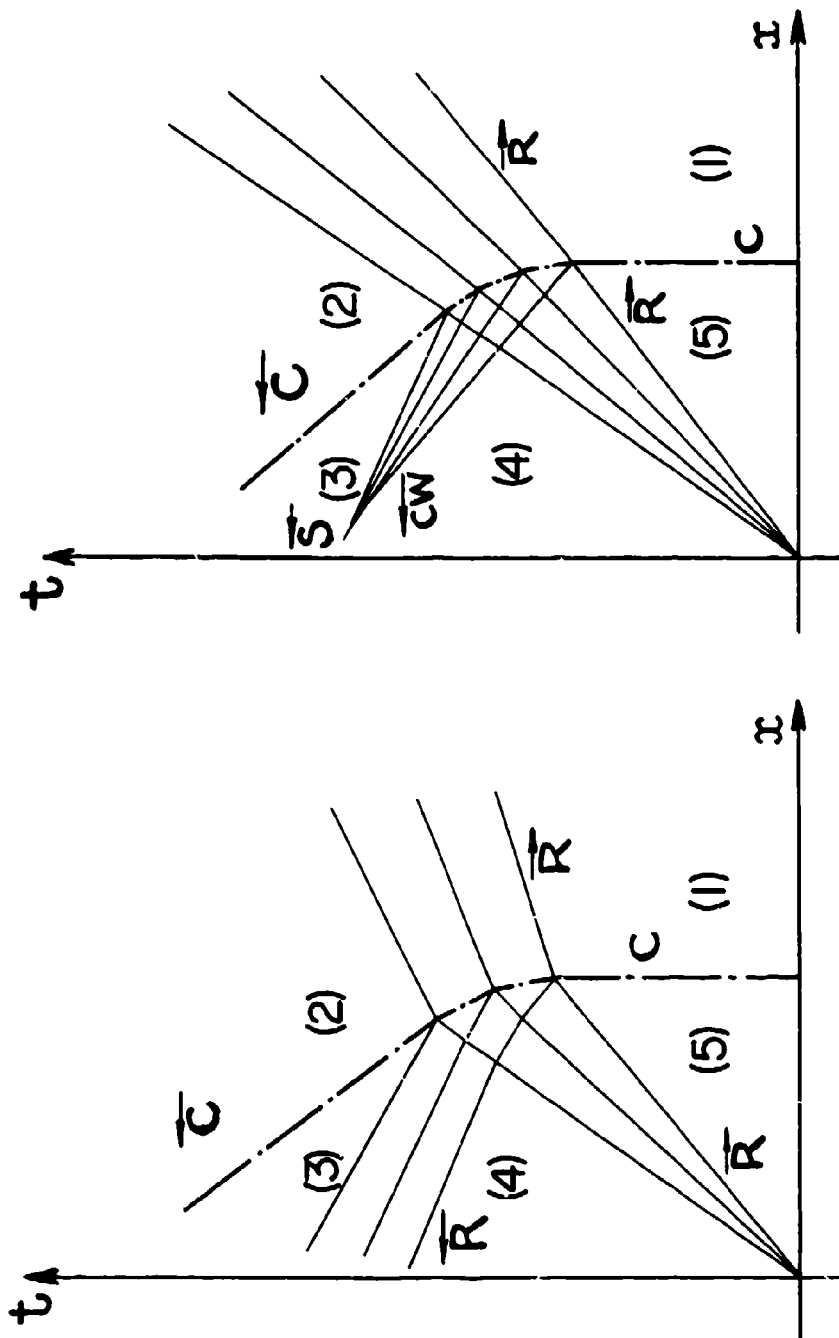


Fig. 2.4-27. Interaction of a rarefaction wave and a stationary contact surface in the (x, t) -plane.

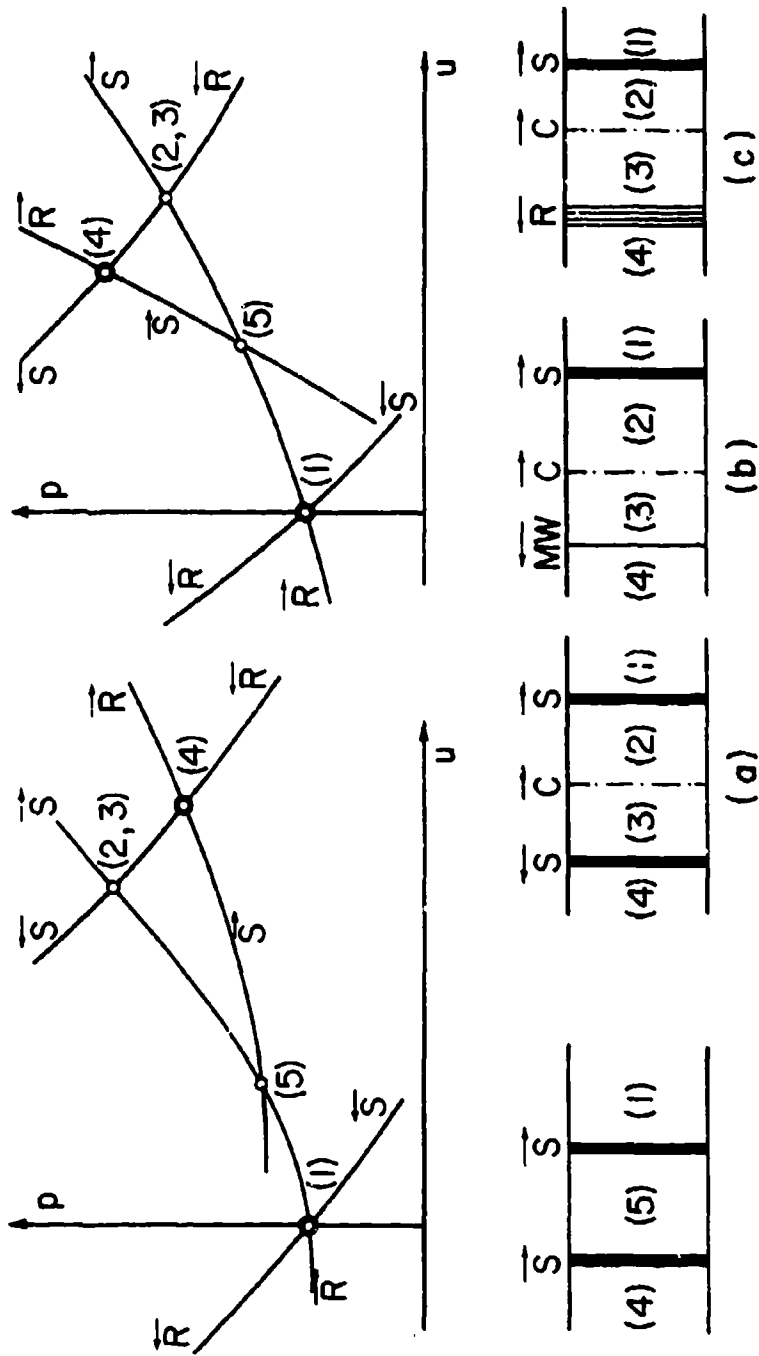
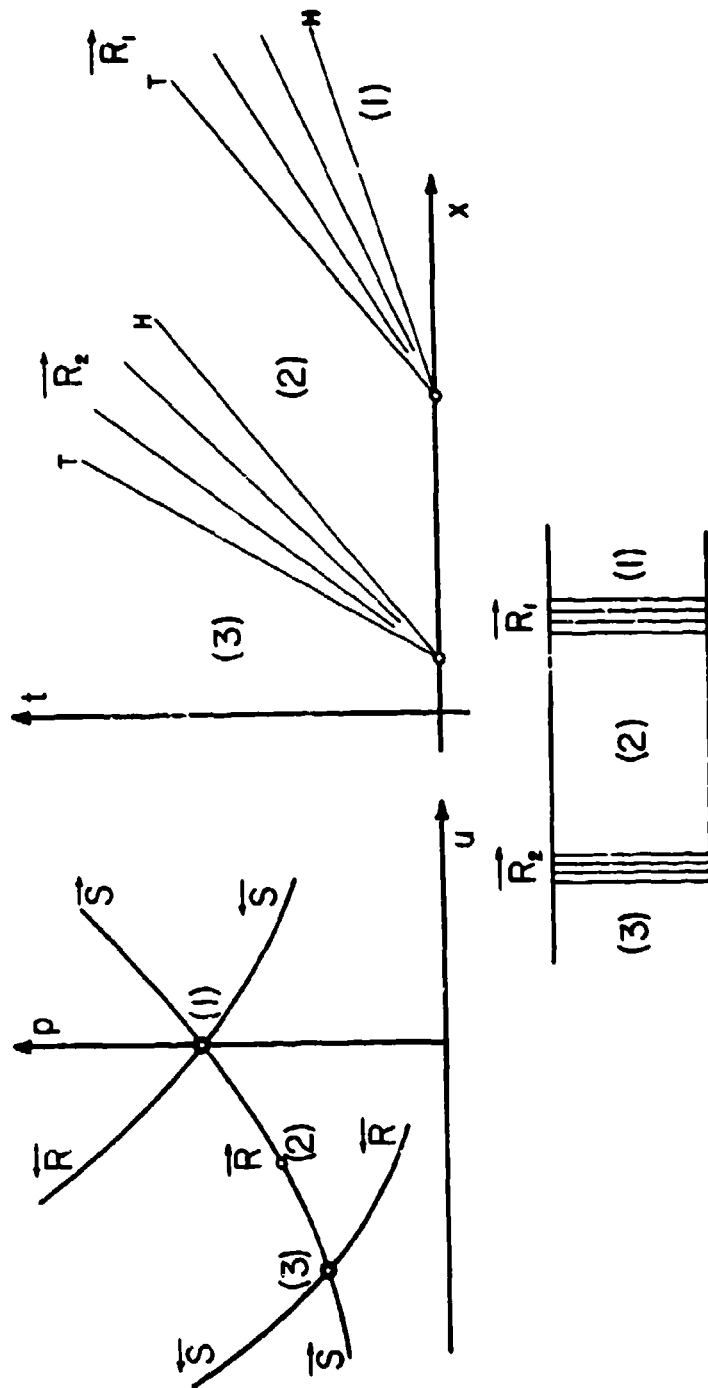


Fig. 2.4-28. Overtaking of two similarly facing shock waves in the (u, p) -plane.



Initial and Final Conditions

Fig. 2.4-30. Overtaking of two similarly facing rarefaction waves in the (x, t) -plane and the (u, p) -plane.

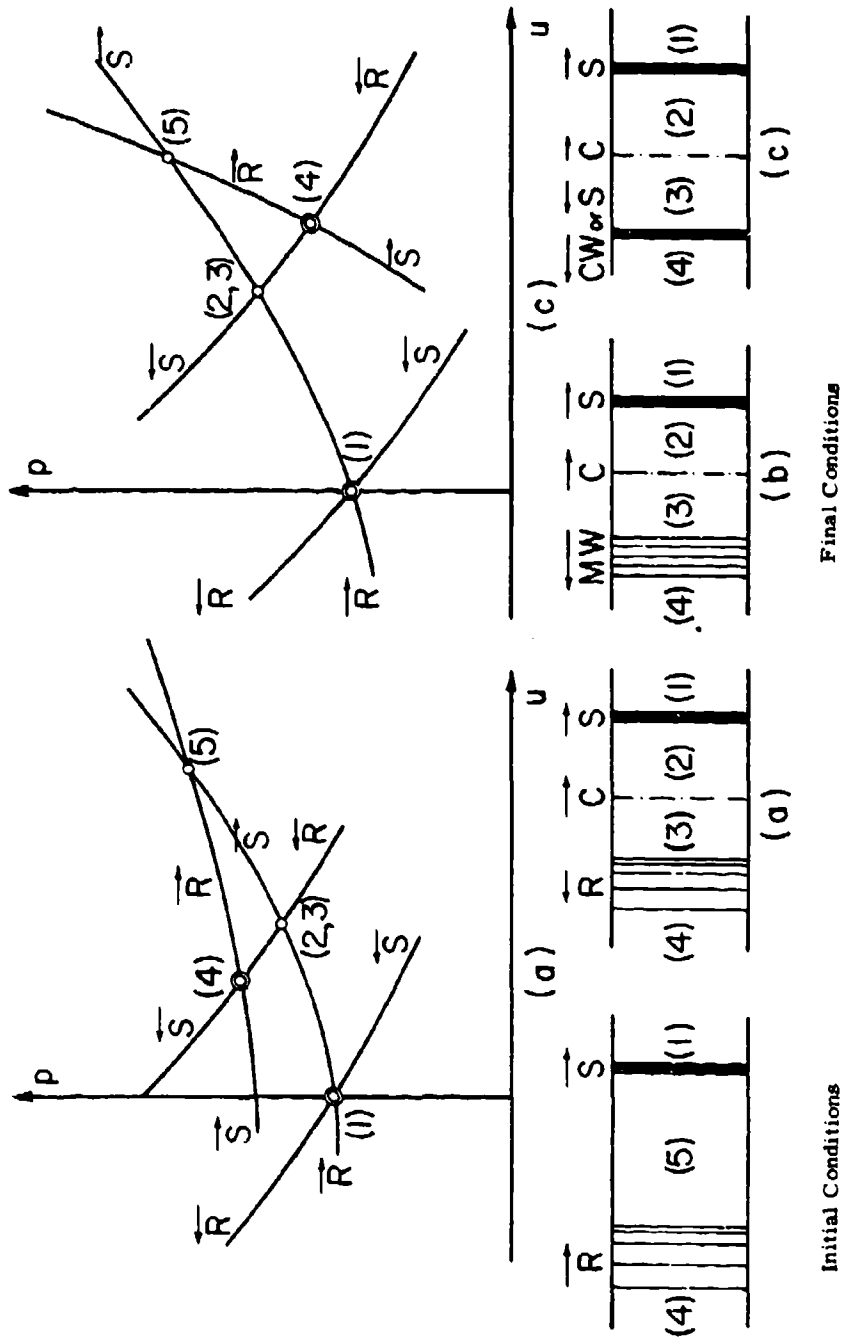


Fig. 2.4-31. Overtaking of a shock wave by a weak rarefaction wave in the (u, p) -plane.

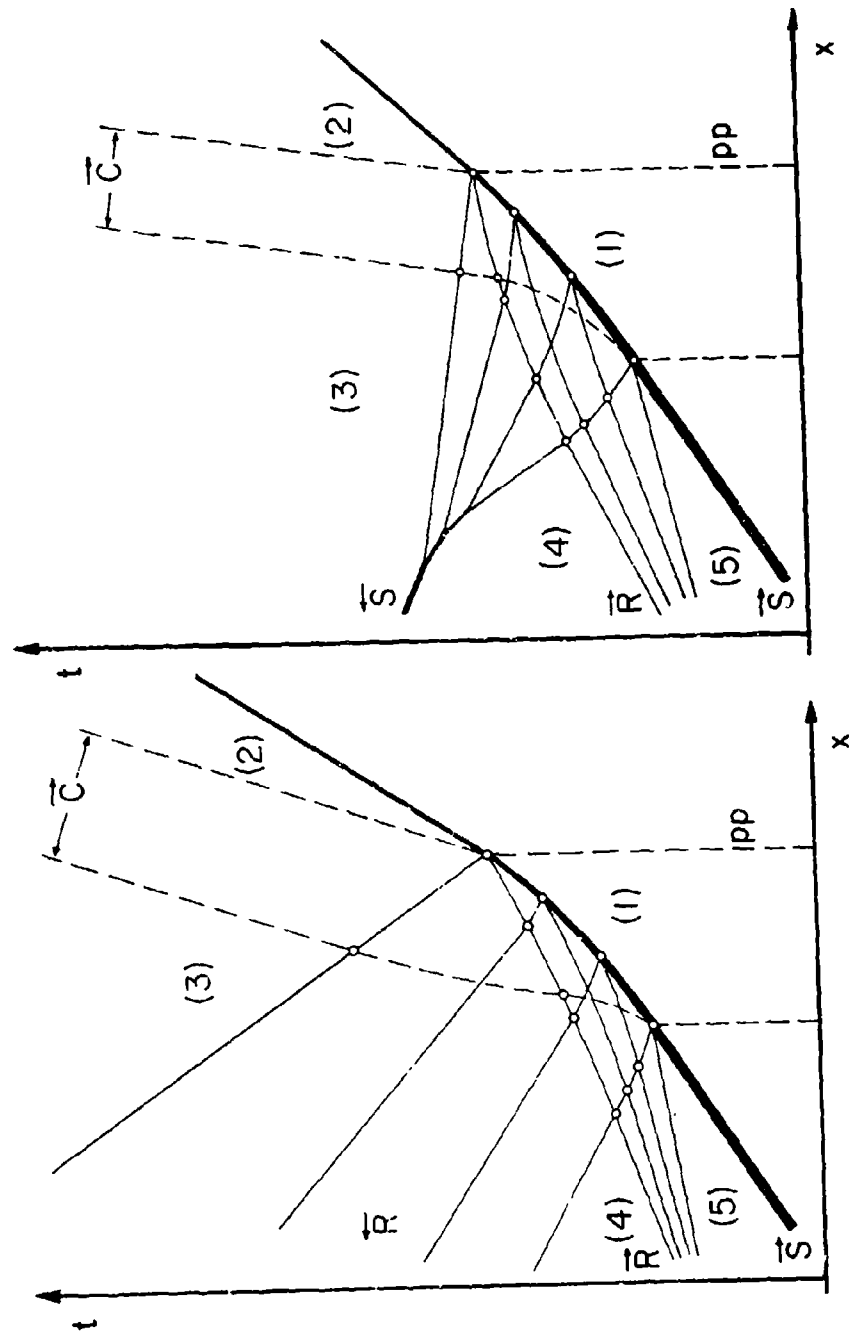


Fig. 2.4-32. Overtaking of a shock wave by a weak rarefaction wave in the (x, t) -plane.

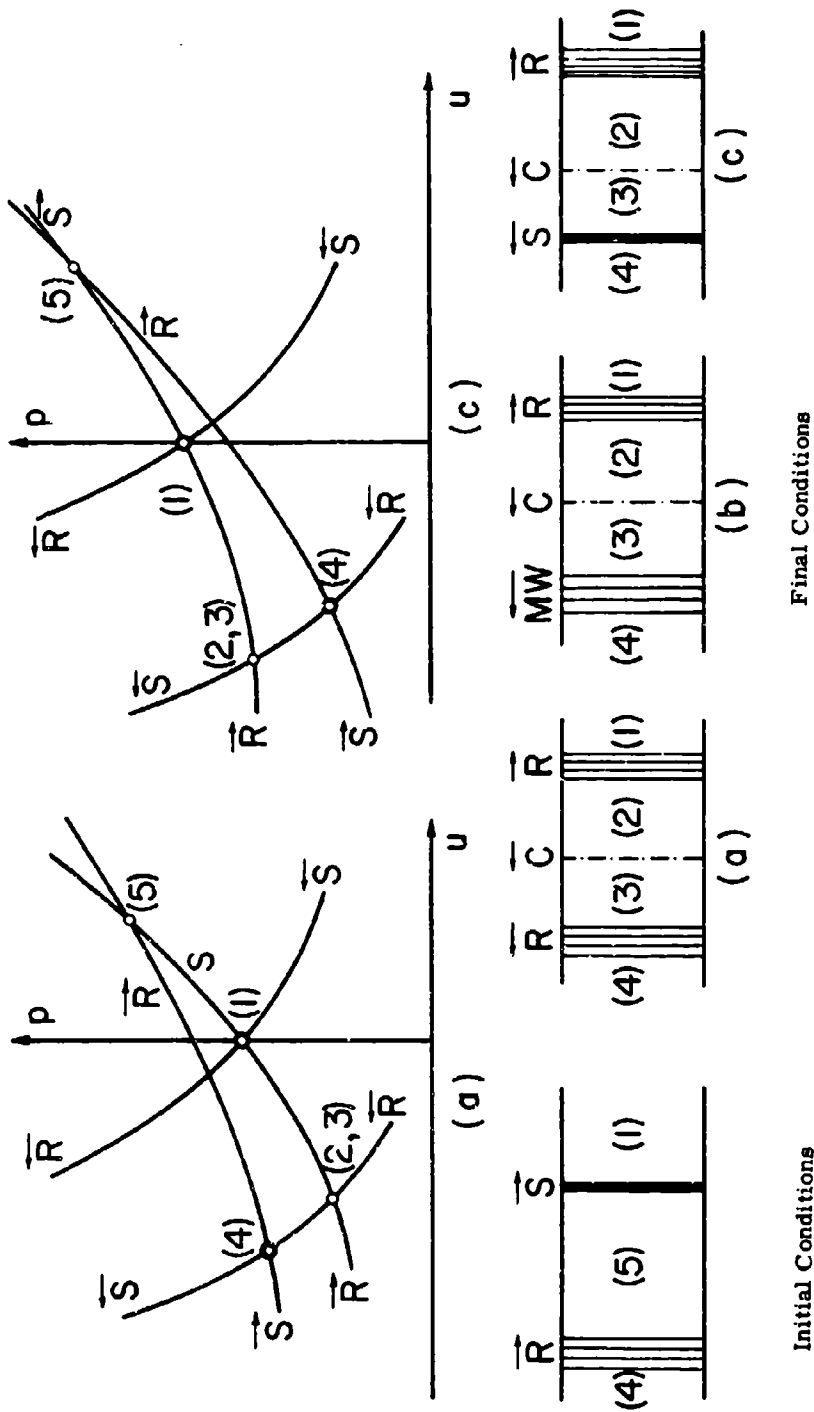


Fig. 2.4-33. Overtaking of a shock wave by a strong rarefaction wave in the (u, p) -plane.

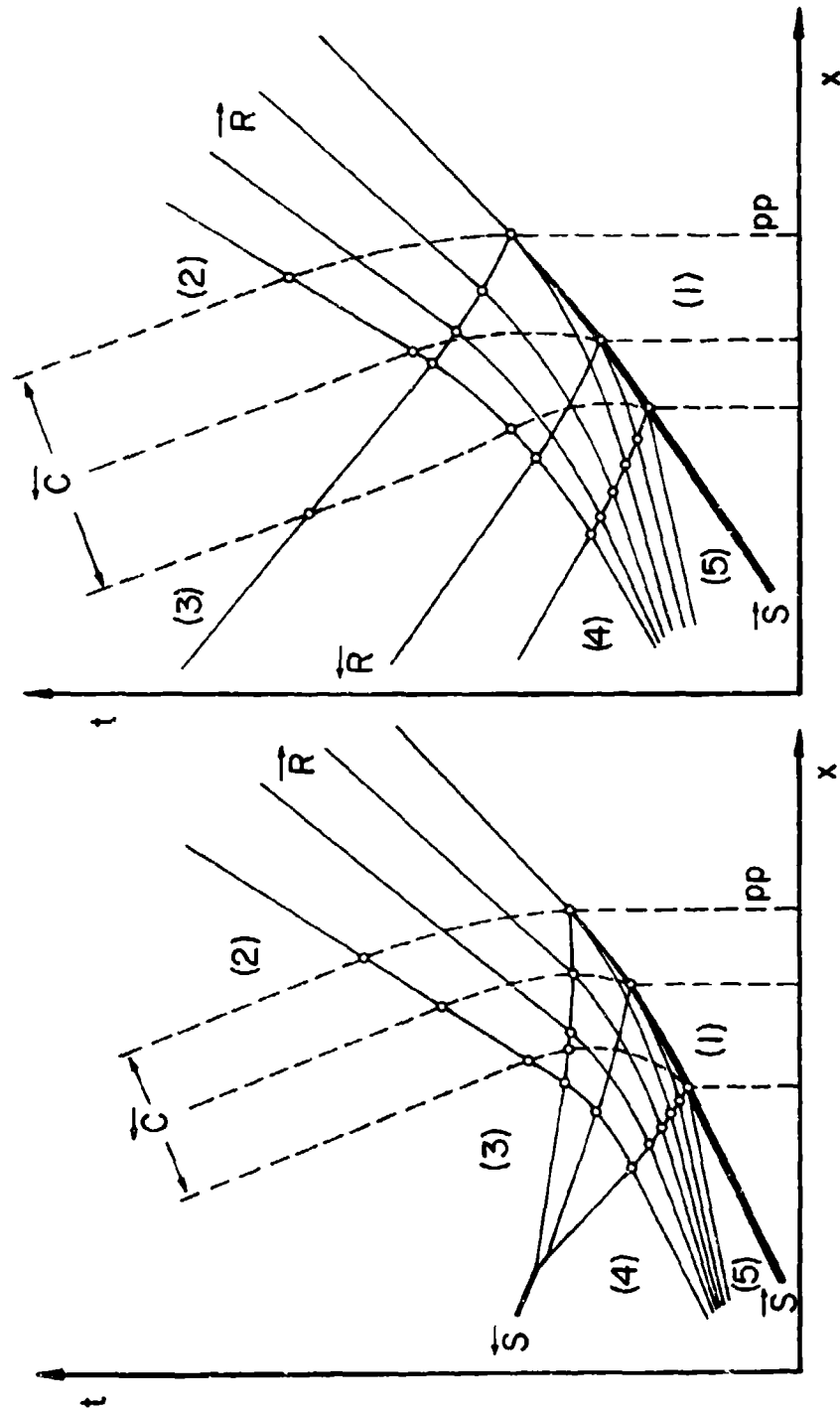


Fig. 2.4-34. Overtaking of a shock wave by a strong rarefaction wave in the (x, t) -plane.

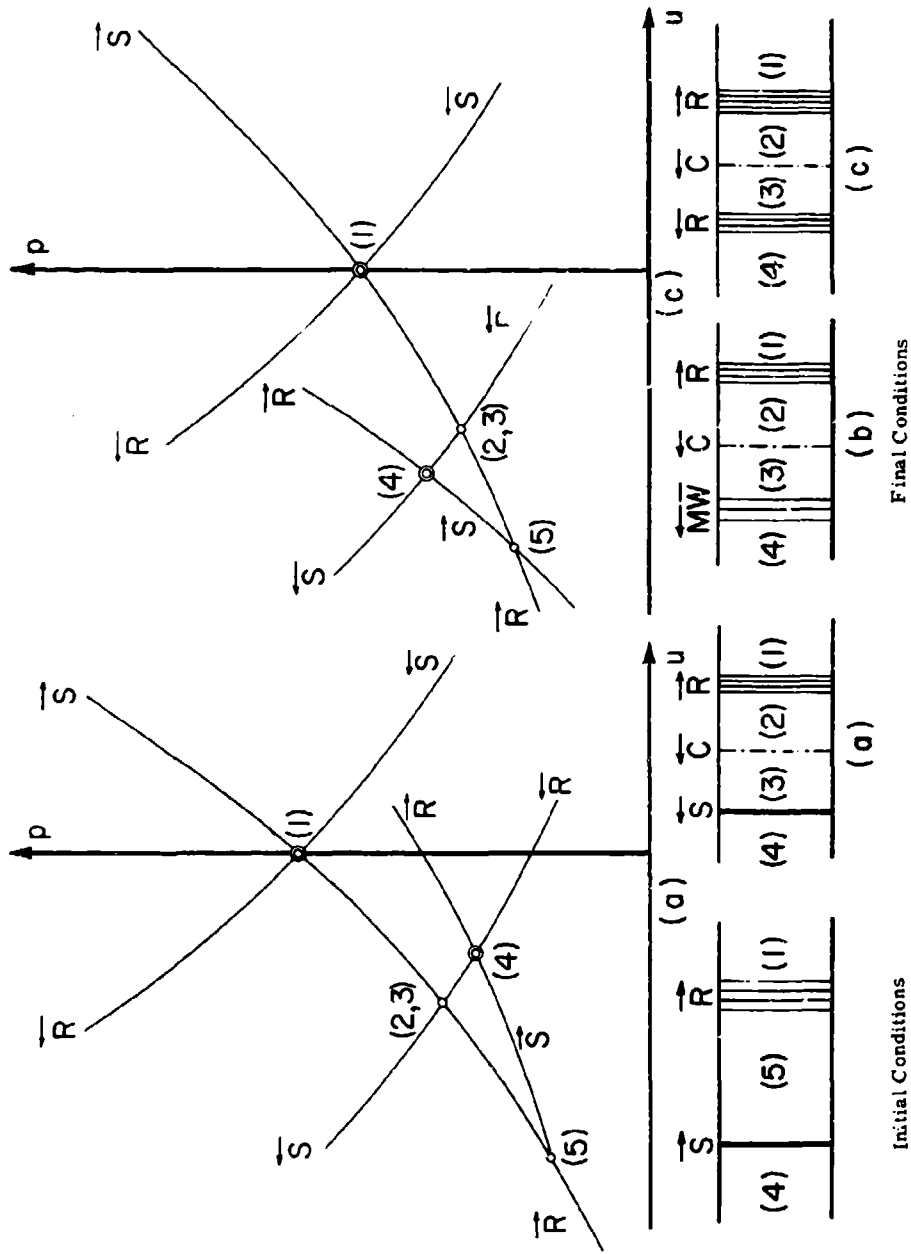


Fig. 2.4-35. Overtaking of a rarefaction wave by a weak shock wave in the (u, p) -plane.

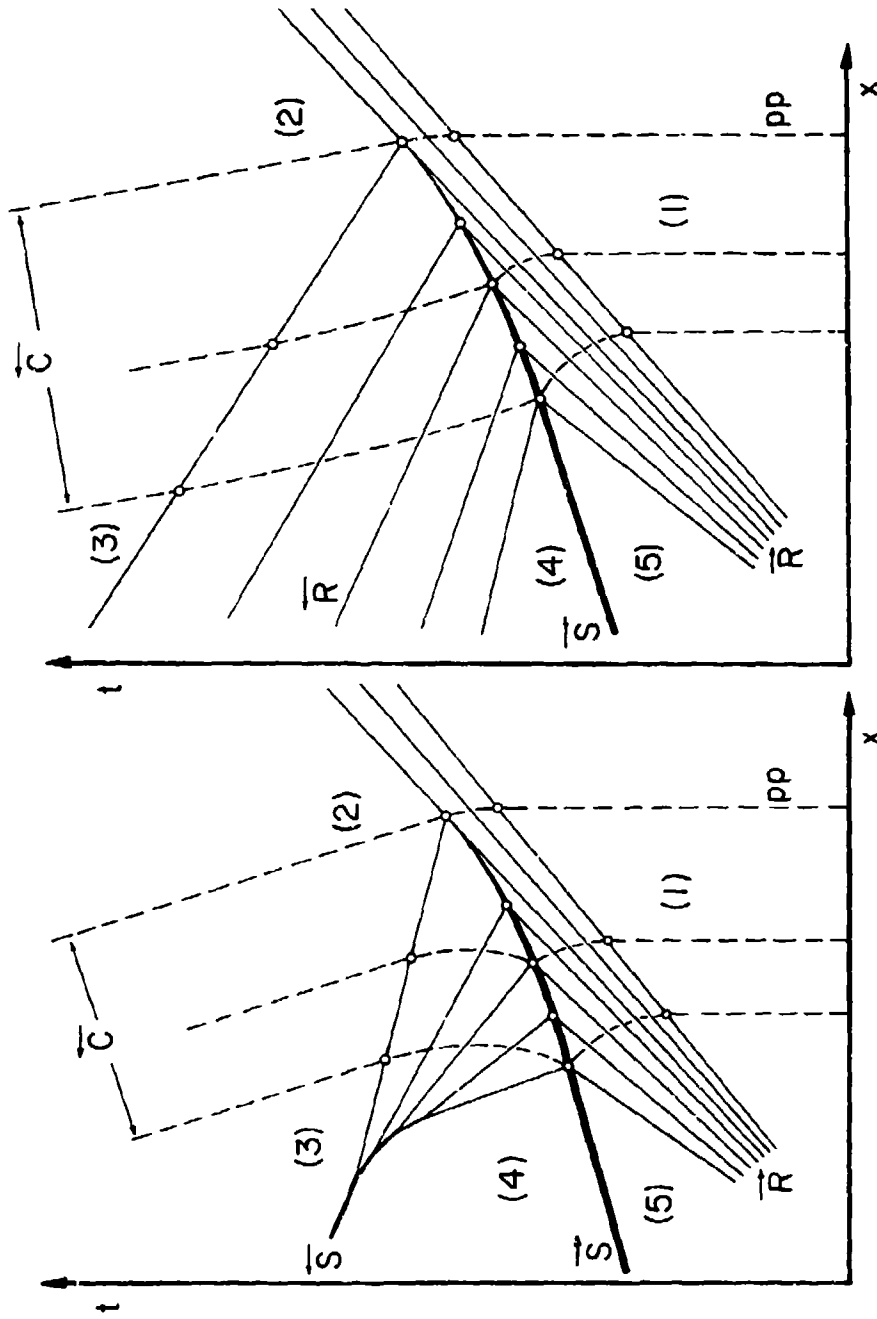


Fig. 2.4-36. Overtaking of a rarefaction wave by a weak shock wave in the (x, t) -plane.

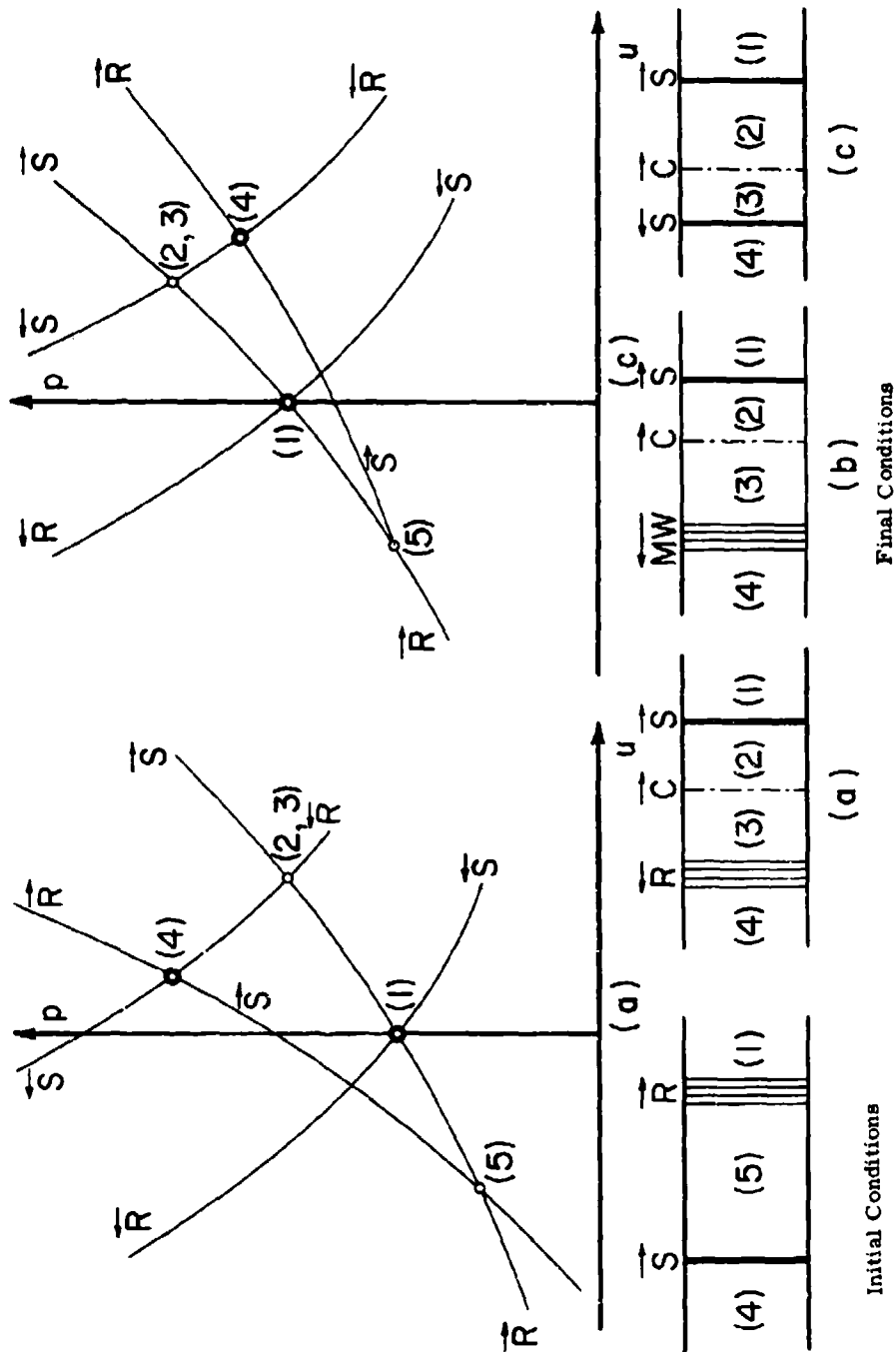


Fig. 2.4-37. Overtaking of a rarefaction wave by a strong shock wave in the (u, p) -plane.

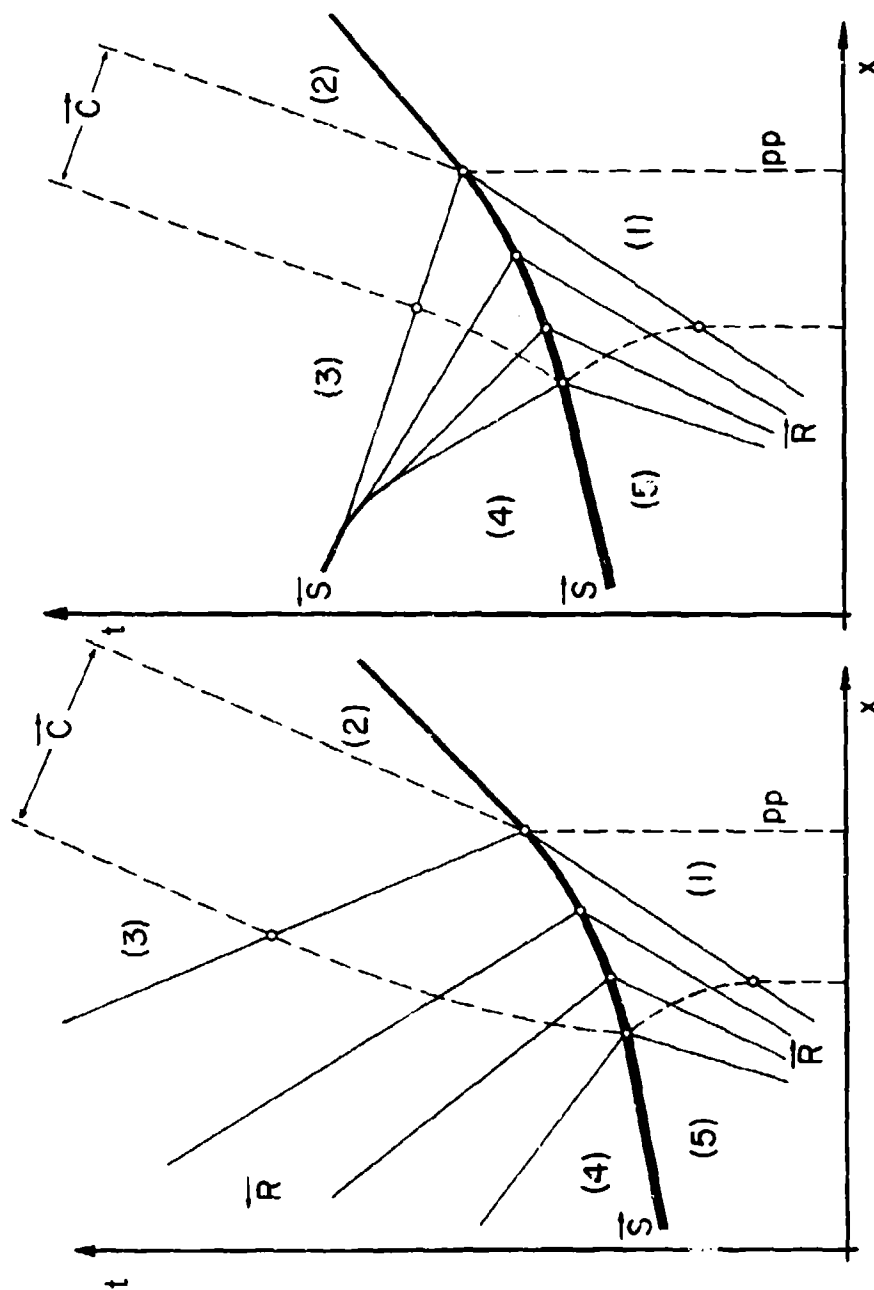
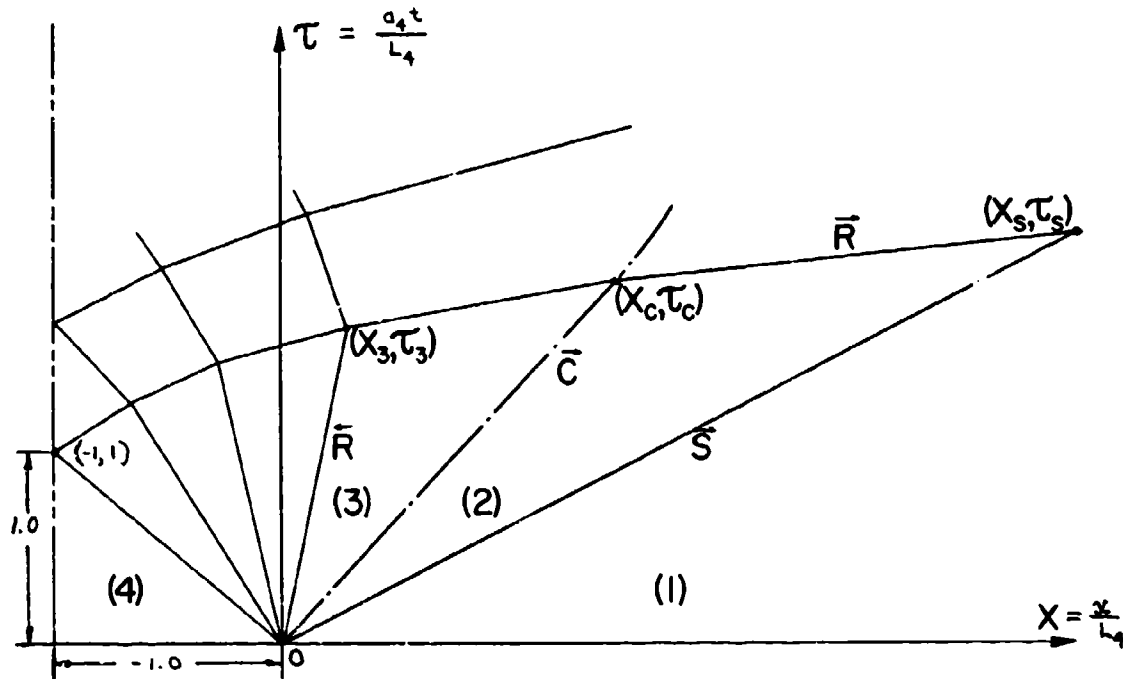


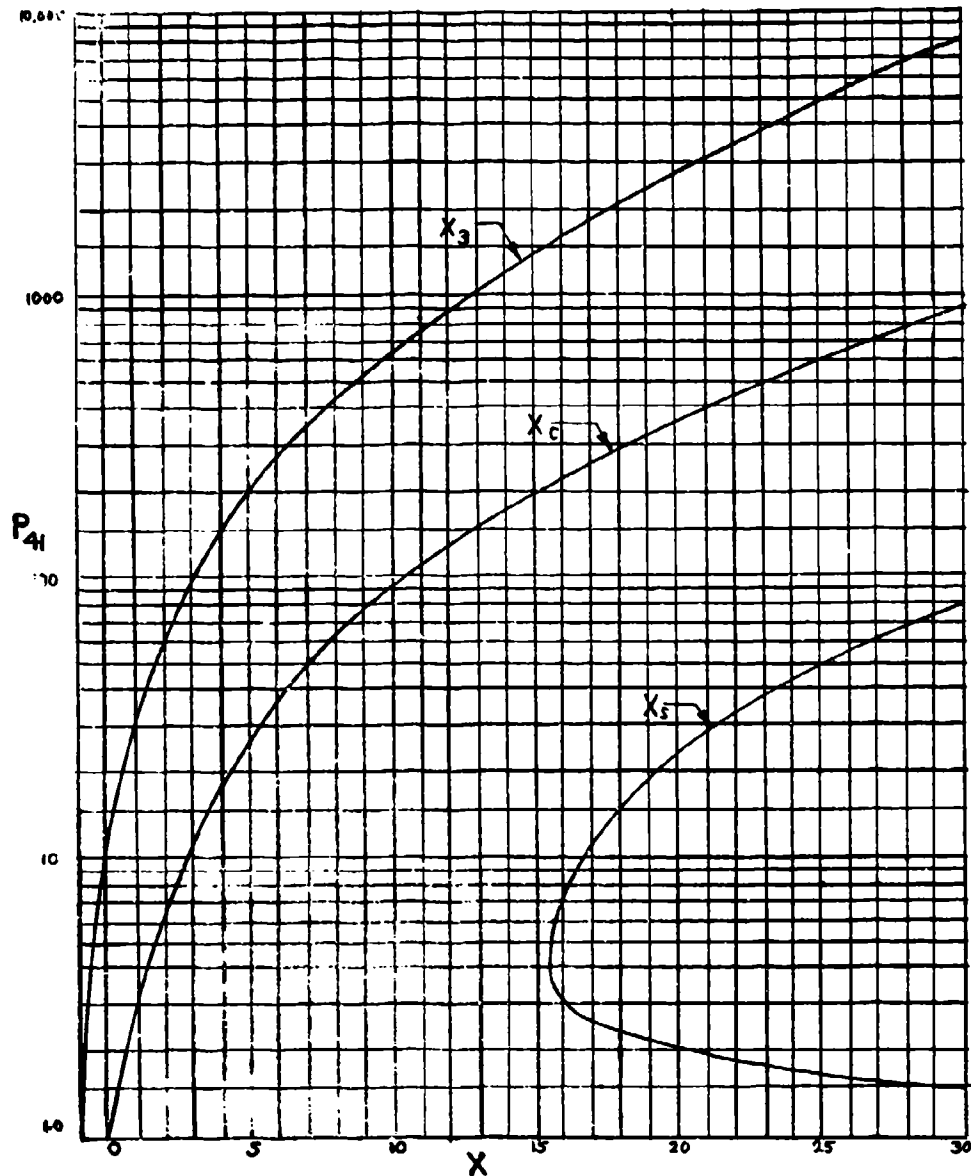
Fig. 2.4-38. Overtaking of a rarefaction wave by a strong shock wave in the (x, t) -plane.



- (a) Point (X_6, τ_6) where the steady state region (6) forms behind the reflected rarefaction wave.
- (b) Point (X_3, τ_3) where the head of the reflected rarefaction wave overtakes the tail of the incident rarefaction wave.
- (c) Point (X_c, τ_c) where the head of the reflected rarefaction wave overtakes the contact surface.
- (d) Point (X_s, τ_s) where the head of the reflected rarefaction wave overtakes the shock wave.
- (e) Point (X_5, τ_5) where the steady state region (5) forms behind the reflected shock wave.

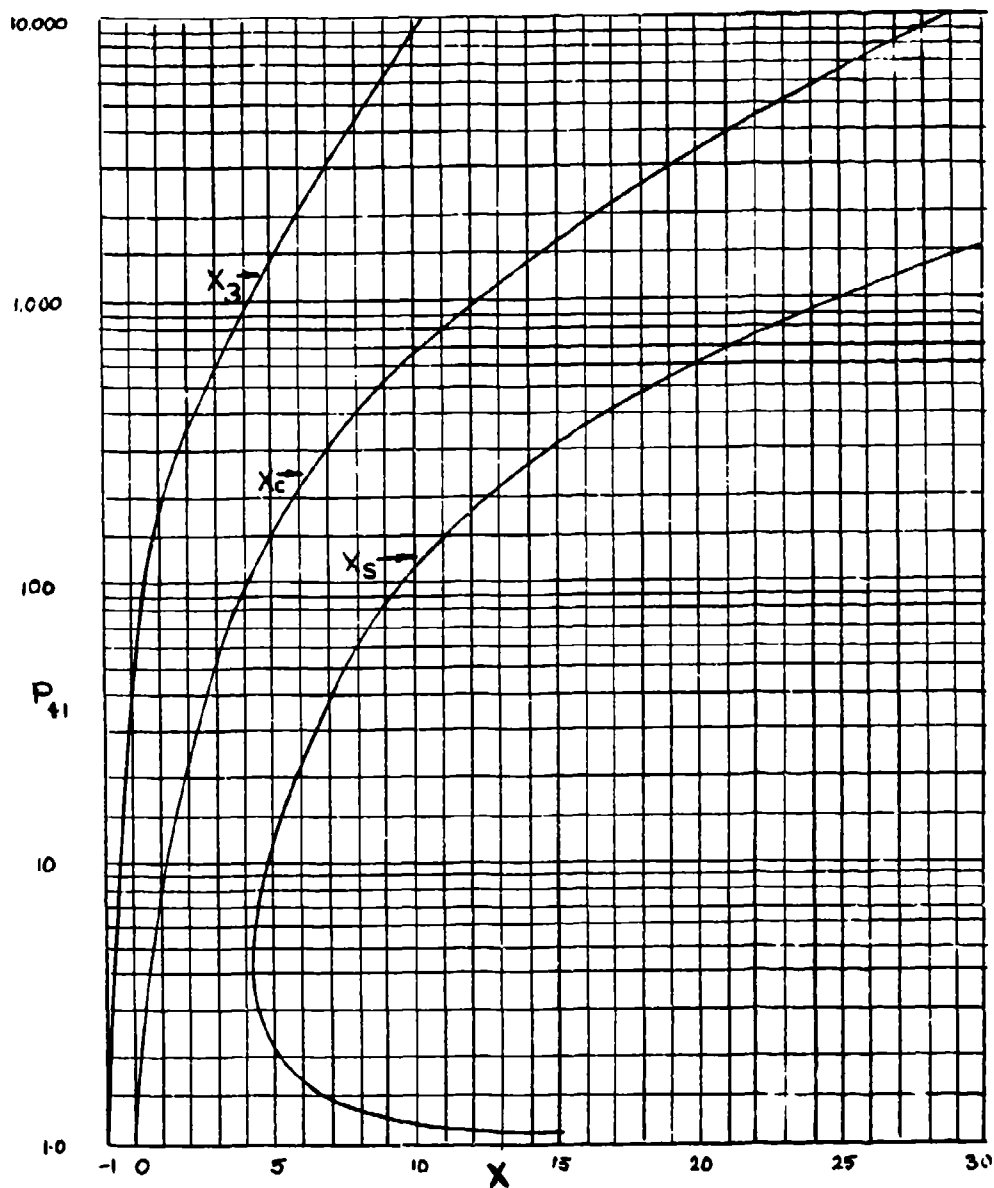
The point (X_6, τ_6) is given by $(-1, \tau_6)$. The value of τ_6 as a function of the diaphragm pressure ratio P_{41} is shown on Fig. 2.4-15 for different gas combinations.

Fig. 2.4-39. Points in the (X, τ) -plane where the head of the reflected rarefaction wave overtakes the tail of the incident rarefaction wave (X_3, τ_3) , the contact surface (X_c, τ_c) , and the shock wave (X_s, τ_s) (L_4 is the chamber length).



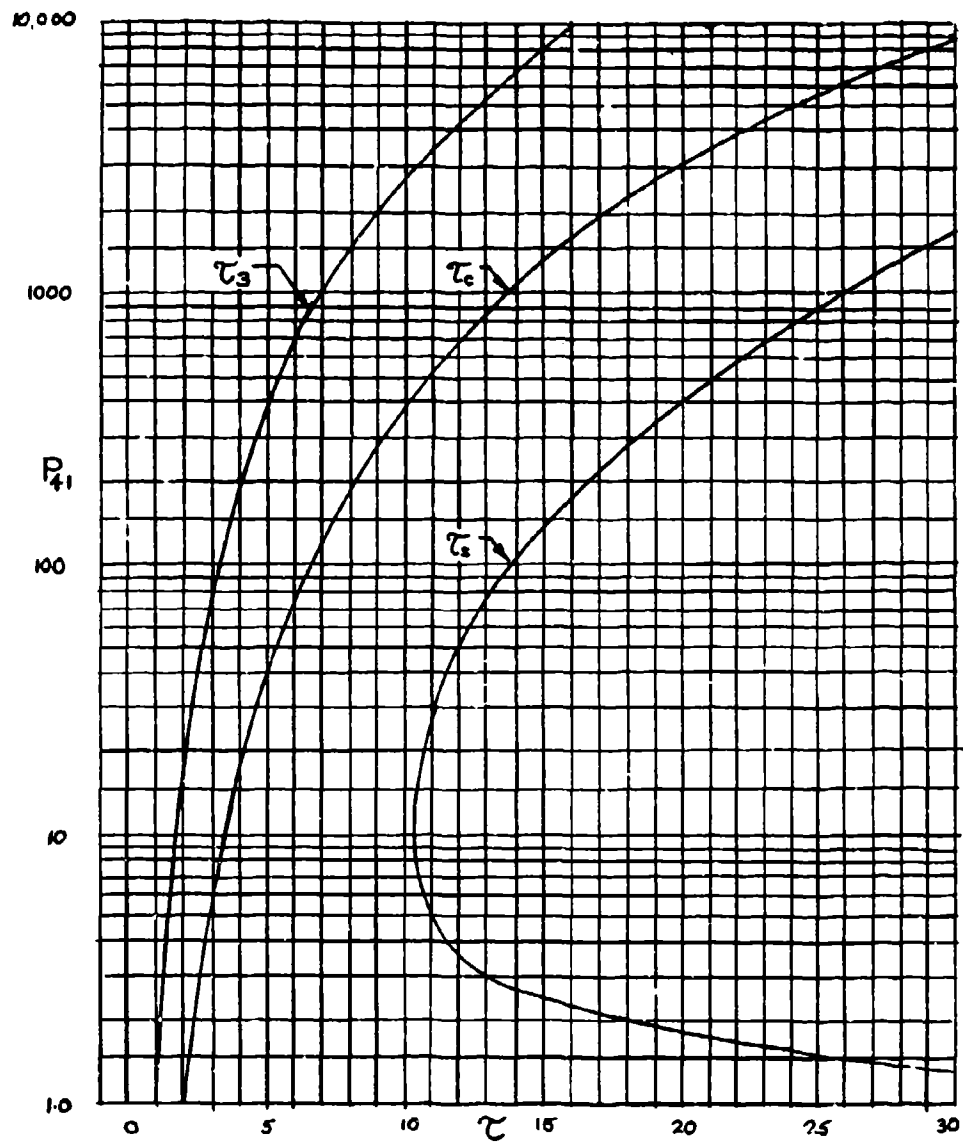
(See Fig. 2.4-39 for definition of X .)

Fig. 2.4-40. Variation of X_3 , X_c , and X_s with the pressure ratio (P_{41}) across the diaphragm for air/air; $T_{14} = 1$ or $E_{14} = 1$.



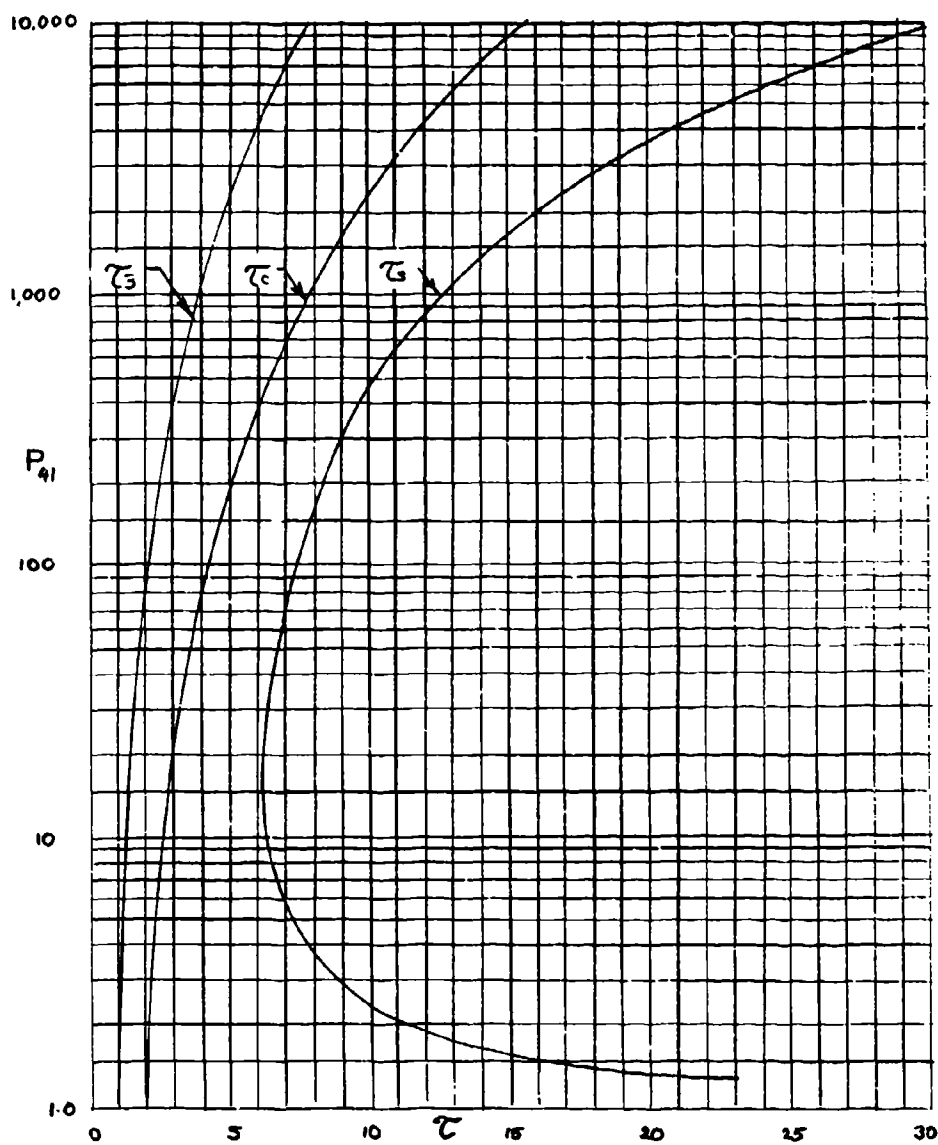
(See Fig. 2.4-39 for definition of X .)

Fig. 2.4-41. Variation of X_3 , X_c , and X_s with the pressure ratio (P_{41}) across the diaphragm for He/air; $T_{14} = 1$.



(See Fig. 2.4-39 for definition of τ .)

Fig. 2.4-42. Variation of τ_3 , τ_c , τ_s with the pressure ratio (P_{41}) across the diaphragm for air/air; $T_{14} = 1$ or $E_{14} = 1$.



(See Fig. 2.4-39 for definition of z .)

Fig. 2.4-43. Variation of z_3 , z_c , z_5 with the pressure ratio (P_{41}) across the diaphragm for He/air; $T_{14} = 1$.

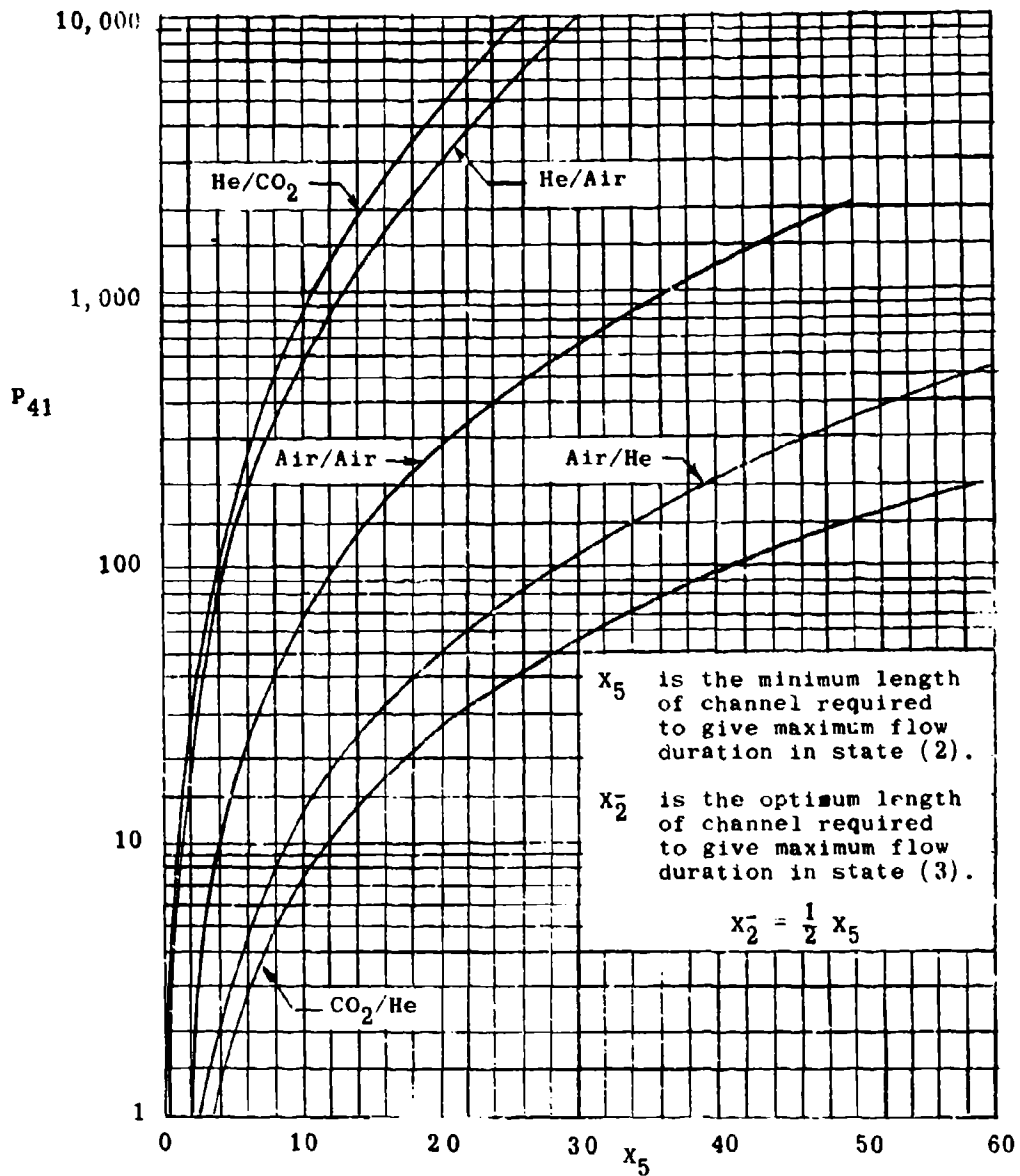
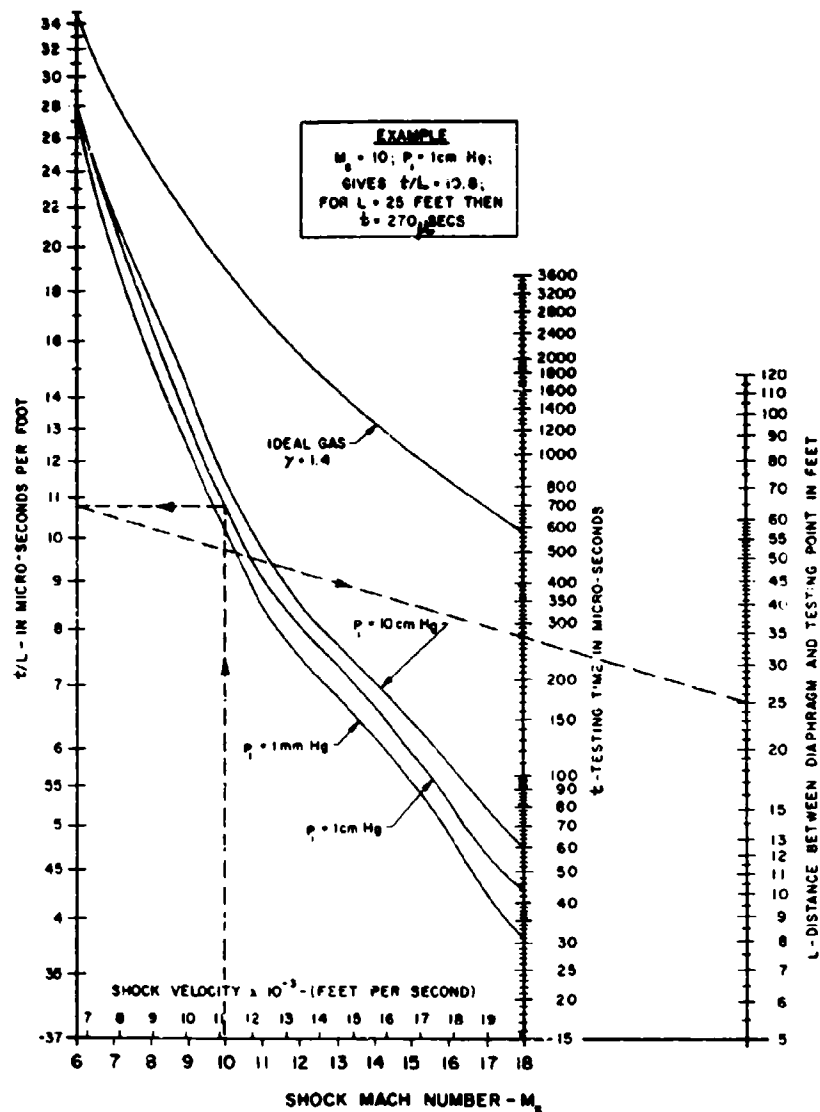


Fig. 2.4-45. Variation of X_5 and X_2 with the pressure ratio (P_{41}) across the diaphragm for different gas combinations.



Nomograph for calculating the time interval between the arrival of the shock wave and the driver gas at a given station in a shock tube. Calculations have been carried out considering air as an ideal gas ($\gamma = 1.4$) and a_0 in equilibrium at all times (recombination rate infinitely fast). For equilibrium air the testing time is greatly reduced.

Enter abscissa at shock Mach number and find intersection with initial pressure curve. Find values of left hand ordinate, t/L , at the latter intersection. Line up the value of t/L with the length of the shock tube on the right hand ordinate and read the testing time, t , on the center ordinate. Experimentally, the values of t are found to be approximately 50% of the values thus calculated.

Fig. 2.4-46. Testing time as a function of shock Mach number and initial pressure (Ref. 53).

REFERENCES

1. Courant, R. and Friedrichs, K. O. Supersonic Flows and Shock Waves. New York: Interscience Publishers, Inc., 1948.
- 1a. _____ . Interaction of Shock and Rarefaction Waves in One-Dimensional Motion, OSRD No. 1567. Washington: Office of Scientific Research and Development, 1943.
2. McLafferty, G. A Generalized Approach to the Definition of Average Flow Quantities in Nonuniform Streams. SR-13534-g. East Hartford, Conn.: Research Department, United Aircraft Corporation, December 1955.
3. Liepmann, H. W. and Roshko, A. Elements of Gas Dynamics. New York: John Wiley and Sons, Inc., 1957.
4. Hilsenrath, J. et al. Tables of Thermal Properties of Gases. NBS Circular 564. Washington: U. S. National Bureau of Standards, November 1955.
5. Allen, C. W. Astrophysical Quantities. London: Athlone Press (University of London), 1955.
6. Eggers, A. J., Jr. One-Dimensional Flows of an Imperfect Diatomic Gas. NACA Report 959, 1950.
7. Rudinger, G. Wave Diagrams for Unsteady Flows in Ducts. New York: Van Nostrand Co., 1955. (See also Boundary Conditions in Non-stationary Flow. Ninth International Congress on Applied Mechanics, Belgium, 1956.)
8. Shapiro, A. H. Dynamics and Thermodynamics of Compressible Fluid Flow. New York: The Ronald Press Co., 1954.
9. Trimpi, R. L. and Cohen, N. B. The Theory for Predicting the Flow of Gases in Shock Tubes with Experimental Verification. NACA TN 3375, March 1955.
10. Petschek, H. and Bryan, S. Approach to Equilibrium Ionization Behind Strong Shock Waves in Argon. Graduate School of Engineering, Cornell University, 1957.
- 10a. Spitzer, L., Jr. Physics of Fully Ionized Gases. New York: Interscience Publishers, Inc., 1956.
11. Bethe, H. A. and Teller, E. Deviations from Thermal Equilibrium in Shock Waves. BRL Report X-117. Aberdeen Proving Ground, Md.: Ballistic Research Laboratory, 1945.
12. Bethe, H. A. The Specific Heat of Air up to 25,000°C. OSRD 369. Washington: Office of Scientific Research and Development, 1942.
13. Salpeter, M. N. "Ionization of the Solar Chromosphere," Phil. Mag., Vol. 40 (1920), p. 472.
- _____ . "Elements in the Sun," Phil. Mag., Vol. 40 (1920), p. 808.

- 13a. Alpher, R. A. "The Saha Equation and the Adiabatic Exponent in Shock Wave Calculations," J. Fluid Mech., Vol. 2, Part 2 (1957), pp. 123-126.
- 13b. Pomerantz, J., Winkler, E. H., and Seigel, A. E. Thermodynamic Properties and One-Dimensional Flow of a Partially Ionized Monatomic Gas. NAVORD Report 4222. White Oak, Md.: U. S. Naval Ordnance Laboratory, 2 February 1956.
14. Herzfeld, K. F. Private Communication, September 1959.
- 14a. McChesney, M. Relaxation Phenomena in Diatomic Gases. Luton Report No. LAM 097. Stevenage, Luton, England: English Electric Co., Ltd., 1957.
15. Timan, B. L. "Heat Capacity of a Gas at High Temperatures," J. Experimental and Theoretical Phys., Vol. 27 (1954), pp. 262-264.
16. Epstein, P. S. Thermodynamics. New York: John Wiley and Sons Inc., 1947.
- 16a. Hansen, C. F. Approximations for the Thermodynamic and Transport Properties of High-Temperature Air. NACA TN 4150, 1958.
- 16b. Hansen, C. F. and Heims, P. H. A Review of the Thermodynamic Transport and Chemical Reaction Rate Properties of High-Temperature Air. NACA TN 4359, 1958.
17. Woolley, H. W. Effect of Dissociation on Thermodynamic Properties of Pure Diatomic Gases. NACA TN 3270, 1955.
18. Logan, J. G., Jr. Relaxation Phenomena in Hypersonic Aerodynamics. IAS Preprint No. 728. New York: Institute of Aeronautical Sciences, January 1957.
19. Gunn, S. C. Relaxation Time Effects in Gas Dynamics. R and M No. 2338. Ministry of Supply, Aeronautical Research Council. London: Her Majesty's Stationery Office, 1952.
20. Schwartz, R. N. and Herzfeld, K. F. "Vibrational Relaxation Times in Gases," J. Chem. Phys., Vol. 22 (1954), p. 767.
- 20a. Smiley, E. F. and Winkler, E. H. "Shock-Tube Measurements of Vibrational Relaxation," J. Chem. Phys., Vol. 22 (1954), p. 2018.
21. Blackman, V. H. "Vibrational Relaxation in Oxygen and Nitrogen," J. Fluid Mech., Vol. 1 (1956), pp. 61-85.
- 21a. Byron, S. R. Interferometric Measurement of the Rate of Dissociation of Oxygen Heated by Strong Shock Waves. Graduate School of Engineering, Cornell University, 1958.
22. Resler, E. L., Jr. "Characteristics and Sound Speed in Nonisentropic Gas Flows with Equilibrium Thermodynamic States," J. Aeronaut. Sci., Vol. 24 (1957), p. 785.
- _____ "Sound Speed in a Reacting Medium," J. Chem. Phys., Vol. 25 (1958), p. 1287.

- _____. "Sound Speed," J. Chem. Phys., Vol. 27 (1957), p. 596.
- 22a. Burgers, J. M. Selected Topics from the Theory of Gas Flow at High Temperature, Parts 1 to 5. TN BN-83. Institute for Fluid Dynamics and Applied Mathematics, University of Maryland, 1956.
- 22b. Kirkwood, J. G. and Wood, W. W. "Characteristic Equations for Reactive Flow," J. Chem. Phys., Vol. 27 (1957), p. 596
- 22c. Penner, S. S. Chemical Reactions in Flow Systems. ACARDograph No. 7. London: Butterworths, 1955.
- 22d. Chu, B. T. Wave Propagation and Method of Characteristics in Reacting Gas Mixtures with Applications to Hypersonic Flow. WADC TN 57-213. Division of Engineering, Brown University, 1957.
- 22e. Lighthill, M. J. Dynamics of a Dissociating Gas, I Equilibrium Flow. ARC 18,837. Ministry of Supply, Aeronautical Research Council. London: Her Majesty's Stationery Office, 1956.
- 22f. Freeman, N. C. Dynamics of a Dissociating Gas, III Non-Equilibrium Theory. AGARD Report 133, 1957.
- 22g. Bray, K. N. C. Departure from Dissociation Equilibrium in a Hypersonic Nozzle. ARC 19,983. Ministry of Supply, Aeronautical Research Council. London: Her Majesty's Stationery Office, 1958.
- 22h. Rudin, M. "Criteria for Thermodynamic Equilibrium in Gas Flow," Phys. of Fluids, Vol. 1, No. 5, (1958), p. 384.
- 22i. Broer, L. J. F. "Characteristics of the Equations of Motion of a Reacting Gas," J. Fluid Mech., Vol. 4, Part 4 (1958), p. 276.
23. Wood, W. W. and Kirkwood, J. G. "Hydrodynamics of a Reacting Relaxing Fluid," J. Appl. Phys., Vol. 28 (April 1957), p. 395.
- 23a. Feldman, S. The Chemical Kinetics of Air at High Temperatures; A Problem in Hypersonic Aerodynamics. AVCO Research Note 25. Everett, Mass.: AVCO Research Laboratory, AVCO Manufacturing Corp., 1957.
- 23b. Wood, W. W. and Parker, F. R. "Structure of a Centered Rarefaction Wave in a Relaxing Gas," Phys. of Fluids, Vol. 1, No. 3 (1958), p. 230.
24. Glass, I. I., Martin, W. A., and Patterson, G. N. A Theoretical and Experimental Study of the Shock Tube. UTIA Report 2. Institute of Aerophysics, University of Toronto, 1953.
25. Guderley, G. Nonsteady Gas Flows in Thin Tubes of Variable Cross-Section. TT No. 82. Ottawa, Canada: National Research Council, 1946.
26. Patterson, G. N. Molecular Flow of Gases. New York: John Wiley and Sons, Inc., 1956.
- 26a. Mandl, P. Transition Through a Weak Shock Front. UTIA Report 14. Institute of Aerophysics, University of Toronto, 1951.
- 26b. Sherman, F. S. A Low-Density Wind Tunnel Study of Shock Wave Structure and Relaxation Phenomena in Gases. NACA TN 3298, 1955.

- 26c. Talbot, L. The Structure of a Shock Wave in a Gas Having a Long Relaxation Time. TR-HE-150-145. Institute of Engineering Research, University of California, 1957.
- 26d. v. Krzywoblocki, M. Z. "On the Bounds of the Thickness of a Steady Shock Wave," Appl. Sci. Res (Netherlands) Section A, Vol. 6, No. 5-6 (1957), p. 337.
27. Christian, R. H., Duff, R. E., and Yarger, F. L. "Equations of State of Gases by Shock Wave Measurements," J. Chem. Phys., Vol. 23, No. 11 (1955), p. 2042.
28. D'iakov, S. P. "Shock Waves in a Relaxing Medium (University of Maryland TMBN-77)," J. Experimental and Theoretical Phys., Vol. 27 (1954), p. 728.
- 28a. Zeldovich, Ya. B. "Shock Waves of Large Amplitude in Air," J. Experimental and Theoretical Phys., Vol. 32, No. 5 (1957), pp. 1126-1135.
- 28b. Shafranov, V. D. "Structure of Shock Waves in a Plasma," J. Experimental and Theoretical Phys., Vol. 32, No. 6 (1957), pp. 1451-1459.
- 28c. Raizer, Yu. R. "On the Structure of the Front of Strong Shock Waves in Gases," J. Experimental and Theoretical Phys., Vol. 32, No. 6 (1957), pp. 1528-1535.
- 28d. Griffith, W. C. and Kenny, A. "On Fully Dispersed Shock Waves in CO₂," J. Fluid Mech., Vol. 3, No. 3 (1957), p. 286.
29. Chapman, D. R. Some Possibilities of Using Gas Mixtures Other than Air in Aerodynamic Research. NACA Report 1259, 1956.
30. Lighthill, M. J. "Viscosity Effects in Sound Waves of Finite Amplitude," Surveys in Mechanics, (edited by Batchelor and Davies). London: Cambridge University Press, 1956.
31. Glass, I. I. and Patterson, G. N. "Contributions to Fluid Mechanics from Shock Tube Research," Fifth International Aeronautical Conference, Los Angeles, Calif., 1955. New York: Institute of Aeronautical Sciences.
32. Kantrowitz, A. "Effects of Heat-Capacity Lag in Gas Dynamics," J. Chem. Phys., Vol. 14 (1946), p. 150.
33. Wood, G. P. Calculation of the Rate of Thermal Dissociation of Air Behind Normal Shock Waves of Mach Numbers of 10, 12, and 14. NACA TN 3634, 1956.
34. Evans, J. S. Method for Calculating Effects of Dissociation on Flow Variable in the Relaxation Zone Behind Normal Shock Waves. NACA TN 3860, 1956.
- 34a. Duff, R. E. The Use of Real Gases in a Shock Tube. Report 51-3. Engineering Research Institute, University of Michigan, 1951.
- 34b. Bird, G. A. Some Methods of Evaluating Imperfect Gas Effects in Aerodynamic Problems. RAE Tech. Note Aero 2488. Farnborough, Hants, England: Royal Aircraft Establishment, 1957.

- 34c. Stollery, J. L. Real Gas Effects on Shock-Tube Performance at High Shock Strengths. RAE Tech. Note Aero 2413. Farnborough, Hants, England: Royal Aircraft Establishment, 1957.
35. Gilmore, F. R. Equilibrium Composition and Thermodynamic Properties of Air to 24,000°K. RM-1543. Santa Monica, Calif.: Rand Corporation, 1955.
36. Hilsenrath, J. and Beckett, C. W. Thermodynamic Properties of Argon-Free Air. NBS Report 3991. Washington: National Bureau of Standards, 1955. (Also published with improvements as AEDC TN-56-12. Tullahoma, Tenn.: Arnold Engineering Development Center, 1956.)
- 36a. Feldman, S. Hypersonic Gas Dynamic Charts for Equilibrium Air. Everett, Mass.: AVCO Research Laboratory, AVCO Manufacturing Corp., 1957.
- 36b. Korobkin, I. and Hastings, M. S. Mollier Chart for Air in Dissociated Equilibrium at Temperatures of 2000 - 15,000°K. NAVORD Report 4446. White Oak, Md.: Naval Ordnance Laboratory, 1957.
- 36c. Hochstim, A. R. Gas Properties Behind Shocks at Hypersonic Velocities (Parts 1 to 4). Convair Physics Section Reports ZPh 002-005. San Diego, Calif.: Convair, 1958.
37. Bleviss, Z. O. and Inger, G. R. The Normal Shock Wave at Hypersonic Speeds. Report SM-22624. Santa Monica, Calif.: Douglas Aircraft Co., 1956.
38. Ames Research Staff. Equations, Tables, and Charts for Compressible Flow. NACA Report 1135, 1953.
39. Romig, M. F. "The Normal Shock Properties in Air in Dissociation Equilibrium," J. Aeronaut. Sci., Vol. 23, No. 2 (1956), p. 185.
- 39a. Bradley, J. C. "General Properties of Normal Shock Waves at Hypersonic Speeds," Heat Transfer and Fluid Mechanics Institute. Stanford, Calif.: Stanford University Press, 1957.
40. Moeckel, W. E. Oblique-Shock Relations at Hypersonic Speeds for Air in Chemical Equilibrium. NACA TN 3895, 1957.
41. Squire, W., Hertzberg, A., and Smith, W. E. Real Gas Effects in a Hypersonic Shock Tunnel. AEDC TN-55-14. Tullahoma, Tenn.: Arnold Engineering Development Center, 1955.
42. Resler, E. L., Lin, S. C., and Kantrowitz, A. "The Production of High Temperature Gases in Shock Tubes," J. Appl. Phys., Vol. 23, No. 12 (1952), p. 1390.
43. Bond, J. W., Jr. The Structure of a Shock Front in Argon. Report LA-1693. Los Alamos, N. Mex.: Los Alamos Scientific Laboratory, 1954.
44. Kolb, A. C. "Experiments at the U. S. Naval Laboratory," Proceedings of Symposium on Magnetohydrodynamics (Lockheed Aircraft). Stanford, Calif.: Stanford University Press, 1956.

45. Hall, J. G. Transition Through a Contact Region. UTIA Report 26. Institute of Aerophysics, University of Toronto, 1953.
46. Glass, I. I. and Patterson, G. N. "A Theoretical and Experimental Study of Shock Tube Flows," J. Aeronaut. Sci., Vol. 22, No. 2 (1955), pp. 73-100.
47. Steketee, J. A. On the Interaction of Rarefaction Waves in a Shock Tube. UTIA Review 4. Institute of Aerophysics, University of Toronto, 1952.
48. Gould, D. G. The Head-On Collision of Two Shock Waves and a Shock and a Rarefaction Wave in One-Dimensional Flow. UTIA Report 17. Institute of Aerophysics, University of Toronto, 1952.
- 48a. Rudinger, G. "The Reflection of Shock Waves at an Orifice at the End of a Duct," ZAMP, Vol. IXb, Fasc. 5/6 (1958), p. 570 (see also additional cited references therein).
49. Bitondo, D., Glass, I. I., and Patterson, G. N. One-Dimensional Theory of Absorption and Amplification of a Plane Shock Wave in a Gaseous Layer. UTIA Report 5. Institute of Aerophysics, University of Toronto, 1950.
50. Billington, I. J. and Glass, I. I. On the One-Dimensional Refraction of a Rarefaction Wave at a Contact Surface. UTIA Report 31. Institute of Aerophysics, University of Toronto, 1955.
51. Bull, G. V., Fowell, L. R., and Henshaw, D. H. The Interaction of Two Similarly-Facing Shock Waves. UTIA Report 23. Institute of Aerophysics, University of Toronto, 1952.
- 51a. Glass, I. I., Heuckroth, L. E., and Molder, S. On the One-Dimensional Overtaking of a Shock Wave by a Rarefaction Wave. UTIA Technical Note 30. Institute of Aerophysics, University of Toronto, 1959.
- 51b. Bremner, G. F., Datar, S. G., Dukowicz, J., and Glass, I. I. On the One-Dimensional Overtaking of a Rarefaction Wave by a Shock Wave. UTIA Technical Note. Institute of Aerophysics, University of Toronto (to be published 1960).
52. Lobb, R. K. On the Length of a Shock Tube. UTIA Report 5. Institute of Aerophysics, University of Toronto, 1950.
53. Rose, P. H. Physical Gas Dynamics Research at the AVCO Research Laboratory. AVCO Research Note No. 37. Everett, Mass.: AVCO Research Laboratory, AVCO Manufacturing Corp., 1957.
54. Matthews, D. L. "Interferometric Measurement in the Shock Tube of the Dissociation Rate of Oxygen," Phys. of Fluids, Vol. 2 (1959), p. 170.
55. Huber, P. W. "Note on Hydrogen as a Real-Gas Driver for Shock Tubes," J. Aeronaut. Sci., Vol. 25 (1958), p. 269.

3. Observed Flow in a Constant-Area Shock Tube

3.1 Comparison of Idealized Theory with Experiment

In the previous section the wave elements and the wave system that might be produced in a simple shock tube of constant area for perfect and imperfect inviscid gases were considered in some detail. The present section will endeavour to compare the experimental results with the theoretical predictions. It will be found that viscosity and heat transfer effects in the wall boundary layer modify the idealized wave system and the physical quantities in the uniform states. The magnitude of these effects depends mainly on the strength of the incident shock wave, the initial conditions, the type of boundary layer, and the area and length of the shock tube channel.

3.1.1 Wave System Produced by Diaphragm Removal

Plate 1.1-1 is typical of the schlieren photographs taken at the origin. These are presented and analysed in Ref. 1. Under pressure the cellophane diaphragm becomes a curved surface. When it ruptures, three-dimensional effects are introduced in the form of shock-wave reflection arising from shock curvature. Shock diffraction and vortices are also produced by the jagged remains of the diaphragm. As a result, the assumption of one-dimensional inviscid flow at the origin is not realized.

All the records are typical, in that the shock wave at the origin appears to be formed within a network of converging characteristic lines representative of a compression wave. However, closer examination of the optical records reveals that the method of characteristics cannot be applied in order to predict the birth point of the shock wave because the apparent compression wave is in fact composed of a number of coalescing shock fronts. These overtake, accelerate, and combine to form the primary shock wave. The wave is initially curved, but the resulting regular and Mach reflections form the mechanism that produces a plane primary shock wave (Ref. 2). It was also noted that the reflections give rise to a train of transverse waves that follow the primary shock wave down the tube (even as far as 50 tube hydraulic diameters). They also propagate upstream of the diaphragm. Eventually the transverse waves become sound waves. However, they form a dissipative mechanism that extracts energy from the flow, and thus they contribute to the total shock-wave attenuation and to the fluctuation of physical quantities in the two uniform regions separated by the contact front.

It is shown in Ref. 1 that even for a weak shock wave ($P_{21} < 3$) contact surface accelerations of the order of 7×10^7 ft/sec may be produced during the first 10 μ sec, and in this respect the rupturing process approximates the ideal case of infinite acceleration.

Plate 1.1-1 also shows that the contact front is in fact a region which, in a matter of 18 in., has grown to a thickness of over 3 in. In a long tube it can grow to several feet, and this seriously affects the available test time when the shock tube is used as an aerodynamic facility.

The region behind the contact front and the rarefaction wave is filled with striations that are indicative of turbulent and eddying

flow. The rough flow is caused by the passage of the gas from the chamber over the jagged remains of the diaphragm.

Since the ideal case of an instantaneous plane shock wave is not attained at the origin, the rarefaction wave is not centred there. The head of the wave appears prominently on Plate 1.1-1, but not the tail of the wave. The nonappearance of this characteristic line cannot be attributed entirely to the fact that the rarefaction wave is not centred, since the order of magnitude of the density derivative which responds to a schlieren system is not too different for the head and tail of the wave. However, when a centred rarefaction wave is produced by means of shock wave refraction, the tail can also be seen in a schlieren photograph (see Subsec. 2, Ref. 31).

Plate 1.1-1 indicates that after some distance from the diaphragm the shock wave becomes well formed. This distance depends on the tube cross-section, the diaphragm material, and the pressure difference across the diaphragm. In Ref. 1, it is noted that for a 3 x 3-in. shock tube the shock velocity was uniform after about 4 to 6 hydraulic diameters ($4A/C$) when the diaphragm was loaded near its bursting strength. If the diaphragm was not well loaded, the shock formation process was longer and the contact front was thicker. Improved shock velocities are obtained with proper diaphragm loading, especially at higher shock strengths, where the formation distance can be an order of magnitude greater (see Ref. 38).

3.1.2 Wave Speed Measurements

Since the head of a rarefaction wave travels into a quiescent gas with the speed of sound, this property can be utilized to determine the sound speed in a gas (Ref. 3). The method makes use of a schlieren record of the (x, t) -plane, such as Plate 1.1-1. The rate of advance of any wave is given by $w = v \tan \alpha / \mu$ (where v is the film speed, α is the acute angle between the t -axis and the wave element, and μ is the optical magnification factor of the x -axis). In the limit, a weak shock approaches a sound wave. This principle can also be used to measure sound speed (Ref. 4).

The results presented in Refs. 3 and 4 are summarized in Table 3.1-1. It is seen that these values are in excellent agreement with the acoustic result $a^2 = \gamma RT$, where γ is based on equilibrium of active and inert degrees of freedom, when applicable. This is to be expected, as the measurements of the head of a rarefaction wave produced by breaking a diaphragm in a shock tube would probably not reveal relaxation effects (in the form of a higher sound speed very close to the origin, Subsec. 2.1.5) since the wave is not centred. Consequently, the flow would probably be in equilibrium since any particle path would have a long effective flow time.

From the relations given in Subsec. 2.3, it might be concluded that once the initial conditions in a shock tube were given, the final-state properties and wave speeds could be found. Alternatively, if the shock speed is known (see Subsec. 7.4 for measurement methods), then the properties behind it can be calculated. Optical devices made it relatively easy to measure this quantity even in the early days of shock tube development. Investigators found that when the shock wave was weak and travelled over relatively short distances in tubes that were not of

small diameter, then agreement with theory was quite good. However, as soon as the above quantities were accentuated, it was found that the shock strength attenuated (Refs. 1, 2, 5, 6, 7, and 8).

Some typical results are shown in Figs. 3.1-1 and 3.1-2.

It has been found (Ref. 1) that the total attenuation in a shock tube can be described as in Fig. 3.1-3a. When the diaphragm ruptures, the compression waves overtake to form a shock front, which gains in strength until it reaches a maximum velocity at x_f , the formation distance. Beyond that, the shock front attenuates with increasing distance. Consequently, the formation decrement and the distance attenuation make up the total attenuation at any given station. Some investigators do not agree that a formation decrement really exists (Ref. 5). However, the results of Refs. 1 and 7 tend to confirm this model. Recently, the work of Ref. 7a has substantiated the type of curve shown in Fig. 3.1-3a for shock waves produced in air by helium or hydrogen in the chamber. Some results appear in Figs. 3.1-3b and 3.1-3c, which show the variation of the shock Mach number M_s with distance x from the diaphragm station. The value of M_s given in the tables on the figures was calculated by using imperfect gas effects behind the shock in accordance with Subsec. 2.3.3. It is seen that in the case of hydrogen, the formation decrement is almost zero, whereas for helium a formation increment appears to result. It is seen from Fig. 3.1-3b that the effect of increasing the initial air pressure from 5 to 100 mm Hg appears to be small. For shocks of the same strength, Fig. 3.1-3c indicates that the attenuation rate with distance is very much greater (double) for hydrogen than for helium as a driver gas. The latter would be preferable for aerodynamic testing. It is worthy of note that the formation distance in these cases is very large, that is, about 20 ft or 64 hydraulic diameters. (Recent attenuation studies reported in Ref. 19 substantiate the trend of the curves given in Ref. 7a.)

Experimenters realized that the above results are probably due to the boundary layer growth in the shock tube. Figure 3.1-4 is a schematic diagram of the flow in a shock tube at a time $t = t_1$. It is seen that a boundary layer exists between the head of the rarefaction wave and the shock front. It starts growing at these two faces (which effectively are leading edges) and increases in thickness until it reaches a maximum at the contact region. Due to the condition of no slip at the wall, the contact front would extend right back to the diaphragm station. It is seen that the boundary layer consists of three main regions. In state (2), which is hot with respect to the tube walls, the growth occurs in a uniform unaccelerated region (if the boundary layer is thin). In state (3), which is cold with respect to the tube walls, the boundary layer growth is similar, but it takes place at a higher free-stream Reynolds number and Mach number. In the rarefaction zone the boundary layer is subjected to a monotonically decreasing pressure and increasing velocity. As indicated in the diagram, at the contact surface where the two main boundary layers meet, the flow would be still more complex. In a real flow this effect is even more pronounced owing to the wide extent of the contact region. As time goes on, the leading edges have raced along the tube in opposite directions, transition to turbulent flow occurs, the boundary layer becomes thicker, and the assumption of a zero pressure gradient in the uniform regions becomes invalid. Finally, after a long enough time has elapsed (assuming the shock tube is of sufficient length), the boundary layer fills the tube and the flow consists predominantly of a turbulent pipe flow.

A review of the early attempts to account for the boundary layer effects is given in Ref. 8. Recently, the theoretical work of Refs. 9, 10, 11, and 12 have given a means of predicting not only the shock attenuation effects, but also the resulting deviations in the flow quantities that one might expect to arise as a result of the boundary layer growth. Basically, the two theories postulate the continuous generation of nonstationary compression and expansion waves by the boundary layer. These pressure waves traverse the flow and change its properties as well as the speed of the shock wave and the contact zone. Consequently, there are no uniform flow regions. All flow properties become a function of x and t . However, the mechanisms for generating the pressure waves are different. Trimpi and Cohen consider that the pressure waves are generated by skin friction and heat transfer effects, whereas Mirels takes the view that they are essentially generated by the vertical velocity at the edge of the boundary layer, that is, a piston-like effect. Both theories predict an attenuation that varies with shock strength, the distance the shock has travelled from the diaphragm, the boundary layer type and profile, the initial conditions across the diaphragm, and the tube cross-section.

In Ref. 12 (p. 46) it is pointed out that for thin boundary layers with an isentropic core the theory developed by Mirels should apply, whereas for thick boundary layers or pipe flow the theory of Trimpi and Cohen can be used since viscous shear affects the entire cross section. (In their theory they averaged the viscous effects over the cross section.) In Ref. 10 (p. 85) some concurrence on this point is also expressed. So far, an integrated and critical comparison of these two theories with experiment has not been made. However, the attenuation results of many investigations do agree quite well where the theory of Ref. 9 was applied.

A good account of this procedure is given in Ref. 8, from which Fig. 3.1-1b has been reproduced. It is seen that the results of Fig. 3.1-1a tend to lie on curves based on the theory of Ref. 9, which assumes a turbulent boundary (compressible or incompressible) layer over the entire flow (T_c, T_{ic}, T), rather than a laminar layer (L_c, L_{ic}).

It was noted above that the contact surface becomes an eddying zone in a real flow that can stretch over many feet, depending on the length of the shock tube or the flow duration. Consequently, one might expect from the previous remarks regarding the boundary layer effects that the velocity of the contact front would not agree with the ideal particle velocity. The behaviour of the front of the contact zone, as recorded by (x, t) -schlieren photographs (Ref. 1), is indicated schematically on Fig. 3.1-5. When the diaphragm is pierced, a jet of air strikes the gas in the channel. The front of this jet moves at a velocity greater than the ideal U_{21} . When the shock is formed at x_f , it has decelerated to a value which is still higher than the ideal U_{21} , and from there on the front of the contact region speeds up with distance along the tube (Fig. 3.1-6). The theory of Ref. 12 predicts an increase in the contact front velocity. However, a quantitative comparison has not been made to date.

3.1.3 Uniform States Separated by the Contact Region

A fairly detailed study of the rarefaction wave and state (3) behind it (in air) was made in Ref. 13, using a piezo gauge and a hot-wire anemometer; and in Ref. 14, using a chrono-interferometer. The

results are shown in Figs. 3.1-7 to 3.1-11 and in Table 3.1-2. It is seen that the rarefaction wave for diaphragm pressure ratios $P_{41} > 1.5$ is much weaker than predicted by theory. The experimental values of Ref. 13 satisfy the isentropic relation $P_{34} = \Gamma_{34}^\gamma$. However, as shown in Fig. 3.1-11, the Riemann invariants P and Q are not satisfied. It was shown in Subsec. 2.1.2 (Eqs. (9) and (10)) that P and Q remain invariant for a tube of constant cross section in an inviscid flow. When a boundary layer forms in a real flow, heat transfer and friction (which are related to the normal component of the velocity at the edge of the boundary layer) act on the entire flow so that P and Q become functions of heat transfer and skin friction at any x and t. Consequently, it would not be surprising that the relations $P = 5A_{34} + U_{34}$ and $Q = 5A_{34} - U_{34}$ might not be satisfied in a flow where viscous effects are present. However, in this case, since the isentropic relation $P_{34} = \Gamma_{34}^\gamma$ is satisfied, it is rather anomalous that the Riemann invariants are not satisfied. A reasonable explanation of the above has not been given to date.

Other investigations in Refs. 15, 16, and 17 show very marked deviations in the physical properties of the flow right from the shock wave to the head of the rarefaction wave as shown on Figs. 3.1-12 to 3.1-15. The theories of Refs. 9 and 12 indicate that such flow changes can be expected to occur. The measured values of density and pressure (Figs. 3.1-14 and 3.1-15, Refs. 14 and 16) and calculated values of temperature (Fig. 3.1-16), entropy, velocity, and mass flow (Refs. 15 and 17) over large portions of the shock-tube flow indicate that the average pressure and density at a cross section increase as a function of time. However, the temperature has a tendency to decrease in state (2) and increase in state (3). It is seen that in Fig. 3.1-13, where the density variation with time is compared with the theory of Trimpi and Cohen, quantitative agreement is only fair although the slope of the theoretical curve corresponds closely to that of the experimental data.

The mass flow and the particle velocity (Fig. 3.1-12) never appear to reach their maximum ideal values and show a tendency to increase with distance between the shock and the rarefaction wave.

Typical measurements of the Mach numbers in states (2) and (3) in air for lower shock wave pressure ratios or shock wave Mach numbers which were determined from schlieren photographs of the oblique shock wave attached to a wedge of known angle (Ref. 2), are shown on Figs. 3.1-16a and 3.1-16b. It is seen that the Mach number in state (2) for lower diaphragm pressure ratios P_{41} is in good agreement with ideal theory. However, the Mach number in state (3) appears to reach a limiting value as P_{41} rises. Other experimenters did not find such a limit (Ref. 18). An experimental decision on this matter is still required.

Some experimental results of the flow Mach number M_2 for stronger shock waves in air are shown in Figs. 3.1-17a and 3.1-17b from Refs. 19 and 19a, respectively. Imperfect gas effects were used to determine the flow velocity and flow sound speed or the flow Mach angle μ_2 . It is seen that the Mach angles μ_2 , measured in a manner indicated on the figures, or the flow Mach numbers M_2 , derived from the experimental measurements of μ_2 , show good agreement with the theory for air treated as an imperfect gas. The perfect gas limit for $M_2 = 1.89$ is exceeded, of course, as the initial pressure p_1 is decreased for strong

shocks. (The reader is referred to Ref. 38 for recent measurements of physical quantities behind strong shock waves in nitrogen. Direct and other measurements have just been reported in Refs. 41, 42, and 43. Very good agreement with theory is indicated in Refs. 42 and 43 for temperatures behind shock waves in air, oxygen, nitrogen, and argon; in the latter case, up to 9000°K.)

It may be stated that in due course, as the physical quantities throughout the shock tube flow will become better known, it should be possible to put the theories of Ref. 9 and 12 (if they are extended to strong shock flows) to a decisive test with regard to shock wave attenuation and the variation of the physical flow quantities in a shock tube (see Refs. 39 and 40 for a recent survey of this problem).

3.1.4 Wave Interaction Results

Not all of the one-dimensional wave interactions considered in Subsec. 2.4 have been tested experimentally. However, those that have been tested agree quite well with the theoretical predictions and lend considerable weight to a (p, u)-plane type of analysis (Subsec. 2.3.1).

A large number of results on the normal reflection of shock waves in argon, nitrogen, and carbon monoxide is given in Ref. 20 (Fig. 3.1-18). When imperfect gas effects and boundary layer effects are taken into account, the results appear quite consistent with theory. (The calculated values for the curves in Fig. 3.1-18 are listed in Table 3.1-3 and were kindly supplied by Greene, Ref. 20a.) A more critical evaluation is given in Subsec. 3.2.5.

In comparison to the above, very little experimental information is available on the normal reflection of rarefaction waves or the uniform state (6) that can be formed behind it.

Some results for the head-on collision of two shock waves and a shock and rarefaction wave (Subsec. 2, Ref. 48) are shown in Figs. 3.1-19 and 3.1-20. It is seen that for this range of experiments the agreement with theory is quite good.

Experimental data on the collision of two rarefaction waves is not yet available. Some (x, t)-plane schlieren records of this interaction and of the normal reflection of a rarefaction wave may be found in Ref. 46, Subsec. 2. Hot-wire anemometer and piezo-pressure gauge records of the latter are given in Ref. 13.

One-dimensional refraction of shock waves and rarefaction waves has been investigated (Refs. 21 to 23), and the results agree quite well with the theory outlined in Subsec. 2.4. Typical experimental data are given in Figs. 3.1-21 to 3.1-27.

The Air || A contact surface in Fig. 3.1-21 was established by using a microfilm of nitrate dope to separate the two gases. Its effect on the interaction could be taken into account (Ref. 21). An increase in shock pressure ratio (amplification) after refraction is evident.

For the single and double refraction problems illustrated in Figs. 3.1-22 to 3.1-24, a slide technique was used to separate the gases. The slide was withdrawn when the shock was generated in the tube, permitting it to interact with the new gas. It can be seen that significant

decrease in shock pressure ratio (attenuation or absorption) can take place in a gas like helium or hydrogen. However, the layer of gas (Air || He || Air) is not suitable for shock attenuation because, far enough away from the layer, overtaking shock waves strengthen the emergent shock and bring its pressure ratio back towards the original value (Fig. 3.1-24).

Figure 3.1-25 illustrates the refraction problem at a moving contact surface generated in a shock tube by using He || Air. It will be seen that at an incident wave Mach number $W_{11} \sim 3.4$ the gas behind the rarefaction wave is cold enough to change the energy ratio across the Air || He contact surface so that it is below the critical value, and now the pressure ratio across the transmitted shock wave is increased. This gives rise to a reflected shock wave after refraction as shown. This shock wave undergoes normal reflection and refraction. It then overtakes the original transmitted shock wave and increases its strength in a manner similar to Fig. 3.1-24. The agreement with theory is quite good. This type of refraction forms the basis for the tailored-interface hypersonic shock tunnel (Subsec. 5.1.2.3).

The above problems involving overtaking shock waves indirectly verifies this type of interaction. The overtaking shock problem has also been studied in Ref. 23, and good agreement with theory is indicated.

The refraction of a rarefaction wave at a contact surface was investigated in Ref. 13. Piezo-gauge data of the interaction are shown in Figs. 3.1-26 and 3.1-27 for Air || A and Air || He, respectively. The agreement with theory is very satisfactory, providing the actual rarefaction, not the one computed from the diaphragm pressure ratio, is used for comparison. A typical hot-wire anemometer trace and piezo-gauge record are shown in Fig. 3.1-28. It should be noted that the hot wire total temperature measurements were found to be close to the theoretical value, whereas the mass flow results showed a considerable scatter (Ref. 13). From a measurement of pressure, mass flow, and total temperature, all other flow quantities can be calculated. Fortunately, the mass flow has a weak effect on the calculations. However, the piezo-pressure gauge measurements across the various states in themselves are quite convincing.

3.2 Boundary Layer Effects

The present Section will consider in more detail the boundary layer that forms on the shock tube walls between the head of the rarefaction wave and the shock wave (see Fig. 3.1-4). It was noted in Subsec. 3.1 that it is this boundary layer which induces the deviations in the wave speeds and the physical quantities in a shock-tube flow.

3.2.1 Laminar Boundary Layer

For a laminar boundary layer with zero pressure gradient, the problem was initially considered as analogous to Rayleigh's analysis (Ref. 24) of an infinite flat plate that has been instantly accelerated from rest to a uniform velocity u_1 at $t = 0$. This was the method adopted in Ref. 25 in order to estimate shock wave attenuation. It was assumed that the defect in mass flow at the contact surface expressed

as a function of the pressure ratio across the shock could be equated to the mass flow defect derived from the viscous incompressible equations of motion (Ref. 1). With this assumption, it is possible to obtain the strength of the attenuated shock wave. The validity of this analogy was not verified and the agreement with experiment for stronger shocks was poor. (It is shown in Ref. 28 that, for weak shocks, by neglecting second order terms, the analogy is exact.)

In Ref. 26 a historical note describes the work that led to the correct formulation and solution of the zero-pressure-gradient, compressible, laminar boundary layer with heat transfer in the region behind a moving shock wave as given by Hollyer (Ref. 27). This work was extended by Mirels (Ref. 28), who showed that for weak shock waves the boundary layer is equivalent to the Rayleigh problem and that an analytical solution is possible. For the stronger shock waves a numerical solution is given for velocity and temperature profiles, recovery factors, and skin friction and heat transfer coefficients. This problem has also been studied in Refs. 29 and 30, with special application to wall surface temperature and heat transfer.

An examination of Fig. 3.1-4 shows that it would be possible to put the two nonstationary boundary layers with their moving leading edges at the shock front and at the rarefaction wave head into a steady-flow frame of reference by fixing a set of co-ordinate axes to the wave front. This imposes no difficulty at the shock but requires an assumption that the rarefaction wave fan can be replaced by a single plane (expansion shock). This assumption becomes progressively worse as the pressure ratio across the diaphragm increases. In the limit, for a perfect gas, state (3) disappears (see Subsec. 2.3.2), and the rarefaction wave fan occupies a length which is sixfold greater (for Air/Air, $\gamma = 1.4$) than the region occupied by state (2), between the shock and the contact surface. The two boundary layers in steady and unsteady co-ordinates are shown in Figs. 3.2-1 and 3.2-2. The gas thermal boundary layer and the wall thermal layer appear in Fig. 3.2-3. (The notation used in Subsec. 2, above, has been retained; that is, for a shock wave $v_1 = w$, $v_2 = w - u_2$, $v_1/v_2 = \rho_2/\rho_1$, and $1 \leq \rho_2/\rho_1 \leq 6$ for $1 \leq v_1/a_1 \leq \infty$, for $\gamma = 1.4$. Similarly, for an expansion wave $v_1 = a_4$ and $v_2 = a_4 + u_3$. For $\gamma = 1.4$, in the range $0 \leq u_3 \leq 5 a_4$, $1 \geq v_1/v_2 \geq 1/6$.) It is seen that, in steady co-ordinates, the wall now has a velocity equal to the wave velocity ($v_1 = v_w$). The expansion wave profile is reminiscent of a boundary layer with slip flow, while behind the shock wave the profile has the largest velocity at the wall and smallest in the free stream.

Following the method used in Refs. 28 and 31, the Prandtl boundary layer equations are applied (except at the leading edges of the two waves) to the compressible flow for $x > 0$ with the assumption $dp/dx = 0$.

Continuity:

$$\frac{\partial(\rho u)}{\partial x} + \frac{\partial(\rho v)}{\partial y} = 0 \quad (1)$$

Momentum:

$$u \frac{\partial u}{\partial x} + v \frac{\partial u}{\partial y} = \frac{1}{\rho} \frac{\partial}{\partial y} \left(\mu \frac{\partial u}{\partial y} \right) \quad (2)$$

Energy:

$$\rho C_p \left(u \frac{\partial T}{\partial x} + v \frac{\partial T}{\partial y} \right) = \frac{\partial}{\partial y} \left(k \frac{\partial T}{\partial y} \right) + \mu \left(\frac{\partial u}{\partial y} \right)^2 \quad (3)$$

State:

$$p = \rho RT \quad (4)$$

Boundary conditions for shock wave (Fig. 3.2-1):

$$\begin{aligned} u(x, 0) &= -w_1 = -v_1 \quad (\text{zero slip}) \\ v(x, 0) &= 0 \\ T(x, 0) &= T_w \quad (\text{constant wall temperature}) \end{aligned} \quad (5)$$

(It was shown in the above references that $T_w = T_1$ except for stronger shocks.)

$$\begin{aligned} u(x, \infty) &= (u_2 - w_1) = -v_2 \\ T(x, \infty) &= T_2 \end{aligned}$$

Boundary conditions for the expansion wave (Fig. 3.2-1):

$$\begin{aligned} u(x, 0) &= a_4 = v_1 \\ v(x, 0) &= 0 \\ T(x, 0) &= T_w \quad (\text{constant wall temperature}) \end{aligned} \quad (6)$$

(It was also shown that $T_w \sim T_4 = T_1$ for all expansions.)

$$\begin{aligned} u(x, \infty) &= a_4 + u_3 = v_2 \\ T(x, \infty) &= T_3 \end{aligned}$$

(Note: The typed "v" signifies a relative velocity in the x-direction, whereas the written "v" is the actual velocity component in the y-direction.)

The assumption of constant wall temperature was shown to be valid for a laminar boundary layer in Ref. 31. It has also been substantiated experimentally in Ref. 26. Even for a turbulent boundary layer, although the temperature varies with distance behind the shock, the approximation is good except possibly for stronger shocks.

Numerical solutions to the above equations in the range $0 \leq v_1/v_2 \leq 6$ are given in Refs. 28 and 31. The case of $v_1/v_2 = 0$ is the Blasius solution for the incompressible flow past a fixed, semi-infinite plate. When $v_1/v_2 = 1 \pm \epsilon$ (where ϵ is a small quantity, $\epsilon \ll 1$; otherwise when $\epsilon = 0$, $v_1/v_2 = 1$, $u_2 = 0$, and a boundary layer is not possible, see Fig. 3.2-2) an analytical solution involving the first order in $(v_1/v_2 - 1)$ is possible, which reduces to the Rayleigh relation for the nonstationary boundary layer:

$$\frac{v_1 - v}{v_1 - v_2} = \frac{u}{u_2} = \operatorname{erf} \sqrt{\frac{v_2}{x \nu_2}} \frac{y}{2} = \operatorname{erf} \frac{y}{2\sqrt{\nu_2 x}} \quad (7)$$

A boundary layer parameter η is defined as

$$\eta = \sqrt{\frac{v_2}{2 \nu_w x}} \int_0^y \frac{T_1}{T} dy \quad (8)$$

The boundary layer thickness δ is defined as that value of y when $y = \delta$ or $\eta = \eta_\delta$, and at that point

$$\frac{v_1 - v}{v_1 - v_2} = 0.99 \quad \text{or} \quad \frac{v}{v_2} = 0.99 \pm 0.01 \frac{v_1}{v_2} \quad (9)$$

(The plus sign is used for $1 \leq \frac{v_1}{v_2} \leq 6$ and the minus sign for $0 \leq \frac{v_1}{v_2} \leq 1$.) The variations of v/v_2 with η are given in Refs 28 and 31. Consequently, when v/v_2 assumes the value of Eq. (9), η_δ is known, and the reduced quantities η/η_δ versus $\frac{v_1 - v}{v_1 - v_2}$ can be plotted. For the Rayleigh case, we write

$$\frac{v_1 - v}{v_1 - v_2} = \operatorname{erf} (K \cdot \eta/\eta_\delta) \quad (10)$$

where $K = \text{constant}$.

When

$$\eta = \eta_\delta, \quad \frac{v_1 - v}{v_1 - v_2} = 0.99 \quad \text{and} \quad K \sim 1.8$$

or

$$\frac{v_1 - v}{v_1 - v_2} = \operatorname{erf} (1.8 \cdot \eta/\eta_\delta) \quad (10a)$$

Equation (10a) along with the reduced values for the Blasius ($v_1/v_2 = 0$) and the strong shock cases ($v_1/v_2 = 6$) are shown on Fig. 3.2-4. It is seen that the velocity profiles encountered in a shock tube on the whole lie closer to the Rayleigh profile, except for strong expansions which are closer to the Blasius profile (with the assumption of an expansion shock). On this plot, it is seen that the slope of the profile at the wall increases from the Blasius to the Rayleigh to the strong shock case, and the curves are also in this order.

From Eq. (8), when $y = \delta$, $\eta = \eta_\delta$ and $T = T_2$,

$$\delta/\eta_\delta = \frac{T_2}{T_1} \sqrt{\frac{2 x \nu_w}{v_2}} \quad (8a)$$

For the Blasius case, when $v/v_2 = 0.99$, $\eta_\delta = 3.5$. For $T_2/T_1 = 1$,

$$\delta = 5 \sqrt{\frac{x \nu_2}{v_2}}$$

(This is the incompressible result for the boundary layer growth.)
From Eq. (7) for the Rayleigh case

$$\operatorname{erf} \sqrt{\frac{v_2}{x \nu_2}} \cdot \frac{\delta}{2} = 0.99$$

or

$$\delta = 3.6 \sqrt{\frac{x \nu_2}{v_2}}$$

For the strong shock case ($v_1/v_2 = 6$), $\frac{v}{v_2} = 1.05$ and $\eta_\delta = 1.55$

or

$$\delta = 2.2 \frac{T_2}{T_w} \sqrt{\frac{x \nu_w}{v_2}}$$

The shear stress τ_w at the wall is given by

$$\tau_w = \left(\mu \frac{\partial u}{\partial y} \right)_w = \mu_w v_2 \sqrt{\frac{v_2}{2 x \nu_w}} f''(0) \quad (11)$$

The friction $f''(0)$ is tabulated in Refs. 28 and 31. If the local skin friction is defined as

$$C_f = \frac{\tau_w}{\frac{1}{2} \rho_w (v_1 - v_2)^2} = \frac{\tau_w}{\frac{1}{2} \rho_w u_2^2} \quad (12)$$

and the Reynolds number as

$$Re = \frac{v_2 x}{\nu_w} \left(1 - \frac{v_1}{v_2}\right)^2 \quad (13)$$

(The reason for this definition of Re is given in Eq. (26) below.)

then

$$C_f \sqrt{Re} = \frac{\sqrt{2} f''(0)}{\left|\frac{v_1}{v_2} - 1\right|} \quad (14)$$

From Ref. 31, when

$$\frac{v_1}{v_2} = 0, \quad f''(0) = 0.4696$$

or

$$C_f \sqrt{Re} = 0.664$$

the incompressible-flow Blasius value.

When

$$\frac{v_1}{v_2} = 1, \quad f''(0) = \sqrt{\frac{2}{\pi}} \left(\frac{v_1}{v_2} - 1\right)$$

and $C_f \sqrt{Re} = 1.128$, the Rayleigh value.

Finally, when

$$\frac{v_1}{v_2} = 6, \quad f''(0) = 8.101 \text{ and } C_f \sqrt{Re} = 2.291$$

Thus, the Rayleigh value of $C_f \sqrt{Re}$ is greater than the corresponding Blasius value by a factor of 1.70, and the strong shock value is greater by a factor of 3.45.

Expressions for the recovery factor and heat transfer functions and their numerical values are also given in the above references over the range $0 \leq \frac{v_1}{v_2} \leq 6$ for a $Pr = 0.72$. It is shown that the recovery factor r rises from $r = 0.845$ (Blasius) to $r = 0.885$ (Rayleigh) to $r = 0.920$ for $v_1/v_2 = 6$.

In addition, it is shown in Ref. 31 that the thermal boundary layer in the wall of the tube can be described in a manner similar to the Rayleigh gas velocity boundary layer. The problem is that of bringing two media (the gas and the wall) at different uniform temperatures into contact at a time $t = 0$, and is given by the one-dimensional heat conduction equation (Fig. 3.2-3):

$$\frac{\partial T}{\partial x} = \frac{\alpha_w}{v_1} \frac{\partial^2 T}{\partial y^2} \quad (15)$$

where

$$\alpha_w = \left(\frac{k}{\rho C_p} \right)_w \quad (16)$$

is the diffusivity of the wall material. The boundary conditions for $x > 0$ are given by

$$T(x, 0) = T_w \quad (17)$$

$$T(x, -\infty) = T_1 \quad \text{and} \quad T(x, \infty) = T_4$$

for the shock wave and expansion wave, respectively.

The solution of Eqs. (15) to (17) is given by

$$\frac{T_w - T}{T_w - T_1} = \text{erf} \frac{-y}{2\sqrt{\frac{x\alpha_w}{v_1}}} \quad (18)$$

For a Prandtl number = 1, the recovery temperature and the total temperature are identical (for $Pr < 1$, $0.9 \leq T_r/T_0 \leq 1$ for $\infty \geq M \geq 1$; that is, the ratio is less than unity). Consequently, from Ref. 31 and Subsec. 2.3.2, for $\gamma = 1.4$, for $v_1/v_2 > 1$,

$$\frac{T_r}{T_1} - 1 = \frac{1}{3} (w_{11}^2 - 1) \quad (19)$$

and for $v_1/v_2 < 1$,

$$\frac{T_r}{T_4} - 1 = -2 \left[3 (P_{34})^{1/7} - 2 \right] \left[1 - (P_{34})^{1/7} \right] \quad (20)$$

Since $w_{11}^2 > 1$, $T_r/T_1 > 1$ and heat transfer always occurs from the gas to the wall behind the shock wave. From Eq. (20) or Figs. 2.1-24 and 2.3-25, it is seen that in the range $-1 \leq N \leq 1$; $1 \geq P_{34} \geq (2/3)^7$; $0 \leq M_3 \leq 2.5$ (see Subsec. 2.1.4, Eqs. (30) and (31)), $T_r/T_4 < 1$, and heat transfer occurs from the wall to the cold gas. For stronger expansion waves $T_r/T_4 > 1$, and heat is transferred from the cold gas to the tube walls. Therefore, it is possible for stronger expansion waves to have heat transfer into the gas for the initial portion of the fan ($N = 1$) and into the tube wall for the latter portion of the fan ($N > 1$) at the same time.

The temperature rise is given in Ref. 31 as

$$\frac{T_w - T_1}{T_1} = A_1 \left(\frac{T_r}{T_1} - 1 \right) \quad (21)$$

for $v_1/v_2 > 1$

where

$$A_1 \sim \sqrt{\frac{\alpha_w}{\alpha_1}} \cdot \frac{k_1}{k_w} \quad (22)$$

and

$$\frac{T_w - T_4}{T_4} = A_4 \left(\frac{T_r}{T_4} - 1 \right) \quad (23)$$

for $v_1/v_2 < 1$

where

$$A_4 \sim \sqrt{\frac{\alpha_w}{\alpha_4}} \cdot \frac{k_4}{k_1} \quad (23a)$$

If $k \propto T$ and $C_p = \text{constant}$, then $k/\sqrt{\alpha}$ is independent of T (depends on \sqrt{p}) for a given gas. (Typical values of α cm²/sec at $\sim 18^\circ\text{C}$ are: gold = 1.209, silver = 1.700, air at 1 atm = 0.179, mild steel = 0.173; for air $k = 0.000055$ cal cm/sec cm² °C, for mild steel (1 per cent carbon) $k = 0.107$ cal cm/sec cm² °C -- Ref. 32.) Consequently $A \sim 0.0005$. With this value of A , Eq. (21) shows that the wall temperature will remain within 1 per cent of its original value behind the shock up to

shock Mach numbers $W_{11} \sim 8$. For the entire range of expansion waves it will remain up to 0.2 per cent of its initial wall temperature. Because the heat conductivity of metals is several orders greater than that of the gas, the metal acts as a very large sink and its temperature remains essentially constant. Mirels (Ref. 31) also shows that the thickness ratio of the metal thermal boundary layer (Δ_T) and the gas thermal boundary layer (δ_T) in the Rayleigh case are of order unity for a gas like air in a steel shock tube (i.e., $\Delta_T/\delta_T \sim \sqrt{\alpha_w/\alpha_1}$).

The theory (independent formulations of Refs. 26 and 28) for the laminar compressible boundary layer (with heat transfer) developed on the wall behind a plane shock has been substantiated by the work of Ref. 26, where the density profiles were measured with an interferometer. By assuming that the Crocco relation (Subsec. 2, Ref. 8) applies, the velocity profiles can be calculated. The results of Ref. 26 appear in Fig. 3.2-5. The discrepancy at the larger values of η is attributed to the thin boundary layer (0.3 to 0.6 mm) and other uncertainties. However, the agreement is considered as "moderately good."

From a computation of the momentum thickness the skin friction can be found. An independent determination of the skin friction was also made from the measurements of a 2-micro-inch film heat gauge (Subsec. 7.3.1). The values checked quite well over the range of the experiments.

3.2.2 Transition

The problem of predicting transition from a laminar to a turbulent layer is more complex in the case of boundary layers developed behind travelling shock waves or expansion waves than in steady flows, owing to the nonstationary nature of the problem. The boundary layer itself in this case generates disturbances which are propagated by the characteristic lines throughout the flow. Where the boundary layer occupies a sizeable fraction of the tube area, the isentropic portion of the flow is no longer uniform.

However, the transition from a laminar to a turbulent boundary layer can be studied experimentally using optical methods (shadowgraph, schlieren, and interferometer) and by means of the thin-film heat gauge (see Subsec. 7.3.1; a historical note of its development is given in Ref. 26). It was noted above that for the laminar boundary layer the wall temperature remains constant. This is indicated by the flat portion of the heat gauge trace (Fig. 3.2-6). When transition to turbulent flow occurs at the wall, then the curve suddenly rises and becomes somewhat wavy. The time between the passage of the shock over the gauge and transition to turbulence is given by $\tau = (t_3 - t_2)$, and the phenomenon moves along with the shock speed w . The flow particle which first goes turbulent on hitting the gauge has been in motion for a total flow time $\Delta t = (t_3 - t_1)$. From the figure,

$$\frac{\Delta t}{\tau} = \frac{a + b}{a} = \frac{w_1 \tau + u_2 \Delta t}{w_1 \tau} \quad (24)$$

or

$$\Delta t = \frac{w_1 \tau}{w_1 - u_2} = \frac{v_1}{v_2} \tau = \Gamma_{21} \tau$$

That is, the particle transition time is equal to the gauge transition time multiplied by the stationary velocity factor v_1/v_2 . In the case of the Rayleigh boundary layer, when $v_1/v_2 = 1$, then $\Delta t = \tau$, i.e., the two transition times are equal, since all particles start instantly. For the strong shock case, in a perfect gas ($\gamma = 1.4$) it is sixfold greater.

It is now possible to define a transition Reynolds number Re_T based on this particle time. The characteristic distance is the particle time multiplied by the external flow velocity u_2 , and is equivalent to the distance b from the leading edge to the transition point in the steady case. That is, in both cases it is the distance that the particle has moved with respect to the wall before undergoing transition.

Therefore,

$$Re_T = \frac{u_2 b}{\nu_w} \quad (25)$$

or

$$Re_T = \frac{u_2^2 \tau}{\nu_w} \cdot \frac{v_1}{v_2} = \frac{u_2^2}{\nu_2} \cdot \frac{T_2}{T_1} \cdot \tau \cdot \frac{v_1}{v_2} \quad (25a)$$

It should be noted that this Re_T is greater by a factor of v_1/v_2 than that based on the Rayleigh flow.

From the point of view of the co-ordinates fixed in the shock wave, an appropriate Reynolds number Re_x for any distance x measured behind the shock wave can be defined because $x = a$ is the distance between the shock and the particle path in question at that station.

Since

$$\frac{b}{a} = \frac{u_2 \Delta t}{w_1 \tau} = \frac{u_2}{w_1} \cdot \frac{v_1}{v_2}$$

therefore

$$Re_x = \frac{u_2^2}{w_1} \cdot \frac{v_1}{v_2} \cdot \frac{x}{\nu_w} = \frac{v_2 x}{\nu_w} \left(1 - \frac{v_1}{v_2}\right)^2 \quad (26)$$

Equation (26) was derived by Mirels in Ref. 31.

Boundary layer transition has been observed in Refs. 26, 33, and 34. Studies of transition are reported in Refs. 35 and 36. From Ref. 35 it appears that Re_T based on the Rayleigh relation and free-stream kinematic viscosity ($Re_T = u_2^2 \tau / \nu_2$) has a constant value of $Re_T = 3.2 \times 10^5$ for shock strengths of $P_{21} = 2.1, 3.2,$ and 5.5 for initial $p_1 = 40$ mm Hg to 760 mm Hg. From Ref. 36 it appears that Re_T based on $Re_T = \frac{u_2^2 \tau}{\nu_2} \cdot \frac{v_1}{v_2}$ has a value of $1/4$ to 2×10^6 . The above

results appear to lie in the same range as steady flow transitions, considering the surface finish and tube geometry that might influence these results. The large heat transfer to the wall that occurs for stronger shocks would have a stabilizing effect on the boundary layer and correspondingly larger transition Reynolds numbers can be expected.

In Ref. 34, it is noted that Re_T , as measured from schlieren and shadowgraph records of the boundary layer, was approximately twice the value obtained from the microfilm heat gauge. This is not surprising, perhaps owing to the difficulty in fixing the transition point on a photograph of the boundary layer. Very little experimental work has been done on the boundary layer behind the rarefaction wave. Some shadowgraphs of the boundary layer development in this region are given in Ref. 8.

It may be concluded that at the present time the information on boundary layer transition in the shock tube is still limited.

3.2.3 Turbulent Boundary Layer

Solutions for the turbulent boundary layer behind moving shock waves are given in Ref. 31. The same concept is used, i.e., that it is possible to reduce the problem to a steady-flow case by fixing the reference axes to the shock front. The usual empirical, semi-infinite flat-plate theory without pressure gradient is applied to the apparently moving wall in the shock tube.

The integral form of the momentum equation is given by

$$\frac{\tau_w}{\rho_2 v_2^2} = \frac{d}{dx} \int_0^{\theta} \frac{\rho v}{\rho_2 v_2} \left(1 - \frac{v}{v_2}\right) dy = \frac{d\theta}{dx} \quad (27)$$

where θ , as defined by Eq. (27), is the momentum thickness of the boundary layer. (Note, as above, the typed "v" is now the average relative velocity ($w_1 - u$) whereas the written "v" is the average velocity component in the y-direction in the boundary layer.) If the boundary layer thickness is given as δ , then a turbulent similarity parameter can be defined as $\zeta = y/\delta$. The velocity profile relative to the shock-tube wall is assumed to follow a power law expressed by

$$\left| \frac{v - v_1}{v_2 - v_1} \right| = \zeta^{\frac{1}{n}} \quad \text{for } 0 \leq \zeta \leq 1$$

and

$$\left| \frac{v - v_1}{v_2 - v_1} \right| = 1 \quad \text{for } \zeta \geq 1 \quad (28)$$

The above assumes that the actually existing boundary-layer profile in the shock tube in region (2) or (3) can be expressed by

$$\frac{u}{u_2} = \zeta^{\frac{1}{n}} \quad \text{or} \quad \frac{u}{u_3} = \zeta^{\frac{1}{n}} \quad (28a)$$

In what follows, region (2) will be used for illustration, but the same procedure also applies to region (3). A value of $n = 7$ is usually accepted for work in steady flow. However, the data of Ref. 34 indicate that $n = 5$ gives a somewhat better fit for shock-tube velocity profiles.

Similarly, the thermal boundary-layer profile is expressed as a function of ζ by using Crocco's relation (usually used for laminar boundary layers) which assumes that $Pr = 1$, or $T_o = T_r$, or that the thermal and velocity profiles have the same thickness (see the bibliography and remarks in Ref. 34),

$$\frac{\rho_2}{\rho} = \frac{T}{T_2} = \frac{T_w}{T_2} \left(1 + b\zeta^{\frac{1}{n}} - c\zeta^{\frac{1}{n}} \right)$$

for

$$0 \leq \zeta \leq 1$$

and

$$\frac{\rho_2}{\rho} = \frac{T}{T_2} = 1 \quad \text{for} \quad \zeta \geq 1$$

where

$$b = \frac{T_r}{T_2} - 1, \quad c = \left(\frac{T_r}{T_2} - 1 \right) \frac{T_2}{T_w} \quad (29)$$

It is shown in Ref. 31 that

$$\frac{T_w - T_1}{T_1} \sim 10\% \quad \text{for} \quad M_s = W_{11} \gg 1$$

when

$$\left(\frac{x v_2}{\nu_2} \right)^{0.3} \cdot W_{11} < \text{order of } 10^4$$

Consequently, even for moderately strong shocks, $T_w \sim T_1$. Thus T_w may be replaced by T_1 , and T_r by T_o in the above equations. (Since for air $Pr \sim 0.72$, T_r is usually retained to give a "better" estimate of T/T_2 .)

Since by definition

$$\delta^* = \int_0^{\alpha} \left(1 - \frac{\rho v}{\rho_2 v_2} \right) dy \quad (30)$$

and from Eq. (27)

$$\theta = \int_0^{\infty} \frac{\rho v}{\rho_2 v_2} \left(1 - \frac{v}{v_2}\right) dy \quad (31)$$

A substitution of Eqs. (28) and (29) into Eqs. (30) and (31) yields

$$\frac{\delta^*}{\delta} = 1 - \left(\frac{n T_2}{T_w}\right) \left[\frac{v_1}{v_2} I_{n-1} + \left(1 - \frac{v_1}{v_2}\right) I_n \right] \quad (32)$$

$$\frac{\theta}{\delta} = n \frac{T_2}{T_w} \left(1 - \frac{v_1}{v_2}\right) \left[\frac{v_1}{v_2} I_{n-1} + \left(1 - 2 \frac{v_1}{v_2}\right) I_n - \left(1 - \frac{v_1}{v_2}\right) I_{n+1} \right] \quad (33)$$

where the I's are functions of b and c and are defined by the integral,

$$I_a = \int_0^1 \frac{z^a dz}{1 + bz - cz^2} \quad (34)$$

where $a = (n - 1)$, n , and $(n + 1)$.

The following results have been developed in Refs. 31 and 34:

$$\frac{\tau_w}{\rho_2 v_2^2} = 0.0225 \theta \left(1 - \frac{v_1}{v_2}\right) \left|1 - \frac{v_1}{v_2}\right|^{3/4} \left(\frac{v_2}{v_2 \delta}\right)^{1/4} \quad (35)$$

for

$$n = 7, \quad \theta = \left(\frac{\mu_m}{\mu_2}\right)^{1/4} \left(\frac{T_2}{T_m}\right)^{3/4} \quad (36)$$

$$\delta = 0.0574 \left(\theta - \frac{1 - v_1/v_2}{\theta/\delta}\right)^{4/5} \left|1 - \frac{v_1}{v_2}\right|^{1/2} \left(\frac{v_2}{v_2 x}\right)^{1/5} \cdot x \quad (37)$$

$$C_f \text{Re}^{1/5} = 0.0920 \left[\left(\frac{T_w}{T_2} \frac{\theta}{\delta} \frac{1}{1 - v_1/v_2}\right) \frac{\nu_m}{\nu_w} \left(\frac{\rho_m}{\rho_w}\right)^4 \right]^{1/5} \cdot \frac{(1 - v_1/v_2)}{|1 - v_1/v_2|} \quad (38)$$

where

$$T_m = 0.5 (T_w + T_2) + 0.22 (T_r - T_2) \quad (39)$$

$$\frac{\tau_w}{\rho_2 v_2^2} = 0.0488 \theta \left(1 - \frac{v_1}{v_2}\right) \left|1 - \frac{v_1}{v_2}\right|^{2/3} \left(\frac{v_2}{v_2 \delta}\right)^{1/3} \quad (40)$$

for

$$n = 5, \quad \theta = \left(\frac{\mu_m}{\mu_2}\right)^{1/3} \left(\frac{T_2}{T_m}\right)^{2/3} \quad (41)$$

$$\delta = 0.130 \left(\theta \frac{1 - v_1/v_2}{\theta/\delta}\right)^{3/4} \left|1 - \frac{v_1}{v_2}\right|^{1/2} \left(\frac{v_2}{v_2 \delta}\right)^{1/4} \cdot x \quad (42)$$

$$C_f Re^{1/4} = 0.195 \left[\left(\frac{T_w}{T_2} \theta \frac{1}{1 - v_1/v_2}\right) \frac{\nu_m}{\nu_2} \left(\frac{\rho_m}{\rho_w}\right)^3 \right]^{1/4} \cdot \frac{(1 - v_1/v_2)}{|1 - v_1/v_2|} \quad (43)$$

$$q_w = C_{p,m} \frac{T_w - T_r}{v_2 \left(1 - \frac{v_1}{v_2}\right)} P_{r,m}^{-2/3} \tau_w \quad (44)$$

$$\frac{T_r}{T_2} = 1 + \left(\frac{v_1}{v_2} - 1\right)^2 \frac{v_2^2 r(0)}{2 T_2 C_{p,m}} \quad (45)$$

$$r(0) = \sqrt[3]{P_{r,m}} \quad (46)$$

Typical experimental results from Ref. 34 for a 2 x 7-in. shock tube are shown in Figs. 3.2-7 to 3.2-11. For these data, the boundary layer thickness δ was defined as the value of y where $u/u_2 = 0.99$ or $\rho_2/\rho = 0.996$. Since it is difficult to determine δ accurately, the ratios T/T_2 and u/u_2 are plotted against y/δ^* in Figs. 3.2-7 and 3.2-8 to avoid scatter, as δ^* is an integrated quantity, and variations in δ do not affect it strongly. The temperature profiles are obtained directly from the interferometric density measurements and the velocity profiles are obtained with the aid of Eq. (29). It is seen that the experimental values tend to follow the 1/5 rather than the 1/7 power law for the given initial conditions. This in itself may not be too indicative. The important point is that the analysis is substantiated by the experimental results. The plots of δ , δ^* , and θ appear on Figs. 3.2-9 and 3.2-10. The experimental points are closer to the 1/5 power law profile for δ , but there is only a small difference between

the 1/5 and 1/7 power law for the theoretical values of δ^* and θ . For the stronger shock wave ($P_{21} = 8$), the scatter in the experimental results are about 25 to 30 per cent for θ and δ^* at the higher Re (10^8), and may be due to the fact that the measurements were close to the eddying contact region. At a fixed Re_x , the theoretical values of δ^* are approximately the same for both cases; δ is greater for $P_{21} = 2.75$; θ and θ/δ are greater for $P_{21} = 8$.

In Fig. 3.2-11 the local skin friction C_f shows the typical decline with increasing Reynolds number Re_x as the boundary layer thickens. For a given Re_x , the theoretical skin friction decreases somewhat with an increase in v_1/v_2 from 2 to 3.5. The agreement with theory shown in Fig. 3.2-11(a) is very good for $v_1/v_2 = 2$, ($U_{21} = 0.79$, $M_2 = 0.67$, $T_2/T_w = 1.38$). The experimental points for $v_1/v_2 = 3.5$, ($U_{21} = 1.88$, $M_2 = 1.25$, $T_2/T_w = 2.3$) are higher than that predicted by theory and are close to the values obtained for $v_1/v_2 = 2$.

It can be concluded that the experimental work of Ref. 34 substantiates the analysis of Ref. 31 of the zero-pressure-gradient, compressible, turbulent boundary layer developed on the wall of a shock tube behind a plane shock wave. Similar data for the flow behind a rarefaction wave are not available as yet. From these results it might be inferred that the variation of the physical quantities in the flow, and the shock wave attenuation induced by a thin boundary layer in a shock tube, should be predictable from the analysis of Refs. 11 and 12.

3.2.4 Boundary-Layer Closure

Of some interest is the distance behind the shock wave when the wall boundary layers have grown to such an extent that they meet and a turbulent pipe flow results. This may be illustrated by referring to Fig. 3.2-6 and by assuming that the boundary layer closes at distance "a" behind the shock wave. It is seen that the total test time that would be available with a case of uniform flow is given by τ . Consequently, there is nothing gained by making the channel longer than (a + b), that is, this particular particle path now becomes the contact surface. As a result, the ratio of the total channel length to the boundary layer closing distance is given by

$$\frac{a + b}{a} = \frac{v_1}{v_2} = \frac{w_1 u_2}{w_1 u_2 - 1} = \frac{1}{1 - u_2 w_1} = \frac{\rho_2}{\rho_1} \quad (24a)$$

This ratio has a value of unity for very weak shocks, and a value of six for strong shocks, in air, considered as a perfect gas. For an imperfect gas, the ratio ρ_2/ρ_1 depends on the initial pressure and can exceed six by sizeable factors (see Subsec. 2, Supplement B).

From Eqs. (37) and (42), it is seen that

$$\delta = \frac{bx}{\text{Re}_x^{2/(n+3)}} = \frac{bx}{\text{Re}_x^\alpha} \quad (47)$$

where

$$b = b\left(\frac{v_1}{v_2}, p_1, T_1\right)$$

is a function of the shock velocity ratio and the initial conditions. The parameter α depends on the power index n . If the Reynolds number is now changed so that it is based on the hydraulic diameter, then

$$\frac{x}{D} = \left(\frac{\delta}{D}\right)^{\frac{1}{1-\alpha}} \left(\frac{\text{Re}_D^\alpha}{b}\right)^{\frac{1}{1-\alpha}} \quad \text{or} \quad \frac{\delta}{D} = c \left(\frac{x}{D}\right)^{1-\alpha} \quad (48)$$

where

$$c = c\left(\frac{v_1}{v_2}, p_1, T_1\right)$$

The results derived from Figs. 3.2-9 and 3.2-10 have been replotted on Fig. 3.2-12 for a 2 x 7-in. shock tube with $D \sim 3$ in. It is seen that for the case of $P_{21} = 2.75$ and the given initial conditions in the channel, Eq. (48) is satisfied using $n = 5$ as the power index, or $(1 - \alpha) = 0.75$. For $P_{21} = 8$, $1 - \alpha \sim 0.6$, or $n \sim 2$; however, since the boundary layer density (velocity) measurements check the $n = 5$ power law, it can be concluded that for $P_{21} = 8$ the boundary layer thickness measurements cannot be considered as reliable as the profile measurements themselves. Additional experimental results from Ref. 37 (of the boundary layer thickness obtained from schlieren records, in a 1.5 x 2.5-in. shock tube, where the 2.5 in. was used as D , instead of $D \sim 2$ in.) show that for stronger shocks ($7 < W_{11} < 12$, $p_1 = 0.1$ atm.) $(1 - \alpha) \sim 0.9$ or $n \sim 17$. This apparent power index is rather high for a turbulent layer.

Under the assumption of a flat plate with zero pressure gradient, the boundary layer would close at a distance behind the shock when $\delta = 1/2 D$, or from Eq. (48),

$$\frac{x}{D} = \left(\frac{1}{2b}\right)^{\frac{1}{1-\alpha}} \text{Re}_D^{\frac{\alpha}{1-\alpha}} \quad (49)$$

From Fig. 3.2-12 it is seen that the closing distance lies in the range of $20 < x/D < 140$ for the shock strengths and initial conditions considered here. It appears that the closing distance is smaller for

stronger shocks. A more detailed plot for a range of initial conditions and several power laws might be more revealing. However, in view of the existing pressure and velocity gradients in an actual flow, it is doubtful whether the boundary layer growth would follow the predictions of Eqs. (37) and (42), and the above results can be taken only as a rough indication of the closing distance for shock tubes of hydraulic diameters of 2 to 3 in. and the initial conditions given above.

3.2.5 Reflected Shock-Wave Boundary-Layer Interactions

If the channel is closed, the incident shock wave reflects and interacts with the boundary layer that it initially induced in the hot gas. Later, the reflected shock wave refracts at the contact region and interacts with the boundary layer in the cold region induced by the rarefaction wave.

The interaction with the boundary layer in the hot region does not appear to be as severe as that with the eddying region and the turbulent boundary layer of the cold gas which has passed through the diaphragm station. Examples of the latter interaction can be seen on the wave-speed records of Refs. 2 and 10, Subsec. 1; Refs. 48 and 49, Subsec. 2; and Refs. 1, 22, and 22a, Subsec. 3. The instantaneous spark schlieren photographs and interferograms of the interaction in the cold region shown in Ref. 22a are especially noteworthy. From the experimental records one can conclude that even for a relatively weak reflected shock wave its interaction with the boundary layer in the cold region leads to severe separation and generates a multiple shock-wave system similar to that of steady supersonic flow in ducts (Ref. 8, Subsec. 2; Ref. 22b, Subsec. 3); whereas such a multiple shock-wave system does not appear to have been observed in the hot region, where the flow Reynolds number per foot is smaller, and more severe viscous effects might have been expected (Ref. 31, Subsec. 2). However, stabilizing effects due to cooling would be greater in the hot gas, as it has a higher recovery temperature.

The interaction of the reflected shock wave and the boundary layer in the hot gas has recently been studied theoretically and experimentally by Mark (Ref. 20c). The problem is analyzed in a co-ordinate system fixed to the reflected shock wave. Consequently, the shock tube walls and the closed end move with the apparent velocity of the reflected shock wave. A simplifying assumption is made by considering the entire boundary layer as having those properties that occur at the cold wall. That is, a cool jet-stream moving against the reflected shock wave.

It is shown that in the laminar case, which lends itself to a theoretical treatment, three interaction regions exist over the range of incident shock Mach numbers (M_1) that are strongly dependent on the specific heat ratio for a perfect gas (γ). These regions depend on whether or not the boundary layer stagnation pressure (in the steady co-ordinate system) is greater or less than the flow pressure in the hot region behind the reflected shock wave. In the range $1.33 \leq M_1 \leq 6.45$, for $\gamma = 1.4$, the boundary layer stagnation pressure is less, and consequently the gas in this jet-like layer rolls up behind the shock wave and grows with time in a pattern that remains geometrically similar. This configuration gives rise to a severe interaction that causes a rapid attenuation of the reflected shock wave and

gives rise to variable flow properties behind it. Above and below this limiting shock Mach number range, the stagnation pressure of the layer is greater and the stream can pass under the foot of the shock wave, and a mild type of interaction occurs. The reflected shock wave and the state properties behind it are not affected very much. A similar mild interaction occurs for the turbulent boundary layer (analogous to the steady type of shock-wave boundary-layer interactions), as it can make up for any stagnation pressure deficiency by drawing additional energy from the free stream. In the case of monatomic gases ($\gamma = 5/3$), the critical shock-wave Mach number region shrinks to $1.6 \leq M_1 \leq 2.8$. Consequently, this region is more difficult to observe experimentally, and the disturbing effect of the reflected shock wave and the changes in state properties behind it would be correspondingly small in a monatomic gas. Recent experimental results (Ref. 20b) appear to substantiate the above analysis. However, sizeable accelerations occur after reflection, especially in a triatomic gas (CO_2), where the shock has a large bifurcation; this has as yet not been resolved.

A similar analysis for the boundary layer in the cold region has not been done to date. Such theoretical and experimental work would be very useful in understanding the severe interactions encountered in this region, as noted in the above references.

Enough data exists to indicate that one must proceed with some caution (Ref. 20b) when using the hot, ideally-stationary gas behind a reflected shock wave for spectroscopic studies or other real gas flow investigations. Similarly, if the hot gas behind the reflected shock wave is used to run a hypersonic shock tunnel, additional deviation in flow properties can be expected over and above those which already exist behind the incident shock wave. These effects will depend on the type of gas and the state of the boundary layer.

Table 3.1-1

Speed of sound in gases

Gas	Air	A	CO ₂	N ₂ O	SF ₆
T°C	20	20	20	20	30
γ	1.400	1.667	1.290	1.275	1.093
a	1126	1046	877	872	451
a _H	1126	1045	875*		455 ⁺
a _S	1126		875	875	455

$$a = \sqrt{\gamma RT} \text{ ft / sec}$$

a_H = Sound speed from head of rarefaction wave

a_S = Sound speed from weak shocks

γ = As calculated at the given temperature

* = Pressure in chamber was approx. 3 atm

+ = Pressure in chamber was 750 mm Hg

Table 3.1-2

Deviations in state (3) behind the rarefaction wave
generated in a shock tube

(a) Measured Results

	<u>Theory</u>	<u>Experiment</u>	<u>% Deviation</u>
P_{34}	.285	.430	+57
T_{034}	.833	.814	-2
Λ_{34}	.332	.230	-30
Γ_{34}	.410	.545	+36

(b) Calculated from (a) (see Ref. 13)

	<u>Theory</u>	<u>Experiment</u>	<u>% Deviation</u>
T_{34}	.70	.79	+13
A_{34}	.838	.89	+6
U_{34}	.81	.33	-60
M_3	.98	.39	-60
$P = 5A_{34} + U_{34}$	5	4.78	-4
$Q = 5A_{34} - U_{34}$	3.38	4.15	+23

Note: Since A_{34} is a large quantity its influence on P is not too great. Consequently, one cannot use the relation for P to obtain U_{34} from an experimentally calculated value of A_{34} . If this is done $U_{34} = 5(1 - .89) = .55$, whereas it is .33.

Example from Figs. 3.1.7 to 3.1.11 for $P_{41} = 10$

Table 3.1-3

Imperfect gas properties behind an incident and reflected shock wave in nitrogen and carbon monoxide (Ref. 20a)

Nitrogen, $l_d = 225$ kcal/mole, $T_1 = 300^\circ\text{K}$, $a_1 = .354$ mm/ μ sec

p_1 mm Hg	M_1	T_2 °K	T_5 °K	ρ_5/ρ_1	w_2 mm/ μ sec	α_5
0.1	3.59	1000	1760	14.9	.434	-
1.0	3.59	1000	1760	14.9	.434	-
0.1	4.78	1500	2800	19.9	.515	-
1.0	4.78	1500	2800	19.9	.515	-
0.1	5.74	2000	3740	23.3	.580	.002
1.0	5.74	2000	3780	23.2	.580	.0007
0.1	6.59	2500	4430	36.9	.594	.015
1.0	6.59	2500	4660	26.1	.618	.010
0.1	7.35	3000	4790	31.0	.584	.036
1.0	7.35	3000	5110	29.7	.620	.037
0.1	8.08	3500	5070	35.7	.576	.066
1.0	8.08	3500	5510	33.3	.621	.050
0.1	8.93	4000	5370	42.2	.571	.106
1.0	8.79	4000	5800	37.9	.611	.080
0.1	10.26	4500	5770	55.7	.570	.100
1.0	9.64	4500	6110	42.8	.614	.126

Carbon Monoxide, $l_d = 256$ kcal/mole, $T_1 = 300^\circ\text{K}$, $a_1 = .354$ mm/ μ sec

p_1 mm Hg	M_1	T_2 °K	T_5 °K	ρ_5/ρ_1	w_2 mm/ μ sec	α_5
0.5	6.41	2350	4500	25.6	.616	.0047
5.0	6.37	2325	4500	25.3	.619	.0015
0.5	7.15	2830	5000	29.2	.619	.0185
5.0	6.84	2630	5000	27.1	.639	.0058
0.5	8.22	3580	5500	34.8	.609	.0507
5.0	7.48	3060	5500	29.8	.648	.0182
0.5	9.66	4510	6000	45.3	.593	.114
5.0	8.36	3690	6000	33.8	.646	.0433
5.0	9.55	4570	6500	40.6	.637	.090

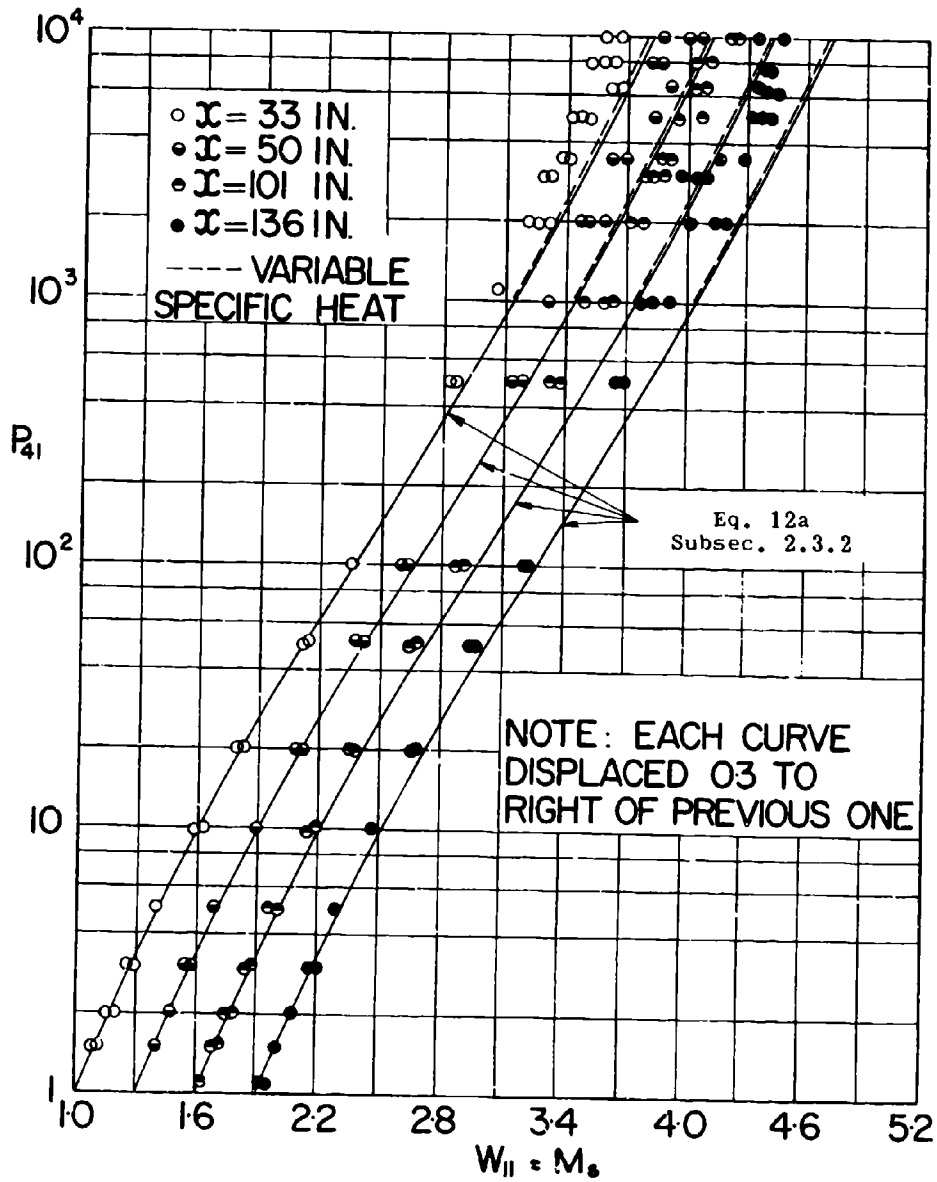


Fig. 3.1-1a. Typical variation of shock Mach number with distance in a 3 x 3-in. shock tube.

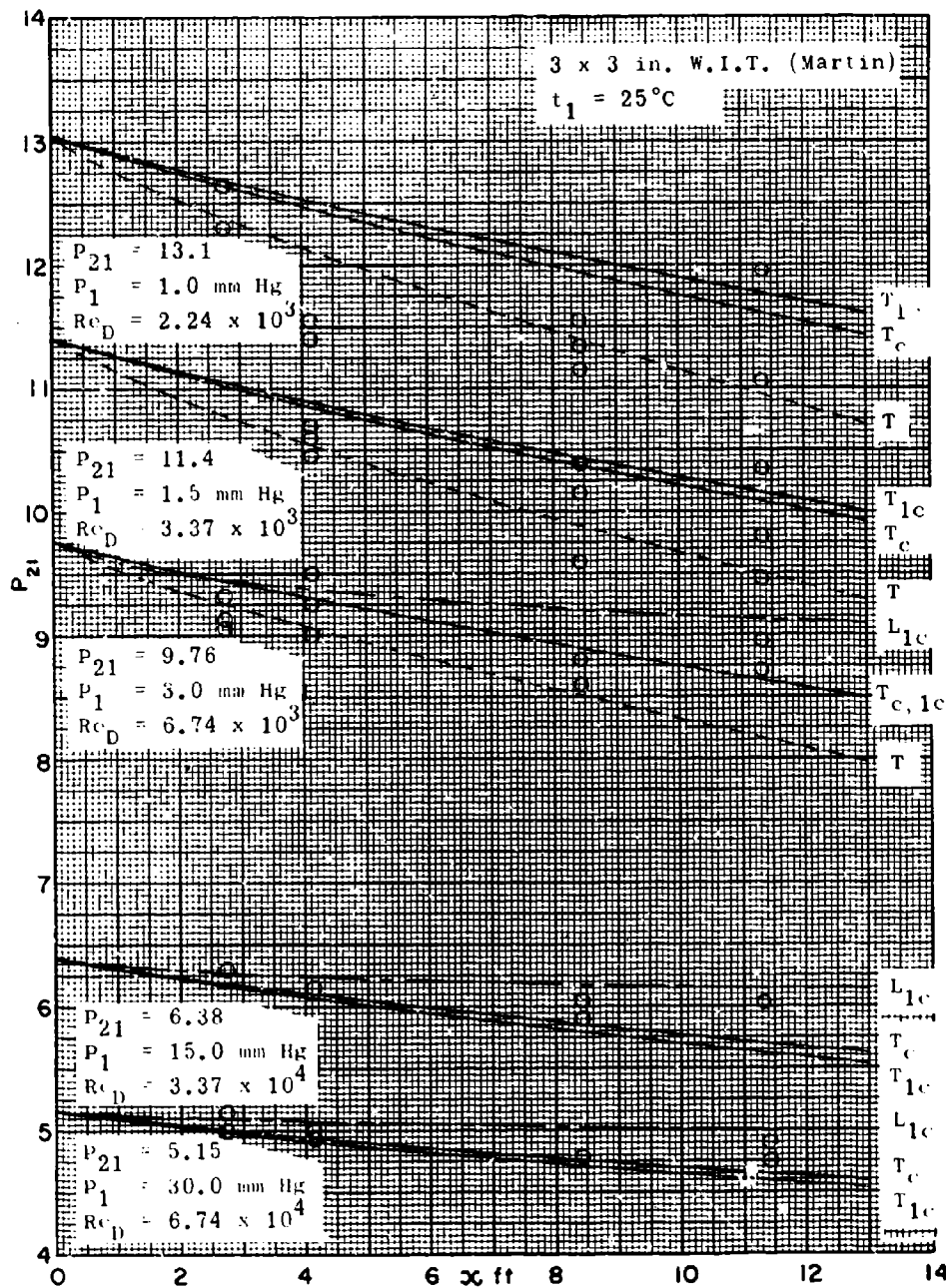


Fig. 3.1-1b. Distance attenuation of shock waves as a function of shock strength: $P_{21} = 5.15$ to 13.1.

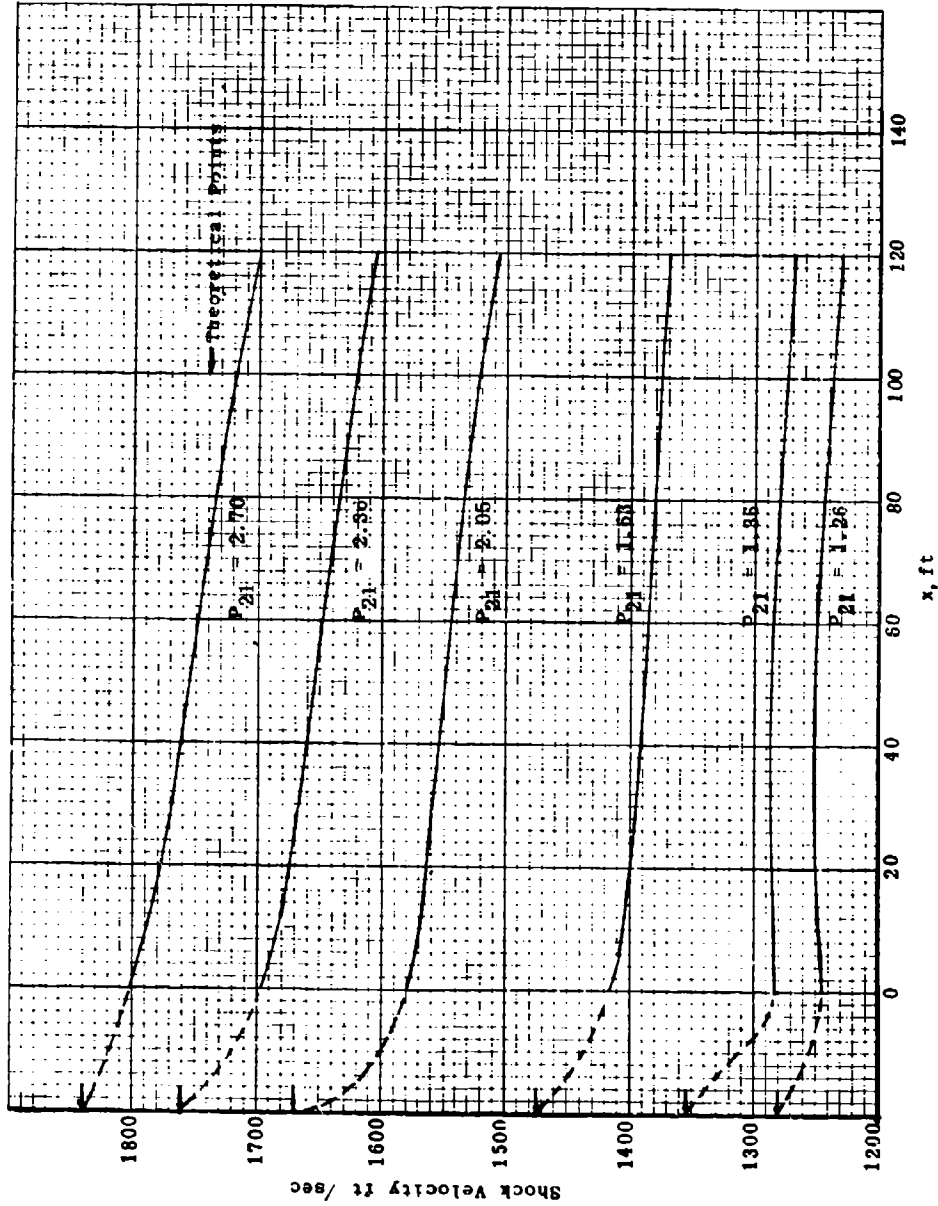


Fig. 3.1-2. Velocity attenuation of shock waves in 24-in. diameter tube (Ref. 7).

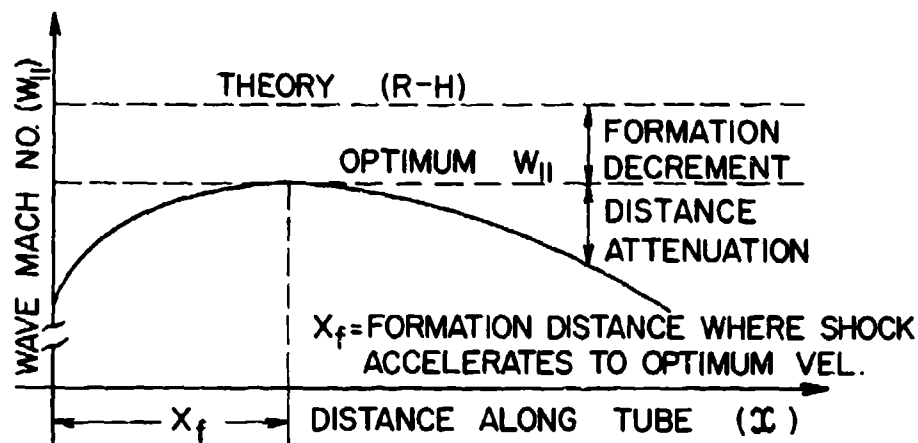


Fig. 3.1-3a. Representation of the total attenuation in a shock tube.

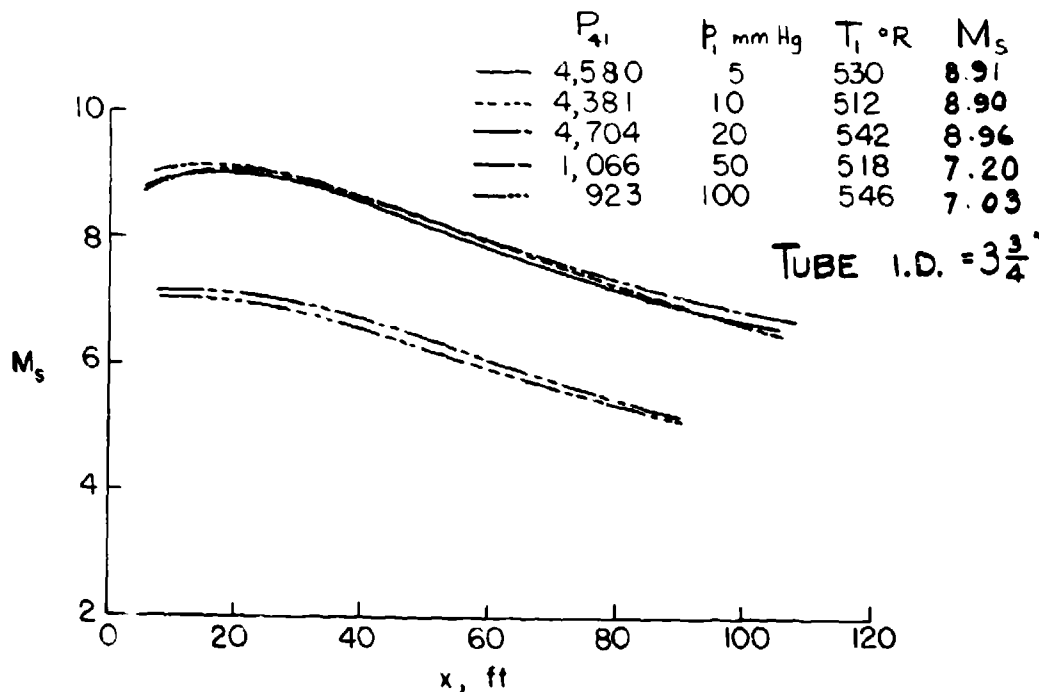


Fig. 3.1-3b. Effect of initial pressure on attenuation with hydrogen as driver gas (Ref. 7a).

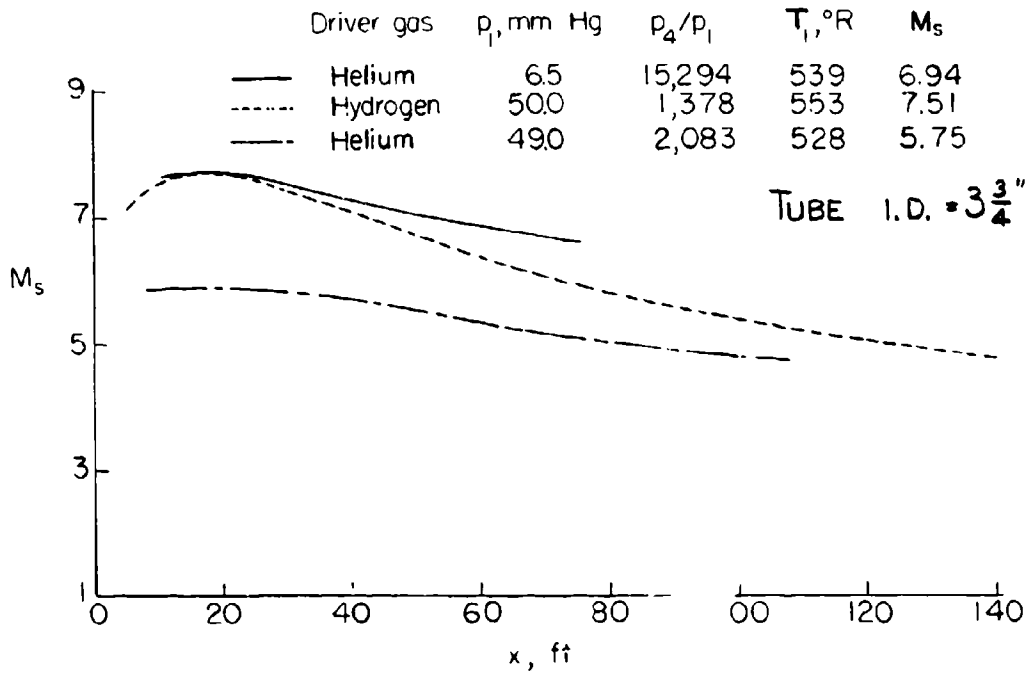


Fig. 3.1-3c. Comparison of the effects of hydrogen and helium driver gases on shock-wave attenuation (Ref. 7a).

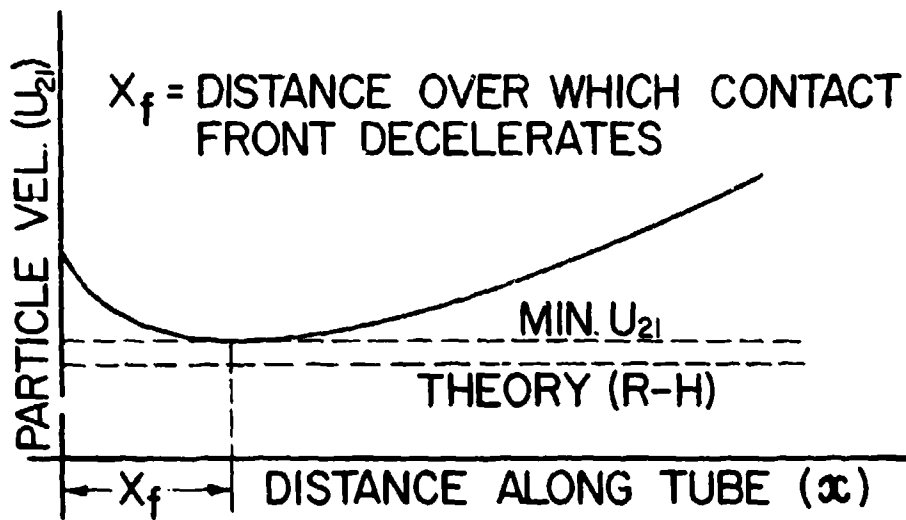


Fig. 3.1-5. Representation of the velocity (U_{21}) of the front of the contact zone in a shock tube.

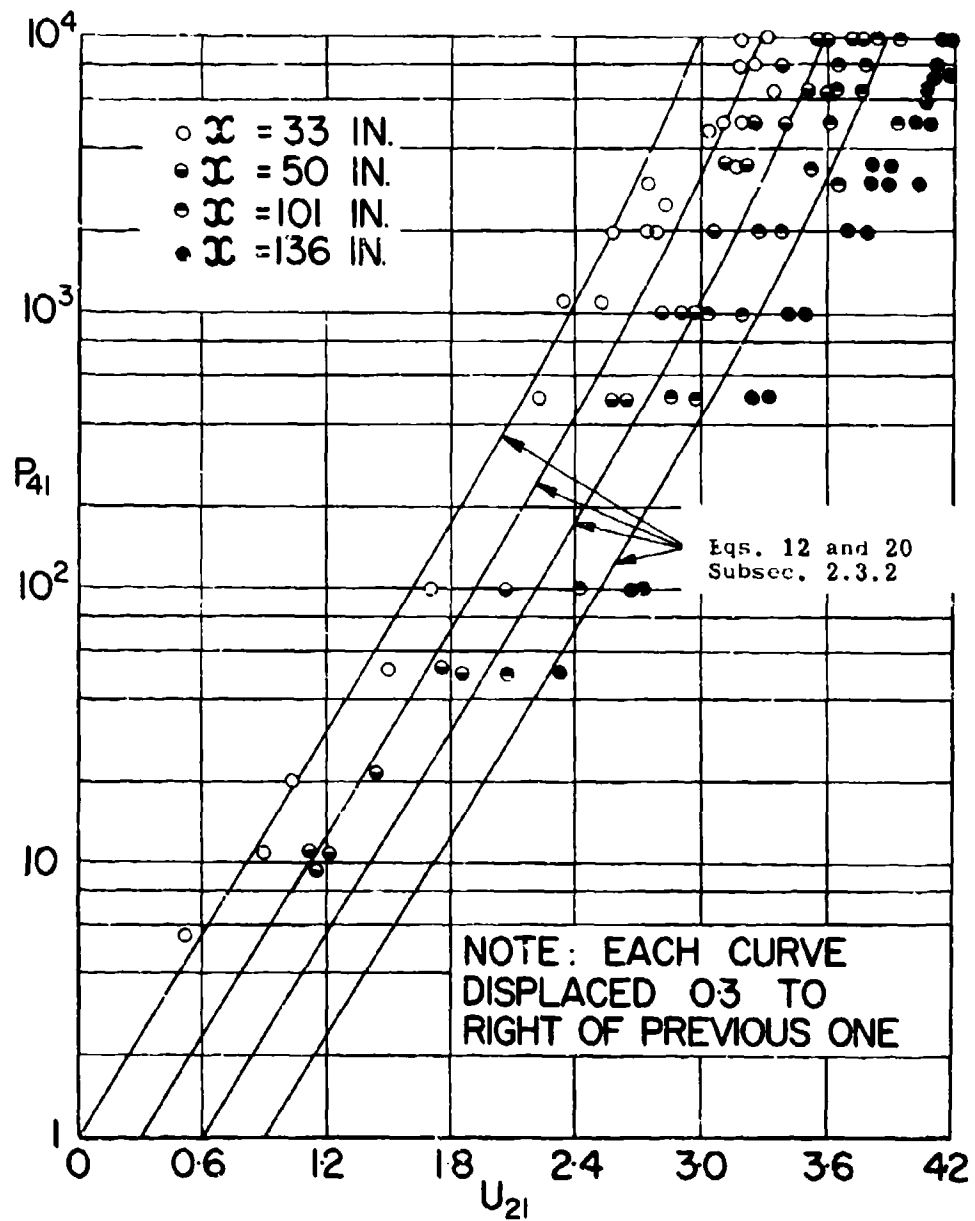


Fig. 3.1-6. Typical variation of the velocity of the contact region front with distance in a 3 x 3-in. shock tube.

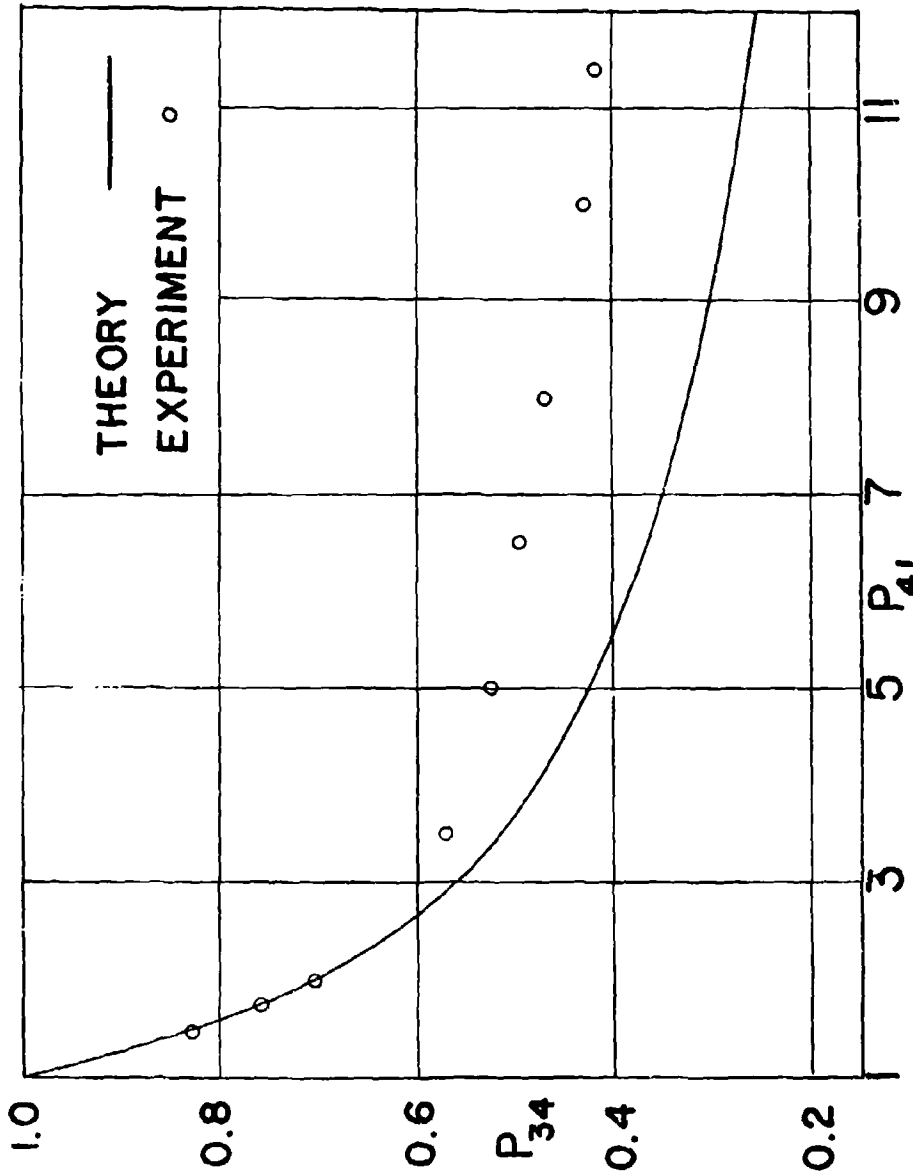


Fig. 3.1-7. Theoretical and experimental variation of rarefaction wave pressure ratio (P_{34}) with diaphragm pressure ratio (P_{41}).

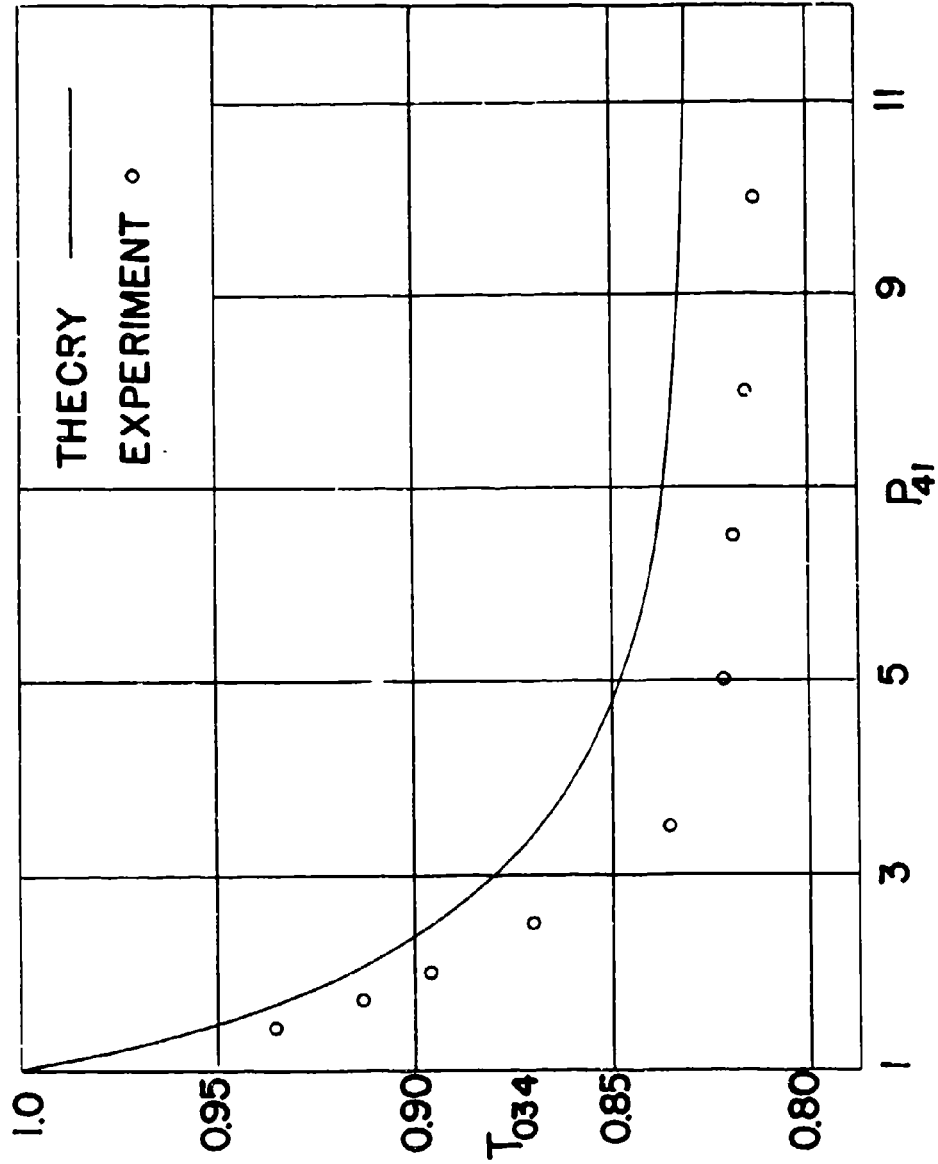


Fig. 3.1-8. Theoretical and experimental variation of rarefaction wave stagnation temperature ratio (T_{034}) with diaphragm pressure ratio (P_{41}).

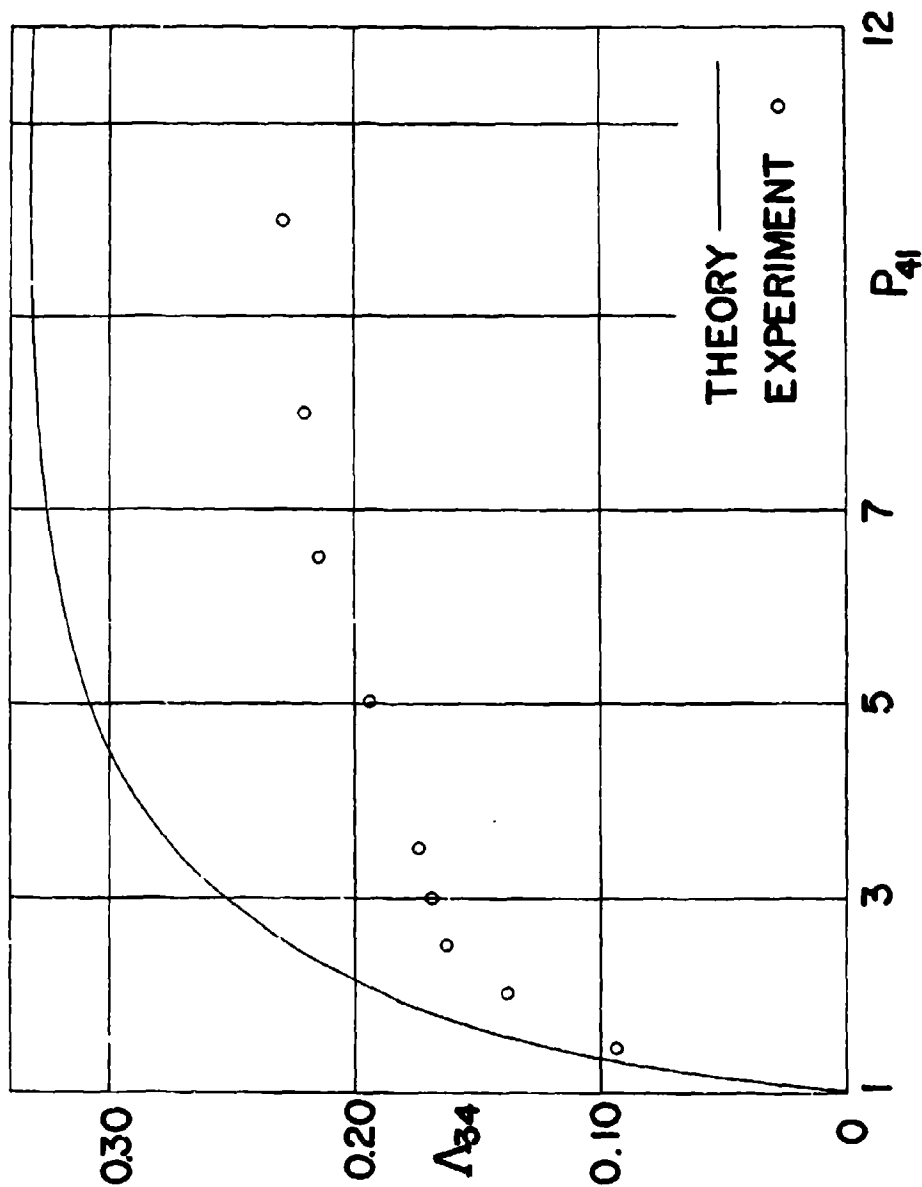
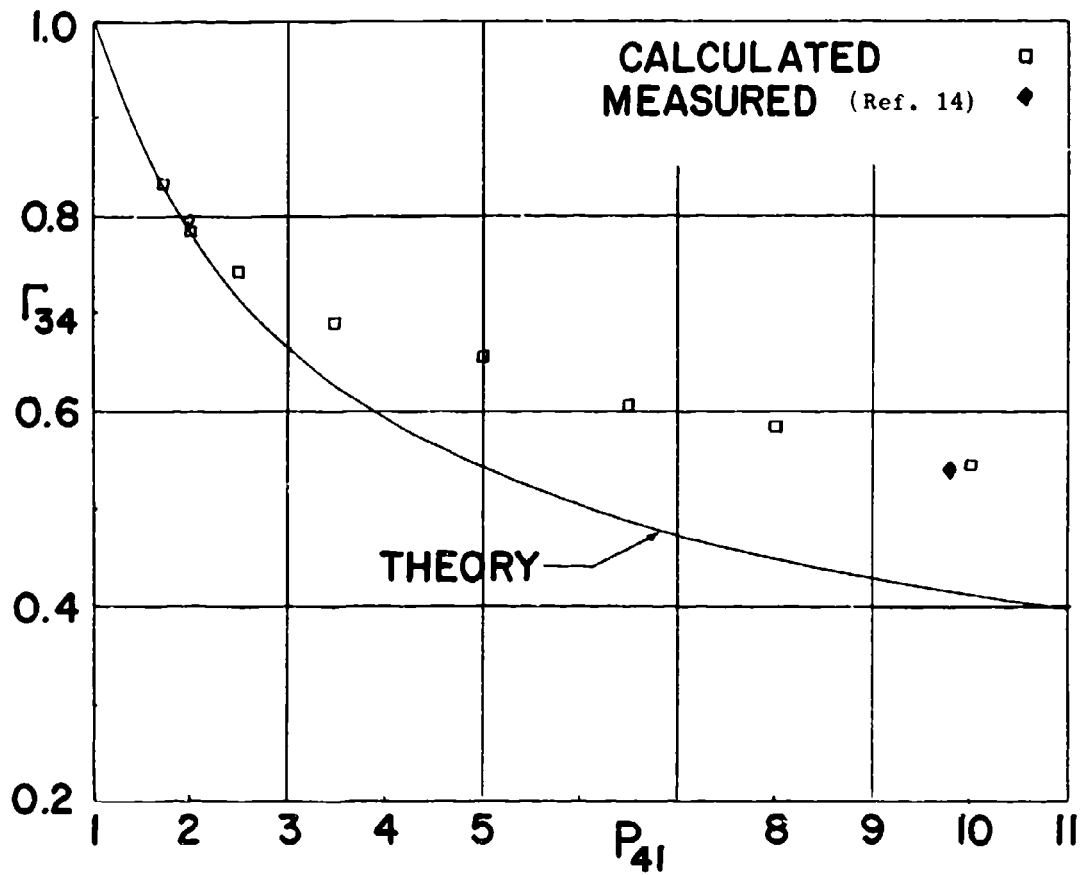


Fig. 3.1-9. Theoretical and experimental variation of rarefaction wave mass flow ratio (Λ_{34}) with diaphragm pressure ratio (P_{41}).



(The values calculated from measured flow parameters are compared with ideal shock tube theory and with direct measurements.)

Fig. 3.1-10. Variation of density ratio (Γ_{34}) across incident rarefaction wave with diaphragm pressure ratio (P_{41}).

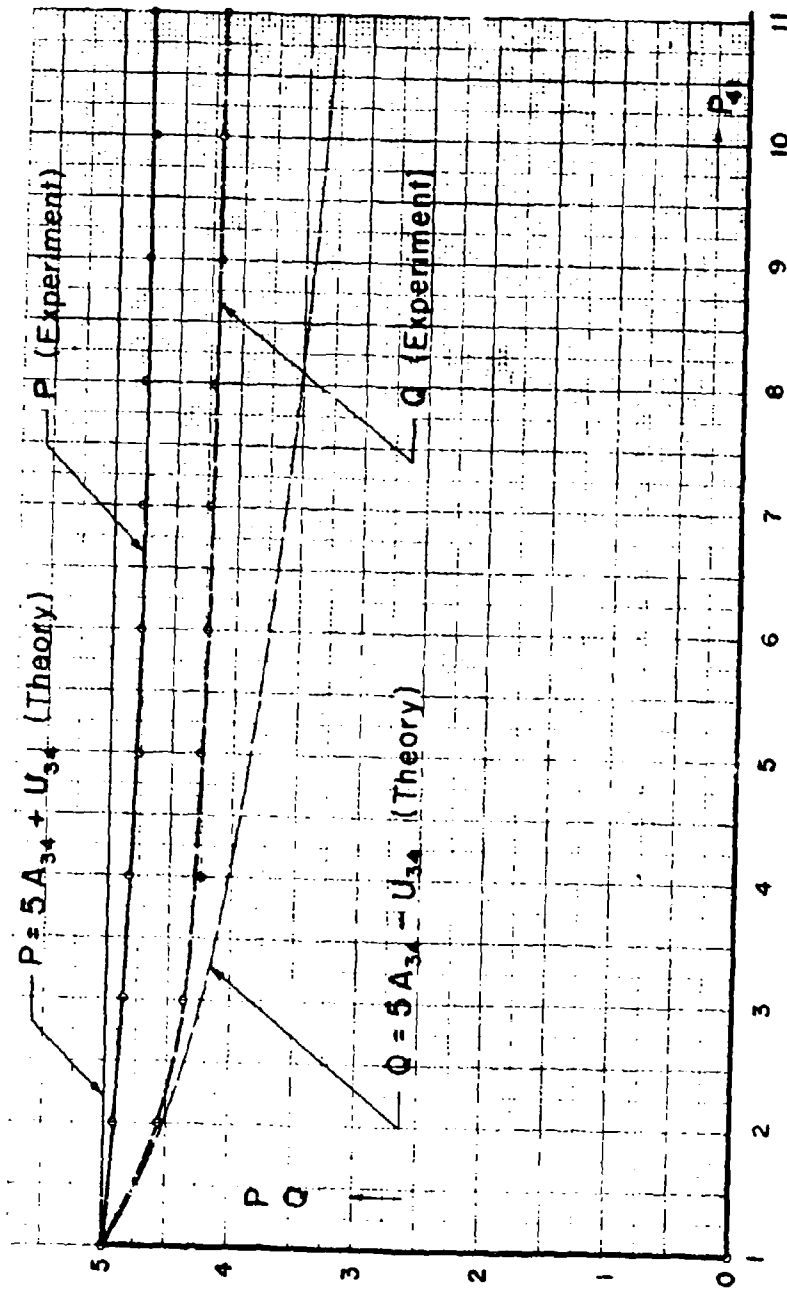


Fig. 3.1-11. Variation of the Riemann invariants P and Q with diaphragm pressure ratio (P_{41}).

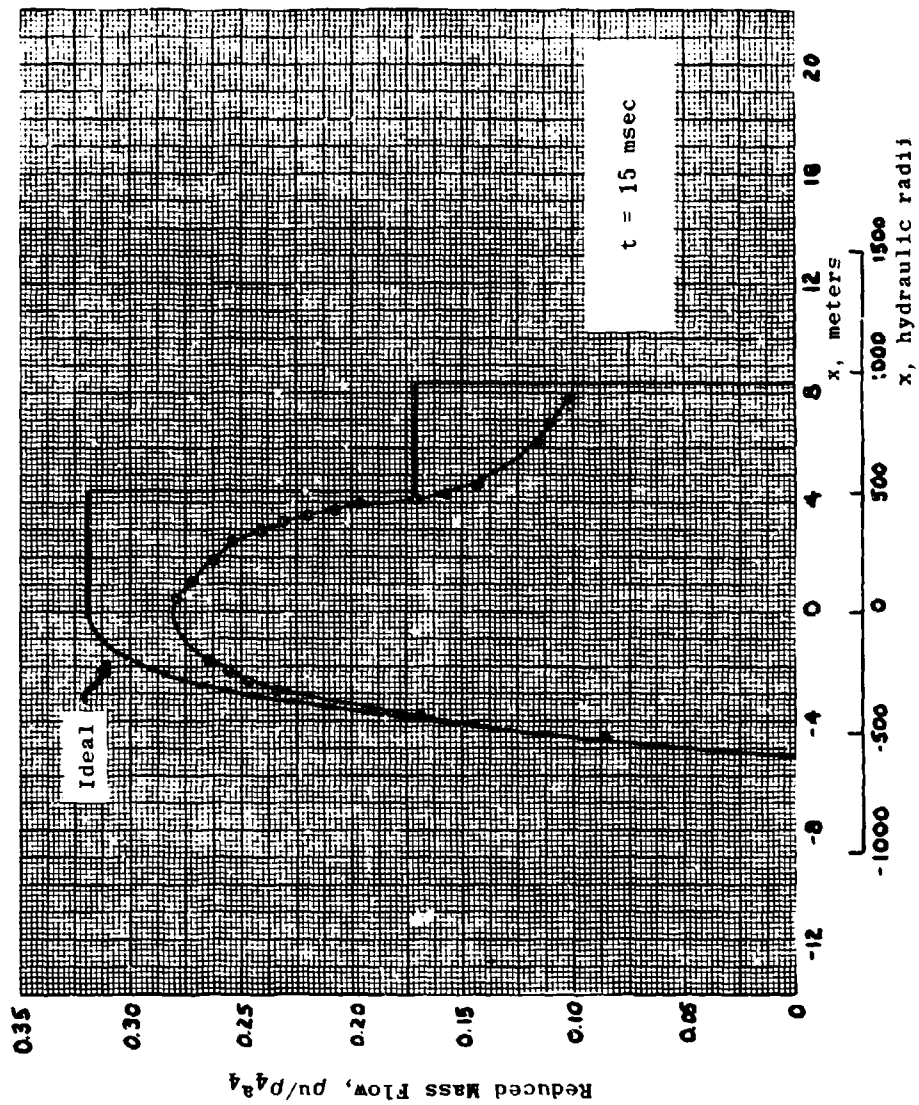


Fig. 3.1-12a. Mass flow distribution derived from density measurements in a 1-3/8-in. diameter shock tube for $P_{41} = 9.6$ (Ref. 15).

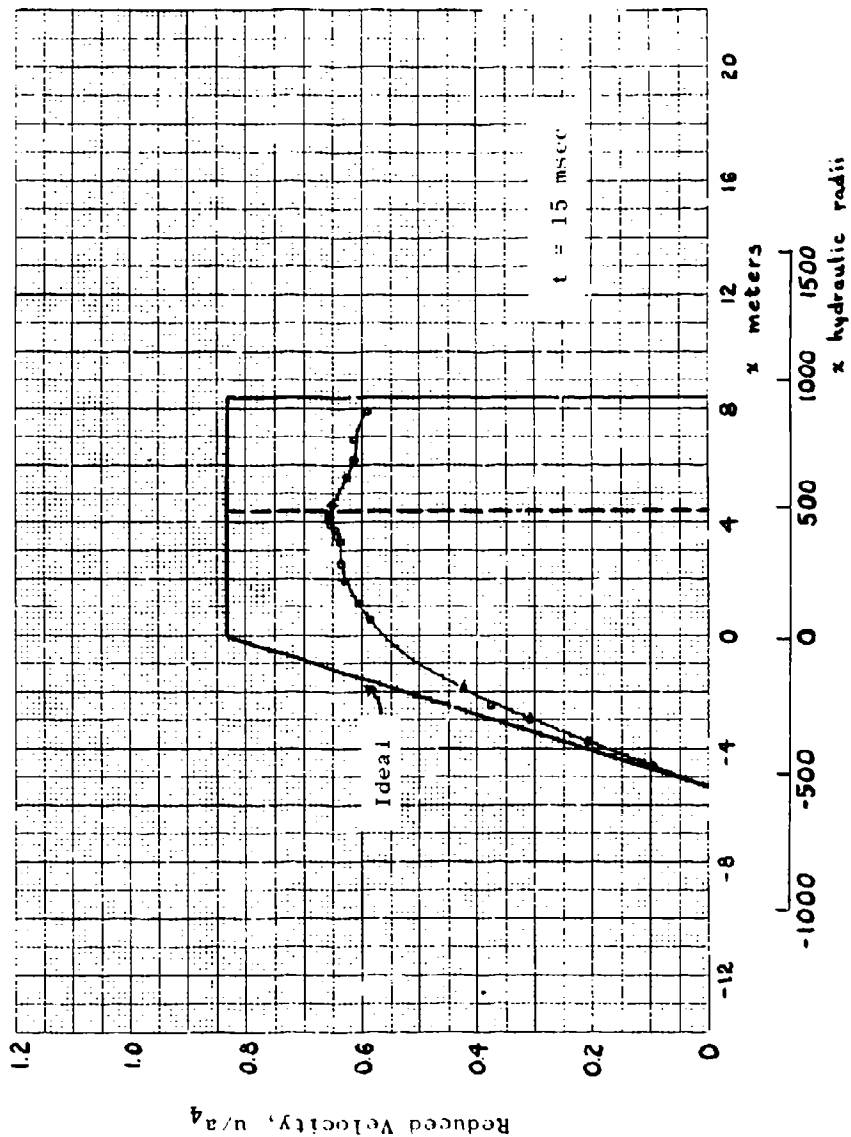
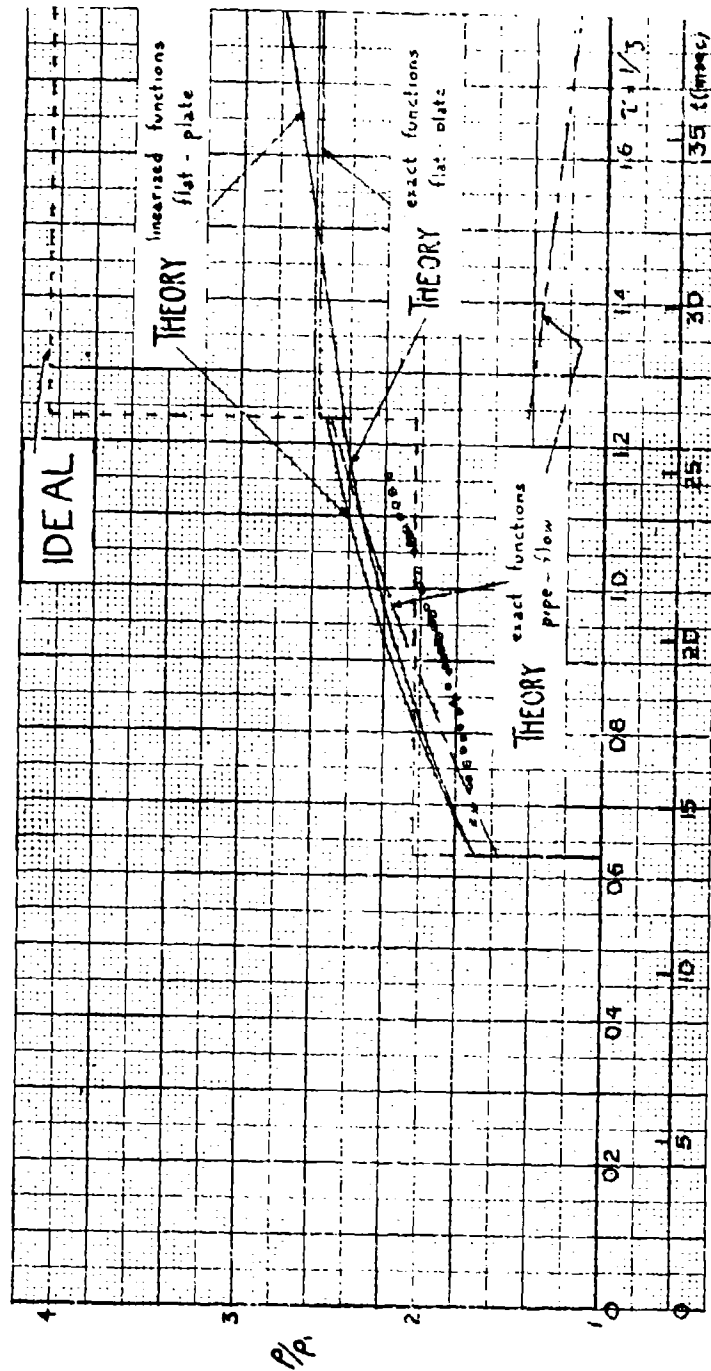


Fig. 3.1-12b. Particle velocity distribution derived from density measurements in a 1-3/8-in. diameter shock tube for $P_{41} = 9.8$ (Ref. 15).



(The ideal profile and theoretical profiles based on the theory of Trimpf and Cohen are shown for comparison.)

Fig. 3.1-13. Density as a function of time for $P_{41} = 9.8$ in a 1-3/8-in. diameter shock tube at $x = 7.622$ meters (Ref. 17).

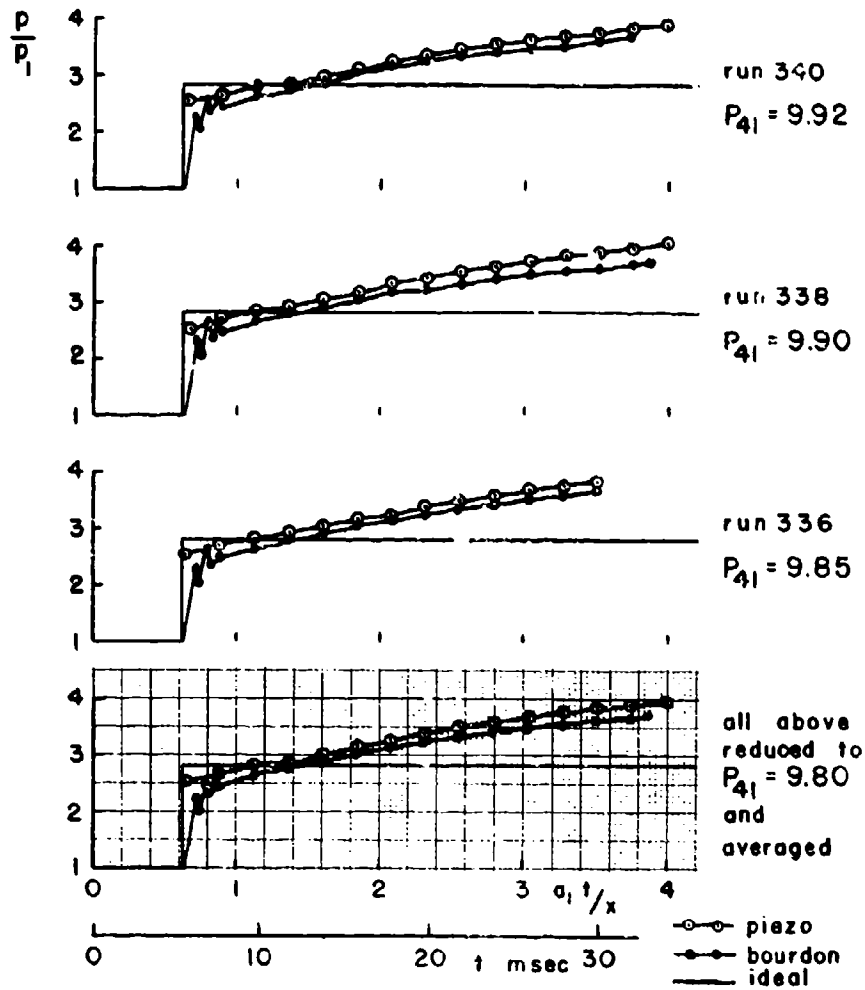
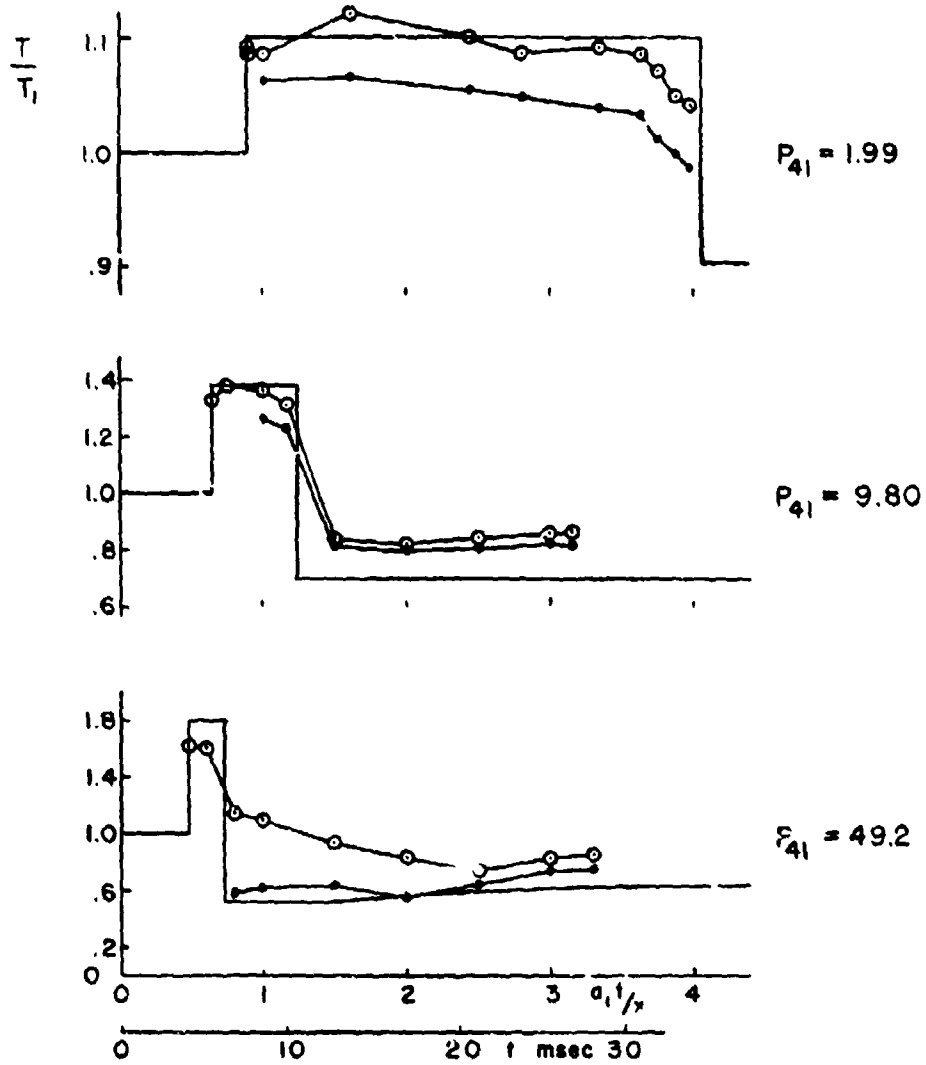


Fig. 3.1-14. Pressure as a function of time in a 1-3/8-in. diameter shock tube at $x = 3$ meters from the diaphragm station (Ref. 16).



Temperature calculated from density and pressure indication of

Piezo \circ — \circ

Bourdon \bullet — \bullet

Ideal theory temperature ———

Fig. 3.1-15. Temperature derived from pressure and density measurements as a function of time in a 1-3/8-in. diameter shock tube at $x = 3$ meters (Ref. 16).

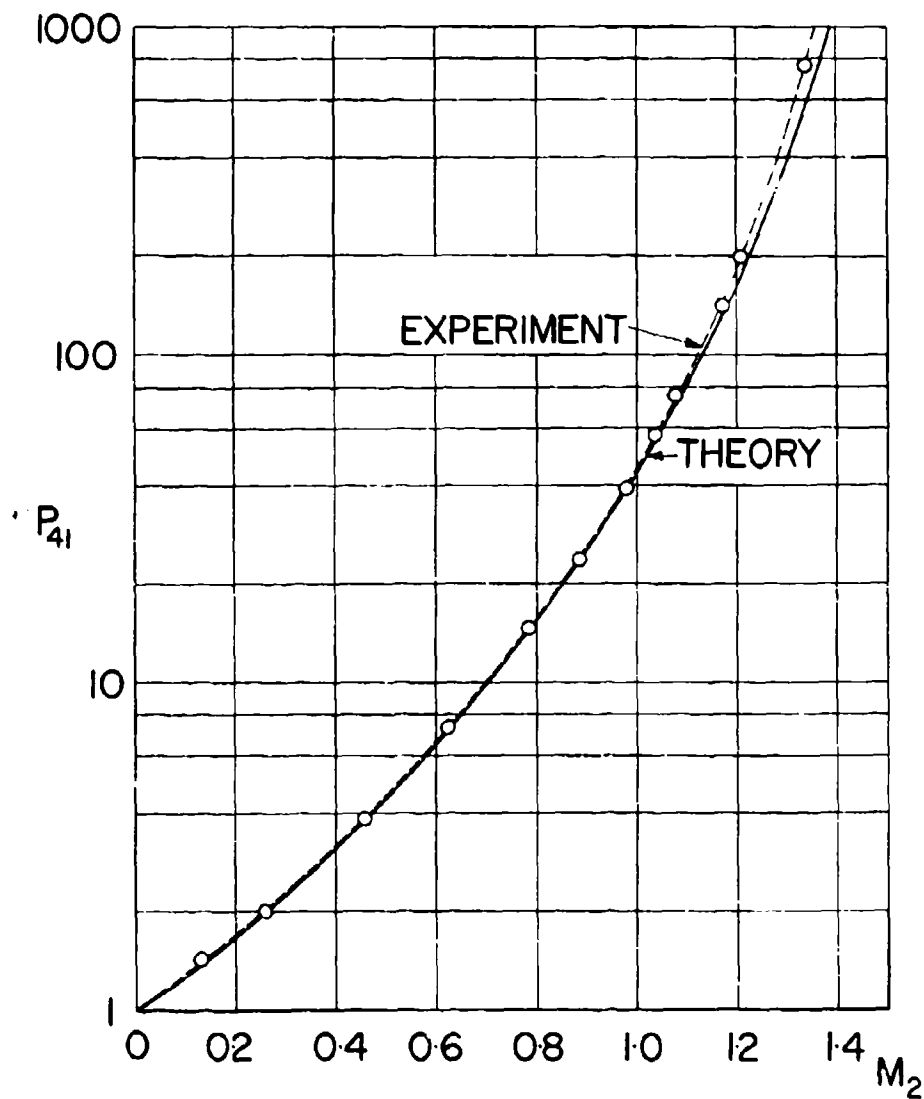


Fig. 3.1-16a. Variation of Mach number (M_2) with diaphragm pressure ratio (P_{41}); case air/air.

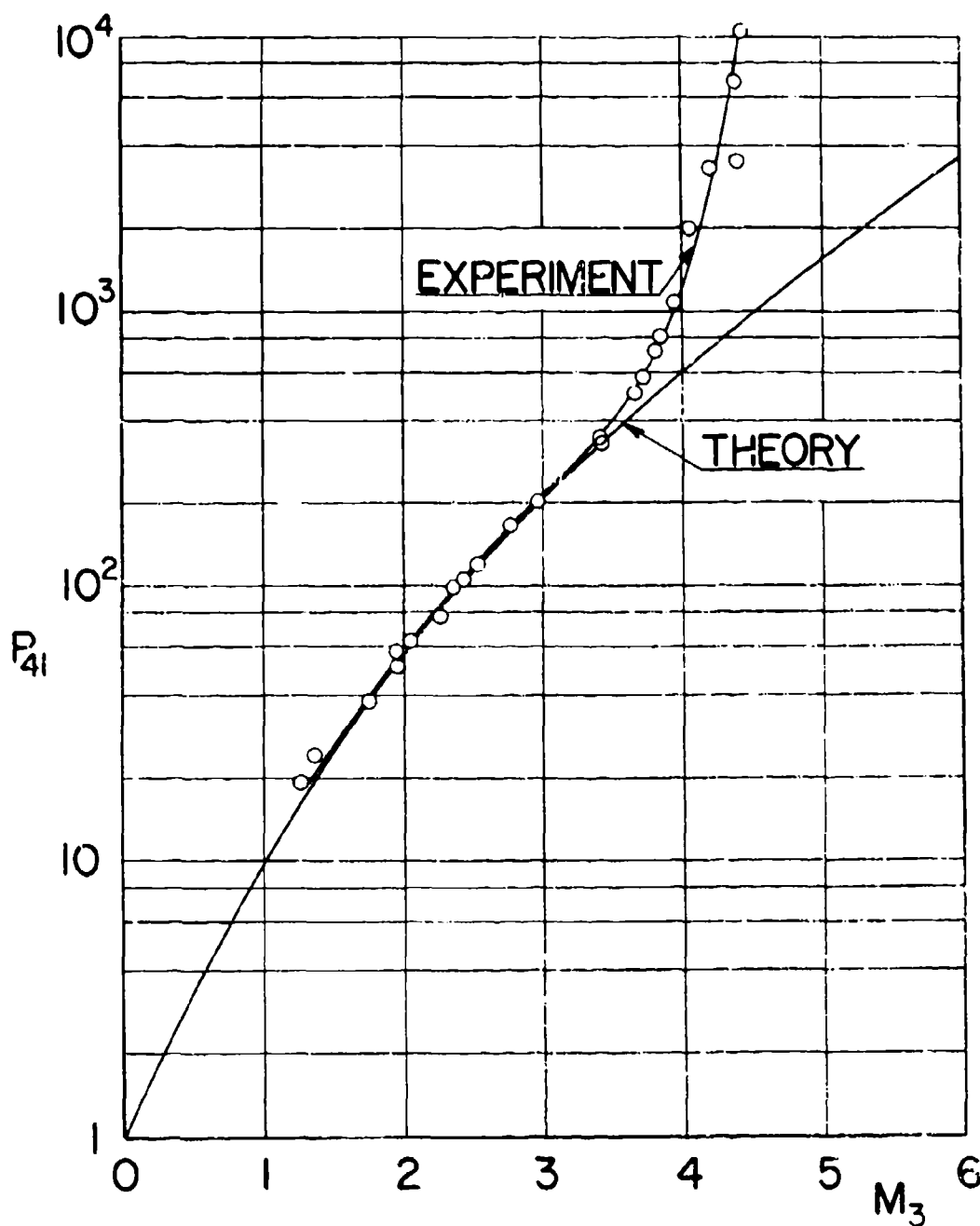


Fig. 3.1-16b. Variation of Mach number (M_3) with diaphragm pressure ratio (P_{41}); case air air.

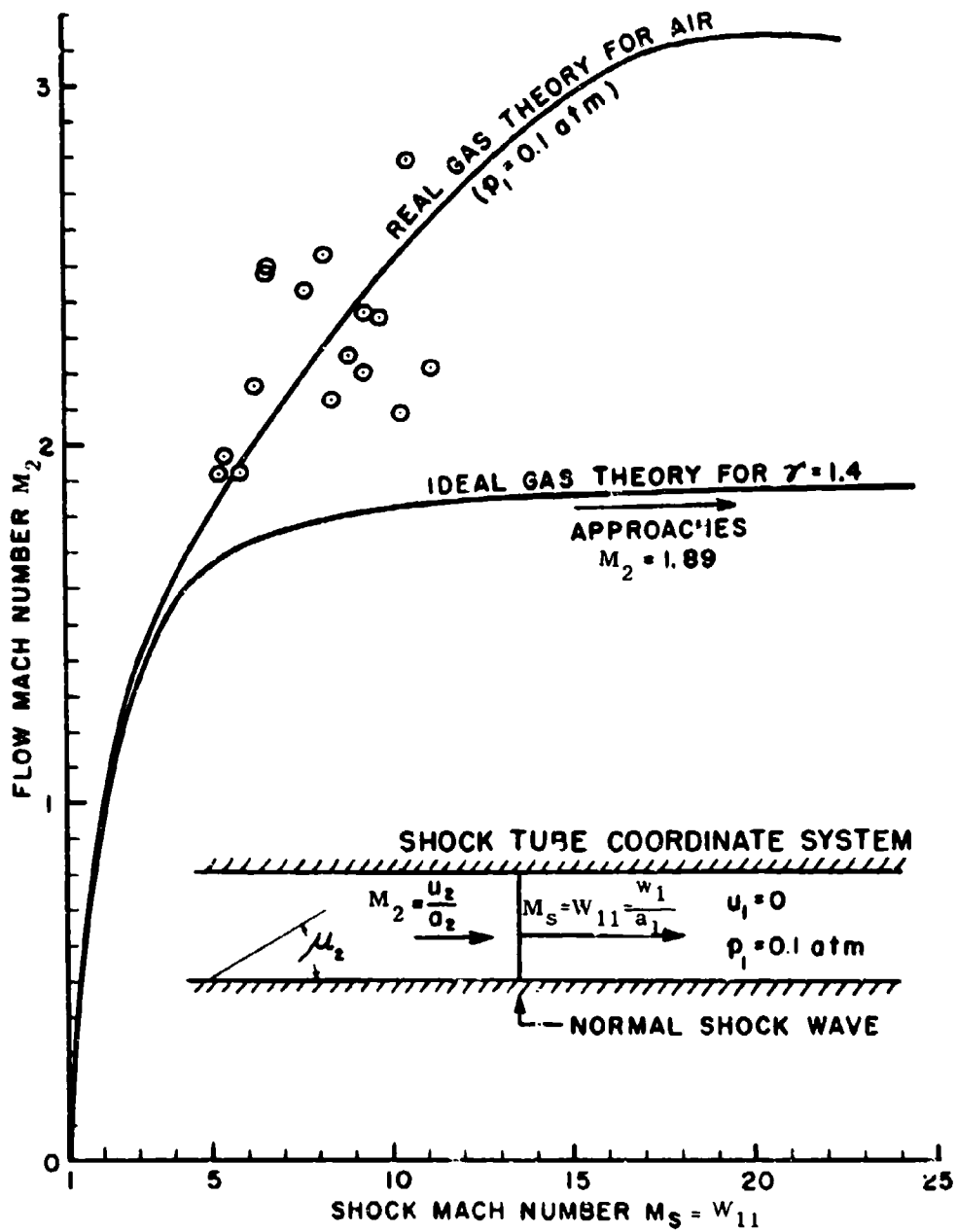


Fig. 3.1-17a. Comparison of flow Mach numbers (M_2) in air, obtained from the Mach angle (μ_2) caused by a small disturbance (scotch tape) on the shock tube wall, with theory considering imperfect gas effects (Ref. 19).

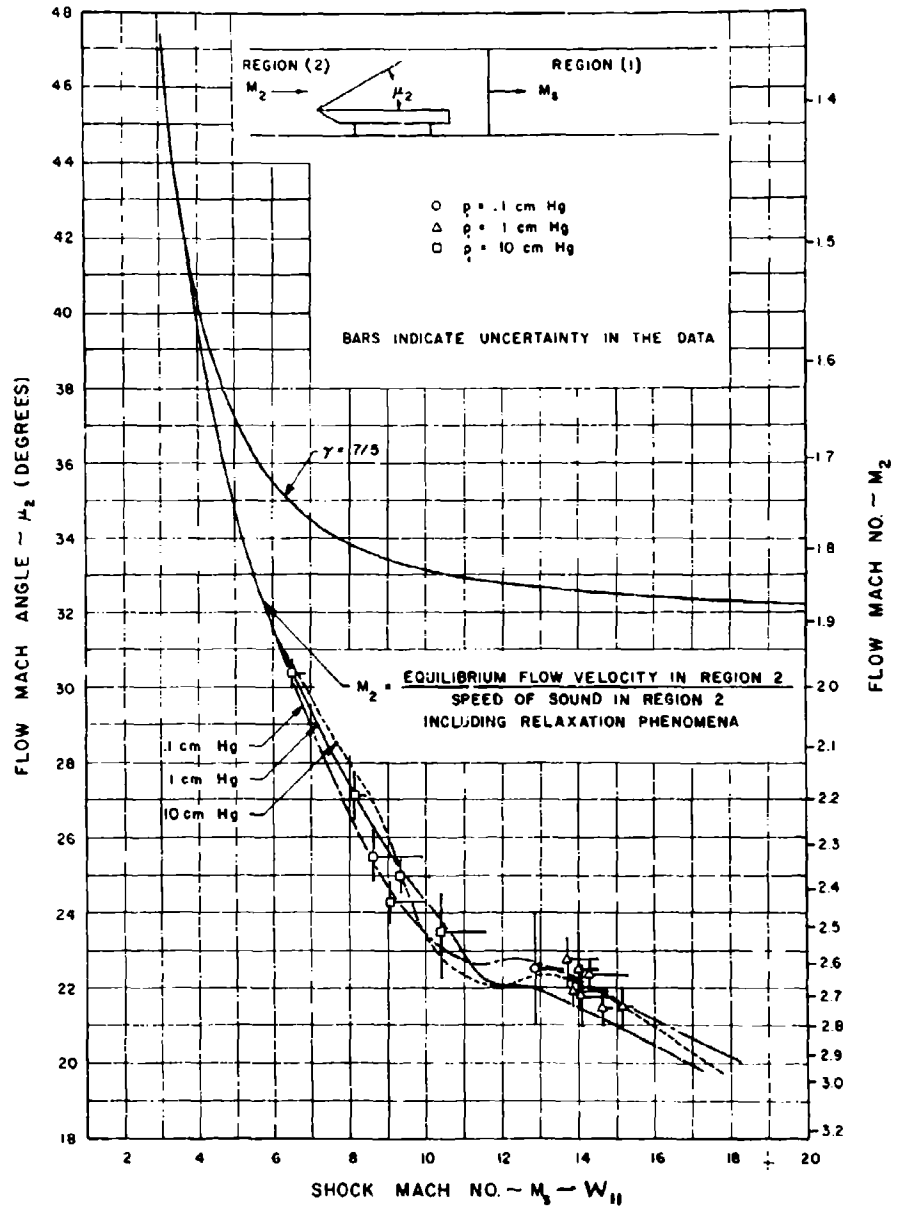
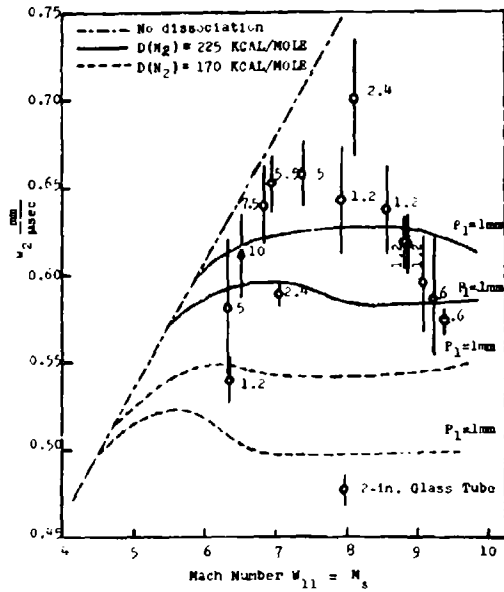
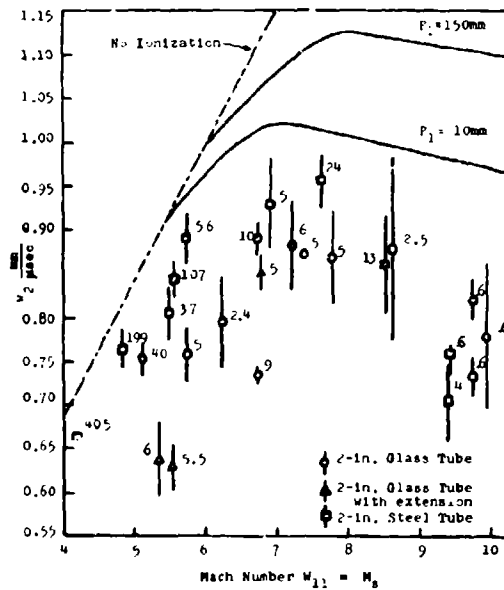


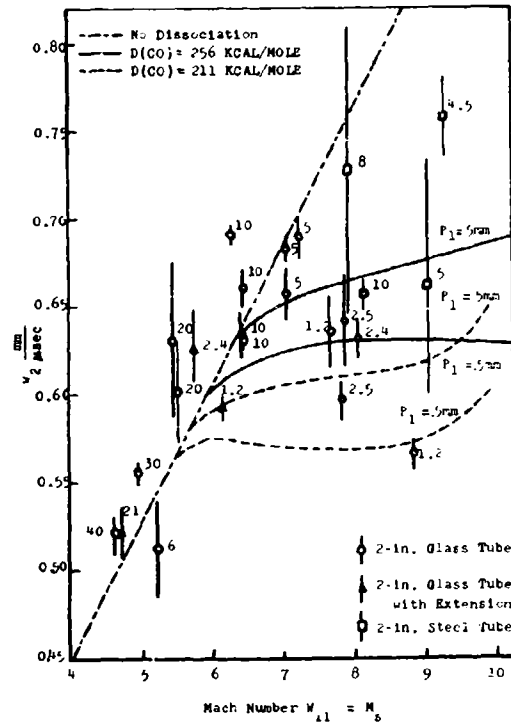
Fig. 3.1-17b. Comparison of flow Mach numbers (M_2) in air, obtained from measurements of the flat plate Mach angle (μ_2), with theory considering imperfect gas effects (Ref. 19a).



(a) Reflected shock velocity as a function of incident shock Mach number for nitrogen. The numbers beside the experimental points give P_1 in mm and the curves show the calculated values for $P_1 = 0.1$ and 1 mm.



(c) Reflected shock velocity as a function of incident shock Mach number for argon. The numbers beside the experimental points give P_1 in mm, and the curves show the calculated values for $P_1 = 10$ and 150 mm.



(b) Reflected shock velocity as a function of incident shock Mach number for carbon monoxide. The numbers beside the experimental points give P_1 in mm, and the curves show the calculated values for $P_1 = 0.5$ and 5 mm.

Fig. 3.1-18. Experimental results for the normal reflection of a shock wave (Ref. 20).

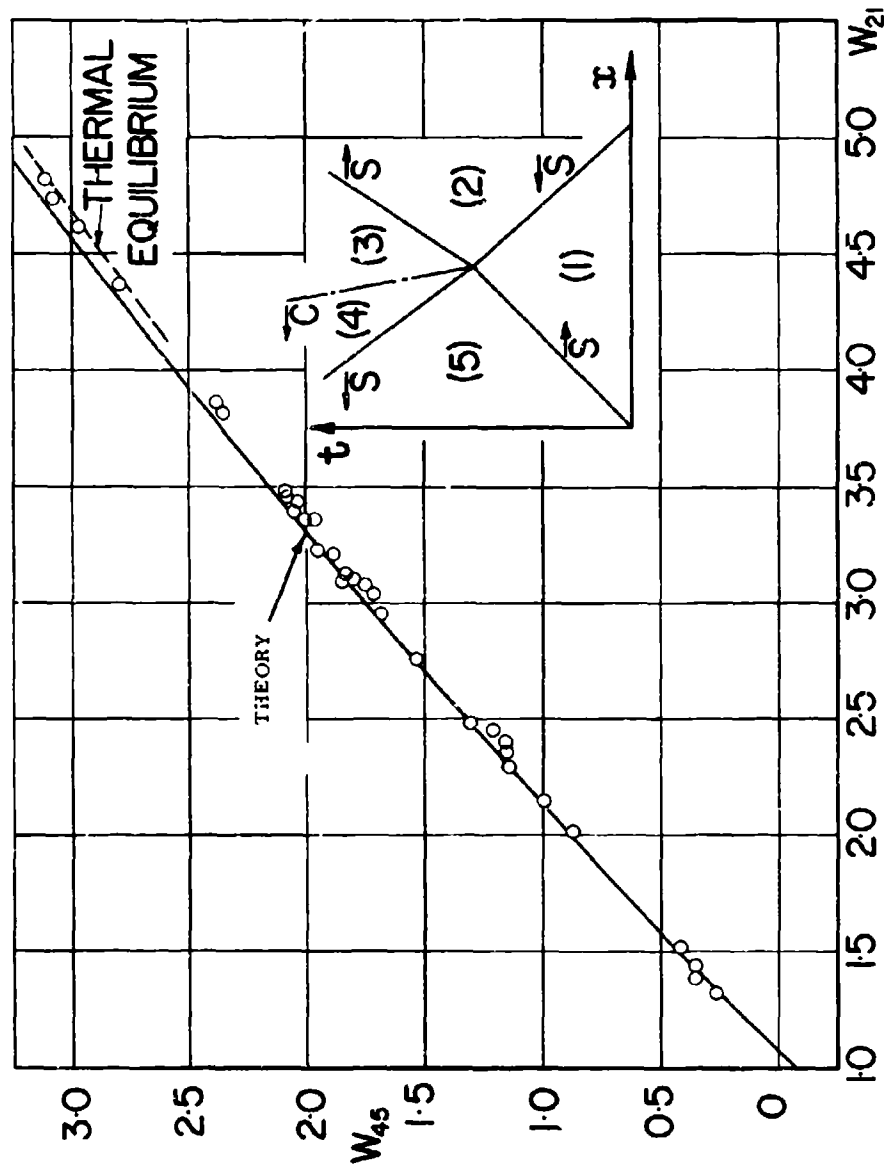


Fig. 3.1-19. Variation of the transmitted wave speed (W_{45}) with the incident wave speed (W_{21}) for the head-on collision of two shock waves in air;

$W_{51} = 2.18$.

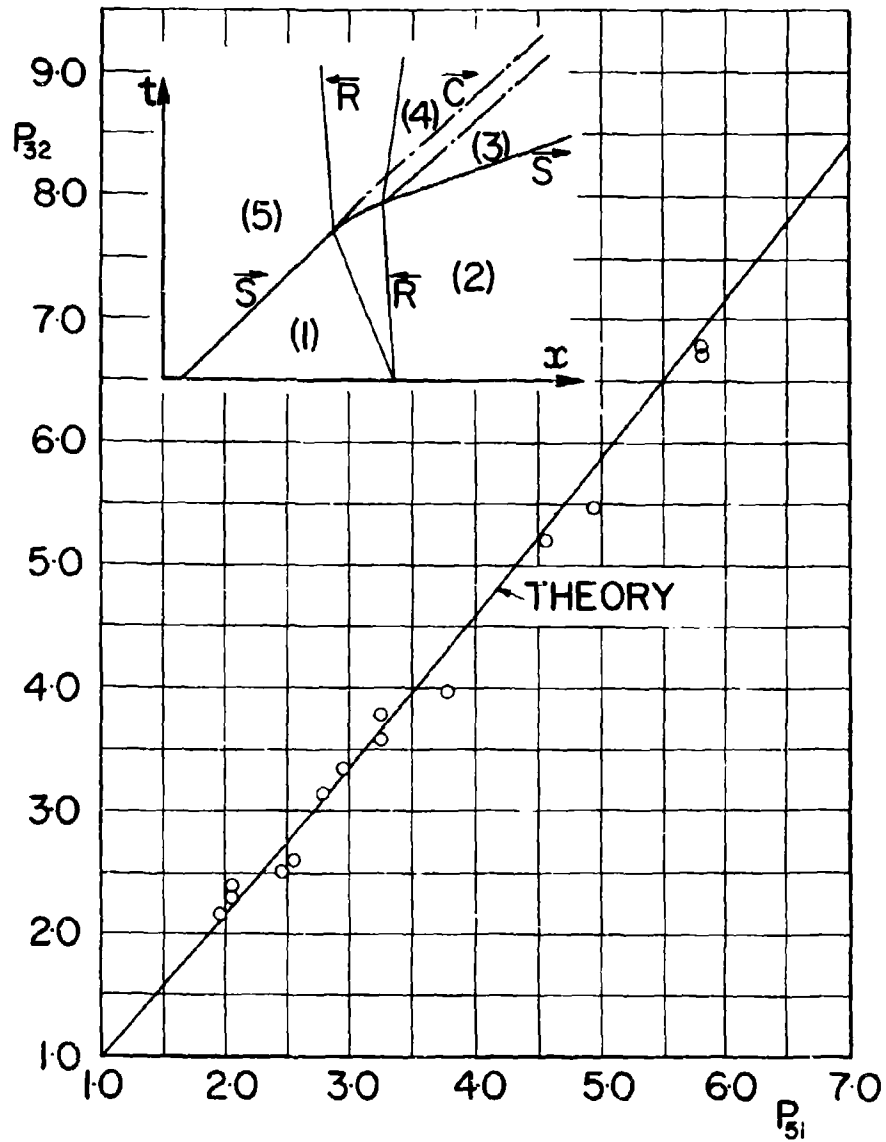


Fig. 3.1-20. Head-on collision of shock and rarefaction waves.
Rarefaction strength $P_{21} = 0.500$.

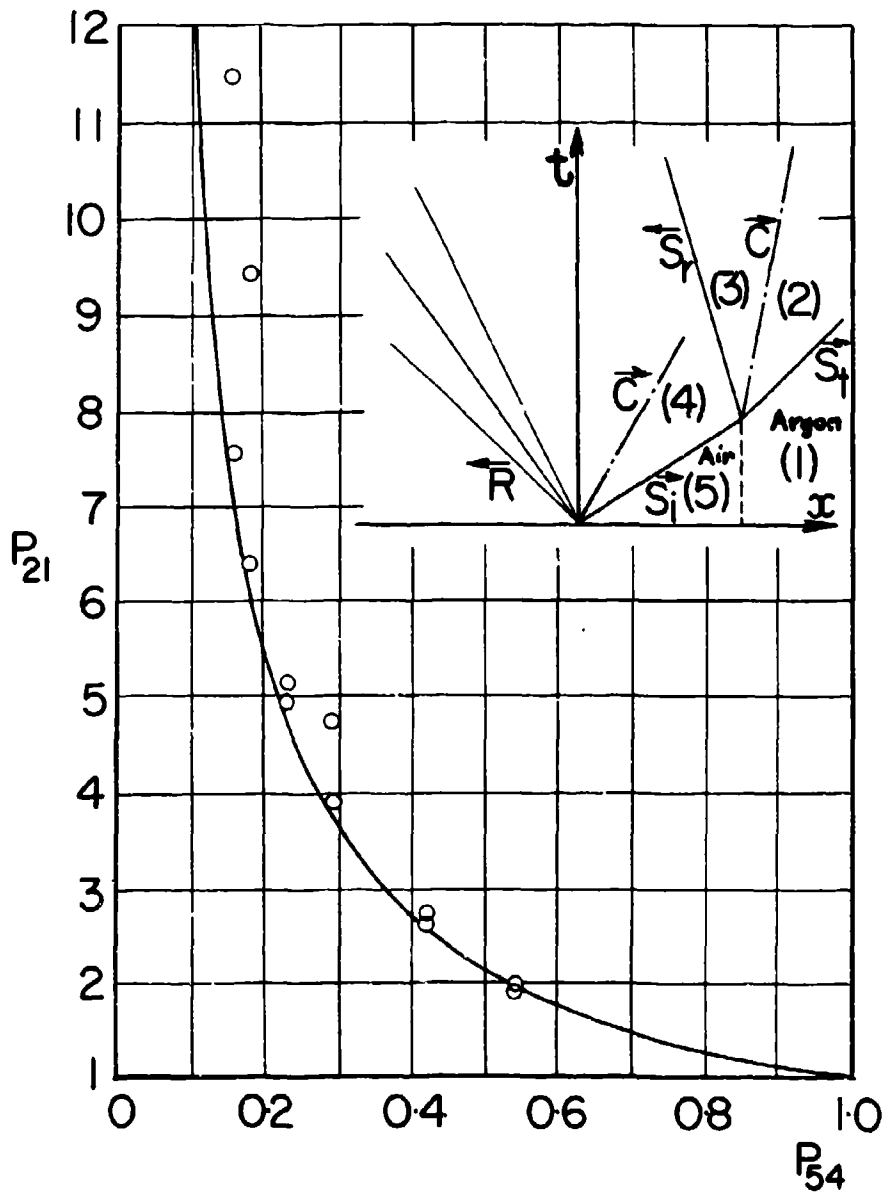
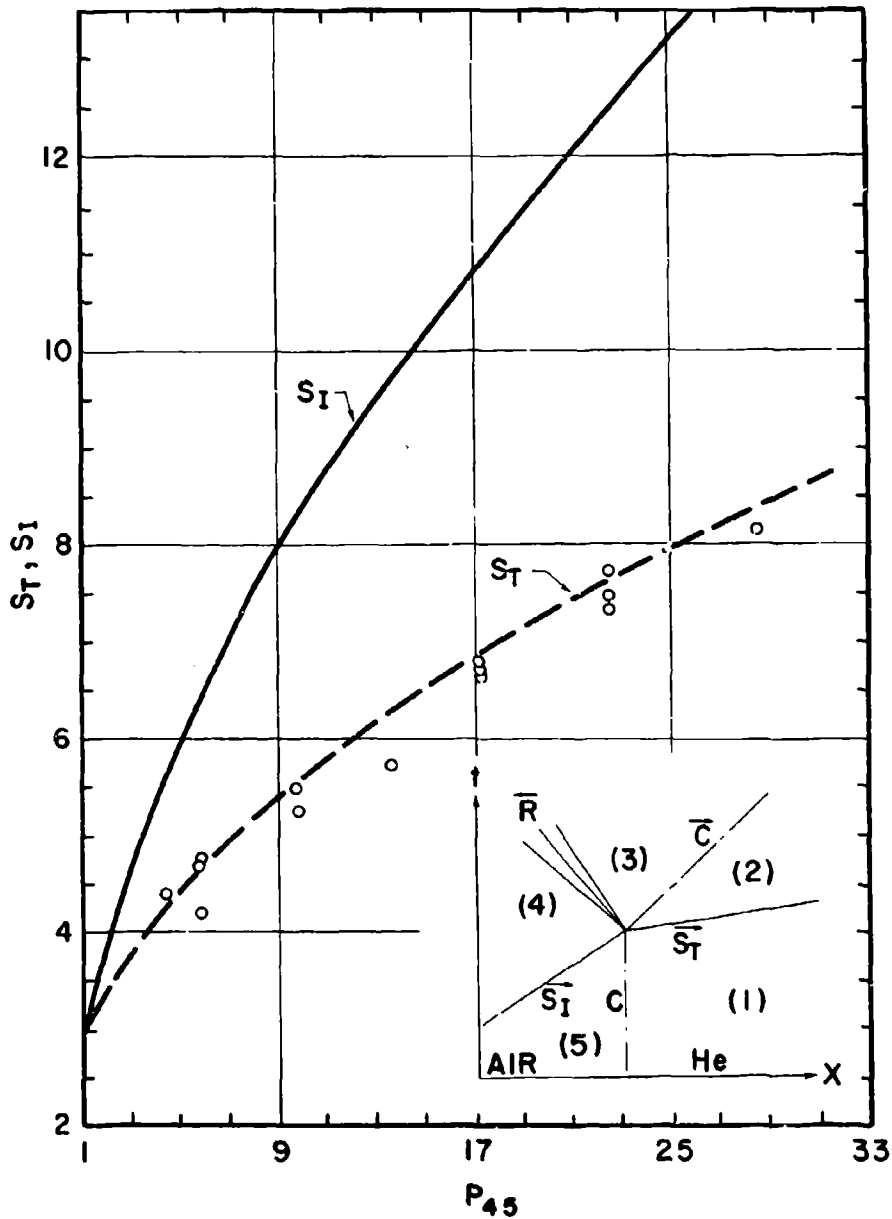
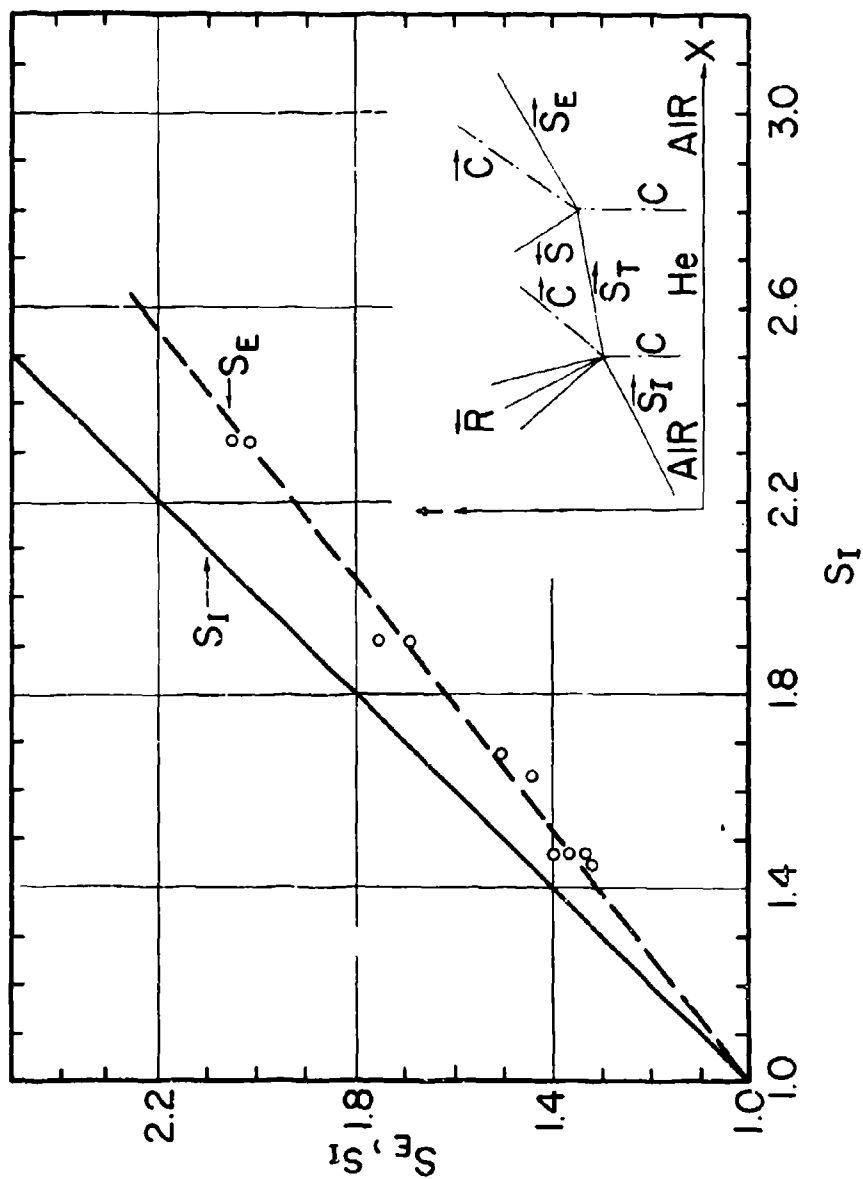


Fig. 3.1-21. Variation of the transmitted shock pressure ratio (P_{21}) for the refraction of a shock wave at a contact surface; case air||argon, $E_{15} = 0.431$.



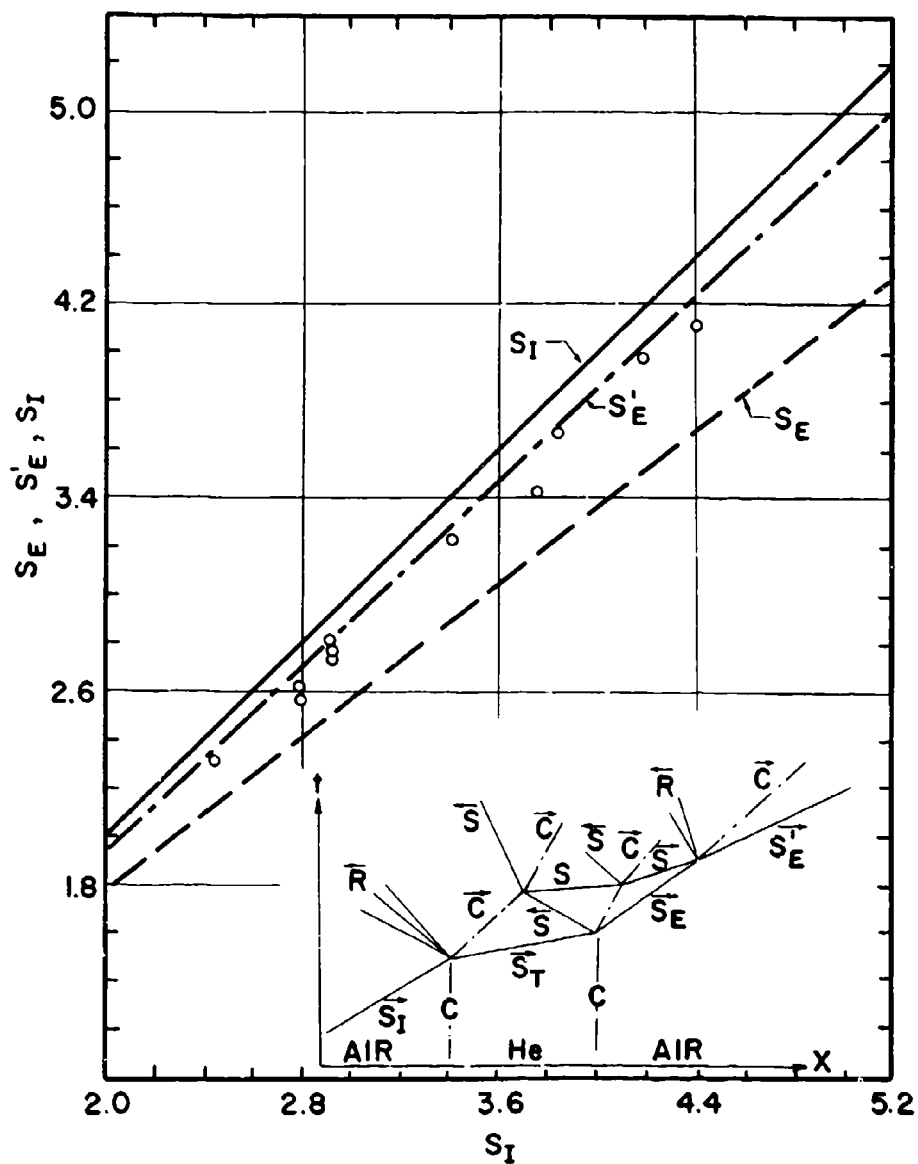
(The Mach number of the incident wave (S_I) referred to helium is plotted as a reference to show the attenuation. Both Mach numbers are referred to the sound speed in air.)

Fig. 3.1-22. Variation of the transmitted shock Mach number (S_T) with the pressure ratio (P_{45}) across the incident shock wave; case air||He.



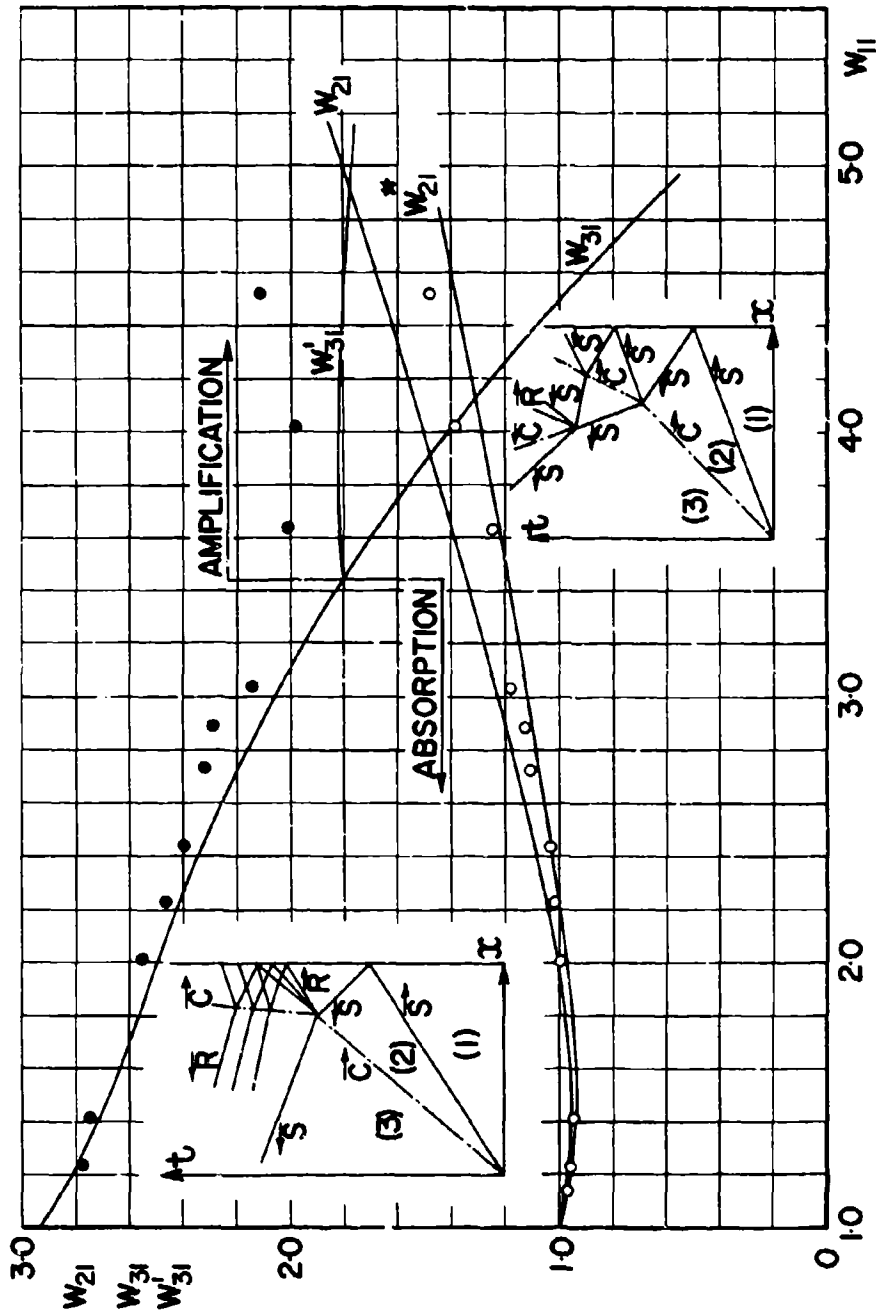
(S_I is plotted as a reference to show the initial shock wave attenuation obtained close to the contact surface.)

Fig. 3.1-23. Double refraction at a layer of helium showing the variation of the emergent shock Mach number (S_E) with the incident wave Mach number (S_I); case air||He||air.



(Experimental points are for the shock-amplified wave (S'_E). It can be seen that overtaking shock waves will bring the final wave close to its original strength.)

Fig. 3.1-24. Double refraction at a layer of helium showing the variation of the emergent shock Mach number (S_E) and the overtaken shock-amplified Mach number (S'_E) with the incident shock Mach number (S_I); case air||He||air.



(W_{21} = perfect gas, W_{21}^* = imperfect gas, no dissociation.)
 Fig. 3.1-25. Variation of the reflected wave speed (W_{21}), the refracted wave speed (W_{31}), and the overtaken shock-amplified wave speed (W_{31}) with the incident wave speed (W_{11}); case He/air.

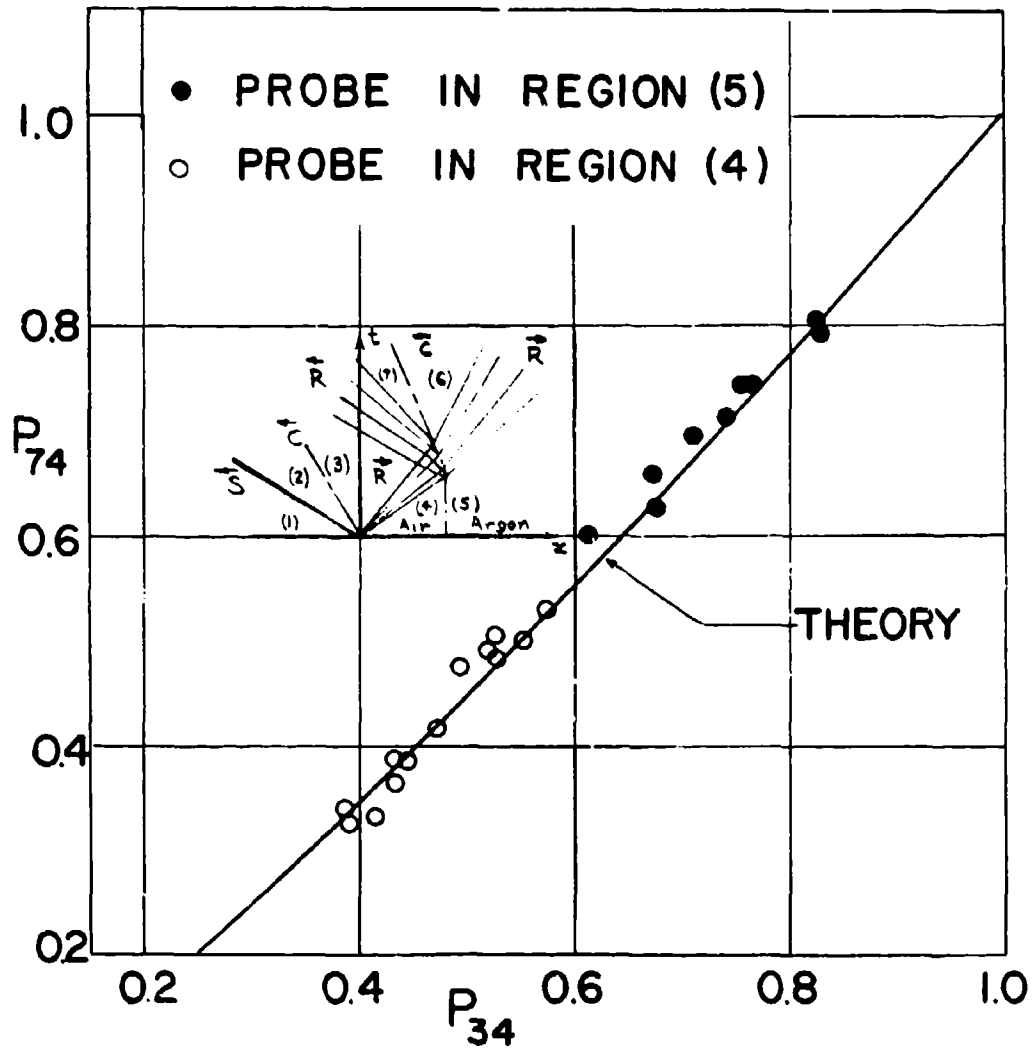


Fig. 3.1-26. Variation of the pressure ratio across the rarefaction waves after the interaction ($P_{74} = P_{65}$) with the pressure ratio across the incident rarefaction wave (P_{34}); case air||argon.

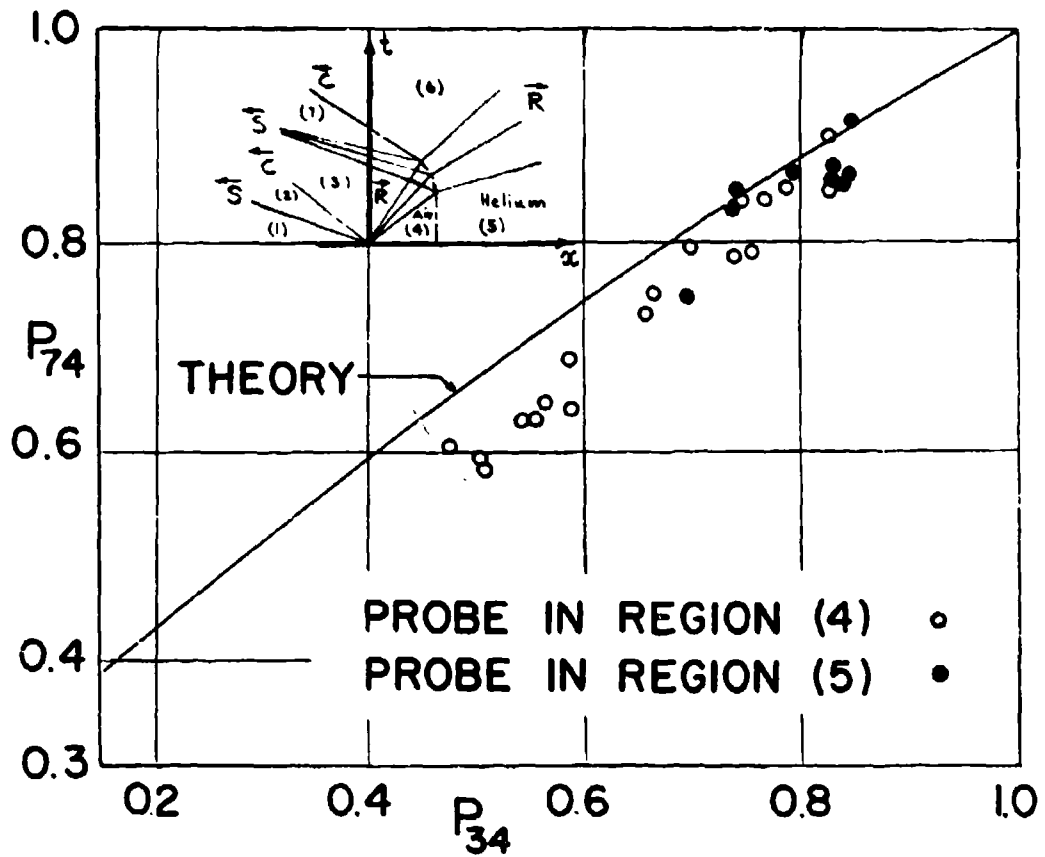
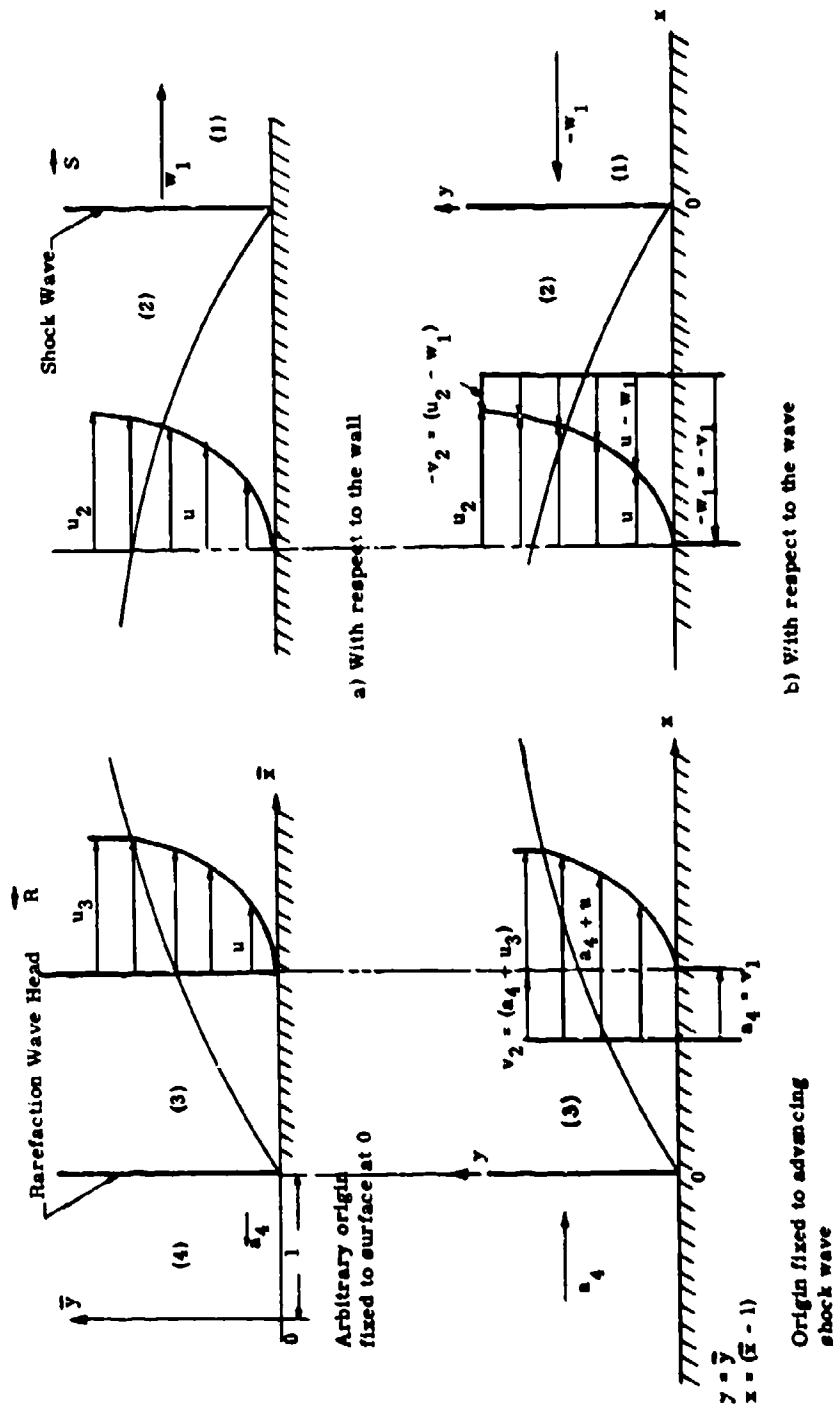
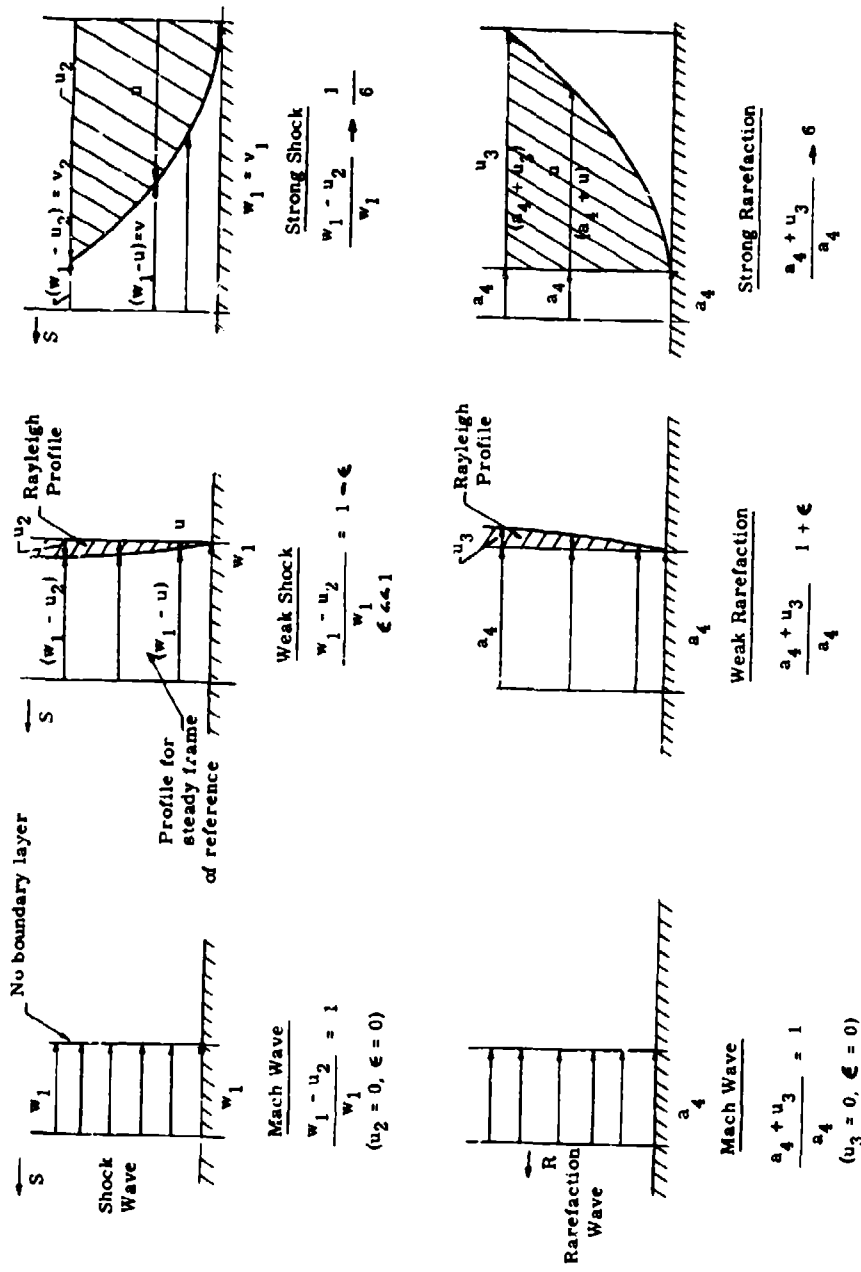


Fig. 3.1-27. Variation of the pressure ratio across the rarefaction waves after the interaction ($P_{74} = P_{65}$) with the pressure ratio across the incident rarefaction wave (P_{34}); case air||He.



(See Fig. 3.1-4)

Fig. 3.2-1. Coordinate axes for a moving and stationary shock wave or expansion wave in a shock tube.



(Both waves shown as moving to the left for illustration)

Fig. 3.2-2. Limiting boundary layer profiles in a shock tube in air; $\gamma = 1.4$.

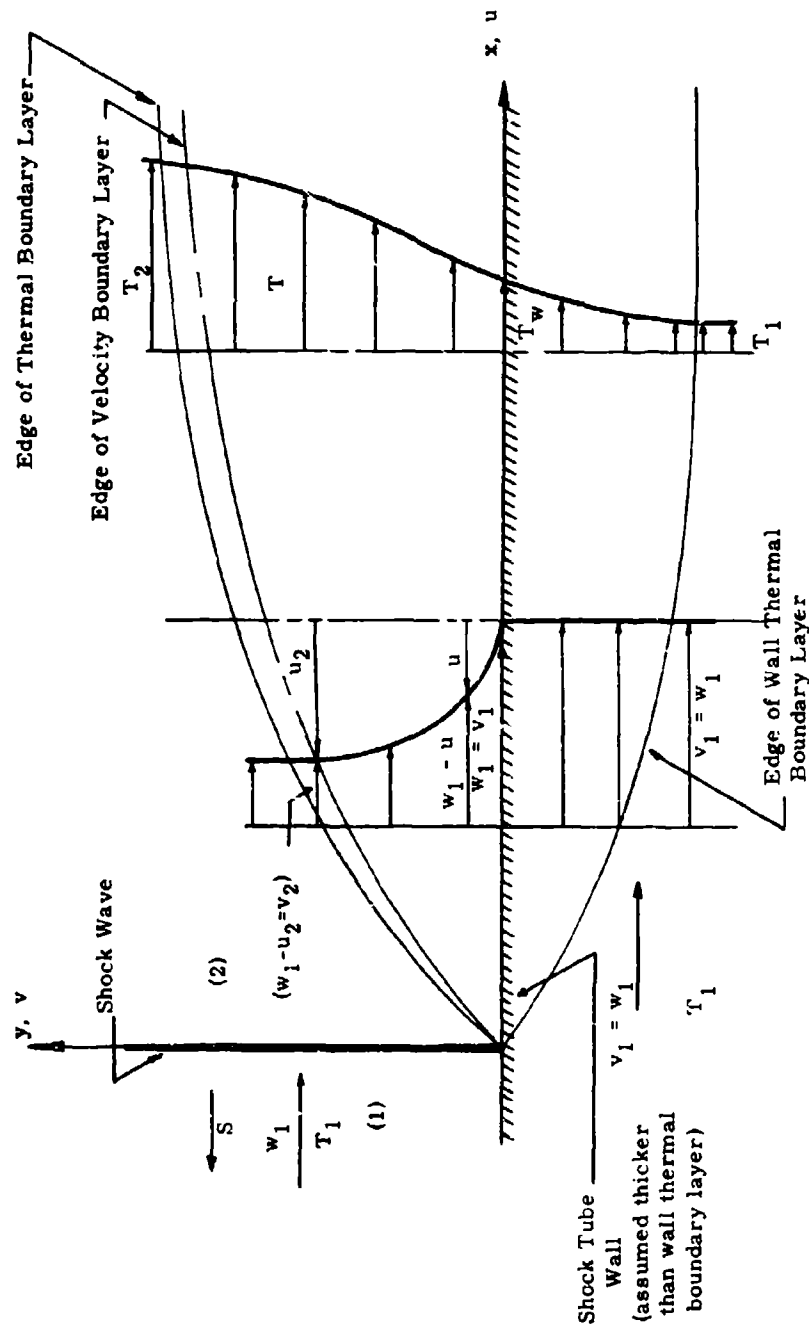


Fig. 3.2-3. Velocity and temperature profiles in the boundary layer behind a moving shock wave (reference axes fixed to shock).

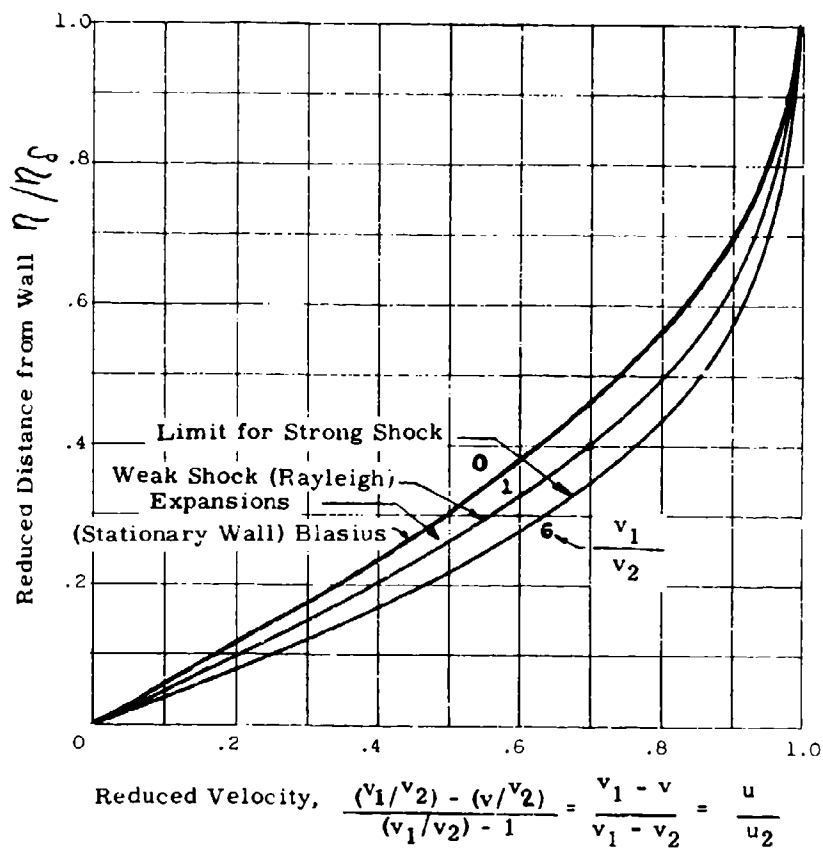


Fig. 3.2-4. Boundary layer velocity profiles for a moving wall in the range of wall to free stream velocity ratios of $0 \leq v_1/v_2 \leq 6$ (after Refs. 28 and 31).

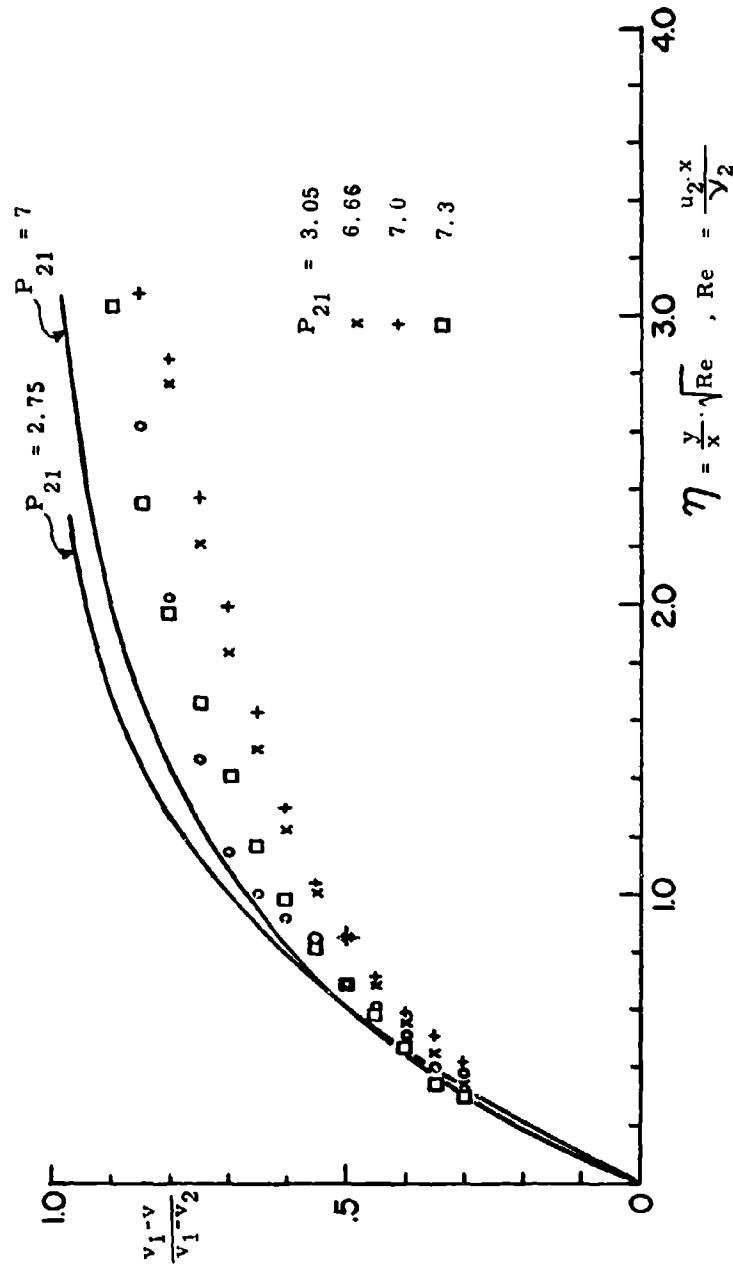


Fig. 3.2-5. Comparison of experimental (interferometric) and theoretical laminar boundary layer velocity profiles (Ref. 26).

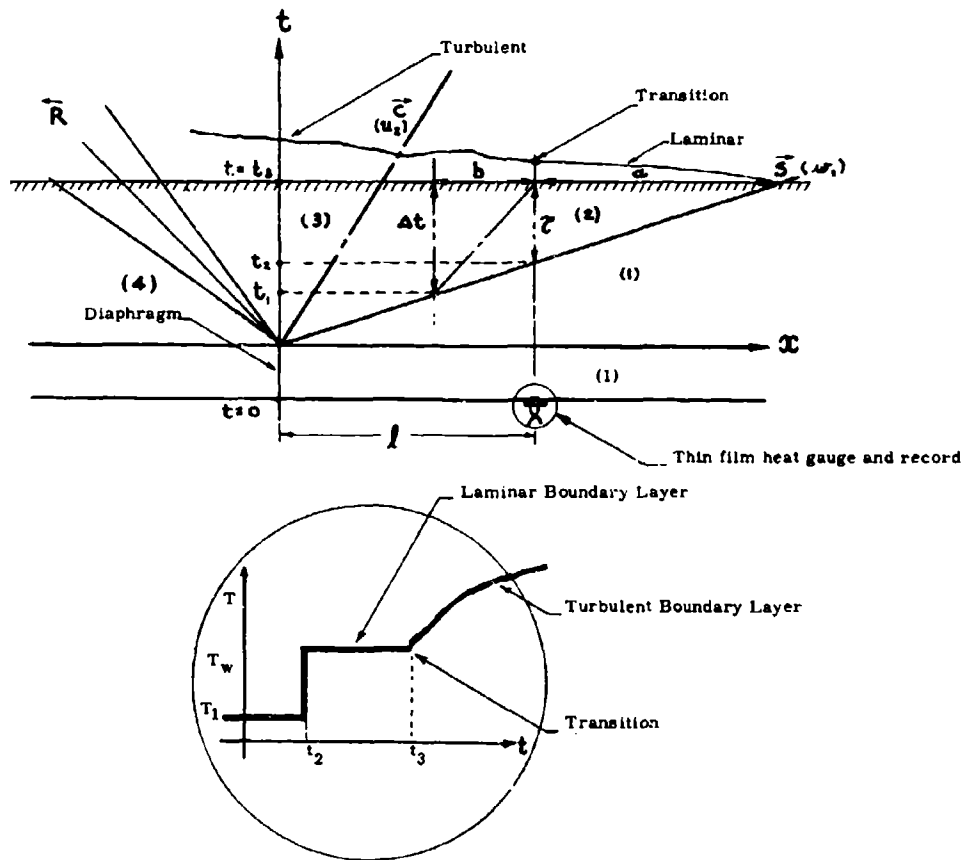


Fig. 3.2-6. Illustration of the measurement of boundary layer transition with a thin film heat gauge.

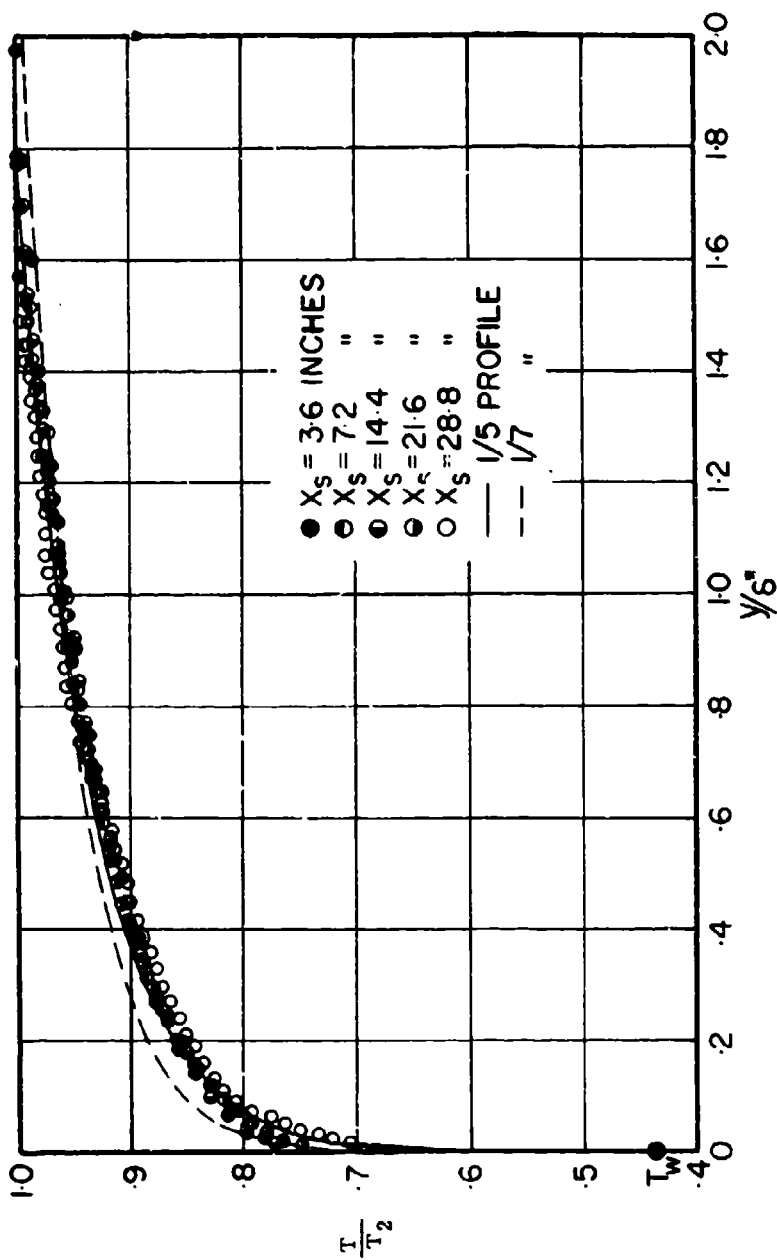


Fig. 3.2-7. Theoretical and experimental temperature profiles T/T_2 in a turbulent boundary layer (y/δ^*) behind a plane shock wave in a 2 x 7-in. shock tube; case He/air; $P_{21} = 8.03$, $P_1 = 120$ mm HG, $T_1 = 533^\circ R$, $W_{11} = 2.65$, $M_2 = 1.25$, $U_{21} = 1.88$; measuring station 141 in. from diaphragm.

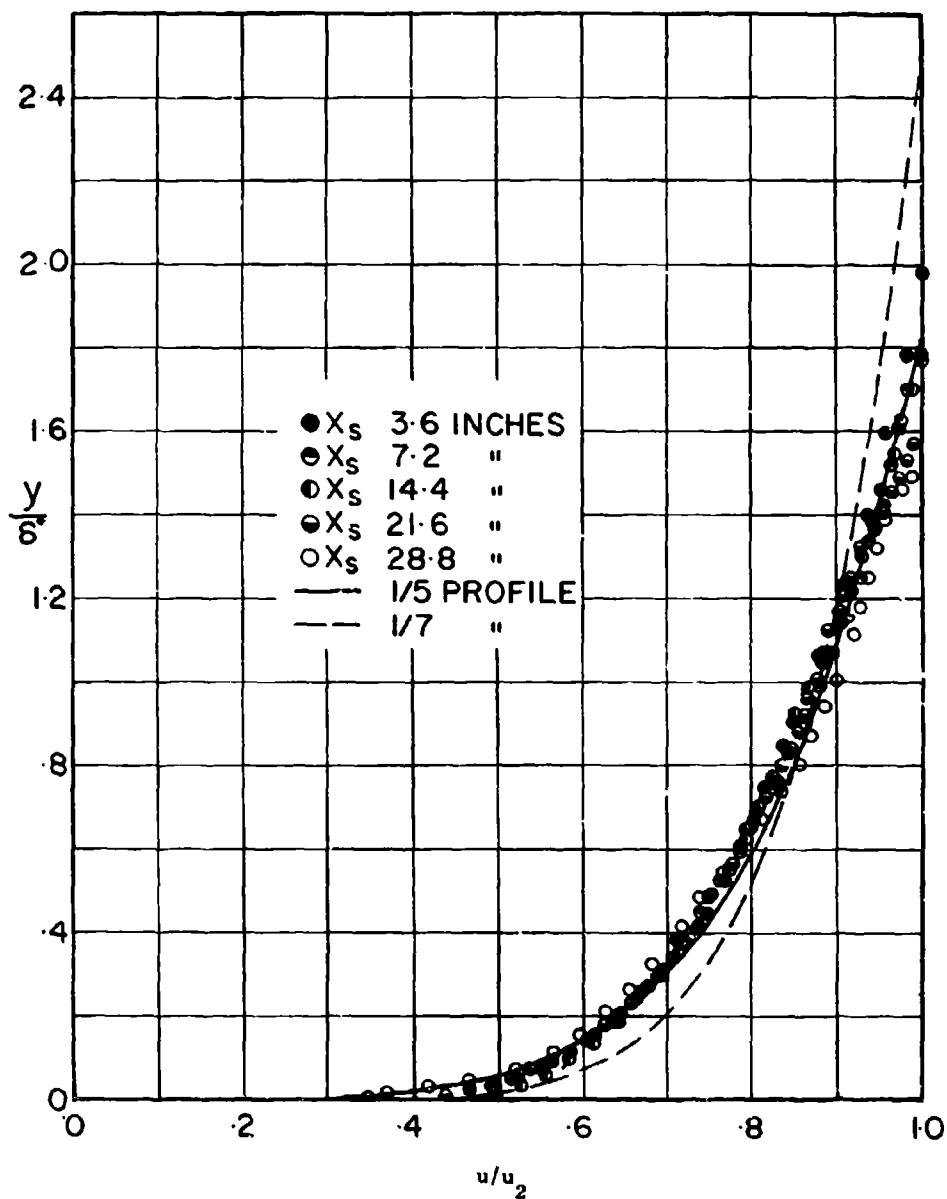


Fig. 3.2-8. Theoretical and experimental velocity profiles (u/u_2) in a turbulent boundary layer (y/δ^*) behind a plane shock wave in a 2 x 7-in. shock tube (derived from Fig. 3.2-7).

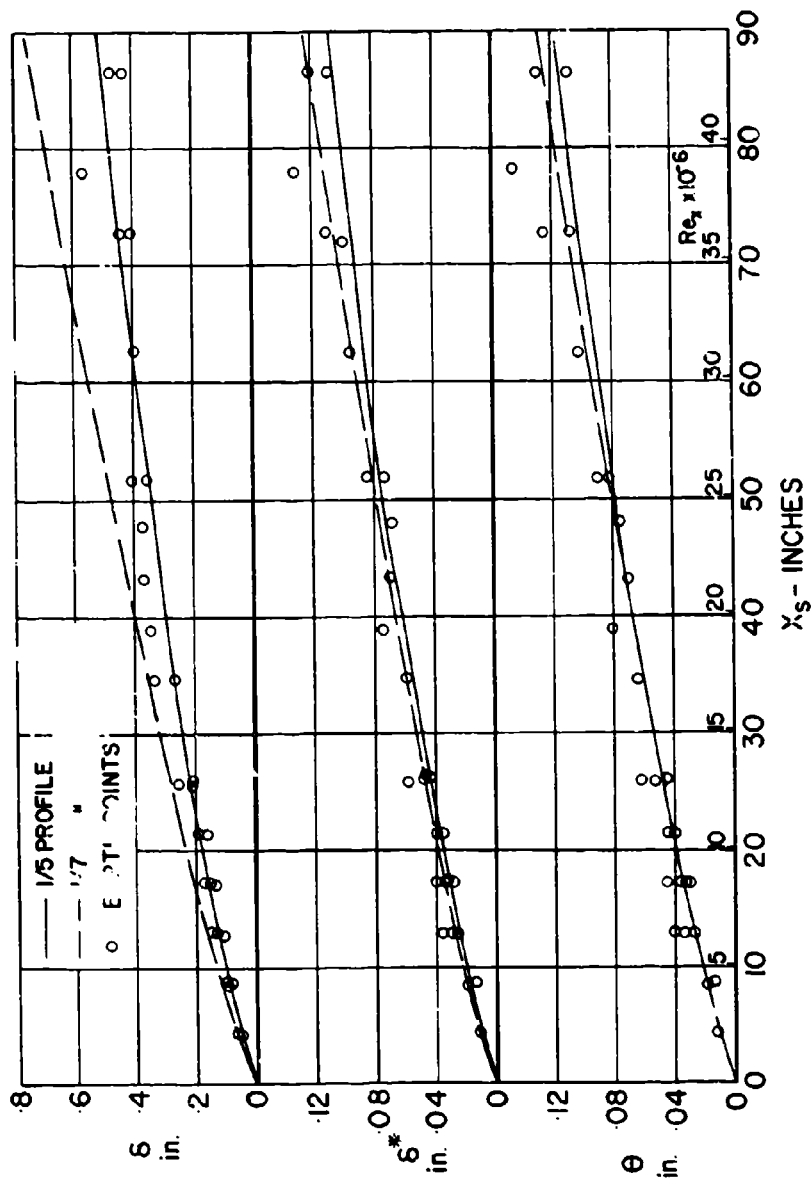


Fig. 3.2-9. Theoretical and experimental variation of the boundary layer thickness (δ), displacement thickness (δ^*), and momentum thickness (θ) with the distance behind the shock wave (X_s) and the Reynolds number (Re_x) in a 2 x 7-in. shock tube; $P_{21} = 2.75$, $P_1 = 300$ mm Hg, $T_1 = 531^\circ R$, $M_{11} = 1.58$, $M_2 = 0.67$, $U_{21} = 0.79$.

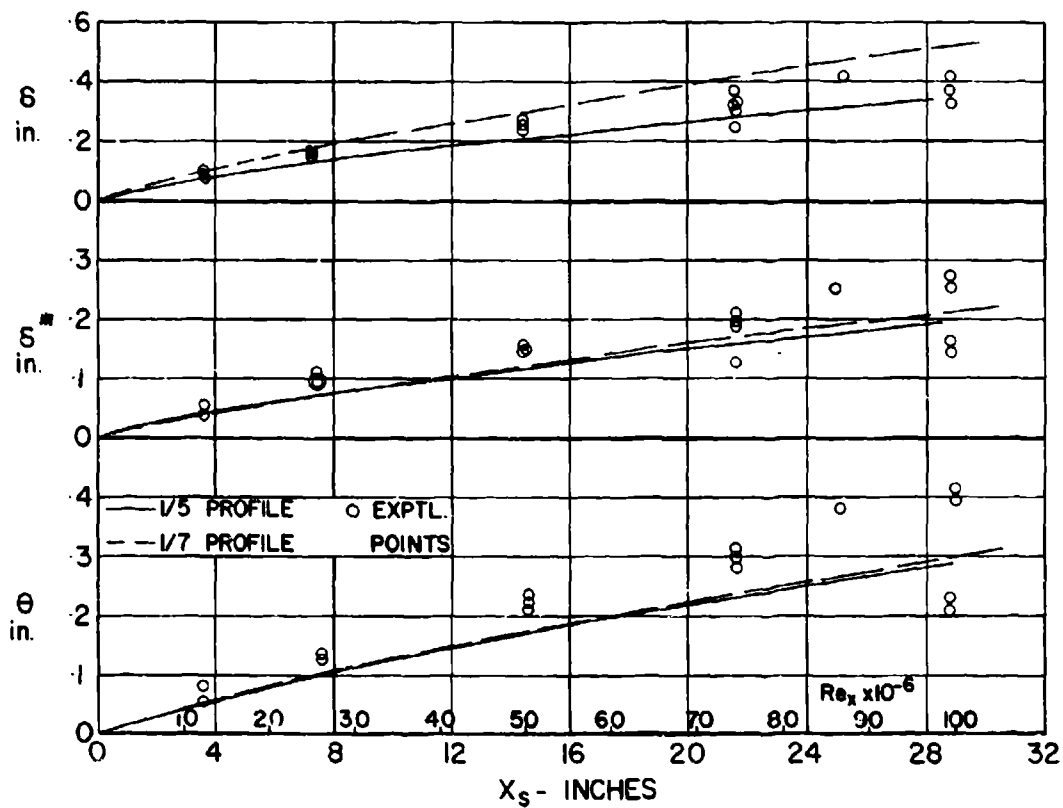


Fig. 3.2-10. Theoretical and experimental variation of the boundary layer thickness (δ), displacement thickness (δ^*), and momentum thickness (θ) with the distance behind the shock wave (X_s) and the Reynolds number (Re_x) in a 2 x 7-in. shock tube; $P_{21} = 8.03$, $p_1 = 120$ mm Hg, $T_1 = 533^\circ R$, $w_{11} = 2.65$, $M_2 = 1.25$, $U_{21} = 1.88$.

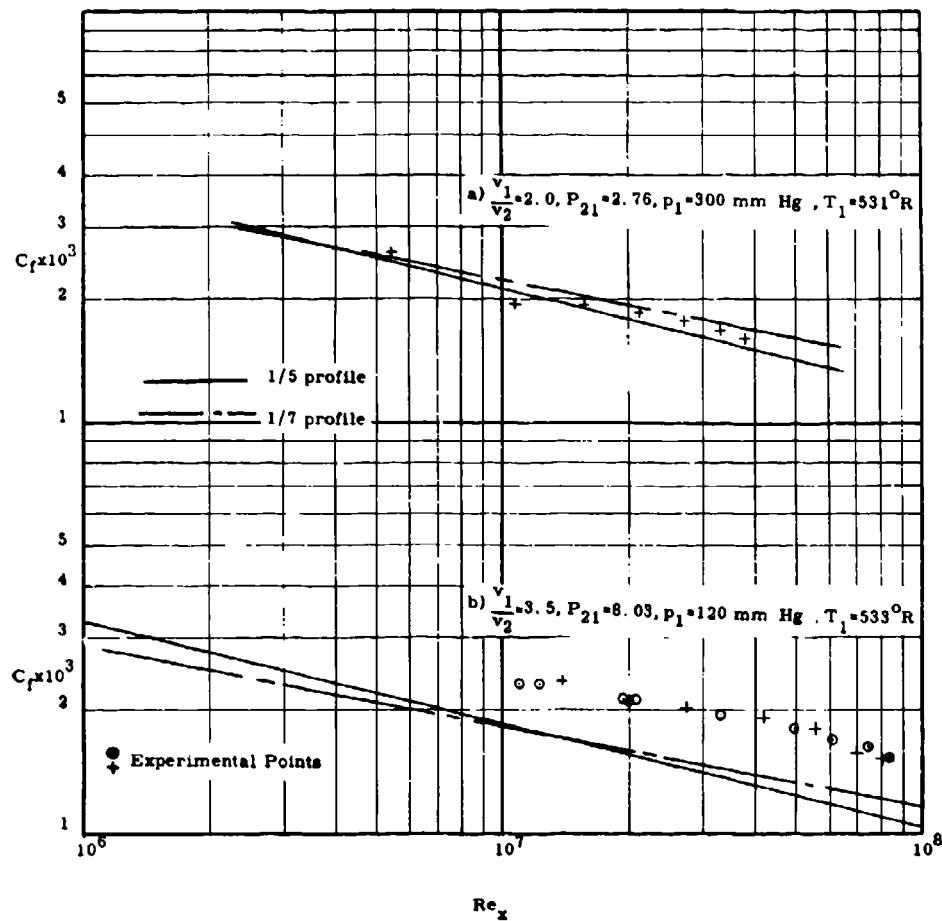


Fig. 3.2-11. Variation of the local skin friction coefficient (C_f) (from interferometric measurements) with Reynolds number (Re_x) for turbulent boundary layer behind a plane shock wave.

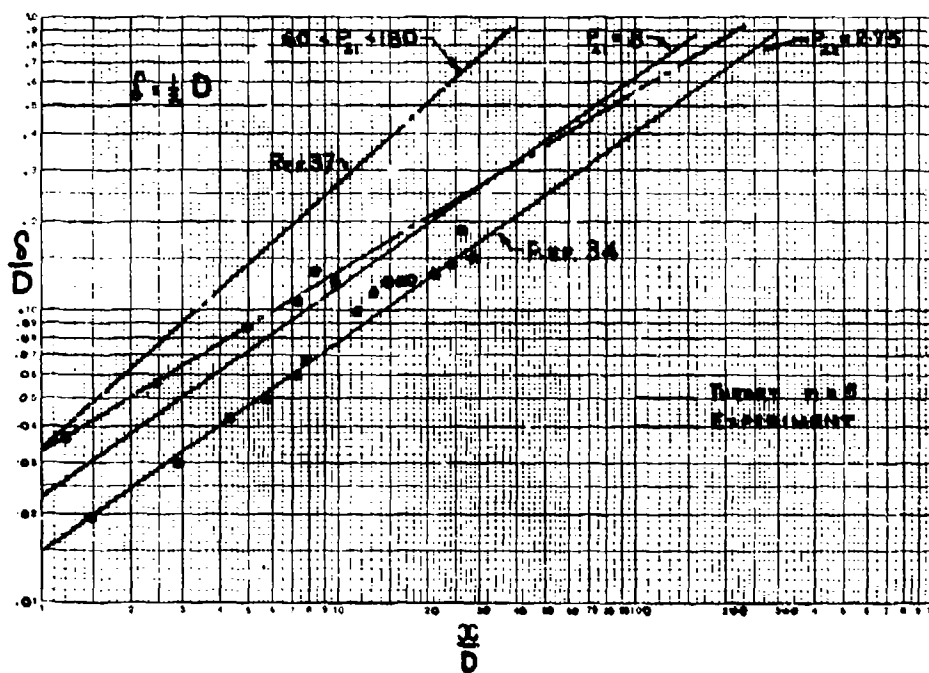


Fig. 3.2-12. Variation of the boundary layer growth (δ/D) behind a moving plane shock wave (x/D).

REFERENCES

1. Glass, I. I., Martin, W. A., and Patterson, G. N. A Theoretical and Experimental Study of the Shock Tube. UTIA Report 2. Institute of Aerophysics, University of Toronto, 1953.
2. Lobb, R. K. A Study of Supersonic Flows in a Shock Tube. UTIA Report 8. Institute of Aerophysics, University of Toronto, 1950.
3. Glass, I. I. An Experimental Determination of the Speed of Sound in Gases from the Head of a Rarefaction Wave. UTIA Report 9. Institute of Aerophysics, University of Toronto, 1952 (also J. Aeronaut. Sci., Vol. 19 (1952), p. 286).
- 3a. Glass, I. I. and Hall, J. G. "Determination of the Speed of Sound in Sulfurhexafluoride in a Shock Tube," J. Chem. Phys., Vol. 27, No. 5 (November 1957).
4. Griffith, W. C. and Bleakney, W. "Shock Waves in Gases," Am. J. of Phys., Vol. 22 (1954), p. 597.
5. Emrich, R. J. and Curtis, C. W. "Attenuation in the Shock Tubes," J. Appl. Phys., Vol. 24, No. 3 (1953).
6. Bannister, F. K. and Mucklow, G. F. "Wave Action Following Sudden Release of Compressed Gas from a Cylinder," Proc. Inst. Mech. Eng., Vol. 159 (1948).
7. Day, J. D. Attenuation of Shock Waves in the BRL 24-Inch Shock Tube. BRL Report 948. Aberdeen Proving Ground, Md.: Ballistic Research Laboratory, 1955.
- 7a. Jones, J. J. Experimental Investigations of Attenuation of Strong Shock Waves in a Shock Tube with Hydrogen and Helium as Driver Gases. NACA TN 4072, 1957.
8. Boyer, D. W. Effects of Kinematic Viscosity and Wave Speed on Shock Wave Attenuation. UTIA TN 8. Institute of Aerophysics, University of Toronto, 1956.
- 8a. White, D. R. Influence of Diaphragm Opening Time on Shock Tube Flows. Report 58-RL-1999. Schenectady, N. Y.: General Electric Research Laboratory, 1958.
9. Trimpi, R. L. and Cohen, N. B. A Theory for Predicting the Flow of Real Gases in Shock Tubes with Experimental Verification. NACA TN 3375, 1955.
10. Trimpi, R. L. and Cohen, N. B. An Integral Solution to the Flat Plate Laminar Boundary Layer Flow Existing Inside and after Expansion Waves and after Shock Waves Moving into Quiescent Fluid with Particular Application to the Complete Shock Tube Flow. NACA TN 3944, 1957.
11. Mirels, H. Attenuation in a Shock Tube Due to Unsteady-Boundary Layer Action. NACA TN 3278, 1956.

12. Mireis, H. and Braun, W. H. Nonuniformities in Shock-Tube Flow Due to Unsteady-Boundary-Layer Action. NACA TN 4021, 1957.
13. Billington, I. J. An Experimental Study of One-Dimensional Refraction of a Rarefaction Wave at a Contact Surface. UTIA Report 32. Institute of Aerophysics, University of Toronto, 1955 (and J. Aeronaut. Sci., Vol. 23 (1956), pp. 997-1006).
14. Mack, J. E. Density Measurements in Shock Tube Flow with the Chrono-Interferometer. Tech. Report 4. Institute of Research, Lehigh University, 1954.
15. Williams, A. C. Mass Flow and Velocity in the Shock Tube. Tech. Report 5. Institute of Research, Lehigh University, 1955.
16. Emrich, R. J. and Peterson, R. L. Pressure Variation in the Shock Tube with Time. Tech. Report 7. Institute of Research, Lehigh University, 1956.
17. Wheeler, D. B., Jr. Density Variation in Shock Tube Flow. Tech. Report 8. Institute of Research, Lehigh University, 1956.
18. Lundquist, G. A. The NOL 8 x 8 Inch Shock Tube; Instrumentation and Operation. NAVORD Report 2449. White Oak, Md.: Naval Ordnance Laboratory, 1952.
19. Hertzberg, A. The Shock Tunnel and its Applications to Hypersonic Flight. Report AD-1052-A-5. Buffalo, N. Y.: Cornell Aeronautical Laboratory, Inc., 1957.
- 19a. Feldman, S. The Chemical Kinetics of Air at High Temperatures: A Problem in Hypersonic Aerodynamics. AVCO Research Note 23. Everett, Mass.: AVCO Research Laboratory, AVCO Manufacturing Corp., 1957.
20. Toennies, J. P. and Greene, E. F. "Dissociation Energies of Carbon Monoxide and Nitrogen from Reflected Shock Wave Studies," J. Chem. Phys., Vol. 26, No. 3 (1957).
- 20a. Greene, E. F. Private Communication, June 1957.
- 20b. Strehlow, R. A. and Cohen, A. "Comment on Reflected Shock Wave Studies," J. Chem. Phys. Vol. 28 (1958), pp. 983-985.
- 20c. Mark, H. The Interaction of a Reflected Shock Wave with the Boundary Layer in a Shock Tube. NACA TM 1418, 1958.
- 20d. Gould, D. G. On the Head-on Collision of Two Shock Waves and a Shock and a Rarefaction Wave in One-Dimensional flow. UTIA Report No. 17. Institute of Aerophysics, University of Toronto, 1952.
21. Bitondo, D. Experiments on the Amplification of a Plane Shock Wave. UTIA Report 7. Institute of Aerophysics, University of Toronto, 1950.
22. Ford, A. and Glass, I. I. An Experimental Study of Shock Wave Reflection. UTIA Report 29. Institute of Aerophysics, University of Toronto, 1954 (and J. Aeronaut. Sci., Vol. 23 (1956), pp. 189-191).

- 22a. McKee, R. M. An Experimental Study of the Interaction of a Plane Shock Wave with a Contact Region. UTIA Tech. Note 1. Institute of Aerophysics, University of Toronto, 1954.
- 22b. Lukasiewicz, J. "Diffusers for Supersonic Wind Tunnels," J. Aeronaut. Sci., Vol. 20 (1953), p. 617.
23. Laporte, O. and Turner, E. B. "On the Interaction of Two Plane Shocks Facing in the Same Direction," J. Appl. Phys., Vol. 25 (1954), p. 678.
24. Goldstein, S. Modern Developments in Fluid Dynamics, Vol. 1. Oxford: Clarendon Press, 1938, pp. 181-186.
25. Donaldson, C. duP. and Sullivan, R. D. The Effect of Wall Friction on Strength of Shock Waves in Tubes and Hydraulic Jumps in Channels. NACA TN 1942, 1949.
26. Bershader, D. and Allport, J. On the Laminar Boundary Layer Induced by a Travelling Shock Wave. Tech. Report II-22. Department of Physics, Princeton University, 1956.
27. Hollyer, R. N., Jr. A Study of Attenuation in the Shock Tube. Report M720-4. Engineering Research Institute, University of Michigan, 1953 (see also J. Appl. Phys., Vol. 27 (1956), pp. 254-261).
28. Mirels, H. Laminar Boundary Layer Behind Shock Advancing into Stationary Fluid. NACA TN 3401, 1955.
29. Bromberg, R. "Use of the Shock Tube Wall Boundary Layer in Heat Transfer Studies," Jet Propulsion, Vol. 26, No. 9 (1956), pp. 737-740.
30. Rott, N. and Hartunian, R. On the Heat Transfer to the Walls of a Shock Tube. OSR-TN-55-422. Graduate School of Engineering, Cornell University, 1955.
31. Mirels, H. Boundary Layer Behind Shock or Thin Expansion Wave Moving into Stationary Fluid. NACA TN 3712, 1956.
32. American Institute of Physics Handbook. New York: McGraw-Hill Book Co., Inc., 1957.
33. Stever, H. G., Witmer, E. A., and Herrmann, W. "The Growth of a Boundary Layer Behind a Shock Wave." Funfzig (50) Jahre Grenzschichtforschung. Eine Festschrift in Originalbeitragen. Herausgegeben von H. Gortler und W. Tollmien. Braunschweig: Fried. Vieweg und Sohn, 1955.
34. Martin, W. A. An Experimental Study of the Boundary Layer Behind a Moving Plane Shock Wave. UTIA Report 47. Institute of Aerophysics, University of Toronto, November 1957.
- 34a. Gooderum, P. B. An Experimental Study of the Turbulent Boundary Layer on a Shock Tube Wall. NACA TN 4243, 1958.
35. Chabai, A. and Emrich, R. J. Private Communication.
36. Boyer, A. G. An Experimental Study of Transition of the Boundary Layer Behind a Moving Plane Shock Wave. UTIA TN. Institute of Aerophysics, University of Toronto (to be issued).

37. Hertzberg, A., et al. Modifications of the Shock Tube for the Generation of Hypersonic Flow. AD-789-A-2 (also AEDC-TN-55-15). Buffalo, N. Y.: Cornell Aeronautical Laboratory, Inc., 1955, and private communications.
38. Waldron, H. F. An Experimental Investigation of the Flow Properties Behind Strong Shock Waves in Nitrogen. UTIA Report 50. Institute of Aerophysics, University of Toronto, March 1958.
39. Emrich, R. J. and Wheeler, D. B., Jr. "Wall Effects in Shock Tube Flow," Phys. of Fluids, Vol. 1, No. 1 (January-February 1958), p. 14.
40. Rose, P. H. and Nelson, W. On the Effect of Attenuation on Gas Dynamic Measurements Made in Shock Tubes. AVCO Research Report No. 24. Everett, Mass.: AVCO Research Laboratory, AVCO Manufacturing Corp., 1958.
41. Model, I., Sh. "Measurement of High Temperature in Strong Shock Waves in Gases," Soviet Physics J. Experimental and Theoretical Phys., Vol. 5, No. 4 (November 1957), p. 589.
42. Clouston, J. G., Gaydon, A. G., and Glass, I. I. "Temperature Measurements of Shock Waves by the Spectrum-Line Reversal Method," Proc. Roy. Soc. London, Vol. 248 (1958), p. 249.
43. Parkinson, W. H. and Nicholls, R. W. Shock Tube Spectroscopy: I Shock Excitation of Powdered Solids; II Spectroscopic Temperature and Intensity Measurements. Science Report, Nos. 1 and 3. University of Western Ontario, 1959.

4. Production of Strong Shock Waves4.1 Limitations of the Simple Shock Tube

The designation "simple shock tube" here refers to a single diaphragm shock tube of constant cross-section area operated with a cold driver gas, i.e., operated with both driver and driven gases at room temperature when the diaphragm is ruptured. The limitations of the simple shock tube for production of strong shocks have been indicated in Subsec. 2.3.2 and will be briefly reviewed here.

The equation relating diaphragm pressure ratio $P_{41} = p_4/p_1$ to resulting shock Mach number M_s for the simple shock tube is (from Subsec. 2.3)

$$P_{41} = \frac{(\gamma_1 - 1)}{(\gamma_1 + 1)} \left[\frac{2\gamma_1}{(\gamma_1 - 1)} M_s^2 - 1 \right] \left[1 - \frac{(\gamma_4 - 1)(M_s^2 - 1)}{(\gamma_1 + 1) A_{41} M_s} \right]^{-\frac{2\gamma_4}{(\gamma_4 - 1)}} \quad (1)$$

where $A_{41} = a_4/a_1$ is the ratio of driver-to-driven gas sound speeds. The assumptions entering Eq. (1) are:

1. Perfect gases, constant specific heats
2. Perfect diaphragm burst
3. One-dimensional flow without viscosity or heat transfer

With weak and moderate strength shocks, discrepancy between experiment and Eq. (1) is due chiefly to violation of assumptions 2 and 3 (see Subsec. 3). With strong shocks and large values of P_{41} , however, assumption 1 will also be violated (see Subsec. 2.3.3). With cold hydrogen driving air at large P_{41} , significant variations in specific heat will occur in both the shock-heated air and the expansion-cooled hydrogen. Air dissociation and eventually ionization will occur behind sufficiently strong shocks. Thus, for strong shocks Eq. (1) can be taken only as a useful general guide to tube performance.

As indicated in Subsec. 2.3.2, the two important parameters governing shock strength are the diaphragm pressure ratio P_{41} and the diaphragm sound speed ratio A_{41} . Shock Mach number M_s increases monotonically with both. With the simple shock tube (cold driver) A_{41} is fixed by the gas combination used, and P_{41} is thus the only variable. The limiting value of $M_s = M_s^*$ attained asymptotically as $P_{41} \rightarrow \infty$, A_{41} finite, is from Eq. (1) above:

$$\lim_{P_{41} \rightarrow \infty} M_s = M_s^* = \frac{\gamma_1 + 1}{2(\gamma_4 - 1)} A_{41} + \sqrt{\left[\frac{(\gamma_1 + 1)}{2(\gamma_4 - 1)} A_{41} \right]^2 + 1}$$

or

$$M_S^* \approx \frac{\gamma_1 + 1}{\gamma_4 - 1} A_{41} \quad \text{for } A_{41} > 1$$

which indicates a need for large A_{41} and low γ_4 to obtain strong shocks. Little effect can be achieved in practice through the specific heat ratios γ_1 and γ_4 . For perfect gases, A_{41} is given by

$$A_{41} = \sqrt{\frac{\gamma_4 m_1 T_4}{\gamma_1 m_4 T_1}}$$

where m_4 and m_1 are the molecular weights, and T_4 and T_1 the initial absolute temperatures of the driver and driven gases, respectively. Thus with the simple shock tube, where $T_4 = T_1$, large values of A_{41} can be achieved by maximizing m_1/m_4 . That is, generation of strong shocks in the simple shock tube requires a light driver gas and a heavy driven gas. Thus hydrogen is the most efficient cold driver gas from this point of view, with helium the next best. Table 4.1-1 shows M_S^* for a number of gas combinations. The combination H_2/N_2 is to be preferred to H_2/Air as hydrogen-oxygen combustion at the contact surface can occur with the latter.

While hydrogen is superior to helium in the above sense, experimental results for strong shock waves show that shock wave attenuation with hydrogen drive is much greater than with helium drive. The attenuation of strong shocks for various driving methods is discussed in Subsec. 4.4.

Figure 4.1-1 shows M_S as a function of P_{41} calculated from Eq. (1) for the gas combinations He/ N_2 , He/Air, He/A, H_2/N_2 , H_2/Air , and H_2/A at cold operation, $T_4 = T_1$. Figures 4.1-2 to 4.1-7 show M_S as a function of P_{41} from Eq. (1) for various values of γ_4 and γ_1 , with A_{41} as independent parameter varying from 1 to ∞ . The latter curves are generally useful for considering modified versions of the simple shock tube (Subsec. 4.2) and will be referred to again. It might be noted here that the limiting case $A_{41} \rightarrow \infty$, P_{41} finite, is approximately attained in practice with so-called "constant-pressure" combustion of the driver gas (Subsec. 4.2.1) and gives shock pressure ratio $P_{21} = P_{41}$. Also, it is evident from Figs. 4.1-2 to 4.1-7 that a low value of γ_4 , as well as a high value of A_{41} , is desirable to attain maximum M_S for given values of P_{41} and γ_1 .

As previously noted, Eq. (1) assumes perfect gases and ideal flow. Figures 4.1-1 to 4.1-7 therefore serve as a general guide only. If desired, the effects of variable specific heat, dissociation, or ionization can be taken into account by iterative solution of the appropriate equations for the rarefaction and shock waves (Subsecs. 2.1.5

and 2.2.2) matching pressure and velocity across the contact surface as discussed in Subsec. 2.3.3. As a first approximation, imperfect gas effects can be neglected across the rarefaction wave and considered only across the shock. For this purpose the simple shock tube equation may be written as

$$P_{41} = P_{21} \left[1 - \frac{(\gamma_4 - 1) U_{21}}{2A_{41}} \right]^{-\frac{2\gamma_4}{\gamma_4 - 1}} \quad (2)$$

and real gas relations for the shock (see Subsec. 2.2.2 and Supplement D) used to obtain P_{21} and U_{21} for a given M_s and p_1 . A useful discussion of the effects of gas imperfections on shock-tube performance is given in Ref. 29.

Comparisons of Eq. (1) above with experime. for cold hydrogen driving argon, and cold helium and hydrogen driving air are shown in Figs. 4.1-8 and 4.1-9, respectively. In Fig. 4.1-9 the experimental shock Mach numbers are the maximum values attained in the low-pressure channel (see Fig. 4.4-1, Subsec. 4.4 for the corresponding shock formation and attenuation results). It will be noted that with both helium and hydrogen drives (Fig. 4.1-9), particularly with the former, the maximum experimental shock strengths exceed those calculated assuming equilibrium air.

As noted in Ref. 2, shock strength may be varied at constant diaphragm pressure ratio P_{41} by varying the molecular weight m_4 of the cold driver gas. Constant P_{41} can be convenient in practice in order to obtain consistent diaphragm rupture. Hydrogen, for example, can be diluted with nitrogen for this purpose. Assuming perfect gases, then for the H_2 - N_2 mixture

$$\gamma_4 = 7/5 \quad (\text{unchanged})$$

$$m_4 = 2.016(p_{H_2}/p_4) + 28.02(p_{N_2}/p_4)$$

$$p_4 = p_{H_2} + p_{N_2}$$

where p_{H_2} and p_{N_2} refer to the partial pressures of hydrogen and nitrogen, respectively. The value of M_s given by Eq. (1) for any value of m_4/m_1 and P_{41} may be estimated from Figs. 4.1-4 and 4.1-5 with the corresponding value of A_{41} .

As a generator of strong shocks, the simple shock tube driven by cold hydrogen rapidly becomes less attractive as the shock Mach number increases beyond 6 or 7 because of the asymptotic approach of M_s to M_s^* with increasing P_{41} . For example, with H_2/N_2 the multiplication of

P_{41} required to give unit increase in M_s is about a factor of 2 at $M_s = 6$, increasing to about 2.5 at $M_s = 13$. The required values of P_{41} at $M_s = 7, 10, \text{ and } 13$ are of orders of magnitude $10^3, 10^4, \text{ and } 10^5$, respectively. Thus, if extremely low densities in the low-pressure channel are to be avoided for M_s beyond 10, the required driver-gas pressure p_4 rapidly becomes undesirably large from the viewpoint of compression chamber strength requirements and complexity of the high-pressure supply. Modifications to the simple shock tube which provide significant increase in M_s beyond 10 without impractically high driver pressures are described in Subsec. 4.2, which follows. Alternative methods to the conventional diaphragm shock tube for generating strong shocks are mentioned in Subsec. 4.3.

4.2 Modifications to the Simple Shock Tube

There are two principal modifications commonly made to the simple shock tube which provide increased shock strength for a given diaphragm pressure ratio. These modifications are heating of the driver gas to increase sound speed ratio A_{41} (Subsec. 4.2.1), and variation of the tube cross-section area (Subsec. 4.2.2). Various combined modifications are considered in Subsec. 4.2.3.

4.2.1 Heating of Driver Gas in Constant-Area Tube

The increase in shock Mach number M_s to be expected for increased sound speed ratio A_{41} at a given diaphragm pressure ratio P_{41} is evident in Figs. 4.1-2 to 4.1-7. With heating of the driver gas, the value of A_{41} obtained will be proportional to $\sqrt{T_{41}}$ for a perfect driver gas, but only approximately so if T_4 is sufficiently high to produce real gas effects as dissociation.

The methods for heating the driver gas which follow are electrical heating, the multiple-diaphragm technique, and combustion heating.

4.2.1.1 Electrical Heating

Possible methods of increasing T_4 by electrical means include the use of direct heating elements placed inside the driver section and short-duration electrical discharge giving rapid ohmic heating of the driver gas. Direct heating elements appear impractical for attaining values of the ratio T_{41} of the order of 3 or more (with $T_1 = 300^\circ\text{K}$). However, this method has been used for limited heating of the driver gas in the tailored-interface hypersonic shock tunnel (Subsec. 5.1.2.3). Pulsed electrical discharge heating was suggested as a possibility by the work of Fowler and associates (Refs. 4, 5, and 6). However, the method has not been developed to a practical degree for other than small tubes.

Fowler and associates studied pulsed discharges through various gases contained in tee and straight pyrex tubes as shown with typical dimensions in Fig. 4.2-1. The discharge was obtained using capacitors with initial stored energies up to about 180 joules. Critical damping of the discharge with small external resistance resulted in the discharge current rising to a peak value (typically 5,000 to 10,000 amp) within 2 to 4 microsecs and then decaying to the order of 1/10 peak in about 15 microsecs (Ref. 6). Various gases including hydrogen, nitrogen, neon, argon, helium, and xenon were used in the discharge tube at initial pressures ranging from 0.2 to 155 mm Hg and initially at room temperature.

Initial studies (Ref. 4) at low densities reported the propagation of a "luminous front" down the side tube of the tee following discharge. Later work (Refs. 5 and 6) with tee and straight tubes confirmed that these fronts were shock waves. Apparent shock Mach numbers obtained ranged from 5 to 30.

As a shock-wave generator, the straight discharge tube of Fig. 4.2-1 may be roughly analysed as a constant-area shock tube having driver section A-B and driven section B-C initially filled with the same gas at the same initial pressures $P_{4i} = p_1$ and temperatures $T_{4i} = T_1$ throughout. At discharge, the driver gas in A-B is assumed to take up a fraction η of the capacitor energy and to be brought instantly to a final equilibrium state (4) (temperature T_4 , sound speed a_4 , pressure p_4 , and isentropic index γ_4^*) by ohmic heating at constant volume. Subsequent generation of a shock wave in the driven gas can then be considered to occur as in the simple shock tube with parameters $A_{41} = a_4/a_1$, $P_{41} = p_4/p_1$, and isentropic index γ_4^* . In Fowler's studies, final temperatures T_4 of the order of 5000 to 25,000°K were obtained. For such temperatures, real gas effects as dissociation and ionization must be considered in calculating the final equilibrium state of the driver gas. Final pressures p_4 obtained were relatively low, however, as the same low initial pressure was used throughout the discharge tube. For shock tube purposes, different driver and driven gases separated by a diaphragm with an initial pressure difference might be advantageous for production of strong shocks.

One obvious difficulty in this very simplified picture of electrical discharge drive is ignorance of the factor η giving the fraction of capacitor energy E_c taken up by the driver gas. Equilibrium calculations of η from Atkinson's results (Ref. 7) for measured shock speeds and capacitor energies indicate values ranging from the order of 2 to 20 per cent. In addition to depending on the gas, η increases with increasing pressure (density).

As a matter of interest, Fig. 4.2-2 is included showing the results of equilibrium calculations as indicated above for a helium/argon combination assuming a constant area tube, $p_1 = 0.1$ psi, $T_{4i} = T_1 = 300^\circ\text{K}$, and $P_{4i} =$ initial driver gas pressure = 10, 1, and 0.1 psi. Shock Mach number M_s is plotted versus energy transferred to unit volume of driver gas, $(\eta E_c)/V$. The final equilibrium state of the driver gas after discharge (T_4 , p_4 , a_4 , γ_4^*) was calculated assuming adiabatic constant-volume

heating from addition of energy ηE_c per unit volume of driver gas taking account of single helium ionization only with no electronic excitation. Because of neglect of electronic excitation and second ionization, the results are qualitative only at the lower pressures (particularly 0.1 psi) and higher energies. The resulting shock Mach number M_s was obtained from Eq. (1), Subsec. 4.1, for the corresponding P_{41} , A_{41} , γ_4^* values and thus assumes ideal one-dimensional flow (no heat transfer or viscosity) with perfect gas behaviour. The relevant equations for determining the final equilibrium state of the driver gas after capacitor discharge are as follows:

Notation: v volume of driver section
 R universal gas constant/initial molecular weight of driver gas = R/m_{41}
 l_1 ionization energy/unit mass of driver gas
 x degree of ionization of driver gas
 E_c capacitor energy
 η fraction of E_c transferred to driver gas
 e internal energy/unit mass

Subscripts: 4 final equilibrium driver gas values after discharge
 4i initial driver gas values
 1 initial channel gas values

$$e_4 = \frac{3}{2} (1 + x) RT_4 + l_1 x \quad (1)$$

Also,

$$e_4 = C_{v4i} T_{4i} + \frac{\eta E_c}{v \rho_{4i}} \quad (2)$$

From (1) and (2), taking $T_{4i} = T_1$

$$T_{4i} = \frac{1 + \frac{2 \eta E_c}{3 v \rho_{4i}} - \frac{2 l_1 x}{3 RT_1}}{1 + x} \quad (3)$$

For helium, $l_1/R = 2.841 \times 10^5 \text{ }^\circ\text{K}$ (Ref. 9).

The assumed equation of state for the driver gas is

$$p/\rho = (1 + x) RT \quad (4)$$

For constant volume, $\rho_4 = \rho_{4i}$ and from (4)

$$p_4/p_{4i} = (1 + x) T_{4i} \quad (5)$$

To solve for p_4 , T_4 , x , a third equation is required. This is taken as the Saha equation (see Supplement B):

$$x = \left[A \frac{p}{T^{5/2}} e^{\frac{B}{T}} + 1 \right]^{-\frac{1}{2}} \quad (6)$$

assuming single equilibrium ionization and neglecting electronic excitation (valid for small x). For helium, the constants A and B are (Ref. 8, pp. 79 and 80) $A = 52,300$ and $B = 284,100$ for p in psi and T in °K. In the present case $p_4 = (1 + x) R \rho_{4i} T_4$ and Eq. (6) can be put in the form

$$x = \frac{D}{2} \left[\sqrt{1 + \frac{4}{D}} - 1 \right] \quad (7)$$

where

$$D = \frac{T_1 T_4^{3/2}}{A p_{4i} e^{B/T_4}} \quad (8)$$

Equations (3), (5), (7), and (8) enable T_4 , p_4 , and x to be determined by iteration for assumed values of E_c , v , p_{4i} , and $T_{4i} = T_1$. The final driver sound speed a_4 and isentropic index γ_4 are given by (see, for example, a general treatment in Ref. 9, pp. 315 to 320; also Supplement B)

$$a_4^2 = \gamma_4^* \frac{p_4}{\rho_4}$$

$$\gamma_4^* = \left(\frac{C_{p4}}{C_{v4}} \right) \frac{2}{2 + x - x^2}$$

where

$$C_{p4} = \frac{5}{2} (1 + x) R + \left(\frac{5}{2} + \frac{1_i}{RT_4} \right)^2 \frac{x(1 - x^2)}{2} R$$

and

$$C_{v4} = \frac{3}{2} (1 + x) R + \left(\frac{3}{2} + \frac{1_i}{RT_4} \right)^2 \frac{x(1 - x)}{2 - x} R$$

are the specific heat capacities (per unit mass) of the driver gas in the final equilibrium state. Knowing p_4 , a_4 , and γ_4^* , the ratios P_{41} , A_{41} , and γ_4^* may be substituted into Eq. (1) of Subsec. 4.1 to obtain M_s .

The use of Eq. (1), Subsec. 4.1, for determining M_s will give only approximate results because of the simplifying assumptions involved. Real gas behaviour, which is neglected in Eq. (1), may be included by iterative solution of the flow equations as discussed in Subsec. 4.1.

The curves of Fig. 4.2-2 suggest that the straight electric discharge drive would involve very large energies to generate strong shocks in equipment of a size suitable for model testing purposes. For example, to generate a shock of $M_s = 20$ with a driver-section volume of 100 cu in. (a driver about 3 ft long with 2-in. diameter) would apparently require of the order of 5×10^4 joules for an initial helium driver pressure $p_{4i} = 10$ psi assuming an efficiency of 10 per cent, 10^5 joules for $p_{4i} = 1$ psi assuming an efficiency of 5 per cent, and at least 2×10^5 joules for $p_{4i} = 0.1$ psi assuming an efficiency of 1 per cent. In Subsec. 4.3 some recent extensions of the discharge method are described which utilize magnetic body forces on the driver gas in addition to ohmic heating. In small-scale equipment this additional magnetic drive has resulted in shock Mach numbers up to the order of 300.

4.2.1.2 Multiple-Diaphragm Technique

Several authors (Refs. 2, 10, 11, 12, 13, and 20) have considered the possibility of using two or more diaphragms in the constant-area shock tube as a means of heating the driver gas. The basic arrangement is illustrated in Fig. 4.2-3 for the so-called "unsteady-expansion" method (Refs. 10 and 12) using two diaphragms. Two high-pressure chambers, 1 and 2, in series constitute the driver section with an initial pressure difference across each diaphragm, i.e., P_{86} and P_{61} are > 1 . In operation, diaphragm D_1 is burst by external means whereupon resulting shock \bar{S}_6 moves into quiet gas (state 6) which is thus accelerated, heated, and compressed to uniform state (4). Diaphragm D_2 is assumed to be of such strength as to burst immediately on impact of shock \bar{S}_6 . The initial resulting channel flow with shock \bar{S}_1 then resembles that of the conventional shock tube except that driver state (4) is at increased temperature $T_4 > T_1$ and has uniform velocity $u_4 > 0$. The initial resulting Mach number M_{s1} of shock \bar{S}_1 is greater than that obtained for single diaphragm operation at over-all pressure ratio P_{81} and over-all temperature ratio $T_{81} = 1$.

A second possibility, termed the reflected-shock method (Refs. 11 and 12), is illustrated in Fig. 4.2-4. The arrangement is similar to that in Fig. 4.2-3 except that the second diaphragm D_2 is

strong enough to withstand impact of shock \bar{S}_6 and is assumed to be burst by external means at controlled time t_D after impact. Thus the driver gas (state 4) in this second method is further heated by the reflection of shock \bar{S}_6 , but is also brought to rest, i.e., $u_4 = 0$. Again, the initial strength of shock \bar{S}_1 is greater than that for single diaphragm operation at over-all ratios P_{81} and $T_{81} = 1$.

It is clear that the wave diagrams of Figs. 4.2-3 and 4.2-4 depict only the initial flow in such tubes and that complicated wave interactions not present in a single diaphragm tube would begin after a time depending on the gases used, the initial pressures, the intermediate compression chamber length l_2 , and the time delay t_D for second diaphragm rupture. An important product of such interactions will be reflected waves which travel in the same direction as, and which eventually overtake, shock \bar{S}_1 . The reflected waves will limit the duration of uniformity of \bar{S}_1 and of the flow in regions (2) and (3). In practice, the first interaction in this respect will involve the first contact surface \bar{C}_1 with the reflected shock \bar{S}'_6 for long time delay t_D , or the overtaking of \bar{S}'_6 by \bar{R}_2 for short time delay t_D (Fig. 4.2-4). For $t_D = 0$ (Fig. 4.2-3), the first interaction will involve \bar{R}_2 and \bar{C}_1 . These wave interactions can be calculated for any specific case by the methods of Subsec. 2.4. Bird (Ref. 13) has computed several typical examples. His results show that such interactions can significantly limit the duration of uniform initial shock Mach number M_{s1} and that the gain in M_{s1} due to the double-diaphragm method is eventually cancelled out by the overtaking reflected waves. The duration of uniform flow behind the shock \bar{S}_1 is seriously reduced and in extreme cases may almost vanish. Careful consideration of intermediate chamber length l_2 and test location would be necessary to avoid such limitations.

The initial flow quantities of Figs. 4.2-3 and 4.2-4, such as M_{s1} , may be calculated with the methods of Subsec. 2. Henshall (Ref. 12) gives general formulae for any gas combination assuming perfect gases and ideal one-dimensional flow. Figure 4.2-5 shows M_{s1} versus P_{61} for a double-diaphragm tube having the same gas throughout with $\gamma = 1.4$. The optimum P_{61} giving maximum M_{s1} is very nearly $(P_{81})^{1/2}$. The results for the unsteady-expansion and reflected-shock methods are very nearly the same. Figure 4.2-6 shows similar results calculated by Yoler (Ref. 11) for He/Air/Air and He/He/Air combinations.

Henshall (Ref. 12) extends the reflected-shock method to include any number of diaphragms n , each having the pressure ratio $(P_o)^{1/n}$, where P_o is the over-all pressure ratio. Theoretical curves of final shock Mach number M_s versus n for the same gas throughout with $\gamma = 1.4$ are shown in Fig. 4.2-7.

It is evident from Figs. 4.2-5 and 4.2-6 that, for the optimum value of P_{61} and at the higher over-all pressure ratios, the double-diaphragm technique theoretically offers significant percentage increase in initial shock Mach number (before attenuation by reflected waves) over that obtained with a single-diaphragm tube having the same over-all pressure ratio. The extension of the method to higher shock strengths by means of a tube cross-section area change at the second diaphragm (Ref. 20) is described in Subsec. 4.2.3. Some recent experimental results which substantiate the advantages of this technique are given in Ref. 20a.

4.2.1.3 Combustion Heating

Combustion of a light gaseous mixture in the driver chamber with spontaneous diaphragm rupture from the resulting increase in pressure has been found a practical method of raising the driver gas temperature to attain a sound speed significantly greater than that of cold hydrogen (Refs. 2, 3, 14, 15, 27, 30, and 31). Oxygen-hydrogen mixtures with either excess hydrogen or helium diluent have been used to meet the requirements of light products of combustion, high heat of reaction, availability, mild corrosion, and ease of handling. Unfortunately, the molecular weight of the combustion products is higher than pure hydrogen, and the temperature rise is limited by dissociation. Optimum oxygen-hydrogen mixtures provide an increase in sound speed of the order of 70 to 80 per cent over that for cold hydrogen assuming adiabatic constant-volume combustion. In the simple constant-area shock tube this increase in sound speed enables a shock Mach number in air of around 16 or 17 to be attained for a peak over-all pressure ratio (after combustion) of the order of 10^5 .

While providing a significant increase in driver gas sound speed, combustion heating is not without inherent difficulties. The resulting primary shock strength and attenuation, and the degree of flow nonuniformity behind the shock with combustion drive depend very much on the method of ignition and on the stage of the combustion process at which the diaphragm ruptures. Various combustion processes approximated in practice include constant-volume combustion, "constant-pressure" combustion, and detonation. Primary shock attenuation is observed to be greater with all these methods than with cold hydrogen drive (see Subsec. 4.4). Constant-volume combustion produces the lowest primary shock strength in general, but has the advantage over the other combustion processes of giving the least shock attenuation.

Adiabatic constant-volume heating is considered in detail below and is followed by brief mention of other combustion methods.

Adiabatic Constant-Volume Heating. -- Adiabatic constant-volume combustion is approximated in practice by igniting the (initial) low-pressure driver mixture at a number of points and using a metal diaphragm (Subsec. 6.2.2) designed to burst spontaneously at a pressure just less than the peak combustion pressure. In actuality, the heating will not be adiabatic since heat losses occur to the cold driver-section walls. Also, in most such arrangements some combustion does occur after diaphragm rupture with adverse effects on the resulting flow. Variations in diaphragm bursting strength must be minimized to attain consistent results from run to run. Reproducibility of primary shock strength in practice is typically in the range of 10 to 20 per cent.

If it is assumed that the driver mixture undergoes adiabatic constant-volume combustion to a final equilibrium state and this is followed by instantaneous diaphragm removal, the tube performance can be calculated. Equilibrium pressure p_4 , temperature T_4 , and mixture composition after combustion may be computed by the methods of Ref. 16. The corresponding isentropic index γ_4^* and sound speed a_4 may be obtained by the methods of Ref. 9. According to Ref. 3, good agreement is obtained between experimental sound speed a_4 and that calculated by considering water vapour dissociation only (neglecting oxygen and hydrogen dissociation). Knowing the equilibrium values of P_{41} , A_{41} , and γ_4 , the resulting shock Mach number M_S may be obtained as in Subsec. 4.1.

The use of Eq. (1), Subsec. 4.1, for determining M_S will give only approximate results because of the simplifying assumptions involved. Real gas behaviour, which is neglected in Eq. (1), may be included by iterative solution of the flow equations as discussed in Subsec. 4.1.

Figure 4.2-8 from Ref. 27 shows calculated equilibrium values of a_4 , γ_4 , and p_4 following adiabatic constant-volume combustion of stoichiometric oxygen-hydrogen plus helium, and oxygen-excess hydrogen mixtures. The calculations neglect all dissociation and thus show no dependence on initial pressure p_{41} . With excess hydrogen as diluent, the maximum value of a_4 , occurring for a 92 per cent hydrogen mixture, is about 1.67 times that for cold hydrogen. The corresponding A_{41} value with air as the driven gas is about 6.35. With helium diluent, the maximum sound speed a_4 is about 1.8 times that for cold hydrogen corresponding to an A_{41} value of about 6.85 with driven air. The maximum a_4 with helium occurs for a helium percentage of about 60. In practice, however, it has been found necessary to use somewhat leaner mixtures than 60 per cent in order to avoid unpredictable detonations which give rise to flow nonuniformities (Refs. 3, 14, 15, and 27). Satisfactory results have been reported for 80 per cent helium mixtures (Refs. 14, 15, and 27) and also through the range 70 to 80 per cent (Ref. 3), with the richest helium mixtures usable without detonation depending on such factors as driver-section geometry, gas mixing, and the number of ignition points.

Figure 4.2-9 from Ref. 27 gives theoretical results illustrating the relative efficiencies of various combustion mixtures for producing strong shock waves in air in a constant-area shock tube. The calculations assume adiabatic constant-volume combustion in the driver section followed by ideal shock-tube flow. Real gas effects are included across the shock wave. Regarding the relative merits of helium and hydrogen diluents for the production of strong shocks, it will be noted that the advantage of higher sound speed with helium is offset by the lower γ_4 obtainable with hydrogen. However, the 70 per cent helium mixture (curve C) is almost as efficient as the best hydrogen mixture (curve E) and is to be preferred from the viewpoint of safety.

Various ignition methods used include distributed spark plugs, distributed fusion plugs containing filament wires fused by electric discharge, and a single wire which is also fused by electric discharge stretched along the chamber axis. A number of distributed ignition points are desirable to promote uniform combustion and avoid detonation. Thorough mixing of the combustion mixture constituents is necessary to

achieve consistent results (see also Subsec. 6.1.2). The handling, mixing, and ignition of oxygen and hydrogen should be viewed as a potentially dangerous process (see also Subsec. 6.4).

Sporadic occurrence of detonation in the constant-volume combustion method is undesirable. Apart from flow nonuniformities introduced, the sudden pressure rise due to reflection of a normal detonation wave can be sufficient to remove parts or all of the metal diaphragm, rather than petal it without loss of weight, which can be very damaging to the tube and models. It appears that detonation can occur over a wide range of mixture compositions depending on such factors as chamber geometry and method of ignition. The possibility of pressure rise due to detonation occurring should be considered in determining combustion chamber strength requirements (see Subsec. 6.1.2). In addition to normal detonation, consideration should be given to the possibility of so-called over-detonation (see, for example, Ref. 28), a phase in the formation of normal detonation in which pressures can attain values three or four times those of normal detonation. For example, Ref. 28 reports measured reflected pressures with over-detonation of stoichiometric hydrogen-air mixtures in a 32-ft long, 3-1/4-in. square tube of the order of five times those for normal detonation.

Few measurements of actual pressure rise in the driver section due to constant-volume combustion have been reported. Reference 27 gives results indicating the maximum experimental pressure increase to be substantially less (of the order of 30 per cent) than theory predicts.

Figure 4.2-10 from Ref. 3 compares experimental and theoretical shock Mach numbers obtained in air by constant-volume combustion of stoichiometric oxygen-hydrogen plus helium mixtures containing 0.70 to 0.75 moles of helium per mole of mixture. The theoretical combustion drive curve is calculated for $A_{41} = 7.3$ and $\gamma_4 = 1.6$ using Eq. (2), Subsec. 4.1, and real gas relations across the shock. The experimental results are from two tubes: a constant-area tube of 1-1/2-in. diameter, and a stepped tube of 6-in. diameter driver and 4-in. diameter driven sections. The results for the stepped tube are converted to equivalent results for a constant-area tube as outlined in Subsec. 4.2.2. It should be noted that the experimental results apply about 20 tube diameters from the diaphragm station. The constant-volume combustion drive is seen to give substantial improvement over cold hydrogen as regards primary shock strength. As discussed in Subsec. 4.4, however, it has the disadvantage of producing greater shock attenuation than hydrogen.

Other Combustion Processes.--Two combustion processes other than constant-volume combustion that have been used for driver gas heating are the so-called "constant-pressure" method (Refs. 14 and 27) and the detonation wave (Refs. 30, 33, and 34). Generally speaking, both methods produce stronger shock waves than constant-volume heating, but they have the disadvantage of considerably increased shock attenuation.

The "constant-pressure" method involves a weak diaphragm intended to rupture immediately after ignition. In this case the driver gas mixture undergoes expansion as combustion proceeds. While producing stronger shock waves than attainable with constant-volume combustion, constant-pressure heating has not proved too useful because of large shock attenuation, large decay of pressure behind the shock, and difficulties in obtaining consistent diaphragm rupture (Ref. 27). The overtaking wave phenomena discussed below for detonation or combustion wave heating are likely a contributing factor in this method, also.

Heating by means of combustion or detonation waves is considered theoretically in Ref. 34. For given initial conditions, examples are calculated for diaphragm rupture by combustion and detonation waves initiated from either end of the driver section. The results are compared to those for ideal constant-volume combustion. From these examples it is evident that the location of the point of ignition, i.e., whether at the diaphragm or at the tube end, and the time of diaphragm rupture greatly influence the resulting flow. For a detonation wave initiated at the tube end which ruptures the diaphragm on impact, the rarefaction wave accompanying the detonation immediately overtakes the primary shock. While the primary shock may initially be of the order of 50 per cent stronger than with constant-volume heating, the attached rarefaction attenuates it continuously and produces a pressure decay in the flow behind. For a detonation wave initiated at the diaphragm, and with immediate diaphragm rupture, the primary shock is initially somewhat weaker than with constant-volume heating but has constant strength until overtaken by the detonation reflected from the tube (driver) end. On being overtaken, the primary shock is first reinforced and then continuously attenuated by the rarefaction wave accompanying the detonation.

Experimental results for detonation wave heating (Refs. 30 and 33) qualitatively substantiate the examples calculated in Ref. 34. The shock attenuation is very large with ignition at the tube end (see Subsec. 4.4), and a large decay of pressure with time is noted following passage of the shock.

4.2.2 Cross-Section Area Change

4.2.2.1 Monotonic Convergence at Diaphragm

The use of a monotonic area reduction from driver to driven sections as shown in Fig. 4.2-11 provides a stronger shock for given diaphragm pressure and sound speed ratios than is obtainable in a constant-area tube. Such a convergent shock tube has been considered by Lukasiewicz (Ref. 17) and others (Refs. 2, 12, 18, and 32). Area reduction is sometimes combined with the combustion heating method of Subsec. 4.2.1.3 to minimize the over-all pressure ratio required for strong shocks.

The improved performance with a monotonic convergence at the diaphragm results because of the greater efficiency at subsonic speeds of steady over unsteady expansion in conversion of thermal to kinetic energy (Ref. 2). At supersonic speeds the reverse is true. The area change in Fig. 4.2-11 is such as to derive an advantage from this fact in the two cases shown:

(a) Mach number $M_3 \leq 1$

(b) $M_3 \geq 1$

Case (a) results from a sufficiently low diaphragm pressure ratio P_{41} . A steady subsonic expansion occurs through the area ratio S_4/S_1 from uniform state (5) generated by the unsteady rarefaction wave R_1 to uniform subsonic state (3). As P_{41} is increased from values giving $M_3 < 1$, the pressure ratio P_{45} across R_1 and the Mach number M_5 increase to

values $P_{45 \text{ cr}}$ and $M_{5 \text{ cr}}$ which give sonic flow in state (3), i.e., $M_e = M_3 = 1$. For steady isentropic one-dimensional flow $P_{45 \text{ cr}}$ and $M_{5 \text{ cr}}$ depend only on the contraction ratio S_4/S_1 and γ_4 . With further increase of P_{41} beyond that giving $M_3 = M_e = 1$, the values of P_{45} , M_5 , and M_e remain fixed at $P_{45 \text{ cr}}$, $M_{5 \text{ cr}}$, and 1, respectively. Expansion from $M = M_e = 1$ at station e - e, area S_1 , to $M = M_3 > 1$ in state (3) occurs through the unsteady rarefaction wave \bar{R}_2 , Fig. 4.2-11 (b). The head of \bar{R}_2 remains at station e - e.

In accordance with what has been said, it can be shown (Ref. 32) that convergent-divergent geometry with the diaphragm at the throat, whereby the unsteady expansion \bar{R}_2 may be completely or partially replaced (depending on P_{41}) by a steady expansion, is less efficient for generating strong shocks than the monotonic-convergent geometry of Fig. 4.2-11 (b). However, the convergent-divergent geometry with steady expansion throughout is advantageous with the tailored-interface hypersonic shock tunnel as it provides a longer test flow duration (see Subsec. 5.1.2.3).

Assuming the idealized wave systems of Fig. 4.2-11 to develop shortly after diaphragm rupture, the convergent-tube performance may be computed by applying usual steady- and unsteady-flow relations to match pressure and velocity of states (2) and (3). For one-dimensional inviscid flow throughout and a perfect driver gas, the relevant equations for performance are (see, for example, Refs. 18 or 32)

$$g P_{41} = P_{21} \left[1 - \frac{(\gamma_4 - 1) U_{21}}{2 A_{41}} (g) \right]^{-\frac{\gamma_4 - 1}{2\gamma_4}} \frac{2\gamma_4}{\gamma_4 - 1} \quad (1)$$

$$g = \left[\frac{2 + (\gamma_4 - 1) M_5^2}{2 + (\gamma_4 - 1) M_e^2} \right]^{\frac{\gamma_4}{\gamma_4 - 1}} \left[\frac{2 + (\gamma_4 - 1) M_e^2}{2 + (\gamma_4 - 1) M_5^2} \right]^{\frac{2\gamma_4}{\gamma_4 - 1}} \quad (2)$$

$$\frac{S_4}{S_1} = \frac{M_e}{M_5} \left[\frac{2 + (\gamma_4 - 1) M_5^2}{2 + (\gamma_4 - 1) M_e^2} \right]^{\frac{\gamma_4 + 1}{2(\gamma_4 - 1)}} \quad (3)$$

$$M_3 = \frac{U_{21}}{A_{41} (g) \frac{\gamma_4 - 1}{2\gamma_4} - \frac{\gamma_4 - 1}{2} U_{21}} \quad (4)$$

The parameter g , introduced in Ref. 2, is useful for analyzing the convergent tube in terms of an equivalent constant-area tube. A comparison of Eq. (1) above with Eq. (2) of Subsec. 4.1 shows that on the basis of the ideal theory a monotonic convergent tube with diaphragm pressure ratio P_{41} and sound speed ratio A_{41} will generate a shock of strength equal to that obtained in a constant-area tube with pressure ratio gP_{41} , sound speed ratio

$$A_{41} (g) = \frac{\gamma_4 - 1}{2\gamma_4}$$

equal γ_4 , and equal γ_1 . Thus, if the factor g is obtained, the performance of a convergent tube can be calculated using the constant-area tube results of Subsec. 4.1. For the subsonic case, $M_3 < 1$, then $M_3 = M_e$ and Eqs. (1) to (4) may be solved for P_{41} with assumed values of A_{41} , γ_4 , P_{21} , U_{21} , and S_4/S_1 . Curves of g as a function of γ_4 , S_4/S_1 , and U_{21}/A_{41} given in Ref. 32 facilitate calculation for $M_3 < 1$. For the supersonic case with $M_3 > 1$, which is of interest for strong shocks, then $M_e = 1$ and g depends only on γ_4 and S_4/S_1 , and may be computed from Eqs. (2) and (3). Curves of g versus γ_4 for $M_3 \geq 1$ and various contraction ratios S_4/S_1 are given in Fig. 4.2-12.

An alternative method of obtaining convergent-tube performance than directly in terms of the equivalent constant-area tube is to use Fig. 4.2-13 (from Ref. 18) containing plots of Eq. (1) above written in the form

$$Y = \left[1 - \frac{\gamma_4 - 1}{2} X \right]^{-\frac{2\gamma_4}{\gamma_4 - 1}} \quad (5)$$

with

$$Y = gP_{41}/P_{21}$$

plotted versus

$$X = \frac{U_{21}}{A_{41}} (g) = \frac{\gamma_4 - 1}{2\gamma_4}$$

for various values of γ_4 . As an example, the diaphragm pressure ratio P_{41} (peak ratio for combustion driver) required to obtain a given strong shock Mach number M_3 with given driven gas, S_4/S_1 , A_{41} , and γ_4 is obtained as follows. The shock parameters U_{21} and P_{21} are obtained from M_3 (Subsec. 2.2) with real gas effects across the shock included if necessary. Assuming $M_3 \geq 1$, g is obtained from Fig. 4.2-12. Then X

is determined, and the corresponding value of Y from Fig. 4.2-13 gives P_{41} . The same method may be used for the constant-area tube by taking $g = 1$.

The advantage of the monotonic-convergent tube over the constant-area tube in operating at lower diaphragm pressure ratios for a given shock strength is illustrated in Fig. 4.2-14. Shown are plots of the ratio of P_{41} for constant area ($P_{41 \text{ c-A}}$) to P_{41} for convergence ($P_{41 \text{ con}}$) against shock Mach number M_s (same M_s in both tubes) for cold hydrogen driving nitrogen at various contraction ratios S_4/S_1 . The gain in pressure ratio of the convergent tube is significant. It may be noted that a contraction ratio S_4/S_1 of about 2.5 achieves approximately one-half of the maximum possible gain for $S_4/S_1 = \infty$. In general, for the same M_s , a_4 , a_1 , γ_4 , γ_1 values in both tubes (Ref. 18),

$$\frac{P_{41 \text{ c-A}}}{P_{41 \text{ con}}} = g \left[\frac{1 - \frac{(\gamma_4 - 1) U_{21}}{2A_{41}}}{1 - \frac{(\gamma_4 - 1) U_{21}}{2A_{41}} (g)^{-\frac{\gamma_4 - 1}{2\gamma_4}}} \right] \quad (6)$$

Reference 32 reports the results of experimental tests to check the foregoing theory. The tests were done for contraction ratios S_4/S_1 of 1.00 and 1.51 using a 3-1/4-in. square section containing air, nitrogen, or argon and driven by helium or hydrogen. Up to shock Mach numbers of about 6 ($P_{41} \sim 1000$), the increase in maximum experimental shock strength (attained some distance from the diaphragm) due to monotonic convergence at the diaphragm is in very good agreement with theory. Above diaphragm pressure ratios of about 1000, the theory becomes increasingly inadequate in describing tube performance, although the shock strength increment due to convergence is still predicted with fair accuracy.

4.2.2.2 Monotonic Convergence Along Tube

Impingement of the primary shock wave on a monotonic area reduction at some point along the driven section of the tube produces a transmitted shock wave \bar{S}_T stronger than the incident primary wave \bar{S}_1 (Refs. 2, 12, and 19). The idealized flow some time after impingement when quasi-steady conditions have been attained is illustrated in Fig. 4.2-15. With a given area ratio S_4/S_1 and sufficiently weak incident shock \bar{S}_1 , case (a) results with Mach number $M_3 = M_e < 1$. The resulting wave system contains reflected shock \bar{S}_R and contact surface \bar{C} in addition to transmitted shock \bar{S}_T . Steady subsonic expansion occurs from uniform state (4), area S_4 , to uniform state (3), area S_1 .

As the incident shock strength increases, M_4 increases until at some value of $M_4 = M_{4\text{ cr}}$ choking occurs at the constriction entrance, i.e., $M_e = 1$. For steady isentropic one-dimensional flow $M_{4\text{ cr}}$ depends only on S_4/S_1 and γ_4 . With further increase in incident shock strength, M_4 remains fixed at $M_{4\text{ cr}}$ and the wave system of case (b) Fig. 4.2-15 results. Steady subsonic expansion occurs from $M_4 = M_{4\text{ cr}}$ at area S_4 , to $M_e = 1$ at the constriction entrance, area S_1 . Further expansion to supersonic state (3) occurs through the unsteady rarefaction wave, \bar{R} , the head of which remains at the constriction entrance.

The wave systems of Figs. 4.2-15 (a) and (b) are similar to those of Fig. 4.2-11 and may be calculated in a similar manner (as in Ref. 19) by application of one-dimensional inviscid flow relations matching pressure and velocity in regions (2) and (3). The calculated results of Ref. 19 for a monatomic gas ($\gamma_1 = 5/3$) show the pressure ratio P_{21} of the transmitted shock \bar{S}_T to increase almost linearly with increasing pressure ratio P_{51} of the incident shock \bar{S}_1 at a given contraction ratio S_4/S_1 . The ratio P_{21}/P_{51} varies from 1.19 at $P_{51} = 3$ to 1.25 at $P_{51} = 50$ for $S_4/S_1 = 2$, from 1.42 at $P_{51} = 6$ to 1.48 at $P_{51} = 50$ for $S_4/S_1 = 5$, and from 1.60 at $P_{51} = 6$ to 1.69 at $P_{51} = 50$ for $S_4/S_1 = \infty$.

4.2.3 Combined Modifications and Comparisons of Theoretical Performance

The modifications to the simple shock tube previously described, i.e., driver-gas heating and area change, may be combined to various degrees to improve strong-shock performance. Several authors (Refs. 2, 11, 12, and 20) have considered a combination of the double-diaphragm technique with monotonic area reduction at the second diaphragm. Figure 4.2-16 illustrates the initial flow with such an arrangement assuming the second diaphragm D_2 to burst immediately on impact of shock \bar{S}_6 and the flow at the entrance to the driven section, area S_1 , to be sonic. Because of the area reduction, immediate rupture of the second diaphragm D_2 in this case gives rise to a reflected shock \bar{S}'_6 . This reflected shock does not occur with the double-diaphragm unsteady-expansion method for a constant-area tube described in Subsec. 4.2.1.2 and Fig. 4.2-3.

Extensive calculated results are given by Russo and Hertzberg (Ref. 20) for the arrangement of Fig. 4.2-16 with the gas combination hydrogen/inert monatomic buffer gas/air, $T_8 = T_6 = T_1$, and large contraction ratio S_8/S_1 . The use of an inert monatomic buffer gas eliminates the problem of combustion at the hydrogen-air interface encountered with direct hydrogen drive and also minimizes real gas effects. The results show that for given over-all pressure ratio P_{81} and atomic weight of the monatomic buffer gas, an optimum value of pressure ratio P_{61} across the second diaphragm exists for which the Mach number M_{s1} of

shock \bar{S}_1 is a maximum (as for the double-diaphragm constant-area tube, Subsec. 4.2.1.2). Over a wide range of buffer-gas atomic weights, this maximum value of M_{S1} is approximately constant. Figure 4.2-17 shows the calculated performance with argon as the buffer gas. A heavy atomic weight buffer gas requires low pressure ratio P_{61} (to achieve maximum shock strength), and this permits a weak and light second diaphragm with advantages of reduced downstream tube damage and diaphragm opening time.

Reference 20 also considers a constant-volume combustion driver with the double-diaphragm convergent tube. The results for stoichiometric hydrogen-oxygen diluted with 80 per cent helium (molar percentage) driving argon as the buffer gas are included in Fig. 4.2-17 for peak over-all pressure ratios of 10^3 and 10^4 .

While the calculated results of Fig. 4.2-17 apply to infinite contraction ratio S_6/S_1 , as noted in Subsec. 4.2.2.1, about one-half of the maximum pressure ratio gain for $S_6/S_1 = \infty$ may be achieved with a contraction ratio as low as 2.5.

A comparison of theoretical performance for various modifications to the simple shock tube previously described is given in Fig. 4.2-18. The curves are based on ideal flow (as Eq. (1), Subsec. 4.1) and assume perfect gases. Infinite contraction ratio is assumed for the convergent tubes. The comparison indicates the relative effectiveness for production of strong shocks at a given over-all pressure ratio of cold-hydrogen drive, constant-volume combustion drive, area reduction at the diaphragm, and the double-diaphragm or buffer-gas technique. It will be noted that the absolute gain in shock Mach number obtained by addition of area reduction to the simple tube remains relatively constant with increasing over-all pressure ratio. By comparison, the further gain due to addition of a buffer gas (maintained at optimum pressure for strong-shock production) increases significantly with pressure ratio.

4.3 Alternatives to the Diaphragm Shock Tube

For generating strong one-dimensional shocks, alternatives to the diaphragm shock tube include tubes with magnetic, solid-explosive, and piston drives.

One type of magnetic drive introduced by Kolb (Ref. 22), which is an extension of the tee-type pulsed discharge drive used by Fowler (see Electrical Heating, Subsec. 4.2.1.1), is illustrated in Fig. 4.3-1. Discharge of a high-voltage low-inductance capacitor produces discharge current \bar{i} which is returned through a heavy lead or strap running adjacent and parallel to the discharge arm and centered in the x-z plane. The magnetic field at the discharge arm axis (x-axis) due to the return current is directed along the y-axis as indicated by the vector \bar{H}_y . Thus the conducting gas in the discharge region is subjected to a Lorentz force ($\alpha \bar{i} \times \bar{H}_y$) directed along the z-axis. This magnetic push in addition to the usual ohmic heating obtained (Subsec. 4.2.1.1) has produced shock waves with Mach numbers of the order of several hundred in small-scale equipment at low initial pressures

(Ref. 22). Shock strength is observed to reach a maximum a short distance from the arc and then decay rapidly (Refs. 22 and 23). Ringing of the discharge circuit produces a succession of secondary shocks. The production of strong shocks requires a large initial rate of rise of discharge current. The initial rate of current rise is proportional to the ratio of discharge voltage to circuit inductance. Additional external field strength has been obtained by adding coils, as indicated in Fig. 4.3-1, which also carry the gas discharge current (Ref. 23), or which are pulsed independently of the gas discharge (Ref. 22).

A magnetic drive without electrodes has been used at Princeton University (Ref. 24) to obtain shock Mach numbers exceeding 200 in air at 0.2 mm Hg pressure. A low-inductance capacitor at high voltage is discharged through a single or two-turn coil wrapped tightly around a 1-in. diameter quartz tube containing gas at low pressure. The resulting induced electric field breaks down the gas to produce circular current loops. The latter interact with the magnetic field to give magnetic forces acting radially inward. As a result of this magnetic squeezing, and also the ohmic heating, very strong shocks are produced moving along the tube away from the coil.

Figure 4.3-2 illustrates direct solid-explosive and piston drives. The solid-explosive drive with an explosive lens or plane-wave generator and expendable tube has been extensively developed at Los Alamos for study of strong plane-shock phenomena (see, for example, Ref. 25). With the piston drive, the piston may be driven by similar explosive means (see, for example, Ref. 26) into gas at rest. A shock wave quickly forms ahead of the piston. If the piston moves at constant speed U_p , state (2) behind the shock is uniform and $U_2 = U_p$. The use of such explosive methods at Los Alamos has produced shock Mach numbers of over 200 in air.

4.4 Attenuation of Strong Shock Waves

Existing theories for shock-wave attenuation and flow non-uniformities produced by tube wall effects are described in Subsec. 3. These theories are small perturbation analyses based on the assumption of a thin boundary layer (relative to the tube diameter) producing small departures from the ideal flow quantities. Also, perfect gas behaviour is assumed. Generally speaking, the existing theories apply in the weak shock range (say M_g less than 2 or 3) but do not accurately predict the attenuation and flow nonuniformities observed for strong shock waves at large distances from the diaphragm station (see, for example, Ref. 27).

Limited experimental data have been published for strong shock attenuation. The most complete study for a cold driver gas is that of Ref. 21, done in a constant-area shock tube of 3.75 in. inside diameter (see also Subsec. 3.1.2). Shock attenuation in air was measured up to 380 tube diameters from the diaphragm station for shock Mach numbers between 5 and 10.5 obtained with cold hydrogen and helium drives. Initial air pressure ahead of the shock was varied from 5 to 100 mm Hg. For a given shock strength, hydrogen drive was found to give about twice the rate of wave-speed decay produced with helium drive (see Fig. 4.4-2 lower). Typical results for hydrogen and helium are shown in Figs. 4.4-1 and 4.4-2, respectively. It will be noted that the maximum shock speed was attained a distance of the order of 60 tube diameters downstream of

the diaphragm. Over the range of pressures studied, the initial air pressure had practically no effect on shock attenuation.

In addition to measurement of shock speed, the work of Ref. 21 included measurement of wall pressure as a function of time at various stations along the low-pressure channel. These studies showed a period of near constant pressure following passage of the shock, after which the pressure increased significantly with time. Figure 4.4-3 shows typical results. It will be noted that the pressure increase begins before arrival of the contact surface, and that the period of constant pressure is relatively insensitive to distance along the tube. It is suggested (Ref. 21) that the pressure gradient change may coincide with wall boundary-layer transition. Evidently, such strong nonuniform flow effects can severely limit the usefulness of the shock tube for aerodynamic testing.

Experimental studies of strong-shock attenuation and wall pressure variation for various combustion and detonation drives, as well as for pure hydrogen and helium, are reported in Refs. 27, 30, and 30a. Reference 30a also reports experimental results for density variation with time behind the shock (obtained by an x-ray method) and, in addition, estimates the effects of shock attenuation on the flow properties and quantities such as heat transfer rate and shock detachment distance. With constant-volume combustion drive, the wall pressure variation after the shock wave is similar to that with cold hydrogen or helium drive (i.e., Fig. 4.4-3), and the rate of shock-speed decay is somewhat less than double that with hydrogen drive. Shock attenuation with detonation-wave heating initiated at the tube end is very large (typically 3 to 4 per cent per foot for shock Mach numbers around 12, Refs. 30 and 33), and exceeds that for "constant-pressure" combustion. The latter method in turn gives greater attenuation than constant-volume combustion (Ref. 27). With detonation initiated at the tube end, and also with "constant-pressure" combustion for sufficient distance from the diaphragm (Ref. 27), wall pressure is observed to decrease with time following passage of the shock wave. This suggests overtaking of the shock by an expansion wave with consequent greater attenuation than from wall effects alone (see also Subsec. 4.2.1.3).

In summary, the present experimental data on strong-shock attenuation indicate the percentage rate of decay of shock speed to increase strongly with increasing driver-gas sound speed but to be only weakly dependent on pressure level and shock strength. The various driving methods in order of increasing shock attenuation are: cold helium, cold hydrogen, constant-volume combustion, "constant-pressure" combustion, and detonation initiated at the tube end. Thus the performance advantage of a high-sound-speed driver gas as predicted by the ideal shock-tube theory (i.e., lower diaphragm pressure ratio) is somewhat offset in practice by the attendant increase in shock attenuation. In applications where strong-shock attenuation must be minimized, a relatively inefficient driver gas may thus be a necessary compromise.

Table 4.1-1
 Maximum shock Mach number M_s^* attainable with cold driver in simple shock tube
 at infinite diaphragm pressure ratio

Driver/Driven Gas (4)	m_4	m_1	γ_4	γ_1	$\frac{a_4}{a_1} = A_{41} = \sqrt{\frac{\gamma_4}{\gamma_1} \frac{m_1}{m_4} \frac{T_4}{T_1}}$	M_s^*
Air/Air	28.95	28.95	1.404	1.404	1	6.16
He/Air	4.003	28.95	1.667	1.404	2.93	10.6
He/N ₂	4.003	28.02	1.667	1.404	2.88	10.4
He/A	4.003	39.94	1.667	1.667	3.16	12.7
H ₂ /Air	2.016	28.95	1.407	1.404	3.80	22.5
H ₂ /N ₂	2.016	28.02	1.407	1.404	3.73	22.1
H ₂ /A	2.016	39.94	1.407	1.667	4.09	26.8

$$(4) \quad \frac{P_4}{P_1} \rightarrow \infty$$

$$T_4 = T_1$$

$$P_4/P_1 \rightarrow \infty$$

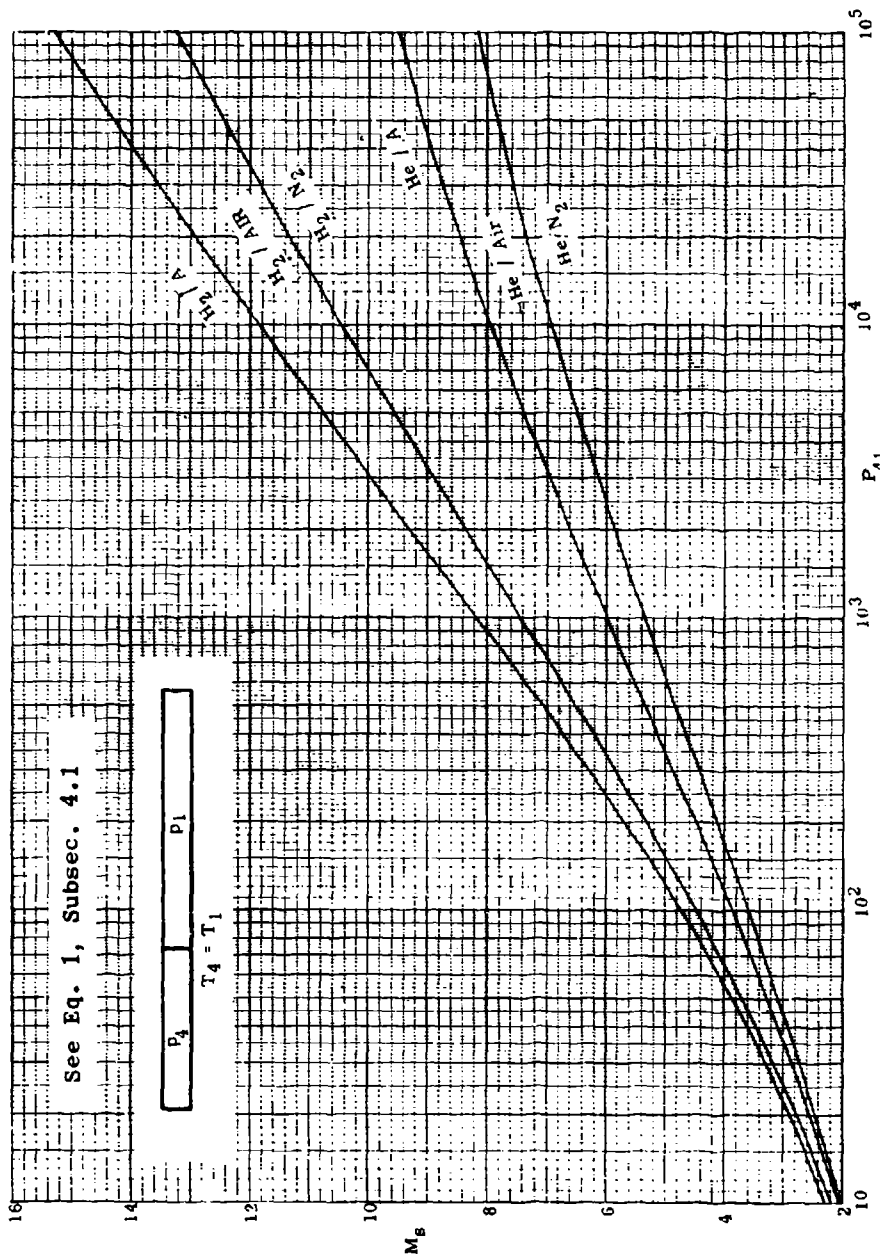


Fig. 4.1-1. Shock Mach number M_s vs diaphragm pressure ratio P_4 for simple constant-area shock tube.

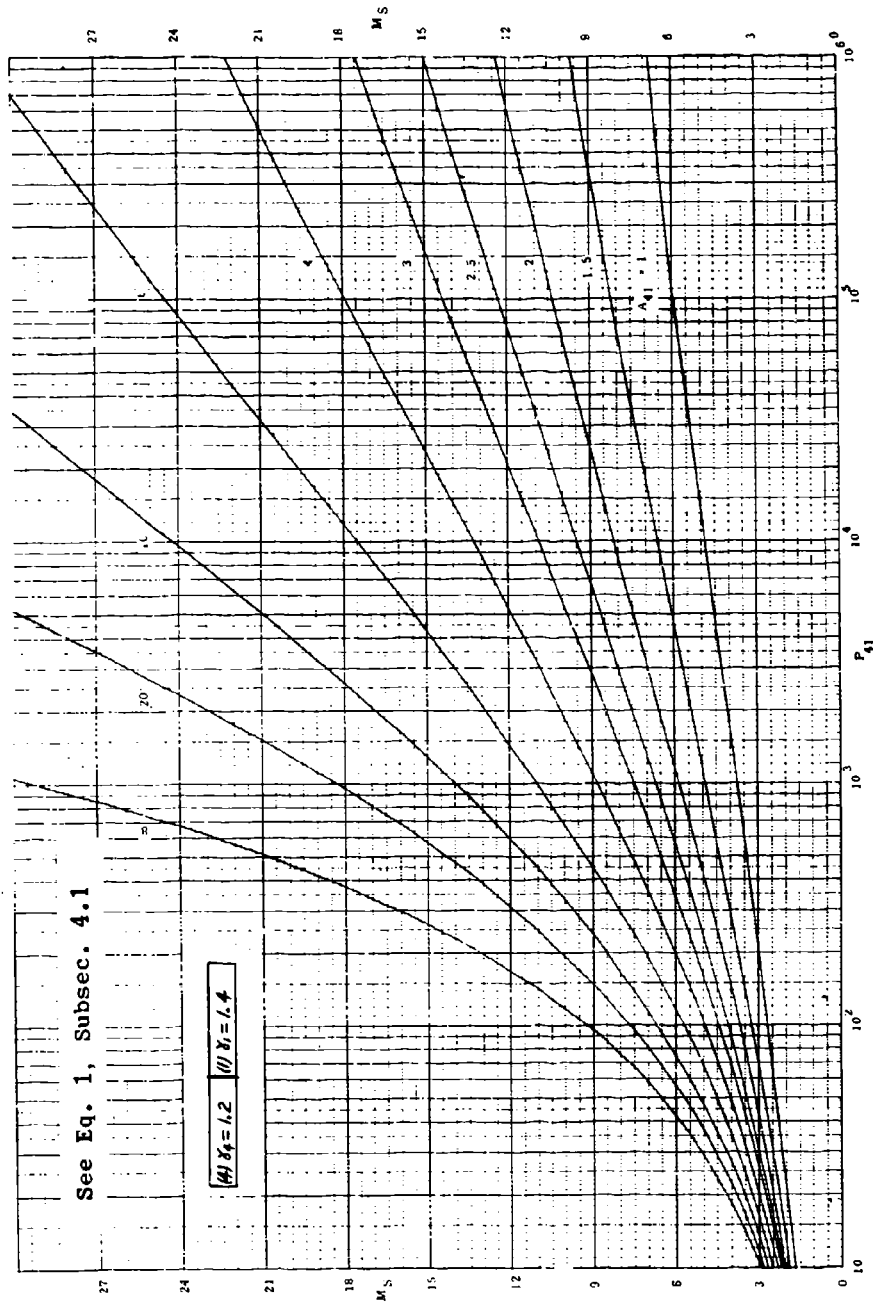


Fig. 4.1-2. Theoretical perfect-gas performance of ideal constant-area shock tube; shock Mach number M_s vs diaphragm pressure ratio P_{41} for various diaphragm sound speed ratios A_{41} ; $\gamma_4 = 1.2$, $\gamma_1 = 1.4$.

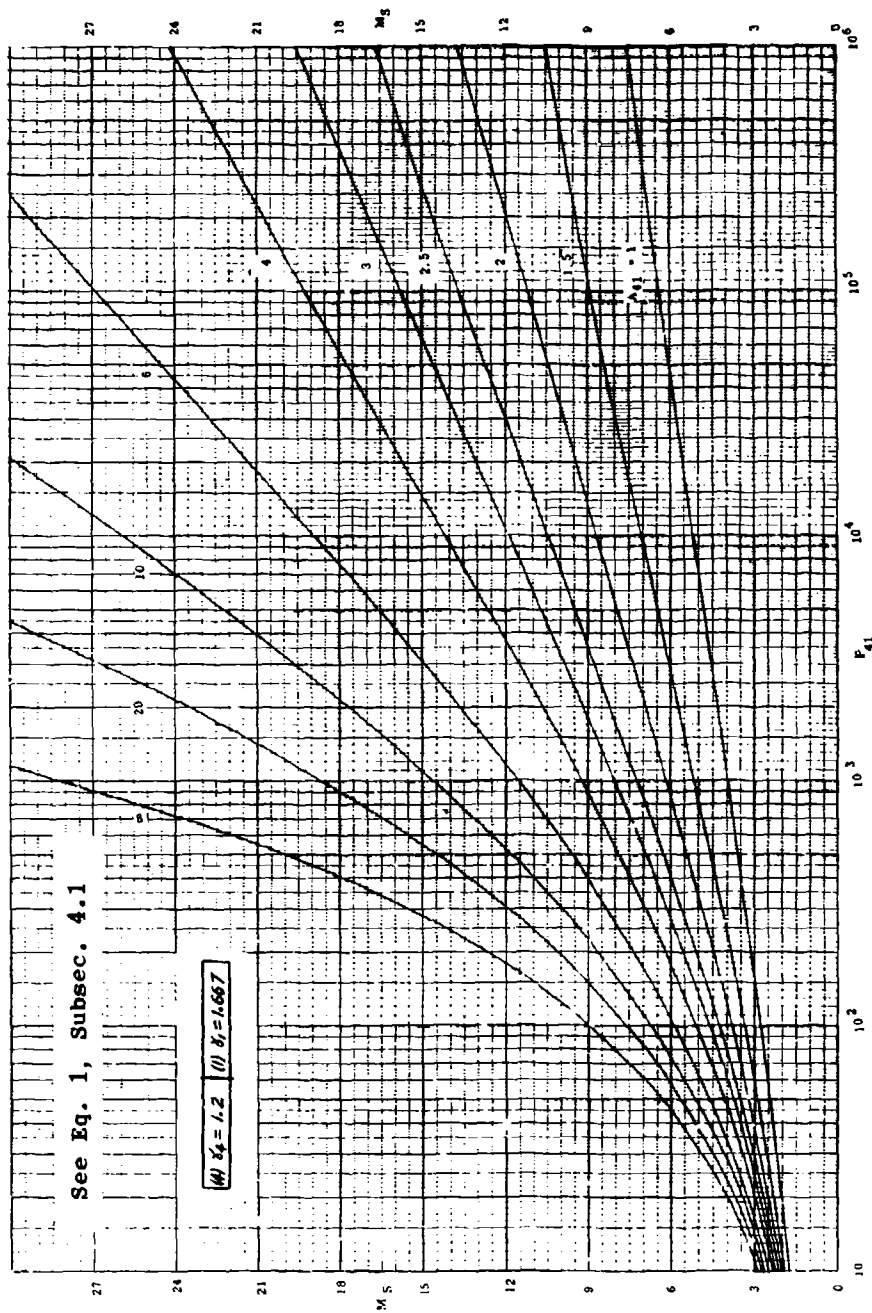


Fig. 4.1-3. Theoretical perfect-gas performance of ideal constant-area shock tube; shock Mach M_g vs diaphragm pressure ratio P_{41} for various diaphragm sound speed ratios A_{41} ; $\gamma_4 = 1.2$, $\gamma_1 = 1.667$.

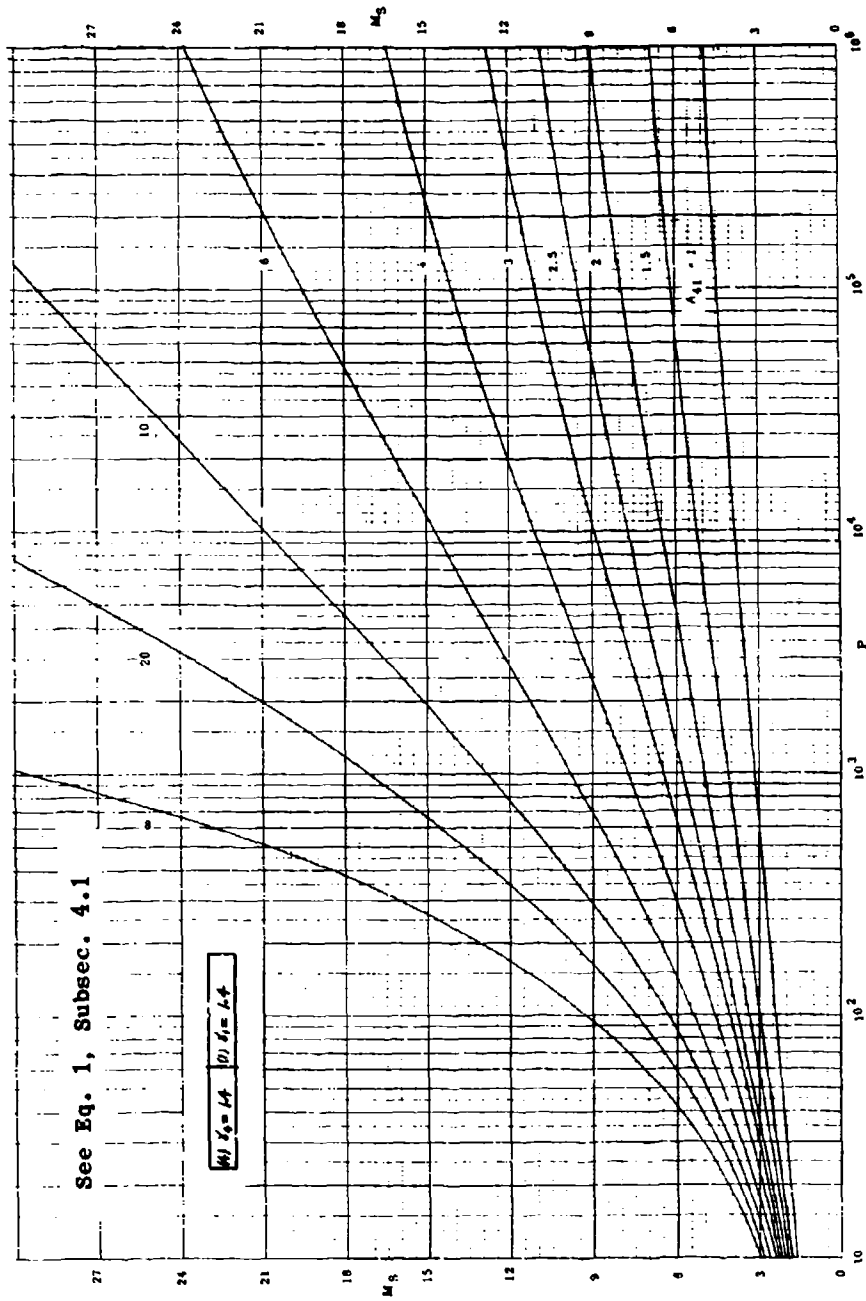


Fig. 4.1-4. Theoretical perfect-gas performance of ideal constant-area snook tube; shock Mach number M_s vs diaphragm pressure ratio P_{41} for various diaphragm sound speed ratios A_{41} ; $\gamma_4 = 1.4$, $\gamma_1 = 1.4$.

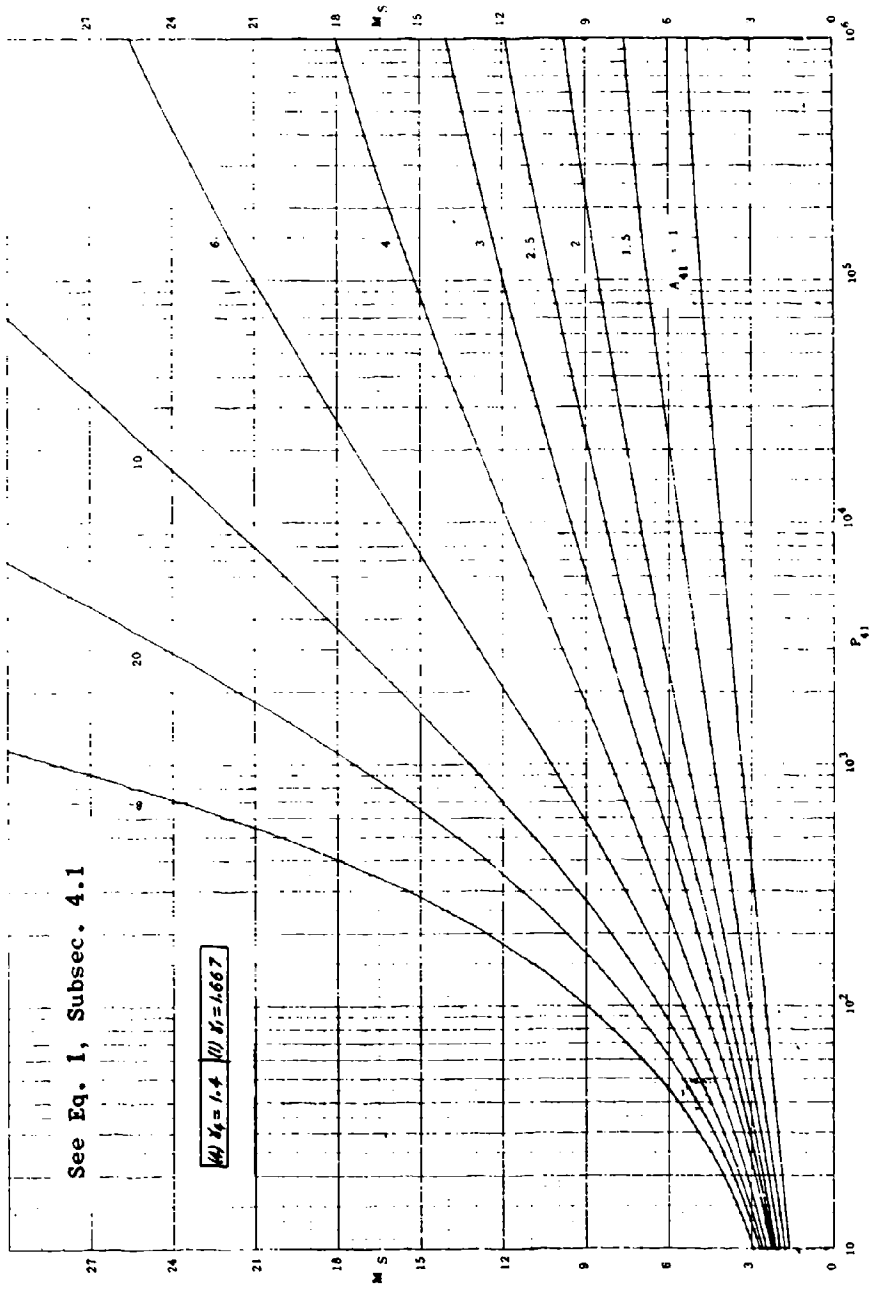


Fig. 4.1-5. Theoretical perfect-gas performance of ideal constant-area shock tube; shock Mach number M_s vs diaphragm pressure ratio P_{41} for various diaphragm sound speed ratios A_{41} ; $\gamma_4 = 1.4$, $\gamma_1 = 1.667$.

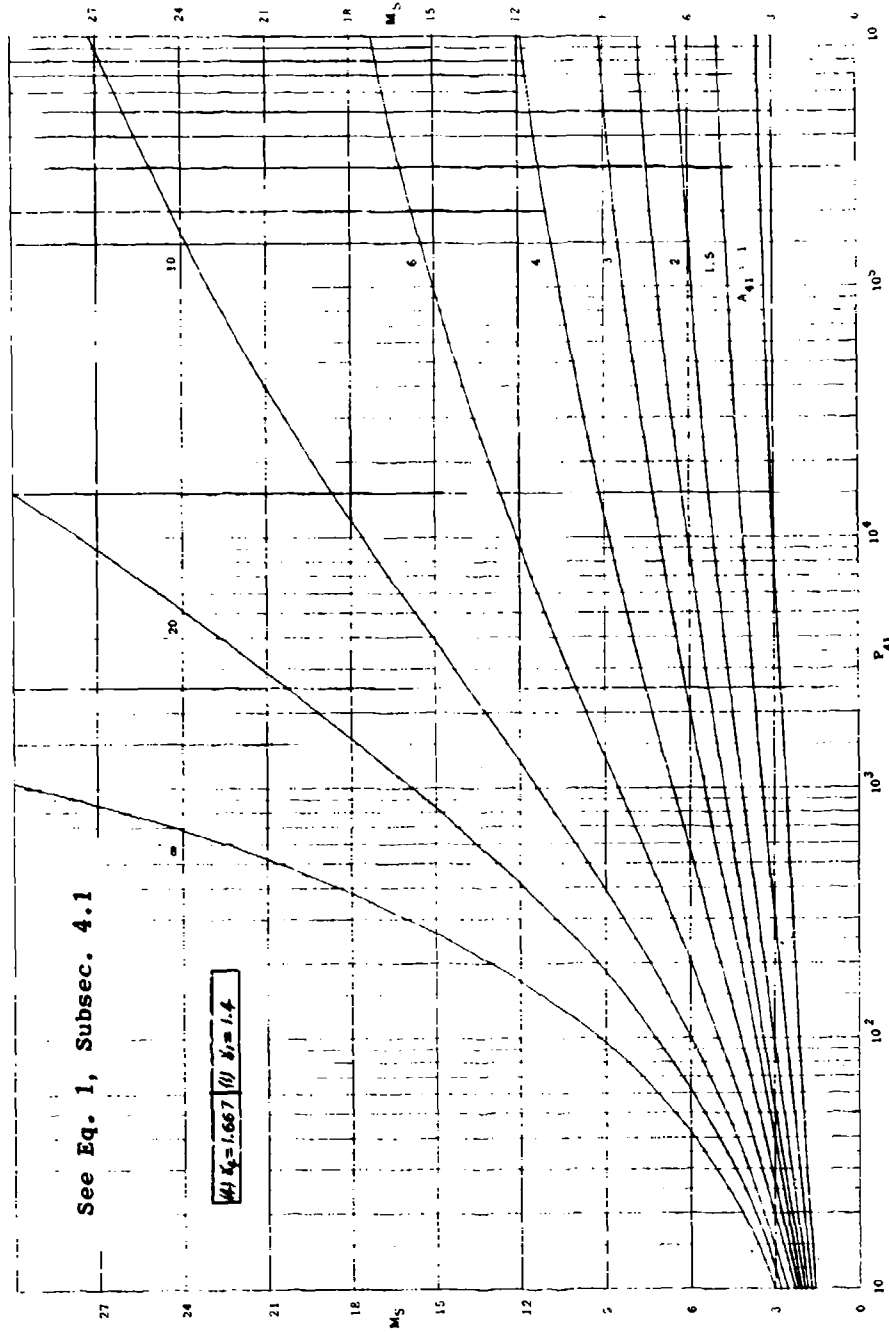


Fig. 4.1-6. Theoretical perfect-gas performance of ideal constant-area shock tube; shock Mach number M_s vs diaphragm pressure ratio P_{41} for various diaphragm sound speed ratios A_{41} ; $\gamma_4 = 1.667$, $\gamma_1 = 1.4$.

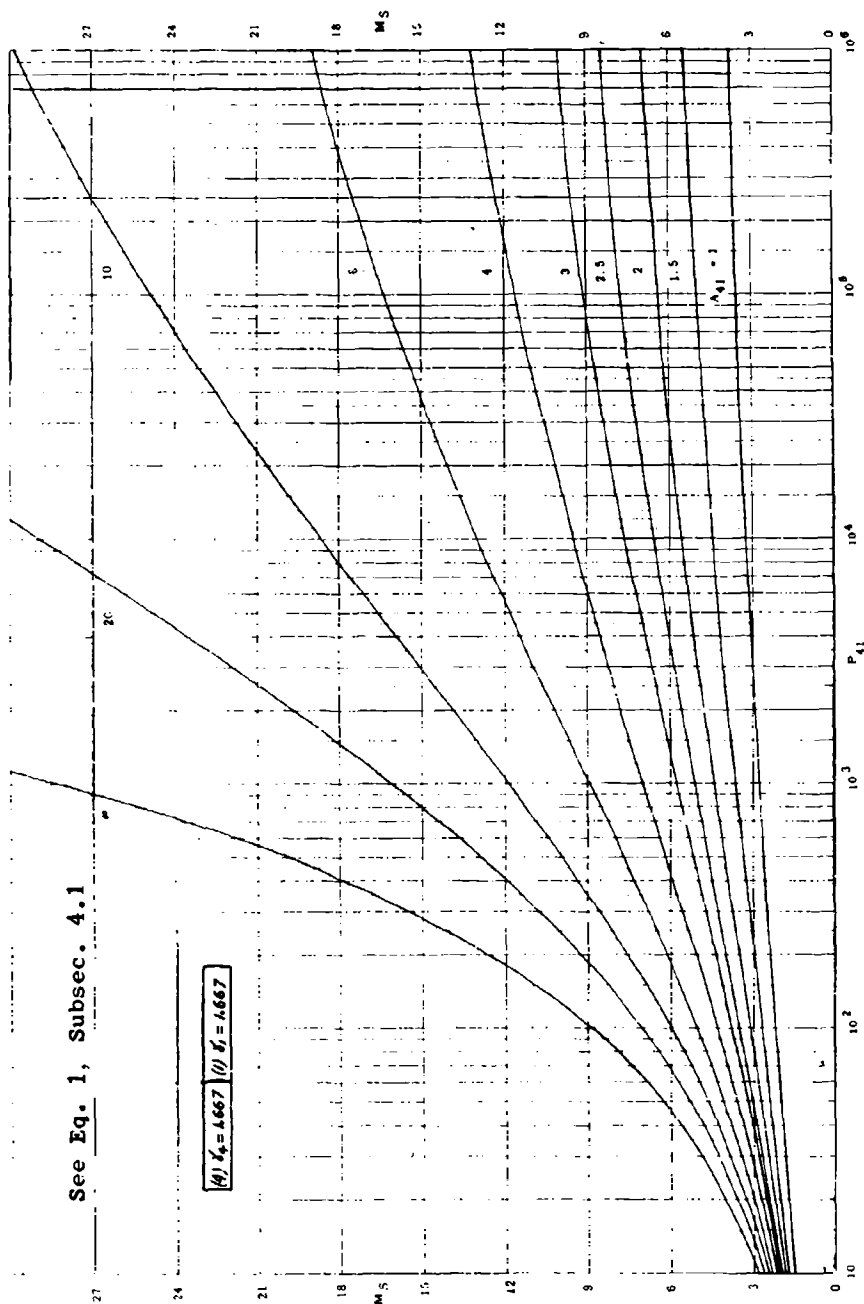


Fig. 4.1-7. Theoretical perfect-gas performance of ideal constant-area shock tube; shock Mach number M_S vs diaphragm pressure ratio P_{41} for various diaphragm sound speed ratios A_{41} ; $\gamma_4 = 1.667$, $\gamma_1 = 1.667$.

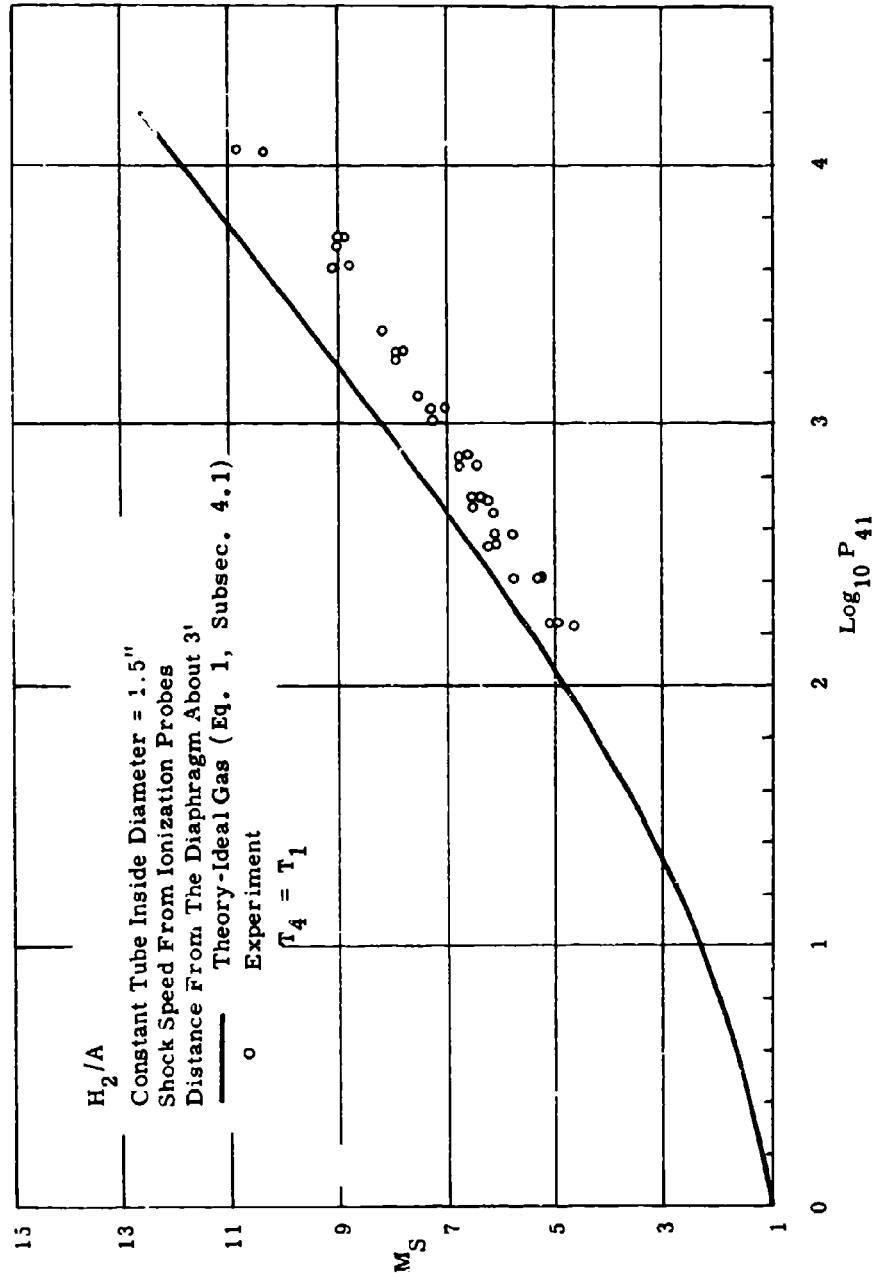


Fig. 4.1-8. Theory and experiment for simple constant-area shock tube (Ref. 2); shock Mach number M_S vs diaphragm pressure ratio P_{41} .

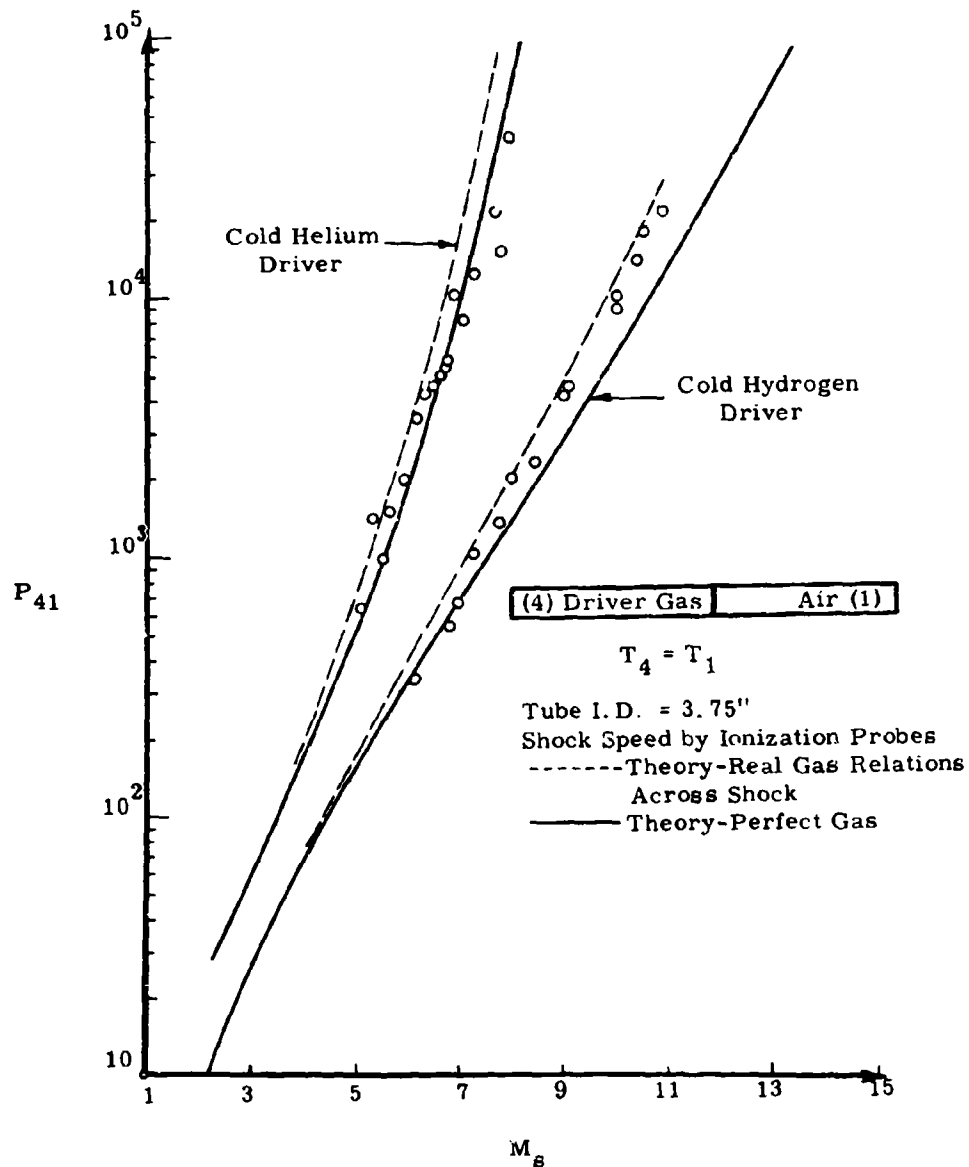
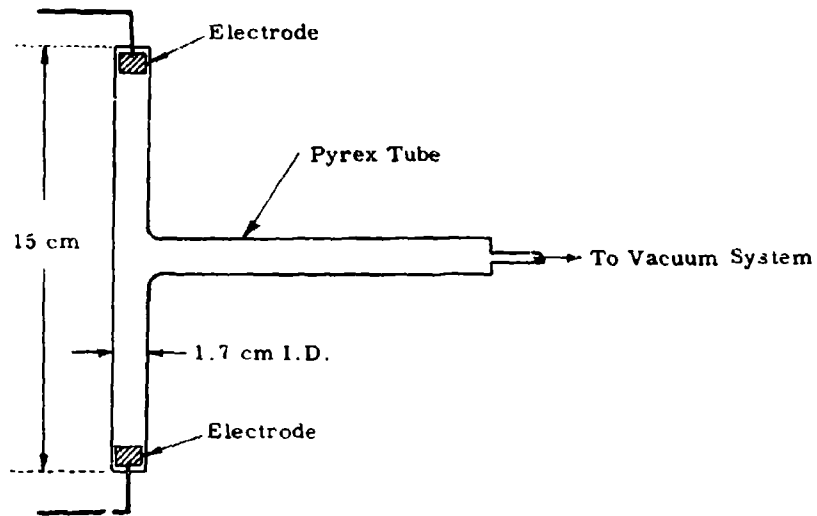
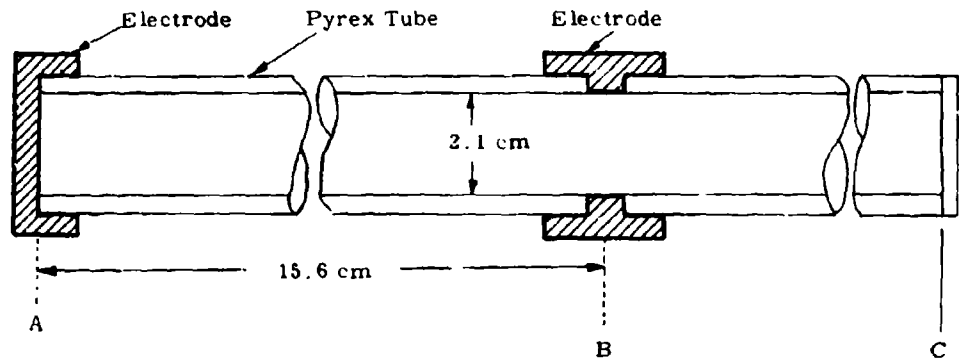


Fig. 4.1-9. Comparison of theory and experiment for simple shock tube (Ref. 21); maximum shock Mach number M_s (about 60 diameters from diaphragm) vs diaphragm pressure ratio P_{41} .



Tee-Type Tube



Straight Tube

Fig. 4.2-1. Pulsed discharge tubes (after Refs. 4 and 6).

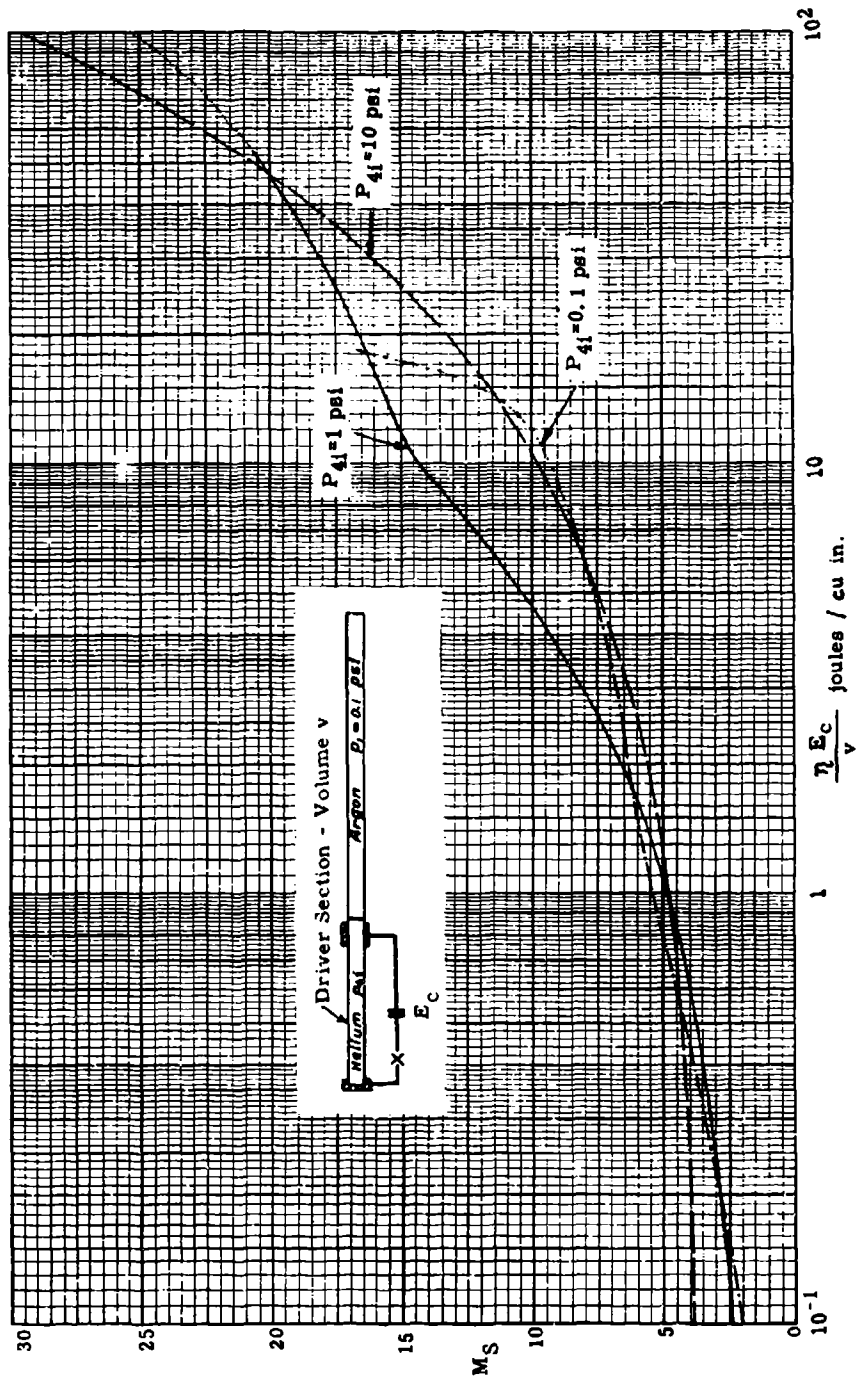


Fig. 4.2-2. Electric discharge drive; shock Mach number M_S vs energy transferred to unit volume of driver gas $\eta E_C/v$.

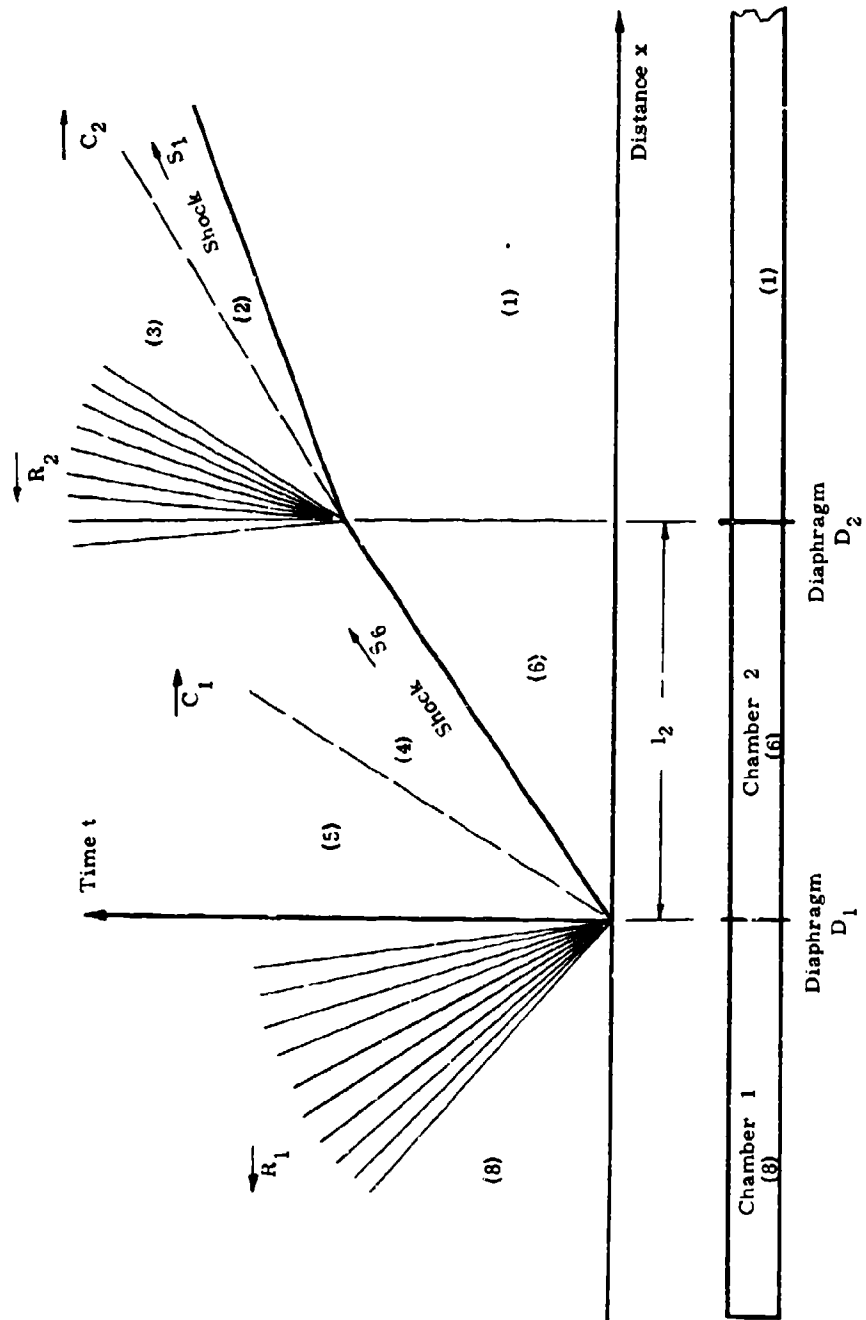


Fig. 4.2-3. Initial flow in double-diaphragm constant-area tube; unsteady expansion method.

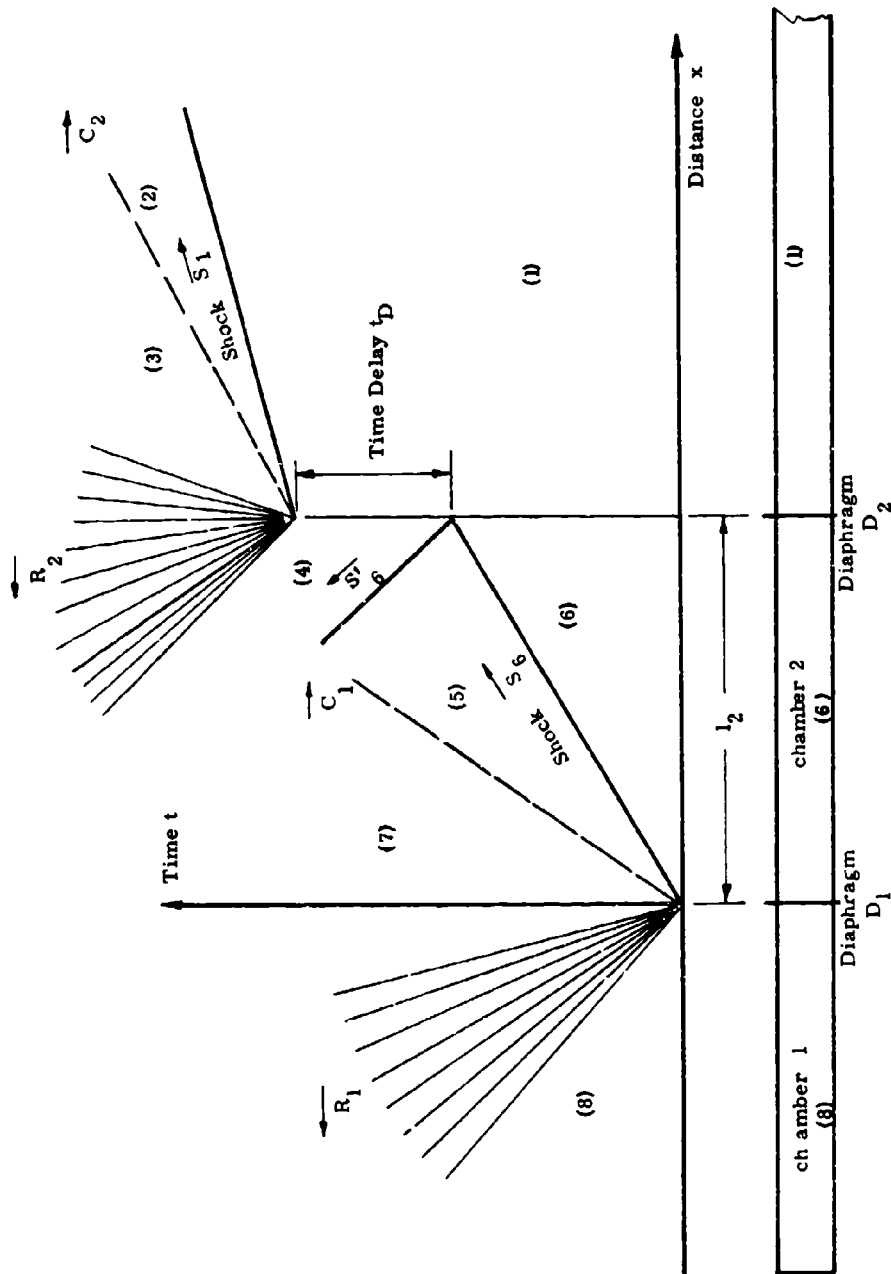
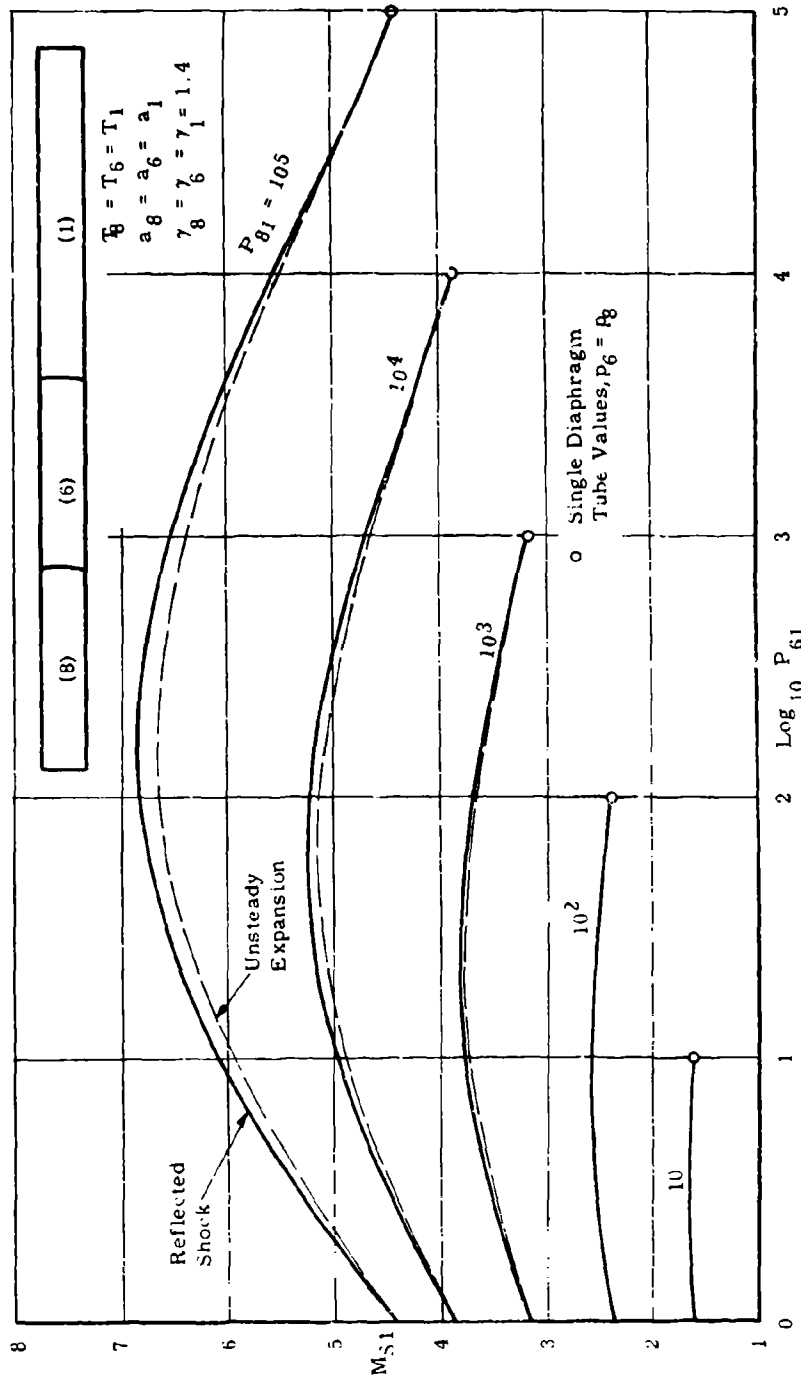
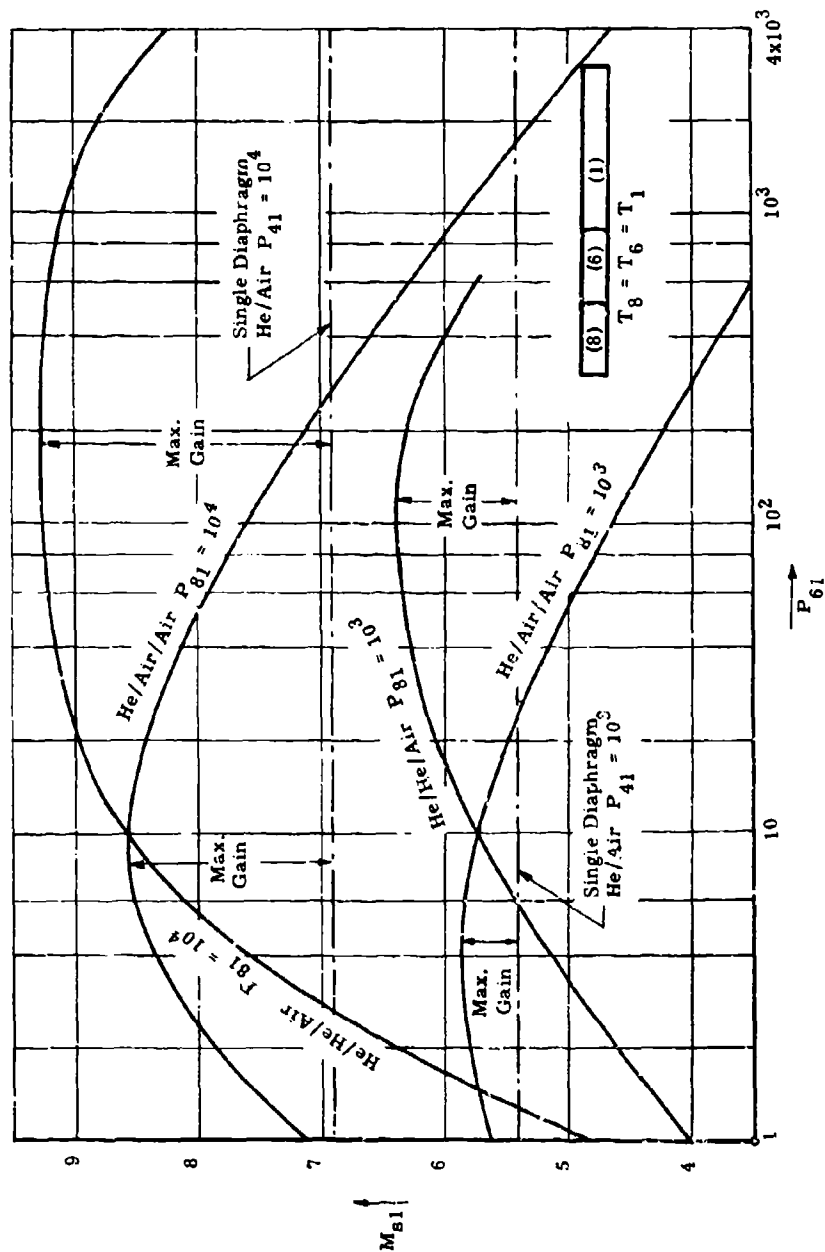


Fig. 4.2-4. Initial flow in double-diaphragm constant-area tube; reflected shock method.



(See also Figs. 4.2-3 and 4.2-4.)

Fig. 4.2-5. Comparison of reflected shock and unsteady expansion methods for double-diaphragm constant-area tube (Ref. 12); second shock Mach number M_{S1} vs pressure ratio P_{61} across second diaphragm.



(See also Fig. 4.2-4.)

Fig. 4.2-6. Double-diaphragm constant-area tube performance for helium-air combinations (after Ref. 11); reflected shock method; second shock Mach number M_{s1} vs pressure ratio P_{61} across second diaphragm.

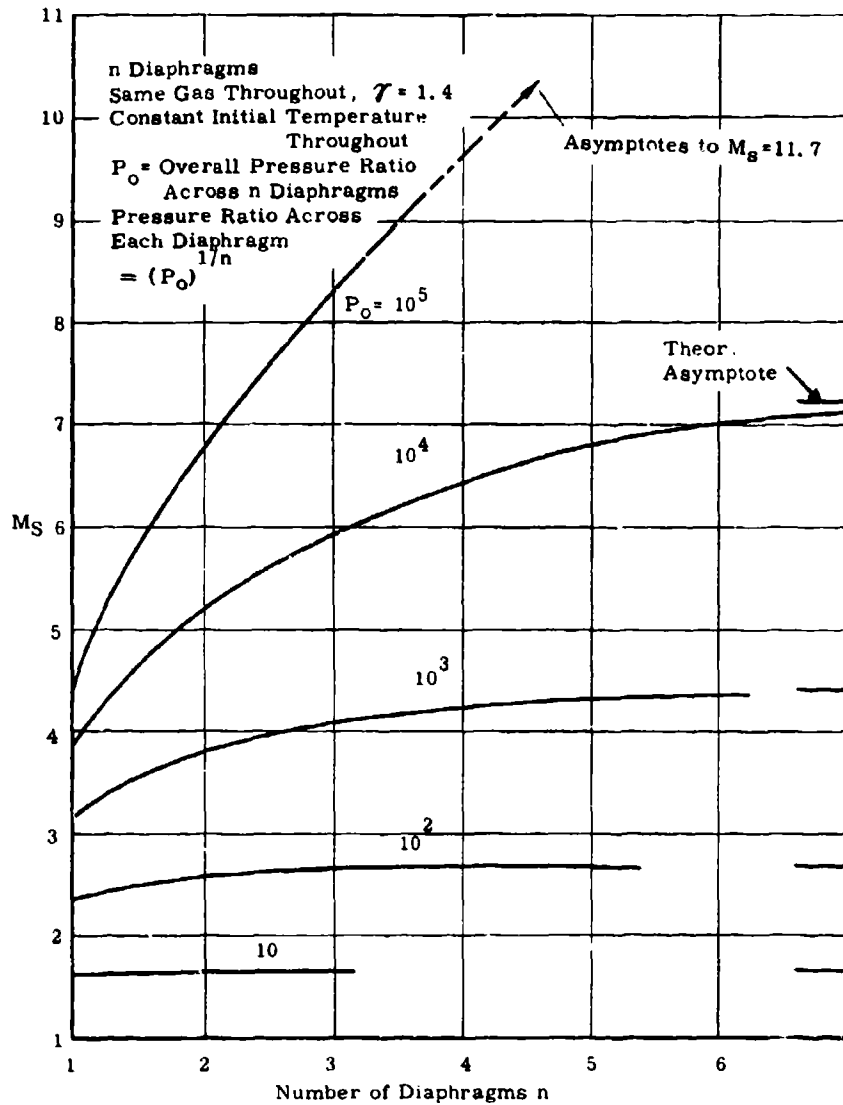


Fig. 4.2-7. Multiple-diaphragm constant-area tube performance; reflected shock method; maximum final shock Mach number M_S vs number of diaphragms, n (Ref. 12).

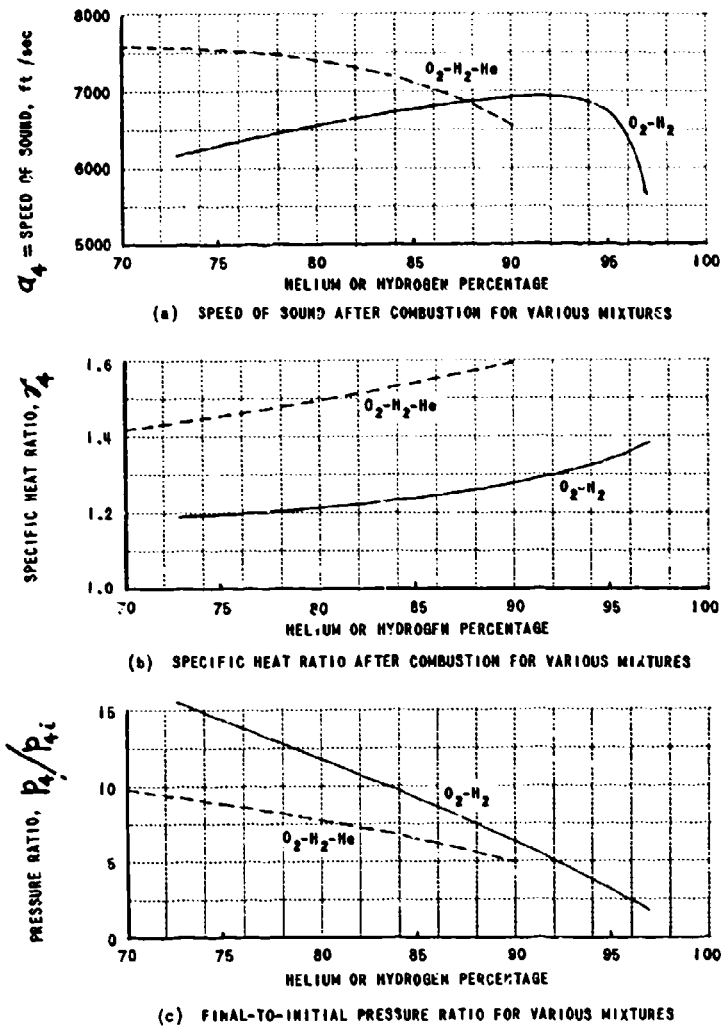


Fig. 4.2-8. Theoretical calculation of adiabatic constant-volume combustion assuming no dissociation; helium or hydrogen percentages on a molar basis; initial temperature 291°K (Ref. 27).

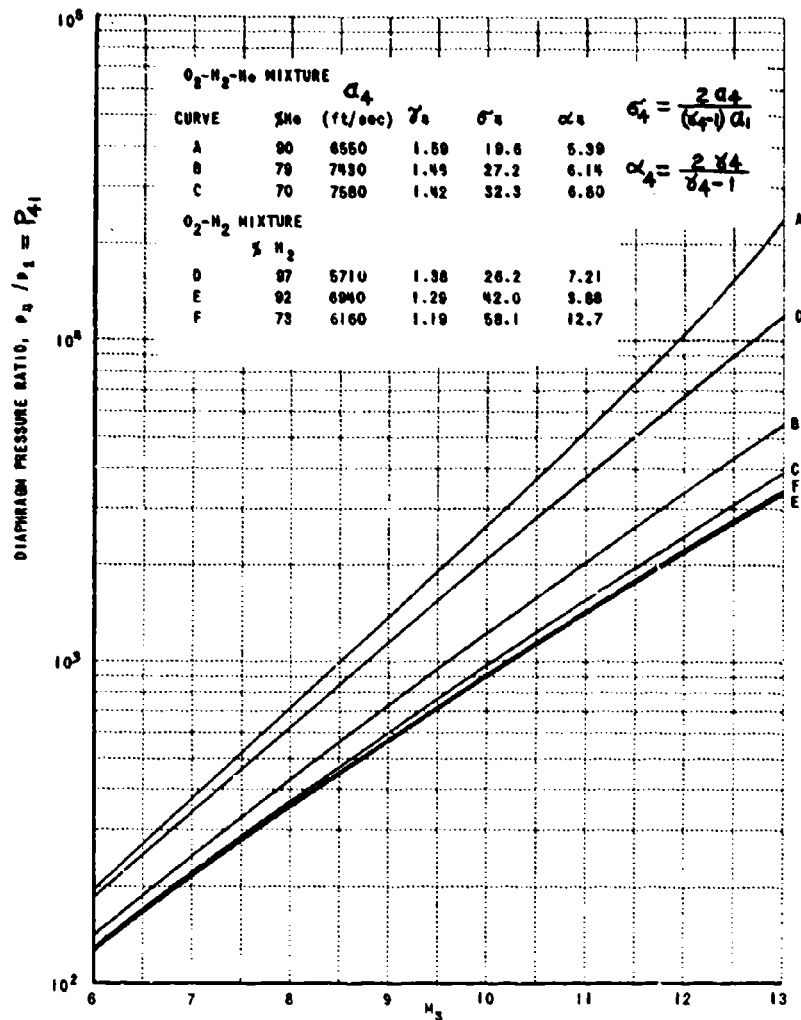
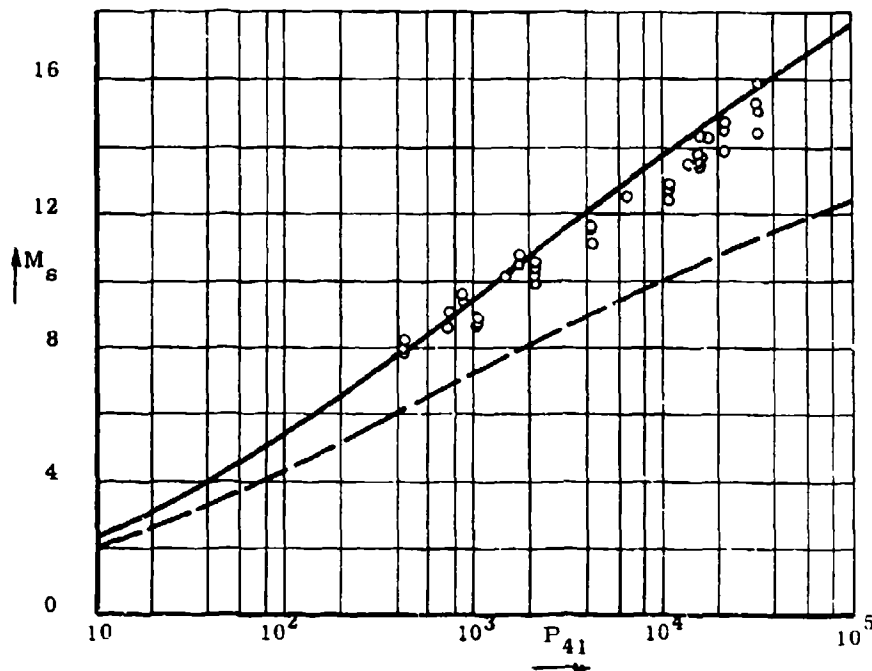


Fig. 4.2-9. Theoretical shock Mach number M_s in constant-area shock tube vs peak diaphragm pressure ratio P_{41} (after combustion) for adiabatic constant-volume combustion of various driving mixtures (Ref. 27).



———— Theory for adiabatic constant-volume combustion of O_2, H_2, He driver, with 70-75% He. Driven gas air. $A_{41} = 7.3, \gamma/4 = 1.6$. Real gas effects across shock included.

----- Theory for cold hydrogen driving air

○ Experimental	3' 1.5" D	20' 1.5" D
	(4)	(1) Air
O_2, H_2, He Driver 70-75% He	20' 6" D	100' 4" D
	(4)	(1) Air

Shock speed by ionization probes about 20 tube diameters from diaphragm station.

Fig. 4.2-10. Comparison of theory and experiment for O_2-H_2-He combustion drive; shock Mach number M_s vs peak diaphragm pressure ratio P_{41} after combustion (Ref. 3).

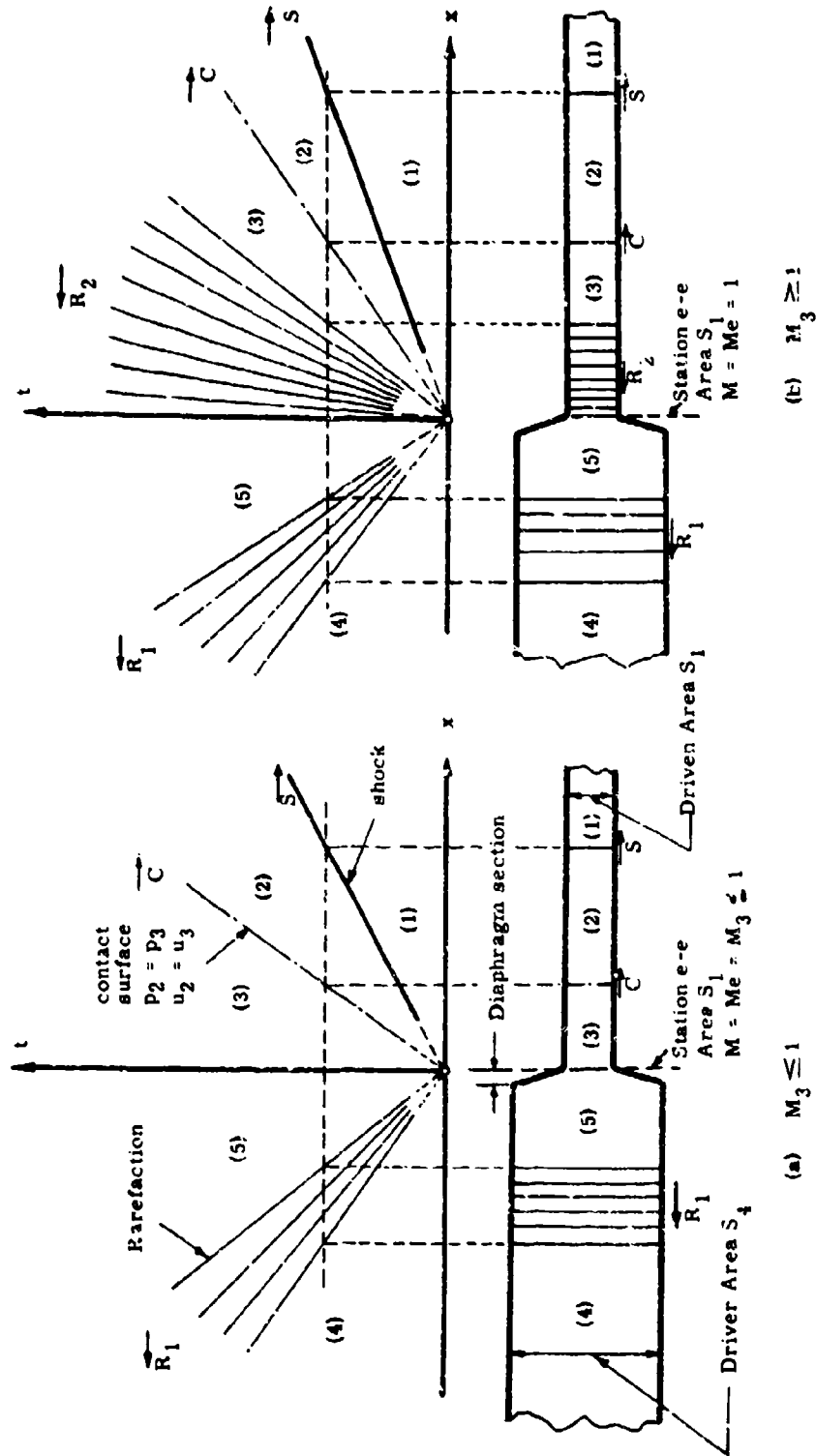
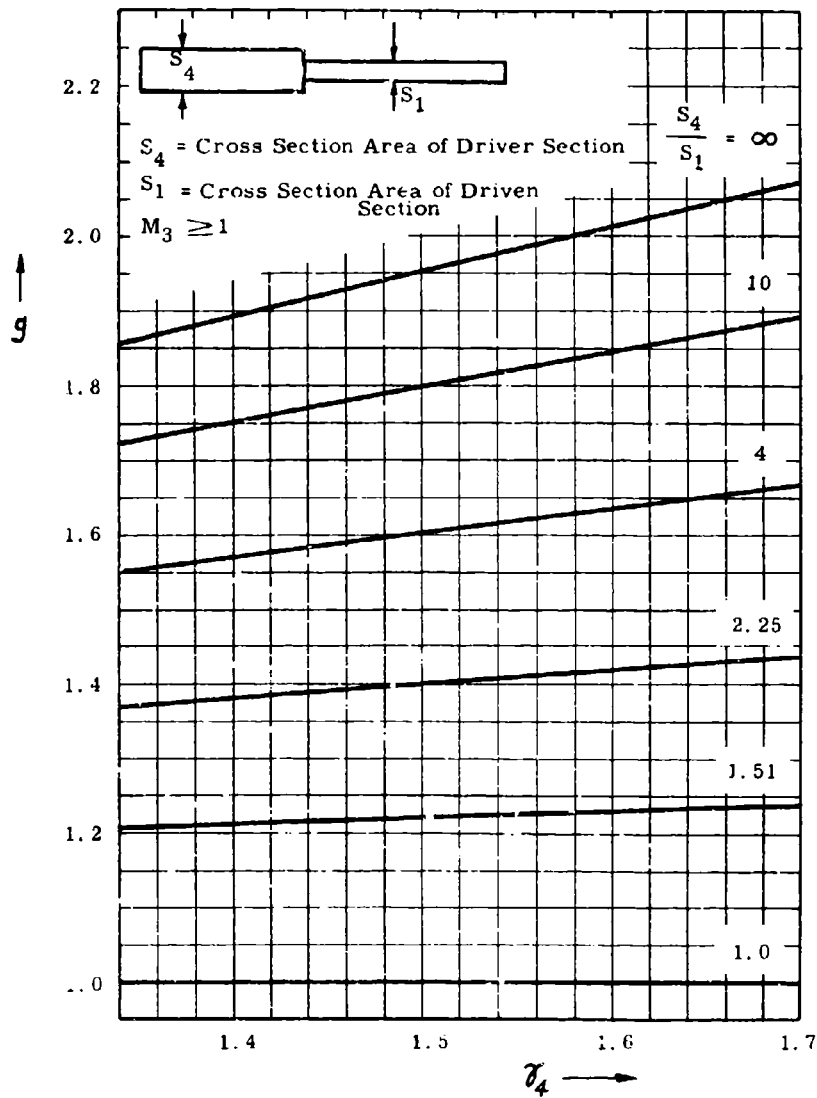


Fig. 4.2-11. Idealized flow with monotonic area reduction at diaphragm.



(Curves apply only for $M_3 \geq 1$: see Fig. 4.2-11;
 for value of g , see Eq. 2, Subsec. 4.2.2.1.)

Fig. 4.2-12. Parameter g for monotonic-convergence shock tube vs isentropic index γ_4 for driver gas (Ref. 18).

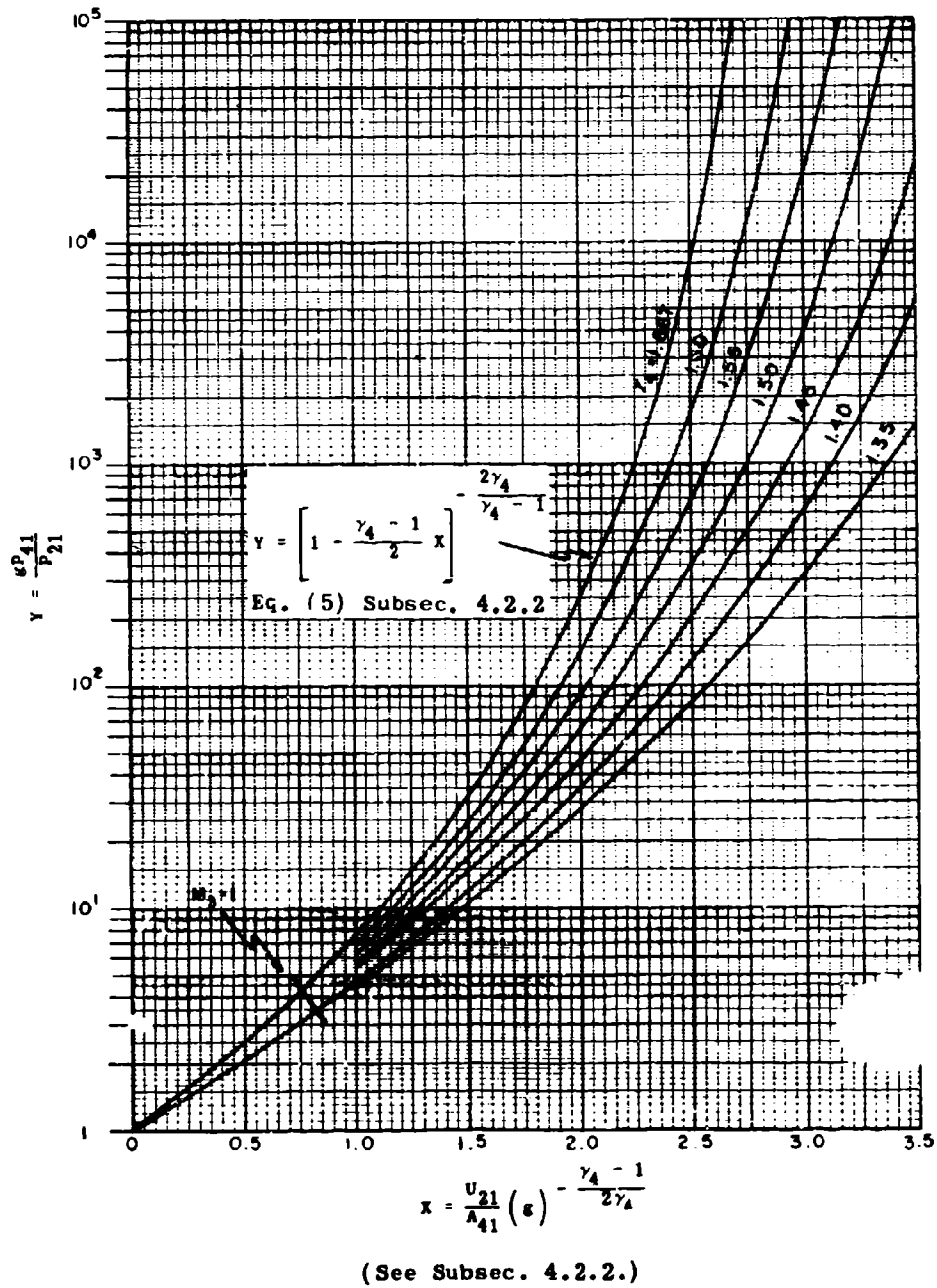


Fig. 4.2-13. General shock-tube performance curves (Ref. 18).

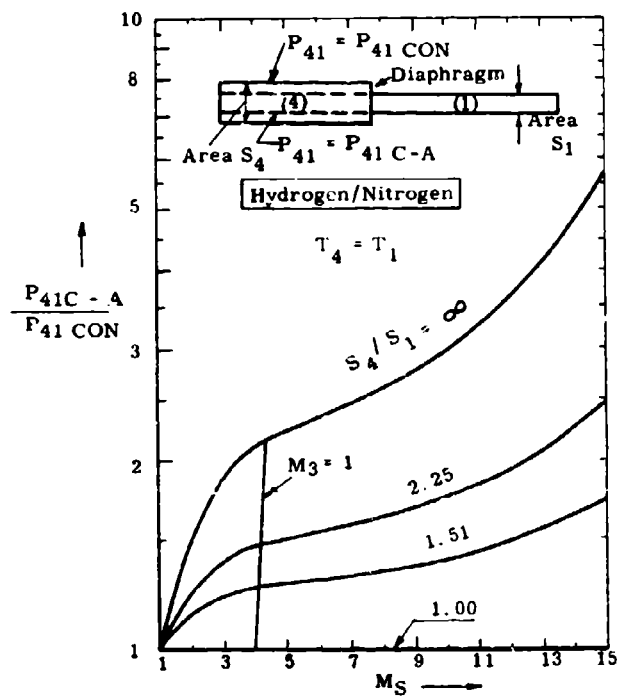


Fig. 4.2-14. Ratio of diaphragm pressure ratio for constant-area tube ($P_{41 \text{ C-A}}$) to diaphragm pressure ratio for convergent tube ($P_{41 \text{ CON}}$) vs shock Mach number M_S in driven N_2 (Ref. 18).

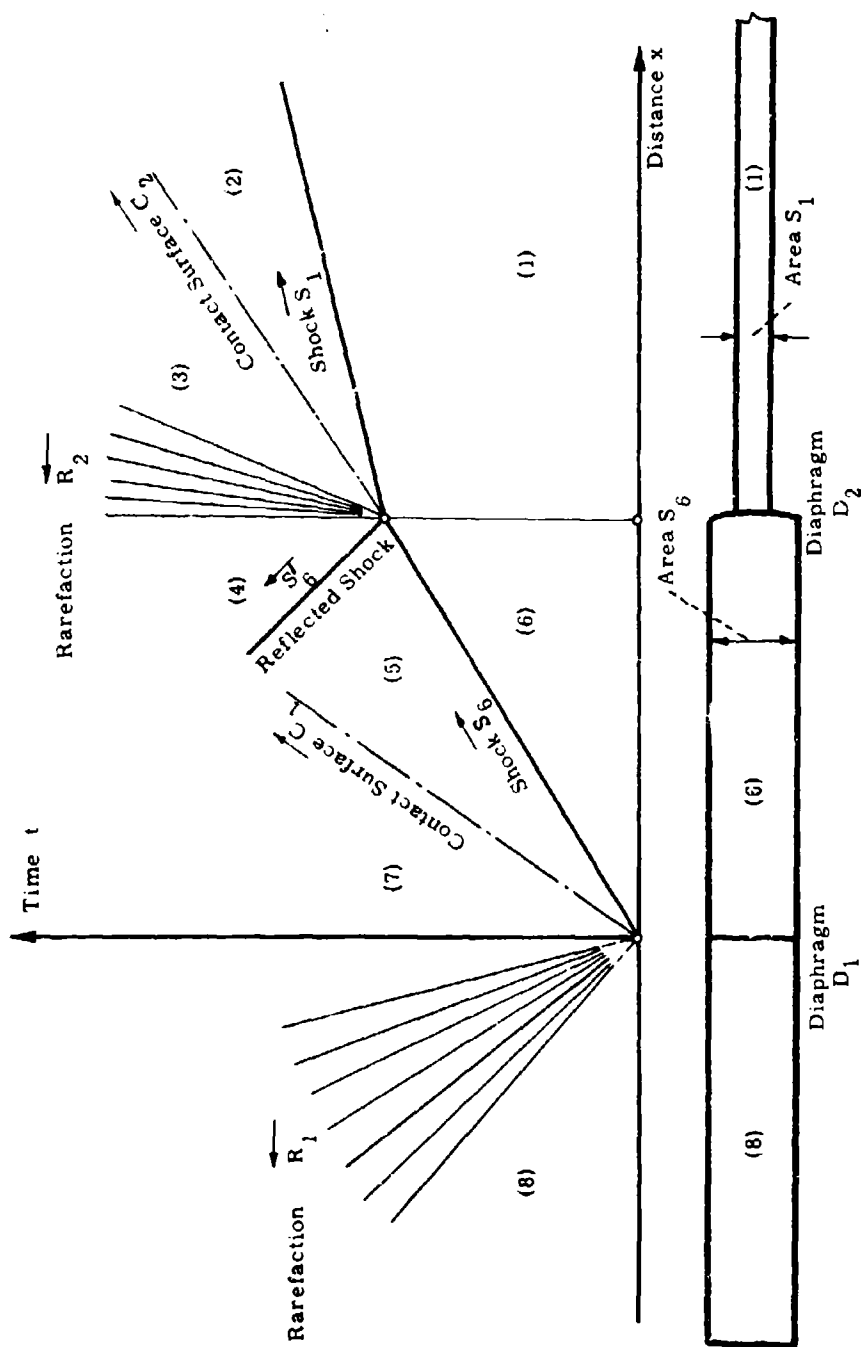


Fig. 4.2-16. Double-diaphragm technique with area reduction; Mach number $M_3 \geq 1$.

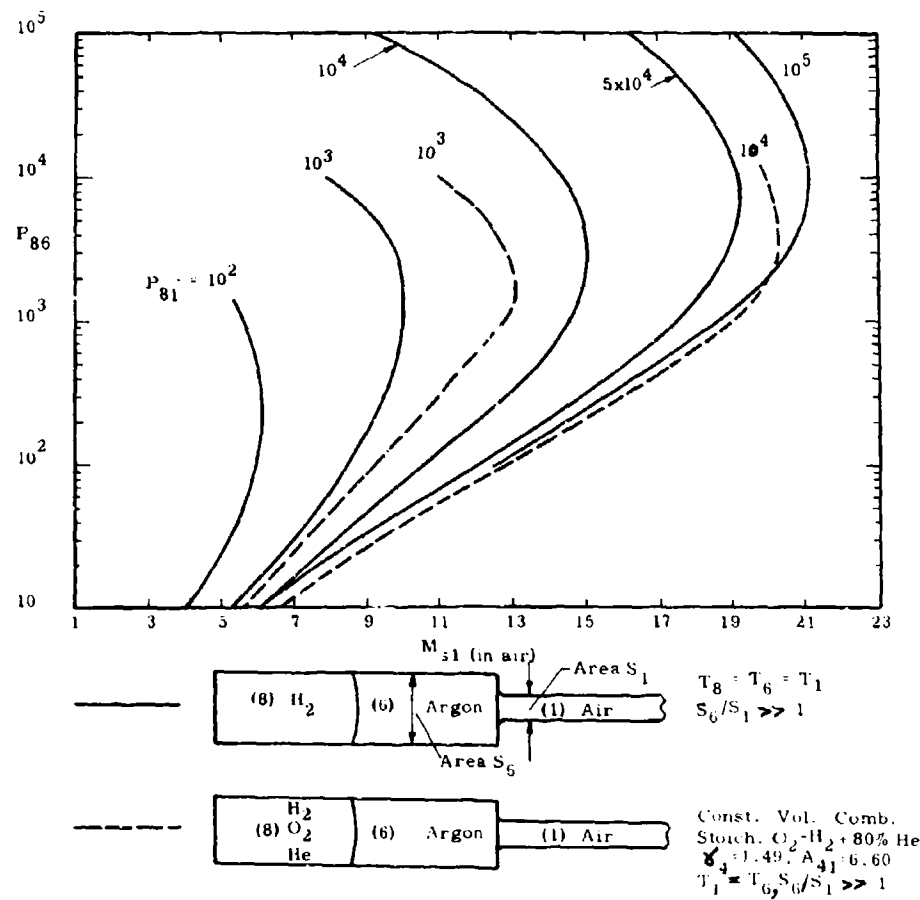


Fig. 4.2-17. Calculated performance of double-diaphragm convergent tube with argon buffer and large contraction ratio S_6/S_1 ; pressure ratio P_{86} across upstream diaphragm vs shock Mach number and combustion drive at various peak over-all pressure ratios P_{81} (Ref. 20).

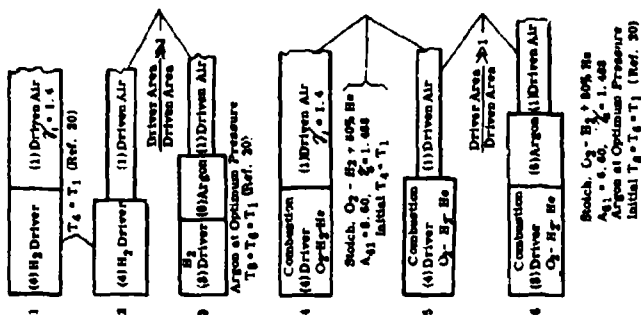
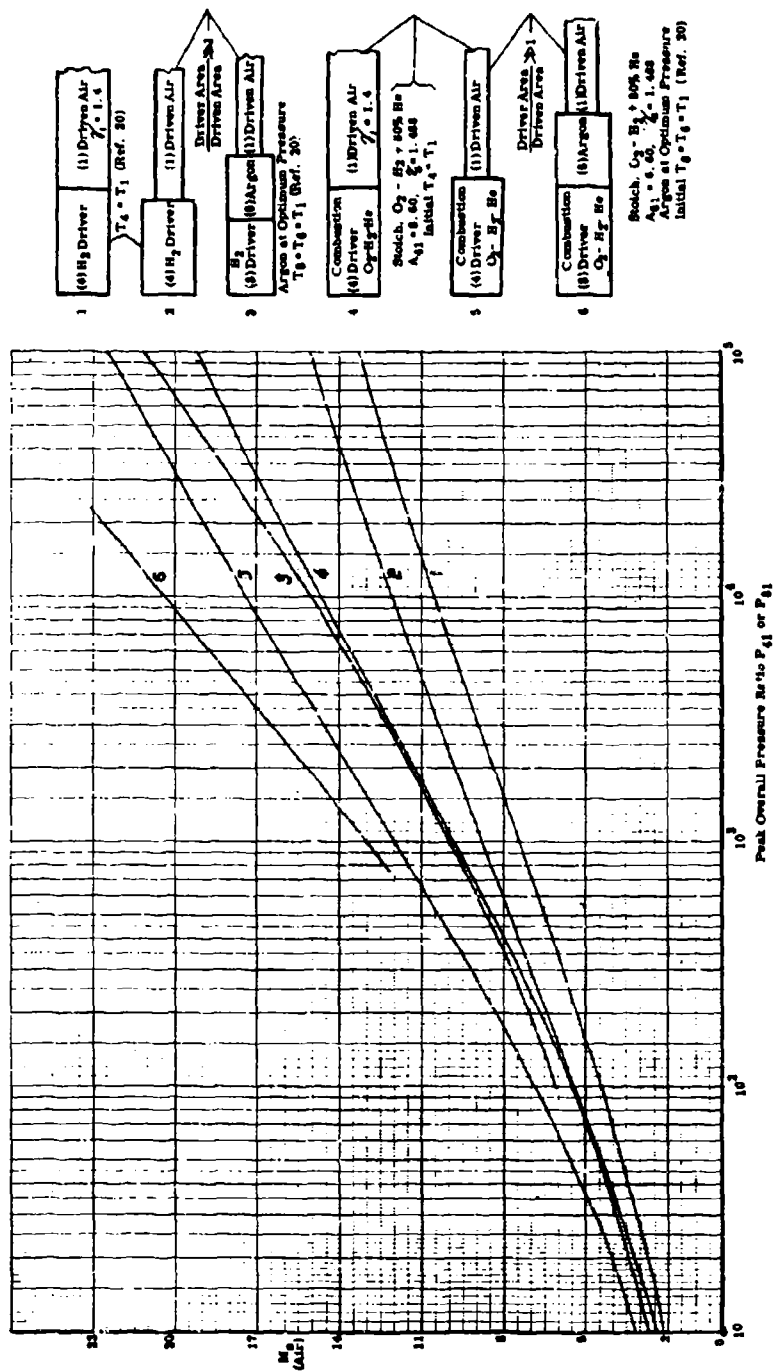


Fig. 4.2-18. Comparison of various modifications to simple shock tube. Theoretical shock Mach number M_s in driven air vs peak over-all pressure ratio P_{01} or P_{01} (after combustion); perfect gases assumed.

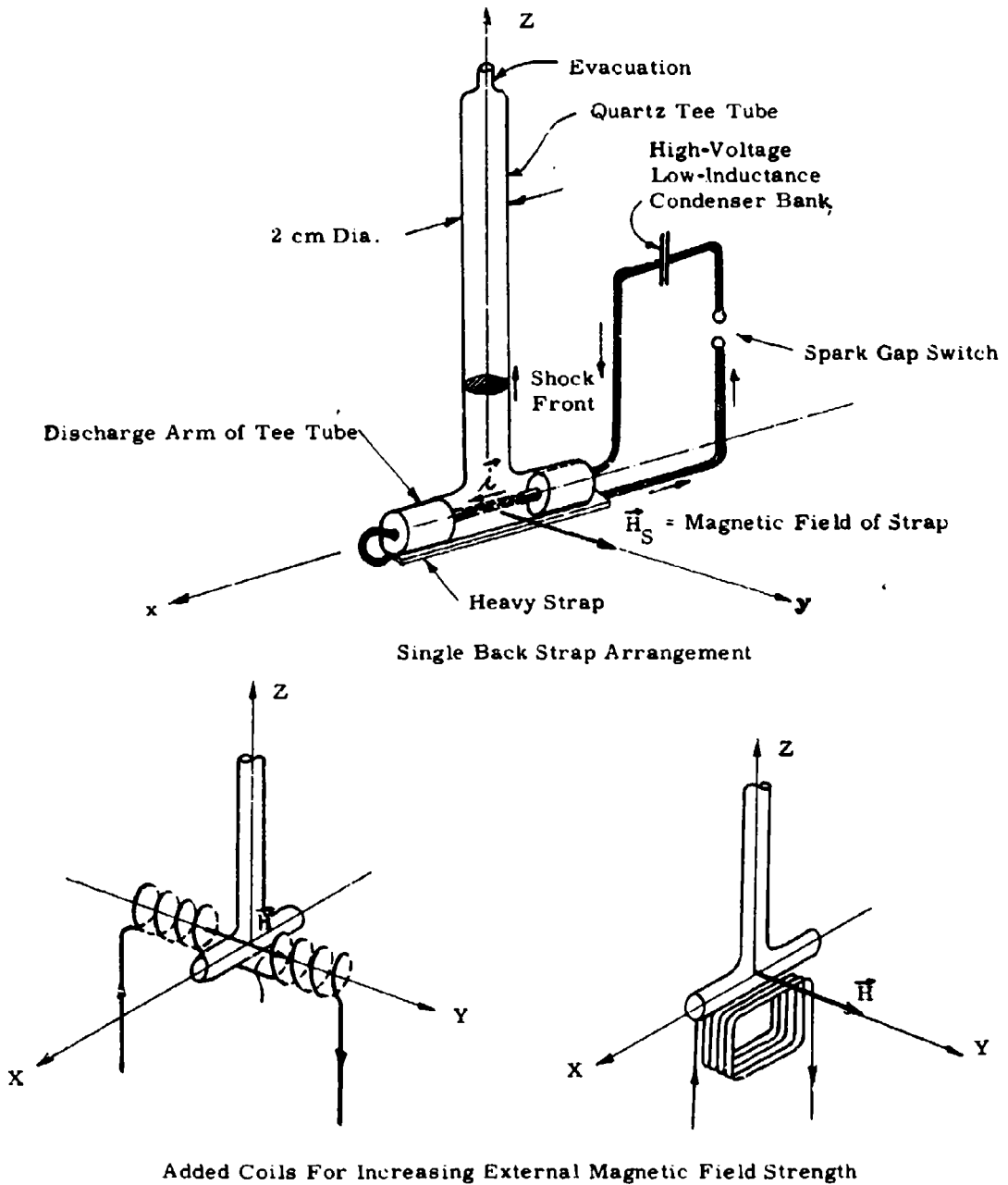
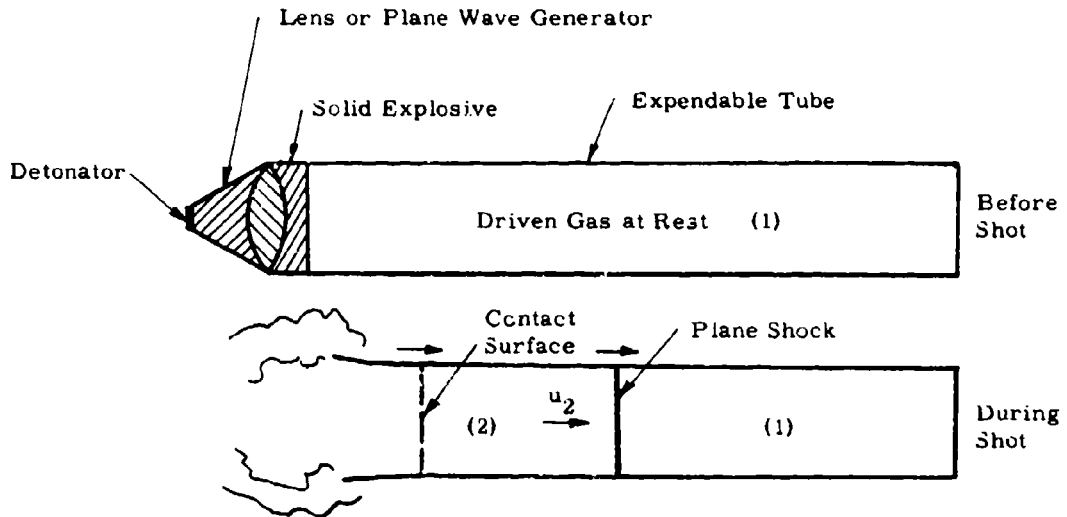
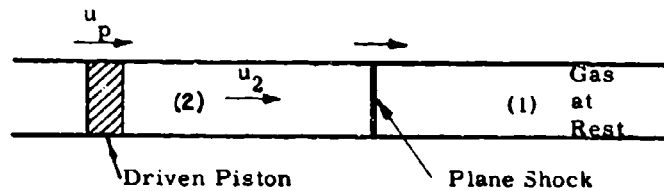


Fig. 4.3-1. Electric discharge shock tube with magnetic push.



Solid-Explosive Drive (see, for example, Ref. 25)



Piston Drive

Fig. 4.3-2. Solid-explosive and piston drives.

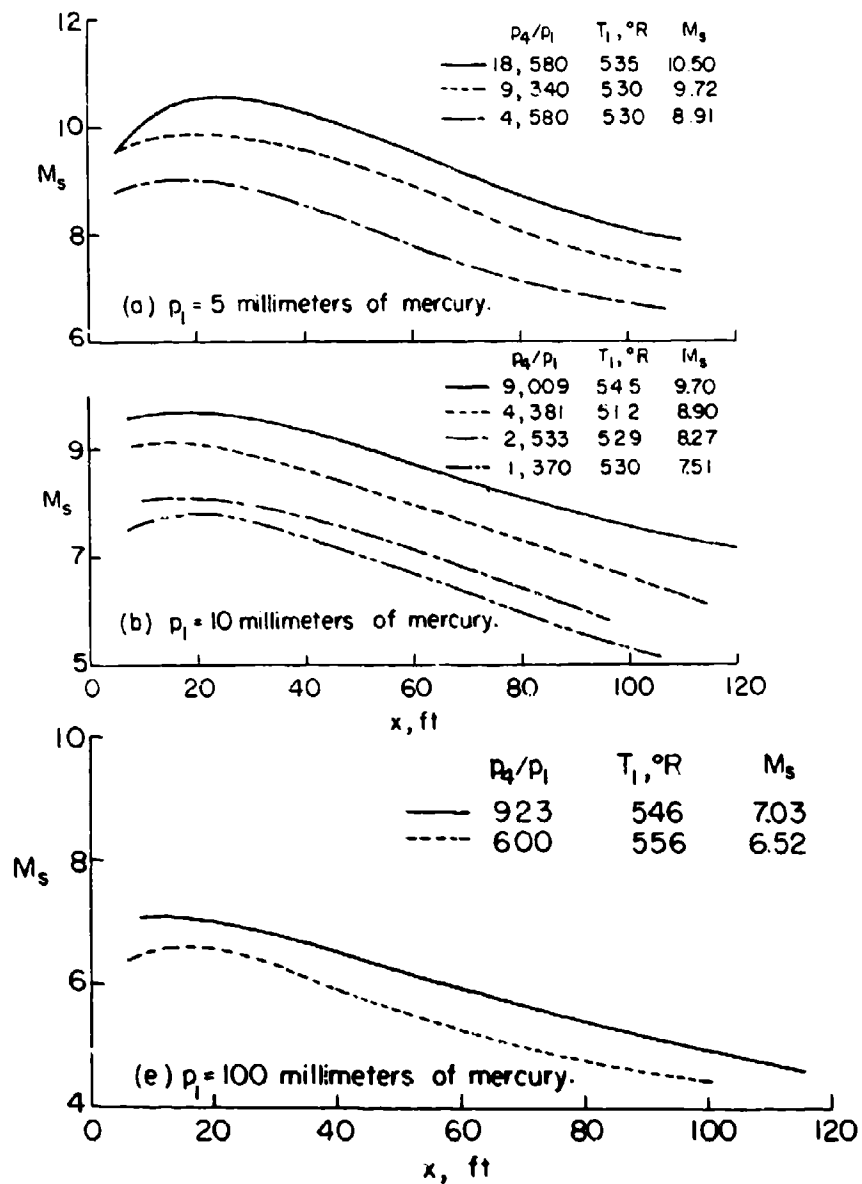
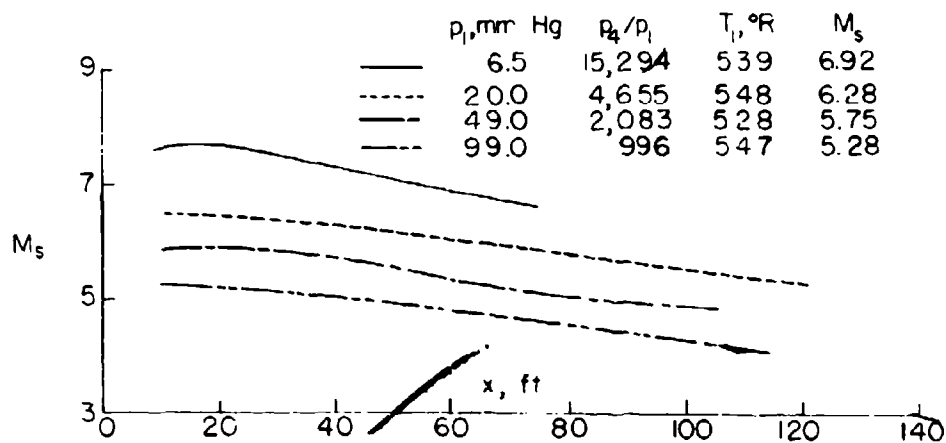
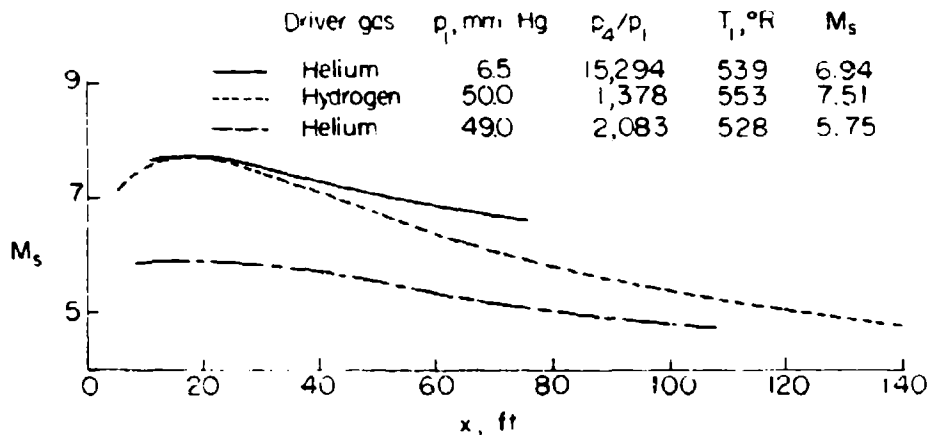


Fig. 4.4-1. Experimental shock-wave attenuation in air with distance x from diaphragm for cold hydrogen drive; constant-area shock tube, 3.75-in. I.D. (Ref. 21).

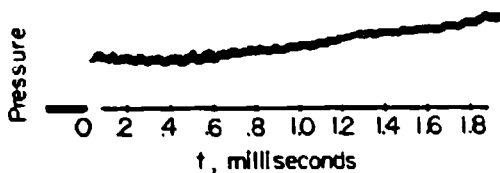


Typical shock-wave attenuation data with helium as driver gas.

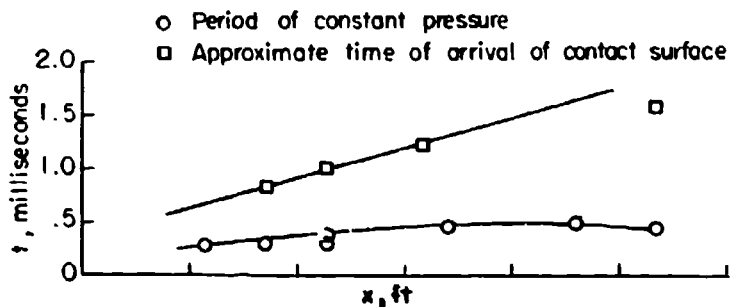


Comparison of the effects of hydrogen and helium driver gases on shock-wave attenuation.

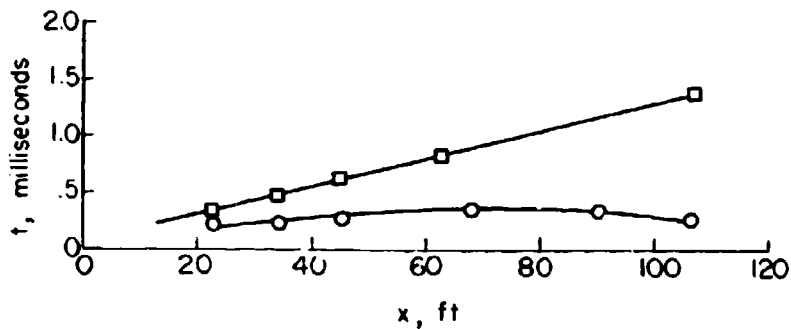
Fig. 4.4-2. Experimental shock-wave attenuation in air with distance x from diaphragm for cold helium drive and for cold helium and hydrogen; constant-area shock tube, 3.75-in. I.D. (Ref. 21).



(a) Typical pressure-indicator record.



(b) $p_1 = 20$ millimeters of mercury; $p_h/p_1 \approx 1,250$.



(e) $p_1 = 10$ millimeters of mercury; $p_h/p_1 \approx 5,000$.

(t is time following arrival of shock wave at station x ft from diaphragm.)

Fig. 4.4-3. Experimental wall pressure results with air in low-pressure channel for cold hydrogen drive. Constant-area shock tube, 3.75-in. I.D. (Ref. 21).

REFERENCES

1. Lin, Shao-Chi. "Electrical Conductivity of an Ionized Gas Produced by Strong Shock Waves." Unpublished Ph. D. Dissertation, Cornell University, 1952.
2. Resler, E. L., Lin, Shao-Chi, and Kantrowitz, A. "The Production of High Temperature Gases in Shock Tubes," J. Appl. Phys., Vol. 23 (December 1952), pp. 1390-1399.
3. Rose, P. Physical Gas Dynamics Research at the AVCO Research Laboratory. AVCO Research Note 37. Everett, Mass.: AVCO Research Laboratory, AVCO Manufacturing Corp., 1957.
4. Fowler, R. G., Goldstein, J. S., and Clotfelter, B. E. "Luminous Fronts in Pulsed Gas Discharges," Phys. Rev., Vol. 82 (June 1951), pp. 879-882.
5. Fowler, R. G., Atkinson, W. R., Compton, W. D., and Lee, R. J. "Shock Waves in Low-Pressure Spark Discharges," Phys. Rev., Vol. 88 (October 1952), pp. 137-138.
6. Fowler, R. G., Atkinson, W. R., Clotfelter, B. E., and Lee, R. J. Final Report, Research on Radiation Transients in Gas Discharges. Project 52. University of Oklahoma Research Institute, December 1952.
- 6a. Bloxson, D. E., Jr. "Electrically Driven Shock Tubes," J. Appl. Phys., Vol. 29 (July 1958), p. 1128.
7. Atkinson, W. R. One-Dimensional Fluid Flow Produced by Confined Sparks. Project 87. University of Oklahoma Research Institute.
8. Allen, L. H. Astrophysics, the Atmosphere of the Sun and Stars. New York: The Ronald Press, 1953.
9. Epstein, Paul S. Textbook of Thermodynamics. New York: John Wiley and Sons, Inc., 1937, pp. 315-321.
10. Bernstein, H. "A Double-Diaphragm Shock Tube to Produce Transient High Mach Number Flow," J. Aeronaut. Sci., Vol. 20 (November 1953), pp. 790-791.
11. Yoler, Y. A. Hypersonic Shock Tube. GALCIT Memo No. 18. Guggenheim Aeronautical Laboratory, Hypersonic Wind Tunnel, California Institute of Technology, 1954.
12. Henshall, B. D. The Use of Multiple Diaphragms in Shock Tubes. ARC 18,062. Aeronautical Research Council, Ministry of Supply. London: Her Majesty's Stationery Office, 1955.
13. Bird, G. A. A Note on Multiple-Diaphragm Shock Tubes. RAE TN Aero 2469. Farnborough, Hants, England: Royal Aeronautical Establishment, 1956.

14. Hertzberg, A. and Smith, W. "A Method for Generating Strong Shock Waves," J. Appl. Phys., Vol. 25 (January 1954), pp. 130-131.
15. Hertzberg, A. "The Application of the Shock Tube to the Study of the Problems of Hypersonic Flight," Jet Propulsion, Vol. 26, No. 7, (July 1956).
16. Lewis, B. and Von Elbe, G. Combustion, Flames, and Explosions of Gases. New York: Academic Press, Inc., 1951, pp. 644-647.
17. Lukasiewicz, J. Shock Tube Theory and Applications. NAE Report 15. Ottawa, Canada: National Aeronautical Establishment, 1952. (Originally published as Reports MT-10 and MT-11. Ottawa, Canada: Division of Engineering, National Research Council, January 1950.)
18. Alpher, R. A. and White, D. R. Ideal Theory of Shock Tubes with Area Change Near Diaphragm. Report 57-RL-1664. Schenectady, N.Y.: General Electric Research Laboratory, January 1957.
19. Laporte, Otto. On the Interaction of a Shock with a Constriction. LA-1740. Los Alamos, N. Mex.: Los Alamos Scientific Laboratory, University of California, August 1954.
20. Russo, A. and Hertzberg, A. "A Method for Improving the Performance of Shock Tubes," Jet Propulsion, Vol. 27, No. 11 (November 1957), p. 1191.
- 20a. Schexnayder, C. J., Jr. "On the Performance of a Double-Diaphragm Shock Tube Using the Reflected-Shock Method and a Light-Gas Buffer," J. Aero/Space Sci., Vol. 25, No. 8 (1958), p. 527. The experimental results substantiate the advantages of the double-diaphragm technique.
21. Jones, J. J. Experimental Investigation of Attenuation of Strong Shock Waves in a Shock Tube with Hydrogen and Helium as Driver Gases. NACA TN 4072, 1957.
22. Kolb, A. C. "Magnetically Driven Shock Waves," Bull. Am. Phys. Soc., Series II, Vol. 2, No. 1 (January 1957). (Also, paper delivered at Lockheed Magnetohydrodynamics Symposium, December 1956, to be published by Stanford University Press.)
23. Kash, S. W., Gauger, J., Starr, W. L., and Vali, V. "Velocity Attenuation of Strong Shocks in Air," Bull. Am. Phys. Soc., Series II, Vol. 2, No. 4 (1957), p. 216. (Also, Private Communication with J. Gauger, Lockheed Missiles Systems Division, Sunnyvale, California.)
24. Blackman, V. H., Niblett, G. B. F., and Schrank, G. "Hydromagnetic Shock Tube," Bull. Am. Phys. Soc., Series II, Vol. 2, No. 4 (1957), p. 216.
25. Schreffler, R. G. and Christian, R. H. "Boundary Disturbance in High-Explosive Shock Tubes," J. Appl. Phys., Vol. 25 (March 1954), pp. 324-331.
26. Deal, W. E. "Shock Hugoniot of Air," J. Appl. Phys., Vol. 28 (July 1957), pp. 782-784.

27. Wittliff, C. E. and Wilson, M. R. Shock-Tube Driver Techniques and Attenuation Measurements. Report AD-1052-A-4. Buffalo, N.Y.: Cornell Aeronautical Laboratory, Inc., August 1957.
28. White, D. R. "On the Existence of Higher than Normal Detonation Pressures," J. Fluid Mech., Vol. 2, Part 5 (July 1957), p. 513.
29. Bird, G. A. Some Methods of Evaluating Imperfect Gas Effects in Aerodynamic Problems. RAE TN Aero-2488. Farnborough, Hants, England: Royal Aircraft Establishment, January 1957.
30. Waldron, H. F. An Experimental Investigation of the Flow Properties Behind Strong Shock Waves in Nitrogen. UTIA Report 50. Institute of Aerophysics, University of Toronto, March 1958.
- 30a. Rose, P. H. and Nelson, W. On the Effect of Attenuation on Gas Dynamic Measurements Made in Shock Tubes. AVCO Research Report 24. Everett, Mass.: AVCO Research Laboratory, AVCO Manufacturing Corp., 1958. Effects on heat transfer rate and shock detachment distance are evaluated.
31. deLeeuw, J. H. and Waldron, H. F. The Combustion Driven Shock Tubes at the Institute of Aerophysics and Their Instrumentation. UTIA Report. Institute of Aerophysics, University of Toronto (to be published).
32. Alpher, R. A. and White, D. R. "Flow in Shock Tubes with Area Change at the Diaphragm Section," J. Fluid Mech., Vol. 3, Part 5 (February 1958), pp. 457-470.
33. Winkler, E. H. Private Communication. White Oak, Md.: Naval Ordnance Laboratory, November 8, 1957.
34. Bird, G. A. A Note on Combustion Driven Shock Tubes. RAE TN Aero-2511. Farnborough, Hants, England: Royal Aircraft Establishment, 1957.

5. Applications of the Shock Tube

Applications of the shock tube to be outlined in this subsection include use as a wind tunnel (Subsec. 5.1) covering both uniform or constant-area channel testing (Subsec. 5.1.1) and the hypersonic shock tunnel (Subsec. 5.1.2); use in aerophysics research for study of phenomena as wave interactions, wave diffraction, transition fronts, boundary layers, and high-temperature phenomena (Subsec. 5.2); use in chemical research for combustion and chemical kinetics studies (Subsec. 5.3); and use for calibration of instruments (Subsec. 5.4). With such a wide coverage of applications, detailed discussion of the results of specific researches cited is generally not attempted. Rather, the intent is to illustrate the method of application and provide sufficient documentation for the reader to pursue further details desired.

5.1 Use as a Wind Tunnel

5.1.1 Shock Tube with Uniform or Constant-Area Channel

5.1.1.1 Use in Subsonic, Transonic, Supersonic, and Hypersonic Research

The use of the uniform-channel shock tube (i.e., a shock tube with the low-pressure channel of constant area) as a short duration wind tunnel for aerodynamic testing has both advantages and disadvantages relative to conventional steady-flow wind tunnels in which equal flow conditions may be attained. Significant advantages of the shock tube are the low initial and operating costs, and the ease with which the flow Mach number and Reynolds number may be controlled by varying the initial driving conditions as diaphragm pressure ratio and the initial channel pressure. Two serious disadvantages are the very short test-flow durations obtained with tubes of convenient lengths, and the fact that, in practice, only the relatively low Mach number region (2) between the primary shock wave and the contact surface provides a useful test flow. In practice, the high theoretical Mach numbers of region (3) upstream of the contact surface are not attained (see Subsec. 3.1), and more important, the flow of region (3) for simple shock tubes of constant area throughout is found to be too nonuniform to be useful for testing (Refs. 4, 5, and 14). The resulting limit on flow Mach number set by the use of region (2) is 1.89 for a perfect diatomic gas (no excitation of inert degrees of freedom) and from 2 to 3 for equilibrium air behind strong primary shocks. Despite this Mach number limitation, however, the uniform-channel shock tube as a wind tunnel has an important application to hypersonic research, as discussed below, in producing high stagnation temperature conditions not attainable in conventional wind tunnel facilities.

The principal difficulty resulting from the very short test-flow durations obtained in the shock tube is the severe requirement placed on instrumentation response. Typical test times in practice might lie in the range of 0.1 to 10 milliseconds. Non-ideal flow and real gas effects aggravate the situation. Test-flow duration is further discussed under Performance below.

The attainment of large model Reynolds numbers in the shock tube presents a further difficulty, particularly so in the transonic range. Structural limitations of the high-pressure driver section

limit the pressure (density) level of region (2) for a given primary shock strength, and the large tube cross-sections required for high model Reynolds numbers create a difficult diaphragm problem.

The possibility of using the uniform-channel shock tube as a very short duration, intermittent wind tunnel for aerodynamic testing was suggested by several workers around 1949 (Refs. 1, 2, and 3). Geiger, Mautz, and Hollyer (Ref. 4) at the University of Michigan first used the quasi-steady flow of hot region (2) in this way in a 2 x 7-in. cross-section tube to study by optical means the development of subsonic, transonic, and supersonic flows about two-dimensional airfoils. Similar studies in a 2 x 7-in. tube were done about the same time by Lobb (Ref. 5) at the University of Toronto who also investigated the use of cold region (3) upstream of the contact surface. Since these initial applications, however, the uniform-channel shock tube as a wind tunnel has not come into common use wherever the same flow conditions may be attained in conventional wind tunnels giving much longer test-flow durations. Undoubtedly the difficult instrumentation problem in the shock tube has been primarily responsible for its limited use in this direction.

Applications as a wind tunnel which have been made have used hot region (2) and relied chiefly on the optical instrumentation techniques of shadowgraph, schlieren, and interferometry (Subsec. 7.2.1). In particular, spark interferometry has proved invaluable for quantitative flow studies. In the subsonic to supersonic research fields, the applications include study of vortex shedding from a circular cylinder (Ref. 7) and study of the transient aerodynamics of two-dimensional airfoils subjected to a step shock wave (Ref. 9) at subsonic speeds; detailed study of flow about two-dimensional wedges (Ref. 8) at transonic speeds; and study of flow past circular cylinders (Ref. 18) at supersonic speeds. Reference 15 gives a thorough discussion of applications to transient aerodynamic and aircraft structures research where the uniform-channel shock tube provides a unique method of studying transient response to gust loading (supplied by the primary shock wave).

Although it has seen limited use for conventional subsonic to supersonic testing, the uniform-channel shock tube now appears to be coming into common use as a wind tunnel for certain hypersonic studies where very high stagnation temperature simulation is required with attendant real gas effects, and where flight Mach number simulation can be disregarded. In this respect, the uniform-channel shock tube can provide flow conditions not attainable in conventional hypersonic wind tunnels. The very high stagnation temperature and the stagnation densities appropriate to hypersonic flight can be achieved without difficulty in the flow of hot region (2) behind sufficiently strong shocks. Kantrowitz (Ref. 10), in 1955, suggested the use of the uniform-channel shock tube in this way to study certain problems critical to extreme hypersonic flight, such as the high aerodynamic heat transfer at the stagnation region of hypersonic blunt bodies. He pointed out that the high flight stagnation temperatures and stagnation densities (required to produce the real gas effects of flight) could be attained in region (2), and that simulation of the stagnation region boundary-layer flow for blunt bodies would not be seriously limited by the low maximum Mach number of region (2) since the blunt body stagnation flow was essentially independent of free-stream Mach number above Mach numbers of about 2. For example, at a free-stream Mach number of 2 (and above) the pressure distribution over the nose of a hemisphere-cylinder closely follows the Newtonian approximation, which is independent of Mach number (Ref. 11).

Following this philosophy, the AVCO Research Laboratory has used the uniform-channel shock tube as a short-duration wind tunnel to simulate and study aerodynamic heat transfer occurring at the stagnation point of a blunt body moving at hypersonic velocities of up to 26,000 ft/sec at altitudes up to 120,000 ft (Refs. 12 and 13). In this work, very fast response thin-film resistance thermometers (Subsec. 7.3.1) and calorimeter gauges (Subsec. 7.3.3) were used to measure stagnation point heat transfer rates on hemispherical pyrex models in the hot flow of region (2) generated behind shocks of Mach numbers up to 17 in air. One-half-inch and 1-in. diameter models were employed in 1-1/2-in. and 4-in. diameter shock tube channels, respectively. The stagnation temperature range of the experiments extended from values giving negligible air dissociation up to values (corresponding to maximum flight velocity of 26,000 ft/sec) where the energy of dissociation accounted for more than 60 per cent of the total stagnation energy of the air.

Reference 14 reports similar use of a 2-7/8 x 2-7/8-in. shock tube to measure local heat transfer rates over the circumference of a normal circular cylinder in the hot flow of region (2) behind shocks of Mach numbers up to 7. A thin-film resistance thermometer of small dimension in the circumferential direction was used, and cylinder pressure distribution was deduced from the measured heat transfer rates. Thin-film thermometer measurements of turbulent heat transfer rates on the aft portion and on the flat base of a hemispherical nosed cylinder (axially aligned) in the same shock tube are reported in Ref. 14a. Turbulent boundary layer over the cylinder afterbody was ensured by deliberate flow separation at the nose.

Figure 5.1-1 from Ref. 12 shows the range of conditions attainable in region (2) of the uniform-channel shock tube which produce the stagnation enthalpy and stagnation density of given flight velocity and altitude. For both the flight and model stagnation boundary layers in either thermochemical equilibrium throughout or else of constant chemical composition (i.e., "frozen" composition) throughout, reproduction of flight stagnation enthalpy and stagnation density in the shock tube achieves effectively complete flow simulation. When the stagnation region boundary layer is neither in equilibrium nor fully "frozen", however, simulation of the flow chemistry requires consideration of the finite atom recombination rate (Ref. 12).

At the present time at least, the uniform-channel shock tube, where applicable as a hypersonic facility, has an important advantage over the hypersonic shock tunnel (Subsec. 5.1.2). This advantage is the fact that the test-flow properties in the uniform channel (region (2)) may be better determined (from measured shock speed) than those in the expanded-flow test section of the shock tunnel.

5.1.1.2 Performance

Considerations relevant to the performance of the uniform-channel shock tube as a wind tunnel using hot region (2) include the driving method used, the flow properties and aerodynamic parameters of region (2), and the useful test-flow duration. Driving methods are covered in Subsec. 4. Test-flow properties and duration are considered below.

Test-Flow Properties.--The general flow properties of hot region (2) as a function of primary shock strength are covered in Subsec. 2.3.2 (perfect gas) and Subsec. 2.3.3 (real gas). Flow nonuniformities and nonequilibrium effects in region (2) will be elaborated on here.

Flow nonuniformities in region (2) (Subsec. 3.1.3) resulting from tube wall boundary-layer development (Subsec. 3.2) require consideration in wind tunnel applications. For sufficiently long hot-flow duration at the test station, the thickening boundary layer will eventually fill the tube cross-section. Thus a criterion for tube cross-section area is that it be sufficiently large to avoid significant boundary-layer interference in the desired test-flow duration.

For model testing, the variations of test flow properties with time at the test station are desired as small as possible. However, some variations with time always exist in practice and may necessitate corrections to test results. When the tube wall boundary layer is thin relative to the tube diameter, the methods reviewed in Subsec. 3 will provide an estimate of time variations of flow properties in region (2) up to moderate shock strengths. In particular, for shock Mach numbers up to 6 in air, Mirels and Braun (Ref. 17) present results in convenient graphical form for both laminar and turbulent wall boundary layers. For a given shock strength, if the state of the boundary layer is known and also the decrement in shock strength at the test station due to attenuation (calculated from Ref. 17, or measured), the variations with time of the free stream properties of region (2) at the test station may be quickly determined.

In wind tunnel applications using region (2) behind primary shock waves in air strong enough to produce excitation of inert degrees of freedom, as vibration and dissociation, the question of whether the test flow is in desired thermodynamic equilibrium is important. For the diatomic gases oxygen and nitrogen, vibrational relaxation times have been well enough established (Ref. 16) to permit a reliable answer for vibration effects. The dissociation relaxation times, however, are as yet not as well known. Figure 5.1-2 from Ref. 13 gives estimated vibration and dissociation relaxation distances for region (2) (i.e., distances a fluid particle moves, after set into motion by the shock wave, before thermodynamic equilibrium is attained) as a function of shock Mach number in air at various densities. For these curves, the vibration relaxation times of oxygen and nitrogen in air at a given total pressure were assumed equal to measured values in either gas alone at the same pressure. The dissociation relaxation times were calculated on the basis of a recombination rate constant of $10^{17} \text{ cm}^6 \text{ mole}^{-2} \text{ sec}^{-1}$ for both oxygen and nitrogen in air. The results of Fig. 5.1-2 indicate a need for care in using the shock tube as a wind tunnel at low densities and with moderately strong shocks where significant non-equilibrium effects in the test flow may be present.

Test-Flow Duration.--For steady-flow tests in hot region (2) the useful test-flow duration is the interval Δt between arrival of the primary shock wave and arrival of the contact surface at the model (assuming no interference from reflected primary shock or rarefaction waves), minus the time required for steady flow to develop about the model. For a given length L_1 of low pressure channel, the optimum model location x_p giving maximum time Δt is at the point of collision of the reflected primary shock with the contact surface, as shown in

the x, t diagram of Fig. 5.1-3. The minimum length L_4 of high pressure chamber to avoid interference from the reflected rarefaction wave is that for which the first reflected characteristic C_0^+ of the rarefaction wave overtakes the contact surface at x_T . Figure 5.1-3 illustrates the minimum length L_4 for a shock tube of constant cross-section area throughout.

Equations for the dimensionless ratios $L_1/(a_1 \Delta t)$, L_1/x_T , and L_1/L_4 are given in Fig. 5.1-3 in a form convenient for taking real-gas effects into account. It will be noted that the ratios $L_1/(a_1 \Delta t)$ and L_1/x_T depend only on the driven gas (state 1) and primary shock Mach number M_S . The ratio L_1/L_4 , however, depends on the driving method also, and the expression given is for a constant-area shock tube with an ideal centered rarefaction wave connecting regions (4) and (3). Graphical results computed from these expressions for air as the driven gas are given as a function of primary shock Mach number in Figs. 5.1-4 to 5.1-7. Results are shown for both equilibrium air in region (2) and also air as a perfect gas with constant specific heat ratio 1.4. Figure 5.1-4 gives $L_1/\Delta t$ in ft/millisecc for $T_1 = 293^\circ\text{K}$. Figure 5.1-5 gives L_1/x_T . For stronger shocks, the real-gas effects across the shock are seen to produce a very large reduction in Δt for a given channel length L_1 . Figures 5.1-6 and 5.1-7 give L_1/L_4 for air, helium, hydrogen, and oxygen-hydrogen combustion drives in a constant-area shock tube. The real-gas effects across the shock wave reduce the required chamber length L_4 for a given channel length L_1 (Fig. 5.1-7).

In practice, the contact surface is an extended region of turbulent mixing which arrives at the test station considerably sooner than predicted by theory (Subsec. 3.1). Consequently, the values of Δt realized in practice are considerably less than those predicted by the real-gas curves of Fig. 5.1-4. Reference 14 reports measurements of Δt for shock Mach numbers in air from about 4 to 8 in a 2-7/8 by 2-7/8-in. channel driven by cold helium. Scribed metal diaphragms, generally burst by pressure alone, were used. The measured values of Δt at $x_T = 20$ ft are roughly 50 per cent of those predicted by the real-gas theory. Reference 12 reports experimental results of the same order for shock Mach numbers in air up to 17.

Rather limited experimental evidence is available as to the time required for the flow about models to become fully developed after passage of the primary shock wave. Lukasiewicz (Ref. 6) gives a rough estimate for flat-plate boundary-layer development as the order of three model chord lengths of flow, assuming a laminar Rayleigh flow buildup to steady flow Blasius boundary layer displacement thickness and wall shear stress. In the subsonic range, Ref. 15 reports that the circulation development about two-dimensional airfoil models is substantially complete experimentally after 10 chord lengths of flow. For supersonic flow in region (2), attached shocks about models will form very rapidly, while detached shocks will require some time to reach the stable detached position. Figures 5.1-8 and 5.1-9 from Ref. 4 show measured detached bow-shock positions as a function of time after passage of the tube primary shock wave for 30-degree and 45-degree wedge-tipped two-dimensional bodies of various thicknesses. The time required

for the detached shock to reach the stable position increases as the flow Mach number M_2 approaches 1. Reference 4 points out that the flow near the trailing edge and at points away from the body may be changing for some time after the central portion of the detached shock has stabilized. In this connection, it is evident also that the body wave system interacts with the shock-tube wall boundary-layer (Subsec. 3.2) which is continually thickening with time.

Stagnation point heat transfer measurements on blunt bodies located in the flow of region (2) generated by strong shocks show steady-flow heat transfer rates to be attained very quickly (Refs. 12 and 14). The results of Ref. 12, for example, at a shock Mach number of 13 in air show steady-flow heat transfer to be attained at the stagnation point of a 1/2-in. diameter hemisphere-cylinder within about 10 microsec following passage of the primary shock. Similar measurements of Ref. 14 for a 1/4-in. diameter circular cylinder normal to the flow and shock Mach numbers around 5 show steady-flow stagnation line heat transfer to result after some 25 to 30 microsec.

Little appears to be known of the times required for the base region and wake flows to become fully established. Shock-tube heat-transfer measurements on the flat base of a hemispherical nosed cylinder aligned with the flow are reported in Ref. 14a. The experiments were done in a 2-7/8 by 2-7/8-in. tube with a 3/4-in. diameter, 2-5/8-in. long model at shock Mach numbers between 3.5 and 4 (limited by choking). Initial air pressures p_1 ranged from 3 to 17 cm Hg giving Reynolds number per cm from 3.5×10^4 to 3×10^5 . Turbulent boundary layer over the cylinder afterbody was achieved by using a spike at the nose to produce flow separation and reattachment. The base heat-transfer results indicate a constant heat-transfer rate to be established after about 100 to 150 microsec of shock-induced flow. Further studies of the establishment of base and wake flows are needed before shock-tube model flow studies can be interpreted with confidence.

5.1.1.3 Instrumentation

General shock-tube instrumentation is considered in detail in Subsec. 7. The basic experimental parameter measured in shock-tube tests is the primary shock wave speed. This can be measured accurately by the methods of Subsec. 7.4.1, and from its value the flow properties of region (2) can be determined. A measure of shock wave attenuation is also desirable for purposes of estimating variations of test-flow properties with time at the test station.

The optical techniques of shadowgraph, schlieren, and interferometry are very useful for shock-tube studies of flow fields about models (Subsec. 7.2.1). Their effective response time can be reduced below one microsecond by the use of very short duration light sources (Subsec. 7.2.1.5). In particular, spark interferometry has proved very useful for quantitative determination of density throughout two-dimensional flow fields.

Heat transfer measurement in the short flow times available in the shock tube has become possible with the development of fast-response thin-film resistance thermometers (Subsec. 7.3.1) and the fast-response calorimeter gauge (Subsec. 7.3.3).

Much remains to be done in the development of small fast-response pressure transducers suitable for direct measurement of model pressure distributions (Subsec. 7.1.2). Development of direct force measuring instrumentation has received little attention as yet (Subsec. 7.8).

5.1.2 Hypersonic Shock Tunnels

5.1.2.1 General Characteristics

Hertzberg in 1951 (Ref. 20) demonstrated that the Mach number limitation of hot region (2) in the uniform-channel shock tube could be overcome by expanding the hot flow in a divergent nozzle fitted to the end of the low-pressure channel. He pointed out that by using sufficiently high temperatures in region (2) (determined by primary shock strength) air in region (2) could be expanded to high hypersonic Mach numbers with static temperatures after expansion amply high enough to avoid the conventional hypersonic wind tunnel problem of air liquifaction. Since 1951, the development of the hypersonic shock tunnel* as a practical facility for hypersonic testing beyond the range of conventional blow-down tunnels has been vigorously pursued (e.g., Refs. 20 to 30, inclusive). In particular, in the U.S.A. the Cornell Aeronautical Laboratory has been active in this development (Refs. 20, 23, 24, 25, 26, and 27). Shock tunnel facilities have also appeared recently in the United Kingdom (Refs. 28, 29, 30, and 32).

It is too early yet to predict the ultimate usefulness of shock tunnels as practical hypersonic test facilities. The bulk of the effort to date has gone into basic development of shock-tunnel technique. Emphasis has been placed on development of model and tunnel instrumentation, and in overcoming tunnel starting losses and problems associated with primary shock wave attenuation and boundary-layer buildup such as limitation of test-flow duration and variation of test-flow properties with time. The most promising technique in development at the present time appears to be the so-called tailored-interface reflected-shock method (Refs. 27 and 94) described below, which avoids the boundary-layer difficulties of the non-reflected method and provides milliseconds of test-flow duration.

While the short durations of (high stagnation temperature) shock-tunnel flows avoid severe structural and metallurgical problems due to heating, the resulting instrumentation difficulties are well known. While model heat-transfer rates are now measurable in the shock tunnel with the development of fast response thin-film and calorimeter heat-transfer gauges (Subsec. 7.3), much remains to be done on development of model-mounted pressure transducers and direct force measuring instrumentation. The accurate determination of the test-section flow properties also remains an outstanding problem.

Regarding simulation, the hypersonic shock tunnels as hitherto developed cannot simulate simultaneously all parameters of interest such as Mach number, model Reynolds number, stagnation temperature, and ratio of (heated) model surface to static stream temperature. However,

* That is, uniform-channel shock tube plus divergent nozzle and test section; also referred to as an impulse tunnel.

this situation is more usual than not in wind tunnel facilities of any kind. In the shock tunnel, hypersonic flight Mach number and stagnation temperature simulation is possible with sacrifice of desired model Reynolds number, although the Reynolds numbers attainable in moderate installations are adequate to give useful data. By lowering the test-flow static temperature to near the liquifaction limit and retaining the Mach number (using same nozzle but a weaker primary shock wave) the Reynolds number is improved considerably and the ratio of model-surface temperature to free-stream static temperature becomes realistically larger. However, the test-flow stagnation temperature is below that of flight. Stagnation temperature and density (or Reynolds number) simulation can be obtained by sacrificing Mach number, and the limiting method here is testing in a uniform channel as discussed in Sub-sec. 5.1.1.

Numerous possible methods of using the shock tube for the generation of high Mach number flows are described in Ref. 23. Three methods in present use are briefly outlined below. These are the so-called non-reflected or straight through method, the (tailored-interface) reflected shock method, and the hypersonic gun tunnel.

5.1.2.2 Non-Reflected Shock Tunnels

In the non-reflected method (Ref. 23) the primary shock wave travels directly through a diverging nozzle and test section after reaching the end of the low-pressure channel, as shown in Fig. 5.1-10. The nozzle expands the hot flow of region (2) at supersonic Mach number M_2 to the higher test Mach number M_T . If region (2) is subsonic, the nozzle must have an initial contraction to a sonic throat preceding the divergence. The test section is followed by a receiver vessel designed to avoid interference from reflection of the primary wave system which initiates flow in the nozzle. A schematic drawing of a hypersonic shock tunnel employing two-stage bilateral expansion in use at the Cornell Aeronautical Laboratory, Buffalo, N. Y., is shown in Fig. 5.1-11.

If the primary shock Mach number M_S is relatively large, M_2 is close to its asymptotic limit and relatively independent of M_S . Thus, for fixed nozzle geometry, M_T is independent of M_S also. Test-section static temperature can then be varied at constant M_T by varying M_S . Test section density is controlled by M_S and the initial channel density in region (1).

The flow in the nozzle and test section requires a finite time to be established, and this results in a certain unavoidable loss of useful testing time from the nominal value of Fig. 5.1-10. The primary shock wave is continuously weakened (and curved) as it travels through the diverging nozzle. The low-pressure channel flow behind region (2) with $M_2 > 1$ undergoes steady expansion in the nozzle, and in effect overexpands. Its pressure and velocity from steady expansion are matched to those induced by the weakening primary shock by formation of a secondary shock wave which faces upstream but is swept downstream. The secondary wave strengthens as it moves downstream, and for sufficiently large nozzle expansions it can strengthen to the point where it becomes stationary with respect to the nozzle walls. To avoid

this condition which prevents the nozzle from starting, and to minimize starting time, a weak secondary diaphragm is used at the nozzle entrance (Fig. 5.1-10), and the nozzle is highly pre-evacuated so that the initial nozzle pressure p_3 is less than p_1 . Pre-evacuation of the nozzle weakens the secondary shock wave and reduces the time for it to be swept through the nozzle. Minimum starting time results when p_3 is sufficiently low to allow the secondary shock to become a sound wave which is swept through the nozzle at local speed $(u - a)$, as in Fig. 5.1-10.

Uniform flow ceases at the test section on arrival of a wave of speed $u + a$ generated when the primary contact surface or interface reaches the end of the low-pressure channel. The minimum loss in testing time due to nozzle starting is then the difference in times taken for the $u - a$ and $u + a$ waves to traverse the nozzle. References 24 and 29 consider the nozzle starting phenomena in detail and give quantitative results for starting losses. Clearly, the nozzle length should be as short as possible to minimize these losses.

To date, nozzle construction has been simplified by the use of straight walled source-flow nozzles rather than the Busemann type giving parallel flow. To limit test-section size and avoid excessive boundary-layer buildup, the nozzle expansion may be done in two stages (Ref. 23) as indicated in Fig. 5.1-10. Only a small central core of uniform flow is expanded in the second stage; the remainder, including the shock-tube wall boundary-layer flow, is bypassed (see also Fig. 5.1-11). With strong primary shock waves giving high temperature T_2 with air, real-gas effects in the nozzle are significant (Ref. 25). For example, the required nozzle expansion ratio for a given test Mach number is considerably increased with equilibrium air flow over that for perfect air flow with constant specific heat ratio 1.4. Significant departures from equilibrium flow may be expected with sufficiently large nozzle cooling rates, although nonequilibrium effects will generally be smaller in non-reflected than in reflected shock tunnels. Relaxation phenomena to be expected from the rapid expansions in hypersonic nozzles are considered in Ref. 18. Calculations of Ref. 18 indicate that frozen flow near the nozzle entrance due to extreme cooling rates there can reduce the final equilibrium test-section Mach number by the order of 50 per cent. Calculation of test-section flow properties from measured test Mach number assuming equilibrium flow throughout can result in large errors (particularly in pressure) if the early nozzle flow is frozen. It is evident that much further work is required (in particular, experimental studies) before nonequilibrium effects in hypersonic nozzles are well understood.

Real-gas effects also have considerable influence on other shock-tunnel parameters as testing time and test-section Reynolds number. For example, at a test Mach number of 10, the (equilibrium) test Reynolds number is reduced by a factor of the order of 10 from the ideal gas value. Perfect-gas testing times are roughly halved for high Mach numbers when real-gas effects are considered. Detailed consideration of the effects of equilibrium real-gas behaviour on shock-tunnel performance is given in Ref. 25.

An outstanding problem encountered with the non-reflected method is the boundary-layer development on the low-pressure channel walls and the consequent attenuation of the primary shock wave (see Subsecs. 3.2 and 4.4, and Ref. 23). The most serious difficulty arising from the boundary-layer buildup is the consequent nonuniformity of

the region (2) free-stream flow. As a result, the flow entering the hypersonic nozzle, and thus the expanded test-section flow downstream, will undergo some variation with time throughout the test-flow duration. The boundary-layer buildup also limits the useful time attainable if the plane of boundary-layer closing (i.e., the plane where the thickening boundary layer first fills the channel completely) arrives at the end of the low-pressure channel before the contact surface. The problem is aggravated by the long low-pressure channel lengths required to achieve adequate test times (e.g., 40 to 50 ft for 1/2 millisec at a test Mach number of 15).

Considerations of the time required for steady flow to be established about a model after passage of the primary shock wave are given in Subsec. 5.1.1.2, under Test-Flow Duration. Suitable shock tunnel driving methods for generation of strong shocks are described in Subsec. 4.

Detailed performance curves for the non-reflected shock tunnel may be found in the references cited. Illustrative results for air considered as a perfect gas with constant specific heat ratio 1.4 are shown in Figs. 5.1-12* and 5.1-13*. Figure 5.1-12 gives primary shock Mach number M_2 required to obtain (perfect-gas) flight stagnation temperature for a flight Mach number M_f with test section static temperature T_T maintained at 218°K corresponding to the isothermal stratosphere. Results are shown for both the non-reflected method and the reflected method discussed below. Figure 5.1-13 gives test section Reynolds number as a function of flight Mach number M_f for stagnation temperatures equal to those in flight. The test section Mach number M_T is a parameter. The curve marked complete simulation represents complete expansion from Mach number M_2 to flight Mach number M_f ($T_T = 218^\circ\text{K}$). Curves of constant M_T represent incomplete expansion from M_2 to $M_T < M_f$, with $T_T > 218^\circ\text{K}$. Nominal testing time, determined by the time difference in arrival of the primary shock and contact surface at the end of the low-pressure channel, is shown in Fig. 5.1-14.

5.1.2.3 Reflected-Shock Tunnels

In the reflected-shock tunnel (Ref. 23), the low-pressure channel is terminated with a converging-diverging hypersonic nozzle as illustrated in Fig. 5.1-15. The area contraction is such as to strongly reflect the incident primary shock wave, thus creating a reservoir of nearly stationary hot gas in region (5). This hot gas then expands through the nozzle to the desired test-section conditions. The test-flow duration is limited by arrival at the nozzle entrance of a shock wave generated from interaction of the reflected primary shock wave with a contact surface.

It is emphasized that these results are illustrative only, given for purposes of comparison of reflected and non-reflected methods. Real gas effects reduce the Reynolds numbers considerably below the values shown.

Compared to the non-reflected method, the reflected method offers only slight increase in nominal testing time per foot. However, some alleviation is obtained from the difficulties caused by channel-wall boundary-layer development. The nozzle starting phenomena and losses are very similar to those for no reflection, and a second diaphragm with pre-evacuation of the nozzle is also required. For equal static pressures at the end of the low-pressure channel during flow through the nozzle (non-reflected $p_2 =$ reflected p_5), the test-section Reynolds number is considerably less with reflection (see Fig. 5.1-17). Thus increased pressures and a correspondingly reinforced low-pressure channel are required to attain the non-reflected Reynolds numbers. Other disadvantages of the reflected method include increased real-gas effects, and nozzle erosion and damage due to higher static temperatures and densities.

A modification of the above reflected-shock method termed the tailored-interface method (Refs. 23, 27, and 94) offers greatly increased testing time per foot of low-pressure channel with consequent elimination of the difficulties in the non-reflected method from boundary-layer development behind the primary shock wave. With the tailored-interface method, the contact surface or interface is "tailored" so that on interaction with the reflected primary shock wave, no reflected shock wave is generated. The maximum nominal testing time is then limited by the overtaking of the interface by a nonsteady rarefaction wave as illustrated in Fig. 5.1-16 (a). Theoretical nominal testing times per foot are of the order of 10 times those for the non-reflected tunnel (Fig. 5.1-14).

Figure 5.1-16 (b) illustrates a second variation of the tailored-interface method. Here, the nonsteady rarefaction wave which limits the maximum testing time in the arrangement of Fig. 5.1-16 (a) is replaced by a steady expansion through addition of a divergence downstream of the diaphragm. Thus the maximum testing time is determined by overtaking of the interface by the shock wave reflected from the diaphragm station. The theoretical increase in testing time per foot of channel over the non-reflected tunnel is about a factor of 25 (Fig. 5.1-14).

Tailoring of the interface to avoid shock reflection is accomplished by careful adjustment of the driver gas initial conditions. With air as the driven gas, cold hydrogen and helium driver mixtures produce a tailored interface up to stagnation temperatures equivalent to flight Mach numbers of 10. Tailoring is achieved up to Mach 15 with cold hydrogen driving a buffer gas (Subsec. 4.2.3), or with hydrogen preheated to about 600°K in a single diaphragm tube (Refs. 27 and 94).

Except for the greatly increased testing times attainable with tailoring, performance of the tailored-interface method is identical to that for the simple reflected-shock method. Figures 5.1-12 and 5.1-17 give theoretical primary shock Mach number and test Reynolds number, respectively, as functions of flight Mach number for simulation of flight stagnation temperature assuming air as a perfect gas. Despite its added complexity, the tailored-interface method is attractive because of the possibility of very large gains in testing time and alleviation of the boundary-layer problem. Reference 94 gives detailed real-gas performance curves for the tailored-interface tunnel and reports initial tests with such a tunnel done at the Cornell Aeronautical Laboratory, Inc., Buffalo, N. Y. The tests indicate that the theoretical advantages of the tailored-interface method can be realized to a substantial degree in practice.

5.1.2.4 Hypersonic Gun Tunnels

In the so-called "hypersonic gun" tunnels, a light piston is projected at supersonic speed into a closed barrel. The accelerating piston generates a shock wave which undergoes multiple reflections (from the piston and closed barrel end) and heats the gas nonisentropically to a high temperature. In a short time the piston comes to rest with the pressure equilibrated throughout. The hot stagnant gas is then expanded through a suitable nozzle at the barrel end.

Such a method has been employed at the Ames Laboratory (Ref. 31) using a nylon piston driven by a powder charge. Stagnation temperatures of around 1400°K at Mach numbers of 10 were obtained. Reference 32 describes a small gun tunnel in which a light compressed gas is used as a more efficient means of driving the piston, thereby increasing the stagnation temperatures obtainable. The testing times attainable in these tunnels are very long by comparison to the shock tunnels--of the order of hundreds of milliseconds--and melting of the nozzle throat can be a limiting factor. The instrumentation problems are accordingly less difficult with the long test times.

The gun tunnel is very similar to the equilibrium-interface modification of the shock tunnel described in Ref. 23. Here, the primary shock wave is reflected from the end of the low-pressure channel, but the interface is not tailored. Multiple shock reflections in this case occur from the tube end and from the moving interface. In the gun tunnel, the piston replaces the gas interface, and this has the advantages of providing stronger shock reflection and avoiding mixing of the driver and driven gases. However, construction of the low-pressure channel (or barrel) with the gun tunnel is complicated by the necessity for a very close-fitting but free-moving piston.

The gun tunnel has thus far been used to obtain only relatively low stagnation temperatures of the order of 1400°K and less. Further studies are required to fully assess the properties and uniformity of the test flows produced. As mentioned, the testing times attainable (after pressure equilibrium is reached) may be several orders of magnitude greater than those in the shock tunnel. At the stagnation temperatures obtained thus far, the heat losses from the gas in the initial period of time required for pressure equilibration (of the order of 50 millisecc in the tunnel of Ref. 32) are not too serious. With increasing temperatures, however, the heat losses in this initial period, particularly radiation losses, will eventually dominate and impose a practical upper limit on attainable stagnation temperature. Thus the advantage of the gun tunnel over the shock tunnel in providing much longer testing times is probably limited to a range of relatively low stagnation temperatures.

5.2 Use in Aerophysics Research

5.2.1 Wave-Interaction and Non-Planar Wave Phenomena

The uniform-channel shock tube has been used extensively for studies of various one-dimensional wave interactions involving collision and overtaking of shock waves, rarefaction waves, and contact surfaces. Many interactions of this type have been investigated by Glass and colleagues at the University of Toronto (Ref. 40; also Subsec. 2.4). The

results of some particular studies are given in Subsec. 3.1.4. Principally, optical instrumentation has been used. In particular, the wave-speed schlieren technique (Subsec. 7.2.1.3), which provides a photographic distance-time record of moving density disturbances, has proved very useful for such work.

In addition to one-dimensional wave interactions, numerous two-dimensional wave interactions have also been studied in the shock tube. Groups at Princeton University under Bleakney and at the University of Michigan under Laporte have been active in this area. The optical methods of shadowgraph, schlieren, and interferometry (Subsec. 7.2.1) have been extensively used to investigate such problems as oblique-shock reflection from plane walls (e.g., Refs. 33 and 34), oblique-shock refraction at a plane gaseous interface (e.g., Ref. 34), and shock-wave diffraction about solid bodies (e.g., Refs. 36 and 37). Interferometry has proved particularly useful in such two-dimensional studies for the quantitative determination of density variation throughout the flow field. The literature in this area of shock-tube research has now become quite extensive, particularly with regard to diffraction studies, and the above references are exemplary only. Reference 38 provides a brief but useful review of much of the work on two-dimensional shock-wave phenomena up to 1954.

Novel modifications of the constant-area shock tube have been used to generate segments of cylindrical and spherical shock waves. Reference 96 describes a wedge tube for cylindrical waves, and Ref. 97 a pyramidal, square cross-section tube for spherical waves. A complete extension of the latter for spherical waves is the shock sphere (Ref. 98) which has the advantage of avoiding any boundary layer effects. Regarding simulation of the peaked pressure profiles of blast waves, this is feasible in the conventional uniform shock tube by use of a short-length driver section such that the expansion wave reflects to overtake and decay the shock.

5.2.2 Condensation Phenomena

The low temperatures and rapid cooling attainable with strong unsteady rarefaction waves generated in the shock tube offer the possibility of studying various aspects of gas condensation phenomena. To date, very limited use has been made of the shock tube in this way. Shadowgraph studies of the formation of condensation shocks near the diaphragm station were made by Lee (Ref. 39). Reference 40 shows wave-speed schlieren records of saturated air flow near the diaphragm with condensation shocks present. Wegner and Lundquist (Ref. 41) used a light-scattering technique (Ref. 42) in the shock tube to demonstrate existence of water vapour condensation for rapid cooling of moist air to below 150°K.

5.2.3 Flow Transition and Boundary-Layer Phenomena

One-dimensional flow transitions that have been studied in the uniform shock tube include the unsteady rarefaction wave, the contact surface, and the shock wave. Rarefaction wave profiles have been investigated by pressure measurement with fast-response wall-mounted pressure transducers (e.g., Refs. 43 and 44; also Subsec. 7.1.2), by density measurement with the chrono-interferometer (Ref. 45; also Subsec. 7.2.1.4), and by mass flow and temperature measurement with the hot-wire anemometer (Ref. 44; also Subsec. 7.3.4). The laminar contact surface transition has been studied by interferometry (Ref. 46). The

shock front transition has been investigated in the shock tube by Hornig and associates at Brown University using the light-reflectivity technique described in Subsec. 7.5. Studies of rotation, vibration, and dissociation relaxation phenomena behind shock fronts are outlined in Subsecs. 5.2.4 and 5.3.2.

Regarding shock-tube boundary-layer studies, analytical and experimental investigations of shock-tube-wall boundary layers are described in Subsec. 3.2. The initial interest in shock-tube-wall boundary layers was primarily with their role in producing departures from ideal tube flow, such as shock attenuation. In recent years, however, somewhat more interest has developed on account of the fact that the shock-induced wall boundary layer is convenient for study of some basic high-temperature effects, such as those involving dissociation or high cooling rates, not easily produced in conventional steady-flow facilities. For small shock attenuation, the shock-induced wall boundary layer is a steady-flow phenomenon relative to the moving shock. Experimental studies might thus be interpreted to yield information relevant to the conventional Blasius-type flat-plate boundary layer in steady flow.

Recent experimental results for shock-tube-wall boundary layers behind shocks of Mach numbers from 1.5 to about 10 in air and over a range of pressures are reported in Ref. 95. Thin-film resistance thermometers mounted on glass shock-tube walls were used to locate transition and measure laminar and turbulent heat-transfer rates. Ratios of wall to free-stream static temperatures ranged from 0.8 to 0.07. The higher cooling rates produced marked stabilization of the laminar layer. Good correlation of transition data was obtained in terms of transition Reynolds numbers based on calculated displacement thicknesses at transition. Measured laminar and turbulent heat transfer rates agree well with the existing theories discussed in Subsec. 3.2.

Several shock-tube studies of steady-flow boundary layers developed on models are outlined in Subsec. 5.1.1.1.

5.2.4 High-Temperature Gas Physics

The relative ease with which a sample of gas can be rapidly and uniformly heated to a known high temperature by a strong shock wave (Subsec. 2.2.2) makes the shock tube an attractive tool for high-temperature gas physics research. For example, room-temperature argon at 1-cm pressure is heated to about 13,000°K by a shock wave of Mach number 16. Normal reflection of the same shock wave increases the temperature to 18,000°K, and under these conditions the argon is about 40 per cent ionized. Ionization and eventually electronic excitation limit the temperature rise. With monatomic gases, ion densities of the order of 10^{15} to 10^{18} ions/cu cm may be achieved at temperatures up to the order of 18,000°K by selection of initial pressure and shock strength. With diatomic or polyatomic gases, the temperatures attained are much lower for the same shock strength as additional energy is required for excitation of molecular vibration and dissociation. For a Mach 16 shock wave in room-temperature air at 1-cm pressure, the temperatures corresponding to the above values for argon are about 6500°K and 9500°K.

Use of the shock tube for the study of partially ionized gases at high temperatures was pioneered by Kantrowitz's group at Cornell University (Refs. 47, 48, 58, and 59), by Fowler's group at the University of Oklahoma (Ref. 49), and by Laporte's group at the University of Michigan (Ref. 50). These groups developed various spectroscopic techniques for the study of emission spectra from luminous gas behind strong shocks. As a spectroscopic light source the shock tube offers some unique advantages in that temperature, ion density, and other equilibrium properties behind incident or reflected shocks may be calculated from measured wave speeds. Further, by comparison with other sources as arcs, the luminous gas properties are very homogeneous. While shock tube spectroscopy has proved a powerful tool, it is not without its difficulties. Low intensity radiation renders time-resolved spectra difficult to obtain. Also, impurities complicate the spectra and are difficult to avoid with frequent exposure of the driven tube interior to the atmosphere and to the driver gases.

References 13, 51, 52, 53, and 54 review applications of the shock tube to the study of high-temperature phenomena in gases. Detailed discussion of shock tube spectroscopic techniques will be found in Refs. 50, 52, 53, 54, and 57. Some specific applications to high-temperature studies are presented below.

5.2.4.1 Radiation Studies

Some of the first shock-tube radiation studies were done by Kantrowitz's group using monatomic argon heated by primary and reflected shocks to temperatures in the range 6000 to 17,000°K (Refs. 47 and 48). Spectroscopic measurements, including time-resolved spectra obtained with a rotating drum camera, were made of the argon line broadening and shift resulting at the high ion concentrations obtained. Ion density behind incident shocks determined from these measurements showed thermodynamic equilibrium to be quickly attained at the higher temperatures (11,000°K). The intensity of the strong visible continuum radiation present above 10,000°K was measured photoelectrically. The rate of cooling of the hot argon was determined by several methods, and the dominant heat loss above about 10,000°K was shown to be due to the continuum radiation.

Similar shock-tube experiments were done by Laporte's group with krypton, neon, and xenon, in addition to argon (Ref. 50). Ionization delay behind incident shocks was determined in xenon. Luminosity of the shock front itself was studied and shown to result from impurities. Quantitative studies were made of first-order broadening of the hydrogen Balmer lines excited behind reflected shocks in neon containing a slight amount of hydrogen.

Radiation heating of the gas ahead of an advancing shock wave with resulting distortion of the shock front near solid boundaries was studied at Los Alamos by Schreffler and Christian (Ref. 55). Photographic studies were made of the distortion of very strong shock waves generated by means of a solid-explosive drive (Subsec. 4.3).

A recent and important application of the shock tube in radiation studies has been to spectroscopic and spectrophotometric measurement of the emissive and absorptive properties of air up to temperatures of the order of 8000°K (Refs. 56 and 57). Further shock-tube radiation studies are described under chemical applications in Subsec. 5.3.

5.2.4.2 Ionization, Conductivity, Magnetohydrodynamic Studies

In addition to spectroscopic studies of the equilibrium region behind strong shocks in argon, the work of Kantrowitz's group included theoretical and experimental studies of the nonequilibrium region by Petschek (Ref. 58) and measurement of electrical conductivity by Lin, Resler, and Kantrowitz (Ref. 59). Experimental investigation of the approach to equilibrium included photoelectric recording of continuum light intensity and measurement of the electrostatic potential created by electron diffusion. The electrical conductivity of shock-heated argon was measured by the magnetic technique described in Subsec. 7.7. The same method has also been applied to air (Ref. 60).

The production of ionized gas in the shock tube offers the possibility of studying magnetohydrodynamic phenomena involving interaction of the electrically conducting gas with magnetic fields. Shock-tube experiments have been done to demonstrate interactions of partially ionized gases behind strong shocks with externally applied fields (Refs. 13, 61, and 62). For example, in the work of Ref. 61 the conducting gas region behind a shock wave of Mach 11 in argon was accelerated with an external field applied by means of a pulsed transmission line coaxial with the shock tube. Attainment of fully ionized flow conditions at low densities is possible with electromagnetically driven shock tubes (Ref. 13; also Subsec. 4.3). Temperatures of the order of 0.5×10^6 °K estimated from measured shock speeds have been claimed behind electromagnetically driven shocks (Ref. 13).

5.2.4.3 Relaxation Studies

The shock tube has been extensively used to study relaxation phenomena behind shock fronts in gases. The light-reflectivity technique (Subsec. 7.5) which measures the optical reflectivity of the shock wave density transition was used to investigate the rapid equilibration of rotational degrees of freedom in shocked diatomic gases (Ref. 63). Various other optical methods have been employed in the shock tube to study vibrational relaxation behind shock fronts in oxygen, nitrogen, air, and CO₂. These methods include conventional spark interferometry (Refs. 64 and 65), a special schlieren technique utilizing a narrow light beam with photoelectric recording (Ref. 66), and conventional schlieren with knife edge oriented parallel to the shock front (Ref. 67).

Recently, intensive application of the shock tube has been made to the study of chemical relaxation phenomena in reactive flows of oxygen, nitrogen, and air. This application is included in Subsec. 5.3.2 below.

5.3 Use in Chemical Research

The ability of the shock tube to produce very rapid and homogeneous changes in the thermodynamic state of a gas sample offers unique advantages for the study of many high-temperature chemical reactions. The method of shock wave heating is particularly useful in chemical reaction studies because, apart from the high temperatures attainable, the reaction conditions may be accurately determined from measured shock-wave speed. Use of the shock tube for chemical research has become

widespread, as attested by the large volume of research literature which now exists in this area. Reviews of chemical applications are given in Refs. 51, 52, 53, and 68. In particular, Refs. 52 and 53 give detailed discussion of measurement techniques suitable for chemical reaction studies in the shock tube. Some specific chemical applications are outlined below.

5.3.1 Combustion Studies

A considerable amount of research on detonation and combustion phenomena in gaseous mixtures has been done in long flame tubes. However, applications of shock-tube (diaphragm) technique in this area are relatively limited. One application has been the determination of ignition temperatures of combustible gaseous mixtures heated by passage of a plane step shock wave (Refs. 69, 70, and 71). In this work, the shock wave was generated either directly in the combustible mixture employed as the driven gas, or else in an intermediate buffer gas, and occurrence of ignition was detected by eye and by photocell recording. Similar studies have been done with converging cylindrical shock waves generated in the shock tube by diffraction of a plane wave (Ref. 72).

Another application of shock-tube technique in combustion research has been to the interaction of a shock wave with an initially laminar flame front (Ref. 73). In this work, the shock tube was oriented vertically to stabilize the flame generated in a combustion chamber forming the bottom section of the low-pressure channel. The flame was generated by ignition of the combustion chamber mixture just prior to rupture of the diaphragm separating the high-pressure driver gas from an intermediate buffer gas. Detailed study of interaction of the flame front with the impinging primary shock wave, and with subsequent reflected waves, was made by schlieren optical methods.

A shock-tube method has been used to study ignition in transient boundary-layer flow over a hot isothermal surface (Ref. 74). In this work, a slug of cold combustible mixture was accelerated by a weak plane shock wave and caused to flow downstream over a heated plate set flush in the shock tube wall. Subsequent ignition of the mixture by the hot plate was observed optically by schlieren.

Several shock-tube studies have been made of thermal decomposition of organic fuels by heating with strong shock waves. Reference 75 reports optical studies of carbon formation behind reflected shock waves in acetylene. Simultaneous light-absorption and emission measurements (see also Subsecs. 5.3.2 and 7.6) were made using a Kerr cell as a light-beam chopper. Spectroscopic study of the emission spectra excited in various hydrocarbons and hydrocarbon plus argon mixtures by heating with strong shock waves is reported in Ref. 76. Comparison is made with spectra from flames, and from spark and shock-initiated detonations. The shock-excited spectra resemble those produced by flames rather than discharge tubes, which suggests possible use of the technique for study of fundamental processes in flames.

5.3.2 Chemical Kinetic Studies

A fruitful application of shock-tube methods has been to the quantitative determination of chemical reaction rates of fast high-temperature reactions with half-lives of the order of a millisecond or

less. Most kinetic studies have been of relatively simple reactions with the mechanism of the reaction assumed known. Very limited work has been done on complex combustion reactions (see above).

Two main experimental approaches discussed below have been used in kinetic studies. These utilize either the optical methods, which obtain information on the reaction at first hand while it is proceeding, or the chemical shock tube, which subjects the reactant gas to a predetermined temperature-pressure pulse after which a sample is drawn off and analyzed for chemical composition by conventional methods.

5.3.2.1 Optical Methods

The optical methods have been extensively used to study reaction kinetics behind strong shock waves. Early application was made to measurement of the rate of dissociation of N_2O_4 to NO_2 when heated by weak shocks (Ref. 77). The dissociation reaction was followed in time by photoelectric recording of the intensity of a narrow beam of light crossing normal to the shock tube axis which underwent absorption by the coloured NO_2 molecule (see light-absorption measurement, Subsec. 7.6). Later application of this absorption technique using strong shock waves was made to high-temperature dissociation of weak concentrations of molecular iodine (Refs. 78 and 79) and bromine (Refs. 80 and 81) in inert diluents, and to hydrogen-bromine reactions (Ref. 82). With high dilution of the dissociating gas, changes in temperature and density are small as dissociation proceeds and determination of the rate constants is considerably simplified. Dissociation of undiluted gas was also studied.

Recently, intensive application of the shock tube has been made to studies of chemical relaxation of the constituents of high-temperature air (Refs. 67, 83, 84, 85, and 86). The (ultra-violet) light-absorption method above has been used to determine both vibration and dissociation relaxation times of oxygen in shock-heated mixtures containing oxygen or air highly diluted with argon (Ref. 83). In addition to absorption studies, photoelectric recording of the intensity of emission spectra from high-temperature shock-heated gases over a limited wave length region has also been employed (Ref. 83). Dissociation rates for shock-heated nitrogen, oxygen, and air have been obtained in this way. Other optical methods used to study chemical relaxation behind strong shocks include: conventional schlieren with knife edge parallel to the shock front, used to obtain the width of the dissociation relaxation zone in oxygen (Ref. 67); conventional short-duration spark interferometry, used for quantitative determination of spatial density distribution through the dissociation relaxation zone in oxygen (Ref. 84); and a combined interferometer and rotating-drum camera arrangement used to record quantitative density change with time at a fixed station swept by the travelling shock and dissociation relaxation zone in air (Ref. 85).

Optical studies in the shock tube have also been made of chemical relaxation occurring for very rapid cooling of hot dissociated air (Ref. 86) and nitrogen (Ref. 83) with the object of measuring recombination rates. The method involved steady flow of gas heated by the primary shock about a two-dimensional triangular cross-section model. The hot gas was first decelerated to slightly supersonic speed across an oblique shock attached at the model leading edge and then rapidly cooled by Prandtl-Meyer expansion at a sharp corner downstream

of the leading edge. Schlieren observation of Mach waves produced by scribing the model surface provided local Mach angles through the flow sensitive to the local flow chemistry.

5.3.2.2 Chemical Shock Tube

The chemical shock tube (Refs. 87 and 88) offers an alternative to optical methods for obtaining rate data on high-temperature reactions whose product species may be "frozen in" or permanently preserved at any stage by sudden cooling. The tube arrangement is shown in Fig. 5.3-1. To the conventional constant-area shock tube is added a large evacuated tank separated from the driver section by a second diaphragm. In operation, the reactant gas fills the low-pressure section. The diaphragm separating the driver and reactant gases is broken first, and the reactant gas is compressed and heated by the incident and reflected primary shock wave. Effectively, the reactant gas is subjected to a single high-temperature and pressure pulse. For a controlled time of the order of a millisecond the reacting mixture remains at the high-temperature conditions left by the reflected shock. It is then cooled very rapidly by an expansion wave generated from breaking of the second diaphragm at the evacuated tank. This expansion wave reflects from the closed end of the low-pressure section to further cool the reacting gas and bring it to rest. If the reaction is one in which the high-temperature reaction products can be "frozen in" by the rapid cooling, then the duration of the high-temperature pulse and the final chemical composition of the processed reactant (determined from a sample withdrawn immediately after a run) provide quantitative data on the reaction rates.

The duration and magnitude of the high-temperature pulse is controlled by the ratio of driver to reactant section lengths, the time delay between breaking of the two diaphragms, the length of the reactant or low-pressure section, and the primary shock strength. Initial cooling rates of the order of 5×10^5 °K/sec have been obtained with the tank-generated expansion wave (Ref. 88). Use of the tailored-interface technique (Subsec. 5.1.2.3) avoids disturbing the high temperature reaction with reflected waves from interaction of the reflected primary shock with the contact surface. Sonic inflow into the large evacuated tank also prevents any secondary temperature pulses from occurring. Detailed design and performance information on the chemical shock tube is given in Ref. 87. Methods for controlled bursting of the two diaphragms are described in Refs. 75 and 87, and in Subsec. 6.2.3.

The chemical shock-tube technique is limited to the study of those reactions which can be frozen by rapid cooling. It has been successfully applied to the study of the kinetics of the formation of nitric oxide in the temperature range of 2000 to 3000°K (Ref. 88). Interesting attempts have also been made to use the method for production of chemicals (e.g., hydrazine, Ref. 75).

5.3.3 Dissociation Energies

Several methods utilizing dissociation by strong shock waves have been employed for measurement of dissociation energies. In one study, the actual pressure-density (Hugoniot) relation across strong shocks in nitrogen was obtained from the mass and momentum equations by substitution of measured shock and particle velocities (Ref. 89).

The shocks were generated by an explosive driven plate, and the shock and plate (particle) velocities were recorded photographically. Comparison of the experimental Hugoniot with theoretical curves calculated for dissociation energies of 7.385 and 9.764 eV provided additional support for the latter value. In another study, plane shock waves in carbon monoxide and nitrogen were reflected from the end of the low-pressure channel, and incident and reflected wavespeeds were measured (Ref. 90). Comparison of measured reflected-versus-incident wave speed curves was made with corresponding theoretical curves for different dissociation energies. After allowance for relaxation and viscous effects, the results supported the dissociation energies of 11.1 and 9.76 eV for carbon monoxide and nitrogen, respectively.

5.4 Use for Calibration of Instruments

The principal application of the shock tube in instrument calibration has been to the calibration of pressure transducers. However, the shock tube has also been used to study the response of a hot-wire anemometer to the step function changes in mass flow and temperature occurring across a shock wave (see Subsec. 7.3.4).

The first application of shock tubes in America was made by Bleakney's group at Princeton University to the calibration of piezoelectric blast-pressure gauges (Refs. 91 and 92). This method, utilizing the step pressure increase across a shock wave, has since been widely adopted for the determination of dynamic transducer response. Calibration using shock waves has advantages not only for transducers designed for shock tube use, but also for transducers for use at high acoustic pressure levels. The production of sinusoidal pressure variations for determining sinusoidal frequency-phase characteristics of acoustic transducers is difficult if not impractical at high pressure levels. However, the desired frequency-phase characteristics can be calculated from the measured transducer response to a known aperiodic pressure change such as a shock wave. The mathematical techniques involved are outlined in Ref. 93. Further discussion of the use of pressure transducers in shock tubes is given in Subsec. 7.1.2.

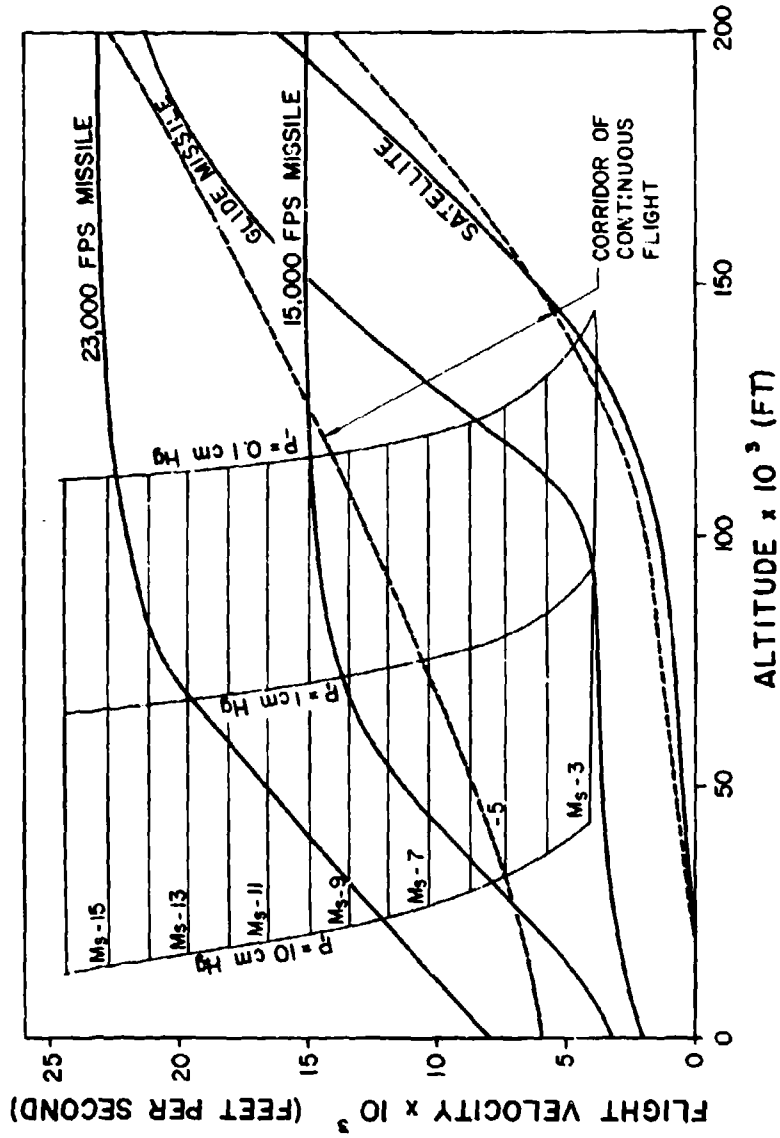
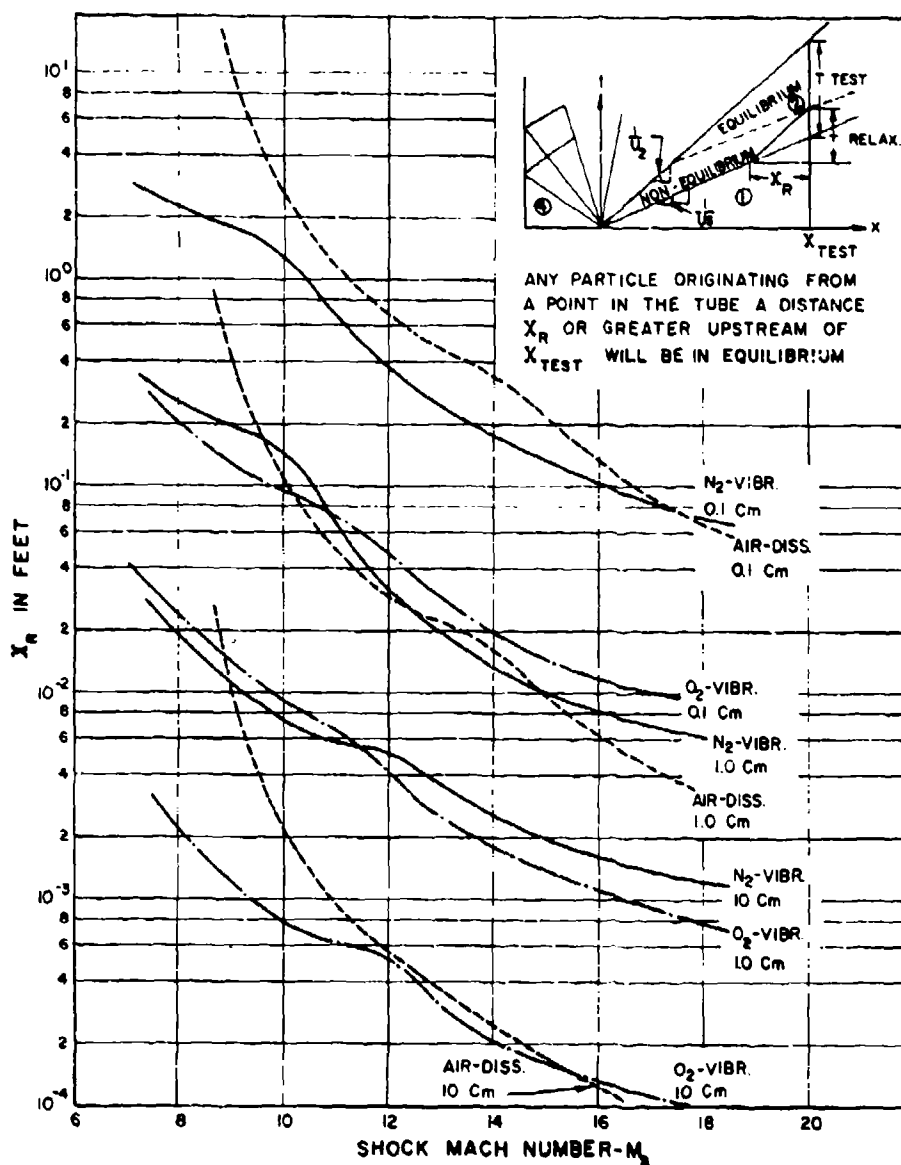
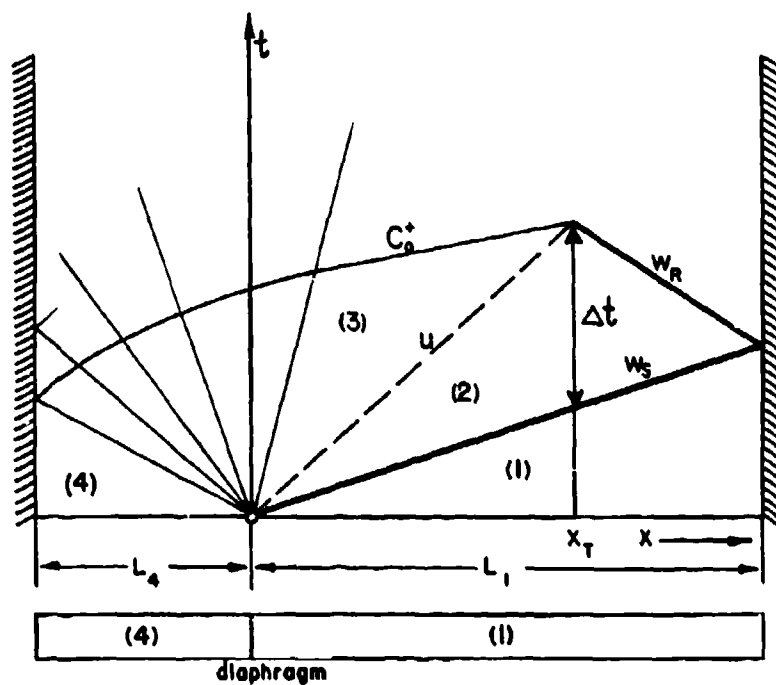


Fig. 5.1-1. Range of shock Mach numbers M_s in air and pressure P_1 ahead of shock producing hypersonic flight stagnation enthalpy and stagnation density in region (2) of uniform channel shock tube (Ref. 12; trajectories from Ref. 18).



(Pressure P_1 given in cm Hg.)

Fig. 5.1-2. Estimated vibration and dissociation relaxation distance X_R for air set into motion by shock wave of Mach number M_s (Ref. 13).



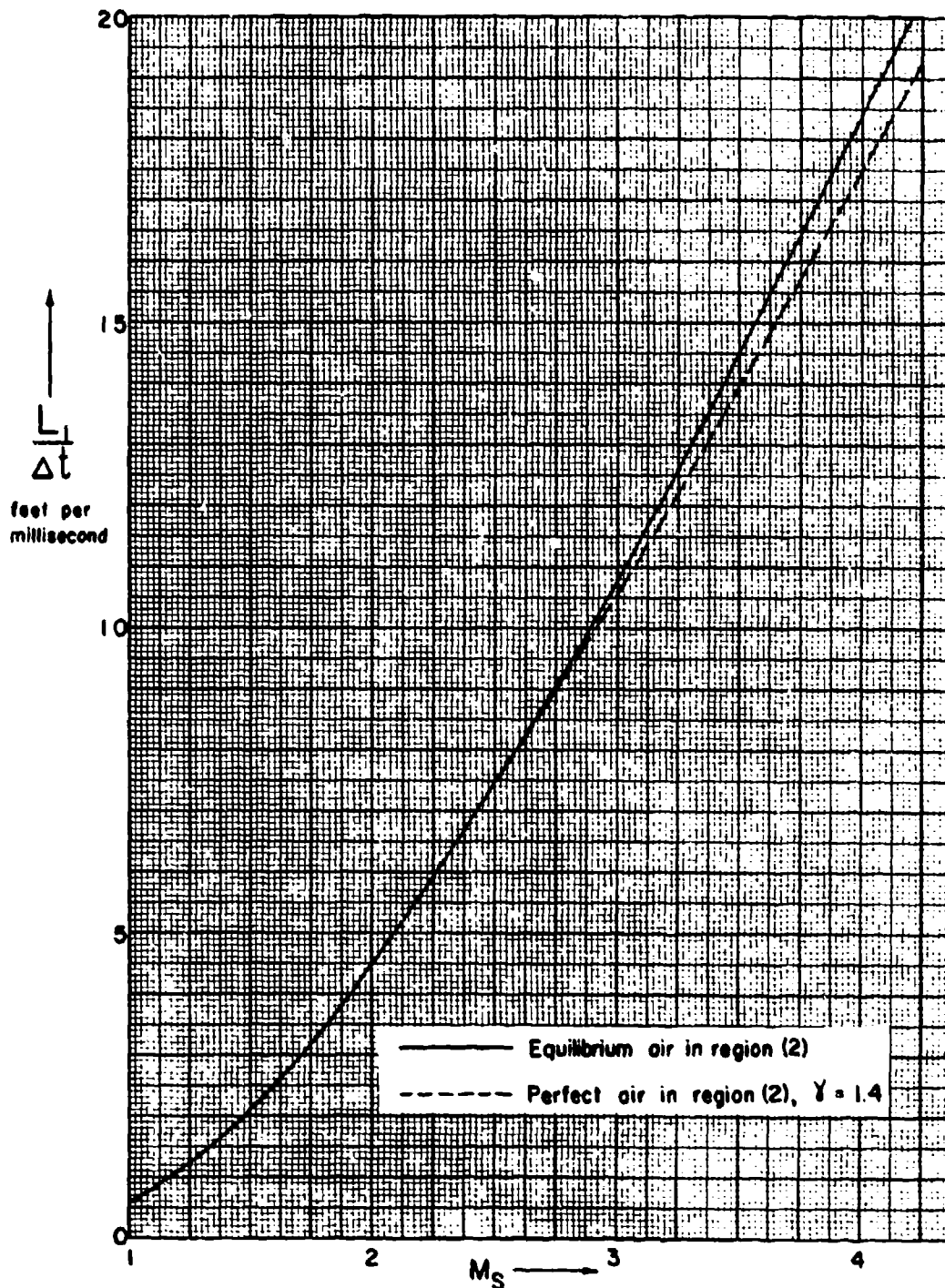
$$\frac{L_1}{a_1 \Delta t} = \frac{M_s M_{SR}}{M_s + M_{SR}} + U_{21} \frac{\gamma_2}{\gamma_1}, \quad \text{where } M_{SR} = \frac{w_R}{a_1}$$

$$\frac{L_1}{x_T} = \frac{M_s}{U_{21}} \left[\frac{U_{21} + M_{SR}}{M_s + M_{SR}} \right],$$

$$\frac{L_1}{L_4} = \frac{2 M_s}{A_{41}} \left[1 - \frac{\gamma_4 - 1}{2 A_{41}} U_{21} \right]^{-\frac{\gamma_4 + 1}{2(\gamma_4 - 1)}} \left[\frac{U_{21} + M_{SR}}{M_s + M_{SR}} \right],$$

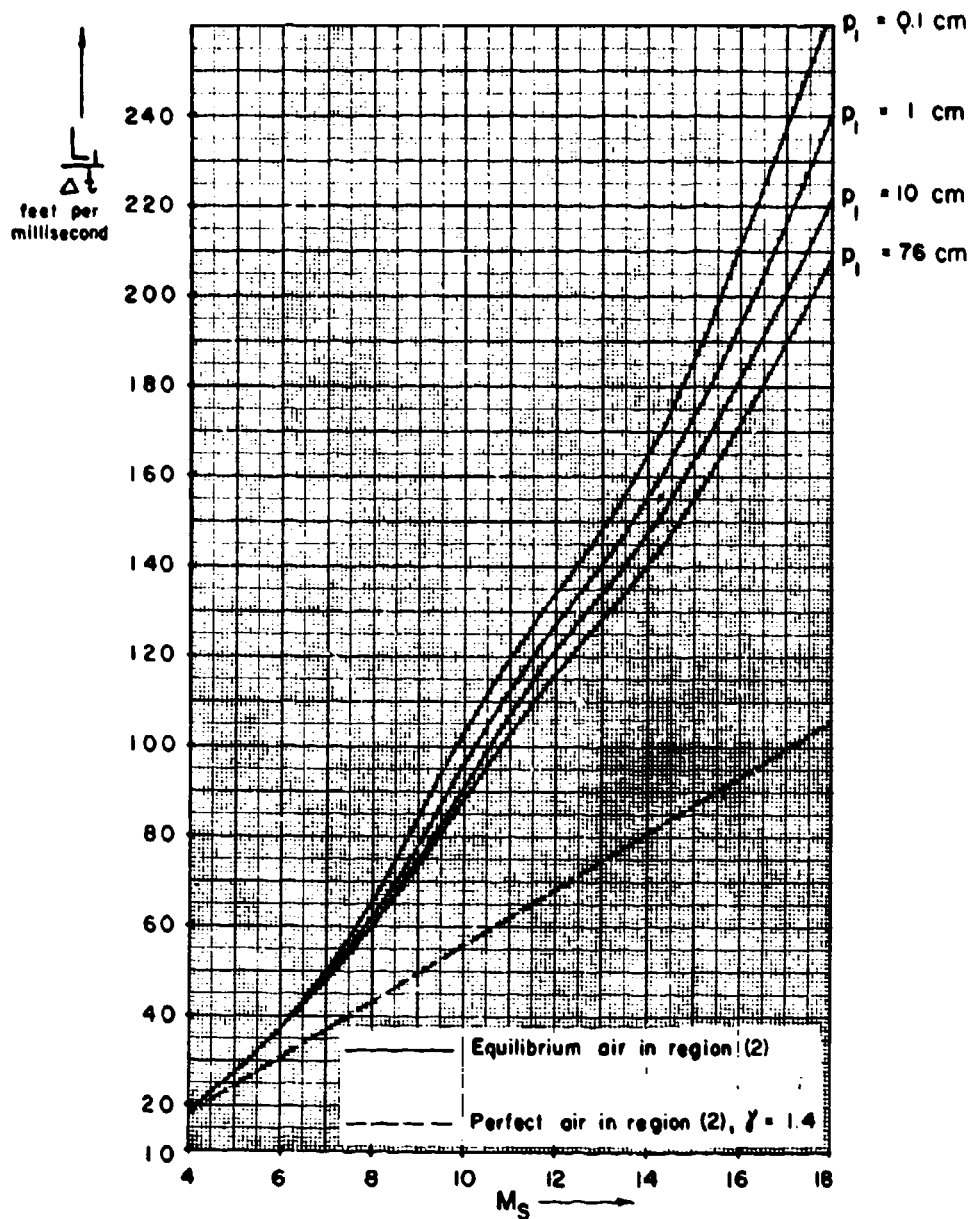
(constant area tube; ideal rarefaction wave).

Fig. 5.1-3. Distance (x)-time (t) diagram showing minimum chamber length L_4 and minimum channel length L_1 giving maximum hot flow duration Δt at station x_T .



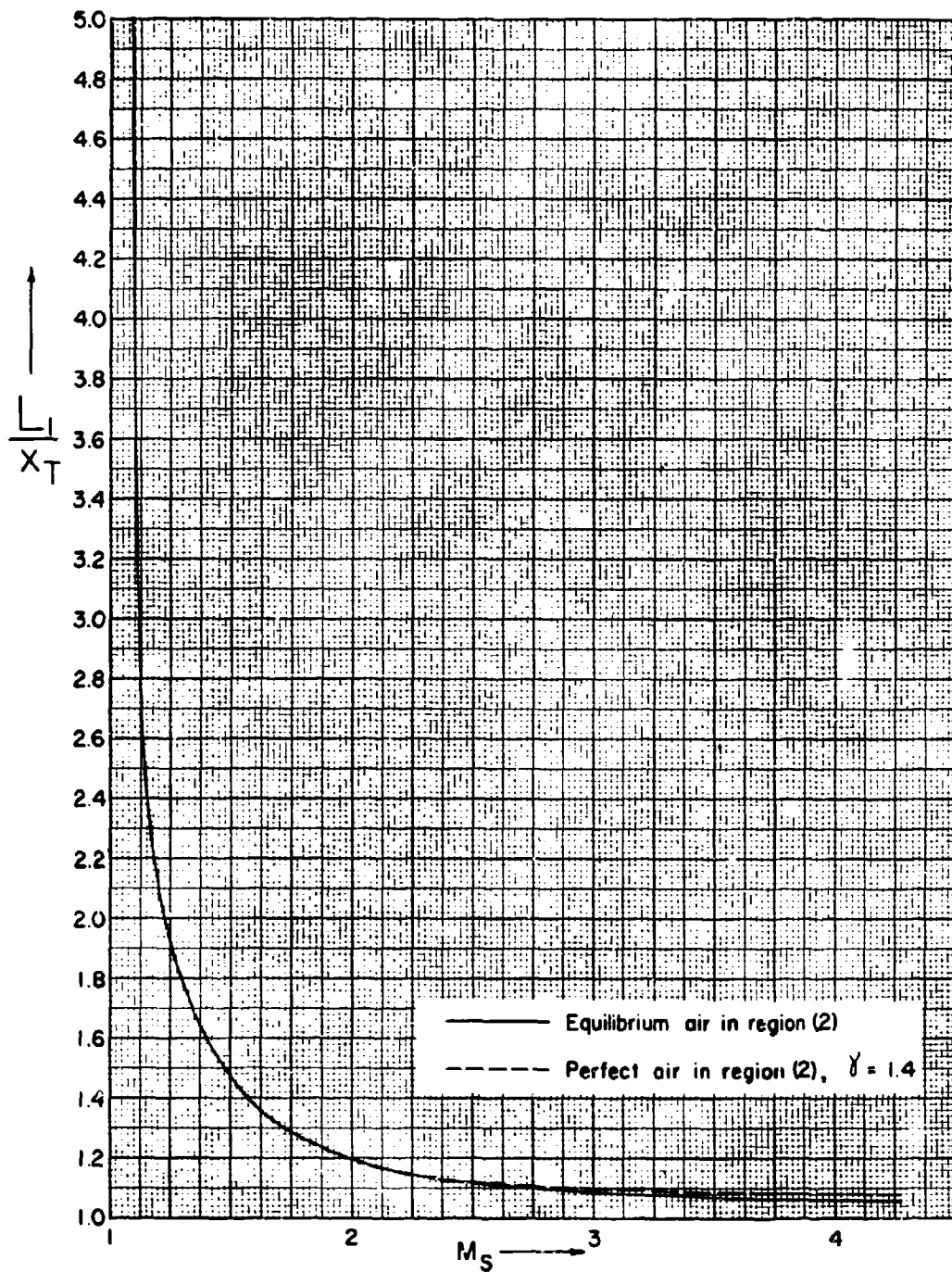
(For higher values of M_s see Fig. 5.1-4b. For notation see Fig. 5.1-3.)

Fig. 5.1-4a. $L_1/\Delta t$ for air as a function of shock Mach number M_s ; $T_1 = 293^\circ\text{K}$.



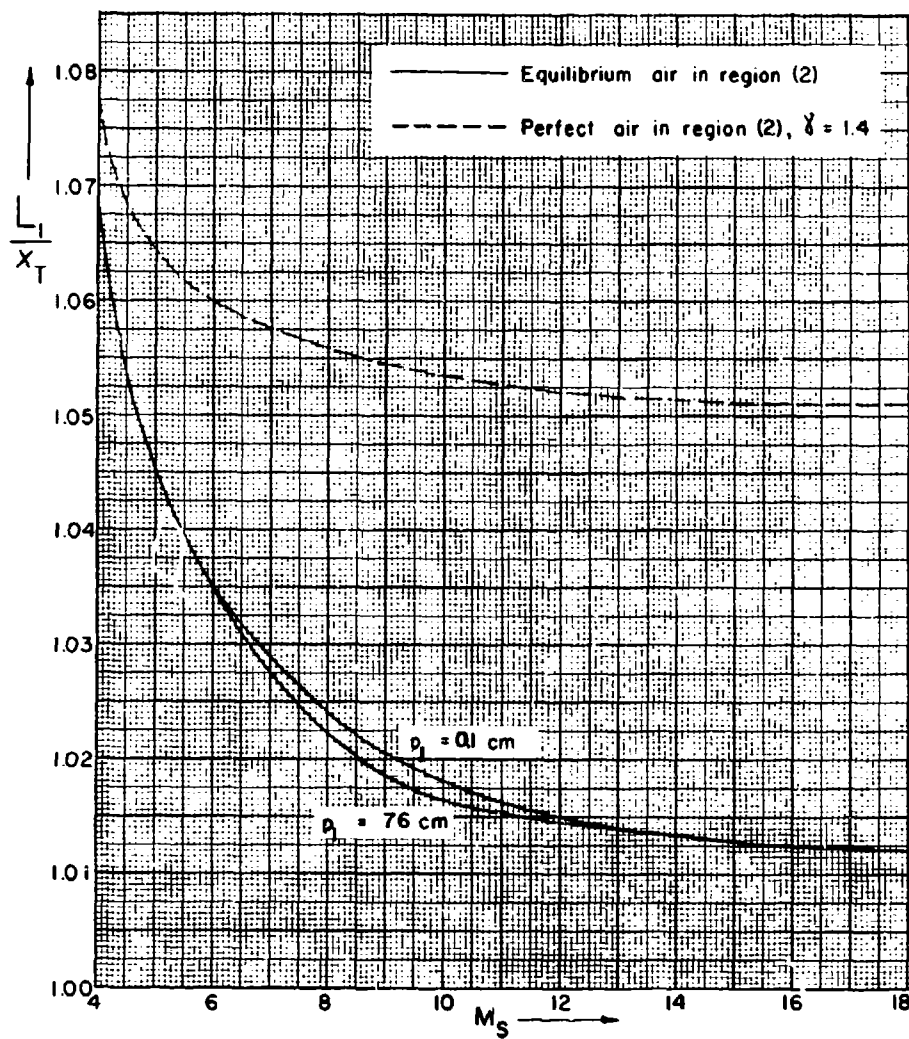
(For lower values of M_s see Fig. 5.1-4a. For notation see Fig. 5.1-3.)

Fig. 5.1-4b. $L_1/\Delta t$ for air as a function of shock Mach number M_s ; $T_1 = 293^\circ\text{K}$.



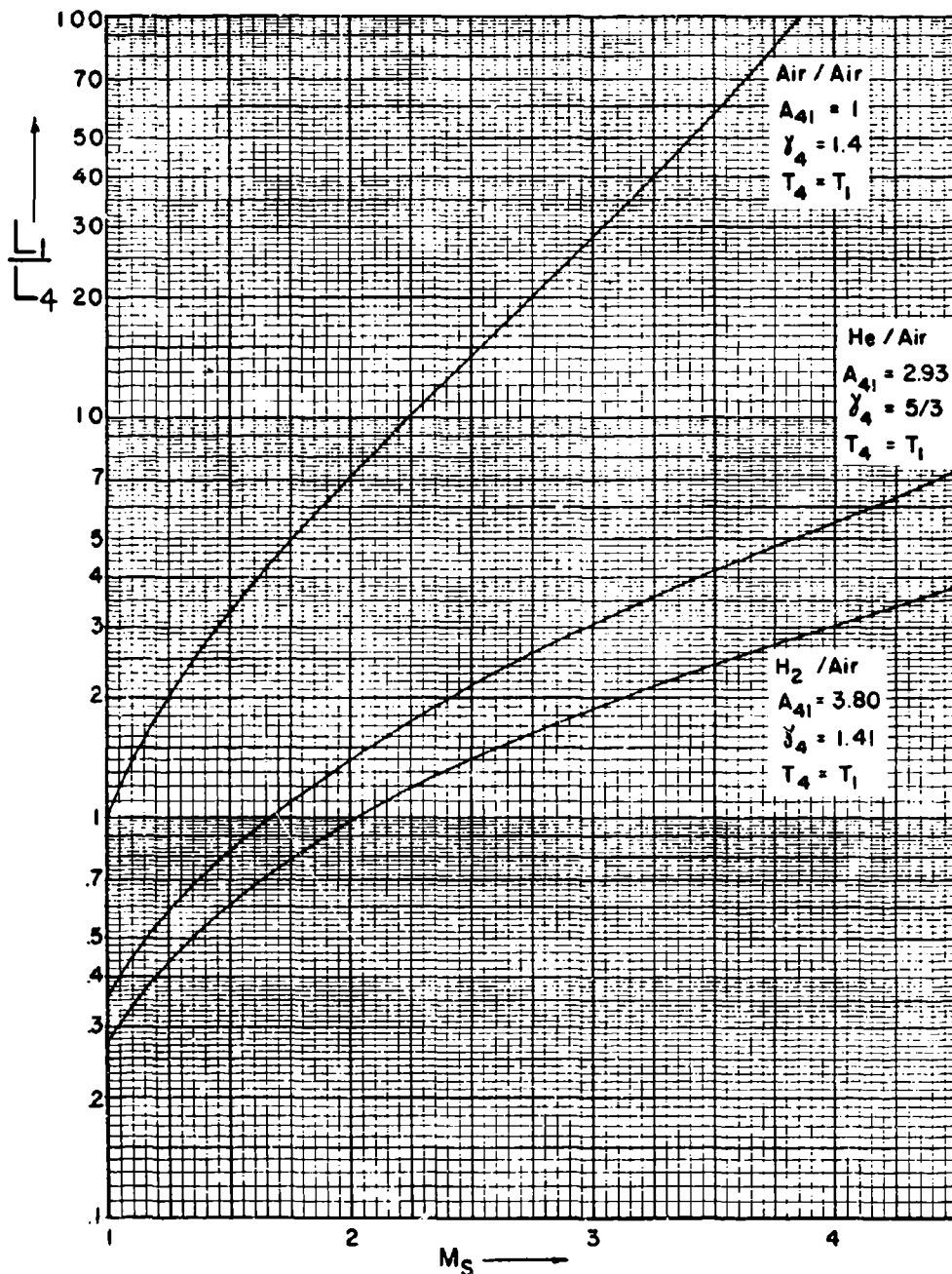
(For higher values of M_S see Fig. 5.1-5b. For notation see Fig. 5.1-3.)

Fig. 5.1-5a. L_1/X_T for air vs shock Mach number M_S .



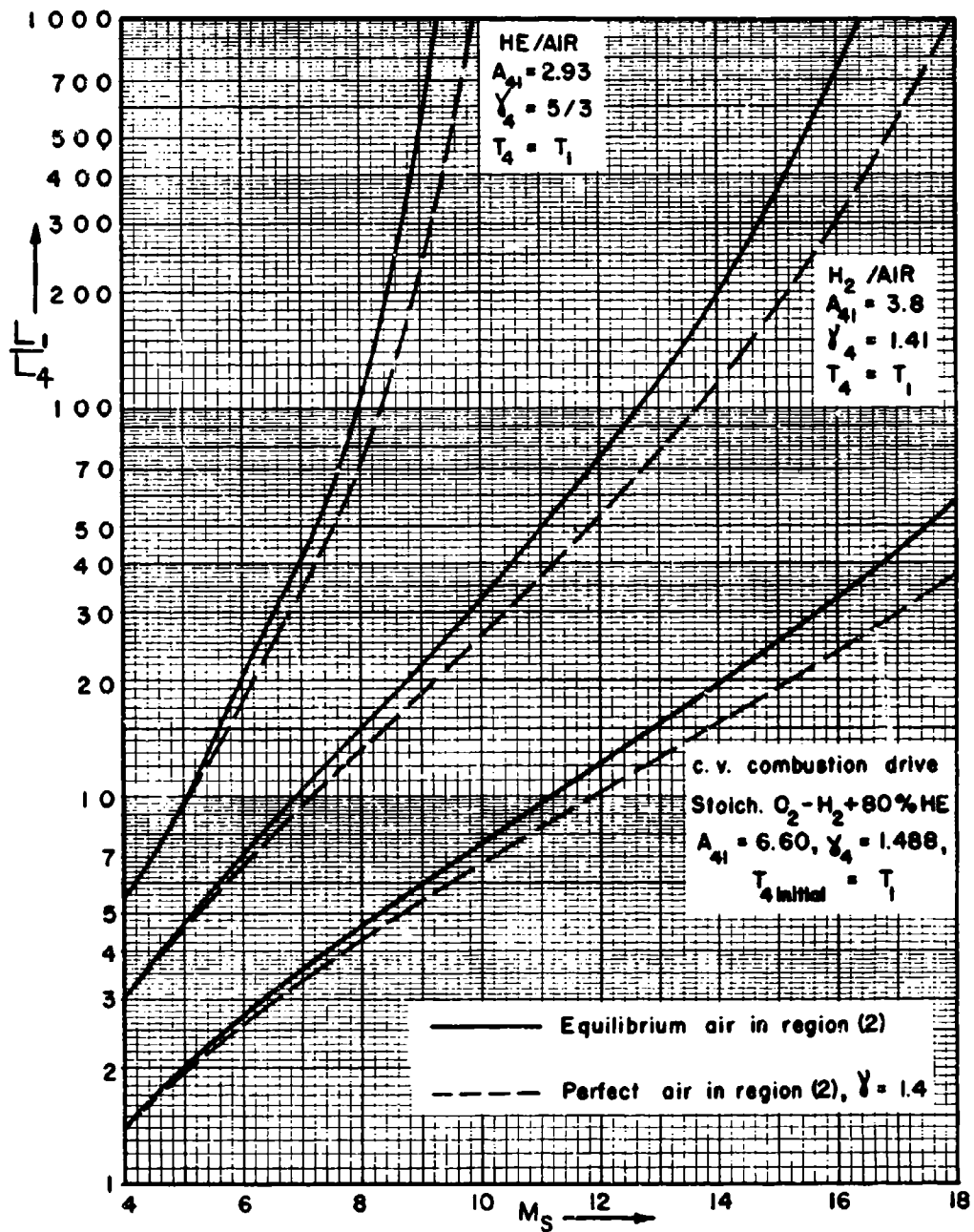
(For lower values of M_S see Fig. 5.1-5a. For notation see Fig. 5.1-3.)

Fig. 5.1-5b. L_1/X_T for air vs shock Mach number M_S .



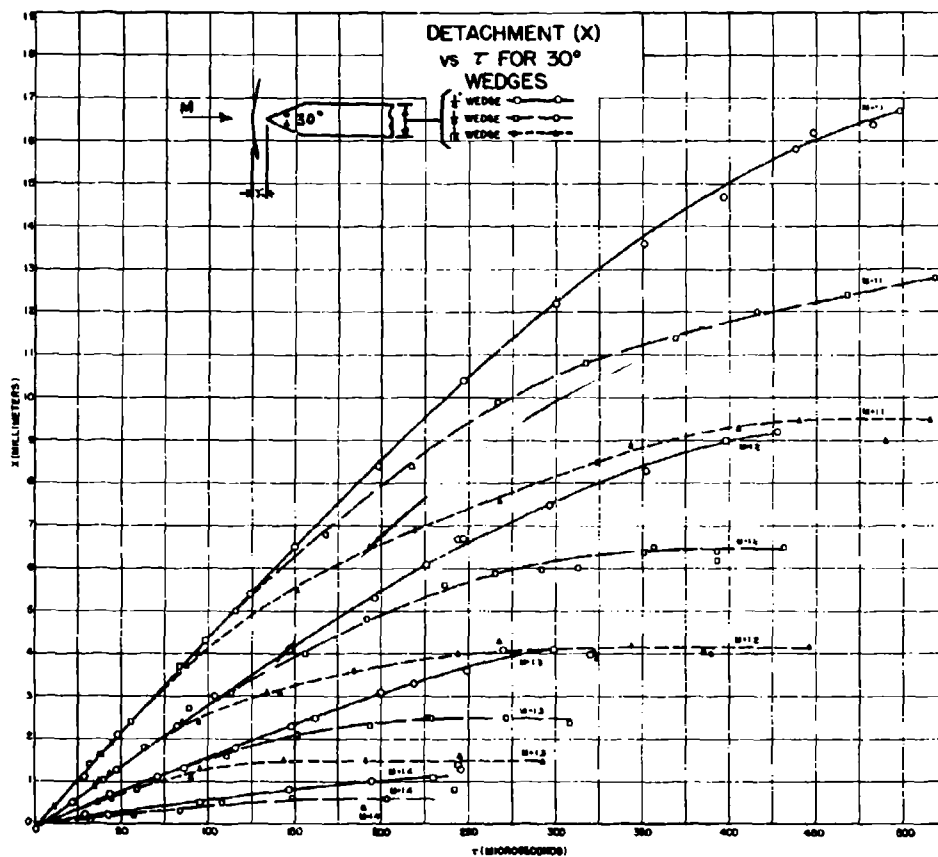
(For higher values of M_s and combustion drive see Fig. 5.1-7.
For notation see Fig. 5.1-3.)

Fig. 5.1-6. L_1/L_4 for constant-area shock tube with various drives and air as driven gas as a function of shock Mach number M_s .



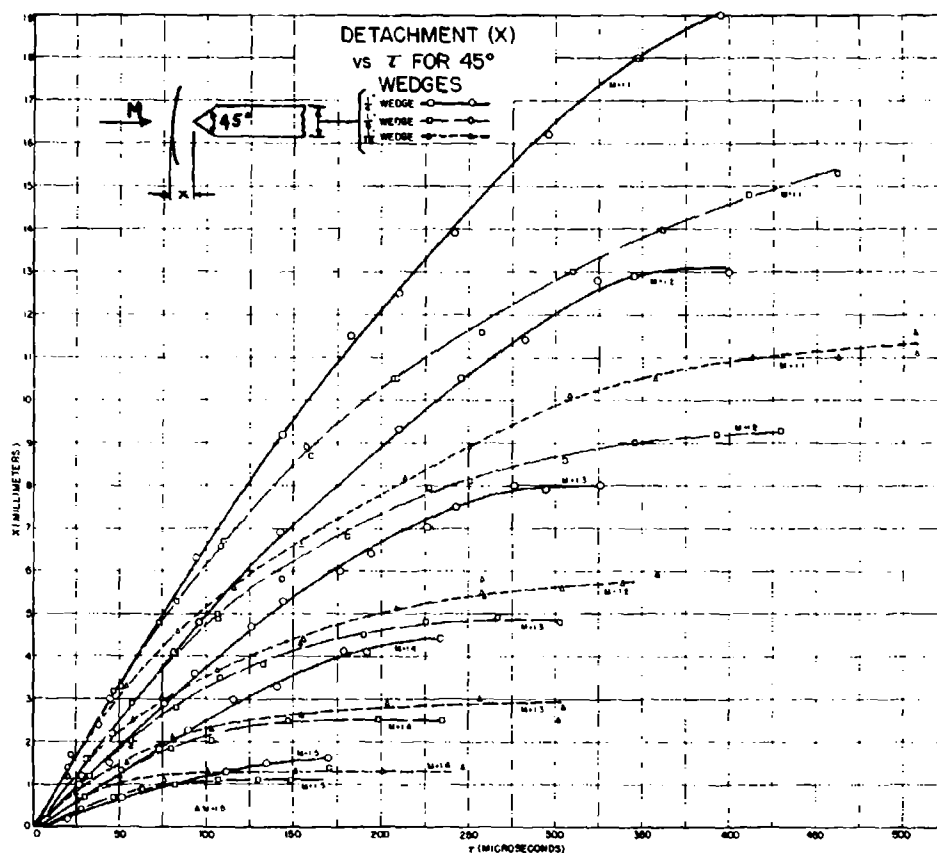
(For lower values of M_s see Fig. 5.1-6. For notation see Fig. 5.1-3.)

Fig. 5.1-7. L_1/L_4 for constant-area shock tube with various drives and air as driven gas as a function of shock Mach number M_s .



(Mach number M refers to region (2).)

Fig. 5.1-8. Measured shock detachment distance x as a function of time τ following passage of primary shock wave for two-dimensional 30-degree wedges (Ref. 4).



(Mach number M refers to region (2).)

Fig. 5.1-9. Measured shock detachment distance x as a function of time τ following passage of primary shock wave for two-dimensional 45-degree wedges (Ref. 4).

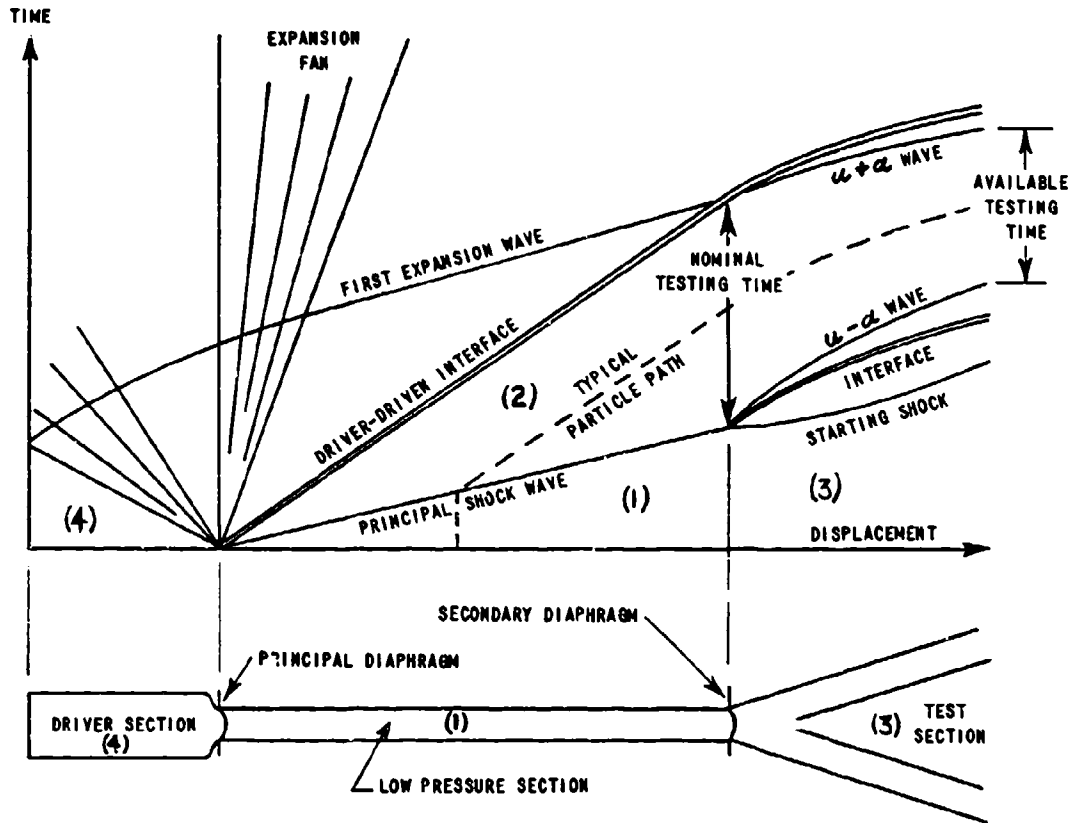
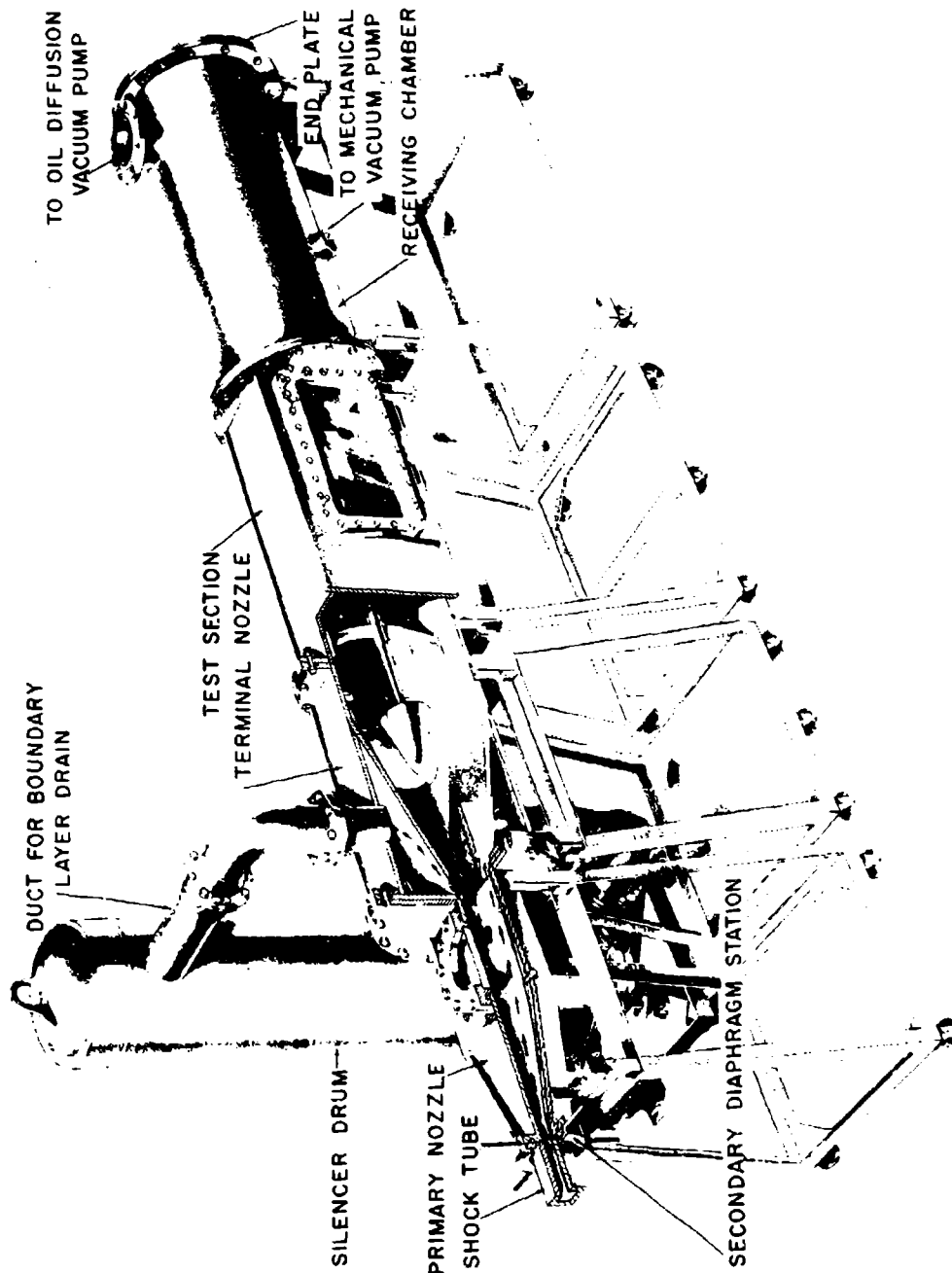


Fig. 5.1-10. Wave diagram of non-reflected shock tunnel (Ref. 27).



(Note two-stage expansion nozzle.)

Fig. 5.1-11. Cornell Aeronautical Laboratory 11 x 15-in. hypersonic shock tunnel (Ref. 27).

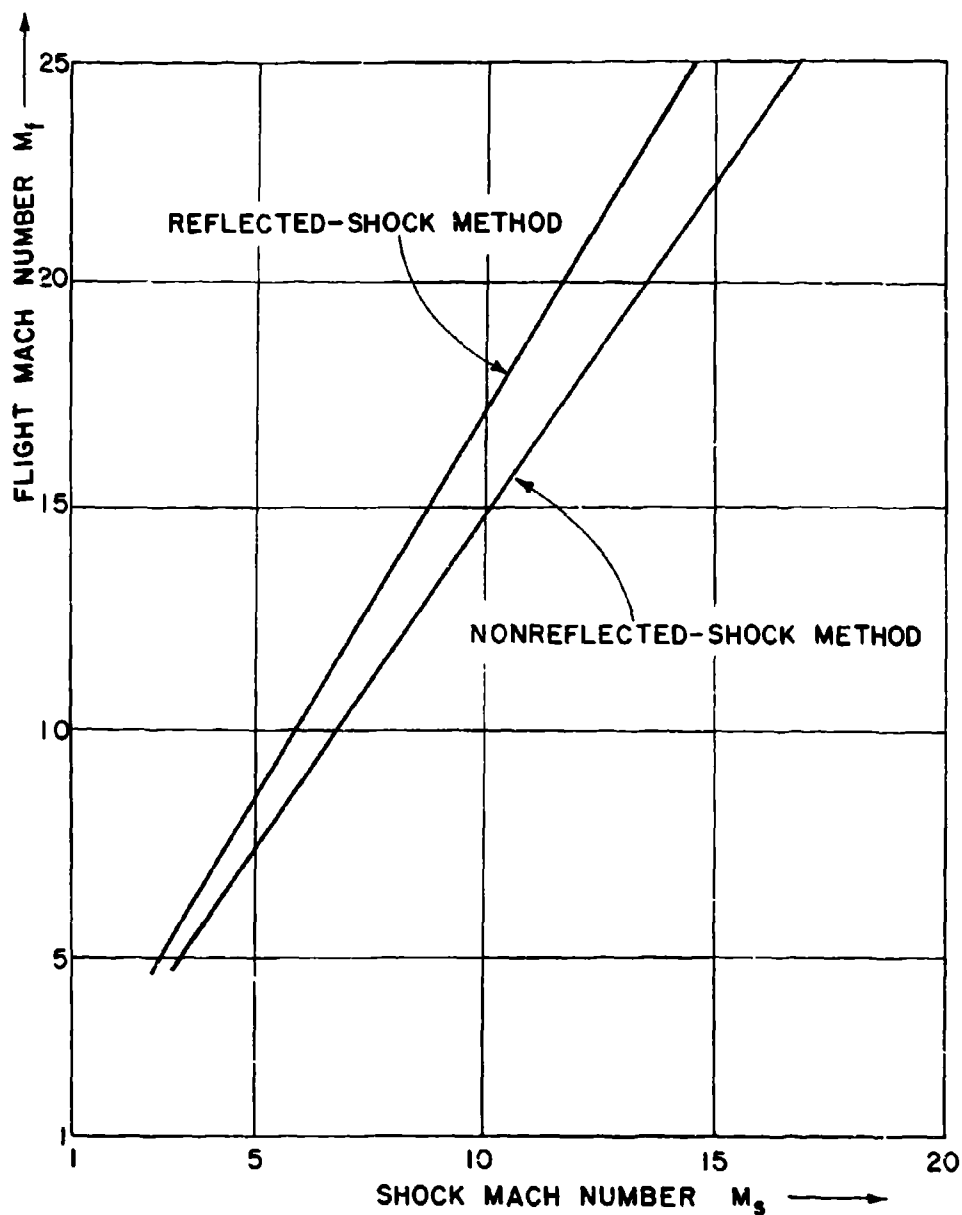


Fig. 5.1-12. Primary shock Mach number M_s required to produce perfect gas flight stagnation temperature for flight Mach number M_f ; flight static temperature $T_f = 392^\circ\text{R}$ (218°K), $T_1 = 518^\circ\text{R}$, $\gamma = 1.4$ (Ref. 23).

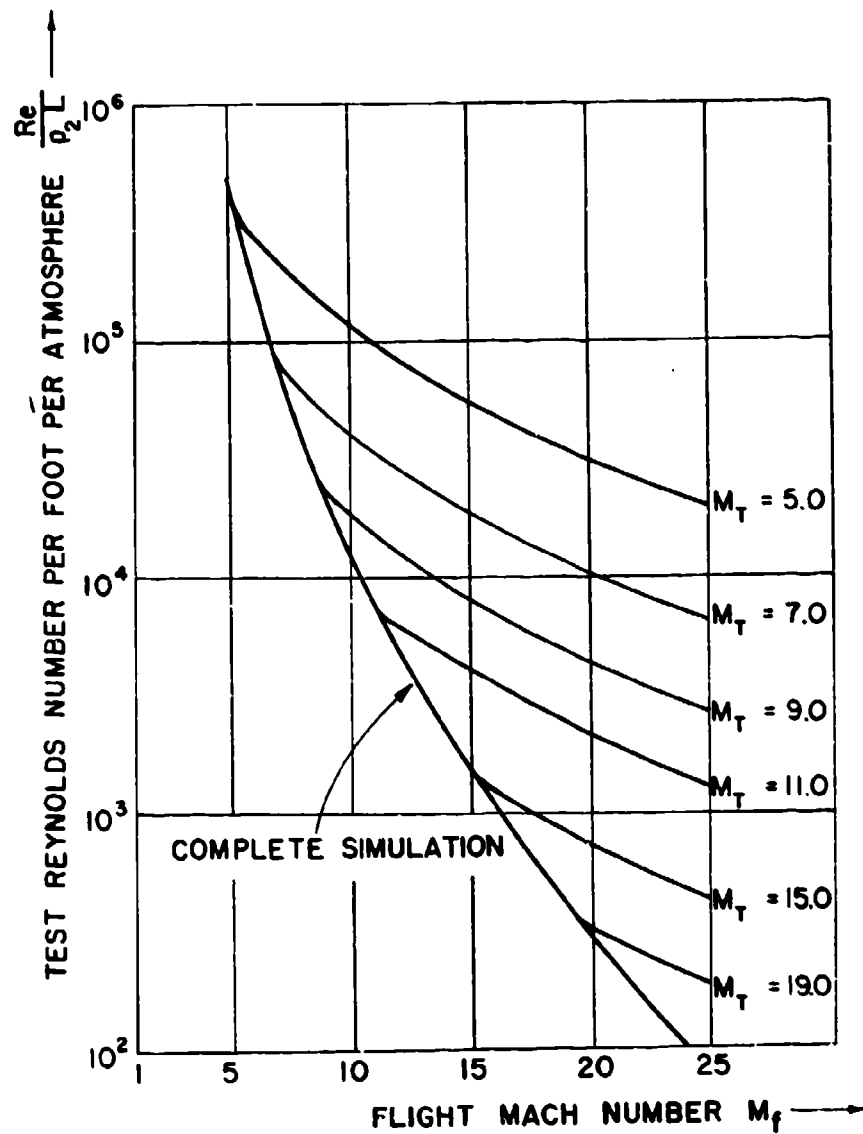


Fig. 5.1-13. Reynolds number performance of non-reflected shock tunnel for stagnation temperatures equal to those in flight at M_f ; perfect gas assumed; M_T = test section Mach number; P_2 = static pressure (atm) behind primary shock wave; $T_f = 392^\circ\text{R}$ (218°K), $T_1 = 518^\circ\text{R}$, $\gamma = 1.4$ (Ref. 23).

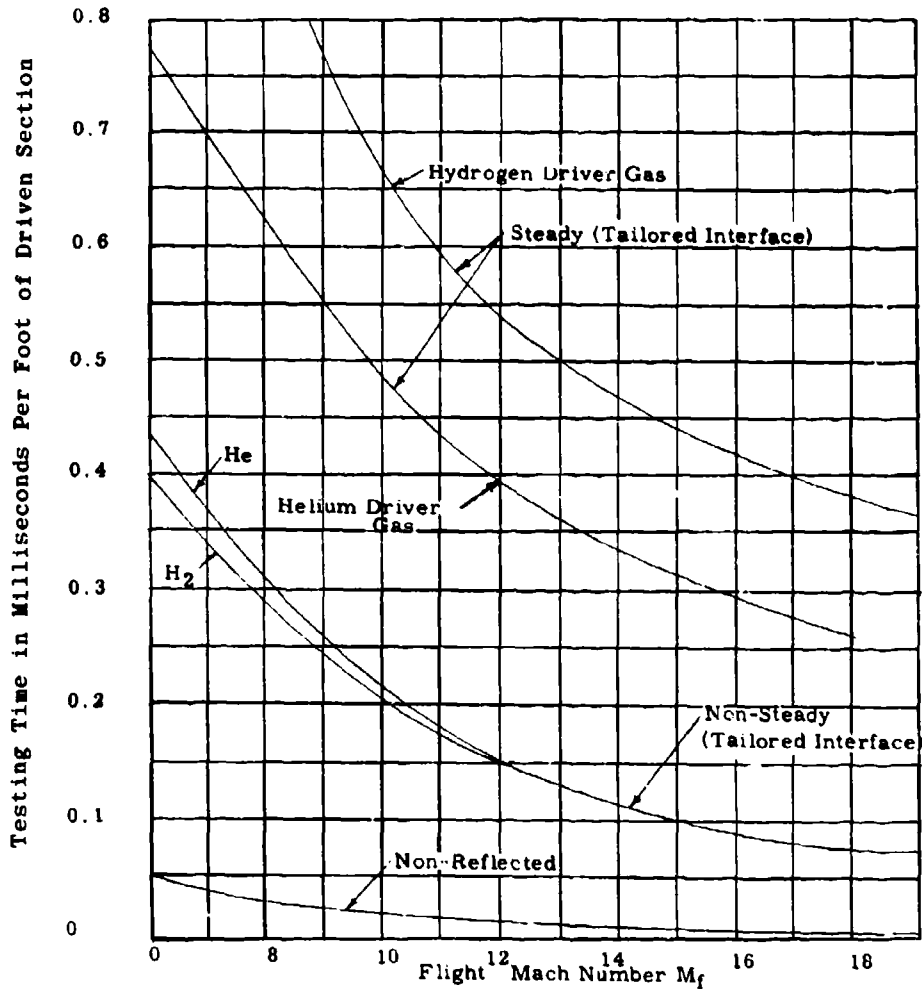


Fig. 5.1-14. Nominal testing times of hypersonic shock tunnel modifications based on equilibrium real-gas calculations; stagnation temperatures equal to those in flight at M_f ; $T_f = 392^\circ\text{R}$ (218°K), $T_1 = 518^\circ\text{R}$ (Ref. 27).

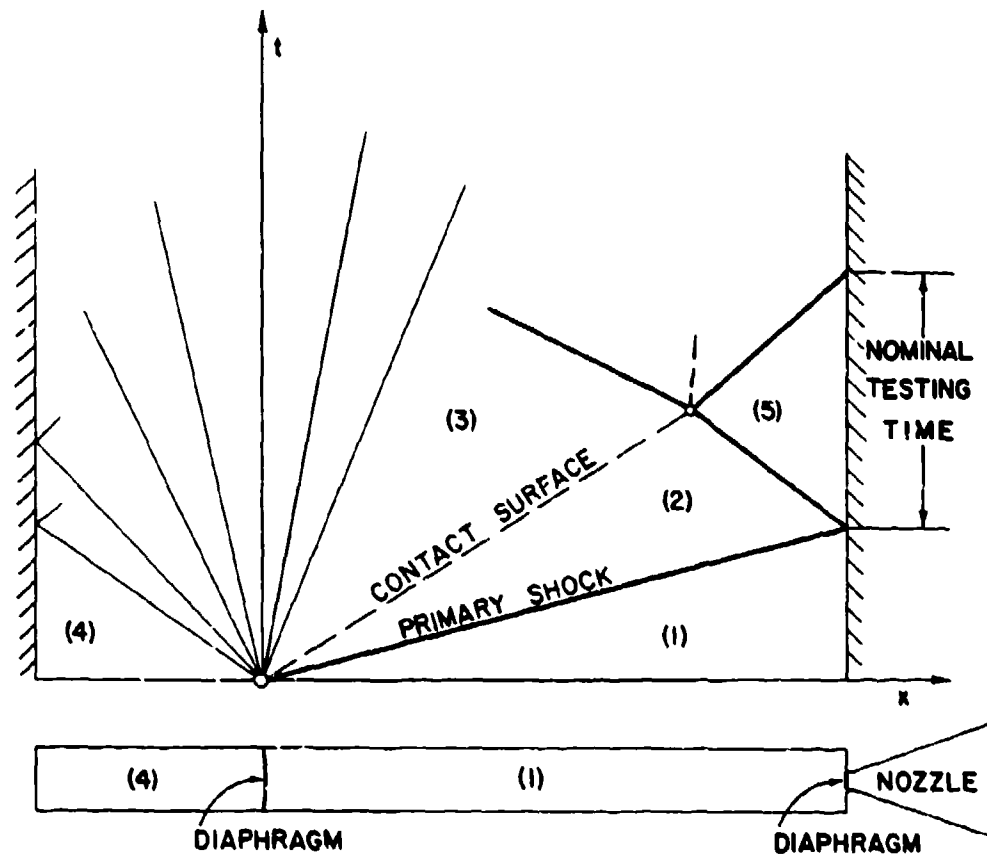


Fig. 5.1-15. Wave diagram for reflected shock tunnel.

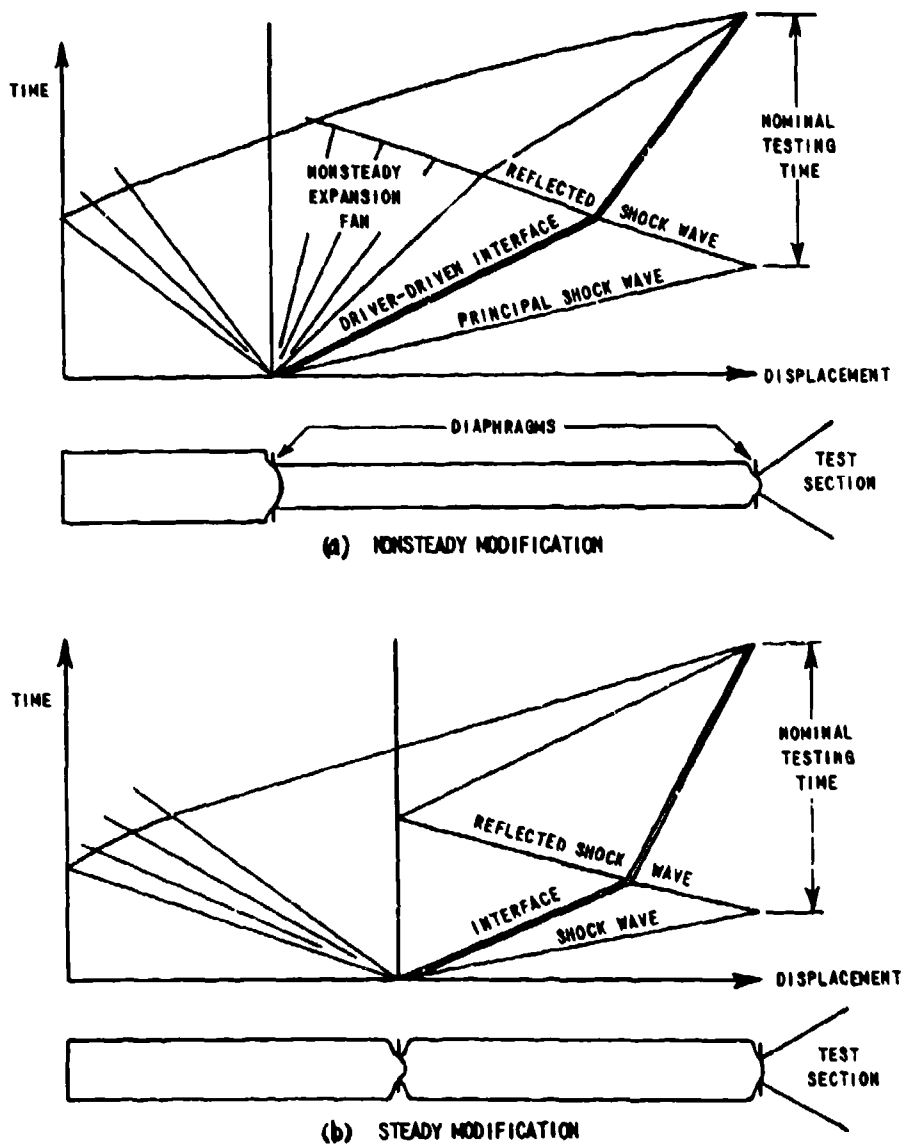
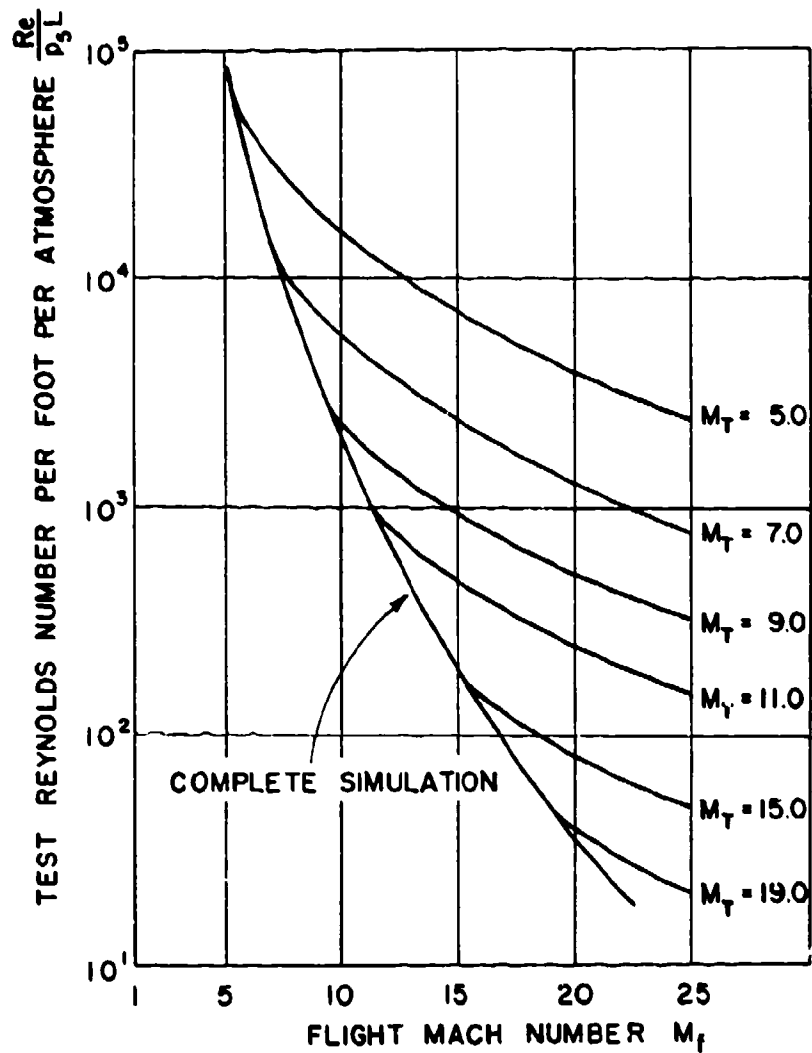


Fig. 5.1-16. Wave diagrams illustrating variations of the tailored-interface modification to the shock tunnel which gives increased testing times (Ref. 27).



(For reflected shock wave see Fig. 5.1-15.)

Fig. 5.1-17. Reynolds number performance of reflected shock tunnel for stagnation temperatures equal to those in flight at M_f ; perfect gas assumed; M_T = test section Mach number; P_5 = static pressure (atm) behind reflected shock wave; $T_f = 392^\circ\text{R}$ (218°K), $T_1 = 518^\circ\text{R}$, $\gamma = 1.4$ (Ref. 23).

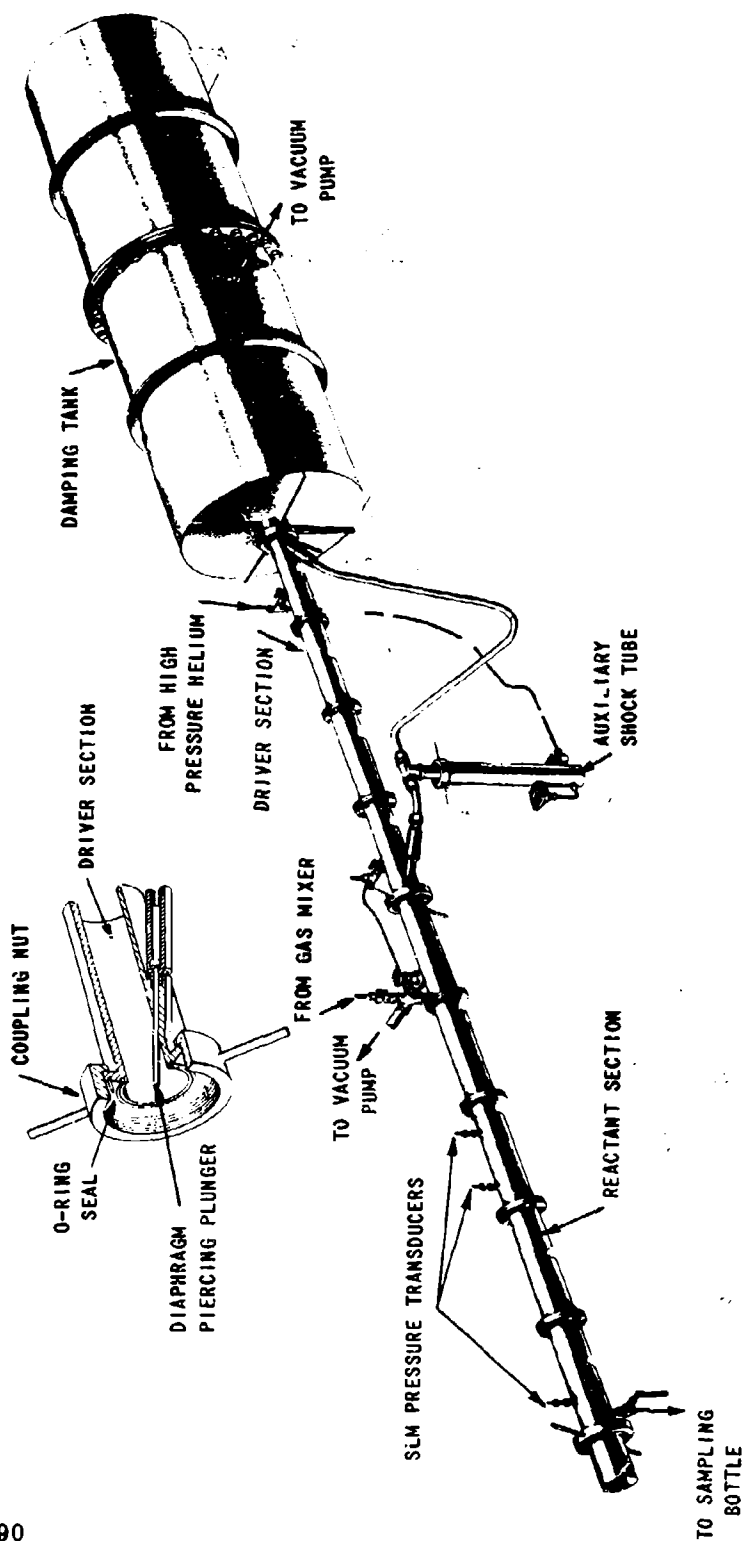


Fig. 5.3-1. Chemical shock tube for producing a single high-temperature pulse (Ref. 88).

REFERENCES

1. Mautz, C. W., Geiger, F. W., and Epstein, H. T. "On the Investigation of Supersonic Flow Patterns by Means of the Shock Tube," Phys. Rev., Vol. 74 (December 1948), p. 1872.
2. Rudinger, G. "Note on the Use of the Shock Tube as an Intermittent Supersonic Wind Tunnel," Phys. Rev., Vol. 75 (June 1949), p. 1948.
3. Weimer, D. K., Fletcher, C. H., and Bleakney, W. "Transonic Flow in a Shock Tube," J. Appl. Phys., Vol. 20 (April 1949), p. 418.
4. Geiger, F. W., Mautz, C. W., and Hollyer, R. N. The Shock Tube as an Instrument for the Investigation of Transonic and Supersonic Flow Patterns. Engineering Research Institute, University of Michigan, June 1949.
5. Lobb, R. K. A Study of Supersonic Flows in a Shock Tube. UTIA Report 8. Institute of Aerophysics, University of Toronto, May 1950.
6. Lukasiewicz, J. Shock Tube Theory and Applications. NAE Report 15. Ottawa, Canada: National Aeronautical Establishment, 1952. (Originally published as Reports MT-10 and MT-11. Ottawa, Canada: Division of Engineering, National Research Council, January 1950.)
7. Bingham, H. H., Weimer, D. K., and Griffith, W. The Cylinder and Semicylinder in Subsonic Flow. Tech. Report JJ-13. Department of Physics, Princeton University, 1952.
8. Griffith, W. "Transonic Flow over Wedge Profiles," J. Aeronaut. Sci., Vol. 19 (1952), p. 249.
9. Witmer, E. A., Herrmann, W., and Beals, V. L., Jr. Transient Aerodynamics of Two-Dimensional Airfoils: Part I--Interferometric Measurements of Two-Dimensional Airflow Development about a Symmetrical Double-Wedge Airfoil in Shock-Initiated Flow. WADC TR 54-368, Part I. Massachusetts Institute of Technology Aircraft Laboratory, August 1954.
10. Kantrowitz, A. Problems of High Mach Number Simulation. (Talk given at Joint Session of AGARD Wind Tunnel Panel and Flight Test Panel, Ottawa, Canada, June 1955.)
11. Lees, L. "Hypersonic Flow," Fifth International Aeronautical Conference, Los Angeles, Calif., 1955. New York: Institute of Aeronautical Sciences, pp. 241-276.
12. Rose, P. H. and Stark, W. I. Stagnation Point Heat Transfer Measurements in Air at High Temperature. Research Note 24. Everett, Mass.: AVCO Research Laboratory, AVCO Manufacturing Corp., December 1956. (See also J. Aeronaut. Sci., Vol. 25 (February 1958), pp. 86-97.)

13. Rose, P. H. Physical Gas Dynamics Research at the AVCO Research Laboratory. Research Note 37. Everett, Mass.: AVCO Research Laboratory, AVCO Manufacturing Corp., May 1957. (Also AGARD Report 145. July 1957.)
14. Rabinowicz, J. Aerodynamic Studies in the Shock Tube. Hypersonic Research Project Memorandum 38. Guggenheim Aeronautical Laboratory, California Institute of Technology, June 1957.
- 14a. Rabinowicz, J. Measurement of Turbulent Heat Transfer Rates on the Aft Portion and Blunt Base of a Hemisphere-Cylinder in the Shock Tube. Hypersonic Research Project Memo. 41. Guggenheim Aeronautical Laboratory, California Institute of Technology, November 1957.
15. Stever, H. G. and Bisplinghoff, R. L. "The Shock Tube in Aerodynamic and Structural Research," Proc. Nat. Acad. Sci., Vol. 40 (1954), pp. 557-565.
16. Logan, J. G., Jr. Relaxation Phenomena in Hypersonic Aerodynamics. IAS Preprint No. 728. New York: Institute of Aeronautical Sciences, 1957.
17. Mirels, H. and Braun, W. H. Nonuniformities in Shock-Tube Flow Due to Unsteady Boundary Layer Action. NACA TN 4021, May 1957.
18. Kim, C. S. "Supersonic Flow Past Circular Cylinder," J. Phys. Soc. of Japan (April 1956), pp. 439-445.
19. Masson, D. J. and Gazely, Carl, Jr. Surface Protection and Cooling Systems for High Speed Flight. Rand Corporation P-829 (Revised April 1956). Santa Monica, Calif.: Rand Corporation, March 1956.
20. Hertzberg, A. "A Shock Tube Method of Generating Hypersonic Flows," J. Aeronaut. Sci., Vol. 18 (December 1951), pp. 803-805.
21. Parks, E. K. Supersonic Flow in a Shock Tube of Divergent Cross-Section. UTIA Report 18. Institute of Aerophysics, University of Toronto, 1952.
22. Yoler, Y. A. Hypersonic Shock Tube. GALCIT Memo. No. 18. Guggenheim Aeronautical Laboratory, California Institute of Technology, July 1954.
23. Hertzberg, A., Smith, W. E., Glick, H. S., and Squire, W. Modifications of the Shock Tube for the Generation of Hypersonic Flow. Report AD-789-A-2, AECD-TN-55-15. Buffalo, N. Y.: Cornell Aeronautical Laboratory, Inc., March 1955.
24. Glick, H. S., Hertzberg, A., and Smith, W. E. Flow Phenomena in Starting a Hypersonic Shock Tunnel. Report AD-789-A-3, AECD-TN-55-16. Buffalo, N. Y.: Cornell Aeronautical Laboratory, Inc., March 1955.
25. Squire, W., Hertzberg, A., and Smith, W. E. Real Gas Effects in a Hypersonic Shock Tunnel. Report AD-789-A-1, AECD-TN-55-14. Buffalo, N. Y.: Cornell Aeronautical Laboratory, Inc., March 1955.

26. Hertzberg, A. "The Application of the Shock Tube to the Study of the Problems of Hypersonic Flight," Jet Propulsion (July 1956), pp. 549-568.
27. Hertzberg, A. The Shock Tunnel and its Application to Hypersonic Flight. Report AD-1052-A-5. Buffalo, N. Y.: Cornell Aeronautical Laboratory, Inc., June 1957. (Also AGARD Report 144, July 1957.)
28. Busing, J. R. Reynolds Numbers in the Hypersonic Shock Tunnel. Report LA. t. 074. Stevenage, Luton, England: English Electric Company Ltd., February 1956.
29. Henshall, B. D. and Gadd, G. E. Factors Affecting the Performance of the Nozzle of a Hypersonic Shock Tube. ARC 18,201. Aeronautical Research Council, Ministry of Supply. London: Her Majesty's Stationery Office, 1956.
30. Schultz, D. L. and Henshall, B. Hypersonic Shock Tube Equipment at the National Physical Laboratory, U. K. AGARD Report 147. July 1957.
31. Stalder, J. R. and Seiff, A. The Simulation and Measurement of Aerodynamic Heating at Supersonic and Hypersonic Mach Numbers. (Paper presented at the Seventh Meeting of the AGARD Wind Tunnel and Model Testing Panel, Ottawa, Canada, June 1955.)
32. Cox, R. N. and Winter, D. F. T. The Light Gas Hypersonic Gun Tunnel at A. R. D. E. AGARD Report 139. Fort Halstead, Kent, England, July 1957.
33. Smith, L. G. Photographic Investigations of the Reflection of Plane Shocks in Air. OSRD Report 6271. Washington: Office of Scientific Research and Development, 1945.
34. Fletcher, C. H. and Taub, A. H. "The Mach Reflection of Shock Waves at Nearly Glancing Incidence," Revs. Modern Phys., Vol. 23 (July 1951), pp. 271-286.
35. Jahn, R. G. "The Refraction of Shock Waves at a Gaseous Interface," J. Fluid Mech., Vol. 1, Part 5 (November 1956), pp. 457-489.
36. Bleakney, W., White, D. R., and Griffith, W. C. "Measurements of Diffraction of Shock Waves and Resultant Loading of Structures," J. Appl. Mech., Vol. 17 (December 1950), pp. 439-445.
37. Griffith, W. and Brickl, D. E. "The Diffraction of Strong Shock Waves," Phys. Rev., Vol. 89 (January 1953), pp. 451-453.
38. Griffith, W. C. and Bleakney, W. "Shock Waves in Gases," Am. J. Phys., Vol. 22 (December 1954), pp. 597-612.
39. Lee, J. D. Condensation in Supersonic Flow. Unpublished M. A. Sc. Thesis. Institute of Aerophysics, University of Toronto, 1950.
40. Glass, I. I., Martin, W., and Patterson, G. N. A Theoretical and Experimental Study of the Shock Tube. UTIA Report 2. Institute of Aerophysics, University of Toronto, 1953.

41. Wegner, P. and Lundquist, G. "Condensation of Water Vapour in the Shock Tube Below 150°K," J. Appl. Phys., Vol. 22 (1951), pp. 233-234.
42. Winkler, E. M. "Condensation Study by Absorption or Scattering of Light." High Speed Aerodynamics and Jet Propulsion, Vol. IX, Part I (edited by R. W. Landenberg). Princeton: Princeton University Press, 1954, p. 289.
43. Huber, P. W., Fitton, C. E., and Delpino, F. Experimental Investigation of Moving Pressure Disturbances and Shock Waves and Correlation with One-Dimensional Unsteady-Flow Theory. NACA TN 1903, 1949.
44. Billington, I. J. "An Experimental Study of the One-Dimensional Refraction of a Rarefaction Wave at a Contact Surface," J. Aeronaut. Sci., Vol. 23 (November 1956), pp. 997-1006.
45. Mack, J. E. Density Measurements in Shock Tube Flows with the Chrono-Interferometer. Tech. Report 4. Institute of Research, Lehigh University, 1954.
46. Hall, J. G. "Transition Through a Contact Region," J. Appl. Phys., Vol. 26 (June 1955).
47. Resler, E. L., Lin, Shao-Chi, and Kantrowitz, A. "The Production of High Temperature Gases in Shock Tubes," J. Appl. Phys., Vol. 23 (1952), p. 1390.
48. Petschek, H. E., Rose, P. H., Glick, H. S., Kane, A., and Kantrowitz, A. "Spectroscopic Studies of Highly Ionized Argon Produced by Shock Waves," J. Appl. Phys., Vol. 26 (January 1955), pp. 83-95.
49. Fowler, R. G., Atkinson, W. R., and Marks, L. W. "Ion Concentrations and Recombination in Expanding Low Pressure Sparks," Phys. Rev., Vol. 87 (1952), p. 966.
50. Turner, E. B. The Production of Very High Temperatures in the Shock Tube with an Application to the Study of Spectral Line Broadening. Report ASOSR TN-56-150. University of Michigan, May 1956.
51. Hertzberg, A. "The Application of the Shock Tube to the Study of High Temperature Phenomena in Gases," Appl. Mech. Rev., Vol. 9 (December 1956), pp. 505-509.
52. Penner, S. S., Harshbarger, F., and Vali, V. An Introduction to the Use of the Shock Tube for the Determination of Physico-Chemical Parameters. Jet Propulsion Center, California Institute of Technology, June 1956.
53. Ferri, A. (editor). Fundamental Data Obtained from Shock Tube Experiments. AGARDograph (to be published).
54. Penner, S. S. The Determination of Absolute Intensities and F-Numbers from Shock-Tube Studies. TR-5. Jet Propulsion Laboratory, California Institute of Technology, 1957.

55. Schreffler, R. G. and Christian, R. H. "Boundary Disturbances in High Explosive Shock Tubes," J. Appl. Phys., Vol. 25 (1954), p. 324.
56. Keck, J., Kivel, B., and Wentink, T. "Emissivity of High Temperature Air," Heat Transfer and Fluid Mechanics Institute. Stanford, Calif.: Stanford University Press, 1957, p. 279.
57. Wurster, W. H., Glick, H. S., and Treanor, C. E. Radiative Properties of High Temperature Air. Report QM-997-A-1. Buffalo, N. Y.: Cornell Aeronautical Laboratory, Inc., 1957.
- Wurster, W. H. and Glick, H. S. "Ultraviolet Spectrum of Air at 5750^bK," J. Chem. Phys., Vol. 27 (November 1957), p. 1218.
58. Petschek, H. E. "Approach to Equilibrium Ionization Behind Strong Shock Waves in Argon." Unpublished Ph. D. Dissertation, Cornell University, 1955.
- Petschek, H. E. and Byron, S. "Approach to Equilibrium Ionization Behind Strong Shock Waves in Argon," Annals. Phys., Vol. I, No. 3 (June 1957), pp. 270-315.
59. Lin, Shao-Chi, Resler, E. L., and Kantrowitz, A. "Electrical Conductivity of Highly Ionized Argon Produced by Shock Waves," J. Appl. Phys., Vol. 26 (January 1955), p. 95.
60. Lamb, L. and Lin, Shao-Chi. "Electrical Conductivity of Thermally Ionized Air Produced in a Shock Tube," J. Appl. Phys., Vol. 28 (July 1957), p. 754.
61. Patrick, R. M. and Kantrowitz, A. "Review of Recent Work on Strong Shock Waves Done at Cornell University." Proceedings of the Gas Dynamics Symposium on Aerothermochemistry. Evanston, Ill.: Northwestern University, 1956.
62. deLeeuw, J. H. The Interaction of a Plane Strong Shock Wave with a Steady Magnetic Field. UTIA Report 49. Institute of Aerophysics, University of Toronto, 1958.
63. Greene, E. F. and Hornig, D. F. "The Shape and Thickness of Shock Fronts in Argon, Hydrogen, Nitrogen, and Oxygen," J. Chem. Phys., Vol. 21 (1953), p. 617.
64. Blackman, V. "Vibrational Relaxation in Oxygen and Nitrogen," J. Fluid Mech., Vol. 1 (1956), p. 61.
65. Smiley, E. F., Winkler, E. H., and Slawsky, Z. I. "Measurement of the Vibrational Relaxation Effect in CO₂ by Means of Shock Tube Interferograms," J. Chem. Phys., Vol. 21 (1952), p. 924.
66. Resler, E. L. and Scheibe, M. "Instrument to Study Relaxation Rates Behind Shock Waves," J. Acoust. Soc. Am., Vol. 27 (September 1955), pp. 932-938.
67. Glick, H. S. and Wurster, W. H. "A Shock Tube Study of Dissociation Relaxation in Oxygen," J. Chem. Phys., Vol. 27 (November 1957), p. 1224.

68. Greene, E. F. "Chemical Reactions in Strong Shock Waves," J. Am. Chem. Soc., Vol. 76 (1954), p. 2127.
69. Shepherd, W. C. F. "Ignition of Gas Mixture by Impulsive Pressure," Third Symposium on Combustion, Flame, and Explosion Phenomena. Baltimore: The Williams and Wilkins Co., 1949, p. 301.
70. Fay, J. A. "Some Experiments on the Ignition of Detonation in $2 \text{ H}_2\text{-O}_2$ Mixtures by Uniform Shock Waves," Fourth Symposium (International) on Combustion. Baltimore: The Williams and Wilkins Co., 1953, p. 501.
71. Steinberg, M. and Kaskan, W. E. "The Ignition of Combustible Mixtures by Shock Waves," Fifth Symposium (International) on Combustion. New York: Reinhold Publishing Corp., 1955, p. 664.
72. Fay, J. A. and Lekawa, E. "Ignition of Combustible Gases by Converging Shock Waves," J. Appl. Phys., Vol. 27 (March 1956), p. 261.
73. Markstein, G. H. "A Shock-Tube Study of Flame-Pressure Wave Interaction," Sixth Symposium (International) on Combustion. New York: Reinhold Publishing Corp., 1957, p. 387.
74. Bitondo, D., Thomas, N., and Perper, D. "Ignition in Transient Flows," Heat Transfer and Fluid Mechanics Institute. Stanford, Calif.: Stanford University Press, 1957, p. 343.
75. Harshbarger, F. C. "Physico-Chemical Processes Behind Shock Front." Unpublished Ph. D. Dissertation, California Institute of Technology, 1957.
76. Fairbairn, A. R. and Gaydon, A. G. "Spectra Produced by Shock Waves, Flames, and Detonations," Proc. Roy. Soc., Series A (April 1957), pp. 464-475.
77. Carrington, P. and Davidson, N. "Photo Electric Observation of the Rate of Dissociation of $\text{N}_2 \text{ O}_4$ by a Shock Wave," J. Chem. Phys., Vol. 19 (1951), p. 1313.
78. Britton, D., Davidson, N., and Schott, G. "Shock Waves in Chemical Kinetics. The Rate of Dissociation of Molecular Iodine," Faraday Soc. Discussion, No. 17 (1954), p. 58.
79. Britton, D., Davidson, N., Gehman, W., and Schott, G. "Shock Waves in Chemical Kinetics: Further Studies on the Rate of Dissociation of Molecular Iodine," J. Chem. Phys., Vol. 25 (November 1956), p. 804.
80. Britton, D. and Davidson, N. "Shock Waves in Chemical Kinetics: Rate of Dissociation of Molecular Bromine," J. Chem. Phys., Vol. 25 (November 1956), p. 810.
81. Palmer, H. B. "Study of Shock Waves by Light Absorption and Emission," J. Appl. Phys., Vol. 27 (September 1956), p. 1105.
82. Britton, D. and Davidson, N. "Hydrogen-Bromine Reaction in a Non-steady State," J. Chem. Phys., Vol. 23 (December 1955), p. 2461.

83. Camac, M., Camm, J., Feldman, S., Keck, J., and Petty, C. Chemical Relaxation in Air, Oxygen, and Nitrogen. IAS Preprint No. 802. New York: Institute of Aeronautical Sciences, 1958.
84. Matthews, D. L. Shock Tube Interferometer Measurements of the Rate of Dissociation of Oxygen. Paper 88. (Presented at the American Physical Society Fluid Dynamics Division Meeting, November 1957.)
85. Resler, E. L., Jr. and Cary, B. B. "Dissociation of Air Behind Strong Shock Waves," Proceedings of the Conference on Chemical Aeronomy. New York: Pergamon Press, 1957, p. 320.
86. Feldman, S. "The Chemical Kinetics of Air at High Temperatures: A Problem in Hypersonic Aerodynamics," Heat Transfer and Fluid Mechanics Institute. Stanford, Calif.: Stanford University Press, 1957, p. 173.
87. Glick, H. S., Squire, W., and Hertzberg, A. "A New Shock Tube Technique for the Study of High Temperature Gas Phase Reactions," Fifth Symposium (International) on Combustion. New York: Reinhold Publishing Corp., 1955, p. 393.
88. Glick, H. S., Klein, J. J., Squire, W. "Single-Pulse Shock Tube Studies of the Kinetics of the Reaction $N_2 + O_2 \rightleftharpoons 2NO$ Between 2000-3000°K," J. Chem. Phys., Vol. 27 (October 1957), p. 850.
89. Christian, R. H., Duff, R. E., and Yarger, F. L. "Equation of State of Gases by Shock Wave Measurements, the Dissociation Energy of Nitrogen," J. Chem. Phys., Vol. 23 (1955), p. 2045.
90. Toennies, J. P. and Greene, E. F. "Dissociation Energies of Carbon Monoxide and Nitrogen From Reflected Shock Wave Studies," J. Chem. Phys., Vol. 26 (March 1957), p. 655.
91. Reynolds, G. T. A Preliminary Study of Plane Shock Waves Formed by Bursting Diaphragms in a Tube. Armor and Ordnance Report A-192 (OSRD No. 1519). Princeton University Station. Washington: National Defense Research Committee of the Office of Scientific Research and Development, June 1953.
92. Fletcher, C. H., Read, W. T., Stoner, R. G., and Weimer, D. K. Final Report on Shock Tube, Piezoelectric Gauges and Recording Apparatus. NDRC Report No. A-356, (OSRD Report No. 6321). Princeton University Station. Washington: National Defense Research Committee of the Office of Scientific Research and Development, November 1945.
93. P. ... , C. G. and Bowersox, R. B. Experimental and Mathematical Techniques for Determining the Dynamic Response of Pressure Gauges. JPL Memo. 20-68. Jet Propulsion Laboratory, California Institute of Technology, 1953.
94. Wittliff, C. E., Wilson, M. R., and Hertzberg, A. "The Tailored-... Hypersonic Shock Tunnel (Cornell Aeronautical Laboratory, Inc.)." Paper presented at the ASME-ARS Aviation Conference, Dallas, Texas, March 16-20, 1958. (Also appears in J. Aero/Space Sci., Vol. 26, No. 4, April 1959.)

5. References

NAVORD Report 1488 (Vol. 6, Sec. 18)

95. Hartunian, R., Russo, A., and Marrone, P. "Boundary-Layer Transition and Heat Transfer in Shock Tubes." (Paper presented at the Heat Transfer and Fluid Mechanics Institute, University of California, 1958.)
96. Laporte, O. and Cole, A. L. Construction of a Sector Shock Tube. Progress Report No. 7. Engineering Research Institute, University of Michigan, June 1957.
97. Campbell, G. R. "Initial Wave Phenomena in a Weak Spherical Blast," J. Appl. Phys., Vol. 29 (January 1958), p. 55.
98. Glass, I. I. and Hall, J. G. "Shock Sphere - An Apparatus for Generating Spherical Flows," J. Appl. Phys., Vol. 28 (April 1957), p. 424.

6. Shock-Tube Materials, Design, and Construction

With the rather widespread use of the shock tube as a research tool in recent years, shock tube designs have naturally become somewhat specialized according to application. An example is the chemical shock tube, Subsec. 5.3.2.2. This subsection is concerned with some of the general design or construction aspects common to most applications, and is limited to conventional shock tubes employing diaphragms.

6.1 Tube Design and Construction

6.1.1 Tube Length and Internal Cross-Section

Shock tube length and internal cross-section shape and area are, of course, determined by the particular application and the funds available. For model testing in a uniform channel tube, for example, the required test time and the driving method would determine the driver and driven section lengths as considered in Subsec. 5.1.1.2. Choice of tube internal cross-section geometry would be influenced by factors such as shock attenuation and boundary-layer development on the tube walls (Subsecs. 5.1.1.2 and 3.2), flow Mach number and model Reynolds number required (which determine model size and the tube pressure loading), whether the model flow is to be two or three dimensional, and the type of instrumentation to be used for flow measurement.

Use of the optical techniques of shadowgraph, schlieren, and interferometry is simplified with rectangular tube cross-sections which can accommodate plane parallel windows. Quantitative interferometry is most often applied to two-dimensional flows for which the rectangular geometry is a natural choice. The tube width along the light path in this case must be sufficient to give adequate optical sensitivity without introducing excessive refraction effects (Subsec. 7.2.1.4). Typically, for two-dimensional interferometric work at relatively low pressure levels the tube height might be several times the width to avoid or delay wave interaction with the tube walls.

While advantageous for certain optical studies, the rectangular or square cross-section is inferior to the circular cross-section as regards structural strength and general ease of construction and sealing. A common construction method for use of the rectangular cross-section at high pressure levels is described below (Subsec. 6.1.2). If the application permits, the driver section of the tube may be of circular cross-section with transition to a rectangular or square cross-section driven channel at the diaphragm station.

Table 6.1-1 from Ref. 1 gives the geometries of a number of (unclassified) shock tubes in the U.S.A. and Canada. The bulk of the tube geometries listed fall into the following ranges (Ref. 1):

1. Tube diameter (or area equivalent): 1 to 4 in.
2. Tube length/tube diameter: 40 to 150.
3. Driver section length/driven section length: 0.15 to 0.25.

Also, roughly an equal number of tubes have rectangular as circular internal cross-sections.

6.1.2 Tube Structure

With many shock tubes the desired driver or driven tube lengths are achieved by coupling together a number of short sections of similar construction. This approach provides flexibility in tube arrangement and is advantageous when various driver or driven tube lengths are likely to be required. The short component sections may have individual supports with wheels for convenient assembly, or else a single two-rail support to carry all sections may be used. A disadvantage of a large number of short sections is the increased number of joints which increase the possibility of leaks, waviness in the tube, and interior steps due to slight misalignment.

The almost universal method of sealing at joints is by means of commercial Neoprene or Teflon "O" rings. These are very efficient when properly used and are available in a large range of sizes. Alignment of sections is aided with dowels in smaller tubes and male-female joints in larger tubes. Common methods of coupling sections together include bolting through end flanges and threaded couplings. Rapid coupling or clamping at the diaphragm joint and of tube end plates which are frequently removed to permit cleaning of the tube is a worthwhile operating convenience. Hydraulic or pneumatic diaphragm clamping mechanisms have been used on large tubes. For smaller tubes at suitably low pressures, the commercial "Vise Grip"* is a very useful device for rapid clamping. Diaphragm clamping is further discussed in Subsec. 6.2 below.

Regarding tube cross-section, the circular cross-section has obvious structural advantages over the rectangular geometry. It lends itself to the use of commercial steel pipe which is available in length in a considerable range of steels, diameters, and wall thicknesses.

Also, short lengths of commercial pyrex glass** or quartz pipe may be included in the driven tube for luminosity studies. For the highest pressure level shock tubes, tube lengths of circular cross-section have been forged from high-strength alloy steels. Stainless steels have proved popular because of their high resistance to corrosion and high strength. A number of shock tubes for high pressure use have been constructed from standard gun barrels (see Table 6.1-1).

Rectangular or square cross-section tube lengths may be constructed in a number of ways. For example, metal side plates may be bolted to top and bottom members with a sealing arrangement as shown in Fig. 6.1-1. Another alternative, which reduces the number of seals, is a milled or cast U-channel with the fourth closing side bolted on. Welded construction is preferable to bolting if distortion can be avoided. For high-pressure work, the structural limitations of the rectangular or square cross-section channel can be overcome by encasing it in a steel pipe with "incompressible" filler material, as illustrated in Fig. 6.1-2. Various filler materials used include concrete, plastic metals, and Woods metal. The last is relatively expensive but expands on cooling and can be readily melted out. The rectangular channel insert can be relatively thin walled. Waveguide elements or stainless steel angle or channel are convenient insert materials.

* Manufactured by Petersen DeWitt Mfg. Co., Nebraska.

** Manufactured by Corning Glass Co., for example.

For any application the circular cross-section is preferable from the structural viewpoint, particularly for the driver section of the tube. A combination of a circular driver section and a square driven section is sometimes the most practical arrangement. Transition from round to square can be made at or downstream of the diaphragm. Another alternative, described in Ref. 2, is a rectangular testing channel with an open knife-edged entrance which projects axially into a circular driven tube so as to capture or cut out the central portion of the impinging primary shock wave.

The ASME Code for Unfired Pressure Vessels and standard references such as Refs. 3 and 4 will provide data for the design of tube sections for adequate static strength. However, the most severe stress conditions arise from transient loadings during operation of the tube. Provision for transient stressing usually reduces to estimation of what is considered an adequate safety factor over expected maximum static loadings. With a driver section intended for constant-volume combustion, the possibility of greatly increased loading due to detonation or over-detonation occurring should be considered (see also Subsec. 4.2.1.3). Reflection of normal detonation waves in stoichiometric hydrogen-oxygen mixtures can increase the reflection wall pressure by factors of the order of 40. Wall pressure increases of the order of 4 times this amount have been observed with the phenomenon of over-detonation (Ref. 5). Thus, in a driver section designed and operated with a safety margin adequate only for constant-volume combustion, where the expected pressure rise is by a factor of the order of 10 at most, the occurrence of detonation could produce serious overloading. In particular, reflection of detonation from the end cap of the driver section can result in hazardous blowout of the cap. One way of avoiding this is to mount a standard rupture disc in the end cap which will burst at a safe pressure loading. The possibility of detonation occurring can be materially reduced by using a large number of ignition points.

High-pressure loading of the low-pressure section can result from reflection of the primary shock wave. With combustion drive, for example, the pressure following primary shock reflection can be of the same order of magnitude as the peak driver pressure. Hence, with reflection of the primary shock wave, part or all of the low-pressure section may require structural strength comparable to the driver section. Unwanted shock reflection can be avoided by terminating the low-pressure section with a large-volume surge tank.

With small tubes, the axial impulse loads set up in the tube structure and supports which restrain axial movement following the diaphragm burst are usually unimportant. With large diameter tubes at high driver pressures, however, limited recoil of the tube may be desirable to avoid unduly high stressing.

It is common to provide a number of standard type wall openings along the tube length for mounting of various transducers such as shock detectors. A convenient method for doing this with circular tubes made up of short sections is to use tapped instrumentation blocks that are a few inches in length. These blocks have the same bore as the tube and can be inserted at the tube joints. Openings are also required for gas inlets, vacuum system outlets, and windows. For combustion drive, adequate gas mixing before combustion is important for best results. Various gas inlet systems have been used to promote good mixing. One system uses a large number of wall entry holes distributed along the driver section. A simpler method uses an internal, drilled feeder pipe which passes through the driver-section end plate.

A common method of window mounting with a Woods metal seal is illustrated in Fig. 6.1-1. Windows also may be bonded directly to metal with high strength bonding agents such as Hysol cement. Information on the strength of windows may be obtained from the glass manufacturer. Regarding window quality, usually selected plate glass is adequate for shadowgraph and schlieren work. Good quality plate may also make suitable windows for interferometry (see Subsec. 7.2.1.4).

Tolerances on tube internal geometry and alignment are usually necessary to avoid unduly large steps at joints and excessive wall angularity. Practice varies rather widely on this question, depending on the application and on the tube construction and method of manufacture. In the most accurately constructed tubes for more or less general use, step height is limited to the order of 0.001 in. and wall angularity to about 0.15 deg. For many applications, however, these limits are probably unnecessarily severe. Also, often only the low-pressure driven section, or a part of it, is important in this regard. Wall smoothness also varies widely in practice, from honed surfaces of a few micro-inches RMS finish to the standard finishes of commercial smooth pipe or as produced by regular machining operations.

Stainless steels resist corrosion and abrasion, but other steels should be plated for protection. Hard platings are required as the standard soft platings, such as cadmium, are ineffective under the severe conditions present with combustion drives and high temperature operation. Hard chromium is good, but a superior shock-tube plating is "Kanigen" nickel plate, also termed "electrodeless nickel plate". This is a chemically deposited hypophosphite of nickel of excellent homogeneity, which follows any surface contour, however intricate. It can be heat treated to greater hardness than attainable with chromium.

Further useful information on shock-tube design will be found in Refs. 6 to 11, and 18, which describe the construction of specific tubes having constant cross-section area throughout. References for design information on hypersonic shock tunnels and the chemical shock tube are cited in Subsecs. 5.1.2 and 5.3.2.2, respectively.

6.2 Diaphragms

Despite the wealth of shock-tube literature published in recent years, relatively little information of a systematic nature has been reported on the behaviour and bursting characteristics of suitable diaphragm material. This is unfortunate, as successful operation of the shock tube hinges on obtaining suitable diaphragms. Their development from tests is often quite time consuming, particularly so with metallic diaphragms for use at large pressure differences. This subsection attempts to summarize what data have been reported on diaphragm materials and characteristics.

6.2.1 Nonmetallic Diaphragms

The diaphragm materials in common use are most naturally considered according to the range of pressure difference for which they are suited. In the lowest pressure difference range, say from 1 psi to the order of 200 psi across the diaphragm, nonmetallic materials such as cellophane or cellulose acetate are very much used. Table 6.2-1, summarizing reported data for such materials, gives diaphragm material,

thickness, and bursting pressure difference, as well as the tube cross-section geometry and diaphragm supplier. The figures for bursting pressure can be taken as approximate only. Bursting pressures with cellophane type diaphragms depend somewhat on the method of clamping and on their moisture content. A very commonly used laminated cellophane is that known as "Red Zip" (see Table 6.2-1), which shreds into very small pieces when burst. Unfortunately, it is not obtainable in a range of thicknesses. Cellulose acetate is obtainable in various thicknesses but tends to shatter into large jagged fragments. Mylar comes in various thicknesses and can be burst without shattering.

The clamping of cellophane type diaphragms usually presents no problem. The material is clamped between rubber gaskets to provide a seal and a friction grip. The edge of the downstream opening may be smoothed to avoid cutting through the material when the diaphragm is bulged under a pressure difference. Nonmetallic diaphragms are very often burst by controlled mechanical means, rather than allowed to rupture at the natural burst pressure, in order to obtain precise control of effective diaphragm pressure ratio (see Subsec. 6.2.3).

In order to increase the bursting pressure difference of non-metallic diaphragms, several adjacent thicknesses of material may be used. Roughly speaking, the bursting pressure is proportional to the total thickness for a given material and tube cross-section. With such multilayer diaphragms, however, as the number of layers is increased, the bursting characteristics become increasingly less consistent and desirable as regards the primary shock wave formation. In addition to this type of multilayer diaphragm, which effectively acts as a single membrane supporting the total pressure difference, combination diaphragms have been used wherein the various diaphragm layers are separated by gas at intermediate pressures so that the total pressure difference is achieved stepwise. The bursting of such a multi-diaphragm system may be initiated by controlled mechanical bursting of the first layer on the high pressure side.

6.2.2 Metallic Diaphragms

Above pressure differences of the order of a few hundred psi, metal diaphragms are commonly used. Considerable effort has gone into the testing and development of various types of metallic diaphragms with the object of attaining good burst characteristics. Ideally, it is desired that the metal diaphragm burst by petalling cleanly without loss of weight, and that the petals fold back against the tube walls so as not to obstruct the flow. If the diaphragm is fragmented with loss of weight, the detached pieces are accelerated along the tube and are likely to cause considerable damage. Thus the need for proper metal diaphragm rupture is clear.

American practice with metal diaphragms tends to employ a square tube cross-section supporting the diaphragm on the downstream (low-pressure) side, presumably to aid in producing clean petalling. British practice, on the other hand, seems to favour a circular supporting cross-section downstream. Satisfactory petalling has been obtained for both arrangements with natural bursting pressures reproducible to within a few per cent. In both cases, provision of a generous edge radius on the downstream cross-section over which the diaphragm petals can fold, is found desirable. Unfortunately, very little American data on metal diaphragm characteristics have been reported. The quantitative results discussed below are largely derived from British tests employing circular downstream tube cross-sections, as reported in Refs. 12, 13, and 14.

Roughly speaking, ductile metals such as annealed copper and aluminum are found satisfactory for pressure differences from a few hundred psi up to the order of 1500 psi for cross sections of the order of 3-in. diameter. For larger pressure differences, cold-rolled mild steel, nickel, and stainless steel have proved very satisfactory. With constant-volume combustion drive, the diaphragm is allowed to burst naturally from the pressure increase after combustion. With cold driver gas operation, however, controlled bursting by mechanical piercing may also be used (see Subsec. 6.2.3). Controlled scribing of the diaphragm is done by some experimenters to vary the diaphragm bursting pressure and/or promote good petalling (see below).

Reference 12 reports extensive tests on soft aluminum, nickel, and cold-rolled mild steel diaphragms clamped between blocks of 2-in. nominal internal bore diameter as illustrated in Fig. 6.2-1. Single diaphragms of varying thickness and multilayer diaphragms of similar and dissimilar metals were tested for natural bursting characteristics over a range of bursting pressures up to 10,000 psi. The tests included both cold and hot (combustion) bursts. The effects of initial doming of the diaphragm and of scribing were also studied. Reference 13 reports similar tests on natural cold bursting up to 3000 psi of cold-rolled mild steel diaphragms clamped between tube sections of 6-in. nominal internal bore diameter. Reference 14 gives results for the natural burst pressures of unscribed aluminum diaphragms for a 3-in. bore diameter.

The above cold burst tests, including hydraulic loading tests (Ref. 12), show that just before failure the diaphragm is deformed to a near hemispherical shape, particularly so with the less ductile materials. Initial failure is in tension with splitting in the central region along a great circle line. If it is assumed that the deformed diaphragm at failure is a true hemisphere of diameter D , that the original diaphragm thickness t remains unchanged, and that failure occurs in tension at stress f_{ult} , the natural bursting pressure difference P is given to a first approximation by the spherical shell result

$$p = \frac{4t f_{ult}}{D}$$

Cold burst test results for P are compared to the above relation in Fig. 6.2-2 from Ref. 12. The original figure of Ref. 12 has here been replotted in terms of t/D , rather than the original abscissa t , in order to include the test results of Refs. 13 and 14. The general agreement of the test results with the spherical shell prediction is surprisingly good, particularly considering the different bore diameters. The observed values of P are of the order of 10 per cent (or less) low, attributed to the (observed) thinning of the deformed diaphragm at the dome center. The test results from Ref. 12 and 13 include values of P for multilayer diaphragms of steel, in addition to single diaphragm results. Thus, for multilayer diaphragms of the same metal, P is proportional to the total thickness. For multilayer diaphragms of dissimilar metals, P is equal to the sum of the individual diaphragm bursting pressures.

The tests showed no difference in the behaviour of initially flat and initially domed diaphragms. As regards petalling, the high tensile materials such as steel showed a natural tendency to form four

petals as against six petals for low-tensile copper and aluminum. As regards scribing, with ductile metals such as copper and aluminum, this is ineffective in promoting petalling unless the scribing is of such depth as to substantially reduce the natural bursting pressure. The preference (Refs. 12 and 14) is not to scribe the ductile metals. For less ductile mild steel, however, Ref. 12 reports that light, sharp scribing on two perpendicular diameters, which leaves the bursting pressure essentially unchanged, is very effective in producing good petalling (on a 2-in. bore diameter). The effectiveness of the scribing is attributed to the scores acting as local stress raisers in the less ductile steel. Reference 13, on the other hand, reports such scribing of mild steel to be ineffective with a 6-in. bore diameter.

In addition to the limits imposed by the bursting pressure, the diaphragm thickness is limited to a range which provides good petalling. With diaphragms which are too thin, the petals tend to be torn off at the roots. Recommended minimum thicknesses are 0.015 in. for aluminum or mild steel on a 2-in. bore (Ref. 12) and for aluminum on a 3-in. bore (Ref. 14), and 0.064 in. for mild steel on a 6-in. bore (Ref. 13). With diaphragms which are too thick, excessive bending resistance at the petal roots prevents satisfactory folding back, and the flow is obstructed. Recommended maximum thickness is 0.062 in. for a 2-in. bore (Ref. 12). A large radius over which the petals can fold is also helpful.

Reference 12 reports no difference in petal formation between cold and hot (combustion) natural bursts. With combustion, avoidance of combustion pressures much larger than the minimum necessary for bursting is helpful in preventing fragmentation or tearing of petals. Detonation is to be carefully avoided as it can produce blowout of the entire diaphragm with considerable damage to the tube.

Figures 6.2-3 and 6.2-4 from Ref. 12 show burst diaphragms which have petalled nicely. Figure 6.2-3 shows cold and hot burst, scribed steel diaphragms of single and two layers, while Fig. 6.2-4 shows cold burst, scribed (deeply) and unscribed copper diaphragms. Scribed diaphragms are mounted with the scores downstream; the scores are aligned in coincidence for multilayer combinations.

Metal diaphragms are usually clamped between "O"-ring seals. Difficulty is sometimes experienced with excessive "drawing in" of the diaphragm as the gas pressure loading is increased, particularly with the larger diameters. With simple bolting, exterior to the diaphragm clamp area, the increasing driver gas pressure tends to elongate the bolts and weaken the clamping action. Excessive drawing in is lessened by passing the bolts, or dowels, through the diaphragm clamp area, or else by providing a male-female peripheral joint to indent the diaphragm. Another method, effective for large diaphragms, is the free-piston clamp of Ref. 13, illustrated in Fig. 6.2-5. With this arrangement, as the gas pressure is increased the free piston provides clamping action which is unaffected by any bolt elongation. Adequate diaphragm clamp area is also important. For the steel diaphragms tested in the 6-in. bore arrangement of Fig. 6.2-5, Ref. 13 reports a minimum (outer) diaphragm diameter of 16 in. required to avoid excessive drawing.

6.2.3 Methods for Controlled Diaphragm Rupture

Induced rupture of the diaphragm by mechanical or electrical means is often preferable to natural bursting by pressure alone in order to gain precise control of the bursting pressure. The commonest method of inducing metal or nonmetal diaphragms to burst involves mechanical piercing with a sharpened plunger. For nonmetal diaphragms at low pressure loadings, the simplest arrangement is to pass the plunger through the driver section end cap or obliquely through the wall by means of a moving "O"-ring pressure seal, and operate it manually. An oblique spring-driven plunger actuated by a solenoid which avoids the moving seal is shown in Fig. 6.2-6. This unit was actually designed for the synchronized piercing of two diaphragms (see below). Direct solenoid drive of the plunger is also commonly used. By using magnetic coupling through a nonmagnetic housing, such as of stainless steel, electrical leads passing through the housing can be avoided. Pneumatically driven plungers are another possibility. Particularly with metal diaphragms, the plunger is best located on the upstream or high-pressure side to minimize damage from the diaphragm. Best results are always obtained if the diaphragm is pierced at a pressure loading close to that producing a natural burst.

Frequently, as with the chemical shock tube or in some wave-interaction studies, the controlled bursting of two diaphragms spaced at an accurate time interval is necessary. Both mechanical and electrical methods of weakening the diaphragm have been employed to accomplish this. Two assemblies of the type shown in Fig. 6.2-6 were used (Ref. 15) to burst cellophane diaphragms with time delays reproducible to the order of 0.1 millisecon. The two solenoids were pulsed simultaneously and the time delay adjusted by varying the length of stroke of one plunger. An arrangement which uses shock waves to drive the plungers is described in Ref. 16 and illustrated in Fig. 6.2-7. The plungers are located at the ends of two pressure lines which emanate from a tee connection at the low-pressure end of an auxiliary shock tube. Firing of the auxiliary tube sends a shock wave along each line. In piercing aluminum diaphragms, variable time delays reproducible to within 0.1 millisecon were obtained by changing the length of one line.

An electrical method of inducing the rupture of thin metal diaphragms by burning a small central hole with a spark discharge is described in Ref. 17. Figure 6.2-8 illustrates the technique. A high-voltage probe with the tip encased in a dielectric nozzle is held against the diaphragm by a cantilever spring as shown. The spark discharge, switched by a thyratron, takes place from the probe to the diaphragm and is confined to a small area of the diaphragm by the nozzle. For the controlled rupture of two diaphragms, the time delay between the electronic switching of the two discharges can easily be controlled to a few microseconds. From this point of view, this method is an order of magnitude or more better than the mechanical methods. However, there is some question as to whether microsecond accuracy is warranted in view of the probable variations in the diaphragm bursting process following the spark discharge.

6.3 Pressure and Vacuum Technique

The requirements of shock-tube pressure and vacuum technique depend on the application, but in general, the procedures used follow conventional practice. Regarding vacuum technique, two of the more

demanding shock-tube applications are the outgassing of impurities from relatively small surface area tubes, such as might be required for spectroscopic studies, and high pre-evacuation of the large volume nozzle and test section of the hypersonic shock tunnel. Standard texts such as Refs. 19 and 20 may be consulted as a guide in the design of vacuum systems and selection of commercial vacuum components to meet specific requirements as to degree of vacuum and evacuation time.

Commercial cylinders of compressed gas are a convenient source of pure dry gases for most applications. Up to the limits imposed by their maximum pressure on delivery (of the order of 2000 psi) they form a convenient high-pressure supply for the driver. Higher pressures require special compression equipment. High-pressure plumbing required for the shock tube, such as valves, tubing, etc., is usually available commercially.

Measurement of initial pressures in the driver and driven sections is discussed in Subsec. 7.1.1.

6.4 Shock-Tube Hazards

There are some obvious potential hazards in shock-tube experimentation which in the interests of human safety should not be taken lightly. So far as is known to date, there have been no deaths or serious injuries resulting from shock-tube operations. However, accidents have occurred, and in some instances at least the avoidance of serious injury has been more a matter of good fortune than of adequate precaution.

Four sources of major hazard, one or more of which are present in most shock-tube laboratories, are:

1. High-voltage electrical equipment
2. Storage containers of high-pressure gases, in particular of hydrogen and oxygen
3. Use of hydrogen and/or oxygen in the shock tube
4. Shock-tube components which can be pressurized, either by intent or in error

Safeguards in the use of high-voltage electrical equipment include thorough grounding of cabinets, controls, chassis, etc., adequate insulation where needed, bleeder resistances across high-voltage capacitances, foolproof power removal when adjustments are made, and proper labelling and screening off, if possible, of the equipment. Storage of high-pressure gases is, of course, best done off the laboratory premises within a protective enclosure. However, in many cases this is not practical. Commercial gas cylinders are sometimes located in the laboratory close to the shock tube. Common sense precautions with such cylinders include secure upright fastenings to avoid inadvertently knocking them over and releasing the internal gas through damage to the regulator stem, avoidance of a high-temperature environment, and use of proper regulators and lines which are free of any oils or greases. In particular, flammable oils or greases must be kept from contact with high-pressure oxygen else spontaneous combustion results.

With storage and use of hydrogen, hydrogen detection equipment and ample room ventilation should be provided to avoid the possibility of dangerous concentrations of hydrogen in the laboratory. Provision should be made for the safe disposal of unexploded combustible mixtures from the tube. With oxygen-hydrogen combustion drive, the preferred order of gas charging is to add hydrogen last.

Failure of shock-tube components from high pressures is an obvious major hazard and can occur for a number of reasons. Supposed safe and normal pressurization can produce failure through ignorance of actual safe pressure limits. Hydrostatic testing provides only limited assurance against such failure and must be employed with some caution to avoid permanent strain. In equipment which is ill conceived from a safety viewpoint, a slight and easily made deviation from a safe operating procedure, perhaps from ignorance or carelessness, can often produce a hazardous failure. An example of this is accidental admission of high-pressure gas into a low-pressure gauge system not protected with safety blowoff diaphragms or valves.

A study of the explosion hazard presented by a high-pressure shock-tube driver is made in Ref. 21. The summary of this study is presented below.

"The problem of explosive hazards connected with shock tube experimentation has been studied.

From general consideration of the problem it is concluded that experience of others to date is too meager to allow confidence in evaluation of the relative hazard of shock tube experimentation. Of the factors that can be controlled, provision of an enclosure or other protection will probably be the most practical means of reducing the hazard.

A study has been made with a number of simplifying assumptions to determine the wall thickness required to successfully withstand explosions of typical high pressure shock tube drivers. A long enclosure of 10 feet by 10 feet internal cross section was assumed to be constructed with re-inforced concrete walls. A 4-inch I.D. by 8 feet long driver pressurized to 7000 psi working pressure would require walls about 12 inches thick. A 2-inch I.D. by 4 feet long driver pressurized at 11,000 psi would require walls about 8 inches thick. Variation of enclosure size (from the 10 ft. dimension) by a factor of several would cause little variation in wall thickness required.

Fragment velocities (similar to pressure gage blow out) have been estimated to be about 650 ft/sec for a 1-inch diameter mass of 0.01 slug (about 5 ounces) propelled from a vessel containing a pressure of 15,000 psi. Comparison with mild steel plate penetration data shows that a steel plate thickness greater than 1/8 inch would be required to stop such a moving mass."

Table 6.1-1
Survey of unclassified shock tubes in the U.S.A. and Canada up to 1956 (Ref. 1)

No.	Type	Length feet	Driver Section		Design P, psi	Gases	Operate P, psi	Length feet	Low Pressure Section		Design P, psi	Gases	Operate P, psi	Material	Discharge	Remarks
			Finish	Wall thickness, in.					Finish	Wall thickness, in.						
American Radiator and Standard, Illinois Institute of Technology																
1	combustion	2.42	2.0	steel	20,000	H ₂ + O ₂	3,000	15 (20 total)	same as driver section	same as driver section	air	0.02 (mm)	0.02 (mm)			Material erosion
2	cold	3 to 6	3 x 3	1.0		air	100	total	same as driver section	same as driver section	air	0.02 (mm)	0.02 (mm)			
3	cold	20	24			air	100	400	same as driver section	same as driver section	air	15	15			Classified
4	cold	10 to 40	-72	1.0		air	100	250	same as driver section	same as driver section	air	15	15			Classified
Arnold Engineering Development Center (operated by AEC, Inc.)																
1	electric	0.05	0.5	steel	2,000	air		15	same as driver section	same as driver section	air	0.002 (5.1 mm)	0.002 (5.1 mm)	to 15	none	Sustained electrical discharge
AEC Manufacturing Corporation, Research Laboratory (operated by AEC, Inc.)																
1	gun	20	6	steel	40,000	H ₂ , O ₂ , He	to 4,000	100	14.19 in. steel	1.00 in. steel	synthetic air	Can be used to 1 atmosphere	any initial pressure used.			at peak pressure
2	gun	2	2.5	steel	10,000	H ₂ , O ₂ , He	2500	10-18	1.5	0.25	air	any initial pressure used.				
3	gun	3	1.5	steel	10,000	H ₂ , O ₂ , He	2500	10-18	1.5	0.25	air	any initial pressure used.				
4	gun	3	2.5	steel	40,000	H ₂ , O ₂ , He	2500	15-18	1.5	0.25	air	any initial pressure used.				
5	gun	3	1.5	steel	40,000	H ₂ , O ₂ , He	2500	15-18	1.5	0.25	air	any initial pressure used.				
6	gun	3	1.5	steel	10,000	H ₂ , O ₂ , He	2500	15-18	1.5	0.25	air	any initial pressure used.				
7	gun	3	1.5	steel	40,000	H ₂ , O ₂ , He	2500	15-18	1.5	0.25	air	any initial pressure used.				
8	gun	3	1.5	steel	10,000	H ₂ , O ₂ , He	2500	15-18	1.5	0.25	air	any initial pressure used.				
Brown University - Metallurgical Research Laboratory																
1	cold	4	3	steel	1,000	H ₂ , O ₂ , He	< 780	6	3	0.19	air	500	200	brass, Cu	needle	Chemical studies
2	cold	3	3	brass	150	H ₂ , O ₂ , He	500	7	3	0.19	air	50	20	brass	needle	Chemical studies of carbon formation, etc.
California Institute of Technology - DuSautois Astrophysical Laboratory																
1	cold	6	3	steel	2,000	H ₂ , O ₂ , He	200	20	2.88 x 2.88	steel	air	down to 0.01 (mm)	down to 0.01 (mm)	pressure		Shock tunnel; heat transfer
2	electric	1	1	quartz liner	1,500	He	1000	20	cold rolled	0.38	air	0.002 (mm)	0.002 (mm)	pressure		Shock tunnel; heat transfer
General Electric Research and Development Center																
Equipment being designed																
General Electric Research and Development Center																
1	gun	9	3	steel	15,000	H ₂ + O ₂ + He	to 1,000	40 to 1.5 x 2.5	steel	50 x 4.5	air	5000	15	see text		Shock attenuation shock
2	gun	6	3	steel	15,000	H ₂ , O ₂ , He	2,000	14	1.5 x 2.5	steel	air, O ₂ , He	10-5 mm	to 10 mm	pressure		Shock attenuation and chemical reactions, shock
3	gun	6	3	steel	1,000	He	to 600	12	same as driver section	1000	air	2 to 6	to 6	pressure		Shock attenuation, shock, heated gases

Table 6.1-1 (continued)
 Survey of unclassified shock tubes in the U.S.A. and Canada up to 1956 (Ref. 1)

No.	Type	Driver Section			Low Pressure Section			Major Use and Remarks	
		Length ft	Wall Thick. in	Design P, psi	Length ft	Wall Thick. in	Design P, psi		
Cornell Aeronautical Laboratory, Ithaca, (Continued)									
4	cold	12	3.25 brass	400	3 brass	400	air	thin film plunger	Weak shocks reflected from open end
5	cold	2.5	3.15 Alum.	100	same as driver section	100	air	thin film	Interaction of shock waves and combustion
6	cold	9	3.5 steel	100,000	2.5 x 2.5 steel, steel	90,000	air	steel	High speed shock tunnel for hypersonic flow
7	cold	14	3.5 steel	100,000	3 steel	100,000	air	steel	Wallated interface hypersonic shock tunnel
Cornell University - Graduate School of Aeronautical Engineering									
Insufficient data available									
Ford Motor Company, Department of Chemistry, Scientific Laboratory									
Insufficient data available									
General Electric Company, Research Laboratory									
1	cold	10	5.10 steel	20,000	4 steel, steel	4,000	various	various	Operation as a hypersonic reflected-shock tube
2	cold	6.5	5.5 steel	5,000	1.0 steel	1,000	various	various	Physical and chemistry of plungers
General Electric Company, Missile and Ordnance Systems Division									
1	cold	22	3.5 steel	20,000	2 steel	1,500	air	various	Wide variety of intended uses
Johns Hopkins University - Applied Physics Laboratory									
1	cold	3	3 steel	500	2 steel	500	air	various	Electrical signals on probes
Lehigh University, Physics Department									
1	cold	2	3.75 steel	250	same as driver section	250	air, H ₂	various	Shock attenuation, boundary layer, etc.
2	cold	1	3.75 brass, Lucite	500	same as driver section	500	air, H ₂	various	Shock attenuation, boundary layer, etc.
Lockheed Aircraft Corporation - Missile Systems Division									
Insufficient data available									
Los Alamos Scientific Laboratory									
Insufficient data available									
MCA - Langley Aeronautical Laboratory									
Insufficient data available									
MCA - Lewis Flight Propulsion Laboratory									
Equipment being designed									

Table 6.1-1 (continued)
 Survey of unclassified shock tubes in the U.S.A. and Canada up to 1956 (Ref. 1)

Inst. No.	Driver Section		Nozzle Section		Nozzle Section		Major Use and Remarks
	Length, feet	Wall thickness, inches	Length, feet	Wall thickness, inches	Length, feet	Wall thickness, inches	
National Bureau of Standards - Heat and Power Division							
1	3	1.500	3	1.500	3	1.500	air
2	1.5	1.500	1.5	1.500	1.5	1.500	air & helium
3	1.5	1.500	1.5	1.500	1.5	1.500	air & helium
Naval Ordnance Laboratory							
1	2	1.79 (3mm)	2	1.79 (3mm)	2	1.79 (3mm)	argon
Princeton University, Physics Department							
1	1.5	1.500	1.5	1.500	1.5	1.500	air
2	1.5	1.500	1.5	1.500	1.5	1.500	air
McMaster-Bridge Corporation - Aeronautical Research Laboratory							
Equipment being designed							
University of Maryland, Institute for Fluid Dynamics and Applied Mathematics							
1	1.5	1.500	1.5	1.500	1.5	1.500	air
2	1.5	1.500	1.5	1.500	1.5	1.500	air
3	1.5	1.500	1.5	1.500	1.5	1.500	air
4	1.5	1.500	1.5	1.500	1.5	1.500	air
University of Michigan, Physics Department							
1	1.5	1.500	1.5	1.500	1.5	1.500	air
2	1.5	1.500	1.5	1.500	1.5	1.500	air
3	1.5	1.500	1.5	1.500	1.5	1.500	air
University of Oklahoma, Physics Department							
1	1.5	1.500	1.5	1.500	1.5	1.500	air
2	1.5	1.500	1.5	1.500	1.5	1.500	air
University of Toronto, Institute of Aerophysics							
1	1.5	1.500	1.5	1.500	1.5	1.500	air
2	1.5	1.500	1.5	1.500	1.5	1.500	air
3	1.5	1.500	1.5	1.500	1.5	1.500	air
4	1.5	1.500	1.5	1.500	1.5	1.500	air

Table 6.2-1
Nonmetallic diaphragm materials

Thickness t in inches, bursting pressure difference P in psi

Internal Tube Cross Section	No. Diaphragms	Diaphragm Mat'l or Trade Name	Manufacturer or Supplier	t in.	P psi	Remarks and/or References
	1	Mst. 600 cellophane	Canadian Industries Ltd. (CIL) Toronto, Ont.	.003	12	Ref. 8
2 in. x 7 in.	1	Red Zip Cellophane (Amer. Tobacco Co. Red Zip Tape) CIL MSTL 600	Dobekmun Co., Cleveland, Ohio, CIL	.002)) .0025	15-17	Refs. 6, 8, 10 Shreds
8 in. x 24 in.	1	Kodapak	Eastman Kodak	.01	19.5	Mass. Inst. Tech.
	1	Vuepak	Monsanto	.012	18	Dept. Aer. Eng.
	1	Vuepak	Monsanto	.019	30	
3 in. x 3 in.	1	MSC 300 Red Cellophane	CIL	.001	9	Ref. 10
	1	Red Zip Cellophane	Dobekmun, CIL	.0025	25	Shreds
	2	"	"	.0025 each	48	
	3	"	"	.0025 each	72	
8 in. x 8 in.	1	Cellulose Acetate		.010	15	Ref. 9
1 in. dia.	1	Cellophane		.001	22	Ref. 22
	1	Kodatrace	Eastman Kodak	.0045	130	
2 in. dia.	4	Kodatrace	Eastman Kodak	.0045 each	175	Ref. 22
3 in. dia.	1	Mylar	Du Pont	.001	20	Ref. 14
	1	Polyethylene		.002	47	No shattering
	1	Tetraphthalate		.0075	129	
1-3/4 in. x 4 in.	1	Cellulose Acetate		.001	11	Ref. 18
	1			.002	24	
	1			.003	38	
	1			.005	55	
	1			.010	110	
	1			.020	140	

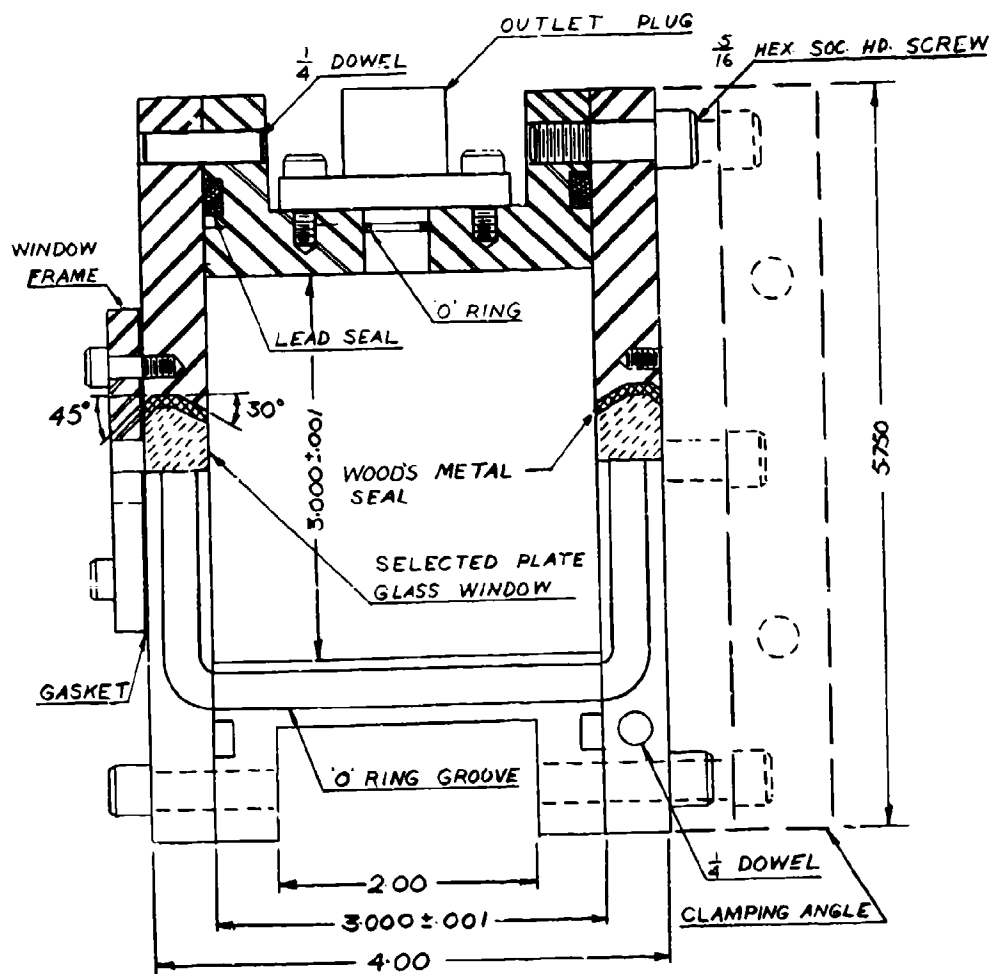


Fig. 6.1-1. Example of square cross-section construction; 3 x 3-in. wave interaction tube (Ref. 10).

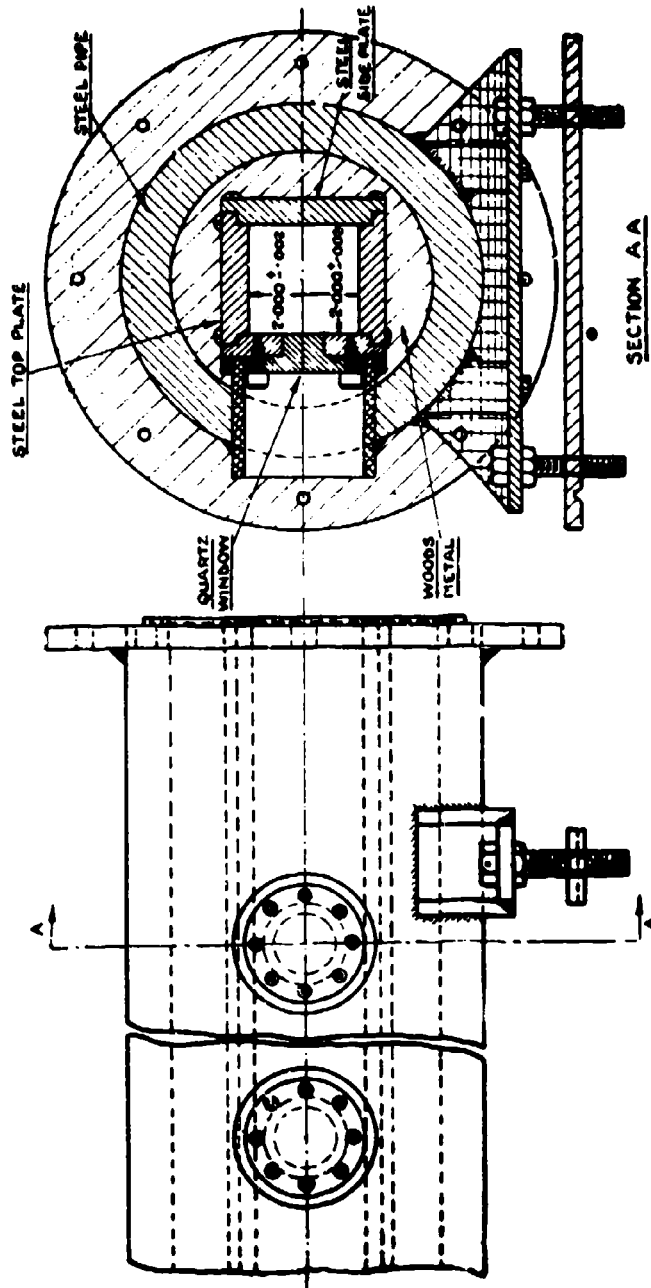


Fig. 6.1-2. Square cross section encased in circular pipe; 2 x 2-in. combustion driven tube (University of Toronto, Institute of Aerophysics).

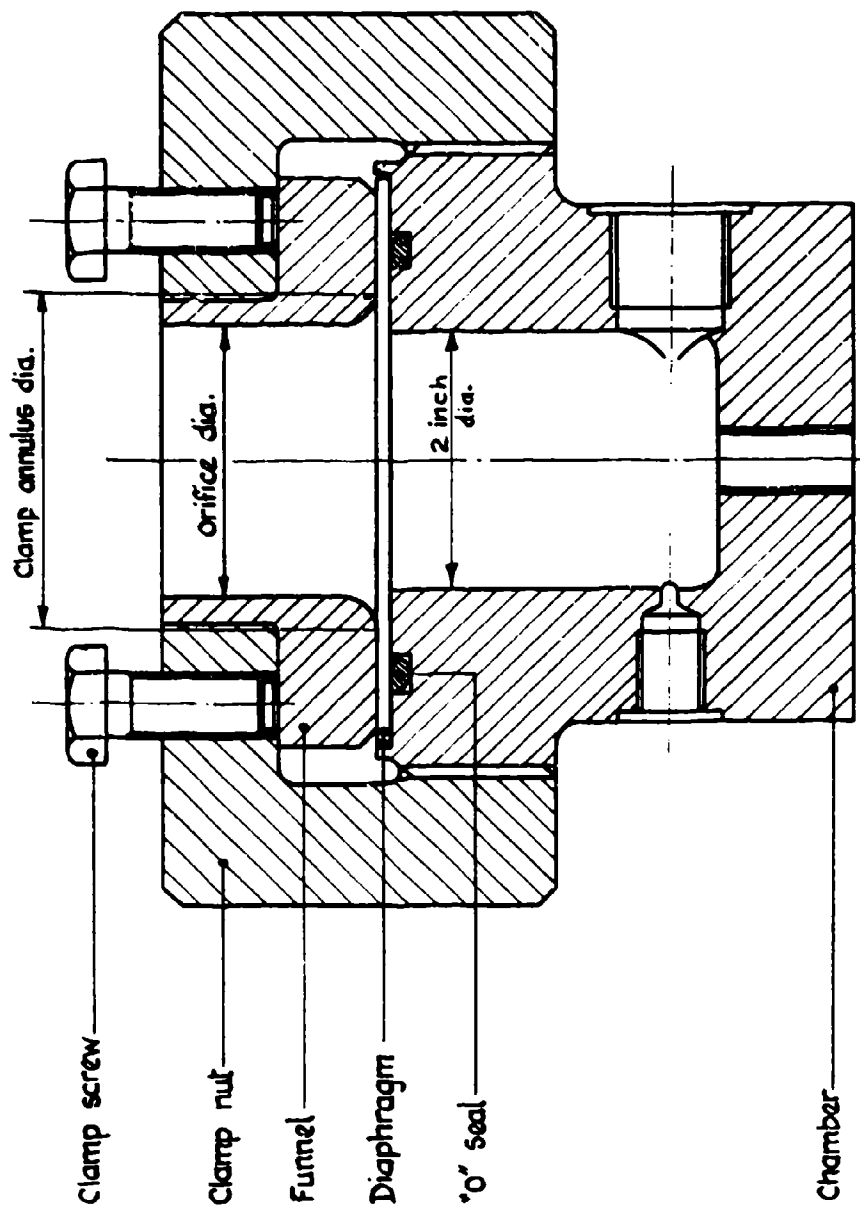


Fig. 6.2-1. Clamping arrangement for diaphragm tests (Ref. 12).

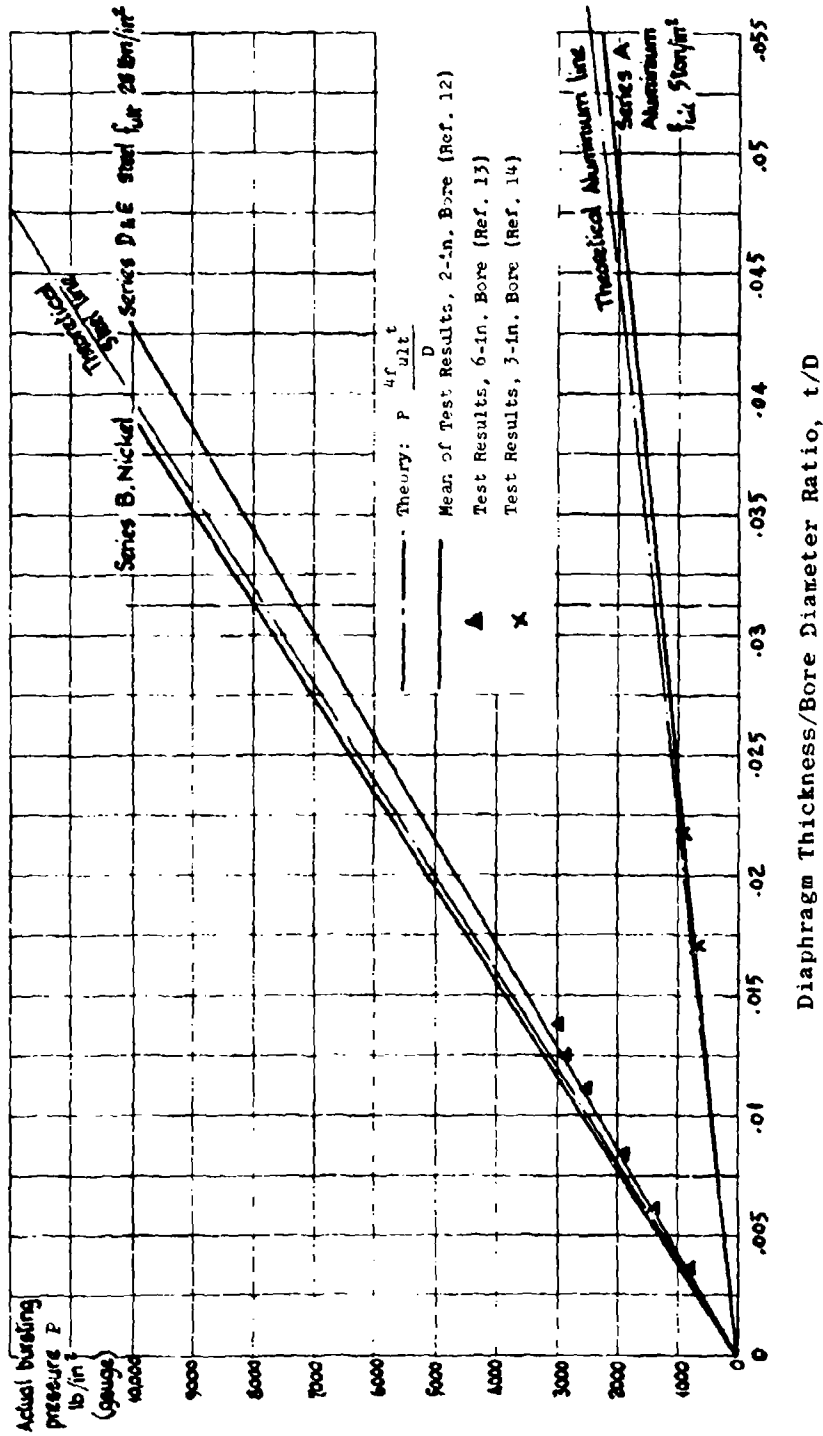


Fig. 6.2-2. Diaphragm bursting test results; bursting pressure difference P in psi vs thickness-diameter ratio t/D .



Hot Burst, Single Layer



Hot Burst, Double Layer



Cold Burst, Single Layer

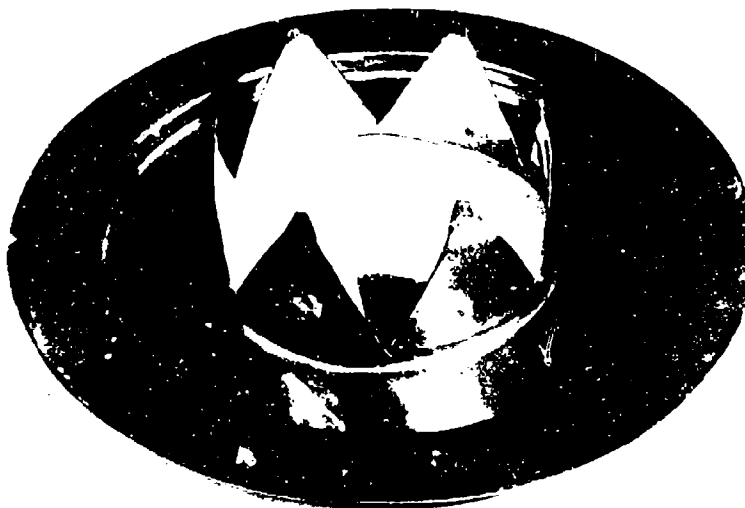


Cold Burst, Double Layer

Fig. 6.2-3. Examples of diaphragm petalling; scribed cold-rolled mild steel, 2-in. bore diameter (Ref. 12).



Unscribed



Deep Scribed

Fig. 6.2-4. Examples of diaphragm petalling; cold-burst annealed copper, 2-in. bore diameter (Ref. 12).

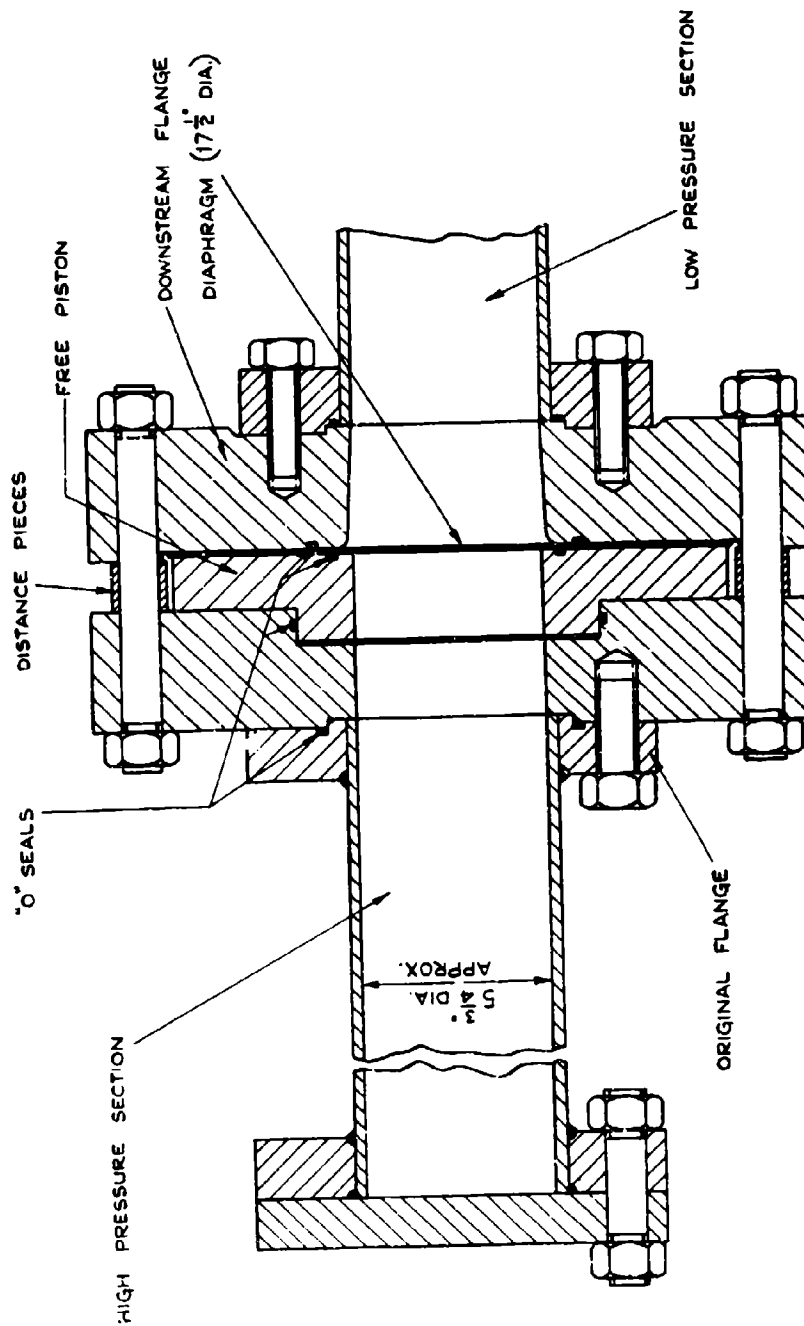


Fig. 6.2-5. Free-piston clamping arrangement for diaphragm tests (Ref. 13).

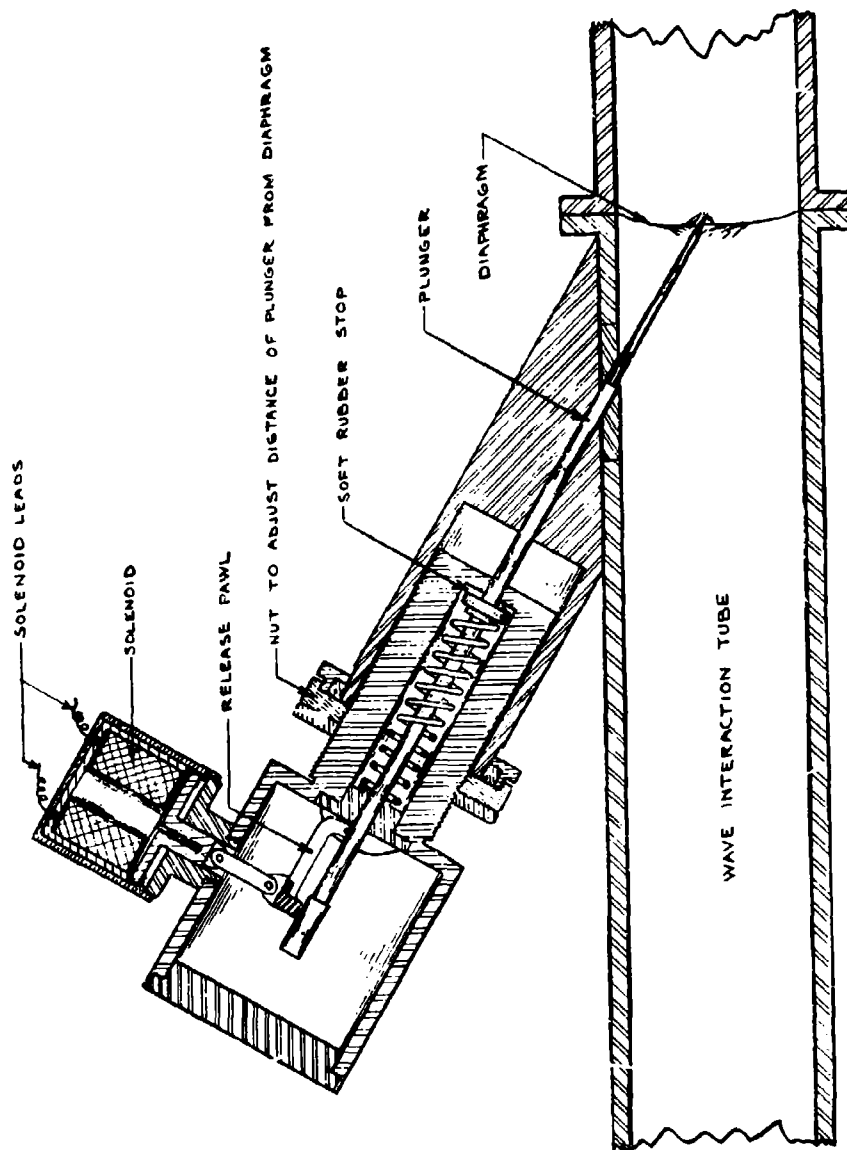


Fig. 6.2-6. Spring-driven, solenoid-actuated diaphragm breaker (Ref. 15).

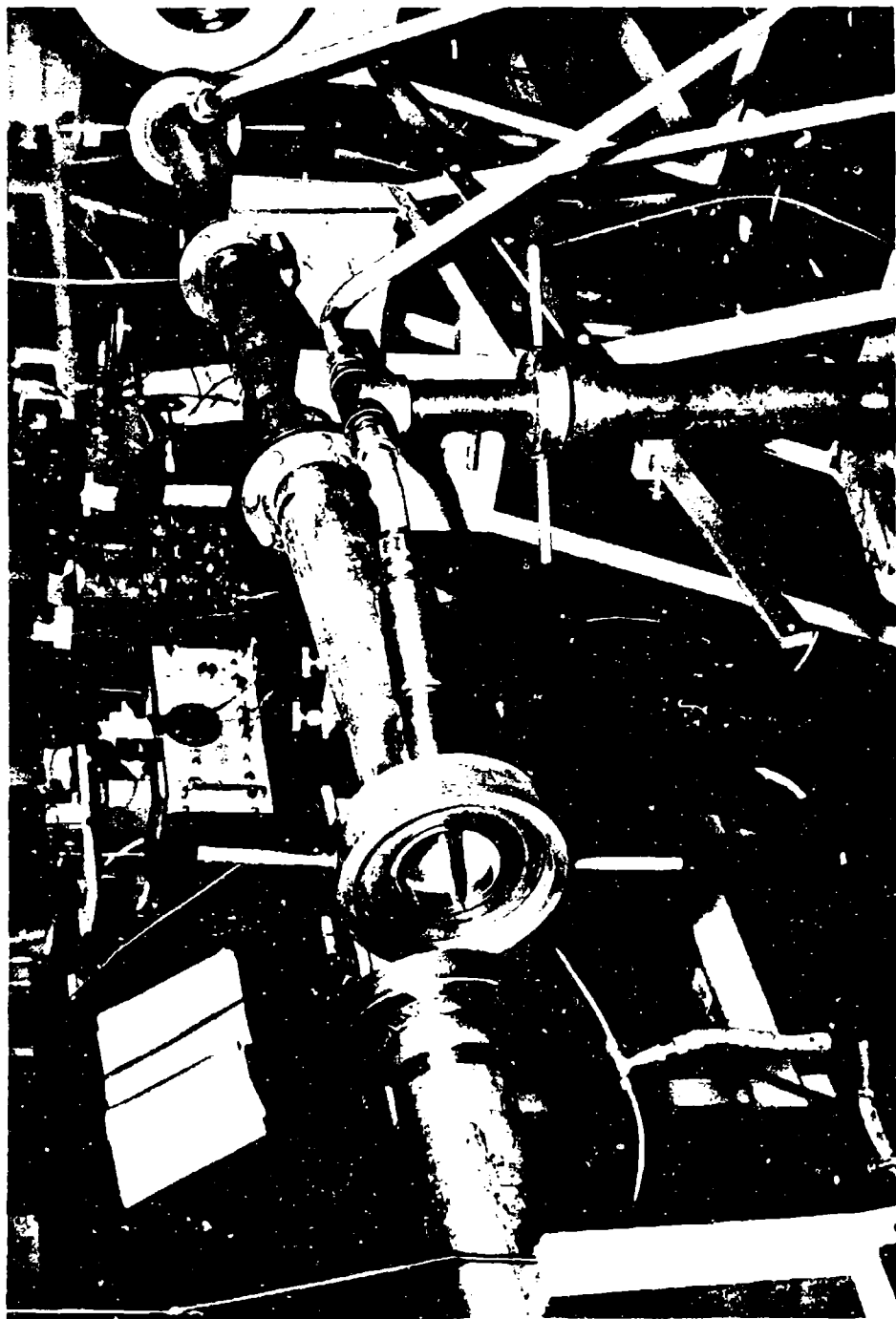


Fig. 6.2-7. Diaphragm-piercing plungers driven by shock waves generated in the auxiliary shock tube at Cornell Aeronautical Laboratory (Ref. 16).

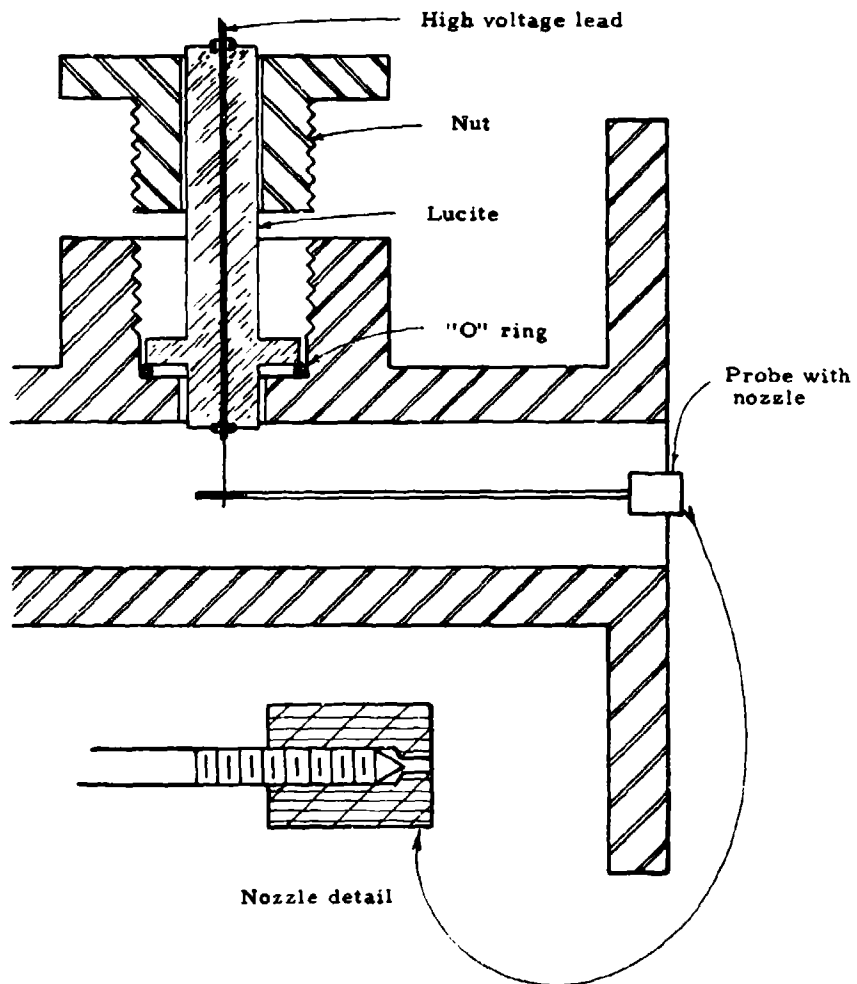


Fig. 6.2-8. Electrical method of diaphragm rupture (Ref. 17).

REFERENCES

1. Streiff, M. L. A Survey of Shock Tube Uses, Equipment, and Instrumentation. Convair Astronautics Report AZR-002. San Diego, Calif.: Convair Astronautics, June 1957.
2. Blackie, J. and Hurdle, C. V. A Schardin Type Shock Tube. ARDE Memo. (B) 19/57. Fort Halstead, Kent, England: Armament Research and Development Establishment, 1957.
3. Roark, R. J. Formulas for Stress and Strain. New York: McGraw-Hill Book Company, Inc., 1954.
4. Seely, F. B. Resistance of Materials. New York: John Wiley and Sons, Inc., 1952.
5. White, D. R. "On the Existence of Higher than Normal Detonation Pressures," J. Fluid Mech., Vol. 2, Part 5 (July 1957), p. 513.
6. Geiger, F. W., Mautz, C. W., and Hollyer, R. N. The Shock Tube as an Instrument for the Investigation of Transonic and Supersonic Flow Patterns. Engineering Research Institute, University of Michigan, 1949.
7. Bleakney, W., Weimer, D. K., and Fletcher, C. H. "The Shock Tube: A Facility for Investigations in Fluid Dynamics," Rev. Sci. Inst., Vol. 20 (November 1949), p. 807.
8. Bitondo, D. and Lobb, R. K. The Design and Construction of a Shock Tube. UTIA Report 3. Institute of Aerophysics, University of Toronto, 1950.
9. Lundquist, G. A. The NOL 8 x 8 Inch Shock Tube: Instrumentation and Operation. NAVORD Report 2449. White Oak, Md.: Naval Ordnance Laboratory, June 1952.
10. Glass, I. I., Martin, W., and Patterson, G. N. A Theoretical and Experimental Study of the Shock Tube. UTIA Report 2. Institute of Aerophysics, University of Toronto, 1953.
11. deLeeuw, J. and Waloron, H. F. The Combustion Driven Shock Tubes at the Institute of Aerophysics and their Instrumentation. UTIA Report. Institute of Aerophysics, University of Toronto (to be published).
12. Freeman, A. J. M. Investigation and Development of High Pressure Burster Discs and Diaphragms. Report No. LM. U. 005. Stevenage, Luton, England: English Electric Company Ltd., 1956.
13. Cox, S. G. Development of the R. A. E. 6-inch Diameter Shock Tube. Part I. Bursting of Diaphragms at 200 Atmospheres. RAE TN Aero 2510. Farnborough, Hants, England: Royal Aeronautical Establishment, 1957.
14. Schultz, D. L. and Henshall, B. D. Hypersonic Shock Tube Equipment at the National Physical Laboratory, U. K. AGARD Report 147. July 1957.

15. Gould, D. G. The Head-on Collision of Two Shock Waves and a Shock and Rarefaction Wave in One-Dimensional Flow. UTIA Report 17. Institute of Aerophysics, University of Toronto, 1952.
16. Glick, H. S., Squire, W., and Hertzberg, A. "A New Shock Tube Technique for the Study of High Temperature Gas Phase Reactions." Fifth Symposium (International) on Combustion. New York: Reinhold Publishing Corp., 1955, p. 393.
17. Harshbarger, F. C. "Physico-Chemical Processes Behind Shock Fronts." Unpublished Ph.D. Dissertation, California Institute of Technology, 1957.
18. Henshall, B. D. On Some Aspects of the Use of Shock Tubes in Aerodynamic Research. ARC R and M No. 3044. Ministry of Supply, Aeronautical Research Council. London: Her Majesty's Stationery Office, 1955.
19. Strong, J. Procedures in Experimental Physics. Englewood Cliffs, N. J.: Prentice-Hall, 1939.
20. Dushman, S. Scientific Foundations of Vacuum Technique. New York: John Wiley and Sons, Inc., 1949.
21. Streiff, M. L. Results of Shock Tube Hazard Studies. Convair Astronautics Report AZR-001. San Diego, Calif.: Convair Astronautics, January 1957.
22. Greene, E. F. Chemical Reactions in Strong Shock Waves. Report 1. Metcalfe Research Laboratory, Brown University, 1953.

7. Shock-Tube Flow Measurement and Instrumentation

Successful use of the shock tube as a research or test facility is, of course, entirely dependent on suitable instrumentation for flow measurement. Because of the highly transient nature of the flows involved, an essential requirement of the measuring instrument is very fast response. Generally speaking, response times of microsecond order are desired. This requirement, in addition to other demands of adequate sensitivity, range, and accuracy, greatly compounds the technical difficulties of shock tube instrumentation.

With the increased use of shock tubes for experimental studies, not only in aerodynamics but also in high-temperature gas physics and chemical kinetics, the variety of instrumentation has expanded and become very broad indeed. A detailed coverage in all three applications mentioned would be very lengthy and has not been attempted. In general, the emphasis here is placed on the aerodynamic side and on techniques which have been reasonably well tested and proved. Increased usage of the shock tube as a steady-flow test facility has forced serious attention to the accompanying instrumentation problem, and new developments may be expected from efforts currently under way.

7.1 Pressure Measurement

Two types of pressure measurements are made in the shock tube: measurement of initial hydrostatic channel and chamber pressures before flow is generated and measurement of transient pressures during flow. The first is discussed in Subsec. 7.1.1. Direct and indirect measurement of transient pressure is described in Subsec. 7.1.2.

7.1.1 Hydrostatic Pressure Measurement

Measurement of hydrostatic channel and chamber pressures prior to tube operation is relatively straightforward and may be done with commercial indicators. For the medium- and high-pressure ranges, mercury manometers and mechanical Bourdon type gauges are common. For the lower pressure ranges, butylphthalate manometers are common, and in recent years absolute dial reading gauges* obtainable down to the range of 0 to 10 mm Hg have become popular. The latter require frequent calibration but are convenient to use. For pressures around a few millimeters of mercury and below, there are such well known instruments as the McLeod and Pirani gauges.

Conventional manometry techniques are described in Refs. 1 and 2, while low pressure measurement is fully treated in Refs. 3 and 4.

7.1.2 Transient Pressure Measurement

7.1.2.1 Direct Measurement

A variety of transient pressure measuring systems have been developed over the years, and an extensive literature on this subject now exists. General reviews are given in Refs. 5, 6, and 7.

* Manufactured by Wallace and Tiernan Co.

Most measurements of transient shock-tube pressure to date have been made at the tube walls using small flush-mounted transducers which convert mechanical deformation from pressure change into an electrical signal. The transducer output may be amplified and recorded by cathode ray oscillography. Single-sweep time base recording is common. The sweep may be triggered at the desired instant by a pulse from one of the shock detectors described in Subsec. 7.4.1 fed via an adjustable time-delay circuit. A similar technique for models to obtain pressure distribution has been hindered by a lack of suitably small transducers, but is currently receiving attention.

The requirements of a pressure transducer for shock tube application are as follows.

1. Good Frequency Response

In general, the useful bandwidth cannot be too wide because good low-frequency response is needed for quasi-steady flow regions, while good high-frequency response is necessary for shock-wave pressure changes. Specific requirements on frequency response depend somewhat on the application. Some applications might require a rise time to a shock front of the order of one microsecond, while for others, 100 microsec might be acceptable. A high mechanical natural frequency and sufficient damping are necessary to avoid excessive ringing following step pressure changes.

2. Linearity

It is usually desirable to have output proportional to input to facilitate calibration and record interpretation.

3. Sensitivity and Pressure Range

A high sensitivity is desirable but usually must be compromised with high-frequency response. For a given interference level the sensitivity determines the lower useful pressure limit and, usually, nonlinear response the upper limit.

4. Accuracy

Dynamic errors, such as those from poor frequency response, and interference errors from other than pressure inputs must be within acceptable limits. Important interference effects are electrical noise, temperature response, and acceleration response. Ideally the transducer should have no response to temperature or acceleration. In the shock tube, temperature changes always accompany pressure changes, but the transducer response to temperature is always delayed with respect to pressure. This delay may be increased by insulating the transducer face with a thin layer of grease. Regarding acceleration, anti-vibration mounting of the transducer may sometimes be necessary to minimize the acceleration response. Vibration of the tube walls, for example, on firing of the tube can produce significant response from wall-mounted transducers.

5. Size and Shape

The transducer should not disturb the flow, and the sensing face should be as small as sensitivity permits to obtain the best spatial resolution possible. Small size is necessary for fast response to a shock wave. The fastest piezoelectric transducers show a rise

time of the order of the transit time of the shock across the sensing face. Flow disturbance may be avoided with accurate flush mounting. Small projections can produce significant shock-wave diffraction effects.

6. Calibration

Calibration is always necessary. Dynamic calibration in the range of pressures to be measured is desirable but usually not possible, and static calibration is usually used. The shock tube itself may be used for dynamic calibration if the primary shock pressure rise can be obtained from theory or from independent measurement (see Subsec. 7.4).

7. Stability and Reproducibility

For consistent results, the transducer and associated circuitry must be thermally, mechanically, and electrically stable.

Usually the transducer is the weakest link in the pressure measuring system and involves compromises in the foregoing requirements. The transducers commonly used in shock tubes include the piezoelectric types and the diaphragm deflection types. Both are commercially available, but their applications are presently limited to relatively high pressure levels. While the high-frequency response of recent piezoelectric models is quite adequate for most shock-tube studies (see end of following section), their compromised sensitivity is inadequate at pressures of a few millimeters of mercury such as exist in hypersonic shock-tunnel nozzles.

Piezoelectric Transducer.--The piezoelectric transducer utilizes the piezoelectric effect whereby a change in the stress (pressure) applied to a piezoactive crystal generates a proportionate electrical charge over certain crystal faces. The magnitude and character of the effect depends on the orientation of applied stress with respect to the crystallographic axes. A crystal transducer might use a number of adjacent disks, a so-called pile, in correct polarity as indicated in Fig. 7.1-1 for a two-pile element. The charge Q generated by a pressure change P is $Q = n K A P$ where

n = number of disks

K = constant, the piezoelectric modulus

A = area of one side of one disk

For most practical purposes the equivalent electrical circuit may be represented by a generator of emf $E = (n K A P / C_c)$ in series with the total crystal element capacitance C_c and shunt leakage resistance R_c , as shown in Fig. 7.1-2. The external load has shunt capacitance C_L and shunt resistance R_L . Usually C_c is $\ll C_L$.

If p is sinusoidal of amplitude P and angular frequency ω , then

$$E_L = \frac{j\omega T n K A P}{1 + j\omega R_c C_c + C_L}$$

where

$$\tau = R(C_c + C_L)$$

$$R = \frac{R_c R_L}{R_c + R_L}$$

$$j^2 = -1$$

For $\omega\tau \gg 1$, (high frequencies)

$$E_L \approx \frac{n KAP}{C_c + C_L}$$

and output is independent of ω as desired. External shunt capacitance C_L decreases sensitivity. With decreasing ω , E_L drops off and phase shift increases. If p is a step increase P at $t = 0$,

$$E_L = \frac{n KAP}{C_c + C_L} e^{-\frac{t}{\tau}}$$

and E_L drops off exponentially at a rate determined by τ . The piezo transducer thus has inherently poor low-frequency response. The time constant τ should be very large compared to flow durations to be measured. Crystal capacitance C_c is small and increase of τ by increasing C_L is limited by sensitivity requirements. Therefore R must be large. Typically, R_c might be of the order of a thousand megohms. A cathode follower (Ref. 8) or electrometer tube (Ref. 9) input directly following the transducer is commonly used to maintain R_L large. Long connecting cables between transducer and amplifier input introduce difficulties as they cannot be terminated properly.

The natural crystals, quartz and tourmaline, and barium titanate ceramics have been the most used materials for shock tube applications. Quartz and tourmaline are excellent mechanically with modulus K insensitive to temperature and about $11 \mu\text{C}$ coulombs/lb. The ceramics are made piezoelectric by electric polarization whereby K can be made as much as 50 times that for quartz. Their form and the direction of the crystallographic axes may be controlled. A limitation on barium titanate is its narrow stable temperature range (about 20 to 100°C).^{*} Tourmaline and barium titanate are hydrostatically sensitive in that they produce a net charge when all crystal faces experience the same pressure change. Quartz is not hydrostatically sensitive, which necessitates the shielding of certain faces from the applied pressure change.

^{*}The National Bureau of Standards has recently developed lead oxide based ceramics superior in this respect.

All piezo transducers exhibit pyroelectric effect, i.e., charge generation due to thermally induced stresses. The hydrostatically sensitive crystals show response even to uniform temperature change. A 1°C rise in tourmaline, for example, is equivalent to a pressure decrease of about 200 psi. Quartz is much superior in this respect.

In calibration, calibrating pressure changes must be applied rapidly enough to avoid errors due to finite τ and consequent charge leakage. The transducer response to the primary shock wave may be used if the shock pressure rise is determined independently (see Subsec. 7.4). The microcoulometer technique (Ref. 10) uses very long input time constant equipment to record response to a relatively slow pressure change by needle swing of a microammeter. Commercial transducers such as the Kistler SLM unit use the latter technique with a dead-weight tester.

Apart from its inherent poor low-frequency response and high output impedance, making it susceptible to electrical interference, the piezo transducer has several advantages for shock tube application. The high-frequency response is generally excellent; a high mechanical natural frequency can be maintained with sufficient damping in the mounting to avoid ringing. Charge generation with pressure change is linear over an enormous pressure range for quartz and tourmaline. The ceramics provide high sensitivity and thus permit good spatial resolution. The Armour Research Foundation has developed small barium-titanate transducers suitable for mounting in models.* Typical characteristics are face diameter, 11/64 in.; sensitivity, 18.6 μC coulombs per psi; internal resistance, 200 megohms; pressure range, 1 to 100 psi; rise time to shock front, 15 microsec; and over-all height, 1/4 in. Of the commercially available piezo transducers, the recently developed SLM miniature quartz transducer** has outstanding characteristics for many shock tube applications (natural frequency, 500 kc; 1/4 in. diameter; resolution, 1 psi; 1 to 2 microsec rise to shock wave).

In addition to references cited, useful information on design and construction of piezo transducers will be found in Refs. 11, 12, and 103.

Diaphragm Transducer.---The diaphragm transducer uses the small deflection from pressure change of a thin metal diaphragm to vary circuit capacitance, resistance, or inductance, and to generate a proportionate electrical output signal. The simplest diaphragm is flat, without tension (all stiffness), and permits accurate flush mounting. Commercial diaphragm transducers use a number of interchangeable diaphragms to cover an extended pressure range.

High frequency response is limited by the lowest natural frequency of the diaphragm. In the fundamental mode, the diaphragm dynamic behaviour may be approximated by (Refs. 13, 14, and 15)

$$m \frac{d^2x}{dt^2} + c \frac{dx}{dt} + kx = A p(t)$$

* Private communication from S. Hoenig, Armour Research Foundation, Illinois Institute of Technology, Chicago 16, Illinois.

** Manufactured by the Kistler Instrument Company, 15 Webster Street, North Tonawanda, N. Y.

where

- x = diaphragm deflection from equilibrium
- p(t) = pressure difference across diaphragm
- m = effective diaphragm mass
- k = effective spring stiffness constant
- c = effective damping constant
- A = effective diaphragm area

i.e., as an effective mass and spring with damping. This equation may be rewritten

$$\frac{d^2x}{dt^2} + 2\zeta\omega_n \frac{dx}{dt} + \omega_n^2 x = S\omega_n^2 p(t)$$

where

- ω_n = undamped lowest natural angular frequency = $\sqrt{\frac{k}{m}}$
- ζ = damping ratio = $\frac{c}{2\sqrt{mk}}$
- S = static sensitivity = $\frac{A}{k}$

Damping ζ of the order of 0.6 is desirable to reduce ringing in response to a shock wave, but in most commercial transducers ζ is < 0.1 . The time t_D , Fig. 7.1-3, for the ringing maxima to damp to a given level is

$\propto \frac{1}{\zeta\omega_n}$ and can be significant compared to flow duration unless ω_n is high. A useful criterion of diaphragm performance (Ref. 14) is the mass per unit area $\frac{m}{A}$. From the foregoing,

$$\frac{m}{A} = \frac{1}{S\omega_n^2}$$

and a small $\frac{m}{A}$ is necessary for desired high sensitivity S and high natural frequency ω_n .

Values of ω_n , S, and $\frac{m}{A}$ are listed in Table 7.1-1 (Ref. 14) for the flat diaphragm without tension, the stretched-membrane diaphragm (all tension, no stiffness), and a spherical-segment diaphragm. For the latter two, sensitivity S can be increased through thickness t without reducing natural frequency ω_n . The spherical segment has the lowest

$\frac{m}{A}$ for given thickness and provides superior high-frequency response. The tension diaphragm is very temperature sensitive.

All diaphragm transducers have acceleration response. If, with no pressure change, the entire transducer is subjected to sinusoidal vibration of amplitude x_v and circular frequency ω_v , the amplitude x of diaphragm displacement from equilibrium is

$$x = \beta^2 \frac{x_v}{[(1 - \beta^2)^2 + 4 \zeta^2 \beta^2]^{1/2}} ; \quad \beta = \frac{\omega_v}{\omega_n}$$

The acceleration response can be significant for small ζ and $\omega_v \rightarrow \omega_n$. Anti-vibration mounting in the tube walls may sometimes be necessary.

A common method of generating an electrical output from diaphragm deflection uses the diaphragm as one plate of a capacitor. Capacitance change is nonlinear with plate spacing, and the maximum diaphragm deflection is small for linear operation. The capacitance variation may be used to amplitude-, frequency-, or phase-modulate a high-frequency carrier in order to provide static or D-C response. Such a system using amplitude modulation is described in Ref. 16.

High performance transducers using strain-gauge resistance variation are described in Refs. 14 and 15. In one of these references (Ref. 15), a catenary diaphragm transmits the load directly to a circular strain tube with longitudinal and circumferential bonded windings connected in a bridge to give additive output. The physical arrangement achieves very low temperature sensitivity.

Variable inductance may also be utilized by using the diaphragm to vary core position in a coil or the air gap of a magnetic circuit.

Calibration of the diaphragm transducer may be done with the shock tube or statically with a dead weight tester if the transducer has D-C response.

Most commercial diaphragm transducers use flat diaphragms and have poorer high-frequency response in the low-pressure ranges than the piezoelectric types. The possible low impedance level of the diaphragm transducer, as with strain gauge resistance windings, for example, gives it an advantage where electrical interference is a problem. Commercial flat diaphragm transducers are available for the pressure range 0 to 1 psi and up with diaphragm diameters around 3/16 to 1/8-in. minimum. Natural frequencies for the 0 to 1 psi range are around 30 kc.

7.1.2.2 Indirect Measurement

Instantaneous pressure distribution throughout an extended region of a transient flow may be determined with spark interferometry (Subsec. 7.2.1.4) provided the pressure-density relation is known. The method has been used, for example, by Bleakney and co-workers (Refs. 17 and 18) to study transient loading of structures from shock diffraction and by the M.I.T. shock-tube group to study transient aerodynamics of two-dimensional airfoils in shock induced flow (Ref. 19).

7.2 Density Measurement

7.2.1 Optical Methods--Schlieren and Interferometry

The well known optical methods of shadowgraph, Toepler schlieren, and interferometry, which utilize the dependence of refractive index of a gas on density to record some aspect of density variation, have proved exceedingly useful for shock-tube studies when used with high-speed photography. The advantages are no inertia lag, no disturbing probes, and recording of conditions throughout an extended flow region. On the other hand, the methods record an integrated or average effect along the light path and are primarily useful for studying two-dimensional or axi-symmetric flows. Their usefulness is ultimately limited by insufficient density change or gradient, for example with very weak shocks or at very low densities. With very strong shocks, the self luminescence of the gas behind the shock may also cause some difficulty.

The optical methods have been extensively documented and only brief descriptions and results will be given here. For recent comprehensive treatments, see, for example, Refs. 20 and 21.

For sufficient accuracy in most instances, the index of refraction n is related to gas density ρ by

$$n = 1 + K\rho$$

where K is the Gladstone-Dale constant depending on the gas and on wavelength λ . Values of K for numerous gases have been tabulated as a function of wavelength by Edelman and Bright (Ref. 22). Table 7.2-1 gives λ and K for commonly used gases.

Both shadowgraph and schlieren utilize the bending of light from gradients in n . From Snell's law for refraction, radius of curvature R of a light ray is given by (see Fig. 7.2-1)

$$\frac{1}{R} = \frac{\tilde{N} \cdot \text{grad } n}{n}$$

and total angular deflection α by

$$\alpha = \int \frac{1}{R} ds$$

where s is arc length measured along the light path. In practice α is usually small. It is convenient to consider component deflections α_x and α_y shown in Fig. 7.2-2 for the incident ray normal to the xy plane. For α small,

$$\frac{1}{R_x} \approx \frac{\partial n}{\partial x} \quad \text{and} \quad \frac{1}{R_y} \approx \frac{\partial n}{\partial y}$$

where R_x and R_y are local radii of curvature of the ray traces in the xz and yz planes, respectively. Then

$$\alpha_x \simeq \int_0^l \frac{1}{R_x} dz = \int_0^l \frac{\partial n}{\partial x} dz = K \int_0^l \frac{\partial \rho}{\partial x} dz$$

$$\alpha_y \simeq \int_0^l \frac{1}{R_y} dz = \int_0^l \frac{\partial n}{\partial y} dz = K \int_0^l \frac{\partial \rho}{\partial y} dz$$

where l = test section width. If the flow depends only on x and y ,

$$\alpha_x = Kl \frac{\partial \rho}{\partial x}$$

$$\alpha_y = Kl \frac{\partial \rho}{\partial y}$$

7.2.1.1 Shadowgraph

The simplest optical technique is direct shadowgraph (Ref. 23). A typical arrangement shown in Fig. 7.2-3 uses a lens to collimate light from a small intense source S . The collimated beam passes through the flow field normal to the flow direction and falls directly on the screen or photographic plate. Without flow, or with uniform flow density throughout, the illumination E of the screen has a constant value

$$E_0 = \frac{BS}{f_1^2} \text{ lumens/ft}^2$$

where

B = source brightness, candles/ft²

S = source emission area, ft²; $\frac{\pi d_s^2}{4}$

f_1 = focal length of L , ft

With flow having density gradients, refraction occurs, and a shadow pattern is cast on the screen. Illumination E with flow is obtained from the foregoing as

$$\frac{E}{E_0} = \frac{1}{\left(1 + hK \int_0^l \frac{\partial^2 \rho}{\partial y^2} dz\right) \left(1 + hK \int_0^l \frac{\partial^2 \rho}{\partial x^2} dz\right)}$$

For flow with weak derivatives this gives

$$\frac{E}{E_0} - 1 \approx -hK \int_0^l \left(\frac{\partial^2 \rho}{\partial x^2} + \frac{\partial^2 \rho}{\partial y^2} \right) dz$$

and the change in illumination is thus proportional to the integrated second derivative of density.

While, in principle, measurement of illumination in the image with subsequent double integration would give the density for certain flows of simple structure, quantitative use of shadowgraph in this way is seldom attempted because of the inherent difficulties involved. The chief use of shadowgraph is for detection of regions containing large second derivatives of density such as shock waves, turbulence, wakes, and boundary layers. A shock wave is shown by shadowgraph as adjacent dark and light lines due to change in sign of the second derivative of density. Turbulence is recorded with a characteristic grainy pattern. Quantitative application of shadowgraph technique to determination of density change across shock waves is reviewed by Weyl (Ref. 20). Kovaszny has employed shadowgraph for quantitative study of certain statistical aspects of turbulent flow (Ref. 20).

The parameters in the arrangement of Fig. 7.2-3, i.e., B , d_s , f_1 , and h , must be suitably chosen to obtain good results. Also, of course, for transient flows the exposure time must be very short, preferably below 1 microsecond. A spark light source (Subsec. 7.2.1.4), which has very high brightness, is commonly used for such short exposures.

Sensitivity is proportional to h , but increase in h is limited by lack of sharpness in the image. Each point is imaged by a circle of confusion of diameter $\frac{hd_s}{f_1}$ because of the finite source size. Thus the source angle $\frac{d_s}{f_1}$ should be as small as possible. Values of $\frac{hd_s}{f_1}$ of the order of 0.010 in. or less are desirable. A lower limit is set by the need for sufficient exposure. Usually, h is determined by trial and error for optimum results and is often $\leq f_1$. For large fields, L is often a concave first-surfaced mirror of diameter D with $\frac{f_1}{D}$ in the range of 6 to 10. Additional optics and a camera focussed on the screen position of Fig. 7.2-3 may be used for magnifications less than unity and increased illumination ($E_0 \sim \frac{1}{(\text{Mag.})^2}$).

7.2.1.2 Toepler Schlieren

A basic Toepler schlieren system (Ref. 24) using near parallel light from a rectangular source of dimensions $a \times b$ is shown in Fig. 7.2-4. Consider first a uniform density field. Each point as P in the flow centerplane is imaged by L_2 and camera lens L_3 at a conjugate point P' on the screen or photographic plate by a "cone" of light

(shown solid) having small divergence angle $\theta_s = \frac{a}{f_1}$ in the plan view shown. An image of the source of dimensions $a_i \times b_i$ is formed a distance f_2 from L_2 at which point there is a knife edge K. The source image may be thought of as a superposition of separate images formed by light through all points as P. Each point of the source image receives light from all such points P. If knife edge K is moved in at the position shown to partially cut off the beam (cut-off edge parallel to dimension b_i perpendicular to paper), the field image will thus darken uniformly.

In use, K is inserted to partially cut off the beam and darken the field image uniformly. Suppose a density gradient at P is such as to deflect the cone imaging P as shown dotted, i.e., off the knife edge. Then P', the image of P, receives more light than neighbouring image points. The opposite effect results for deflection onto the knife edge. Thus ray deflections α perpendicular to the knife edge produce corresponding changes in screen illumination E.

If K cuts off all but η of the width a_i , the background illumination E is

$$E = \frac{B \eta b}{f_1 f_2 m^2}$$

where $m = \text{magnification} = \frac{\text{Image size}}{\text{Object size}}$

If rays through P are deflected through angle α_y perpendicular to K, the corresponding change ΔE in E at P' is

$$\Delta E = \frac{B b \alpha_y}{f_1 m^2}$$

Thus the contrast $\frac{\Delta E}{E}$ is

$$\frac{\Delta E}{E} = \frac{f_2 \alpha_y}{\eta} = \frac{f_2}{\eta} K \int_0^{\ell} \frac{\partial \rho}{\partial y} dz$$

and the schlieren technique records the integrated first derivative of density perpendicular to the knife edge. The sensitivity S is defined as

$$S = \frac{d}{d\alpha_y} \left(\frac{\Delta E}{E} \right) = \frac{f_2}{\eta}$$

If α_y is sufficiently large, the cone through P is completely deflected on or off the knife edge. No further change in E with α_y results, and the system is said to be overloaded. For equal maximum deflection α_{\max} in either direction, $\eta = a_1/2 = f_2 \alpha_{\max}$.

Thus

$$S = \frac{f_2}{\eta} = \frac{1}{\alpha_{\max}}$$

and high sensitivity implies small maximum deflection before overloading. The overloading problem is alleviated with the use of a variable transmission filter (Ref. 25) rather than a knife edge.

Apart from overloading, use of high sensitivity S is limited by the minimum useful background illumination, since $E \propto 1/S$ (Ref. 26). Over a large range of E, the smallest change in E detectable by the eye is directly proportional to E (Weber-Fechner Law), i.e., $\frac{\Delta E_{\min}}{E}$ is a constant. This desirable relation fails for E sufficiently small whereupon $\frac{\Delta E_{\min}}{E}$ increases rapidly with decreasing E.

With large-diameter fields, parabolic or spherical first-surface mirrors are often used in place of lenses L_1 and L_2 , Fig. 7.2-4, for economic reasons. Mirrors avoid chromatic aberration completely. The usual single-pass layout with mirrors is shown in Fig. 7.2-5. The source and knife edge are offset in the same plane, but to opposite sides of the axis. The off-axis source gives astigmatic and comatic aberrations in the source image. Coma is essentially cancelled with $\theta_1 = \theta_2$ and $f_1 = f_2$. Astigmatism is not serious for θ less than about 8 deg. Values of $\frac{f_1}{D}$ or $\frac{f_2}{D}$ range from about 5 with the largest mirrors ($D \sim 50$ in.) up to 10 with the smaller mirrors ($D \sim 12$ in.).

Further information on schlieren system design will be found in Refs. 25, 26, and 27. A recent review of shadowgraph and Toepler schlieren has been given by Beams (Ref. 20).

In principle, for flows of sufficiently simple structure the integration of local image illumination produced by schlieren would yield local density variation. As with shadowgraph, however, quantitative use of schlieren in this way is inherently difficult and seldom attempted. A complication with knife-edge schlieren arises from consequent diffraction effects which are neglected in the foregoing theory. In this connection, it may be noted that such diffraction effects may be eliminated in practice by use of a variable transmission filter rather than a knife-edge (Ref. 25). Quantitative use of schlieren is discussed in some detail in articles by Weyl and Beams (Ref. 20).

While seldom used for quantitative density measurement, schlieren is a powerful method for detection and location of density gradient regions as shock waves, expansion zones, or boundary layers. Shock waves are recorded as a single white or dark line depending on knife-edge orientation. Schlieren will often clearly reveal very weak

shock or expansion waves which are difficult to detect by interferometry because of small over-all density change. One of the many possible applications of schlieren in shock-tube studies is to measurement of attached shock angle for a thin wedge in supersonic flow, from which flow Mach number may be deduced. Other applications for determining primary shock wave strength and the flow properties behind the wave are given in Subsec. 7.4.2. The schlieren light-screen technique for measuring shock speed is described in Subsec. 7.4.1. The wave-speed schlieren technique follows.

7.2.1.3 Wave-Speed Schlieren

The Toepler schlieren technique has been used to obtain distance-time or x-t photographic records of density gradients in shock tube flows (Refs. 28, 29, and 30) by masking the image plane to a long narrow slit in the flow direction and recording with a rotating drum camera. The arrangement, shown schematically in Fig. 7.2-6, samples a depth $\frac{t}{m}$ of the flow where t is the image plane slit opening and m the magnification. With the film rotating at constant linear speed V , a sharp density gradient, such as a shock wave, moving across the field at speed w would leave a trace on the film as in Fig. 7.2-7. The local speed w at any point as P is

$$w_p = \frac{V}{m} \tan \alpha_p$$

The slit opening t must be small, of the order of 1/32 in. or less, to obtain thin, well defined traces.

In the UTIA apparatus (Refs. 29 and 30) a steady light source is used and is collimated and imaged by parabolic mirrors ($D = 12$ in., $f = 72$ in.) rather than lenses. A focal plane shutter uncovers the image plane slit for one drum revolution. Drum speed is accurately measured with a photocell-chronograph system, and reference timing marks may also be placed on the film. The accuracy in wave-speed measurement is about 2 per cent at high wave speeds ($\alpha \sim 75$ deg) and less than 1/2 per cent at low wave speeds ($\alpha \sim 45$ deg). Usable shock traces are obtained with channel pressures down to 0.4 mm Hg at diaphragm pressure ratios of 10,000 (air/air). The apparatus has been used to study numerous aspects of the basic shock-tube flow and many one-dimensional wave interactions. A typical wave-speed record obtained with this equipment is shown in Plate 1.1.1.

Similar drum-camera recording has been used to obtain x-t records of self-luminous strong shock fronts (Ref. 31). The technique required no schlieren effect nor external light source. The test section windows were masked to a 1-mm slit parallel to the flow direction.

7.2.1.4 Interferometry

Whereas shadowgraph and schlieren depend on the bending of light rays by refractive index gradient, the interferometric method depends on variation with refractive index of the light ray transit time across the flow. The Mach-Zehnder (M-Z) interferometer (Refs. 32 and 33), most commonly used in aerodynamics, is illustrated in Fig. 7.2-8.

Here S_1 and S_2 are plane parallel splitting plates of equal thickness designed to reflect 50 per cent and transmit 50 per cent of light incident at angle α , while M_1 and M_2 are full reflecting first-surface plane mirrors. Light from a single small source S is collimated to a parallel beam incident on S_1 at angle α with the normal. This incident beam is split into two beams by S_1 , over paths 1 and 2, which are recombined following splitter S_2 . Path 2 contains the test section bounded by suitable windows perpendicular to the Z-axis. Flow may occur along the X-axis perpendicular to the paper. Path 1 contains a compensating chamber which equalizes the total glass thicknesses of the two paths (equal dispersion) and in which gas density is kept constant. The angle α is shown as 45 deg, but a smaller value is advantageous.

Assume a monochromatic point source of wavelength λ and perfect optics. With uniform density throughout the test section and all plates parallel the illumination over any plane as z-z following S_2 will be uniform. If any plate, S_2 for example, is then rotated through a small angle ϵ , the plane wavefronts will recombine at angle 2ϵ and straight interference fringes of spacing $b = \frac{\lambda}{2\epsilon}$ (to first order) parallel to the axis of plate rotation will be visible at z-z. At points of maximum light intensity the difference in optical path length

$$\int_{\text{source}}^{z-z} ndz = \text{OPL}_{1,2}$$

for the two paths, i.e., the optical path length difference (OPLD) is $N\lambda$, where $N = 0, 1, 2$ denotes the fringe order. At points of minimum light intensity, $\text{OPLD} = (N + \frac{1}{2})\lambda$. If the test-section density is changed uniformly by $\Delta\rho$, the OPL 2 changes by $l\Delta n = lK\Delta\rho$, and all fringes of the above system shift transverse to their direction a constant distance

$$\xi = \frac{l\Delta n}{\lambda} b = \frac{lK\Delta\rho}{\lambda} b$$

The M-Z arrangement may be operated in one of two ways. In the so-called infinite fringe method, the angle ϵ is zero ($b \rightarrow \infty$) and with uniform density in the test section illumination is uniform over z-z. With flow containing gradients in ρ , and thus gradients in n , a fringe pattern is formed such that

$$\int_{-l/2}^{l/2} ndz = \int_{-l/2}^{l/2} (1 + K\rho) dz$$

is constant on any one fringe and changes by λ for adjacent fringes. Thus for two-dimensional flow, $\rho = \rho(x, y)$, $(1 + K\rho) l$ is constant along any one fringe, and if ρ is known on any fringe it is known on all fringes throughout the field.

In the initial fringe method, plate rotation ϵ is used to obtain an initial uniform fringe pattern of spacing $b = \frac{\lambda}{2\epsilon}$ with no flow and uniform density ρ_1 . With flow, local OPL z changes by

$$\int_{-l/2}^{l/2} n dz - l n_1 = K \int_{-l/2}^{l/2} (\rho - \rho_1) dz$$

and the corresponding local fringe shift ξ_i from the initial fringe position is

$$\xi_i = \frac{Kb}{\lambda} \int_{-l/2}^{l/2} (\rho - \rho_1) dz$$

Usually, some part of the flow field has known uniform density ρ_1 and contains uniform parallel fringes of spacing b . The local fringe shift ξ_p from this uniform flow condition is then

$$\xi_p = \frac{Kb}{\lambda} \int_{-l/2}^{l/2} (\rho - \rho_1) dz$$

as illustrated in Fig. 7.2-9. For two-dimensional flow

$$\xi_p = \frac{Kl b}{\lambda} (\rho_p - \rho_1)$$

or

(1)

$$\rho_p = \rho_1 + \frac{\lambda}{Kl} \frac{\xi_p}{b}$$

Thus measurement of fringe shift ξ enables ρ to be determined.

In practice, the initial fringe method is more commonly used, as the true infinite fringe condition is almost impossible to attain due to slight plate imperfections. (The infinite fringe result can also be attained by superposition of flow and no-flow initial fringe interferograms.) The constant $\frac{Kl}{\lambda}$ in Eq. (1) may be computed, but is best checked by determining fringe shift produced with a known density change, such as that across a shock wave of known strength.

Any real interferometer differs in several respects from the ideal instrument described. A light source of finite size has the effect of focussing the fringes, i.e., they are of highest contrast in

one particular plane, and limits the number of distinct fringes attainable on either side of the zero order fringe. In practice, a field lens (or mirror) and camera follow S_2 with the camera focussed on some plane of the test section. The plane of maximum fringe contrast should coincide with this camera object plane, and to obtain this condition rotation controls are necessary for other plates as well as S_2 . A polychromatic source produces a beat effect. Two discrete wavelengths, for example, give a superposition of two sets of fringes of different spacings $b_{1,2} = \frac{\lambda_{1,2}}{2\epsilon}$. For white light, this superposition washes out all but the zero-order fringe and a few coloured fringes on either side--the so-called white light fringes. Interference filters are commonly used to obtain half-bandwidths of 150 Å or less with 30 or 40 per cent peak transmission. As a consequence of real source effects, in practice the optical path lengths 1 and 2 must be closely equal to obtain useful fringes. Towards this end, one plate is usually provided with a pure translation movement. The appearance of white light fringes is the criteria for correct adjustment.

The interference optical components such as splitting plates and mirrors must be of high quality to produce good interference fringes. Local surface unevenness, for example, should preferably be less than 1/4 wavelength. It would seem that requirements for windows can be relaxed somewhat, as good results have been obtained with windows of selected polished plate glass (Ref. 37). Regarding the specification of optical components, an over-all system specification for acceptable fringe quality, such as a maximum fringe waviness or curvature of 1/4 fringe spacing, is preferable to stating tolerances for the individual components.

Good mechanical design should achieve convenient plate control and beam alignment with the test section, insensitivity to vibration and to ambient temperature change, and minimum physical size.

An excellent general review of practical M-Z interferometry has been given by Landenberg and Bershader (Ref. 20). For a detailed analysis of the effects of non-ideal optical components, see Ref. 34. Specific instruments and operating techniques are described in Refs. 35, 36, and 37.

The M-Z interferometer has been extensively used in shock-tube studies for quantitative density measurement, for example, by Bleakney and co-workers at Princeton in the study of shock wave diffraction, refraction, and gas relaxation phenomena (Refs. 17, 38, 39, 40, 41, and 42). It has also been applied to shock-tube boundary-layer studies (Refs. 43, 44, and 45). In the boundary layer, refraction effects can be significant. Corrections for refraction and for other secondary effects not included in Eq. (1), such as boundary layer on the windows, are given in Ref. 46.

A Michelson interferometer with 1/8-in. diameter field and phototube recording of light intensity in the interfering beams (Ref. 47) has been used to obtain time variation of density at a fixed position in the shock tube.

7.2.1.5 Light Sources and Recording

The foregoing optical techniques require very short exposure in shock-tube studies to avoid significant movement of the image on the photographic film or plate. The simplest and commonest method for single exposures uses a short-duration spark gap light source. The spark may be triggered at the desired instant by a pulse from one of the shock detectors, described in Subsec. 7.4-1, fed via an adjustable time delay circuit. In the usual arrangement the spark discharge occurs in air with energy supplied from a low-inductance capacitor. The discharge current is oscillatory because of the small gap resistance, of the order of an ohm or less. Added damping resistance decreases the energy delivered to the gap. For effective durations of 0.1 to 1 microsec, the inductance of the capacitor and discharge circuit must be kept to a minimum. Special low-inductance capacitors are sometimes used. If the discharge energy is too large the light output may be maintained despite current oscillations and decay (Ref. 48). The discharge energy should not exceed about 5 joules for minimum duration. Usual capacities and voltages are in the ranges of 0.01 to 0.2 μ fd and 5 to 30 kv. The unconstrained gap provides less light but shorter duration than when constrained and is commonly viewed end on (as in Fig. 7.2-10). The size of the viewing hole depends on the application, and might vary from 0.015 in. diameter for shadowgraph to 0.25 in. diameter for interferometry, where light losses through the instrument are very large. Regarding electrode materials, the volatile metals as magnesium or aluminum vaporize readily. They give higher intensity but have a longer duration than tungsten or steel.

The spark gap designed by Kovaszny (Ref. 49) uses six tubular capacitors* located concentric about the gap electrodes to minimize circuit inductance. Figure 7.2-10 shows the arrangement. The spark is fired by application of a voltage pulse to the trigger electrode. The resulting trigger spark between it and the rear electrode initiates the main discharge. Measurement of spark duration with a rotating-mirror camera for 6000-volt discharge showed a light intensity decay to 1/50 maximum value in 0.8 microsec.

Figure 7.2-11 illustrates the transmission-line technique used by Beams et al (Ref. 50) to achieve effective durations of the order 0.1 microsec. The discharge energy is stored in the capacitance of a coaxial line connected to the gap through its characteristic resistance R_0 (non-inductive) and open ended. On gap discharge, a wave travels down the line and reflects. If, when the reflected wave arrives back at the input end, the gap resistance has dropped to a negligible value compared to R_0 , no further reflection occurs and the potential at the input end is reduced to zero. Beams used a line giving 0.1 microsec for the discharge wave round trip (about 9 ft of An RG 8/U coaxial cable, $R_0 = 52$ ohms). Additional lines may be added in parallel to increase the energy of discharge.

The disadvantage of the foregoing transmission-line spark is the large energy loss in the necessary matching resistance R_0 . This has been overcome by Fitzpatrick et al (Ref. 51) through the use of a barium titanate cylinder with fired conductors as the transmission line.

*Condenser Products Glassmike, non-inductive type.

The surge impedance of this line was of the order of an ohm, and no added matching resistance was required. Also, for the dimensions used (I.D. 2.5 cm, O.D. 5 cm, length 16.5 cm for 0.1 microsec discharge) the titanate line had about 20 times the capacitance of an equivalent length of RG 8/U cable (about 9.5 m). The resultant gain in light intensity was a factor of about 900 over RG 8/U cable with 0.3 microsec total period from initial zero to $\frac{1}{e}$ of peak.

While single spark exposure is simple, it does necessitate successive shock tube runs to obtain time histories. An alternative is a repetitive source-moving film camera arrangement or a continuous source with a high-speed framing camera (Refs. 52 and 53). Commercial high-speed framing cameras used include the Beckman and Whitley* camera, which provides 25 frames at up to 2×10^6 frames/sec, and the Fastax camera, which was applied usefully at about 7000 frames/sec in the C.A.L. hypersonic shock tunnel (Ref. 54).

Regarding recording materials, it is well known that published data pertaining to photographic emulsions used at ordinary long exposure times does not apply for microsecond exposure. However, most of the fast films such as Kodak Tri-x panchromatic and Linagraph pan**, or Ilford H.P. 3 hypersensitive pan***, are found satisfactory for spark exposure. For quantitative interferometric studies, spectroscopic plates such as the Kodak type 103-J** are satisfactory. They avoid film shrinkage and may be obtained with a narrow sensitivity range to match the wavelength used. Overdevelopment of negatives and printing on hard paper is usual to obtain maximum contrast.

7.2.2 Absorption Methods

Methods of density measurement depending on absorption of an X-ray or charged corpuscular beam by the gas have as yet received little application in shock-tube studies (Refs. 56, 57, and 61). Winkler (Ref. 55) has reviewed absorption methods and points out certain advantages they hold over conventional optical techniques. In particular, the usual difficulties encountered in interferometry or diffraction by steep density gradients and diffraction with solid surfaces are largely avoided. Charged particle beams, such as α particles, neutrons, or electrons, offer the possibility of measurement at densities well below the useful limits of interferometry.

Kistiakowsky (Ref. 56) used moderate soft X-ray absorption to observe density transition in the deflagration zone behind a detonation wave. A continuous X-ray beam (20-kv tube, 30-ma current) of the order of 3 mm wide was shot across the shock tube (through beryllium windows) onto a terephthal crystal masked from ambient light by an aluminum film. A photomultiplier converted the crystal output to an electric signal which was coupled to a cathode-ray oscilloscope. The fluctuation in photomultiplier output was only a few per cent of the mean value. The

* Manufactured by Beckman and Whitley, Inc., 985 San Carlos Ave., San Carlos, Cal.

** Manufactured by Eastman Kodak Company, Rochester, N.Y.

*** Manufactured by Ilford Limited, London, England.

technique has recently been improved with use of a flash X-ray tube (Ref. 57).

Schopper and Schumacher (Ref. 58) studied the suitability of α particles, protons, and electrons for charged particle probing beams. Later (Refs. 59 and 60), steady low-density gas jets were studied by shadowgraph with low-energy electron beams (3 to 30 kev), and by after-glow with sharply defined high-energy electron beams (50 to 100 kev). The shadowgraph technique is applicable down to 10^{-3} mm Hg.

Venable and Kaplan (Ref. 61) have used electron beam absorption in the shock tube to measure density rise across a shock wave in gas at low density. A 10-kev electron beam crossed the tube onto an activated photomultiplier detector with the output displayed on an oscilloscope. The time and space resolution claimed is 1 microsec and less than 0.5 mm (beam diameter), respectively. The lowest expansion chamber pressure mentioned is 0.05 mm Hg with argon.

7.3 Heat Transfer and Temperature Measurement

Techniques for heat transfer and temperature measurement in the shock tube include the thin-film resistance thermometer (Subsec. 7.3.1) and thermocouple (Subsec. 7.3.2) giving body surface temperatures, the calorimeter gauge (Subsec. 7.3.3) giving heat transfer, the hot-wire anemometer (Subsec. 7.3.4) giving flow stagnation temperature, and interferometry (Subsec. 7.3.5) giving static temperature from measured density. Very high temperatures attained in ionized flows behind strong shock waves have been estimated from spectroscopic studies of the radiation emitted (Ref. 107).

7.3.1 Thin-Film Resistance Thermometer

Thin-film resistance thermometers for measuring body surface temperature change with time in shock-tube flows have been developed in recent years by a number of workers (Refs. 62, 63, 41, 64, 65, 66, and 70). From the measured change in surface temperature with time, surface heat transfer rates may be calculated. A recent review of thin-film techniques is given in Ref. 112.

The thermometer consists of a very thin metal film on an insulating backing operated at small constant current. In practice, the operating procedure is similar to that for a constant-current hot-wire anemometer, and for measurement of film cold resistance R_0 and current I_0 it is convenient to make the film one arm of a bridge as indicated in Fig. 7.3-1. If film temperature changes are not too large,

$$R_F = R_0 [1 + \alpha(T_F - T_0)]$$

where T_F is film temperature, R_0 is film resistance at temperature T_0 , and α is a constant coefficient. The voltage E_F across the film is

$$E_F = I_0 R_F = I_0 R_0 [1 + \alpha(T_F - T_0)]$$

Thus an oscilloscope record of E_F gives T_F from

$$T_F = T_O + \frac{1}{\alpha} \left(\frac{E_F}{I_O R_O} - 1 \right) \quad (1)$$

The device is made practical for shock-tube studies by using gold, platinum, or rhodium films of the order of 10^{-5} cm thick. The heat diffusion time constant of such a film is (Ref. 65)

$$\tau_D \sim \frac{\rho_F C_F \delta^2}{k_F}$$

where

ρ_F = density of film

C_F = specific heat capacity of film

δ = thickness of film

k_F = thermal conductivity of film

For platinum or gold with $\delta = 10^{-5}$ cm, then τ_D is of the order of 10^{-10} sec. Thus for practical purposes the film records instantaneous surface temperature of the backing. This recorded surface temperature, however, lags the surface temperature the backing would have with zero film thickness, as the film has a small but non-zero thermal capacity. The time lag can be made very small. In the case of a suddenly applied heat transfer rate $q \sim \frac{1}{\sqrt{t}}$ (t = time), where surface temperature jumps instantly to a constant new value T_B with zero film thickness, the surface temperature with finite film thickness (recorded by the film) attains about 94 per cent of T_B in a time (Ref. 68)

$$\tau_l \approx 100 \frac{(\rho_F C_F \delta)^2}{k_B \rho_B C_B}$$

where subscript B refers to backing material. With gold film on quartz backing τ_l is roughly 3×10^{-6} sec for $\delta = 10^{-5}$ cm and 3×10^{-8} sec for $\delta = 10^{-6}$ cm. Thus with $\delta = 10^{-5}$ cm or less, for many practical purposes the thin-film thermometer records a temperature T_F equal to the true body surface temperature T_B attained with zero film thickness.

The insulating backing for the film may be the model itself made of quartz or glass (Refs. 65, 67, and 70), a plug designed to fit flush in the model or shock-tube wall (Refs. 62 and 63), or a piece of

tape (Refs. 41 and 64). With the usual duration t_D of shock tube flows the depth y_h of heat penetration into the backing is very small and is given approximately by (Ref. 66)

$$y_h \approx 3 \sqrt{\frac{k_B t_D}{\rho_B C_B}}$$

Usually y_h is much smaller than the backing thickness. Also, temperature gradients along the surface are usually small compared to gradients normal to the surface. Thus the backing acts as a semi-infinite heat sink in which the heat flow is essentially one-dimensional and normal to the surface. As the backing surface temperature $T_B = T_F$ is known as a function of time from an oscilloscope record of E_F , the rate of surface heat transfer

$$q(0, t) = -k_B \left(\frac{\partial T}{\partial y} \right)_{y=0}$$

where y is distance normal to the backing surface, can be obtained by solution of the classical one-dimensional heat conduction equation (Ref. 69) as

$$q(0, t) = \sqrt{\frac{k_B \rho_B C_B}{\pi}} \int_0^t \frac{1}{\sqrt{t-\tau}} \frac{dT_B}{d\tau} d\tau$$

In terms of E_F , this is

$$q(0, t) = \frac{\beta}{I_0 R_0 \alpha} \int_0^t \frac{1}{\sqrt{t-\tau}} \frac{dE_F}{d\tau} d\tau \quad (2)$$

where

$$\beta = \sqrt{\frac{k_B \rho_B C_B}{\pi}}$$

A more refined analysis of the thin-film thermometer which includes a first order correction for film thickness is given by Vidal (Ref. 65). It is shown that in the case of a constant heat transfer rate $q(0, t)$, the difference in actual backing surface temperature from that for zero film thickness becomes less than 6 per cent within 10 microsec for $\delta \leq 10^{-5}$ cm with platinum on quartz. The per cent difference is shown in Fig. 7.3-2 as a function of time for various values of δ .

Various film techniques used include bonded gold foil (Refs. 62 and 65), gold and rhodium evaporation under vacuum (Refs. 3, 41, 64, and 65), platinum sputtering (Refs. 3 and 66), and simple painting with special metallic paints or pastes such as Hanovia liquid Bright Platinum No. 05 - x[†] (Refs. 65, 67, and 70). With the last method, the film is baked at high temperature to drive off the vehicle which carries the metal salts in suspension. Application of the paint in thin layers, with each layer baked, produces a very durable film. Evaporation and sputtering methods perhaps offer the best control of film thickness. Typical film dimensions are 1 mm by 1 cm with cold resistance $R_0 \sim 50$ ohms and operating current $I_0 \sim 10$ to 20 ma. Typical voltage output is then of the order of 1 mv/°C for gold and platinum. Connection of electrical leads to the film is aided with conducting paint.

Use of the thin-film thermometer for surface temperature measurement requires knowledge of I_0 , R_0 , and α , Eq. (1). Both I_0 and R_0 can be measured by conventional bridge methods for each run. The thermal coefficient of resistance α is usually considerably less than that for the homogeneous bulk material (typically one-half or less) and must usually be determined by calibration for each film. The required temperature range of calibration depends, of course, on the application. The maximum temperature rise on insulated models in hypersonic shock tunnel flows of the order of one millisecond duration is of the order of 150°C. For heat transfer measurement, the additional constant β , Eq. (2), of the film backing must be known. Again, bulk values may be inaccurate and calibration is desirable. The value of $\frac{\beta}{\alpha}$ may be determined by measurement in the shock tube under conditions where the heat transfer is known. For example, the film may be located at the stagnation point of a blunt body or on a flat plate airfoil and its output recorded for flow induced by a weak shock of known strength (Refs. 65 and 67). A transient method for determining $\frac{\beta}{\alpha}$ which involves no flow is to supply a sudden and known constant rate of heat input by means of a long time constant condenser discharge through the film (Ref. 66). The known theoretical solution for film temperature ($T_F \sim \sqrt{t}$) and the recorded output E_F for the first few hundred microseconds enable $\frac{\beta}{\alpha}$ to be determined.

The thin-film thermometer has been used to measure surface temperature rise and heat transfer at shock-tube walls (Refs. 62, 63, 64, 66, and 45), as an indicator to determine boundary layer transition (Ref. 113), and as a shock wave detector (Ref. 41)**. Sputtered and painted films have proved sufficiently durable for measurement of heat transfer to models in hypersonic shock tube tunnel flows (Refs. 63, 65, 66, 67, and 70). While the thin film has a wide range of application in shock tube aerodynamic studies, its quantitative use becomes difficult under certain extreme conditions. Such conditions include, for

* Manufactured by Hanovia Chemical and Manufacturing Co., Ceramic Division, 1 West Central Ave., East Newark, N.J.

** A recent note on some aspects of thin-film response in ionized flows is given in Ref. 109.

example, very high heat transfer rates and/or long flow times giving excessive film temperature rise; sufficiently high gas temperatures to produce thermal ionization, in which case the film may be partially short circuited by the electrically conducting gas (e.g., Refs. 109 and 113); the presence of foreign particles, such as dust in the gas stream, which erode the film; or the presence of high electrical interference as from arc discharges. Difficulties experienced with thin-film resistance thermometers under such extremes of operation have led to development of "thick-film" surface calorimeters (Subsec. 7.3.3) for use where thin films are not feasible.

When mounted on the shock tube wall the thin-film thermometer shows a step rise ΔT_B in backing temperature (see Subsec. 7.4.1) on passage of the shock wave due to heat transfer $q(0, t) \sim \frac{1}{\sqrt{t}}$ with the initially laminar boundary layer induced by the shock (Subsec. 3.2). A typical wall record is shown in Fig. 7.3-3. The transition to turbulent boundary layer is marked by the sudden change in slope. Use of the film thermometer as a shock detector is further discussed in Subsec. 7.4.1.

7.3.2 Thin-Film Thermocouple

A thermocouple design introduced by Hackemann (Ref. 71) for use in gun barrels has been improved by Bendersky (Ref. 72) to the point where the response is sufficiently fast for shock tube application. The couple junction (Ref. 72) consists of a 1-micron thick film of nickel evaporated onto the polished end face of a 0.090-in. outside diameter steel cylinder. The cylinder houses a nickel wire insulated by nickel oxide from the steel but contacting the nickel film. The film is exposed to the flow.

Attempts to use this thermocouple in shock tube applications, have been reported as unsuccessful due to the fragility of the film which was destroyed on the first or second run. It might be noted that the thermocouple output is of the order of 0.03 mv/°C (Ref. 72) as compared to 1 mv/°C for the thin-film resistance thermometer. For the range of surface temperatures measured in shock tube flows, the thin-film resistance thermometer appears preferable to the thermocouple because of its greater output, simplicity, and ruggedness.

7.3.3 Calorimeter Heat-Transfer Gauge

An alternative to the thin-film resistance thermometer for heat transfer measurement is the fast response calorimeter gauge described in Ref. 70. The calorimeter gauge is mechanically similar to the thin-film thermometer except that the thickness (heat capacity) of the calorimeter resistance element is made sufficiently large for the element to retain essentially all the heat received in the required test time. For one-dimensional heat flow into a plane resistance element and no losses to the dielectric backing, the instantaneous rate of surface heat transfer $q(0, t)$ per unit area can be written

$$q(0, t) = \rho_M C_M \delta_M \frac{d}{dt} \Delta T_{AV}$$

where

ρ_M = density of metal resistance element

C_M = specific heat capacity of resistance element

δ_M = thickness of resistance element

ΔT_{AV} = average temperature rise through resistance element at time t :

$$\frac{1}{\delta_M} \int_0^{\delta_M} [T(y, t) - T_0] dy$$

T_0 = initial uniform temperature of resistance element

y = distance normal to exposed surface of resistance element

For small times, if the temperature rise ΔT_{AV} is small, the approximate relation

$$\frac{d}{dt} \Delta T_{AV} \approx \frac{1}{\alpha_M I R_0} \frac{dE}{dt}$$

may be assumed, where

E = voltage across metal resistance element

I = constant current through resistance element

R_0 = electrical resistance of element at temperature T_0

α_M = temperature coefficient of resistivity of element

Thus

$$q(0, t) \approx \frac{\rho_M C_M \delta_M}{\alpha_M I R_0} \frac{dE}{dt}$$

and the instantaneous heat transfer rate at the exposed surface of the element may be obtained from the corresponding slope of a voltage-versus-time oscilloscope record.

In practice, there is heat loss to the dielectric backing on which the resistance element is mounted. This may be calculated and corrected for. The losses can be reduced by increasing the element thickness δ_M and by leaving a small air gap between the element and the backing. An upper limit to the thickness δ_M is set by the need for sufficient average temperature rise in the short test times to provide

measurable voltage change across the element with practical currents. It is convenient to refer the element thickness to the characteristic heat diffusion length ℓ_M for the element material and test time t , defined by

$$\ell_M = \sqrt{\frac{k_M}{\rho_M C_M} t}$$

where

t = test time

k_M = thermal conductivity of element material

For the thin-film thermometer, the film thickness is made much smaller than ℓ_M . For the calorimeter gauge, the heat losses are relatively small if the element thickness δ_M is equal to or greater than ℓ_M . Figure 7.3-5 shows calculated ratios of heat loss to a pyrex backing to heat input into a metal element versus t/δ_M^2 for several element materials, assuming perfect contact between element and pyrex. With platinum, for example, taking $\delta_M = \ell_M$ gives $t/\delta_M^2 = 4.14 \text{ sec/cm}^2$ for which the heat loss to the pyrex is about 5 per cent. For a test period t of 100 microsec, the required element thickness δ_M is then about $0.5 \times 10^{-2} \text{ cm}$, or of the order of 100 times greater than the thickness for a thin-film thermometer.

The much lower temperature rise experienced by the calorimeter as compared to the thin film permits its use for much larger heat transfer rates and longer flow times. The low electrical resistance of the calorimeter makes it less susceptible to electrical interference than the film, although relatively large measuring currents are thereby required. Data reduction from oscillograph records is simpler for the calorimeter gauge than for the thin film, although the measurement of slopes is inherently inaccurate.

Reference 70 reports the use of a platinum calorimeter gauge to measure heat-transfer rates in the range 0.5 to 20 kw/cm^2 at the stagnation point of a pyrex hemisphere-cylinder body in flows behind shocks of Mach numbers up to 17. One considerable advantage of the calorimeter gauge is its greater durability resulting from the increased element thickness. Also, Ref. 70 reports that bulk properties of the metal resistance element proved sufficiently accurate with the element thicknesses used (of the order of 0.003 cm).

7.3.4 Hot-Wire Anemometer

The hot-wire anemometer has to date had limited application in shock-tube studies. Kovaszny and co-workers (Refs. 73 and 74) first studied the transient response of a constant-current hot wire in shock-tube flows and applied it to measurement of mass flow and stagnation temperature jumps and as a wave detector for timing and triggering purposes (Ref. 75). Billington (Ref. 76) used a constant-current hot wire to measure mass flow and stagnation temperature in a shock tube study

of refraction of a rarefaction wave at a contact surface. A recent comprehensive review of hot-wire anemometry has been given by Kovasznay (Ref. 77). In addition to references cited, use of the hot wire in the shock tube is further described in Ref. 78.

Basically the hot-wire anemometer consists of a very fine wire (typical diameter $d = 0.0001$ in., length $l = 0.1$ in.) mounted between two conducting probes which is placed in the flow and heated by an electric current I (Fig. 7.3-4). Usually, the wire forms one arm of a Wheatstone bridge. The principal wire heat loss is to the flow by forced convection and is dependent on mass flow and flow stagnation temperature. Changes in either produce changes in wire temperature or electrical resistance which generate an electrical signal. The simplest type of operation is with constant heating current I obtained with a large current source impedance. In this case, the output signal is the wire voltage change which is a direct measure of wire resistance or temperature change. A second type of operation is with constant wire temperature or resistance. This is accomplished by varying the heating current I with negative feedback circuitry to closely compensate wire temperature changes resulting from flow changes. The hot wire is a low-impedance device with typical resistance values being 50 ohms or less.

The instantaneous energy balance for the wire may be expressed as

$$W - H = C_w \frac{dT_w}{dt} \quad (1)$$

where

C_w = wire thermal heat capacity

T_w = effective wire temperature

W = rate of heat input to wire = $I^2 R_w$

$R_w = R_f [1 + \alpha(T_w - T_f)]$ = effective wire resistance (for small range of $T_w - T_f$)

T_f = reference temperature

α = constant, resistance coefficient

H = total rate of heat loss from wire

A crucial term in Eq. (1), insofar as practical use of the hot wire is concerned, is the total rate of heat loss H . It is usually assumed that the instantaneous heat loss is that which would exist in steady flow under the same instantaneous conditions. The contributions to H come principally from forced convection, but there can also be radiation, free convection, and conduction, including losses to the supports. Usually radiation is negligible and support losses are small enough to treat as a correction. Free convection effects become significant only for very low mass flows. The complexity of the heat transfer problem is such that no general theoretical solution exists and empirical heat

loss laws based on experiment guided by dimensional analysis must be relied on. In dimensionless form, the heat loss can be expressed in terms of the Nusselt number Nu as

$$Nu = \frac{H}{\pi \ell k (T_w - T_r)}$$

where

k = thermal conductivity of fluid

T_r = temperature attained by unheated wire ($I = 0$)

ℓ = wire length

Dimensional analysis shows that Nu depends on the following dimensionless ratios (Ref. 77):

M = Mach number = $\frac{V}{a}$

Re = Reynolds number = $\frac{\rho V d}{\mu}$

Pr = Prandtl number = $\frac{\mu C_p}{k}$

γ = Specific heat ratio = C_p/C_v

τ = temperature loading = $\frac{T_w - T_r}{T_o}$, T_o = stagnation temperature

ℓ/d = length-diameter ratio of wire

θ = angle giving orientation of wire

A much used heat transfer relation for low speeds is that due to L. V. King (Ref. 79). King's law was derived theoretically for incompressible potential flow about an infinite cylinder normal to the flow direction. In dimensionless form, King's law may be expressed as (Ref. 77)

$$Nu = C_1 \sqrt{Re} + C_2$$

for constant Pr . Most experimental studies at incompressible speeds bear out the linear \sqrt{Re} dependence of Nu although the experimental constants C_1 and C_2 differ considerably from King's theoretical values. Spangenberg (Ref. 80) has observed additional dependence of Nu at incompressible speeds on the Knudsen number λ/d , where λ = mean free path. At compressible subsonic speeds the linear \sqrt{Re} dependence of Nu also applies (Ref. 80), but there is also dependence on Mach number,

temperature loading, and Knudsen number. At supersonic speeds the \sqrt{Re} dependence persists (Re based on conditions behind normal shock wave) with further dependence on temperature loading but only slight dependence on Mach number (Refs. 80, 81, and 82). Most measurements of recovery temperature T_r indicate it to decrease from T_o at $M = 0$ to about $0.96 T_o$ at $M \sim 1$, to remain constant for $M > 1$, and to have practically no dependence on Re (Refs. 80, 81, and 82).

If King's law is assumed, H can be expressed as

$$H = (A' \sqrt{\rho u} + B') (T_w - T_r)$$

where

$$B' = kl, \quad A' = l \sqrt{2\pi k C_p d}$$

may be determined at a given temperature by calibration. Thus from Eq. (1) it follows that

$$I^2 R_w - (A' \sqrt{\rho u} + B') (T_w - T_r) = C_w \frac{dT_w}{dt} \quad (2)$$

Equation (2) has been used (Refs. 73, 74, and 76) as the basis for constant-current hot-wire measurement in the shock tube of quasi-steady flow regions bounding sudden flow changes. In the quasi-steady end states, $\frac{dT_w}{dt} = 0$ and from Eq. (2)

$$I^2 R_w = \frac{R_w - R_r}{\alpha R_r} (A' \sqrt{\rho u} + B') \quad (3)$$

taking $T_f = T_r$ in expressing T_w in terms of R_w . Operation at constant current I enables changes in R_w to be obtained from oscilloscope recordings of wire voltage $E_w = I R_w$. Changes in R_w result from either mass flow change (ρu) or recovery temperature change ($R_r \propto T_r \approx T_o$). With high heating current the wire is mainly mass flow sensitive, while with low heating current it is mainly temperature sensitive. The two effects produce changes of opposite sign in wire voltage and may be separated by duplicate shock tube runs with different currents. Equation (3) then gives two algebraic equations solvable for the unknown mass flow and recovery temperature. The recovery temperature is equal to the flow stagnation temperature to within a few per cent.

Where the time derivative term $\frac{dT_w}{dt}$ cannot be neglected, the wire response for small fluctuations of flow parameters is characterized by a thermal lag time constant \bar{M} (Ref. 77)

$$\bar{M} = \frac{C_w}{\frac{\partial H}{\partial T_w} - \frac{\partial W}{\partial T_w}}$$

In terms of wire voltage fluctuation ΔE_w , Eq. (1) leads to

$$\Delta E_w + \bar{M} \frac{d}{dt} \Delta E_w = \Delta E_s$$

for constant current operation, where ΔE_s is the ideal response with zero lag, $\bar{M} = 0$, (or the static response). For King's law heat loss,

$$\bar{M} = \frac{na_w}{I^2}$$

where

$$n = \text{constant of wire} = \frac{C_w}{\alpha R_f}$$

$$a_w = \text{mean overheating ratio} = \frac{R_w - R_r}{R_r}$$

Thus \bar{M} depends not only on the properties of the wire but also on the mean wire operating conditions. Usually \bar{M} lies in the range 0.1 to 1 millisecc with practical equipment. The desired ideal response ΔE_s may be recovered from the distorted wire output ΔE_w by passing ΔE_w through an electronic compensating amplifier having the inverse characteristics of the wire (Ref. 77).

The constant-current compensation technique is only applicable for small fluctuations in flow parameters about constant mean values where \bar{M} can be considered constant. Thus the technique is of little use in the shock tube for studying transitions in mean flow parameters such as, for example, mass flow and temperature change through a rarefaction wave. For shock-tube transition studies the constant temperature system is superior as $\frac{dT_w}{dt}$ is made negligibly small and the steady state relation (3) applies. Duplicate shock tube runs at different initial heating currents then provide information for two algebraic equations solvable for mass flow and temperature at each step of the transition. The same technique may be used with constant-current operation without compensation (Refs. 76 and 78), but in this case the time derivative terms must be included. This involves measurement of slopes as well as amplitudes from the oscilloscope records of E_w , and the data reduction becomes cumbersome.

The hot-wire anemometer is not a simple instrument, and its reliable use necessitates great care. Accurate quantitative measurement usually requires a separate calibration of each wire. A particular disadvantage for shock-tube studies is the extreme fragility of the wire, which makes it a vulnerable target for diaphragm particles. The use of the hot wire as a shock detector and trigger is further described in Subsec. 7.4.1.

7.3.5 Interferometry

Indirect measurement of static flow temperature can be made by interferometry (Subsec. 7.2.1.4) provided a relation between density and temperature is known. This method has been used to determine temperature distribution through the shock-tube wall boundary layer (Refs. 43, 44, and 45) by assuming static pressure constant and temperature inversely proportional to measured density.

7.4 Primary Shock Strength Measurement

Primary shock wave refers to the initial shock wave propagated into gas at rest in the low-pressure channel after diaphragm removal. The strength of the primary shock is an important parameter in most shock-tube studies, and it seems worthwhile to note under one heading the methods commonly used for its measurement.

Any one of the ratios P_{21} , T_{21} , ρ_{21} , M_s , or U_{21} may be taken as a measure of primary shock strength. Here, subscript 2 refers to the final equilibrium state behind the shock, i.e., after all relaxation phenomena are completed. By virtue of the mass, momentum, and energy relations for the over-all shock transition, and the thermal equation of state for the gas, any one of the above ratios defines the others. The normal shock relations are given in Subsec. 2.2.

Three possible methods of measuring primary shock strength have been mentioned in previous sections. These are the measurement of shock pressure rise with a pressure transducer (Subsec. 7.1.2.1), density rise with the interferometer (Subsec. 7.2.1.4), and mass flow and stagnation temperature change with the hot-wire anemometer (Subsec. 7.3.4). Two further methods which follow are direct shock-speed measurement (Subsec. 7.4.1) and a reflected-wave technique (Subsec. 7.4.2).

7.4.1 Direct Shock-Speed Measurement

Direct measurement of shock speed w is perhaps the most common method of determining primary shock strength. Shock speed w and the sound speed a_1 of the gas at rest ahead of the shock give the shock Mach number M_s . Methods of directly measuring shock speed include those giving continuous wave speed, as wave-speed schlieren, for example, and those using two or more shock detectors spaced along the tube to give an average wave speed measurement over a known distance.

7.4.1.1 Continuous Wave-Speed Methods

The continuous shock-speed measurement methods of wave-speed schlieren and drum-camera streak photography for luminous fronts have been outlined in Subsec. 7.2.1.3. Another method involves microwave reflection from the moving shock wave using the shock tube itself as an electromagnetic wave guide (Refs. 105 and 114). Measurement of the Doppler frequency change of the reflected waves gives a measure of the shock speed. The method is particularly applicable with strong shocks producing ionization and a sufficient electron density to give large reflection coefficients. Large reflection is attained if the number of electrons per cubic centimeter becomes significant in comparison to

$1.24 \times 10^4 f^2$, where f is the microwave frequency in megacycles per second (Ref. 105). A lower limit to f is set by the tube cross section. A successful application of the microwave technique at 5000 Mc/sec with a 5.4-cm square tube is described in Ref. 105.

7.4.1.2 Shock Detector Methods

The shock detector method uses sensing elements (shock detectors) spaced along the tube which respond to some property of the shock transition and provide a fast electrical pulse upon passage of the wave. Measurement of the time interval between pulses from two such detectors located a known distance apart provides an average shock speed. The simplest arrangement has two detectors but more than two may be used to study wave speed variation.

The usual arrangement involves two or more detectors with appropriate coupling circuitry, such as an amplifier and connecting cables, and a chronograph to measure the time interval between pulses. Accurate measurement of average shock speed requires detectors with near identical and fast response, and good spatial resolution. The coupling circuitry may be individual for each detector or common to all. Whichever, the response must be fast, and if individual coupling is used the individual circuits should be closely matched. Regarding spatial resolution, the detector should preferably have the smallest dimension possible in the direction of shock motion to minimize uncertainty in the base length used to compute wave speed. Also of course, the detector should not significantly disturb the flow.

Requirements on response time and electronic technique become more severe with increasing shock speed and decreasing detector spacing. For example, at $M_s = 1.5$ a detector spacing of 12 in. gives a shock transit time of 600 microsec at room temperature, and an error as large as 6 microsec would be tolerable. At $M_s = 15$, however, the same error would be quite significant. At higher shock strengths particularly, where shock attenuation may be large and detector spacing accordingly small, signal rise times of one microsecond or better with time interval measurements to one microsecond or better are desirable.

Commercial interval timers, such as the Potter chronograph, are commonly used for measuring time intervals. These are readily available with resolution to 10^{-6} sec and are convenient as they display the time interval directly. One unit, however, is ordinarily required for each detector pair. Oscilloscope techniques which expand the time scale, such as the raster method using simultaneous X and Y sweep (Ref. 96) or the moving film method where film movement is equivalent to the Y sweep (Refs. 88 and 92) have been used to attain 10^{-7} to 10^{-8} sec resolution with short rise time detector pulses. Measurement is made between the beginning of successive detector signals. The oscilloscope methods have the advantage that one trace can record signals from a number of detectors. However, the time intervals must be measured from a photographic record.

Various shock detectors in use will now be described. Coupling circuitry is generally omitted as this follows customary electronic technique for which Refs. 83 and 84 may be consulted as a general guide. In addition to application to shock speed measurement, the detectors described are, of course, useful for other triggering applications in shock tube studies.

Pressure Contactor.--The pressure contactor is perhaps the simplest detector. It consists of a mechanical on-off switch actuated by the pressure rise across the shock and may be used to switch an R-C circuit for pulse generation. The device can have many forms. Figure 7.4-1 shows a design used by Lundquist (Ref. 85).

Although they appear simple, such mechanical switches suffer numerous defects and usually require frequent and careful adjustment. In general they have not proved too reliable.

Pressure Transducer.--Pressure transducers have been discussed in Subsec. 7.1.2.1. Small transducers with sufficiently fast rise time to a shock front may be used flush in the tube wall as shock detectors. The step electrical output from the shock pressure rise may be differentiated electrically to provide a short duration pulse. Usually some care is required in the mounting to minimize transducer response to wave transmission through the tube walls initiated when the tube is fired. Because of the high sound speed in metals as compared to gases, disturbances transmitted through the walls precede the gas shock, except possibly for very strong shocks. The pressure transducer is ultimately limited with weak shocks by background noise level and similarly with strong shocks when the pressure ahead of the shock is sufficiently low.

Piezoelectric transducers, such as the SLM miniature quartz gauge, make excellent detectors because of their wide operating range and generally fast response. Improved spatial resolution (down to 1/8-in. diameter face) with somewhat less sacrifice of sensitivity may be obtained using barium titanate ceramics (see Ref. 110 for a recent design for low pressures). A good arrangement using a separate amplification and thyratron trigger circuit for each of seven tourmaline transducers (used to measure detonation velocities) is described in Ref. 86. A disadvantage of the commercial pressure transducer as a detector is the relatively high cost compared to other methods such as the ionization probe or resistance thermometer, discussions of which follow in subsequent paragraphs

Light Screens.--The light-screen method was one of the earliest shock-tube measuring techniques developed (Ref. 87) and is still used extensively in the shock Mach number range from 1 to 4. Many specific arrangements have been described over the years (Refs. 85, 87, 88, 89, 90, 92, and 93), and a good general account has been given by Bleakney (Ref. 91).

Many variations of the method are possible. Figure 7.4-2 illustrates the simplest system (Refs. 85 and 90) involving the Toepler-schlieren principle which requires only one lens. The light source S is a line or narrow ribbon filament lamp with the long dimension normal to the plane of the drawing. The lens L images S on the knife edge K preceding a photomultiplier tube P. The optical axis is normal to the flow direction. A narrow light beam in the flow direction (of the order of 0.1 in.) is obtained with suitable stops or slits. In operation, K is adjusted with uniform density in the shock tube to just cut the beam off so only stray light reaches P. As the shock wave passes through the beam the steep density gradient in the wave momentarily deflects each ray of the beam towards the high density side and thus off the knife edge. The photomultiplier thus receives a fast pulse of light and the desired voltage pulse (Fig. 7.4-2(b)) may be obtained from the

corresponding change in photomultiplier current. Pulse rise times of one microsecond may be obtained.

The sensitivity of the system increases directly with f . Values of l of the order of 4 or 5 in. prove adequate in practice. The dimension of the source image in the direction of shock motion should be as small as possible, i.e., the system should have small range, and the source should have high brightness. Elimination of stray light is very important in obtaining a high over-all signal-to-noise ratio. More sophisticated schlieren arrangements (Ref. 89) than that of Fig. 7.4-2 use additional lenses which help towards this end.

The arrangement of Fig. 7.4-3 (Refs. 91 and 92) uses no lenses and depends on total reflection from the shock front, i.e., on the shock acting as a mirror. The three knife edges K_1 , K_2 , and K_3 are carefully adjusted so that their edges lie in a plane normal to the flow direction. Then, only rays from the finite light source S lying in the plane so defined reach the photomultiplier tube P. As the shock wave passes, some rays normally cut off by K_3 (as shown dashed) momentarily suffer total reflection from the back of the shock and escape K_3 to reach P. The rate of change of light flux on P is approximately proportional to shock speed, and the signal voltage initially rises linearly with time.

With both schlieren and reflection methods, the beginning of the output signal rise may be located to a few tenths of a microsecond in time with oscilloscope recording. This permits very accurate average wave speed measurement using two or more light-screen stations with raster or moving film oscillography (Refs. 88, 92, and 93). For multiple stations, light from three detectors can be "piped" to a single photomultiplier by a lucite guide (Ref. 93) as illustrated in Fig. 7.4-4.

To avoid adverse effects from shock-tube vibration it is preferable to have the light screens as mechanically independent of the tube as possible. The references cited may be consulted as a guide to construction methods and detailed electronic circuitry. The optical performance of a given system may be calculated roughly using geometrical optics with simplifying assumptions for shock wave structure, such as constant density gradient. Mair (Ref. 94) gives useful results for light ray refraction through a shock front.

Light screens, when once carefully adjusted, function reliably over a wide range of operating conditions and are capable of good precision. Their use is ultimately limited by the over-all noise level for insufficient density rise occurring for very weak shocks or at sufficiently low density. Their operation may sometimes be unreliable if used so close to the diaphragm that the shock is curved and not fully formed.

Glow-Discharge Probe.--The glow-discharge probe as used by Lundquist (Ref. 85) has proved useful at low densities (see also Ref. 111 for a recent design). Figure 7.4-5 shows the arrangement used. Glow discharge takes place between the steel pin and the shock tube wall with the discharge current depending on gas density, electrical parameters, and pin spacing. The abrupt change in density on passage of the shock wave produces a corresponding change in current and the

electrical circuit provides a fast output voltage pulse. The glow-probe has proved useful in the range of low densities (e.g., channel pressures of 0.1 to 25 mm with air) where light-screen methods may become unreliable and where shock strength is too low for ionization probes (see the next paragraph) to function. Channel pressures must be low enough to obtain glow discharge. The operating range may be extended by adjustment of voltage and pin spacing.

Ionization Probes.--For shock Mach numbers above about 4.5 in air at room temperature, the increased temperature behind the shock front gives a sufficient increase in ionization and gas conductivity to permit use of simple ionization probe detectors. A typical arrangement is shown in Fig. 7.4-6. Glow discharge is avoided. The capacitor discharges through the projecting needles on passage of the shock front because of the sudden decrease in gas resistance. For weaker shocks the large gas resistance and stray shunt capacitance present tend to limit rise times to around one microsecond, but for stronger shocks this can be improved considerably.

The shaped probe shown in Fig. 7.4-7 is reported by Morrison (Ref. 95) to be useful down to shock Mach numbers of 1.5. A local shock wave propagates into the opening on passage of the main wave and is intensified by the converging cross section.

A sequence of ionization detectors of the type shown in Fig. 7.4-6 were used by Knight and Duff (Ref. 96) as shown in Fig. 7.4-8 to measure detonation velocities with high precision. Six pin detectors decoupled by diodes were connected electrically in parallel and spaced at 10 cm along the tube. Each consisted of two copper pins projecting from a Teflon plug set flush. A cathode follower output fed the signals via a 300-ohm line to the plates of a raster oscilloscope. For weaker waves, rise times were sharpened by additional circuitry to permit time resolution to 10^{-8} sec.

Ionization probes have generally fast response, excellent spatial resolution, and are relatively simple and inexpensive. One disadvantage is that any water present after a run condenses on the probes and they require frequent cleaning.

Thin-Film Resistance Thermometer.--Because of its very fast response, insensitivity to vibration, and relative simplicity, the thin-film resistance thermometer discussed in Subsec. 7.3.1 is an excellent detector when mounted flush in the shock tube wall with the long dimension perpendicular to the direction of shock travel. Blackman (Ref. 41) used thin gold films evaporated on tape (stuck onto lucite wall plugs) to measure shock speeds in the range of M_s from 7.5 to 10 with accuracy better than 1 per cent. Signal rise times were determined by the transit time of the shock across the narrow film and were of the order of one-half microsecond or less for the one-half millimeter width used.

For use as a detector, the film is mounted on an insulating plug made of quartz, glass, or lucite (depending on the film technique used) and designed to insert in the tube wall flush with the inside surface. Any of the film techniques described in Subsec. 7.3.1 may be used, i.e., evaporation, sputtering, or painting with metallic paint or paste. Film widths of 0.05 in. or less in the direction of shock motion are desirable, with lengths from 1/2 to 1 in. and resistances of the order of 50 ohms. A simple heating circuit as shown in Fig. 7.4-9 may

be used to operate the film at essentially constant current. Several films could be so heated in parallel.

As discussed in Subsec. 7.3.1, on passage of the shock wave the surface temperature T_B of the insulated backing or plug on which the film is mounted initially undergoes a step increase ΔT_B and the film resistance R_F accordingly increases by $\Delta R_F = \alpha R_O \Delta T_B$. For constant current I_O , the initial step increase in voltage across the film is then $\Delta E_F = I_O \alpha R_O \Delta T_B$. This may be differentiated as indicated in Fig. 7.4-9 to provide a short duration pulse. The film response is so rapid with the thin films used (see Subsec. 7.3.1) that the rise time of the leading edge of the pulse is essentially the transit time of the shock across the film. For purposes of estimating the initial voltage rise ΔE_F to a shock wave, an expression for ΔT_B due to Bromberg (Ref. 68) may be used. In the present notation this is

$$\frac{\Delta T_B}{T_1} = \frac{M_s^2 C_{p1} (\gamma_1 - 1) \bar{U} \sqrt{\frac{1}{2} \rho_2 \mu_2}}{\beta + \frac{M_s C_{p1} \bar{U}}{u_{21}} \sqrt{\frac{1}{2} \rho_2 \mu_2}}$$

where

$$\beta = \sqrt{\frac{k_B \rho_B C_B}{\pi}}$$

for insulated backing (see Subsec. 7.3.1), and \bar{U} is given in Fig. 7.4-10

$$u_{21} = \frac{u_2}{a_1}$$

(Subscripts 1 and 2 refer to gas states ahead and behind the shock.)

This relation for ΔT_B assumes the product $\rho\mu$ as constant across the boundary layer, a Prandtl number of 1, and equilibrium zero-pressure-gradient flow.

Because of its excellent characteristics, the thin-film resistance thermometer is perhaps the best and most generally useful shock detector. Its use is ultimately limited by insufficient temperature rise ΔT_B with weak shocks. It can probably be used without difficulty down to $M_s = 1.5$, at least.

Hot-Wire Anemometer.--The hot-wire anemometer described in Subsec. 7.3.4 has been used by Dosanjh (Ref. 75) as a shock-detector probe to measure wave speeds in the range of M_s from about 1.01 to 4. The mechanical arrangement is shown in Fig. 7.4-11. Some relief from

particle damage is obtained with the protecting well. The wire is used at constant current, uncompensated, with the exponential wire response to the shock wave (see Subsec. 7.3.3) differentiated before amplification. Circuit details are given in Ref. 75.

The polarity of the change in wire voltage due to passage of the shock depends on the amount of heating of the wire. For small heating, temperature response dominates and the wire voltage (wire resistance) increases. For large heating, mass flow response dominates and wire voltage decreases. Figure 7.4-12 shows typical wire voltage jump as a function of shock pressure ratio P_{21} and overheating ratio a_w .

Compared to other detectors such as the resistance thermometer, the hot wire has a number of disadvantages. In particular, it is very fragile and vulnerable to particle damage, and has relatively slow response when uncompensated (0.1 to 1-millisecond time constants). Its use appears advantageous only for detection of very weak shocks where, as indicated by Fig. 7.4-12, good mass-flow sensitivity is maintained with sufficient overheating.

Positive-Ion Beam Detector.--Venable (Ref. 97) has described a detector using a positive-ion beam perpendicular to the direction of shock motion which is useful at low densities. Figure 7.4-13 shows the arrangement schematically. The positive-ion beam is obtained from an electric discharge tube with a drilled cathode opening into the shock tube. The ion current emerging from the cathode hole is collected by a needle about 90 volts negative with respect to the cathode (glow discharge avoided), and passes through a high resistance to ground. Interruption of the beam by passage of the shock provides a sudden voltage change across the resistance.

Ion currents of around one micro-ampere provided adequate output signals (10 to 100 mv) at pressures ahead of the shock of 0.05 to 5 mm Hg in helium, argon, and nitrogen for the range of shock strengths employed ($M_s = 1.6$ to 3).

7.4.2 Reflected-Wave Technique

The reflected-wave technique for shock strength measurement requires the use of instantaneous shadowgraph or schlieren records to compare distances moved by the primary shock and a reflected wave in equal times. If both wavespeeds are constant, this gives a comparison of velocities from which the primary shock strength may be inferred from theory. Numerous practical arrangements are possible. Two applications made by Hertzberg and Kantrowitz (Ref. 98) are typical and will be briefly described.

Cylindrical wave reflection involves a single thickness of Scotch tape across the tube floor which generates two cylindrical acoustic waves on passage of the shock. The resulting wave configuration as recorded optically a short time t after the passage of the shock is shown in Fig. 7.4-14 for subsonic flow in state (2). All velocities are assumed constant. Then,

$$\frac{a_2 - u_2}{w} = \frac{d_3}{d_2}$$

and

$$\frac{a_2}{w} = \frac{d_1}{d_2}$$

For constant specific heats, these two ratios are related to primary shock pressure ratio P_{21} by (Subsec. 2.2)

$$\frac{a_2 - u_2}{w} = \frac{d_3}{d_2} = \frac{\gamma \left[\frac{\gamma - 1}{2\gamma} P_{21} \left(\frac{\gamma + 1}{\gamma - 1} + P_{21} \right) \right]^{1/2} + 1 - P_{21}}{\gamma \left[\frac{\gamma - 1}{2\gamma} \left(1 + \frac{\gamma + 1}{\gamma - 1} P_{21} \right) \right]^{1/2}}$$

$$\frac{a_2}{w} = \frac{d_1}{d_2} = \frac{\left[P_{21} \left(\frac{\gamma + 1}{\gamma - 1} + P_{21} \right) \right]^{1/2}}{\left(\frac{\gamma - 1}{2\gamma} \right)^{1/2} \left(1 + \frac{\gamma + 1}{\gamma - 1} P_{21} \right)}$$

Thus the shock strength P_{21} may be found from either ratio. The ratio d_3/d_2 is the more sensitive to changes in P_{21} .

Normal shock wave reflection involves reflection of a portion of the primary shock from a rigid wall as indicated in Fig. 7.4-15. For constant wavespeeds,

$$\frac{w_R}{w} = \frac{d_1}{d_2}$$

and using the theory of normal shock reflection for constant specific heats (Subsec. 2.4.1)

$$\frac{w_R}{w} = \frac{d_1}{d_2} = \frac{1 + (\gamma - 1) P_{21}}{\frac{\gamma - 1}{2} \left(1 + \frac{\gamma + 1}{\gamma - 1} P_{21} \right)}$$

from which P_{21} may be obtained. In the work of Ref. 98 the reflecting block and splitter plate were made up as a probe unit, and weak shock strengths as low as $M_s = 1.01$ were measured.

Referring to the Scotch-tape technique, when state (2) of Fig. 7.4-14 is supersonic no upstream propagation is possible. Instead, a pseudo-stationary Mach wave results from which the Mach angle

$$\mu_2 = \sin^{-1} 1/M_2$$

and hence M_2 , can be measured. This technique has been used (Ref. 99) to determine M_2 , and the ratio a_2/w with strong shocks. The geometry of the wave configuration a short time t after the shock passes a small disturbance is shown in Fig. 7.4-16. From the figure,

$$\sin \mu_2 = \frac{a_2}{u_2} = \frac{1}{M_2}$$

and

$$\frac{a_2}{w} = \frac{d_1}{d_2}$$

Independent measurement of w by ionization probes enabled a_2 to be determined.

7.5 Light-Reflectivity Measurement (Shock-Wave Transition)

Measurement of the optical reflectivity of shock wave density transitions has been used to determine shock wave thickness and to study equilibration of rotational degrees of freedom in shocked polyatomic gases (Refs. 100, 101, and 102). The experimental arrangement is shown schematically in Fig. 7.5-1. Light from an intense source is filtered and collimated to a near monochromatic parallel beam which is directed through a window at angle θ to the shock tube axis. A plane shock wave travelling down the tube intercepts the beam momentarily and the sharp density gradient in the wave reflects a weak pulse through a second window to the photomultiplier P. The photomultiplier output is recorded on an oscilloscope; the pulse height gives a measure of reflected light intensity. By suitable calibration of the apparatus the variation of optical reflectivity

$$R = \frac{\text{intensity of reflected light}}{\text{intensity of incident light}}$$

with wave length λ , angle θ , and pressure p_1 ahead of the shock may be determined for a given shock strength. The absolute value of R is very small (10^{-5} to 10^{-7}), and the noise due to stray light must be kept very low to obtain useful measurements.

A significant variation of R with λ and θ can be obtained if λ is of the same order as the shock front thickness. The reflectivity can be expressed theoretically as (Ref. 100)

$$R = \frac{(1 + \tan^4 \theta)}{4} |F(y)|^2$$

where

$$F(y) = \int_{-\infty}^{\infty} \frac{dn}{dx} e^{-2\pi i y x} dx$$

n = index of refraction = $n(x, L, \Delta n)$

x = co-ordinate normal to shock front

y = $(2 \cos \theta)/\lambda$

Δn = $n_2 - n_1$ = total refractive index change across shock

L = shock wave thickness = $\frac{\Delta n}{\left(\frac{dn}{dx}\right)_{\max}}$

The measured variation of R was utilized (Ref. 100) by fitting it with the above theoretical variation of R calculated for various assumed profiles $n(x, L, \Delta n)$. The shock thickness parameter L was chosen to give the best fit.

In the limit for small values of $y(\theta \rightarrow \frac{\pi}{2}$ or $\lambda \rightarrow \infty)$ the theoretical reflectivity becomes

$$R = \frac{1 + \tan^4 \theta}{4} (\Delta n)^2$$

which is independent of shock profile, and the shock front appears as a step change. Thus measurement of R (relative) near grazing incidence provides the shock front density change. In a diatomic gas this density change depends on the extent of equilibration between translational and rotational energies, and such measurements have yielded information on rotational heat capacity lag in strong shock waves (Refs. 101 and 102).

7.6 Light-Absorption Measurement

Light absorption has been utilized in shock-tube chemical kinetic studies (see also Subsec. 5.3) to measure rates of dissociation and recombination for certain reactions initiated by shock wave heating, where a reactant or product absorbs light. A typical reaction studied by this method was molecular iodine dissociation over the temperature range of 1000 to 1860°K (Ref. 103). The shock wave is propagated into a mixture of diluent inert gas, such as argon or nitrogen, and a weak concentration (i.e., a few per cent) of the gas to be dissociated. The intensity of a narrow sheet of near monochromatic light crossing normal to the shock tube axis is recorded with a photomultiplier tube and oscilloscope. The scope sweep is triggered just prior to the arrival of the shock. For light of intensity I_0 incident on the shock tube flow the emergent light intensity I is

$$\log_{10} \frac{I}{I_0} = - \epsilon c l$$

where

l = length of light path through absorbing gas

c = concentration of absorbing gas

ϵ = extinction (absorption) coefficient of absorbing gas, a function of wavelength and temperature.

If ϵ is known, a record of I for flow behind the shock then provides the change of concentration c with time. Quantitative interpretation of the light transmission records to obtain dissociation and recombination rate constants is possible. Evaluation is complicated by the fact that the temperature changes as dissociation and recombination proceed. With polyatomic diluents, vibrational relaxation of the diluent behind the shock front must also be considered. Wall boundary layer effects can be significant if the boundary layer thickness increases to an appreciable fraction of the tube width (Ref. 104).

The extinction coefficient ϵ may be determined as a function of temperature for a given wave length from the changes in I immediately across shock fronts of known strength. If no dissociation has occurred immediately behind the front, the concentration is known from that ahead of the shock and the shock density ratio. For polyatomic diluents, the shock front density ratio used to calculate c behind the front, and thus ϵ , depends on the degree of vibrational equilibration assumed. Thus a comparison of ϵ for monatomic and polyatomic diluents can yield information on vibrational relaxation time for the latter (Ref. 103).

7.7 Electrical-Conductivity Measurement

Measurement of the electrical conductivity of argon ionized by strong shock wave heating has been made by Lin, Resler, and Kantrowitz (Ref. 31).

The first technique tried employed a metal probe at the end of the shock tube swept over by the incident and reflected shock wave as shown in Fig. 7.7-1. The probe voltage measured as a function of time with an oscilloscope enabled an average ionized gas resistance to be determined and from this the conductivity could be calculated. The results obtained with this method differed markedly from theoretical expectations. A large effect from the cool boundary layers on the tube walls and probe was indicated. The probe technique was abandoned in favour of a magnetic method which avoided surface effects.

The magnetic experiment, shown schematically in Fig. 7.7-2, utilized interaction between the axisymmetric steady magnetic field supplied by a field coil encircling a glass section of the shock tube and the moving ionized gas behind the shock wave. Passage of the conducting gas through the magnetic field displaced the field lines causing them to cut across a small search coil and thereby induce an emf which was recorded on an oscilloscope. The essential features of the conductivity distribution behind the shock front could be calculated from the recorded search coil voltage with the aid of the search coil response to a metallic rod (with the same inside diameter as the shock tube) shot through the glass section and magnetic field at constant speed. The technique was successfully used to measure the conductivity of shock-heated argon over the temperature range of 4000 to 14,000°K (shock Mach number 7.5 to 16) at various initial pressures. The same technique has been applied to measure the electrical conductivity of shock-heated air (Ref. 106).

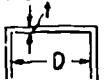
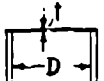
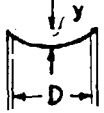
7.8 Model Force Measurement

Rather limited effort has been applied to development of instrumentation for the direct measurement of aerodynamic forces on shock-tube models. Reference 65 describes an internal model balance

system under development which uses commercial accelerometers to measure model accelerations. Figures 7.8-1 and 7.8-2 illustrate the arrangement. When assembled as in Fig. 7.8-1, the model and accelerometers form an integral unit attached to the rigid sting support through soft rubber springs. The latter permit relatively free movement of the model and give a natural period of model oscillation that is large compared to the available testing time. Under these conditions, the rubber spring restoring forces which arise due to model displacement during a shock-tube test can be neglected, and the aerodynamic forces can be obtained from the measured model accelerations.

Table 7.1-1

Transducer diaphragm performance parameters (Ref. 14)

		$\frac{\omega D}{C}$	$\frac{S E}{D}$	$\frac{m}{A} \text{ (eff.)}$	$\frac{P_{MAX}}{\sigma_{MAX}}$
FLAT NO TENSION		$12.2 \frac{t}{D}$	$.011 \frac{D^3}{t^3}$	$.6 \rho t$	$\frac{16}{3} \frac{t^2}{D^2}$
FLAT ALL TENSION		$4.8 \sqrt{\frac{\epsilon}{E}}$	$.13 \frac{E D}{\epsilon t}$	$.6 \rho t$	$8.8 \frac{t}{D} \sqrt{\frac{\sigma_{MAX} - \epsilon}{E}}$
SPHERICAL SEGMENT $\frac{y}{D} < \frac{1}{10}$		$16 \frac{y}{D}$	$.0058 \frac{D^3}{t y^2}$	$\frac{1}{6} \rho t$	$16 \frac{y t}{D^2}$

- C = Sound Speed of Diaphragm Material
 ρ = Density of Diaphragm Material
 E = Youngs Modulus of Diaphragm Material
 ϵ = Tensile Stress / Unit Area in Diaphragm
 p_{max} = Maximum Allowable Pressure Difference Across Diaphragm
 σ_{max} = Maximum Allowable Tensile Stress in Diaphragm

Table 7.2-1

Values of Gladstone-Dale constant K (Ref. 22)

AIR		OXYGEN		NITROGEN		ARGON	
* λ	K						
1 2620	3.886×10^{-3}	3 1920	4.027×10^{-3}	3 4358	3.874×10^{-3}	1 2620	2.700×10^{-3}
1 2960	3.813	3 2000	3.861	3 4811	3.833	3 2894	2666
1 3340	3.762	3 3000	3.245	3 5461	3.834	1 2960	2657
3 4358	3.676	3 4000	3.114	2 5850	3.826	3 3342	2620
1 4360	3.679	3 4358	3.100	3 5876	3.825	1 3350	2622
1 4700	3.663	2 4800	3.064	4 5893	3.794-3.819	3 4109	2576
3 4798	3.656	3 5000	3.062	2 6140	3.815	1 4280	2574
2 4800	3.654	2 5090	3.054	3 6362	3.802	3 4358	2572
1 5050	3.646	2 5210	3.049	3 6564	3.810	3 4917	2551
2 5090	3.644	2 5460	3.042	2 6680	3.805×10^{-3}	1 5110	2551
3 5100	3.646	3 5461	3.055			1 5220	2549
2 5210	3.640	2 5770	3.036			1 5460	2548
1 5460	3.635	3 5876	3.046			3 5461	2546
3 5461	3.636	4 5893	3.041-3.052			3 5462	2538
3 5769	3.629	3 5897	3.037			3 5677	2537
1 5780	3.628	2 6440	3.022			1 5700	2541
3 5786	3.627	3 6564	3.030			1 5770	2542
2 5790	3.625-3.628	2 6710	3.016×10^{-3}			3 5876	2539
1, 2,							
4 5890	3.627					3 5876	2539
2 6140	3.619					4 5893	253
3 6147	3.622					1 6560	2533
1 6440	3.617×10^{-3}					3 6564	2.527×10^{-3}

λ in Angstroms, $K = \frac{n-1}{\rho}$ in cu ft/lb

- * References: 1. Landolt-Bornstein; Physikalisch-Chemische Tabellen, Erster Ergänzungsband. Verlag Von Julius Springer, Berlin, 1927, p 525.
 2. As 1, pp 814-815
 3. As 1, pp 1677-1679
 4. Handbook of Chem. and Pys., 30th Ed., Chem. Rubber Pub. Co., Clev., 1946.

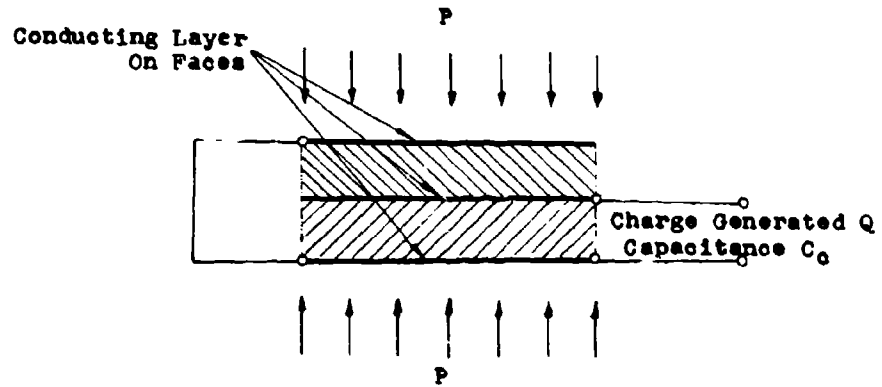


Fig. 7.1-1. Two-pile crystal element.

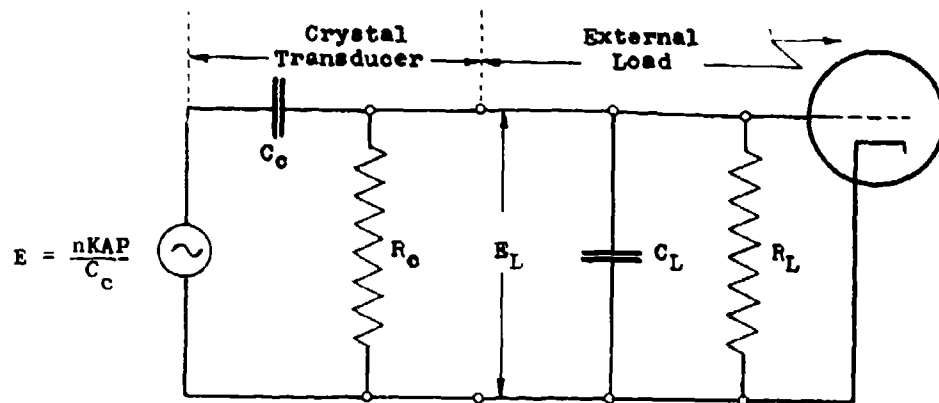


Fig. 7.1-2. Equivalent circuit of piezo transducer.

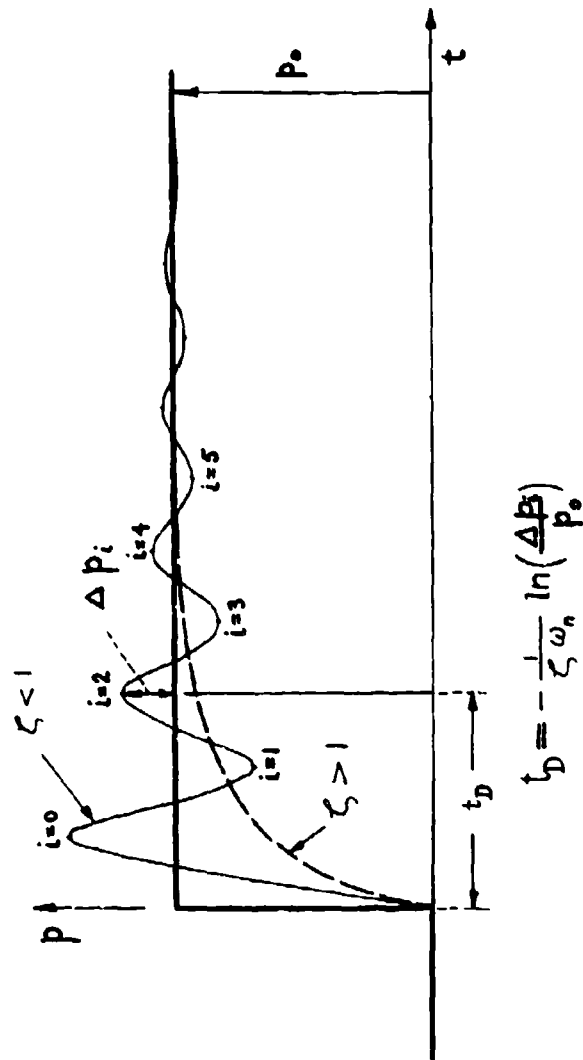


Fig. 7.1-3. Response to shock wave (ringing).

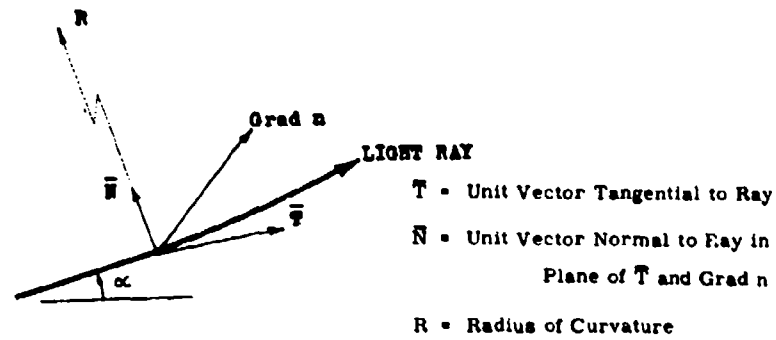
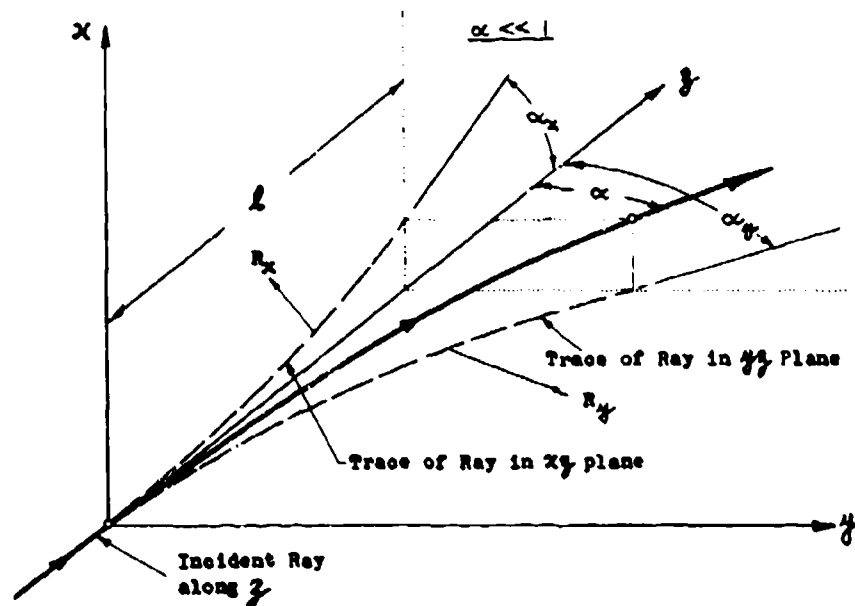


Fig. 7.2-1. Refraction of light ray.

Fig. 7.2-2. Component angular deflections α_x and α_y .

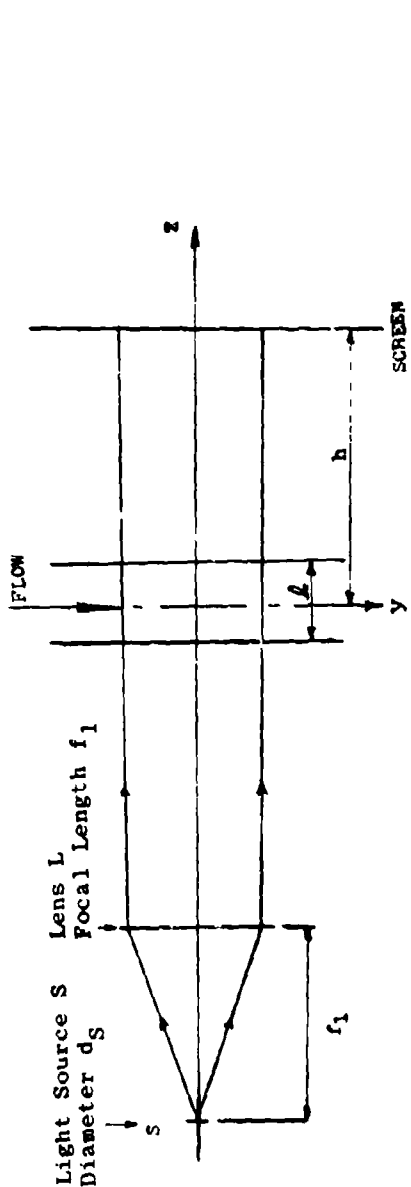


Fig. 7.2-3. Direct shadowgraph method.

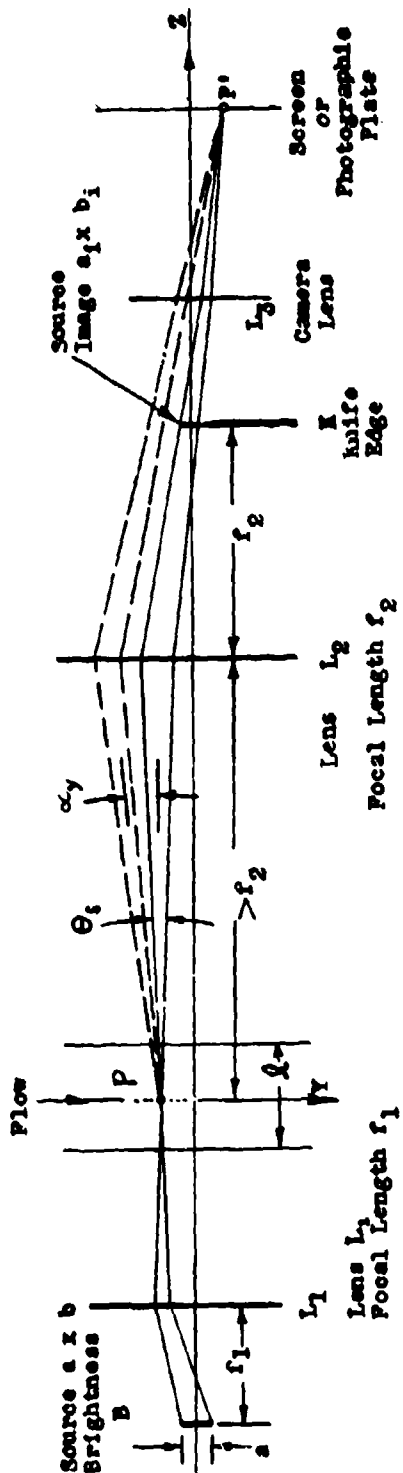


Fig. 7.2-4. Toepler schlieren system.

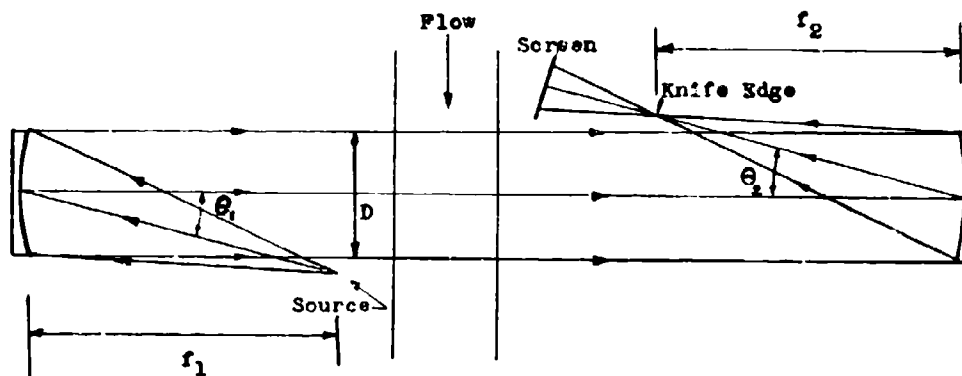


Fig. 7.2-5. Offset schlieren system.

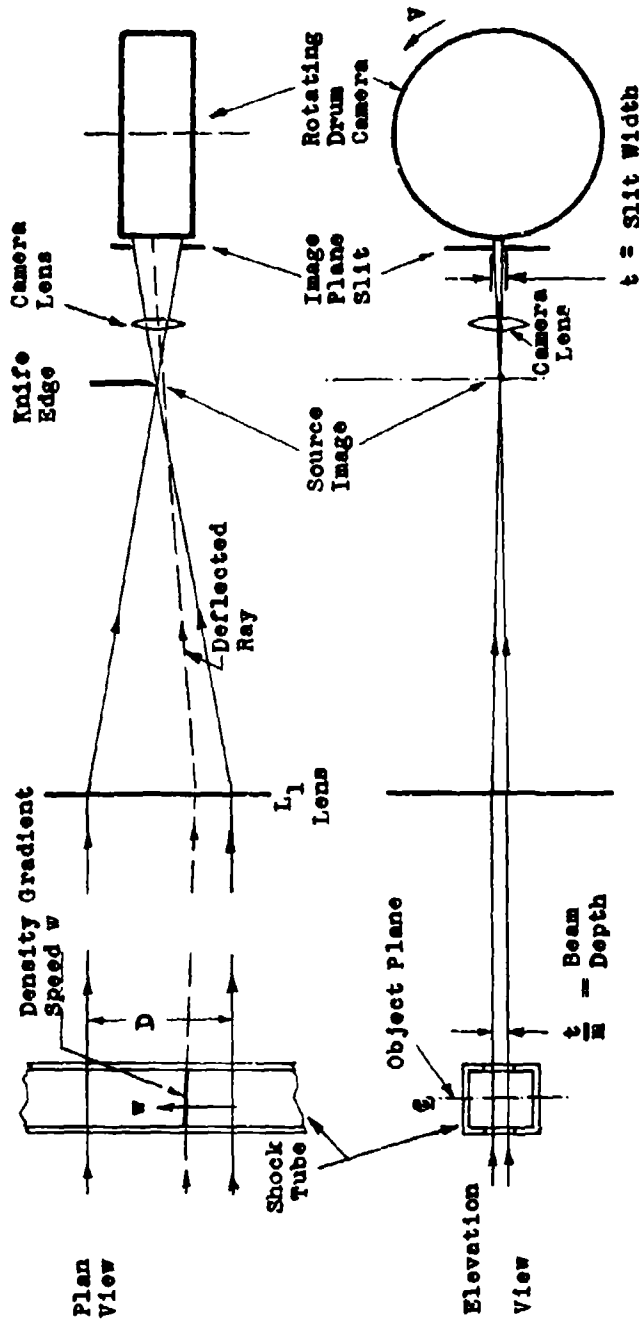


Fig. 7.2-6. Wave-speed schlieren system.

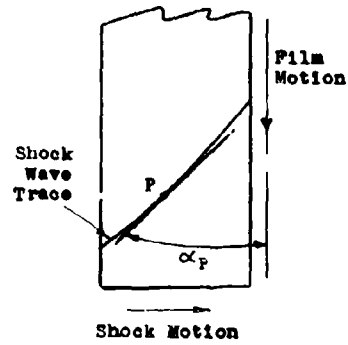


Fig. 7.2-7. Shock trace on wave-speed record.

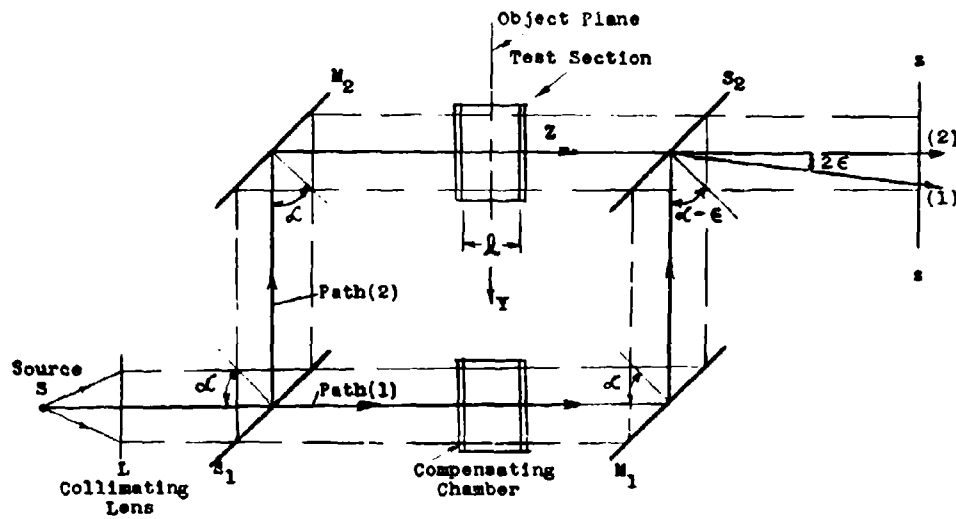


Fig. 7.2-8. Mach-Zehnder interferometer.

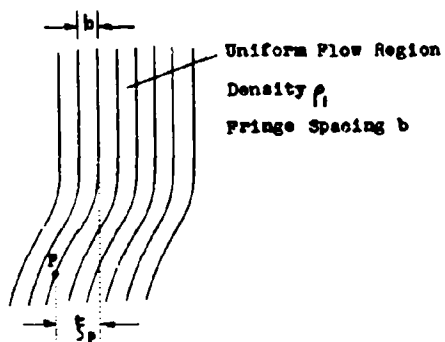


Fig. 7.2-9. Fringe shift referred to uniform flow region.

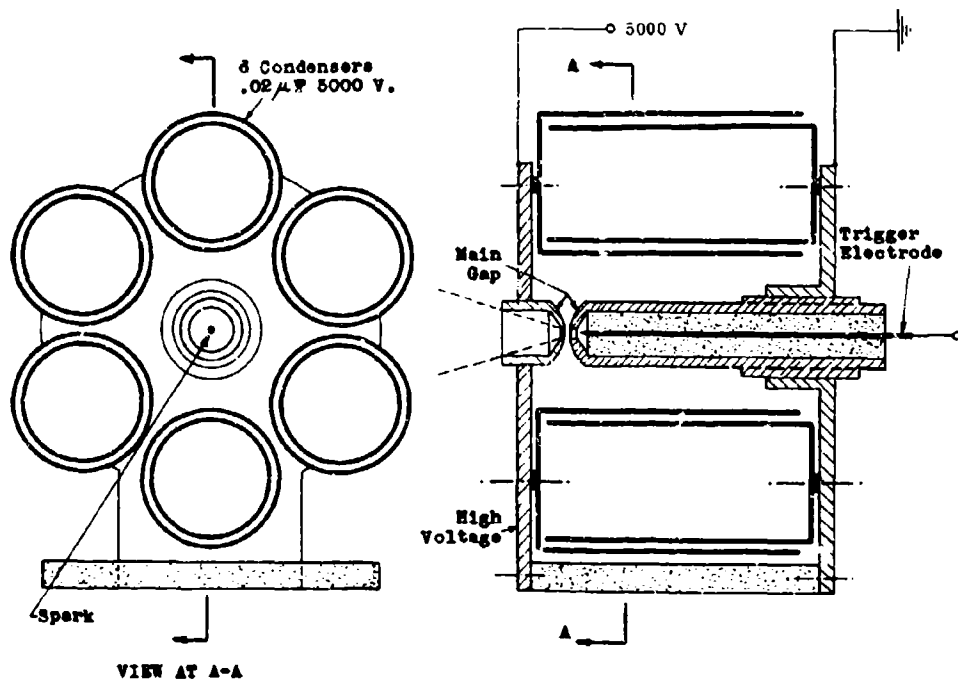


Fig. 7.2-10. Low-inductance spark gap (after Ref. 49).

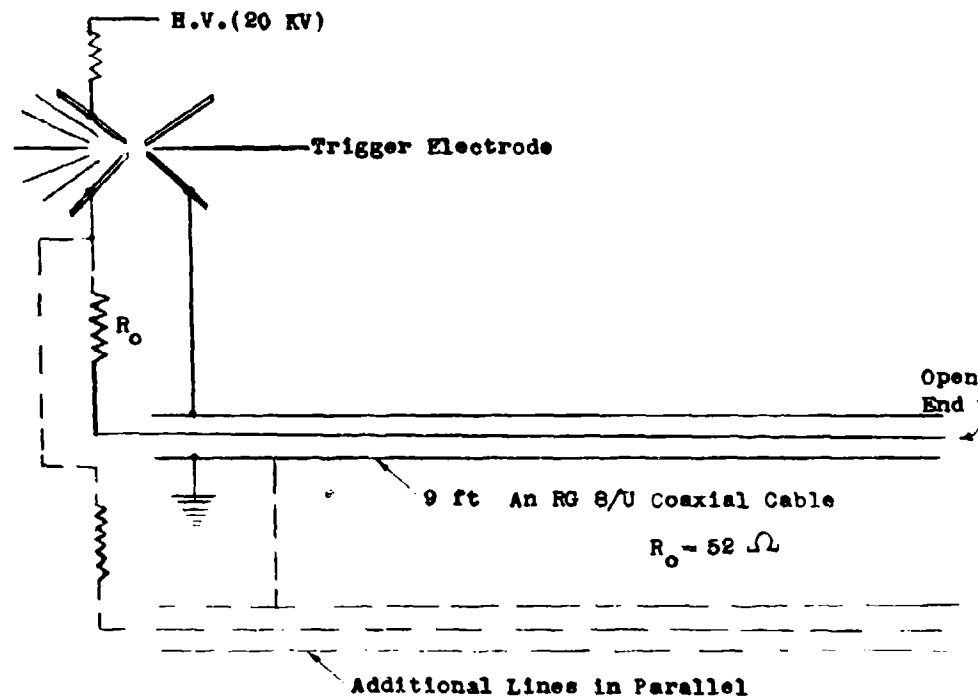


Fig. 7.2-11. Transmission-line spark gap (after Ref. 50).

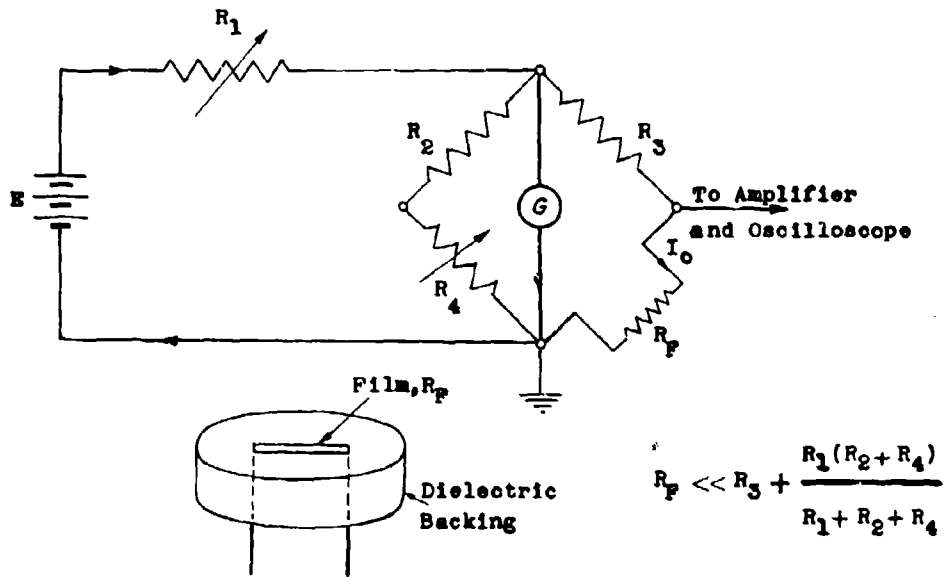


Fig. 7.3-1. Thin-film surface thermometer.

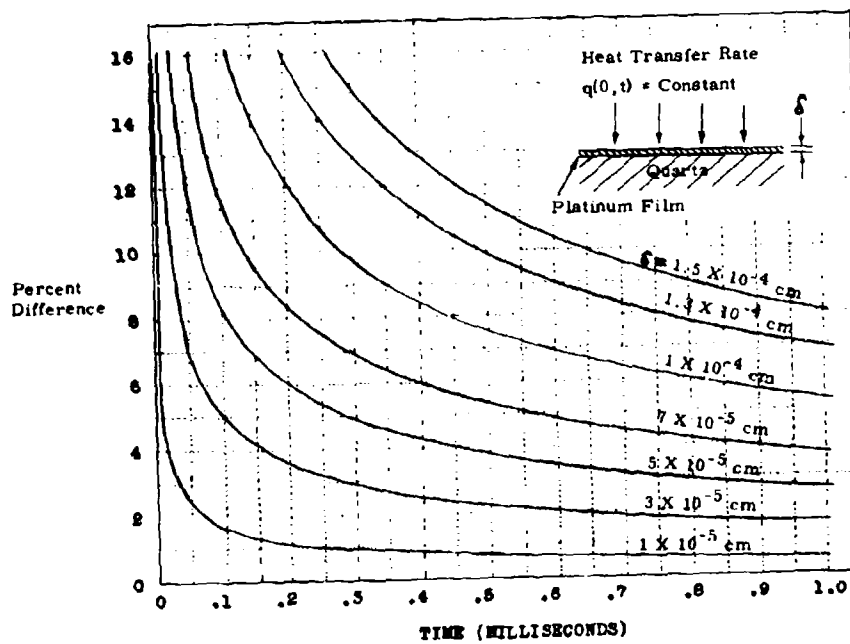
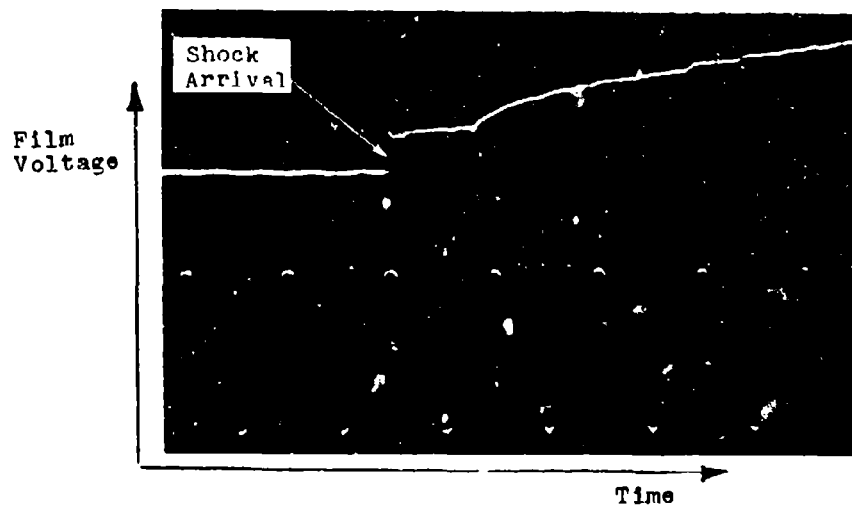


Fig. 7.3-2. Per cent difference between actual surface temperature and that for film thickness $\delta = 0$; constant heat transfer rate; platinum film on quartz (Ref. 65).



$$P_{21} = 4 \quad P_1 = 100 \text{ mm Hg} \quad T_0 = 24^\circ\text{C} \quad I_0 = 10 \text{ ma}$$

$$R_0 = 60.62 \text{ ohms} \quad \text{Calib. } 5\text{Kc} \quad 1 \text{ mv rms}$$

Fig. 7.3-3. Response of thin-film thermometer mounted flush in shock tube wall to passage of shock wave (University of Toronto, Institute of Aerophysics).

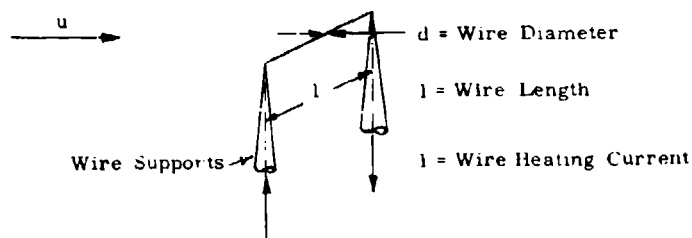


Fig 7.3-4. Hot-wire anemometer.

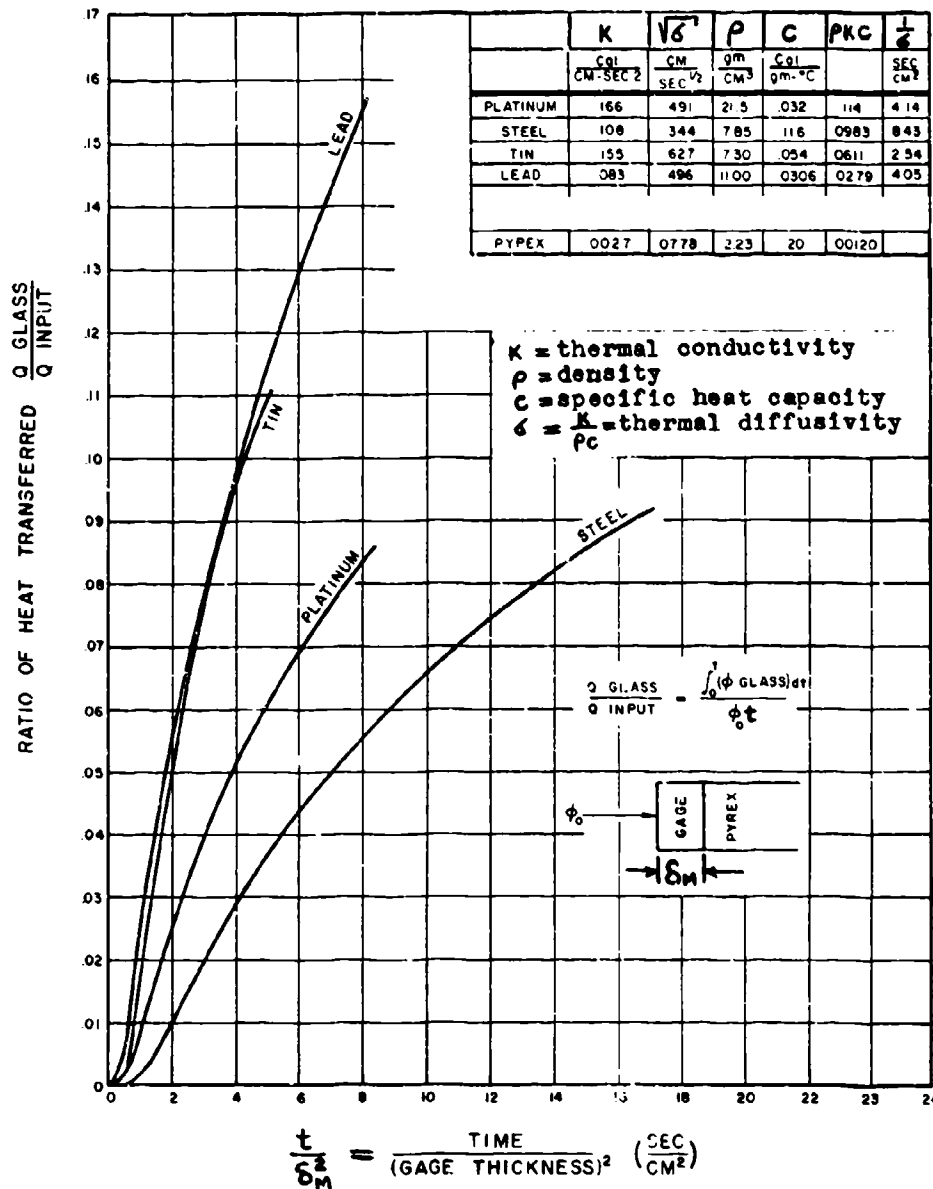


Fig. 7.3-5. Calculated heat loss from calorimeter gauge element of thickness δ_m to infinite pyrex backing for various element materials; constant rate of heat input ϕ_0 to element and perfect contact with pyrex (Ref. 70).

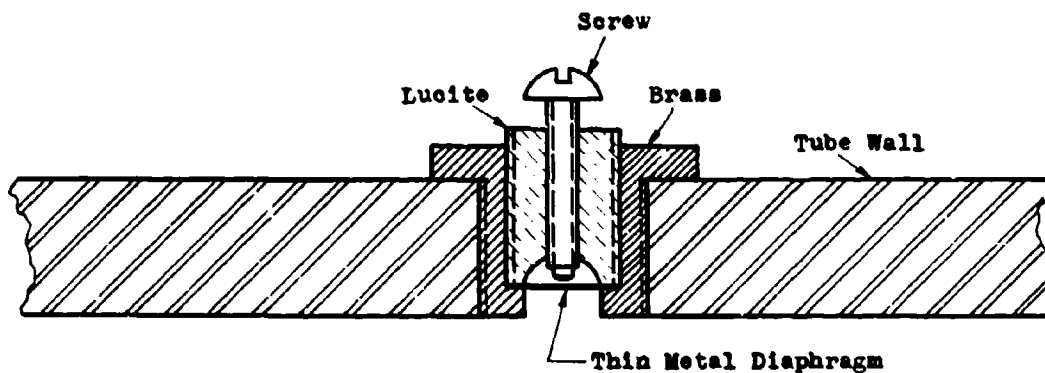
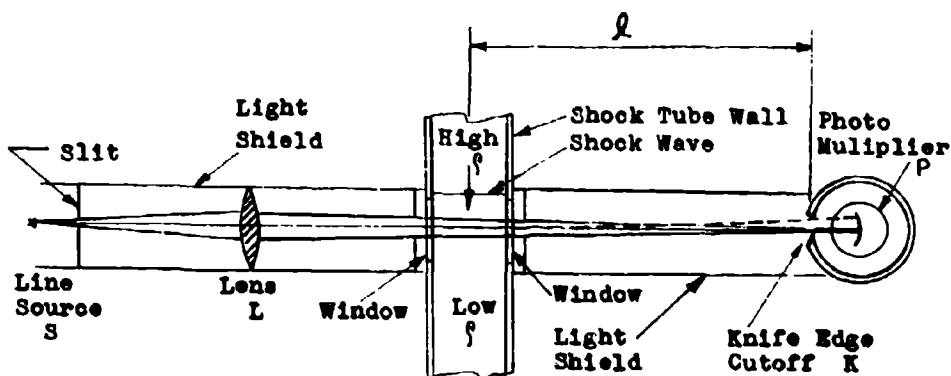
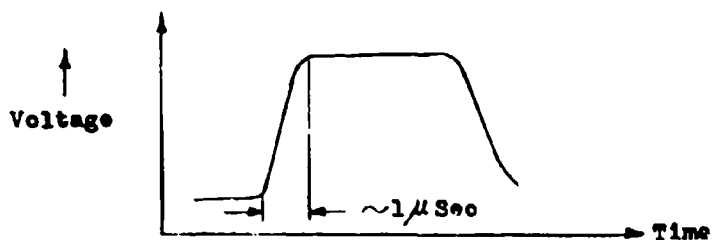


Fig. 7.4-1. Pressure contactor (after Ref. 85).



(a) Plan View of Arrangement



(b) Output Voltage

Fig. 7.4-2. Schlieren light screen, using one lens.

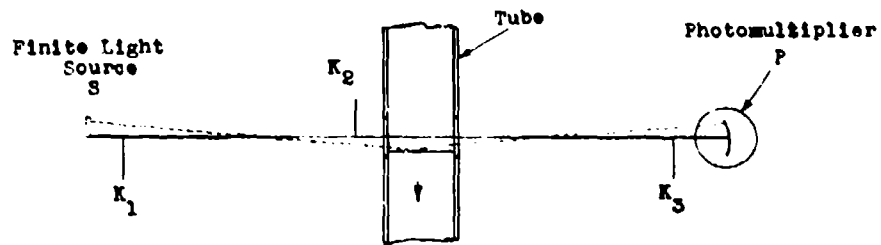


Fig. 7.4-3. Reflection light screen (after Refs. 91 and 92).

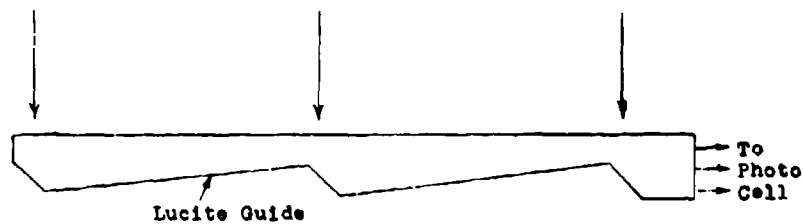


Fig. 7.4-4. Use of lucite guide enabling one photocell to serve three stations (after Ref. 93).

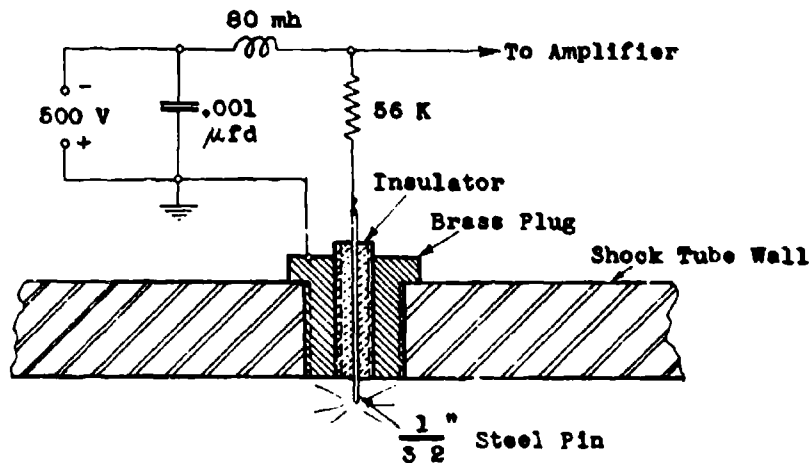


Fig. 7.4-5. Glow discharge probe (after Ref. 85).

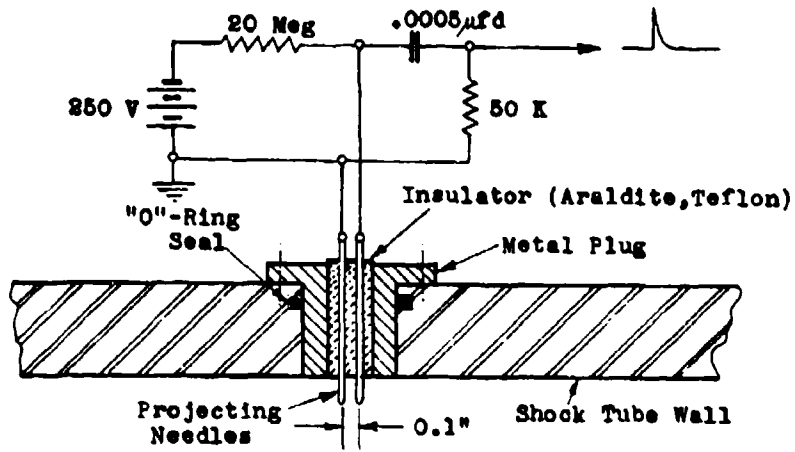


Fig. 7.4-6. Ionization probe.

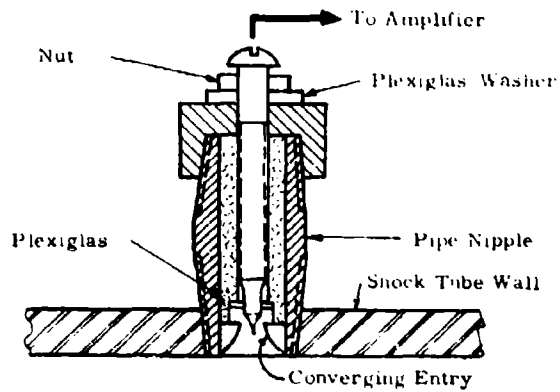


Fig. 7.4-7. Shaped ionization probe (after Ref. 95).

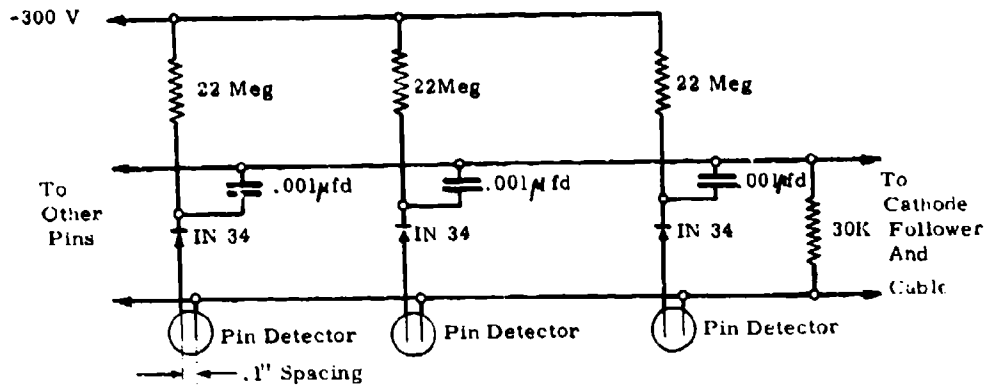


Fig. 7.4-8. Multiple ionization probe unit (after Ref. 96).

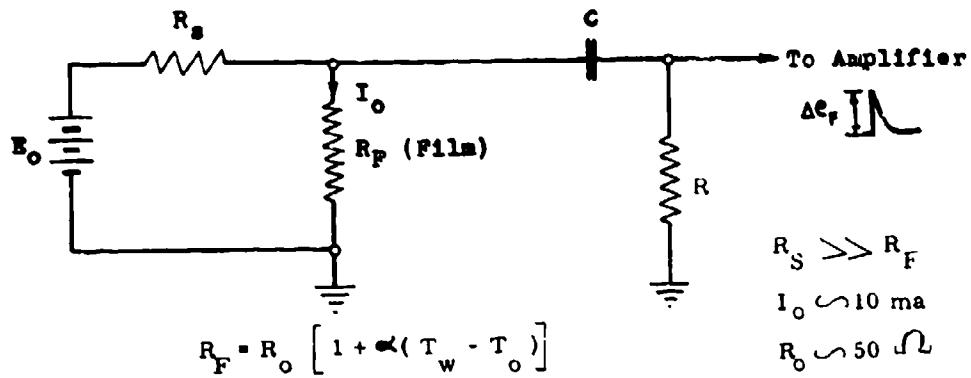


Fig. 7.4-9. Film-resistance thermometer as shock detector.

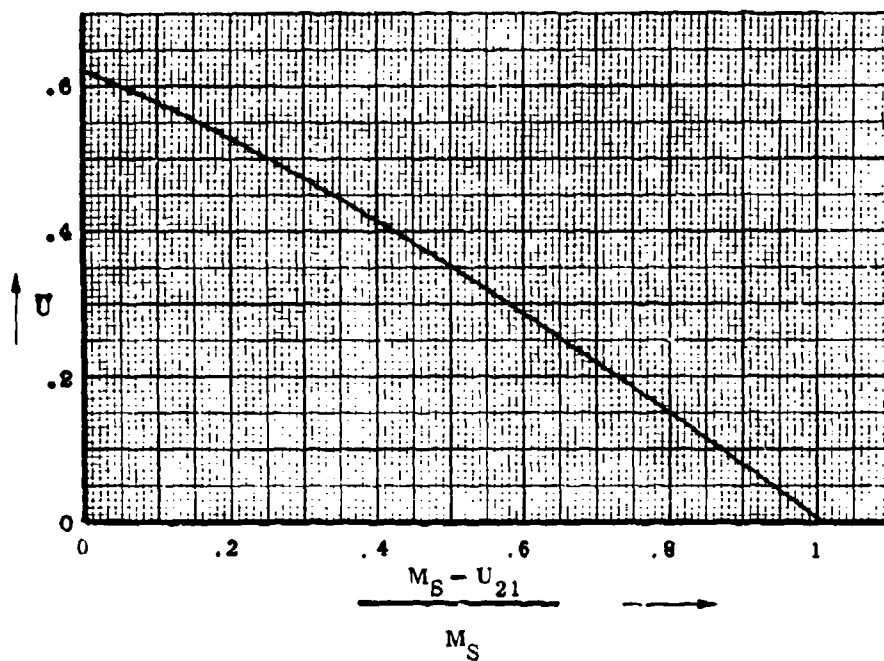


Fig. 7.4-10. \bar{U} function (Ref. 68).

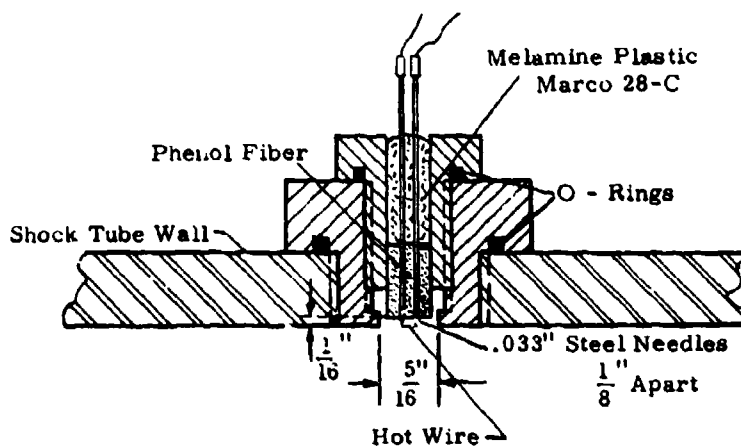


Fig. 7.4-11. Hot-wire shock detector (after Ref. 75).

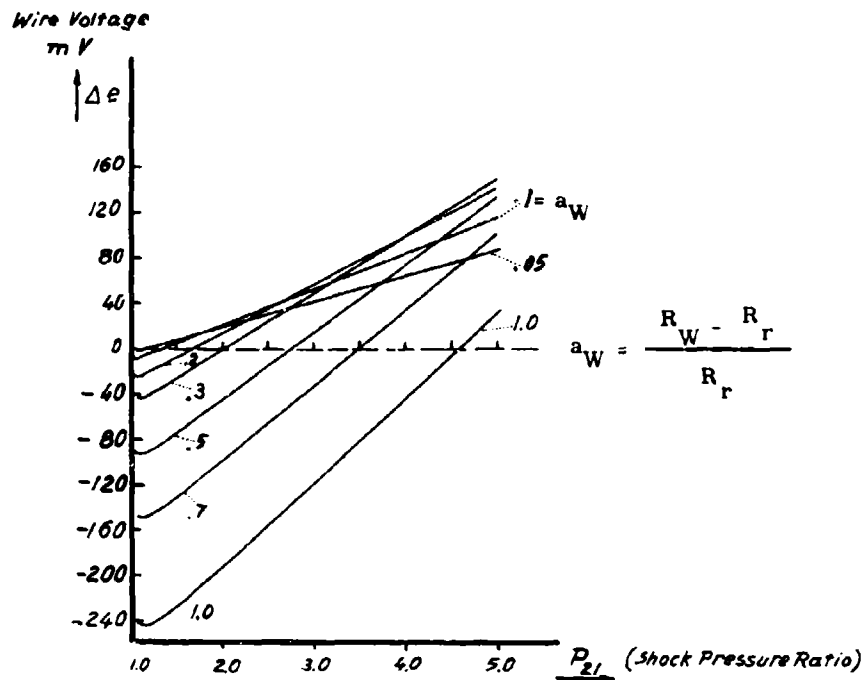
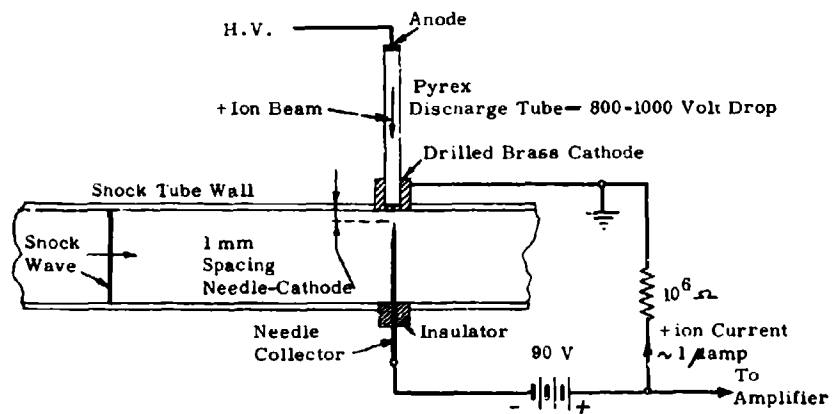


Fig. 7.4-12. Hot-wire response to primary shock wave in air. Tungsten wire; 0.00015 in. diameter, 0.080 in. long; $R_r = 10$ ohms; $p_1 = 1$ atmosphere; $T_1 =$ room temperature (Ref. 75).



Ref. 7.4-13. Positive-ion beam trigger (after Ref. 97).

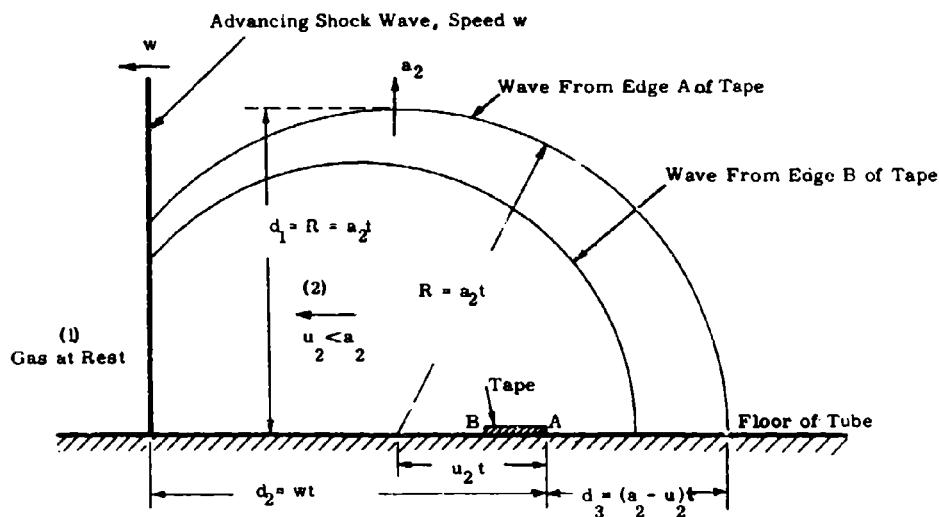


Fig. 7.4-14. Cylindrical-wave reflection method of shock strength measurement; state (2) subsonic (after Ref. 98).

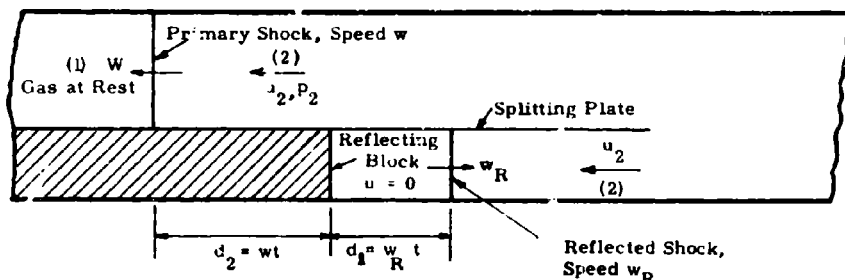


Fig. 7.4-15. Normal shock reflection method of shock measurement (after Ref. 98).

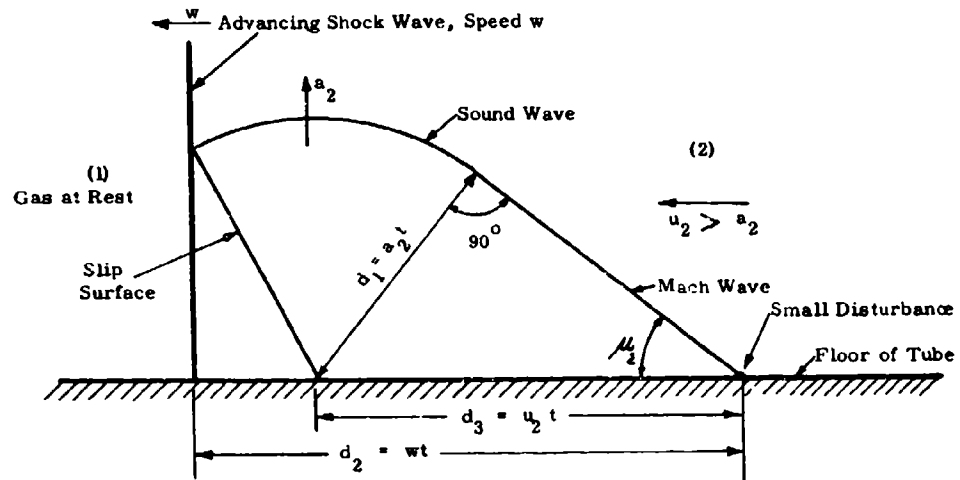


Fig. 7.4-16. Cylindrical-wave reflection method of shock strength measurement; state (2) supersonic (after Ref. 99).

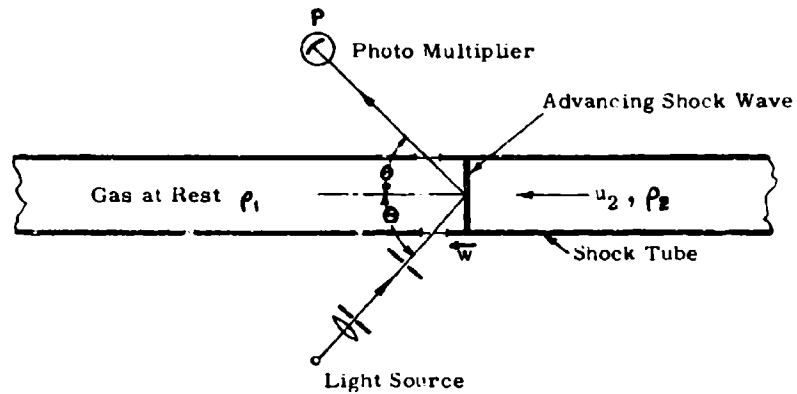


Fig. 7.5-1. Light-reflectivity measurement (after Ref. 100).

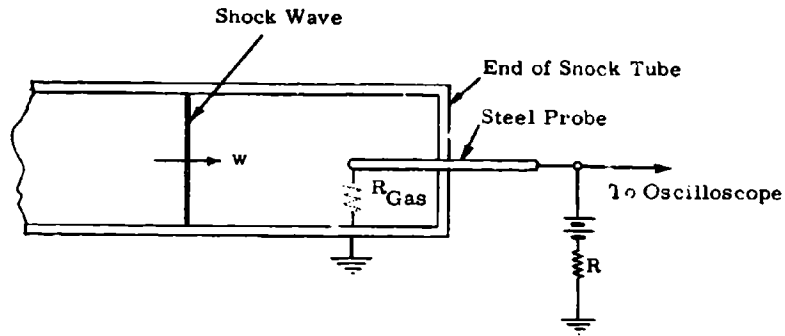


Fig. 7.7-1. Probe technique for measuring gas conductivity (after Ref. 31).

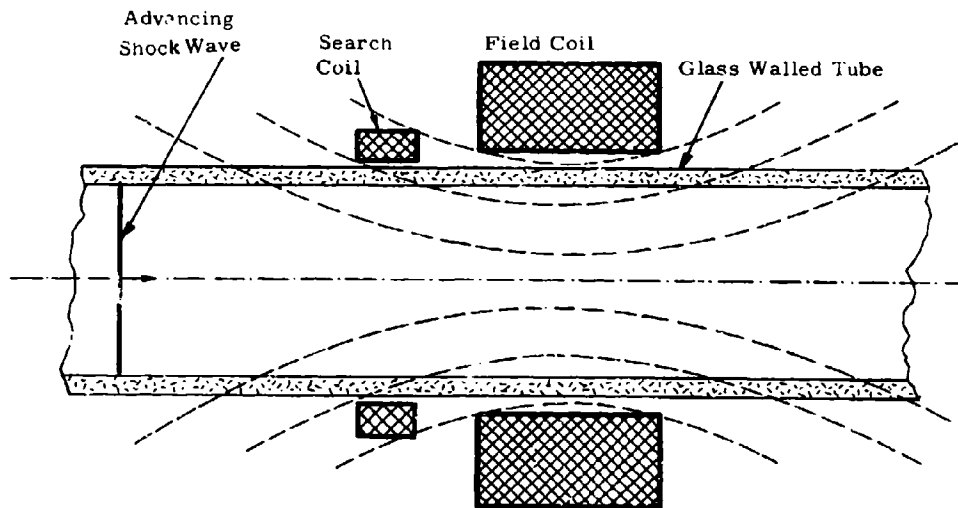
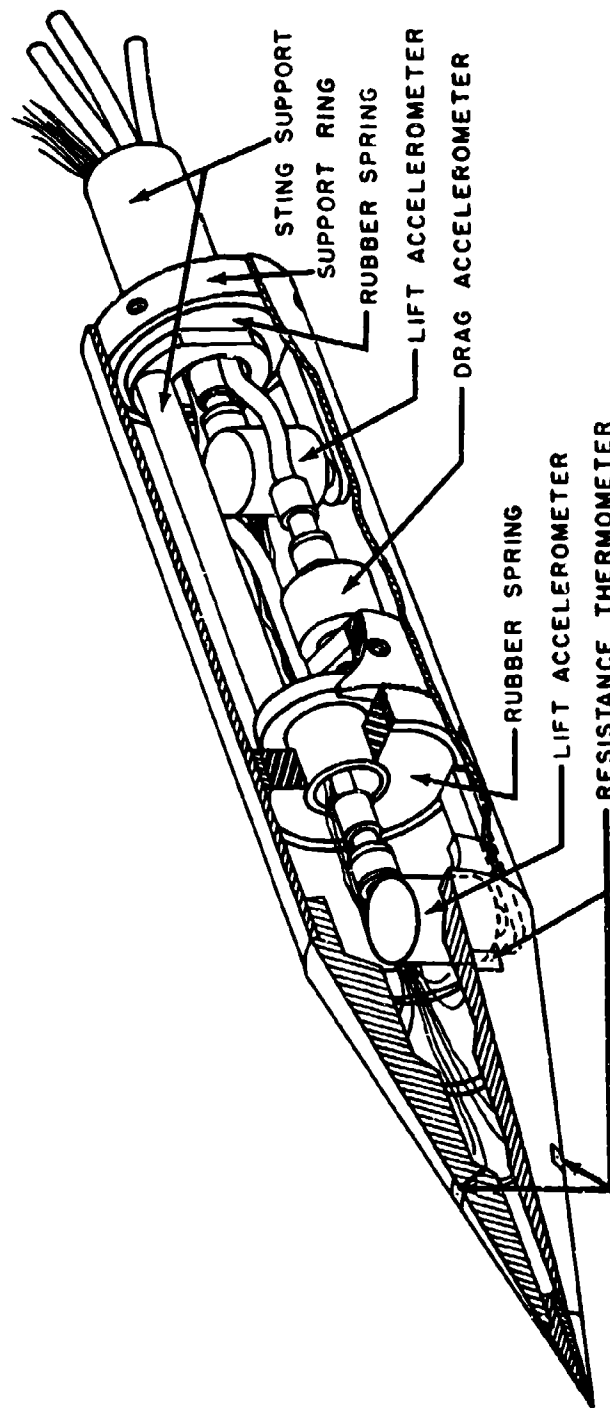


Fig. 7.7-2. Magnetic method for measuring gas conductivity (after Ref. 31).



(See also Fig. 7.8-2.)

Fig. 7.8-1. Internal balance system of shock-tube cone-cylinder model; Cornell Aeronautical Laboratory (Ref. 65).

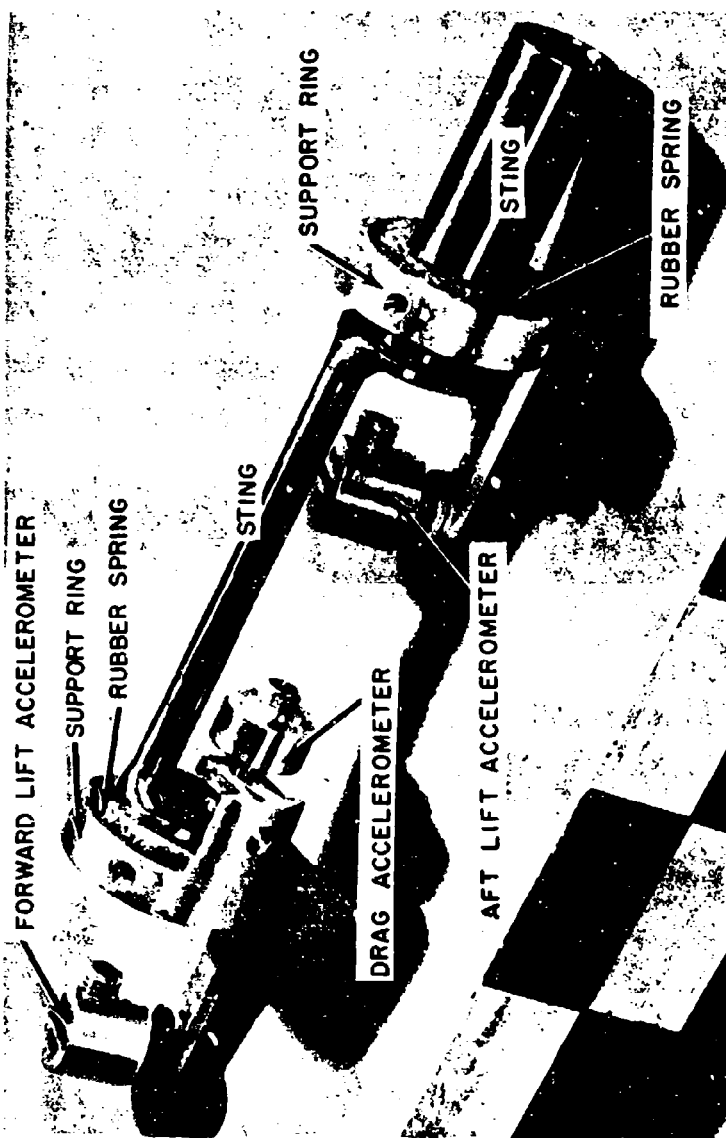


Fig. 7.8-2. Balance system with cone-cylinder shell removed; cylinder diameter, 1 in.; Cornell Aeronautical Laboratory (Ref. 65).

REFERENCES

1. Applied Physics Laboratory, The Johns Hopkins University. Handbook of Supersonic Aerodynamics. NAVORD Report 1488, Vol. 6, Sec. 20, "Wind Tunnel Instrumentation and Operation." Washington: U. S. Government Printing Office (to be published).
2. Pankhurst, R. C. and Holder, D. W. Wind Tunnel Technique. London: Sir Asaac Pitman and Sons Ltd., 1952.
3. Strong, J. Procedures in Experimental Physics. Englewood Cliffs, N. J.: Prentice-Hall, Inc., 1939.
4. Dushman, S. Scientific Foundations of Vacuum Technique. New York: John Wiley and Sons, Inc., 1949.
5. Titman, H. Measurement of Dynamic Pressures. Research Report 12. Safety in Mines Research Establishment. Sheffield, England: Ministry of Fuel and Power, 1950.
6. Eckenrode, R. T. and Kirshner, H. A. "Measurement of Transient Pressures," Rev. Sci. Inst., Vol. 25 (January 1954).
7. Bleakney, W. and Arons, A. B. "Pressure Measuring Manometers and Gauges." High Speed Aerodynamics and Jet Propulsion, Vol. IX, (edited by R. W. Landenberg). Princeton: Princeton University Press, 1954, pp. 124-135.
8. Cole, R. H., Stacey, D., and Brown, R. M. Electrical Instruments for Study of Underwater Explosions and other Transient Phenomena. NDRC Report No. A-360, OSRD Report No. 6238. Washington: National Defense Research Committee of the Office of Scientific Research and Development, November 1954.
9. Nicholl, C. I. H. The Head-On Collision of Shock and Rarefaction Waves. UTIA Report 10. Institute of Aerophysics, University of Toronto, 1951.
10. Arons, A. B. and Tait, C. W. Design and Use of Tourmaline Gauges for Piezoelectric Measurement of Air Blast. NDRC Report No. A-372, OSRD Report No. 6250. Washington: National Defense Research Committee of the Office of Scientific Research and Development, 1946.
11. Arons, A. B. and Cole, R. H. "Design and Use of Piezoelectric Gauges for Measurement of Large Transient Pressures," Rev. Sci. Inst. Vol. 21 (January 1950).
12. Shunk, R. A., Dranetz, A. I., and Budenstein, P. P. "Ring-Shaped Piezoelectric Gauge for Shock Tube," Rev. Sci. Inst., Vol. 24 (1953), p. 1069.
13. Draper, C. S., McKay, W., and Lees, S. Instrument Engineering. Vol. III, Part I, Ch. 3. New York: McGraw-Hill Book Company, Inc., 1955.

14. Li, Y. T. High-Frequency Pressure Indicators for Aerodynamic Problems. NACA TN 3042, November 1953.
15. Draper, C. S. and Li, Y. T. "A New High-Performance Engine Indicator of the Strain-Gauge Type," J. Aeronaut. Sci., Vol. 16 (October 1949), pp. 593-610.
16. Grinstead, C. E., et al. "An Improved Indicator for Measuring Static and Dynamic Pressures," SAE Jour., Vol. 52 (November 1944), pp. 534-556.
17. Bleakney, W., White, D. R., and Griffith, W. "Measurements of Diffraction of Shock Waves and Resultant Loading of Structures," J. Appl. Mech., Vol. 17 (December 1950), p. 439.
18. Bleakney, W. "A Shock Tube Investigation of the Blast Loading of Structures." Proc. of the Symposium on Earthquake and Blast Effects on Structures. Los Angeles: University of California, 1952, p. 46.
19. Witmer, E. A., Herrmann, W., and Beals, V. L., Jr. Transient Aerodynamics of Two-Dimensional Airfoils: Part I--Interferometric Measurements of Two-Dimensional Airflow Development about a Symmetrical Double-Wedge Airfoil in Shock-Initiated Flow. WADC TR 54-368, Part I. Massachusetts Institute of Technology Aircraft Laboratory, August 1954.
20. "Density Measurements." High Speed Aerodynamics and Jet Propulsion, Vol. IX, Part I, Sec. A (edited by R. W. Landenberg). Princeton: Princeton University Press, 1954.
21. Applied Physics Laboratory, The Johns Hopkins University, Handbook of Supersonic Aerodynamics. NAVORD Report 1488, Vol. 6, Sec. 20, "Wind Tunnel Instrumentation and Operation." Washington: U. S. Government Printing Office (to be published).
22. Edelman, G. M. and Bright, M. H. The Specific Refractivity of Gases for Various Wavelengths of Light. Report No. 6. Gas Turbine Laboratory, Massachusetts Institute of Technology, 1948.
23. Dvorak, V. "Ueber eine neue einfache, Ort der Schlierenbeobachtung," Ann. der Physik und Chem. (Wiedemann), Vol. 9 (1880), pp. 502-512.
24. Toepler, A. Ann. der Physik und Chem. (Poggendorff), 5th Series, Vol. 127 (1866), pp. 556-580.
 _____, Vol. 128 (1866), pp. 126-139.
 _____, Vol. 131 (1867), pp. 33-35.
 _____, Vol. 131 (1867), pp. 180-215.
 _____, Vol. 134 (1868), pp. 194-218.
25. Holder, D. W. and North, R. J. Schlieren Methods for Observing High Speed Flows. ARC 16,023. Aeronautical Research Council, Ministry of Supply. London: Her Majesty's Stationery Office, 1954.

26. Holder, D. W. and North, R. J. The Toepler Schlieren Apparatus. R and M 2780 (13,068). Aeronautical Research Council, Ministry of Supply. London: Her Majesty's Stationery Office, 1953.
27. Schardin, H. "Das Toepplersche Schlierenverfahren," Ver. deut. Ing. Forschungsheft, Vol. 5 (1934), pp. 1-32.
28. Payman, W., Shepherd, W. F. C., and others. "Explosions, Waves, and Shock Waves. VI. The Disturbance Produced by Bursting Diaphragms with Compressed Air," Proc. Roy. Soc. London, Series A, Vol. 186 (1946).
29. Glass, I. I. The Design of a Wave Interaction Tube. UTIA Report 6. Institute of Aerophysics, University of Toronto, 1950.
30. Glass, I. I., Martin, W., and Patterson, G. N. A Theoretical and Experimental Study of the Shock Tube. UTIA Report 2. Institute of Aerophysics, University of Toronto, 1953.
31. Lin, Shao-Chi, Resler, E. L., and Kantrowitz, A. "Electrical Conductivity of Highly Ionized Argon Produced by Shock Waves," J. Appl. Phys., Vol. 26 (January 1955), p. 95.
32. Mach, L. "Uber einen Interferenzrefraktor," Z. Instrumentenk., Vol. 12 (1892), pp. 89-93.
"Uber einen Interferenzrefraktometer," Sitzber. Akad. Wiss. Wien, Math. Naturw. Kl. Abt. IIA, Vol. 101 (1892), pp. 5-10.
33. Zehnder, L. "Ein neuer Interferenzrefraktor," Z. Instrumentenk., Vol. II (1891), pp. 275-285.
34. Winkler, E. H. Analytical Studies of the Mach-Zehnder Interferometer. Part I, NOL Report 1077, December 1947; Part II, NOL Report 1099, December 1950. White Oak, Md.: Naval Ordnance Laboratory.
35. De Frate, L. A., Barry, F. W., and Bailey, D. Z. A Portable Mach-Zehnder Interferometer. Meteor Report 51. Guided Missiles Program, Massachusetts Institute of Technology, February 1950.
36. Ashkenas, H. I. and Bryson, A. E. "Design and Performance of a Simple Interferometer for Wind-Tunnel Measurements," J. Aeronaut. Sci., Vol. 18 (February 1951).
37. Hall, J. G. The Design and Performance of a 9-inch Plate Mach-Zehnder Interferometer. UTIA Report 27. Institute of Aerophysics, University of Toronto, 1954.
38. Bleakney, W., Weimer, D. K., and Fletcher, C. H. "The Shock Tube. A Facility for Investigations in Fluid Dynamics," Rev. Sci. Inst., Vol. 20 (November 1949), pp. 807-815.
39. Bleakney, W. and Griffith, W. C. "Shock Waves in Gases," Am. J. Phys., Vol. 22 (December 1954), pp. 597-612.
40. Griffith, W. C., Brickl, D., and Blackman, V. "Structure of Shock Waves in Polyatomic Gases," Phys. Rev., Vol. 102 (June 1956), pp. 1209-1216.

41. Blackman, V. "Vibrational Relaxation in Oxygen and Nitrogen," J. Fluid Mech., Vol. 1, Part I (May 1956).
42. Jahn, R. G. "The Refraction of Shock Waves at a Gaseous Interface," J. Fluid Mech., Vol. 1, Part 5 (November 1956), pp. 457-489.
43. Stever, H. G., Witmer, E. A., and Herrmann, W. "The Growth of a Boundary Layer Behind a Shock Wave," Funfzig (50) Jahre Grenzschichtforschung, Eine Festschrift in Originalbeitragen. Herausgegeben von H. Gortler und W. Tollmien. Braunschweig: Fried. Vieweg und Sohn, 1955, p. 272.
44. Bershader, D. and Allport, J. On the Laminar Boundary Layer Induced by a Travelling Shock Wave. Tech. Report II-22. Department of Physics, Princeton University, May 1956.
45. Martin, W. A. An Experimental Study of the Boundary Layer Behind a Moving Plane Shock Wave. UTIA Report 47. Institute of Aerophysics, University of Toronto, 1957.
46. Howes, W. L. and Buchele, D. R. Practical Considerations in Specific Applications of Gas Flow Interferometry. NACA TN 3507, July 1955.
Generalization of Gas Flow Interferometry Theory and Interferogram Evaluation Equations for One-Dimensional Density Fields. NACA TN 3340, 1955.
47. Mack, J. E. Density Measurement in Shock Tube Flow with the Chrono-Interferometer. Tech. Report 4. Institute of Research, Lehigh University, April 1953.
48. Standring, W. G. and Looms, J. S. T. "Light Output from a Spark Point Source," Nature, Vol. 165 (March 1950), p. 358.
49. Kovaszny, L. G. "High Power Short Duration Spark Discharge," Rev. Sci. Inst., Vol. 20 (September 1949), p. 696.
50. Beams, J. W., Kuhlthau, A. R., Lapsley, A. C., McQueen, J. H., Snoddy, L. B., and Whitehead, W. D. "Spark Light Source of Short Duration," J. Opt. Soc. Am., Vol. 37 (1947), pp. 868-870.
51. Fitzpatrick, J. A., Hubbard, J. C., and Thaler, W. J. "A High Intensity Short Duration Spark Light Source," J. Appl. Phys., Vol. 21 (December 1950), p. 1269.
52. Chesterman, W. D. The Photographic Study of Rapid Events. Oxford: Clarendon Press, 1951.
53. Jones, G. A. High Speed Photography. London: Chapman and Hall Ltd., 1952.
54. Glick, H. S., Hertzberg, A., and Smith, W. E. Flow Phenomena in Starting a Hypersonic Shock Tunnel. Report AD-789-A-3, AEDC-TN-55-16. Buffalo, N. Y.: Cornell Aeronautical Laboratory, Inc., March 1955.
55. Winkler, E. M. "X-Ray Technique." High Speed Aerodynamics and Jet Propulsion, Vol. IX, Part I (edited by R. W. Landenberg). Princeton: Princeton University Press, 1954, pp. 97-107.

56. Kistiakowsky, G. B. "Density Measurements in Gaseous Detonations," J. Chem. Phys., Vol. 19 (December 1951), p. 1611.
57. Duff, R. E. and Knight, H. T. "Precision Flash X-Ray Determination of Density Ratio in Gaseous Detonations," J. Chem. Phys., Vol. 25 (December 1956), p. 1301.
58. Schopper, E. and Schumacher, B. "Messung von Gasdichten mit Korpuskularstrahlsonden," Z. Naturforsch., Vol. 6a (1951), pp. 700-705.
59. Grun, A. R., Schopper, E., and Schumacher, B. "Electron Shadowgraphs and Afterglow Pictures of Gas Jets at Low Densities," J. Appl. Phys., Vol. 24 (December 1953), pp. 1527-1528.
60. Schumacher, B. "Abbildung von Gasströmungen mit Elektronenstrahlen," Ann. der Physik, Vol. 13 (1953), pp. 404-420.
61. Venable, D. and Kaplan, D. E. "Electron Beam Method of Determining Density Profiles Across Shock Waves in Gases at Low Densities," J. Appl. Phys., Vol. 26 (May 1955), pp. 639-640.
62. Chabai, A. J. and Emrich, R. J. "Measurement of Wall Temperature and Heat Flow in the Shock Tube," J. Appl. Phys., Vol. 26 (June 1955), pp. 779-780.
63. Rabinowicz, J., Jessey, M. E., and Bartsch, C. A. "Resistance Thermometer for Transient High Temperature Studies," J. Appl. Phys., Vol. 23 (November 1955), p. 97.
64. Bershader, D. and Allport, J. On the Laminar Boundary Layer Induced by a Travelling Shock Wave. Tech. Report II-22. Department of Physics, Princeton University, May 1956.
65. Vidal, R. Model Instrumentation Techniques for Heat Transfer and Force Measurements in a Hypersonic Shock Tunnel. Report AD 917-A-1. Buffalo, N. Y.: Cornell Aeronautical Laboratory, Inc., 1956.
66. Rabinowicz, J., Jessey, M. E., and Bartsch, C. A. Resistance Thermometer for Heat Transfer Measurement in a Shock Tube. GALCIT Hypersonic Research Project Memo. 33. Guggenheim Aeronautical Laboratory, California Institute of Technology, July 1956.
67. Hertzberg, A. "The Application of the Shock Tube to the Study of the Problems of Hypersonic Flight," Jet Propulsion, Vol. 26 (July 1956), pp. 549-554.
68. Bromberg, R. "Use of the Shock Tube Wall Boundary Layer in Heat Transfer Studies," Jet Propulsion, Vol. 26 (September 1956), pp. 737-740.
69. Carslaw and Jaeger. Conduction of Heat in Solids. Oxford: Clarendon Press, 1947.
70. Rose, P. H. and Stark, W. I. Stagnation Point Heat Transfer Measurements in Air at High Temperature. Research Note 24. Everett, Mass.: AVCO Research Laboratory, AVCO Manufacturing Corp., December 1956.

71. Hackemann, P. A Method for Measuring Rapidly Changing Surface Temperatures and its Application to Rifle and M. G. Barrels. ZWB Publication FB1346. TPA3/TIB Translation No. GDC10/1230T. Ministry of Supply. London: Her Majesty's Stationery Office, June 1941.
72. Bendersky, D. "A Special Thermocouple for Measuring Transient Temperatures," Mech. Eng., Vol. 75 (February 1953).
73. Dosanjh, D. S., Kovaszny, L. S. G., and Clarcken, P. C. Study of Transient Hot-Wire Response in a Shock Tube. JHU Report CM-725. Department of Aeronautics, The Johns Hopkins University, March 1952.
74. Dosanjh, D. S. Use of a Hot-Wire Anemometer in Shock Tube Investigations. NACA TN 3163, 1954.
75. Dosanjh, D. S. "Use of the Hot-Wire Anemometer as a Triggering and Timing Device for Wave Phenomena in a Shock Tube," Rev. Sci. Inst., Vol. 26 (January 1955), pp. 65-70.
76. Billington, I. J. "An Experimental Study of the One-Dimensional Refraction of a Rarefaction Wave at a Contact Surface," J. Aeronaut. Sci., Vol. 23 (November 1956). (Also UTIA Report 32. Institute of Aerophysics, University of Toronto, 1955)
77. Kovaszny, L. S. G. "Turbulence Measurements." High Speed Aerodynamics and Jet Propulsion, Vol. IX, Section F (edited by R. W. Landenberg). Princeton: Princeton University Press, 1954.
78. Billington, I. J. The Hot-Wire Anemometer and its Use in Non-Steady Flow. UTIA Tech. Note 5. Institute of Aerophysics, University of Toronto, 1955.
79. King, L. V. "On the Convection of Heat from Small Cylinders in a Stream of Fluid," Phil. Trans. Roy. Soc. London, A214 (1914), p. 373.
80. Spangenberg, W. G. Heat Loss Characteristics of Hot-Wire Anemometers at Various Densities in Transonic and Supersonic Flow. NACA TN 3381, May 1955.
81. Kovaszny, L. S. G. "The Hot-Wire Anemometer in Supersonic Flow," J. Aeronaut. Sci., Vol. 17 (1950), pp. 565-572.
82. Laufer, J. and McClellan, R. "Measurements of Heat Transfer from Fine Wires in Supersonic Flows," J. Fluid Mech., Vol. 1, Part 3 (September 1956), p. 276.
83. Elmore, W. C. and Sands, M. L. Electronics, National Nuclear Energy Series, Vol. 1. New York: McGraw-Hill Book Company, Inc., 1949.
84. M.I.T. Radiation Laboratory Series, Vols. 18, 19, and 22. New York: McGraw-Hill Book Company, Inc., 1949.
85. Lundquist, G. A. The NOL 8 x 8-Inch Shock Tube: Instrumentation and Operation. NAVORD Report 2449. White Oak, Md.: Naval Ordnance Laboratory, June 1952.

86. Kistiakowsky, Knight, and Malin. "Gaseous Detonations. III. Dissociation Energies of Nitrogen and Carbon Monoxide," J. Chem. Phys., Vol. 20 (1952), p. 876.
87. Smith, L. G. Photographic Investigation of the Reflection of Plane Shocks in Air. OSRD Report 6271. Washington: Office of Scientific Research and Development, November 1945.
88. Bleakney, W., Weimer, D. K., and Fletcher, C. H. "The Shock Tube: A Facility for Investigations in Fluid Dynamics," Rev. Sci. Inst., Vol. 20 (November 1949), pp. 807-815.
89. Geiger, F. W. and Mautz, C. W. The Shock Tube as an Instrument for the Investigation of Transonic and Supersonic Flow Patterns. Engineering Research Institute, University of Michigan, 1949.
90. Bitondo, D. and Lobb, R. K. The Design and Construction of a Shock Tube. UTIA Report 3. Institute of Aerophysics, University of Toronto, May 1950.
91. Bleakney, W. "Velocity of Shock Waves by the Light Screen Technique." High Speed Aerodynamics and Jet Propulsion, Vol. IX (edited by R. W. Landenberg). Princeton: Princeton University Press, 1954, pp. 159-163.
92. Emrich, R. J. Velocity Loss Measurements on Shocks in a Shock Tube. Tech. Report II-2 NR 061-020. Department of Physics, Princeton University, November 1948.
93. Emrich, R. J. and Curtis, C. W. "Attenuation in the Shock Tube," J. Appl. Phys., Vol. 24 (March 1953), pp. 360-363.
94. Mair, W. A. "The Sensitivity and Range Required in a Toepler Schlieren Apparatus for Photography of High-Speed Air Flow," Aeronaut. Quart., Vol. IV (August 1952).
95. Morrison, R. B. A Shock Tube Investigation of Detonative Combustion. UMM-97. Willow Run Research Center, Engineering Research Institute, University of Michigan, January 1952.
96. Knight, H. T. and Duff, R. E. "Precision Measurement of Detonation and Strong Shock Velocity in Gases," Rev. Sci. Inst., Vol. 26 (March 1955).
97. Venable, D. "Positive Ion Oscilloscope Trigger for Shocks in Low-Density Gases," Rev. Sci. Inst., Vol. 26 (July 1955), p. 729.
98. Hertzberg, A. and Kantrowitz, A. "Studies with an Aerodynamically Instrumented Shock Tube," J. Appl. Phys., Vol. 21 (September 1950), pp. 874-878.
99. Squire, W., Hertzberg, A., and Smith, W. E. Real Gas Effects in a Hypersonic Shock Tunnel. Report AD-789-A-3, AEDC-TN-5514. Buffalo, N. Y.: Cornell Aeronautical Laboratory, Inc., March 1955.
100. Cowan, G. R. and Hornig, L. F. "The Experimental Determination of the Thickness of a Shock Front in a Gas," J. Chem. Phys., Vol. 18 (August 1950), pp. 1008-1016.

101. Greene, E. F., Cowan, G. R., and Hornig, D. F. "The Thickness of Shock Fronts in Argon and Nitrogen and Rotational Heat Capacity Lags," J. Chem. Phys., Vol. 19 (1951), pp. 427-434.
102. Greene, E. F. and Hornig, D. F. "The Shape and Thickness of Shock Fronts in Argon, Hydrogen, Nitrogen, and Oxygen," J. Chem. Phys., Vol. 21 (1953), p. 617.
103. Britton, D., Davidson, N., and Schott, G. "Shock Waves in Chemical Kinetics. The Rate of Dissociation of Molecular Iodine." Faraday Soc. Discussion, No. 17 (1954).
104. Palmer, H. "Study of Shock Waves by Light Absorption and Emission," J. Appl. Phys., Vol. 27 (1956), p. 1105.
105. Hey, J. S., Pinson, J. T., and Smith, P. G. "A Radio Method of Determining the Velocity of a Shock Wave," Nature, Vol. 179 (June 1957), pp. 1184-1185.
106. Lamb, Lawrence and Lin, Shao-Chi. "Electrical Conductivity of Thermally Ionized Air Produced in a Shock Tube," J. Appl. Phys., Vol. 28 (July 1957), pp. 754-759.
107. Petschek, H. E., Rose, P. H., Glick, H. S., Kane, A., and Kantrowitz, A. "Spectroscopic Studies of Highly Ionized Argon Produced by Shock Waves," J. Appl. Phys., Vol. 26 (January 1955), pp. 83-95.
108. Willmarth, W. W. "Small Barium Titanate Transducer for Aerodynamics or Acoustic Pressure Measurements," Rev. Sci. Inst., Vol. 29 (March 1958), p. 218.
109. Jahn, R. G. and Weimer, D. "On the Performance of Thin-Film Gauges in High-Temperature Shock Tube Flows," J. Appl. Phys., Vol. 29 (April 1958), p. 741.
110. Knight, H. "Piezoelectric Detector for Low-Pressure Shock Waves," Rev. Sci. Inst., Vol. 29 (February 1958), p. 174.
111. Harrison, H. "Glow Discharge Trigger for Shock Wave Studies," Rev. Sci. Inst., Vol. 29 (February 1958), p. 175.
112. Hall, J. G. and Hertzberg, A. "Recent Advances in Transient Surface Temperature Thermometry," Jet Propulsion, Vol. 28 (November 1958).
113. Hartunian, R., Russo, A., and Marrone, P. "Boundary Layer Transition and Heat Transfer in Shock Tubes." 1958 Heat Transfer and Fluid Mechanics Institute. Stanford, Calif.: Stanford University Press.
114. Winkler, E. H. "The Latest Results in the NOL Shock Tube Wind Tunnel. (Paper presented at the Conference on Supersonic Flow, University of Maryland, March 1954.)

INDEX

- absorption methods of density measurement
 optical, 563
 X-ray, 542
- adiabatic combustion (constant-volume heating of driver gas), 402
- anemometer, hot-wire, 549
- applications
 instrument calibration, 470
 shock tubes
 in aerophysics research, 452
 for calibration of instruments, 470
 chemical, 469
 for chemical research, 466
 for wind tunnels, 451, 453
 transient aerodynamic studies, 531
- area change in a shock tube (see cross-section area change)
- attenuation of strong shock waves, 411
- balance, internal model, 564
- Blasius solution for laminar boundary layer, 326, 327
- boundary layer, 323
 closure, 337
 effect on test flow, 454, 460
 interactions with reflected shock wave, 339
 laminar, 323
 laminar, Blasius equations, 326
 transition, 331, 463
 turbulent, 333
- calibration
 of instruments, 470
 of pressure gauges, 527, 529
- calorimeter heat-transfer gauge, 547
- centred compression wave, 15
- centred rarefaction wave, 15
- characteristics, method of, in (x, t) -plane, 9
- chemical kinetic studies, 467
- chemical research, applications to, 466
- chemical shock tube, 469
- collisions of waves, 90ff
- condensation phenomena, 463
- constant-area channel, 451
- constant-area shock tube, 317ff, 393
- contact region, 320
- contact surface
 definition of, 79
 experimental study of, 320, 322
- continuous shock-speed measurement, 554
- combustion heating of driver gases
 constant-pressure, 404
 constant-volume, 402
 detonation, 405
- combustion studies, 467
- compression waves
 definition of, 5
 in imperfect gases, 35
 in perfect gases, 12
- cross-section area change, 405
 monotonic convergence at diaphragm, 405
 monotonic convergence along tube, 408
- cross section, constant, 451
- density measurement, 532
- design of shock tube, 499
 alternative to diaphragm type, 410
 effects of tube length, 81
 instrumentation, 456
 length and internal cross section, 499
 materials, 499, 502, 504
 methods of heating, 396
- detector, positive ion-beam, 560
- detonation (driver-gas heating), 405
- diaphragm pressure transducer, 529
- diaphragms, 502
 alternatives to, 410
 burst tests, 504
 metallic, 503
 multiple, 400
 nonmetallic, 502
 petalling, 504
 rupture, methods of control, 506
- diffuse shock wave, 48
- direct measurement of transient pressure, 525
- dissociation (energies), 108, 469
- drum camera photography, 554
- duration of test flow, 454
- dynamic pressure, equation for, 31
- electrical heating (driver gas), 396
- electrical conductivity measurement, 564
- equations
 Blasius, 326
 Saha, 111
- equations, inviscid gases
 density ratios, 66
 Mach number, local, 68
 Mach number, shock, 67
 mass flow ratios, 78
 pressures, dynamic, 78
 pressures, pitot, 77
 rarefaction waves, speed of head and tail, 68
 sound speed and temperature ratios, 66
 temperatures, total, 75
 velocity of particle or contact surface, 67
- equilibrium region, flow quantities behind shock wave, 50

- failure of components, high pressure, 508
- film resistance thermometer, shock detector, 558
- finite-length shock tube, effects of, 81
- flow measurement and instrumentation
 - density, 532
 - electrical conductivity, 564
 - light absorption, 563
 - light reflectivity (shock-wave transition), 562
 - model force, 564
 - pressure, 525
 - primary shock strength, 554
 - temperature (and heat transfer), 543
- flow observed in a constant-area shock tube, 317
- force measurements on models, 564
- gas
 - effects in a shock tube, 80
 - high-temperature physics, 464
 - imperfections at low pressures and high temperature, 105
 - rarefaction and compression waves in imperfect gases, 35
 - real, alternative development of equations for, 121
 - relaxation effects, 117
 - thermally imperfect, equation of state, 103
- glow-discharge probe, 557
- gun tunnels, hypersonic, 462
- hazards in shock tubes, 507
- heating of driver gas, 396
 - combustion
 - adiabatic, constant-volume, 402
 - constant pressure, 404
 - detonation, 405
 - electrical, 396
 - multiple diaphragm, 400
 - heat transfer measurement, 543
 - history of shock tubes, 1
 - hot-wire anemometer, 549, 559
 - hydrostatic pressure measurements, 525
- hypersonic
 - gun tunnels, 462
 - research, 451
 - shock tunnels, 457
- ignition methods (for combustion heating), 403
- imperfect gas, definition of, 103
- instrumentation, shock-tube, 456, 525
- interferometry, 532, 537, 554
- internal balance, model, 564
- interval timers, 555
- ion-beam detector, 560
- ionization, 105, 558
- ionization probe, 558
- King's Law, 551
- laminar boundary layer effects, 323
 - Blasius equations, 326
 - length, effect of, on shock-tube flow, 81
- light absorption measurement, 563
- light screens, 556
- light sources and recording, 541
- light reflectivity measurement, 562
- limitations of simple, constant-area shock tubes, 393
- low pressure, gas imperfections at, 105
- Mach numbers, inviscid gases, equation of, 67ff
- Mach-Zehnder interferometer, 537
- magnetic measurements, 564
- magnetohydrodynamics research, 466
- manometer, use of, 525
- mass flow ratios, inviscid gases, equations of, 78
- measurement
 - density, 532
 - flow, 525, 531
 - force on models, 564
 - hydrostatic pressure, 525
 - light absorption and reflectivity, 562, 563
 - model force, 564
 - optical methods, 468, 532
 - interferometry, 532, 537
 - schlieren, 532
 - shadowgraph, 533
 - Toepler-schlieren, 534
 - wave speed-schlieren, 537
 - shock speed, direct, 554
 - shock strength, primary, 554
 - streak photography, 554
 - temperature and heat transfer, 543
 - transient pressure, 525
 - direct, 525
 - diaphragm transducer, 529
 - piezoelectric transducer, 527
 - indirect, 531
 - wave speed, 318
 - metallic diaphragm, 503
 - model force measurements, 564
 - modifications to the simple shock tube, 396
 - multiple diaphragm technique, 400
- nonmetallic diaphragms, 502
- non-reflected shock tunnels, 458
- normal reflection, 82
 - rarefaction wave, 87
 - shock wave, 82
- normal refraction of a shock or rarefaction wave at a contact surface, 93
- Nusselt number, 551
- optical methods of measurement, 468, 532
 - interferometry, 532, 537
 - schlieren, 532
 - shadowgraph, 533
 - Toepler-schlieren, 534
 - wave speed-schlieren, 537

- overtaking
 - of a rarefaction wave by a shock wave, 98
 - of a shock wave by a rarefaction wave, 98
 - of shock waves or rarefaction waves, 96
 - of two rarefaction waves, 97
 - of two similarly facing shock waves, 97
- perfect gas, definition of, 8
- performance of simple, constant-area shock tubes, 5ff, 393
- petalling, diaphragm, 504
- piezoelectric pressure transducer, 527
- positive ion-beam detector, 560
- pressure measurement
 - hydrostatic, 525
 - transient, 525
 - direct method, 525
 - diaphragm transducer, 529
 - piezoelectric transducer, 527
 - indirect method, 531
- pressure technique, 506
- pressure transducer, 556
 - diaphragm, 529
 - piezoelectric, 527
- probe
 - glow discharge, 557
 - ionization, 558
- production of strong shock waves, 393
- properties of test flow, 454
- (p,u)-plane, use of, 60ff
- P-waves, definition of, 10, 11
- Q-waves
 - definition of, 10, 11
 - flow equations in terms of, 25ff
- radiation, 465
- Rankine-Hugoniot shock relations in a perfect gas, 48
- rarefaction waves
 - definition of, 5
 - head-on collision of, 90
 - in imperfect gases, 35
 - overtaking of, 96
 - in perfect gases, 12
 - reflection of, 87
 - refraction of, 95
 - speed of head and tail, 68
- reflected shock tunnels, 460
- reflected wave techniques, 560
- reflection
 - rarefaction wave, 87
 - shock wave, 82
- refraction
 - normal, of shock or rarefaction wave at a contact surface, 93
 - of rarefaction wave at a contact surface, 95
 - of shock wave, 93
- relaxation effects in gases, 117, 466
- research, use of shock tubes in aerophysics, 462
 - chemical, 466
 - chemical kinetic, 467
 - combustion, 467
 - condensation phenomena, 463
 - conductivity, 466
 - ionization, 466
 - magnetohydrodynamics, 466
 - relaxation studies, 466
 - subsonic, transonic, supersonic, hypersonic, 451
 - wave interaction and non-planar wave phenomena, 462
- resistance thermometer, thin film, 543, 558
- Reynolds number in a shock tube, 73
- Riemann variables (sometimes Riemann invariants)
 - P-waves, 10, 11
 - Q-waves, 10, 11, 25
- safety, hazards in shock tubes, 507
- Saha equation, 111
- schlieren technique, 532
 - Toepler, 534
 - wave speed, 537
- shadowgraph, 533
- shock detector methods, 555
 - glow discharge probes, 557
 - hot-wire anemometers, 559
 - ionization probe, 558
 - light screens, 556
 - positive ion-beam detector, 560
 - pressure contactor, 556
 - pressure transducer, 556
 - thin-film resistance thermometer, 558
- shock waves
 - collision of, 90
 - cylindrical, 463
 - diffuse wave, 48
 - interactions in a shock tube of finite length, 81, 462
 - measurement of, 321, 554
 - overtaking of, 96
 - plane, 42
 - in imperfect gases, 47, 80
 - in perfect gases, 43
 - relaxation effects of, 48
 - real gases, alternative development of equations, 121
 - reflection of, 82
 - refraction of, 93
 - spherical, 463
 - strong, attenuation of, 411
 - strong, production of, 393
 - weak shock solution, 48
 - sound, velocity of, 8, 112
 - streak photography, 554
- temperature and heat transfer measurement, 543
- test flow
 - duration, 454
 - properties, 454
- theoretical performance, comparison of, for combined modifications, 409
- thermocouple, thin film, 547

- thermometer, film resistance as shock detector, 558
- thin-film resistance thermometer, 543, 558
- thin-film thermocouple, 547
- timers, interval, 555
- transducer, pressure, 558
 - diaphragm, 529
 - piezoelectric, 527
- transient aerodynamic studies, 531
- transient pressure measurement, 525
- transition, boundary layer, 331, 464
- tunnel
 - hypersonic gun, 462
 - hypersonic shock, 457
 - non-reflected shock, 458
 - performance of shock tube as, 453, 454
 - reflected shock, 460
- turbulent boundary layer, 333
- unequal rarefaction waves, head-on collision of, 92
- unequal shock waves, head-on collision of, 91
- vacuum techniques, 506
- van der Waal equation of state, 103
- velocity
 - of contact surface, 67
 - of particle, 67
- wave, compression, definition of, 1
- wave interaction results, 322
- wave, rarefaction, definition of, 1
- wave speed
 - equation, 80
 - measurement, 318
 - streak photography, 554
- wave system in simple shock tube, 60
 - basic equations in perfect gas, 63
 - imperfect gas effects, 80
- wave system produced by diaphragm removal, 316
- waves
 - centred, in perfect gases, 17
 - compression and rarefaction in imperfect gases, 35
 - compression and rarefaction in perfect gases, 12
 - one-dimensional, 5
 - applications of interactions to a shock tube of finite length, 99
 - effects of interaction and finite tube length, 81
 - experimental results, 322
 - rarefaction and compression, 5
 - P-waves, 10, 11
 - Q-waves, 10, 11, 25
 - rarefaction
 - definition of, 5
 - head-on collision of, 90
 - in imperfect gases, 35
 - overtaking of, 96
 - in perfect gases, 12
 - reflection of, 87
 - refraction of, 93
 - speed of head and tail, 68
 - shock
 - collision of, 90
 - cylindrical, 463
 - interactions in a shock tube of finite length, 81
 - measurement, 321, 554
 - overtaking of, 96
 - plane, 42
 - in imperfect gases, 47, 80
 - in perfect gases, 43
 - relaxation effects of, 48
 - reflection of, 82
 - refraction of, 93
 - spherical, 463
 - strong, attenuation of, 411
 - strong, production of, 393
 - weak shock solutions, 48
 - wind tunnel
 - hypersonic gun, 462
 - hypersonic shock, 457
 - non-reflected shock, 458
 - reflected shock, 460
 - shock-tube performance as, 455
- X-ray measurement, 542